inorganics

Special Issue Reprint

Recent Progress in Perovskites

Edited by
Pengfei Wu

mdpi.com/journal/inorganics

MDPI

Recent Progress in Perovskites

Recent Progress in Perovskites

Guest Editor

Pengfei Wu

MDPI

Basel • Beijing • Wuhan • Barcelona • Belgrade • Novi Sad • Cluj • Manchester

Guest Editor
Pengfei Wu
Chemistry Department
Emory University
Atlanta, GA
USA

Editorial Office
MDPI AG
Grosspeteranlage 5
4052 Basel, Switzerland

This is a reprint of the Special Issue, published open access by the journal *Inorganics* (ISSN 2304-6740), freely accessible at: https://www.mdpi.com/journal/inorganics/special_issues/5887NZUFU8.

For citation purposes, cite each article independently as indicated on the article page online and as indicated below:

Lastname, A.A.; Lastname, B.B. Article Title. *Journal Name* **Year**, *Volume Number*, Page Range.

ISBN 978-3-7258-8633-3 (Hbk)
ISBN 978-3-7258-8634-0 (PDF)
https://doi.org/10.3390/books978-3-7258-8634-0

© 2026 by the authors. Articles in this reprint are Open Access and distributed under the Creative Commons Attribution (CC BY) license. The reprint as a whole is distributed by MDPI under the terms and conditions of the Creative Commons Attribution-NonCommercial-NoDerivs (CC BY-NC-ND) license (https://creativecommons.org/licenses/by-nc-nd/4.0/).

Contents

About the Editor . . . . . **vii**

Preface . . . . . **ix**

Alexei A. Belik, Ran Liu, Lei Zhang, Yoshitaka Matsushita and Kazunari Yamaura
Charge- and Orbital-Order Transitions in the A-Site-Ordered Quadruple Perovskite $NdCuMn_6O_{12}$
Reprinted from: *Inorganics* **2026**, *14*, 174, https://doi.org/10.3390/inorganics14070174 . . . . . **1**

Łukasz Szeleszczuk, Katarzyna Mądra-Gackowska and Marcin Gackowski
Wide-Bandgap A_2TiSiO_6 (A = Ca, Sr, Ba) Double Perovskites for Optoelectronic Applications
Reprinted from: *Inorganics* **2026**, *14*, 130, https://doi.org/10.3390/inorganics14050130 . . . . . **18**

Weiqiang Li, Dan Wang, Wei Zhao, Xiangping Zhu, Yongning He and Guohe Zhang
Enhanced Secondary Electron Emission from Strontium Titanate Films via High-Temperature Annealing
Reprinted from: *Inorganics* **2026**, *14*, 71, https://doi.org/10.3390/inorganics14030071 . . . . . **37**

Jingyu Liu, Xueqiong Su, Lishan Yang, Jiansen Ding, Jin Wang, Xing Ling, et al.
Comparation of Graph Neural Networks and Traditional Machine Learning for Property Prediction in All-Inorganic Perovskite Materials
Reprinted from: *Inorganics* **2026**, *14*, 58, https://doi.org/10.3390/inorganics14020058 . . . . . **48**

Arum Ayuningsih, Nazım Ecebaş, Tran Thi Huyen Tran, John G. Fisher, Jong-Sook Lee, Woo-Jin Choi and Wook Jo
Texturing $(Na_{0.5}Bi_{0.5})TiO_3$-$KNbO_3$-$SrTiO_3$ Electrostrictive Ceramics by Templated Grain Growth Using $(Na_{0.5}Bi_{0.5})TiO_3$ Platelets
Reprinted from: **2025**, *13*, 387, https://doi.org/10.3390/inorganics13120387 . . . . . **66**

Alexei A. Belik, Ran Liu and Kazunari Yamaura
Hidden Magnetic-Field-Induced Multiferroic States in A-Site-Ordered Quadruple Perovskites $RMn_3Ni_2Mn_2O_{12}$: Dielectric Studies
Reprinted from: *Inorganics* **2025**, *13*, 315, https://doi.org/10.3390/inorganics13100315 . . . . . **94**

Pablo V. Tuza and Mariana M. V. M. Souza
A Review of Synthesis, Characterization, Properties, and Applications of Double Perovskite Oxides
Reprinted from: *Inorganics* **2025**, *13*, 372, https://doi.org/10.3390/inorganics13110372 . . . . . **113**

Hongki Kim, Jeongeun Lee, Chae Bin Lee and Yoon Ho Lee
Recent Progress of Plasmonic Perovskite Photodetectors
Reprinted from: *Inorganics* **2025**, *13*, 351, https://doi.org/10.3390/inorganics13110351 . . . . . **142**

Wenguang Li, Tianci Mi, Tian Tian, Meifang Yang and Huan Pang
Mitigating Lead Toxicity in Halide Perovskite Solar Cells: Strategies for Sustainable Development
Reprinted from: *Inorganics* **2025**, *13*, 123, https://doi.org/10.3390/inorganics13040123 . . . . . **169**

About the Editor

Pengfei Wu

Pengfei Wu is a Postdoctoral Research Associate in the Department of Chemistry at Emory University, United States. His research focuses on polymer chemistry, sustainable materials, batteries, and perovskites-related materials, with particular interest in recyclable polymers and their related application in energy and environmental areas. His work combines inorganic/organic synthesis, polymer chemistry, and materials characterization to develop innovative strategies for sustainable materials. He has contributed to research chemistry and materials, publishing in *Nature Chemistry*, *JACS*, *Angew*, and so on. As Guest Editor, he is committed to promoting interdisciplinary research at the interface of perovskites, materials science, and sustainable technologies, and to fostering the development of advanced functional materials for future energy and environmental applications.

Preface

The rapid development of perovskites materials continues to drive advances across a broad range of scientific and technological fields, from optoelectronics and photonics to energy conversion and information technologies. This Reprint was compiled to bring together recent representative contributions that illustrate both the diversity of modern perovskites research and the progress achieved through interdisciplinary collaboration.

The articles collected in this Reprint cover the design, synthesis, characterization, and application of advanced perovskites, with particular emphasis on understanding the relationships between composition, structure, functional properties, and machine learning.

Together, these studies demonstrate how fundamental discoveries can lead to improved material performance and inspire new approaches to emerging challenges in materials science.

As Guest Editor, I hope this Reprint will serve as a valuable resource for researchers, graduate students, and professionals working in chemistry, materials science, physics, and related disciplines. By presenting recent developments within a single volume, the Reprint provides readers with an accessible overview of current research trends while highlighting promising directions for future investigation. I sincerely thank all authors for their high-quality contributions, the reviewers for their thoughtful and constructive evaluations, and the editorial staff for their professional support throughout the publication process. I hope that this collection will stimulate further discussion, collaboration, and innovation in the field of inorganic materials.

Pengfei Wu
Guest Editor

inorganics

MDPI

Article

Charge- and Orbital-Order Transitions in the A-Site-Ordered Quadruple Perovskite $NdCuMn_6O_{12}$

Alexei A. Belik [1,*], Ran Liu [1,2,3], Lei Zhang [1,2], Yoshitaka Matsushita [4] and Kazunari Yamaura [1,2]

1 Research Center for Materials Nanoarchitectonics (MANA), National Institute for Materials Science (NIMS), Namiki 1-1, Tsukuba 305-0044, Ibaraki, Japan; liu.ran@sanken.osaka-u.ac.jp (R.L.); yamaura.kazunari@nims.go.jp (K.Y.)
2 Graduate School of Chemical Sciences and Engineering, Hokkaido University, North 10 West 8, Kita-ku, Sapporo 060-0810, Hokkaido, Japan
3 Institute of Scientific and Industrial Research, Osaka University, Mihogaoka 8-1, Osaka 567-0047, Ibaraki, Japan
4 National Institute for Materials Science (NIMS), Sengen 1-2-1, Tsukuba 305-0047, Ibaraki, Japan; matsushita.yoshitaka@nims.go.jp
* Correspondence: alexei.belik@nims.go.jp

Abstract

AMn_7O_{12} perovskites (with A = divalent elements) show complex structural and magnetic transitions including incommensurate orbital density waves and coupled/decoupled modulated spin helicity originating from charge-ordered Mn^{3+}/Mn^{4+} cations with the 3:1 ratio at the B perovskite sites and unusual apically compressed Jahn–Teller distortions of MnO_6 octahedra. The same Mn^{3+}:Mn^{4+} ratio can be achieved in $RCuMn_6O_{12}$ compositions, where R is a trivalent rare-earth cation. Therefore, the comparison in behavior of AMn_7O_{12} and $RCuMn_6O_{12}$ is of interest. In this work, the A-site-ordered quadruple perovskite $NdCuMn_6O_{12}$ was prepared by a high-pressure high-temperature method. Its structural properties were investigated by synchrotron powder X-ray diffraction between 100 K and 350 K and laboratory powder X-ray diffraction between 5 K and 300 K. It shows a first-order structural phase transition from *Im*-3 symmetry (at high temperatures) to *R*-3 symmetry near 292 K. The structural transition is accompanied by charge (Mn^{3+}/Mn^{4+}) and unusual orbital (on the Jahn–Teller active Mn^{3+} cations located in MnO_6 octahedra) orders. However, no additional structural/orbital modulations were found at lower temperatures in comparison with AMn_7O_{12}. Magnetic properties were investigated by temperature- and field-dependent magnetization and specific heat measurements, where a ferrimagnetic transition was found near 120 K. In addition, low-temperature magnetic anomalies were observed near 20 K, probably originating from the Nd sublattice.

Keywords: A-site-ordered quadruple perovskites; orbital order; charge order; high-pressure synthesis

1. Introduction

Manganites have played an important role in the science of perovskite-structure materials since the 1950s [1,2]. They were used for understanding the interplay between charge, spin, and orbital degrees of freedom and the crystal lattice in transition-metal oxides and developing such concepts as small polarons, double exchange, electron–phonon couplings, and Jahn–Teller (JT) distortions [3–5].

A lot of papers were published on simple perovskite $R_{1-x}A_xMnO_3$ manganites, where R is a rare-earth cation and A is a divalent cation [3–5], and detailed composition–

temperature phase diagrams were constructed [3–6]. Charge-ordering (CO) phenomena were often observed at some special doping levels, such as near $x = 0.5$ (half-doped), $x = 1/3$ (one-third-doped), $x = 1/4$ (quarter-doped), and others. In addition to different CO patterns, orbital ordering (OO) on sites containing Mn^{3+} cations is realized, and complex spin orderings take place coupled with underlying charge-ordered and orbital-ordered structures.

A-site-ordered quadruple perovskites [7–11] with the general composition of $AA'_3B_4O_{12}$ form a different playground to manipulate charge, spin, and orbital degrees of freedom. Such manganites, $AMn_3Mn_4O_{12}$ or AMn_7O_{12} in short [10,11], intrinsically have different ratios of Mn^{3+} and Mn^{4+} cations (at the perovskite B sites) without any doping, depending on the oxidation state of the A cation. With A = Na^+ [12,13], the Mn^{4+}:Mn^{3+} ratio is 1:1 (half-doped). With A = Mn^{2+}, Ca^{2+}, Cd^{2+}, Sr^{2+}, Hg^{2+}, and Pb^{2+} [14–23], the Mn^{4+}:Mn^{3+} ratio is 1:3 (quarter-doped). Among different AMn_7O_{12} compounds, $CaMn_7O_{12}$ (= $[Ca^{2+}Mn_3{}^{3+}][Mn_3{}^{3+}Mn^{4+}]O_{12}$) was the most studied compound because it is the only composition that can be prepared at ambient pressure [15]. $CaMn_7O_{12}$ [10] shows a CO transition below T_{CO} = 409–448 K (T_{CO} is a CO transition temperature) with the *Im*-3 symmetry above T_{CO} and *R*-3 symmetry below T_{CO}. The *R*-3 structure has apically compressed $Mn^{3+}O_6$ octahedra with four longer and two shorter Mn–O distances [16] while usual JT systems have two longer and four shorter Mn–O distances. $CaMn_7O_{12}$ shows another transition below T_{OO} = 260 K with an incommensurate structural modulation and propagation vector, $\boldsymbol{k_S}$ = (0, 0, ~0.92). The incommensurate structure has a complex modulation of Mn–O bond distances interpreted as an incommensurate orbital density wave localized on the B-site Mn^{3+} cations, and the majority of MnO_6 octahedra in this structure are locally elongated along one of two axes with certain periods resulting in the apparent apical compression of MnO_6 octahedra on average. $CaMn_7O_{12}$ shows the first long-range magnetic ordering transition below T_{N1} = 90 K with an incommensurate propagation vector locked to the structural modulation [18]. Below the second magnetic transition at T_{N2} = 48 K, the magnetic structure delocks from the structural modulation giving rise to a complex multi-*k* magnetic ground state [18]. Magnetic structures of $CaMn_7O_{12}$ break the inversion symmetry producing spin-induced ferroelectric polarization [17,18]. The similar picture of complex structural and magnetic phase transitions is realized in other members of the AMn_7O_{12} series with A = Mn, Cd, Sr, Hg, and Pb [10,20–23]. Therefore, AMn_7O_{12} compounds and their variations, such as $CaCu_xMn_{7-x}O_{12}$ solid solutions [24–37] with $0 \leq x \leq 3$, have attracted a lot of attention in the literature. For example, compounds with large Cu contents show robust ferrimagnetic properties above room temperature [31,37], large low-field magnetoresistance [32,33,36], and magnetocaloric properties [34]. AMn_7O_{12} compounds and their variations show good catalytic properties [38].

The Mn^{4+}: Mn^{3+} ratio of 1:3 at the B sites can also be achieved in the following compositions: $RCuMn_6O_{12}$ (=$[R^{3+}Cu^{2+}Mn_2{}^{3+}][Mn_3{}^{3+}Mn^{4+}]O_{12}$), where R is a trivalent rare-earth cation, which are the members of more general solid solutions with the composition of $RCu_xMn_{7-x}O_{12}$ [39–54] and with $x = 1$. Therefore, it could be interesting to compare the structural and magnetic properties of the AMn_7O_{12} and $RCuMn_6O_{12}$ series. In this work, we prepared one member of the $RCuMn_6O_{12}$ series with R = Nd using a high-pressure high-temperature method. $NdCuMn_6O_{12}$ shows a CO transition near 290 K from *Im*-3 symmetry (above 290 K) to *R*-3 symmetry (below 290 K). The *R*-3 symmetry remains down at 5 K without any additional structural distortions/modulations in comparison with the AMn_7O_{12} series. $NdCuMn_6O_{12}$ also shows a ferrimagnetic transition below 120 K and a second magnetic transition near 20 K probably originating from the Nd sublattice, again in comparison with the AMn_7O_{12} series.

https://doi.org/10.3390/inorganics14070174

2. Results and Discussion

No impurity reflections were detected even on high-resolution, high-intensity synchrotron powder X-ray diffraction (XRD) data of the prepared $NdCuMn_6O_{12}$ samples confirming the high quality of the samples. However, room-temperature (RT) XRD data (laboratory and synchrotron) showed the presence of two phases, cubic *Im*-3 and trigonal *R*-3, because a structural phase transition temperature is very close to RT (292 K, see below). Therefore, we show synchrotron XRD patterns at 100 K and 350 K (not at RT) in Figure 1 to demonstrate the sample quality.

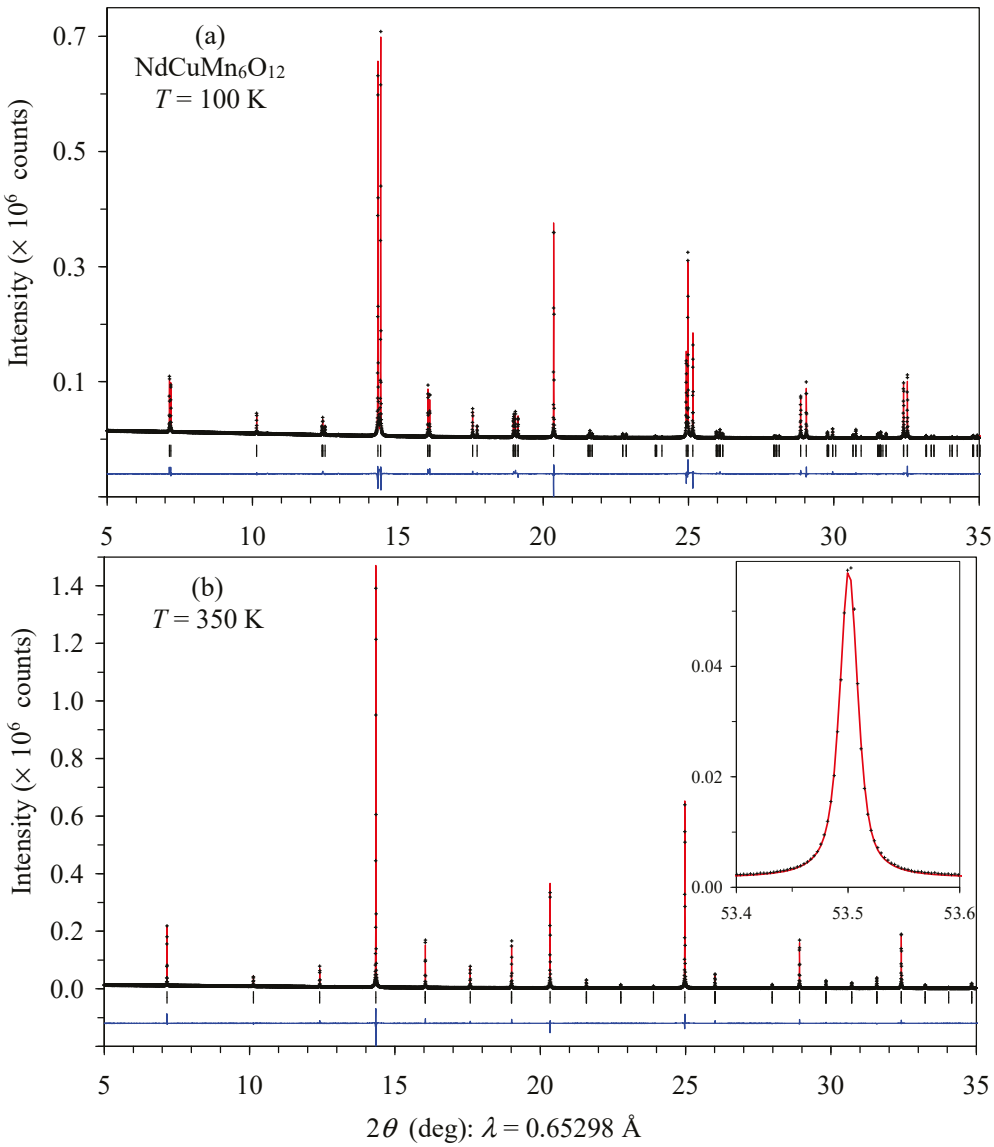

Figure 1. Fragments (between 5° and 35°) of experimental (black crosses), calculated (red line), and difference (blue line at the bottom) synchrotron powder X-ray diffraction patterns of $NdCuMn_6O_{12}$ at (**a**) T = 100 K in the *R*-3 phase and (**b**) T = 350 K in the *Im*-3 phase. The tick marks show possible Bragg reflection positions. The inset in (**b**) emphasizes the shape of reflections in the high 2θ region.

The crystal structures of $NdCuMn_6O_{12}$ were refined by the Rietveld method from synchrotron XRD data. The initial structural models were taken from $CaMn_7O_{12}$ [16]. Structural parameters of $NdCuMn_6O_{12}$ at some selected temperatures are summarized in Tables 1 and 2. Experimental, calculated, and difference synchrotron XRD patterns of $NdCuMn_6O_{12}$ at 100 K and 350 K are shown in Figure 1. In the cubic *Im*-3 modification,

reflections were very sharp and symmetrical (the inset of Figure 1b) indicating good crystallinity and homogeneity of the sample.

Table 1. Structure parameters of charge-ordered $NdCuMn_6O_{12}$ at selected temperatures from synchrotron X-ray powder diffraction data.

***T* (K)**	**100**	**150**	**200**	**250**	**270**
a (Å)	10.48252 (1)	10.48518 (1)	10.48747 (1)	10.48916 (1)	10.48927 (1)
c (Å)	6.35552 (1)	6.35415 (1)	6.35544 (1)	6.35884 (1)	6.36119 (1)
V (Å^3)	604.8011 (7)	604.9781 (6)	605.3652 (7)	605.8845 (7)	606.1211 (8)
B(Nd) (Å^2)	0.145 (7)	0.183 (6)	0.237 (7)	0.282 (7)	0.299 (7)
B(Mn1/Cu1) (Å^2)	0.390 (8)	0.421 (8)	0.478 (8)	0.555 (9)	0.585 (9)
B(Mn2) (Å^2)	0.147 (9)	0.164 (8)	0.192 (8)	0.232 (9)	0.242 (9)
B(Mn3) (Å^2)	0.136 (16)	0.149 (15)	0.169 (15)	0.204 (16)	0.218 (17)
x(O1)	0.2180 (2)	0.2181 (2)	0.2181 (2)	0.2181 (3)	0.2179 (3)
y(O1)	0.2671 (3)	0.2672 (2)	0.2672 (2)	0.2672 (3)	0.2671 (3)
z(O1)	0.0824 (3)	0.0821 (3)	0.0819 (3)	0.0823 (3)	0.0832 (3)
B(O1) (Å^2)	0.22 (4)	0.23 (4)	0.26 (4)	0.37 (4)	0.43 (4)
x(O2)	0.3425 (2)	0.3423 (2)	0.3423 (2)	0.3423 (2)	0.3423 (2)
y(O2)	0.5231 (2)	0.5231 (2)	0.5231 (2)	0.5230 (2)	0.5229 (2)
z(O2)	0.3442 (4)	0.3441 (4)	0.3439 (3)	0.3440 (4)	0.3438 (4)
B(O2) (Å^2)	0.27 (4)	0.26 (4)	0.27 (4)	0.35 (4)	0.39 (4)
R_{wp} (%)	5.54	5.31	5.25	5.46	5.78
R_p (%)	3.58	3.50	3.47	3.57	3.77
R_B (%)	3.09	3.06	3.07	3.16	3.25

Source: Synchrotron powder X-ray diffraction (λ = 0.65298 Å); used *d*-space range: 0.6595–7.485 Å (measured *d*-space range: 0.6595–12.273 Å). Crystal system: trigonal. Space group *R*-3 (No. 148, hexagonal axes), Z = 3. Nd cations occupy the 3*a* site (0, 0, 0); Mn1/Cu1—9*e* site (0.5, 0, 0); Mn2—9*d* site (0.5, 0, 0.5); Mn3—3*b* site (0, 0, 0.5); O3 and O4—18*f* site (*x*, *y*, *z*). The occupation factors of the Nd, Mn2, Mn3, O1, and O2 sites are 1; the occupation of the Mn1/Cu1 site is 2/3Mn + 1/3Cu.

Table 2. Structure parameters of charge-disordered $NdCuMn_6O_{12}$ at selected temperatures from synchrotron X-ray powder diffraction data.

***T* (K)**	**310**	**350**
a (Å)	7.39512 (1)	7.39722 (1)
V (Å^3)	404.4227 (2)	404.7675 (2)
B(Nd) (Å^2)	0.402 (6)	0.429 (5)
B(Mn1/Cu1) (Å^2)	0.801 (9)	0.832 (8)
B(Mn2) (Å^2)	0.332 (7)	0.348 (6)
y(O)	0.30559 (18)	0.30573 (16)
z(O)	0.17458 (20)	0.17457 (17)
B(O) (Å^2)	0.51 (3)	0.58 (3)
R_{wp} (%)	6.37	5.46
R_p (%)	4.03	3.71
R_B (%)	4.77	4.13

Source: Synchrotron powder X-ray diffraction (λ = 0.65298 Å); used *d*-space range: 0.6595–7.485 Å (measured *d*-space range: 0.6595–12.273 Å). Crystal system: cubic. Space group *Im*-3 (No. 204), Z = 2. Nd cations occupy the 2*a* site (0, 0, 0); Mn1/Cu1—6*b* site (0, 0.5, 0.5); Mn2—8*c* site (0.25, 0.25, 0.25); O—24*g* site (0, *y*, *z*). The occupation factors of the Nd, Mn2, and O sites are 1; the occupation of the Mn1/Cu1 site is 2/3Mn + 1/3Cu.

In the crystal structure analysis, Cu^{2+} cations were placed at the square-planar A′ site (together with Mn^{3+} cations) with a fixed occupation as 2/3Mn + 1/3Cu for the Mn1/Cu1 site. Previous structural studies of similar compounds with neutron powder diffraction (which can easily distinguish between Cu and Mn) showed that Cu^{2+} cations are always located at the A′ site due to the strong JT effect of Cu^{2+} cations [25,37,41,47,53,54]. For

unknown reasons, the available synchrotron XRD data were not so sensitive to the location of Cu^{2+} cations in $NdCuMn_6O_{12}$ even though the Cu^{2+} and Mn^{3+} cations differ by five electrons (or about 20%). For example, the refined occupation factor of the Mn1 site (when only Mn was placed at this site) was g(Mn1) = 1.036(1) with refined B = 0.67(9) Å^2 (using the 350 K data in the cubic modification because of the lower number of refined parameters). The obtained g value was within the sensitivity of the method (that is, not noticeably higher) as a similar value was obtained for the Nd site when refined (g(Nd) = 1.035(1) with refined B = 0.497(6) Å^2). g(Mn2) was refined to be 0.983(1) with refined B = 0.289(8) Å^2. Note that two other sets of synchrotron XRD data measured on different batches of $NdCuMn_6O_{12}$ (at T = 380 K with λ = 0.65298 Å) gave g(Nd) = 1.015(1), g(Mn1) = 1.045(2), and g(Mn2) = 1.000(2), and g(Nd) = 1.024(1), g(Mn1) = 1.044(1), and g(Mn2) = 1.014(1). In all cases, the occupation factor of the Mn1 site was slightly larger than that of the Mn2 site (when only Mn was placed at these sites).

Figure 2 shows the temperature dependence of the lattice parameters obtained from laboratory and synchrotron XRD data (see also Tables S1 and S2). Note that the lattice parameters of the R-3 modification were transformed from the hexanogal axes ($a_H \approx 10.5$ Å and $c_H \approx 6.36$ Å) to the rhombohedral axes ($a_R \approx 6.42$ Å and $\alpha_R \approx 109.6°$; $a_R = (a_H \times \beta)/3$, $\alpha_R = 2 \times \arcsin(1.5/\beta)$, $\beta = (3 + (c_H/a_H)^2)^{1/2}$) and then to a different cell choice in the rhombohedral axes ($a_R \approx 7.40$ Å and $\alpha_R \approx 90.3°$) for the better comparison with the cubic Im-3 modification ($a_C \approx 7.40$ Å (and $\alpha_C = 90°$)). The two phases co-existed in a certain temperature range near RT indicating a phase transition of the first order. There were some differences in the a_R parameter for the laboratory and synchrotron XRD data. These differences can be explained by different zero-shift parameters for different XRD sources (zero-shift parameters are usually very small for synchrotron XRD data) and by the fact that samples from different batches were used for the laboratory and synchrotron XRD measurements. The a_R parameter gradually decreases with decreasing temperature and then becomes nearly temperature-independent below about 100 K. The rhombohedral angle α_R shows a dome-like behavior between T_{CO} (≈292 K) and 60 K, and its temperature behavior changes below 50 K, where it slightly decreases with decreasing temperature. No anomalies in the lattice parameters were observed at the first magnetic transition temperature (T_C = 120 K, see below). The R-3 modification was found to be stable below T_{CO} down to 5 K since no (new) modulation reflections were observed on laboratory XRD data down to 5 K and on high-resolution, high-intensity synchrotron XRD data down to 100 K within the sensitivity of both methods. Therefore, the structural behavior of $NdCuMn_6O_{12}$ is different from that of $CaMn_7O_{12}$ [10,16–19] below T_{CO}.

Figure 3 shows the temperature dependence of the bond lengths in $NdCuMn_6O_{12}$ in the R-3 and Im-3 modifications. The Im-3 modification has one crystallographic site for octahedral Mn cations. Therefore, this site should have an average oxidation state of +3.25. The bond-valence sum [55] value of +3.35 (at 350 K) supports the average value (for calculations we used R_0 = 1.76 for all Mn). The R-3 modification has two crystallographic sites for octahedral Mn cations. One octahedral site (Mn3) has short Mn-O distances (which are all the same and, therefore, the octahedral distortion parameter is zero). Therefore, this site should be occupied by Mn^{4+}. The bond-valence sum [55] value of +3.87 (at 270 K) supports this assignment. For the second octahedral site (Mn2), the MnO_6 octahedra have an apically compressed geometry with four longer Mn-O distances and two shorter Mn-O distances (and the resulting octahedral distortion parameter was about 8.4×10^{-4}). Such distortions are caused by the JT effect. This site should be occupied by Mn^{3+}, and the bond-valence sum [55] value of +3.20 (at 270 K) supports this assignment. The same structural features take place in $CaMn_7O_{12}$ [16] below T_{CO}. The bond-valence sum [55] values of the Nd sites remain nearly the same (+3.20 to +3.23) in the R-3 and Im-3 modifications. The larger values

than expected indicate that Nd^{3+} cations are overbonded, and this fact could be a reason why $NdMn_7O_{12}$ [51] and $NdCuMn_6O_{12}$ need a high-pressure high-temperature method for their preparation. The bond lengths remain nearly the same at all temperatures (except in the vicinity of T_{CO}). Therefore, the bond-valence sum values remain nearly constant at different temperatures. We note that the degree of charge separation [56] estimated by bond-valence sum calculations (about 66% in our case at 270 K) is always below ideal values as emphasized in the literature [23,56], and bond-valence calculations just indicate tendencies. The main reason seems to be the nature of bond-valence calculations as they are based on some average parameters obtained from the statistical analysis of many reported crystal structures. In principle, bond-valence parameters can be adjusted for specific materials and coordination numbers and environments. For example, in $R^{3+}MnO_3$ perovskites, where Mn definitely has the fixed oxidation state of +3 and strong JT distortions, the standard bond-valence calculations (with $R_0(Mn^{3+})$ = 1.76 [55]) give values from +3.12 to +3.21 even when structural parameters determined from neutron diffraction (with precise localization of oxygen atoms) are used [57]. The use of $R_0(Mn^{3+})$ = 1.74 gives bond-valence sums close to +3.0 in $RMnO_3$ perovskites and in the Mn2 site of $NdCuMn_6O_{12}$ (for the *R*-3 modification).

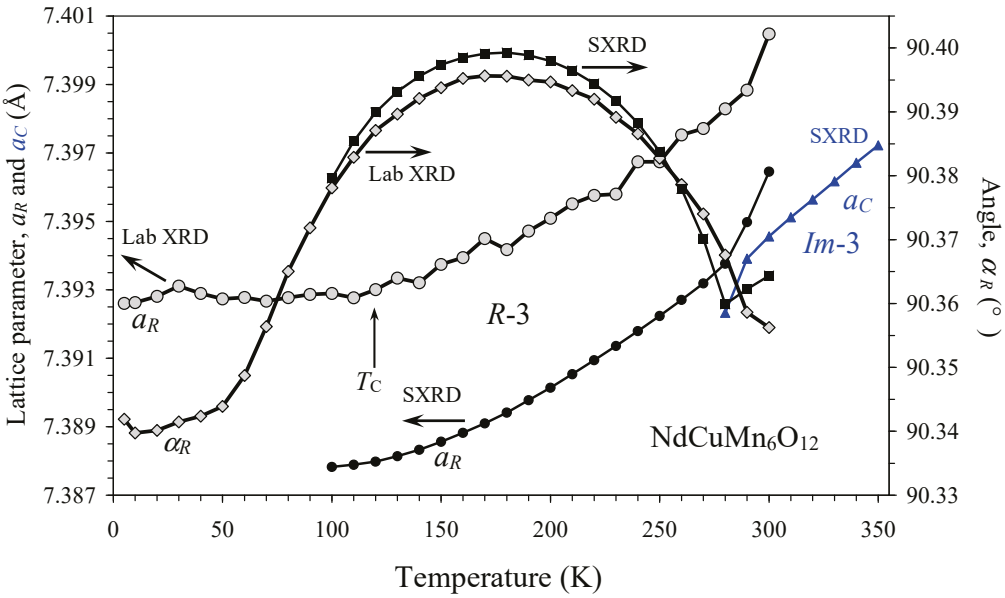

Figure 2. Temperature dependence of the lattice parameters of $NdCuMn_6O_{12}$ on heating. The left-hand axis shows the rhombohedral (a_R) and cubic (a_C) lattice parameter. The right-hand axis shows the rhombohedral angle (α_R). Black and blue symbols show results from synchrotron powder X-ray diffraction (SXRD) measurements; gray symbols show results from laboratory powder X-ray diffraction (Lab XRD) measurements. The vertical arrow shows the position of the magnetic transition temperature, T_C.

The Mn-O bond lengths in $NdCuMn_6O_{12}$ in the *R*-3 modification are nearly temperature-independent (Figure 3). Therefore, the unusual JT distortions in $NdCuMn_6O_{12}$ do not experience any relaxation in comparison with $CaMn_7O_{12}$ [10,16]. However, the rhombohedral distortions/angles (Figure 2) first increased with decreasing temperature from 292 K to about 180 K in $NdCuMn_6O_{12}$; then they reduced on further cooling from 180 K down to 60 K producing the dome-like behavior of the temperature dependence of the rhombohedral angle. Below 60 K, the rhombohedral distortion/angle is nearly locked. This behavior could be related to unusual JT distortions and their tendency to be relaxed.

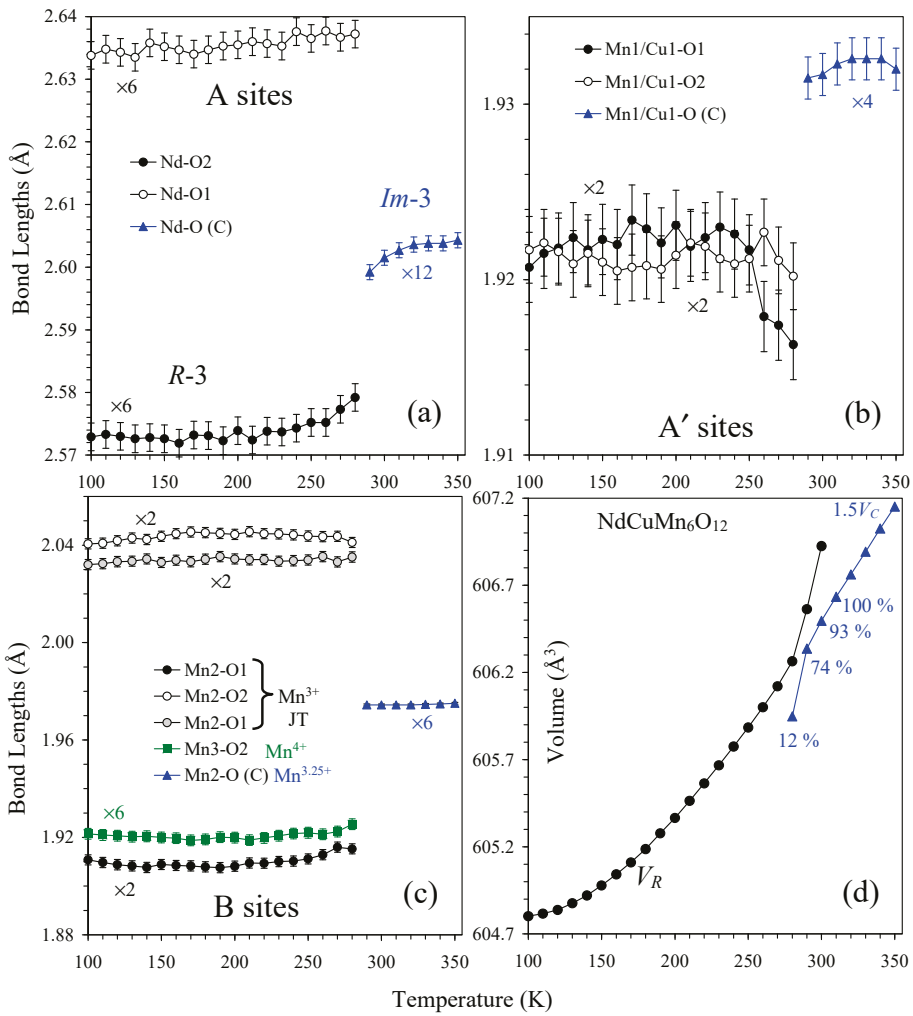

Figure 3. Temperature dependence of (**a**–**c**) bond lengths and (**d**) the (normalized to the *R*-3 cell) unit cell volume of $NdCuMn_6O_{12}$ on heating determined from synchrotron powder X-ray diffraction measurements. Data for the *Im*-3 phase are shown in blue. Numbers in (**d**) show the weight fraction of the cubic (C) *Im*-3 phase. The Nd-O bond lengths are given in (**a**), the Mn1/Cu1-O bond lengths for the square-planar site are given in (**b**), and the Mn-O bond lengths for the octahedral sites are given in (**c**).

Structural behavior of $NdCuMn_6O_{12}$ was also investigated with differential scanning calorimetry (DSC) (Figure 4). $NdCuMn_6O_{12}$ showed sharp and strong DSC anomalies on both heating and cooling curves confirming the presence of a structural phase transition with T_{CO} = 292 K (defined from peak positions on heating curves). DSC anomalies showed good reproducibility on cycling. The sample batch used in this study showed relatively strong and sharp DSC anomalies, and two peaks with nearly the same intensity were clearly resolved plus a shoulder was observed from a high-temperature side. This feature could indicate a phase separation, which was observed in $NdCu_xMn_{7-x}O_{12}$ solid solutions with x = 0.1, 0.2, and 0.3 [52]. However, high-resolution synchrotron XRD data (the inset of Figure 1b) did not detect any evidence of a phase separation. Other batches of $NdCuMn_6O_{12}$ samples showed broader and weaker DSC anomalies (Figures S1 and S2), and no evidence of a phase separation could be seen from such DSC data. Therefore, if a phase separation is present, it is quite small.

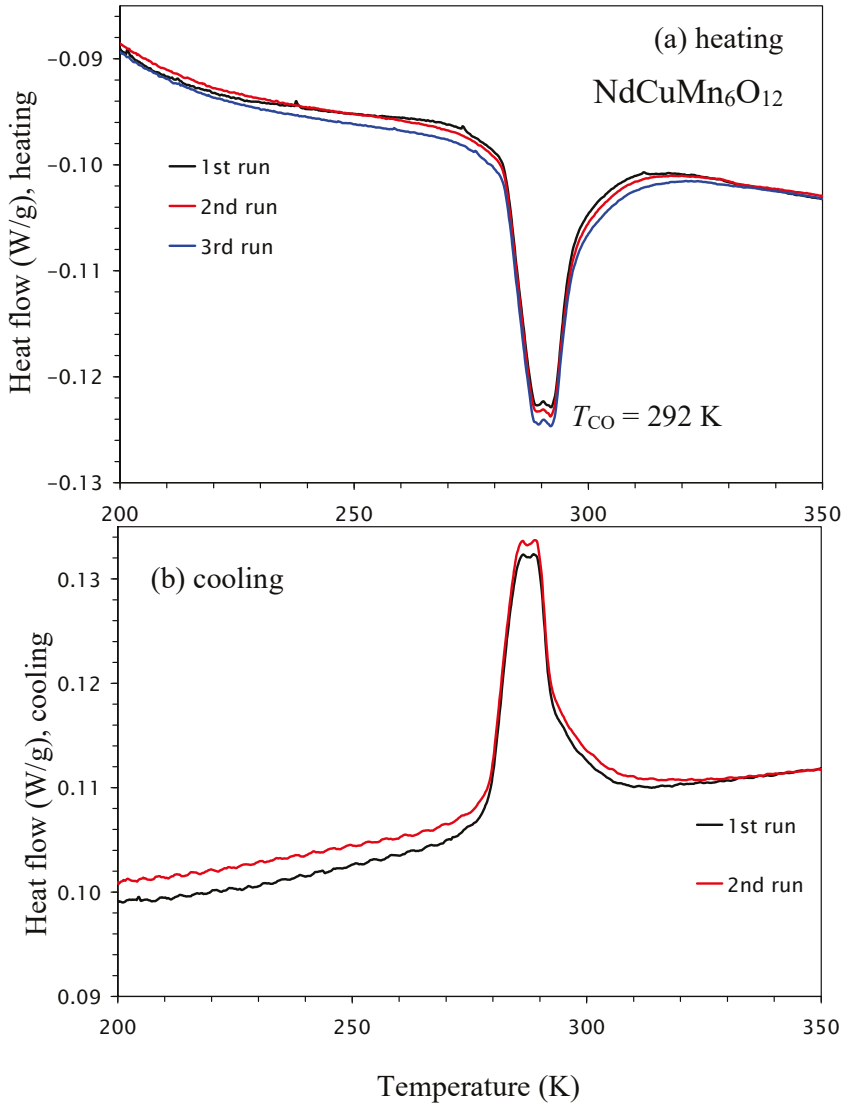

Figure 4. Differential scanning calorimetry (DSC) curves of $NdCuMn_6O_{12}$ (29.40 mg) during (**a**) heating and (**b**) cooling. Three DSC runs were performed (and shown) to check the reproducibility.

Figure 5 shows the direct current (dc) χ versus T curves of $NdCuMn_6O_{12}$ under magnetic fields H = 100 Oe and 10 kOe. There were two clear anomalies (at H = 100 Oe). The first strong anomaly was observed on both zero-field-cooled (ZFC) and field-cooled on cooling (FCC) curves near T_C = 120 K due to a ferrimagnetic transition. T_C was defined from the peak positions on differential curves (Figure S3). The second anomaly (near T_{N2} = 20 K) was quite broadened and was observed as a kink on the ZFC curve and a gradual decrease on the FCC curve. No clear anomalies could be seen at a large magnetic field of H = 10 kOe. Neutron diffraction studies of the undoped $NdMn_7O_{12}$ showed that a gradual small decrease on χ versus T curves is correlated with a gradual increase in the ordered moments on the Nd^{3+} sublattice [50,51], and the Nd^{3+} sublattice orders antiferromagnetically with the ferrimagnetic structure formed by the Mn^{3+} sublattices [50]. However, we note that the decrease on χ versus T curves was observed in $NdMn_7O_{12}$ below T_3 ~ 8 K at higher magnetic fields (e.g., H = 10 kOe); at smaller magnetic fields (e.g., H = 100 Oe), the decrease already started below about 16 K. Therefore, we can assume that the second magnetic anomaly in $NdCuMn_6O_{12}$ also corresponds to the antiferromagnetic (AFM) ordering of the Nd^{3+} sublattice. A similar decrease in magnetic susceptibilities at low temperatures was observed in $NdCu_xMn_{7-x}O_{12}$ solid solutions with x = 1.5−3 [40,41]

and in $NdCu_3Mn_3FeO_{12}$ [58]. Neutron diffraction studies of $NdCu_3Mn_3FeO_{12}$ [58] also allowed suggesting AFM ordering of the Nd sublattice. However, a final conclusion about the origin of the low-temperature susceptibility drops at small magnetic fields and the second magnetic transition in $NdCuMn_6O_{12}$ can only be made from future neutron diffraction studies.

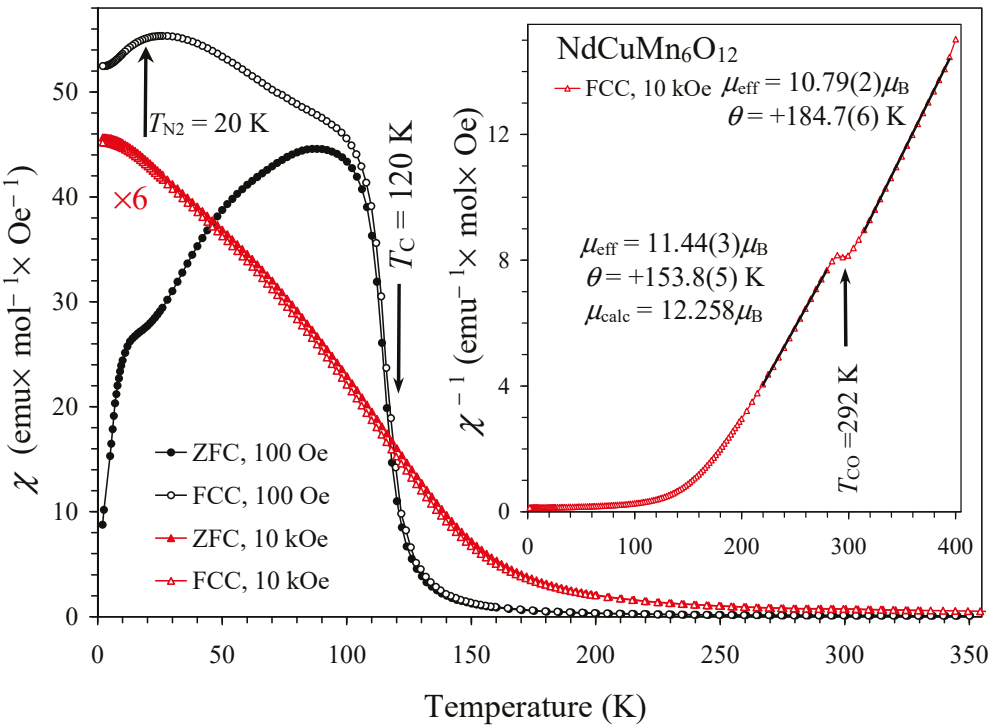

Figure 5. Magnetic properties of $NdCuMn_6O_{12}$. Zero-field-cooled (ZFC: filled curves) and field-cooled on cooling (FCC: empty curves) curves are shown at H = 100 Oe (black curves) and H = 10 kOe (red curves; multiplied by 6). The inset gives the inverse FCC χ^{-1} versus T curve at H = 10 kOe with Curie–Weiss fits (black lines) and fitting parameters in two regions. Vertical arrows emphasize the magnetic transition temperature (T_C) and the charge-order transition temperature (T_{CO}).

Magnetic anomalies were observed at the structural phase transition of T_{CO} = 292 K, where they could be clearly seen as a sharp step on the inverse magnetic susceptibilities (the inset of Figure 5). The Curie–Weiss law was applied to obtain effective magnetic moments and Curie–Weiss temperatures. We fitted the FCC inverse magnetic susceptibilities (at H = 10 kOe) in the temperature ranges of 220–270 K and 320–395 K. The fitting parameters are reported in Figure 5. The Curie–Weiss temperature was positive indicating the predominant ferromagnetic (FM) interactions between magnetic ions. The Curie–Weiss temperature was larger in the *Im*-3 modification in comparison with the *R*-3 modification, while the effective magnetic moment was larger for the *R*-3 modification and closer to the expected value of 12.258 μ_B (for the calculation, we used 3.5 μ_B for Nd^{3+}, 1.732 μ_B for Cu^{2+}, 4.899 μ_B for Mn^{3+}, and 3.873 μ_B for Mn^{4+} [59]). Similar behavior of inverse magnetic susceptibilities was observed in $PrCuMn_6O_{12}$ [43], $CeCuMn_6O_{12}$ [44], and $BiCuMn_6O_{12}$ [53,54].

Isothermal magnetization curves (M versus H) at different temperatures are shown in Figures 6 and S4. They were typical for ferrimagnets with well-defined hysteresis near the origin. However, they did not fully saturate and showed gradual continuous increases in magnetization at higher magnetic fields indicating contributions from AFM interactions. The coercive field was about 600 Oe at T = 2 K, 200 Oe at T = 5 K, and ~0 Oe at T = 20 K. The magnetization values reached ≈ 17.8 μ_B at T = 2 and 5 K (and at H = 70 kOe) and ≈17.3 μ_B at T = 20 K. These values are close to the expected values with the FM interactions

between Cu^{2+} and all Mn^{3+} cations and AFM interactions with Mn^{4+} cations, (1 + 20 − 3) = 18 μ_B (1 μ_B is the maximum ordered moment of Cu^{2+}, 4 μ_B is the maximum ordered moment of Mn^{3+}, and 3 μ_B is the maximum ordered moment of Mn^{4+}). Contributions from Nd^{3+} can be neglected as the ordered moments of Nd^{3+} are usually below 1 μ_B [50,58] and should be negligible at 20 K. In addition, similar saturation values were observed in $CaCu_xMn_{7-x}O_{12}$ solid solutions with $1 \leq x \leq 2$ [34], which do not have magnetic rare-earth cations, and in $NdCu_xMn_{7-x}O_{12}$ solid solutions with x = 1.5 and 2 [40]. $RCu_xMn_{7-x}O_{12}$ and $CaCu_xMn_{7-x}O_{12}$ solid solutions have a tendency to show saturation behavior for large Cu contents and gradual continuous increases in magnetization for smaller Cu contents, such as x = 1 [34,40,44,47].

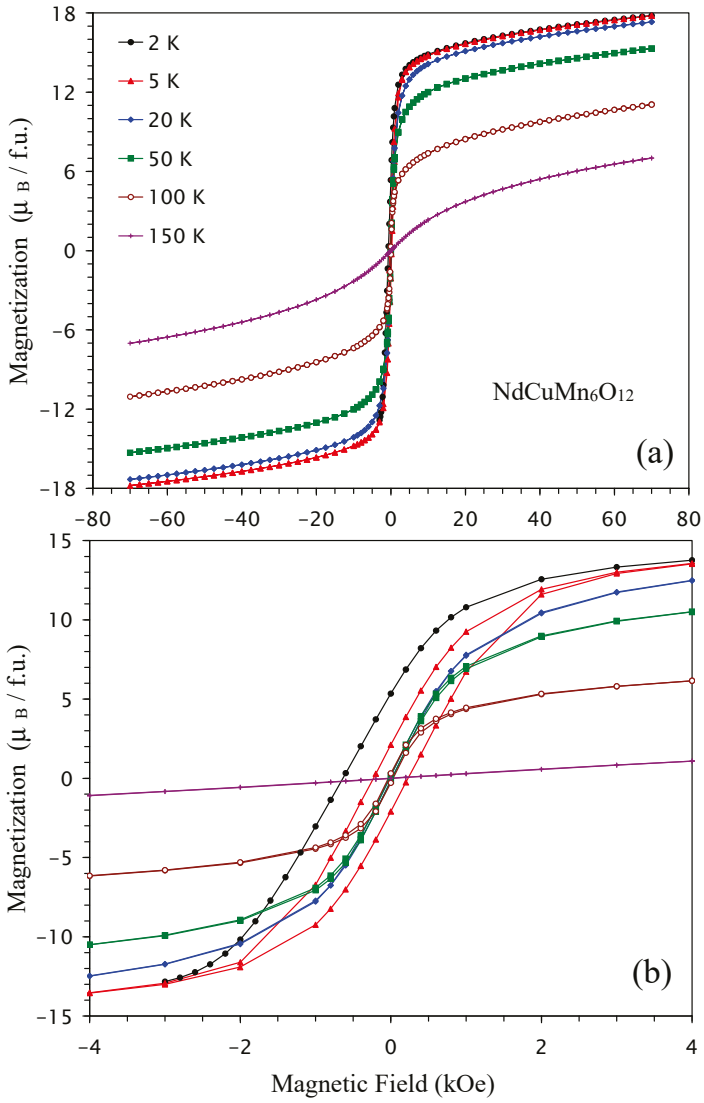

Figure 6. Magnetic properties of $NdCuMn_6O_{12}$: M versus H curves at T = 2, 5, 20, 50, 100, and 150 K. Panel (**a**) shows the full M versus H curves, panel (**b**) shows the zoomed-in M versus H curves near the origin.

Specific heat measurements (Figures 7 and S5) showed a very weak anomaly at T_C = 120 K (the inset of Figure 7), while a stronger anomaly was found near T_{N2} = 20 K. Specific heat data unambiguously confirmed the presence of the second magnetic transition. Magnetic fields slightly suppressed specific heat anomalies at T_{N2} and completely smeared anomalies at T_C and moved magnetic entropy to much higher temperatures. Such effects (near T_C) are typical for FM and ferrimagnetic materials.

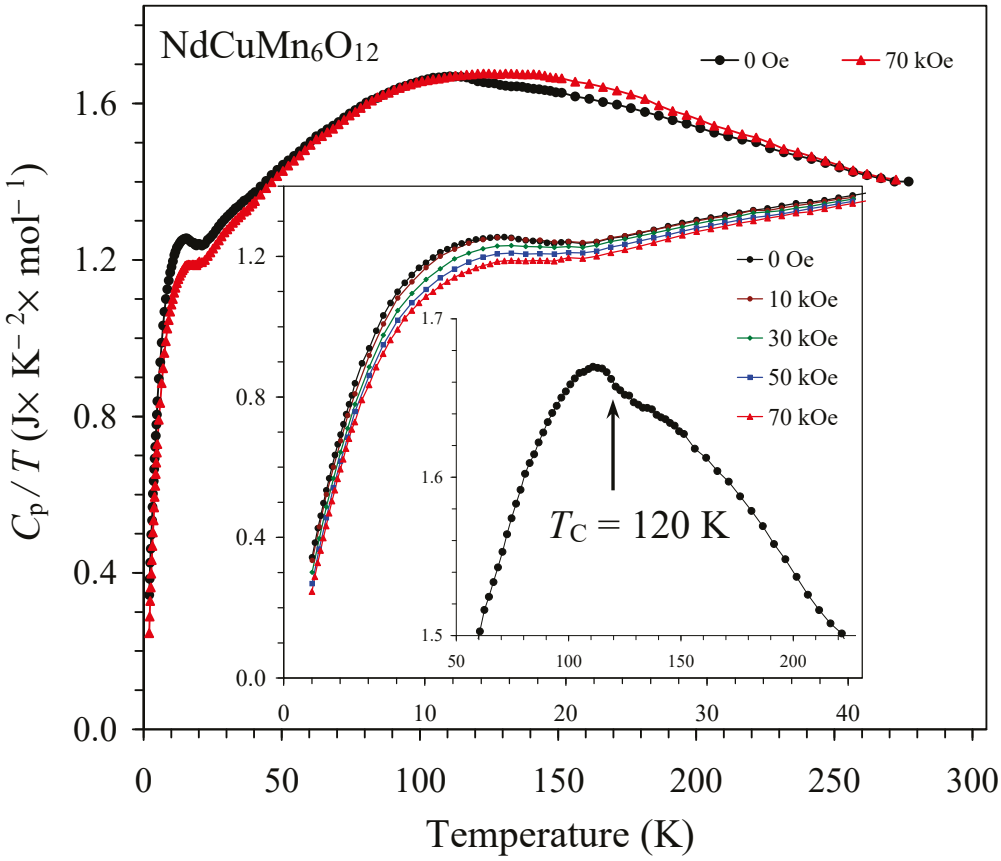

Figure 7. Specific heat data of $NdCuMn_6O_{12}$ plotted as C_p/T versus T at H = 0 Oe (black) and 70 kOe (red). The main inset shows the C_p/T versus T curves at H = 0, 10, 30, 50, and 70 kOe below 40 K. The second inset emphasizes specific heat anomalies near T_C at H = 0 Oe.

Ac susceptibility measurements were performed to get more information about the magnetic properties of $NdCuMn_6O_{12}$ (Figures 8, 9 and S6). Ac susceptibility curves were measured at different frequencies (Figure 8) and different ac fields (Figure 9). Some frequency dependence was observed on the χ' versus T curves between about 60 and 110 K, while much stronger frequency dependence was observed on the χ'' versus T curves between about 20 and 120 K. However, such frequency dependence was not caused by any spin-glass contributions; it was caused by interactions of the ac field with ferrimagnetic domain structures. Non-linear behavior (and the presence of interactions with domain structures) could be more clearly seen from the dependence on the ac field (Figure 9). The χ' versus T curves showed sharp decreases below about 16 K with the appearance of peaks on the χ'' versus T curves near 8–9 K. Anomalies below 20 K showed no dependence on the ac field, indicating the linear response. We note that very similar anomalies were observed below about 20 K in other members of the $RCuMn_6O_{12}$ series (for example, with R = Ce, Sm, and Dy [44]) especially on the χ'' versus T curves. Therefore, their origin could be unrelated to rare-earth elements (Nd in this case) and to the presence of the second magnetic transition in $NdCuMn_6O_{12}$ at T_{N2}.

The synthesis of $NdCuMn_6O_{12}$ was attempted in Ref. [41]. However, because of the presence of large amounts of Mn-containing impurities ($NdMn_2O_5$ and Mn_2O_3), the composition of the main perovskite phase was shifted to the Cu-rich side. As a result, the main perovskite phase remained cubic down to 5 K, and no structural phase transitions were observed. In addition, the magnetic transition temperature was observed at a noticeably higher temperature of 206 K in Ref. [41] (in comparison with 120 K for our sample); our estimation shows that such a transition corresponds to a $NdCu_{1.4}Mn_{5.6}O_{12}$

composition. Our sample was single-phase, suggesting that the target composition was achieved, and our sample showed a structural transition from *Im*-3 symmetry (at high temperatures) to *R*-3 symmetry near 292 K. Such a structural transition was observed at 267 K in $PrCuMn_6O_{12}$ [43], at 297 K in $CeCuMn_6O_{12}$ [44], and at 296 K in $BiCuMn_6O_{12}$ [53,54].

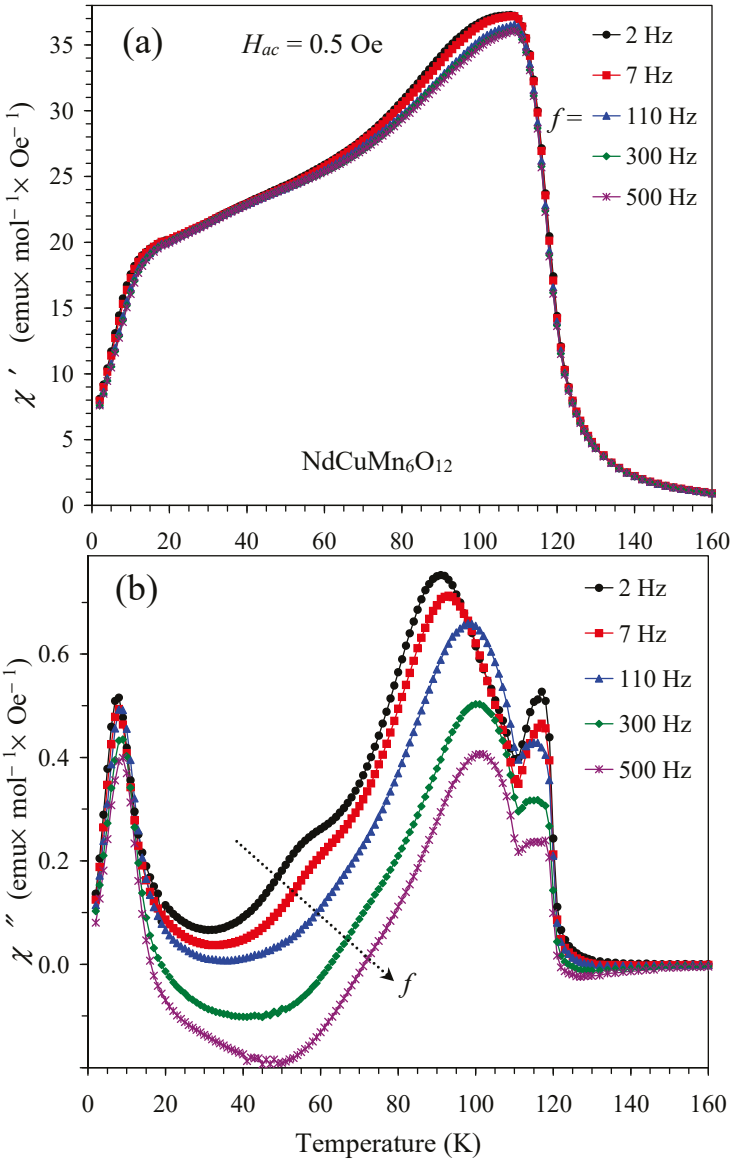

Figure 8. (**a**) The χ' versus T and (**b**) χ'' versus T curves of $NdCuMn_6O_{12}$ at different frequencies (f = 2, 7, 110, 300, 500 Hz) measured with H_{ac} = 0.5 Oe and H_{dc} = 0 Oe.

$AA'_3Mn_4O_{12}$-type perovskites with the 1:3 ratio of Mn^{4+}/Mn^{3+} cations at the B sites show CO structural transitions from *Im*-3 symmetry (at high temperatures) to *R*-3 symmetry and compressed $Mn^{3+}O_6$ octahedra in the average structure of the *R*-3 modification, which is sometimes called an orbital disorder phase [23]. Relaxation of compressed $Mn^{3+}O_6$ octahedra occurs through different mechanisms on further cooling [10]. As mentioned in the introduction, AMn_7O_{12} compounds with A = Ca, Sr, and Pb show incommensurately modulated structures, where $Mn^{3+}O_6$ octahedra become locally elongated [10,20]. $CdMn_7O_{12}$ shows a commensurately modulated structure (space group *P*-3), where a part of $Mn^{3+}O_6$ octahedra restores their typical JT distortions [10,20]. $HgMn_7O_{12}$ shows a polar orthorhombic distortion (space group *Pnn*2), an additional charge transfer, and the restoration of typical JT distortions of $Mn^{3+}O_6$ octahedra [23]. $BiCuMn_6O_{12}$ shows a

unique re-entrant structural transition, where the *R*-3 modification collapses back to the cubic *Im*-3 modification on cooling [53,54]. $CeCuMn_6O_{12}$ demonstrated a phase separation below about 80 K [44]. Therefore, the apparent absence of any further structural transitions in $NdCuMn_6O_{12}$ may need a deeper understanding and further detailed structural characterizations at low temperatures, including more sensitive methods such as electron and neutron diffraction.

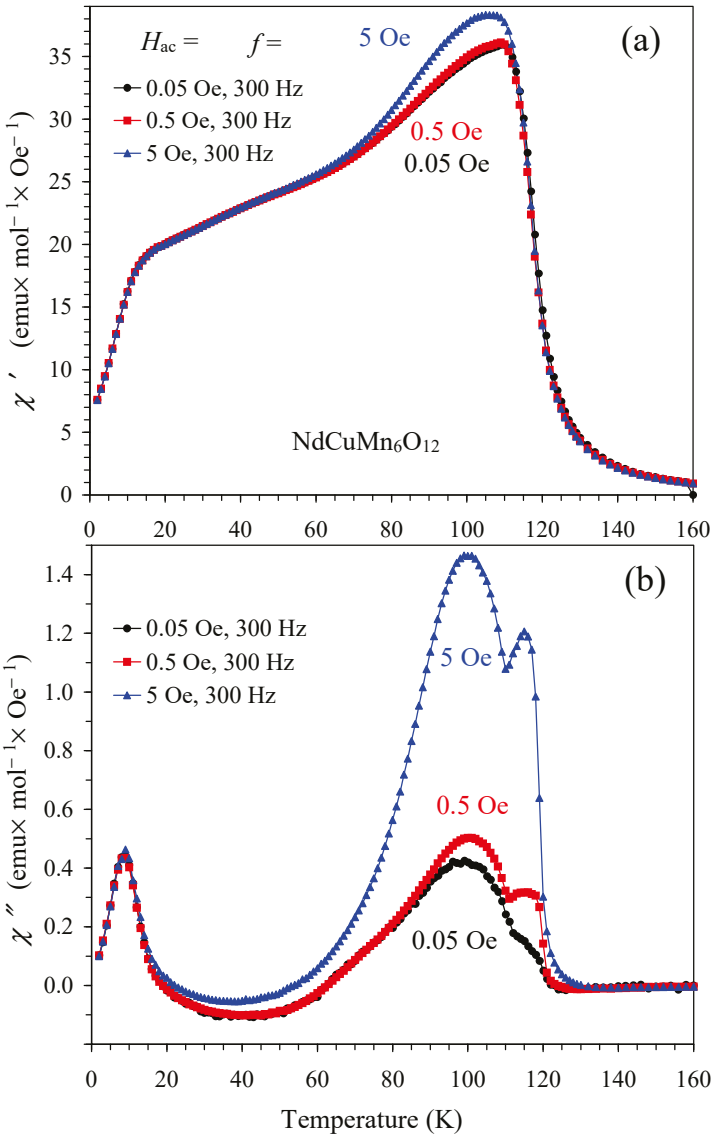

Figure 9. (**a**) The χ′ versus *T* and (**b**) χ″ versus *T* curves of $NdCuMn_6O_{12}$ at different H_{ac} = 0.05, 0.5, and 5 Oe and one frequency of 300 Hz (under H_{dc} = 0 Oe).

3. Materials and Methods

$NdCuMn_6O_{12}$ samples were prepared from stoichiometric mixtures of Nd_2O_3 (Rare Metallic Co., Tokyo, Japan, 99.9%), CuO (Rare Metallic Co., Tokyo, Japan, 99.9%), MnO_2 (Alfa Aesar, Ward Hill, MA, USA, 99.99%), and Mn_2O_3. Single-phase Mn_2O_3 was prepared from a commercial MnO_2 chemical (Rare Metallic Co., Tokyo, Japan, 99.99%) by annealing in air at 923 K for 24 h. The synthesis was performed at 6 GPa and at 1600 K for 2 h in sealed Pt capsules using a belt-type high-pressure (HP) instrument. After annealing at 1600 K, the samples were cooled down to room temperature (RT) by turning off the heating current, and the pressure was slowly released.

Laboratory powder X-ray diffraction (XRPD) data were collected at RT on a MiniFlex600 diffractometer (Rigaku, Tokyo, Japan) using CuKα radiation (2θ range of 10−80°, a step width of 0.02°, and scan speed of 2°/min). Low-temperature laboratory XRPD data were measured on a RIGAKU SmartLab instrument (CuKα_1 radiation at 45 kV and 200 mA; 2θ range of 10−110°, a step width of 0.02°, and scan speed of 1°/min) from 5 K to 300 K (Bragg−Brentano geometry was used for all laboratory XRPD). Synchrotron XRPD data were measured on the BL15XU beamline (the former NIMS beamline) of SPring-8 [60] between 3.05° and 59.35° at 0.003° intervals in 2θ with the wavelength of λ = 0.65298 Å from 100 K to 350 K. The sample was placed into an open Lindemann glass capillary tube (inner diameter: 0.1 mm), which was rotated during measurements. The Rietveld analysis of all XRPD data was performed using the RIETAN-2000 program [61].

Magnetic measurements were performed on a SQUID magnetometer (Quantum Design MPMS-XL-7T, San Diego, CA, USA) between 2 K and 350–400 K in applied fields of 100 Oe and 10 kOe under both zero-field-cooled (ZFC) and field-cooled on cooling (FCC) conditions. Magnetic-field dependence was measured at different temperatures between −70 and 70 kOe. Frequency-dependent alternating current (ac) susceptibility measurements were performed on cooling with a MPMS-1T instrument (Quantum Design, San Diego, CA, USA) at zero static dc field and at different frequencies (f) and different applied oscillating magnetic fields (H_{ac}).

Specific heat, C_p, was measured on cooling from 270 K to 2 K at zero magnetic field and 70 kOe and from 40 K to 2 K at H = 10, 30, and 50 kOe by a pulse relaxation method using a commercial calorimeter (Quantum Design PPMS, San Diego, CA, USA). All magnetic and specific heat measurements were performed using pieces of pellets.

Differential scanning calorimetry (DSC) curves of a powder sample (29.40 mg) were recorded on a Mettler Toledo DSC1 STAR^e system (Columbus, OH, USA) between 173 K and 423 K in open Al capsules with a heating/cooling rate of 10 K/min. Three DSC runs were performed to check the reproducibility.

All the above measurements (except low-temperature laboratory XRPD because such an experiment required a relatively large amount of a sample) were performed using the same batch of the prepared sample.

4. Conclusions

In conclusion, the A-site-ordered quadruple perovskite $NdCuMn_6O_{12}$, with the presence of Mn^{4+}/Mn^{3+} cations with the 1:3 ratio at the B perovskite sites and therefore resembling $CaMn_7O_{12}$, was prepared by a high-pressure high-temperature method. A first-order structural phase transition from *Im*-3 symmetry (at high temperatures) to *R*-3 symmetry was found near T_{CO} = 292 K accompanied by charge ordering and orbital ordering with unusual apically compressed Jahn–Teller distortions of MnO_6 octahedra. In comparison with $CaMn_7O_{12}$, no additional structural transitions were found in $NdCuMn_6O_{12}$ within the sensitivity of the used methods, indicating that compressed Jahn–Teller distortions were not relaxed. $NdCuMn_6O_{12}$ shows a ferrimagnetic transition below 120 K, and the second magnetic transition near 20 K was found in $NdCuMn_6O_{12}$.

Supplementary Materials: The following supporting information can be downloaded at: https://www.mdpi.com/article/10.3390/inorganics14070174/s1, Figure S1 and Figure S2: Differential scanning calorimetry (DSC) curves of a different batch of $NdCuMn_6O_{12}$ on (a) heating and (b) cooling. Three DSC runs were performed (and shown) to check the reproducibility. The peaks were broader in comparison with a sample used in the main text. The inset on (b) shows the shape of cubic reflections ((6 8 2) and (10 2 0)) of synchrotron XRD data (at T = 380 K with λ = 0.65298 Å) for this sample; axes: intensity (counts/10^6) versus 2θ (°); Figure S3: Magnetic properties of $NdCuMn_6O_{12}$. (a) Zero-field-cooled (ZFC: filled curves) and field-cooled on cooling (FCC: empty curves) curves are shown at

H = 5 Oe (black curves). A different (compared with the main text) FCC curve at H = 100 Oe is shown in blue. The inset shows differential curves, $d\chi/dT$ versus T. (b) The ZFC and FCC $d\chi/dT$ versus T curves at H = 10 kOe (red curves); Figure S4: Magnetic properties of $NdCuMn_6O_{12}$: M versus H curves at T = 150, 200, 250, and 300 K; Figure S5: Specific heat data of $NdCuMn_6O_{12}$ (the same batch as used in the main text) in a high-temperature region plotted as C_p versus T (the left-hand axis) and C_p/T versus T (the right-hand axis) at H = 0 Oe on heating (red and pink) and cooling (blue) with a step of 2 K. An H Apiezon grease was used for a better thermal contact between the sample and a sample holder. An addenda contribution was measured with a step of 4 K. Specific heat measurements are in agreement with the DSC measurements (Figure 4) and show a double-peak feature; Figure S6: (a) The χ' versus T and (b) χ'' versus T curves of a different batch of $NdCuMn_6O_{12}$ at different frequencies (f = 2, 7, 25, 110, 500 Hz) measured with H_{ac} = 0.5 Oe and H_{dc} = 0 Oe using MPMS3; Table S1 and Table S2: Numerical data used to plot Figure 2.

Author Contributions: Conceptualization, A.A.B.; methodology, A.A.B.; validation, A.A.B.; formal analysis, A.A.B.; investigation, A.A.B., R.L., L.Z., Y.M. and K.Y.; resources, K.Y.; data curation, A.A.B.; writing—original draft preparation, A.A.B.; writing—review and editing, A.A.B.; supervision, A.A.B. and K.Y.; project administration, A.A.B.; funding acquisition, K.Y. All authors have read and agreed to the published version of the manuscript.

Funding: This work was partially supported by a Grant-in-Aid for Scientific Research (No. JP25K01657) from the Japan Society for the Promotion of Science.

Institutional Review Board Statement: Not applicable.

Informed Consent Statement: Not applicable.

Data Availability Statement: The original contributions presented in this study are included in the article/Supplementary Materials. Further inquiries can be directed to the corresponding author.

Acknowledgments: The synchrotron radiation experiments were conducted at the former NIMS beamline (BL15XU) of SPring-8 with the approval of the former NIMS Synchrotron X-ray Station (proposal numbers: 2016B4504, 2019B4500, and 2020A4501). We thank M. Tanaka and Y. Katsuya for their help at SPring-8. MANA was supported by the World Premier International Research Center Initiative (WPI), MEXT, Japan.

Conflicts of Interest: The authors declare no conflicts of interest.

References

1. Wollan, E.O.; Koehler, W.C. Neutron diffraction study of the magnetic properties of the series of perovskite-type compounds $[(1-x)La, xCa]MnO_3$. *Phys. Rev.* **1955**, *100*, 545–563. [CrossRef]
2. Goodenough, J.B. Theory of the role of covalence in the perovskite-type manganites $[La, M(II)]MnO_3$. *Phys. Rev.* **1955**, *100*, 564–573. [CrossRef]
3. Salamon, M.B.; Jaime, M. The Physics of magnanites: Structure and transport. *Rev. Mod. Phys.* **2001**, *73*, 583–628. [CrossRef]
4. Edwards, D.M. Ferromagnetism and electron-phonon coupling in the manganites. *Adv. Phys.* **2002**, *51*, 1259–1318. [CrossRef]
5. Coey, J.M.D.; Viret, M.; von Molnar, S. Mixed-valence manganites. *Adv. Phys.* **2009**, *58*, 571–697. [CrossRef]
6. Martin, C.; Maignan, A.; Hervieu, M.; Raveau, B. Magnetic phase diagrams of $L_{1-x}A_xMnO_3$ manganites (L = Pr,Sm; A = Ca,Sr). *Phys. Rev. B* **1999**, *60*, 12191–12199.
7. Vasil'ev, A.N.; Volkova, O.S. New functional materials $AC_3B_4O_{12}$ (Review). *Low. Temp. Phys.* **2007**, *33*, 895–914. [CrossRef]
8. Long, Y. A-site ordered quadruple perovskite oxides $AA'_3B_4O_{12}$. *Chin. Phys. B* **2016**, *25*, 078108. [CrossRef]
9. Ding, J.; Zhu, X.H. Research progress on quadruple perovskite oxides. *J. Mater. Chem. C* **2024**, *12*, 9510–9561. [CrossRef]
10. Belik, A.A.; Johnson, R.D.; Khalyavin, D.D. The rich physics of A-site-ordered quadruple perovskite manganites AMn_7O_{12}. *Dalton Trans.* **2021**, *50*, 15458–15472. [CrossRef] [PubMed]
11. Solana-Madruga, E.; Arevalo-Lopez, A.M. High-pressure A-site manganites: Structures and magnetic properties. *J. Solid State Chem.* **2022**, *315*, 123470. [CrossRef]
12. Prodi, A.; Gilioli, E.; Gauzzi, A.; Licci, F.; Marezio, M.; Bolzoni, F.; Huang, Q.; Santoro, A.; Lynn, J.W. Charge orbital and spin ordering phenomena in the mixed valence manganite $(NaMn^{3+}{}_3)(Mn^{3+}{}_2Mn^{4+}{}_2)O_{12}$. *Nat. Mater.* **2004**, *3*, 48–52. [PubMed]

13. Prodi, A.; Daoud-Aladine, A.; Gozzo, F.; Schmitt, B.; Lebedev, O.; van Tendeloo, G.; Gilioli, E.; Bolzoni, F.; Aruga-Katori, H.; Takagi, H.; et al. Commensurate structural modulation in the charge- and orbitally ordered phase of the quadruple perovskite $(NaMn_3)Mn_4O_{12}$. *Phys. Rev. B* **2014**, *90*, 180101. [CrossRef]
14. Bochu, B.; Chenavas, J.; Joubert, J.C.; Marezio, M. High pressure synthesis and crystal structure of a new series of perovskite-like compounds CMn_7O_{12} (C = Na, Ca, Cd, Sr, La, Nd). *J. Solid State Chem.* **1974**, *11*, 88–93. [CrossRef]
15. Horowitz, H.S.; Longo, J.M. Phase relations in the Ca-Mn-O system. *Mater. Res. Bull.* **1978**, *13*, 1359–1369. [CrossRef]
16. Bochu, B.; Buevoz, J.L.; Chenavas, J.; Collomb, A.; Joubert, J.C.; Marezio, M. Bond lengths in $[CaMn_3](Mn_4)O_{12}$: A new Jahn–Teller distortion of Mn_3+ octahedral. *Solid State Commun.* **1980**, *36*, 133–138. [CrossRef]
17. Johnson, R.D.; Chapon, L.C.; Khalyavin, D.D.; Manuel, P.; Radaelli, P.G.; Martin, C. Giant improper ferroelectricity in the ferroaxial magnet $CaMn_7O_{12}$. *Phys. Rev. Lett.* **2012**, *108*, 067201. [CrossRef] [PubMed]
18. Johnson, R.D.; Khalyavin, D.D.; Manuel, P.; Bombardi, A.; Martin, C.; Chapon, L.C.; Radaelli, P.G. Modulated spin helicity stabilized by incommensurate orbital density waves in a quadruple perovskite manganite. *Phys. Rev. B* **2016**, *93*, 180403. [CrossRef]
19. Perks, N.J.; Johnson, R.D.; Martin, C.; Chapon, L.C.; Radaelli, P.G. Magneto-orbital helices as a route to coupling magnetism and ferroelectricity in multiferroic $CaMn_7O_{12}$. *Nat. Commun.* **2012**, *3*, 1277. [CrossRef] [PubMed]
20. Johnson, R.D.; Khalyavin, D.D.; Manuel, P.; Radaelli, P.G.; Glazkova, I.S.; Terada, N.; Belik, A.A. Magneto-orbital ordering in the divalent A-site quadruple perovskite manganites AMn_7O_{12} (A = Sr, Cd, and Pb). *Phys. Rev. B* **2017**, *96*, 054448. [CrossRef]
21. Locherer, T.; Dinnebier, R.; Kremer, R.K.; Greenblatt, M.; Jansen, M. Synthesis and properties of a new quadruple perovskite: A-site-ordered $PbMn_3Mn_4O_{12}$. *J. Solid State Chem.* **2012**, *190*, 277–284. [CrossRef]
22. Ovsyannikov, S.V.; Abakumov, A.M.; Tsirlin, A.A.; Schnelle, W.; Egoavil, R.; Verbeeck, J.; Van Tendeloo, G.; Glazyrin, K.V.; Hanfland, M.; Dubrovinsky, L. Perovskite-like Mn_2O_3: A path to new manganites. *Angew. Chem. Int. Ed.* **2013**, *52*, 1494–1498. [CrossRef]
23. Chen, W.T.; Wang, C.W.; Wu, H.C.; Chou, F.C.; Yang, H.D.; Simonov, A.; Senn, M.S. Improper ferroelectric polarization in a perovskite driven by intersite charge transfer and ordering. *Phys. Rev. B* **2018**, *97*, 144102. [CrossRef]
24. Troyanchuk, I.O.; Balyko, L.V.; Bashkirov, L.A. Crystal structure phase transitions in the perovskites $A(Cu_{1-x}Mn_x)Mn_4O_{12}$ (A = Na+, Ca_2+, Y_3+, La_3+). *Cryst. Res. Technol.* **1986**, *21*, 705–710. [CrossRef]
25. Slawinski, W.; Przenioslo, R.; Sosnowska, I.; Bieringer, M.; Margiolaki, I.; Fitch, A.N.; Suard, E. Phase coexistence in $CaCu_xMn_{7-x}O_{12}$ solid solutions. *J. Solid State Chem.* **2006**, *179*, 2443–2451.
26. Slawinski, W.; Przenioslo, R.; Sosnowska, I.; Bieringer, M.; Margiolaki, I.; Fitch, A.N.; Suard, E. Charge ordering in $CaCu_xMn_{7-x}O_{12}$ (x = 0.0 and 0.1) compounds. *J. Phys. Condens. Matter* **2008**, *20*, 104239.
27. Slawinski, W.; Przenioslo, R.; Sosnowska, I.; Bieringer, M. Structural and magnetic modulations in $CaCu_xMn_{7-x}O_{12}$. *J. Phys. Condens. Matter* **2010**, *22*, 186001. [PubMed]
28. Sławiński, W.; Przeniosło, R.; Sosnowska, I.; Bieringer, M.; Margiolakic, I.; Suard, E. Modulation of atomic positions in $CaCu_xMn_{7-x}O_{12}$ ($x \leq 0.1$). *Acta Crystallogr. Sec. B* **2009**, *65*, 535–542. [CrossRef] [PubMed]
29. Slawinski, W.; Przenioslo, R.; Sosnowska, I.; Petrícek, V. Helical screw type magnetic structure of the multiferroic $CaMn_7O_{12}$ with low Cu-doping. *Acta Crystallogr. Sec. B* **2012**, *68*, 240–249.
30. Glazkova, I.S.; Rusakov, V.S.; Sobolev, A.V.; Matsnev, M.E.; Gapochka, A.M.; Gubaidulina, T.V.; Presniakov, I.A. Probe Mössbauer diagnostics of charge ordering in manganites $CaCu_xMn_{7-x}O_{12}$ ($0 \leq x \leq 1$). *J. Exp. Theor. Phys.* **2019**, *129*, 1017–1028. [CrossRef]
31. Chenavas, J.; Joubert, M.; Marezio, J.C.; Bochu, B. The synthesis and crystal structure of $CaCu_3Mn_4O_{12}$: A new ferromagnetic-perovskite-like compound. *J. Solid State Chem.* **1975**, *14*, 25–32. [CrossRef]
32. Zeng, Z.; Greenblatt, M.; Subramanian, M.A.; Croft, M. Large low-field magnetoresistance in perovskite-type $CaCu_3Mn_4O_{12}$ without double exchange. *Phys. Rev. Lett.* **1999**, *82*, 3164–3167. [CrossRef]
33. Sánchez-Benítez, J.; Prieto, C.; de Andrés, A.; Alonso, J.A.; Martínez-Lope, M.J.; Casais, M.T. Evidence of two different states in $CaCu_3Mn_4O_{12}$ derivatives with colossal magnetoresistance. *Phys. Rev. B* **2004**, *70*, 024419. [CrossRef]
34. Zhang, Q.; Bréard, Y.; Guillou, F.; Hardy, V. Investigation of the magnetocaloric effect in double distorted perovskites $Ca(Cu_{3-x}Mn_x)Mn_4O_{12}$ ($1 \leq x \leq 2$): From standard ferrimagnetism to glassy ferrimagnetism. *Phys. Rev. B* **2011**, *84*, 224430. [CrossRef]
35. Volkova, O.; Goodilin, E.; Vasiliev, A.; Khomskii, D.; Tristan, N.; Kerschl, P.; Skourski, Y.; Mueller, K.-H.; Buechner, B. $CaCuMn_6O_{12}$ vs. $CaCu_2Mn_5O_{12}$: A comparative study. *J. Exp. Theor. Phys. Lett.* **2005**, *82*, 642–645. [CrossRef]
36. Zeng, Z.; Greenblatt, M.; Sunstrom, J.E.; Croft, M.; Khalid, S. Giant magnetoresistance in $CaCu_3Mn_4O_{12}$-based oxides with perovskite-type structure. *J. Solid State Chem.* **1999**, *147*, 185–198. [CrossRef]
37. Sánchez-Benítez, J.; Alonso, J.A.; Martínez-Lope, M.J.; Casais, M.T.; Martínez, J.L.; de Andrés, A.; Fernández-Díaz, M.T. Preparation, crystal and magnetic structure, and magnetotransport properties of the double perovskite $CaCu_{2.5}Mn_{4.5}O_{12}$. *Chem. Mater.* **2003**, *15*, 2193–2200. [CrossRef]
38. Yamada, I. Novel catalytic properties of quadruple perovskites. *Sci. Tech. Adv. Mater.* **2017**, *18*, 541–548. [CrossRef] [PubMed]

39. Samaras, D.; Bochu, B.; Joubert, J.C. Synthesis, composition, and magnetic properties of the ferrimagnetic $NdCu_{3-x}Mn_{4+x}O_{12}$ perovskite-like phases. *J. Solid State Chem.* **1984**, *53*, 323–328. [CrossRef]
40. Zhang, Q.; Bréard, Y.; Hardy, V. Spin-glass-like state and reversible room-temperature magnetocaloric effect in double distorted perovskites $Nd(Cu_{3-x}Mn_x)Mn_4O_{12}$. *Inorg. Chem.* **2022**, *61*, 5792–5799. [CrossRef] [PubMed]
41. Retuerto, M.; Martínez-Lope, M.J.; Sánchez-Benítez, J.; García-Hernández, M.; Fernández-Díaz, M.T.; Alonso, J.A. Synthesis, magnetic properties, and neutron diffraction study of the complex perovskites $R(Cu_{3-x}Mn_x)Mn_4O_{12}$ (R = Pr, Nd and x = 1, 2). *J. Appl. Phys.* **2010**, *108*, 083905. [CrossRef]
42. Sánchez-Benítez, J.; Alonso, J.A.; Falcón, H.; Martínez-Lope, M.J.; de Andrés, A.; Fernández-Díaz, M.T. Preparation under high pressures and neutron diffraction study of new ferromagnetic $RCu_3Mn_4O_{12}$ (R = Pr, Sm, Eu, Gd, Dy, Ho, Tm, Yb) perovskites. *J. Phys. Condens. Matter.* **2005**, *17*, S3063. [CrossRef]
43. Zhang, W.; Yao, L.D.; Yang, L.X.; Liu, Z.X.; Jin, C.Q.; Yu, R.C. Charge ordering in $PrCuMn_6O_{12}$ and its behavior under pressure. *J. Appl. Phys.* **2010**, *107*, 023914. [CrossRef]
44. Zhang, L.; Matsushita, Y.; Katsuya, Y.; Tanaka, M.; Yamaura, K.; Belik, A.A. Charge and orbital orders and structural instability in high-pressure quadruple perovskite $CeCuMn_6O_{12}$. *J. Phys. Condens. Matter.* **2018**, *30*, 074003. [CrossRef] [PubMed]
45. Sanchez-Benitez, J.; Alonso, J.A.; de Andres, A.; Martinez-Lope, M.J.; Martinez, J.L.; Munoz, A. Peculiar magnetic behavior of the $TbCu_3Mn_4O_{12}$ complex perovskite. *Chem. Mater.* **2005**, *17*, 5070–5076.
46. Alonso, J.A.; Sánchez-Benítez, J.; de Andrés, A.; Martínez-Lope, M.J.; Casais, M.T.; Martínez, J.L. Enhanced magnetoresistance in the complex perovskite $LaCu_3Mn_4O_{12}$. *Appl. Phys. Lett.* **2003**, *83*, 2623–2625. [CrossRef]
47. Muñoz, A.; Martínez-Lope, M.J.; Retuerto, M.; Falcón, H.; Alonso, J.A. Ferromagnetic behavior in $La(Cu_{3-x}Mn_x)Mn_4O_{12}$ (x = 1, 2) perovskites. *J. Appl. Phys.* **2008**, *104*, 083911. [CrossRef]
48. Sanchez-Benitez, J.; Alonso, J.A.; Martinez-Lope, M.J.; de Andres, A.; Fernandez-Diaz, M.T. Enhancement of the Curie temperature along the perovskite series $RCu_3Mn_4O_{12}$ driven by chemical pressure of R^{3+} cations (R = rare rarths). *Inorg. Chem.* **2010**, *49*, 5679–5685. [PubMed]
49. Sánchez-Benítez, J.; Martínez-Lope, M.J.; Alonso, J.A. Preparation at moderate pressures, crystal and magnetic structure and magnetotransport of the ferrimagnetic $CeCu_3Mn_4O_{12}$ perovskite. *J. Appl. Phys.* **2010**, *107*, 103904. [CrossRef]
50. Johnson, R.D.; Khalyavin, D.D.; Manuel, P.; Zhang, L.; Yamaura, K.; Belik, A.A. Magnetic structures of the rare-earth quadruple perovskite manganites RMn_7O_{12}. *Phys. Rev. B* **2018**, *98*, 104423. [CrossRef]
51. Belik, A.A.; Liu, R.; Zhang, L.; Terada, N.; Tanaka, M.; Yamaura, K. Multiple magnetic transitions and complex magnetic behaviour of the perovskite manganite $NdMn_7O_{12}$. *J. Solid State Chem.* **2022**, *309*, 122969. [CrossRef]
52. Belik, A.A.; Liu, R.; Yamaura, K. Phase separation phenomena in lightly Cu-doped A-site-ordered quadruple perovskite $NdMn_7O_{12}$. *Molecules* **2025**, *30*, 4561. [CrossRef] [PubMed]
53. Belik, A.A.; Matsushita, Y.; Khalyavin, D.D. Reentrant structural transitions and collapse of charge and orbital orders in quadruple perovskites. *Angew. Chem. Int. Ed.* **2017**, *56*, 10423. [CrossRef] [PubMed]
54. Belik, A.A.; Matsushita, Y.; Tanaka, M.; Johnson, R.D.; Khalyavin, D.D. A plethora of structural transitions, distortions and modulations in Cu-doped $BiMn_7O_{12}$ quadruple perovskites. *J. Mater. Chem. C* **2021**, *9*, 10232–10242. [CrossRef]
55. Brese, N.E.; O'Keeffe, M. Bond-valence parameters for solids. *Acta Crystallogr. Sec. B* **1991**, *47*, 192–197. [CrossRef]
56. Attfield, J.P. Charge ordering in transition metal oxides. *Solid State Sci.* **2006**, *8*, 861–867. [CrossRef]
57. Alonso, J.A.; Martinez-Lope, M.J.; Casais, M.T.; Fernandez-Diaz, M.T. Evolution of the Jahn-Teller distortion of MnO_6 octahedra in $RMnO_3$ perovskites (R = Pr, Nd, Dy, Tb, Ho, Er, Y): A neutron diffraction study. *Inorg. Chem.* **2000**, *39*, 917–923. [CrossRef] [PubMed]
58. Sánchez-Benítez, J.; Kayser, P.; Martínez-Lope, M.J.; de la Calle, C.; Retuerto, M.; Fernandez-Díaz, M.T.; Alonso, J.A. High-pressure preparation and characterization of new metastable oxides: The case of $NdCu_3Mn_3MO_{12}$ (M= Fe, Cr). *J. Phys. Conf. Ser.* **2011**, *325*, 012002. [CrossRef]
59. Kittel, C.; McEuen, P. *Introduction to Solid State Physics*; John Wiley & Sons, Inc.: New York, NY, USA, 2005.
60. Tanaka, M.; Katsuya, Y.; Matsushita, Y.; Sakata, O. Development of a synchrotron powder diffractometer with a one-dimensional X-ray detector for analysis of advanced materials. *J. Ceram. Soc. Jpn.* **2013**, *121*, 287–290. [CrossRef]
61. Izumi, F.; Ikeda, T. A Rietveld-analysis program RIETAN-98 and its applications to zeolites. *Mater. Sci. Forum* **2000**, *321–324*, 198–205. [CrossRef]

Disclaimer/Publisher's Note: The statements, opinions and data contained in all publications are solely those of the individual author(s) and contributor(s) and not of MDPI and/or the editor(s). MDPI and/or the editor(s) disclaim responsibility for any injury to people or property resulting from any ideas, methods, instructions or products referred to in the content.

inorganics

MDPI

Article

Wide-Bandgap A_2TiSiO_6 (A = Ca, Sr, Ba) Double Perovskites for Optoelectronic Applications

Łukasz Szeleszczuk [1,*], Katarzyna Mądra-Gackowska [2] and Marcin Gackowski [3]

[1] Department of Organic and Physical Chemistry, Medical University of Warsaw, 1 Banacha Str., 02-097 Warsaw, Poland
[2] Department of Geriatrics, L. Rydygier Collegium Medicum in Bydgoszcz, Nicolaus Copernicus University in Torun, 9 Skłodowskiej Curie Str., 85-094 Bydgoszcz, Poland; katarzyna.madra@cm.umk.pl
[3] Department of Toxicology and Bromatology, L. Rydygier Collegium Medicum in Bydgoszcz, Nicolaus Copernicus University in Torun, 2 Jurasza Str., 85-089 Bydgoszcz, Poland; marcin.gackowski@cm.umk.pl
* Correspondence: lukasz.szeleszczuk@wum.edu.pl; Tel.: +48-501-255-121

Abstract

The structural, mechanical, electronic, and optical properties of cubic double perovskite oxides A_2TiSiO_6 (A = Ca, Sr, Ba) were systematically investigated using first-principles density functional theory calculations. Structural optimization within the GGA–PBE framework confirms that all compounds crystallize in a stable cubic phase. The negative formation energies indicate thermodynamic stability and potential experimental synthesizability. Ab initio molecular dynamics (AIMD) simulations performed at 300 K further confirm the dynamical stability of all compounds under finite-temperature conditions. The Born–Huang stability criteria performed elastic constant analysis establishes mechanical stability and the derived mechanical moduli indicate the presence of rigid but brittle behavior with moderate amounts of elastic anisotropy. Calculation of the electronic band structure reveals that all the compounds are direct wide-bandgap semiconductors, with the HSE06 bandgaps of Ca_2TiSiO_6, Sr_2TiSiO_6 as well as Ba_2TiSiO_6 being 2.61, 2.50 and 2.37 eV, respectively. The optical property analysis has shown that they are strong in terms of their absorption in the visible–ultraviolet region, with high dielectric constants and good refractive indices, which makes them appropriate in optoelectronics and photovoltaic applications. On the whole, A_2TiSiO_6 double perovskites are promising for use as wide-bandgap materials in the development of superior optoelectronic devices.

Keywords: DFT; thermodynamic stability; elastic properties; direct bandgap; optical properties

1. Introduction

Double perovskite oxides (DPOs) represent an important and highly versatile class of materials, distinguished by their remarkable chemical flexibility and the vast range of possible compositions and structures. These materials typically crystallize in the $A_2BB'O_6$ structure, where A denotes a rare-earth or alkaline-earth metal, B and B′ are transition-metal cations, and O represents oxygen. Owing to this flexible composition, DPOs exhibit a wide variety of unusual and technologically valuable chemical and physical properties [1–3]. These include diverse electronic behaviors such as insulating and metallic states [4], half-metallic spin-polarized conductivity [5], superconductivity, and strong magnetoresistance effects [6–8]. Moreover, DPOs exhibit ionic conductivity, catalytic behavior, ferroelectric and piezoelectric behavior as well as serves as an electrolyte material in fuel cells [9]. In

addition, the operation and improvement of the solar cells depend greatly on the use of the double perovskite oxides [10,11]. DPO materials have attracted much experimental and theoretical attention in the last several years due to their exceptional properties and their technological perspectives [12–14].

The attention of double perovskite oxides has been focused because they exhibit significant magnetoresistance and half-metallic properties, and they are also deemed as significant substances in solar cells and optoelectronic devices [15–18]. The twenty-first century has seen the intensive search of half-metallic (HM) materials that are attractive to spintronic devices, the electron spin degree of freedom which is used to process information and store data. Other material systems have also recently been reported to have half-metallicity, including Heusler alloys [19–21]. A high polarization level, i.e., half-metals with 100 percent spin polarization, is essential in the development of high-performance spin-based devices. The new HM materials, in particular, the double perovskite oxides are of interest as they offer structural as well as compositional flexibility, high spin polarization, and sustained ferromagnetism, often even beyond room temperature [22].

In the last ten years, a wide range of DPOs with divalent alkaline-earth cations (Sr, Ca, and Ba) at the A site, with 3d and 4d/5d transition-metal ions at the B and B sites, have been characterized computationally by density functional theory (DFT) [23–25]. In more recent publications, a number of Ba-based DPOs have been given a significant amount of attention due to their half-metallic character and stability in the cubic form [26,27]. The overall structure of such oxides with transition metals may be expressed as Z_2XMO_6 with Z being an alkaline-earth element, and X and M being the octahedral site elements. The structural, electronic, magnetic, and optical properties can be tailored by substitution of the Z, X, and M sites with alkaline-earth, transition-metal, or other metallic cations. Therefore, one of the key aims of the existing studies is to examine the connection between cation replacement and the resulting structural, electronic, elastic, magnetic, and optical properties of the Z_2XMO_6 compounds.

Of the TMDP oxides, tantalum (Ta)-based materials have been studied extensively experimentally and theoretically, such as Sr_2XTaO_6 (X = Cr, Mn) [28,29], Ba_2ScTaO_6 [30] A_2CrTaO_6 (A: Sr, Ca) [31], Ba_2InTaO_6 [32], A_2SmTaO_6 (A = Ba, Sr, Ca) [33], Ba_2YTaO_6 [34], Ba_2MTaO_6 (M = Cr, Mn, Fe) [35]. In recent years, optoelectronic and magnetic applications have also received a lot of attention in DPOs on the basis of their structural stability and elevated Curie temperature. Theoretically, low-temperature ferromagnetism has been observed in Dy_2NiMnO_6, La_2NiMnO_6 and Lu_2NiMnO_6 DPOs with bandgap values ranging from 1.2 to 1.6 eV [36–39]. Re-based double perovskites like X_2FeReO_6 (X = Ba, Sr, Ca) have also been reported to show ferromagnetic behavior useful in spintronic applications, with the 5d electrons of Re also providing intrinsic magnetic moments [40,41]. Silicate-based perovskites, where silicon (Si) is the center of interest, in particular, are receiving increasing attention due to their tunable physical characteristics, phase transitions triggered by pressure, and their possible technological uses [14]. The cubic quaternary double perovskite Ca_2TiSiO_6 is of special interest in this category. It crystallizes in cubic $Fm\overline{3}m$ space group (No. 225), with Ti and Si fully ordered in alternating octahedral positions, Ca distorted cubo-octahedral coordinated. Leinenweber, Kurt and Parise experimentally optimized the crystal structure of Ca_2TiSiO_6 and reported a lattice constant of a = 7.4105 Å [42]. Also, Husain et al. [43] conducted a theoretical study on the physical properties of the Ca_2TiSiO_6.

Despite these studies, the alkaline-earth analogs Sr_2TiSiO_6 and Ba_2TiSiO_6 remain largely unexplored, both experimentally and theoretically. In this context, the present work provides a systematic first-principles investigation of the structural, mechanical, and optoelectronic properties of silicon-based A_2TiSiO_6 (A = Ca, Sr, Ba) double perovskite oxides. While Ca_2TiSiO_6 has been experimentally realized, the Sr and Ba counterparts are reported

https://doi.org/10.3390/inorganics14050130

here for the first time as theoretically predicted compounds. This enables a comprehensive analysis of A-site cation substitution (Ca → Sr → Ba), where variations in ionic size and polarizability influence lattice structure, Ti–O–Si hybridization, and electronic interactions, resulting in tunable bandgaps and optical responses. By establishing a direct link between A-site substitution, orbital interactions, and dielectric behavior, this study provides deeper insight beyond conventional trend analysis and supports the rational design of wide-bandgap double perovskites for optoelectronic and renewable energy applications.

2. Results and Discussion

2.1. Structural Properties

The parent compound of the current study, the quaternary silicon-based ordered double perovskite oxide Ca_2TiSiO_6, was first experimentally described by Kurt Leinenweber and John Parise in 1997 [42]. Their experiment proved that Ca_2TiSiO_6 forms with a cubic structure with a space group $Fm\overline{3}m$ (No. 225) and an experimental lattice constant of a_0 = 7.4105 Å. The (1/4, 1/4, 1/4) Wyckoff position is occupied by Ca atoms, Ti atoms occupy the (1/2, 1/2, 1/2) position, Si atoms occupy the (0, 0, 0) and O atoms occupy the (0.2372, 0, 0) position.

Motivated by the experimentally confirmed structural stability and successful synthesis of this parent compound, the present study extends the investigation to the isostructural series A_2TiSiO_6 (A = Ca, Sr, Ba), in which the A-site Ca cation is systematically substituted by Sr and Ba. This substitution strategy enables a direct assessment of how A-site cation size and chemistry influence the structural characteristics of the silicon-based ordered double perovskite framework.

Figure 1 illustrates the cubic unit cell of the silicon-based double perovskite structure using Ca_2TiSiO_6 as the representative model, visualized through a ball-and-stick representation.

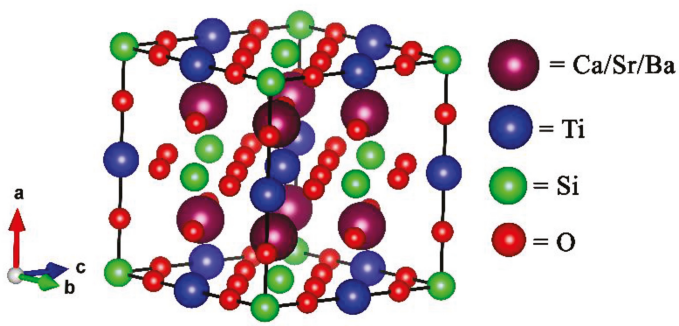

Figure 1. Unit cell of A_2TiSiO_6 (A = Ca, Sr, Ba) compounds.

In the case of the first-principles computations, the crystallographic parameters were used as the starting input structure that were experimentally reported. Complete structural optimization was then done in the context of density functional theory (DFT) with the generalized gradient approximation (GGA) of the exchange correlation functional. During the optimization process, both lattice parameters and internal atomic coordinates were allowed to relax freely until the total energy reached its minimum, yielding the structural ground state of each compound. From the optimized configurations, the equilibrium structural parameters, including the optimized lattice constant (a_0) and the optimized unit cell volume (V) were obtained for all investigated materials.

To determine the thermodynamic stability of the A_2TiSiO_6 (A = Ca, Sr, Ba) compounds, the formation energy (E_f) was determined. Formation energy is also one of the indicators of energetic favorability and it gives an idea whether experimental synthesis could be

feasible. The energy per atom of the formation was calculated by use of the following expression [44]:

$$E_f = \frac{E_{A_2TiSi_6 - n_A \times E_A - n_{Ti} \times E_{Ti}} - n_{Si} \times E_{Si} - n_O \times E_O}{N} \quad (1)$$

where $E_{A_2TiSiO_6}$ is the overall energy of the optimum unit cell of the double perovskite oxide, E_A, E_{Ti}, E_{Si}, and E_O is the total energy of the elemental species (A = Ca, Sr, Ba) in their respective reference states. The N_A, N_{Ti}, N_{Si}, and N_0 represent the number of atoms in the formula unit corresponding to the atoms, and N represents the number of atoms in the formula unit, which is 10 in A_2TiSiO_6.

The calculated formation energies of all investigated compounds are negative, as summarized in Table 1, confirming their thermodynamic stability. These negative values indicate that the formation of A_2TiSiO_6 compounds from their constituent elements is energetically favorable, implying that the materials are intrinsically stable and, in principle, experimentally synthesizable.

Table 1. The lattice constant a_0 (Å), the unit cell volume (V), and formation energy (E_f) (eV/atom) for double perovskite of A_2TiSiO_6 (A = Ca, Sr, Ba) compounds.

Compounds	a (Å)	V (Å^3)	E_f	Ref
Ca_2TiSiO_6	7.4951	421.04	−3.149	This study
	7.4100	406.86		[42]
Sr_2TiSiO_6	7.6292	444.06	−2.824	This study
Ba_2TiSiO_6	7.8372	481.38	−2.324	This study

2.2. Dynamical Stability

Ab initio molecular dynamics (AIMD) simulations were performed at room temperature (300 K) to examine the thermal stability of Ca_2TiSiO_6, Sr_2TiSiO_6, and Ba_2TiSiO_6 through the evolution of their total energies with time (Figure 2). For all three compounds, the total energy fluctuations remain small and well confined within narrow ranges throughout the 10 ps simulation window, indicating stable dynamical behavior under ambient thermal conditions.

Ca_2TiSiO_6 exhibits slightly larger energy fluctuations (~0.0030%) compared to Sr_2TiSiO_6 (~0.0010%) and Ba_2TiSiO_6 (~0.0011%), suggesting relatively higher lattice flexibility or vibrational activity in the Ca-based compound. In contrast, the Sr- and Ba-based systems show more tightly bounded energy variations, reflecting enhanced thermal robustness and stronger lattice stability. The rapid stabilization of the energy profiles after the initial transient region further confirms that all systems quickly reach thermal equilibrium.

The small differences between the maximum, minimum, and mean energies indicate the absence of structural instabilities, bond breaking, or phase transitions over the simulation time scale. These results confirm the dynamical stability of all three compounds at room temperature, validating their structural robustness under realistic thermal conditions. Furthermore, the comparatively lower energy fluctuations observed in Sr_2TiSiO_6 and Ba_2TiSiO_6 suggest that heavier alkaline-earth cations contribute to enhanced lattice stabilization, supporting their suitability for applications where thermal stability is critical. It is also important to note that, in the present work, structural stability has been primarily evaluated using formation energy calculations together with AIMD simulations at 300 K. These approaches provide strong evidence for both thermodynamic and finite-temperature dynamical stability. While additional analyses such as phonon dispersion and Goldschmidt tolerance factor calculations could further complement the stability assessment, they are beyond the current scope of this study and will be addressed in future

work for a more detailed vibrational and structural investigation. Moreover, a comprehensive competing-phase stability analysis has not been performed in the present study; however, it is acknowledged as an important aspect for fully establishing phase stability and experimental feasibility, and will be considered in future work.

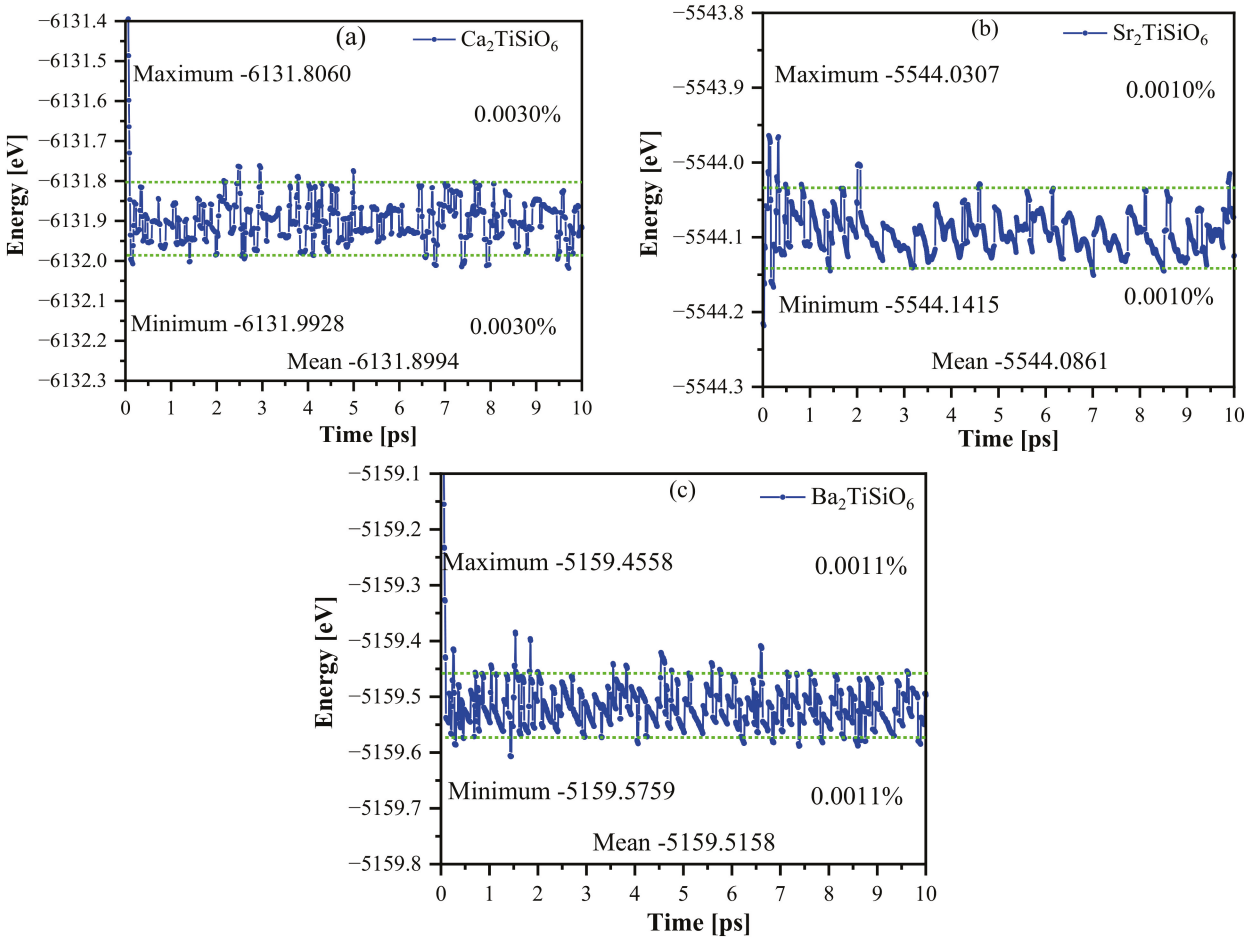

Figure 2. Ab Initio Molecular Dynamics (AIMD) simulations at room temperature (300 K) for total energy fluctuations with time for (**a**) Ca_2TiSiO_6, (**b**) Sr_2TiSiO_6, and (**c**) Ba_2TiSiO_6 compounds.

2.3. Mechanical Properties

The mechanical properties of materials are essential for evaluating their structural stability, reliability, and functional performance during fabrication and practical application. Throughout processing and device integration, materials are frequently exposed to external stresses, making it necessary to understand their elastic behavior and interatomic force interactions at the atomic scale prior to utilization [45]. C_{ij} are the elastic stiffness constants which are the fundamental parameters that directly describe mechanical strength and stability of crystalline solids. Mechanical stability of cubic X_2TiSiO_6 (X = Ca, Sr, Ba) compounds were studied based on the theory of elastic stability of Born–Huang. In the case of a cubic crystal structure, the criteria of mechanical stability are [46]:

$$C_{11} - C_{12} > 0 \tag{2}$$

$$C_{11} + 2C_{12} > 0 \tag{3}$$

$$C_{44} > 0 \tag{4}$$

The conditions provide stability to tetragonal shear deformation, volume compression resistance and stability to shear strain, respectively. A comparatively low C_{12} shows that it is more compressible along the respective crystallographic direction [47].

Table 2 presents the calculated elastic coefficients C_{11}, C_{12}, and C_{44} of A_2TiSiO_6 (A = Ca, Sr, Ba). The compounds all meet the mechanical stability requirements in terms of the equations and attests to their mechanical stability in the cubic form [46]. C_{11} is relatively large, which means that the material is highly resistant to uniaxial deformation, and Ca_2TiSiO_6 has the highest stiffness of the examined materials. The good shear deformation resistance is indicated by the appreciable C_{44} values.

Table 2. Calculated elastic constants (all in GPa) of A_2TiSiO_6 (A = Ca, Sr, Ba) compounds.

Compounds	C_{11}	C_{12}	C_{44}	$C_{11} - C_{12}$	$C_{11} + 2C_{12}$
Ca_2TiSiO_6	341.66	98.33	134.05	243.33	538.32
Sr_2TiSiO_6	302.34	88.39	156.19	391.33	479.72
Ba_2TiSiO_6	275.20	123.52	151.41	398.72	522.24

Moreover, the positive values of $C_{11} - C_{12}$ are indicative that the cubic form is resistant to tetragonal shear deformation, whereas the positive values of $C_{11} + 2C_{12}$ are indicative of a high degree of resistance to uniform compression. Such characteristics indicate high interatomic bonding and mechanically stable cubic phases. The macroscopic elastic parameters were obtained in the form of the Voigt–Reuss–Hill averaging scheme, which is a good compromise between the Voigt and Reuss approximations to determine isotropic mechanical properties [48–50]. The main mechanical descriptors are calculated by the following way:

$$B = \frac{C_{11} + 2C_{12}}{3} \tag{5}$$

$$A = \frac{2C_{44}}{C_{11} - C_{12}} \tag{6}$$

$$\xi = \frac{(C_{11} + 8C_{12})}{7(C_{11} + 2C_{12})} \tag{7}$$

$$Y = \frac{9BG}{3B + G} \tag{8}$$

$$\nu = \frac{3B - 2G}{6B + 2G} \tag{9}$$

$$R_P = \frac{B}{G} \tag{10}$$

$$R_f = \frac{G}{B} \tag{11}$$

$$CP = C_{12} - C_{44} \tag{12}$$

Table 3 shows the calculated values of the bulk modulus (B), shear modulus (G), Young modulus (Y), Poisson ratio (ν), Pugh's ratio (R_P), Frantsevich's ratio (R_f), internal strain factor (ξ), Cauchy pressure (CP), and Zener anisotropy factor (A) of A_2TiSiO_6 (A = Ca, Sr, Ba). The values of the Young's modulus of all compounds are stiffer than the values of the bulk modulus which denote that the compounds will not undergo elastic deformation easily and the compounds are very rigid in their mechanical properties [51].

The increased values of bulk modulus indicate excellent crystal formation and low compressibility. Poisson ratios claim that brittle and ductile materials have a ν of less than 0.26 and over 0.26, respectively [52]. All A_2TiSiO_6 compounds have a calculated value of Poisson's ratio that is less than 0.26, which means that they act brittle. Cauchy

pressure is also in favor of this classification. The negative CP values of all the compounds obtained represent directional (covalent) bonding and brittle nature [53]. In the same manner, the Pugh calculated ratios ($R_P < 1.75$) substantiate brittleness, and the ratios values of Frantsevich's ($R_f > 0.571$) support this finding [51,53].

Table 3. Calculated elastic modulus like the bulk modulus (B), the shear modulus (G), Young's modulus (Y), Poisson's ratio (ν), the Pugh's ratio (R_P), Frantsevich's ratio (R_f), internal strain factor (ξ), Cauchy pressure (CP) and the Zener anisotropy factor (A) for A_2TiSiO_6 (A = Ca, Sr, Ba) compounds.

Compounds	B (GPa)	G (GPa)	Y (GPa)	ν	R_P	R_f	ξ	CP (GPa)	A
Ca_2TiSiO_6	179.44	128.95	312.10	0.210	1.391	0.718	0.299	−35.72	1.101
Sr_2TiSiO_6	159.70	134.21	314.52	0.171	1.189	0.840	0.300	−67.8	1.460
Ba_2TiSiO_6	174.08	114.72	282.18	0.229	1.517	0.659	0.345	−27.98	1.996

The internal strain factor (ξ) is a factor of the resistance of the lattice to internal distortions and is a ratio to the distribution of interatomic forces in the crystal [51]. Values nearer to 1 mean that the crystal is strained in a uniform manner due to stress, whereas values below 1 imply that internal deformation is non-uniform and that the forces are not distributed in an anisotropic manner. In the case of A_2TiSiO_6 compounds, the computed ξ values (Table 3) lie between 0.299, 0.300 and 0.345 and this suggests moderate internal anisotropy. This suggests that the cubic lattice is mechanically stable, but the atomic interactions inside the lattice are a little non-uniform, which is complimentary to the observation of the Zener anisotropy factor ($A \neq 1$) and confirms that these compounds are indeed anisotropic in their elastic behavior at the atomic level. Zener anisotropy factor is not equal to unity in all compounds, which means there is some elastic anisotropy.

Table 4 shows the calculated density (ρ), longitudinal (V_l) and transverse (V_t) and average (V_m) sound velocities as well as the Debye temperature (θ_D) of the cubic double perovskite A_2TiSiO_6 (A = Ca, Sr, Ba) compounds. One of the key thermodynamic parameters is the Debye temperature, which can be used to describe lattice vibrations and is directly connected to such elementary characteristics as the heat capacity, entropy, thermal expansion and thermal conductivity of solids [54]. It also gives an understanding of the interatomic bonding strength and the stiffness of the lattice. The average sound velocity was used to determine the Debye temperature as follows [55]:

$$\theta_D = \frac{h}{k_B}\left[\frac{\left(\frac{3n}{4\pi}\right)N_A\rho}{M}\right]V_m \tag{13}$$

where h is the Planck constant, k_B is the Boltzmann constant, n is the number of atoms in one formula unit, N_A is Avogadro's number, M is the molecular weight, and V_m is the average sound velocity. The longitudinal and transverse sound velocities gave the average sound velocity by:

$$V_m = \left[\frac{1}{3}\left(\frac{1}{v_l^3} + \frac{2}{v_t^3}\right)\right]^{\frac{-1}{3}} \tag{14}$$

Table 4. Calculated density (ρ), transverse, longitudinal, average sound velocity (v_t, v_m, v_l), Debye temperatures (θ_D) and melting temperature (T_m) of Double Perovskite Compounds A_2TiSiO_6 (A = Ca, Sr, Ba) compounds.

Compounds	ρ (kg/m^3)	V_l (m/s)	V_t (m/s)	V_m (m/s)	θ_D (K)	T_m
Ca_2TiSiO_6	6800.96	6230.01	3554.77	3950.49	491.29	2572.25
Sr_2TiSiO_6	3976.49	9400.14	5694.56	6293.59	855.88	2339.84
Ba_2TiSiO_6	5192.39	8075.87	5084.03	5596.12	747.64	2179.46

https://doi.org/10.3390/inorganics14050130

The transverse and longitudinal sound velocities were calculated from the elastic moduli and density as:

$$V_t = [G/\rho]^{\frac{1}{2}} \text{ and } V_l = [(3B + 4G)/3\rho]^{\frac{1}{2}} \tag{15}$$

As Table 4 demonstrates, Sr_2TiSiO_6 has the greatest longitudinal, transverse and average sound velocities and as expected this compound has the highest Debye temperature of the compounds being studied. Conversely, Ca_2TiSiO_6 exhibits lower sound velocities and lower Debye temperature, which implies a weaker lattice stiffness. Ba_2TiSiO_6 exhibits an intermediate behavior to the compounds of Ca and Sr. Debye temperature contrast is very much related to the sound velocities and the elastic moduli, which prove that lattice dynamics and mechanical rigidity have a strong dependence.

The values of higher Debye temperatures are usually associated with a stronger interatomic bond, phonon frequencies, and thermal conductivity [56,57]. Thus, the Debye temperature of Sr_2TiSiO_6 is relatively high implying higher thermal stability and resistance against lattice vibrations, so it can be used in applications that are characterized by high thermal stability. In general, the analysis of the Debye temperature proves the high mechanical strength and good thermodynamic properties of the cubic A_2TiSiO_6 double perovskites compounds.

Table 4 also indicates the melting temperatures that represent the elastic properties of the materials. Generally, materials that are more elastic rigid have a greater bond among atoms and, therefore, greater thermal resistance. In the case of cubic crystals, we can estimate the melting temperature by the empirical relation [47]

$$T_m = (553 + 5.91C_{11})K \tag{16}$$

which shows that a rise in the elastic constant C_{11} is directly proportional to an increase in the melting temperature. Table 4 illustrates a decreasing trend in the melting temperature (T_m) as the compounds were studied. This practice is explained by differences in elastic stiffness and bonding strength, in which the compounds that have high elastic moduli show better thermal stability.

2.4. Electronic Properties

2.4.1. Band Structure

The electronic band structure of a substance gives a basic understanding of its conductivity and forms a direct correlation between the optical and electronic properties of the material and the crystal structure [58]. The band structure, density of states (DOS) and the density of charge are important parameters used to determine the appropriateness of materials to be used in optoelectronic devices. This section will present and analyze in details the calculated band structure, density of states and charge density distribution of the double perovskite A_2TiSiO_6 (A = Ca, Sr, Ba) compounds by Density Functional Theory (DFT) (Table 5).

Table 5. Calculated bandgap values in (eV) of A_2TiSiO_6 (A = Ca, Sr, Ba) compounds.

Compounds	**Ca_2TiSiO_6**	**Sr_2TiSiO_6**	**Ba_2TiSiO_6**
GGA PBE	2.409	2.309	2.212
HSE06	2.610	2.501	2.372
Nature	Direct	Direct	Direct

Both the GGA–PBE and HSE06 exchange correlation functional were used to compute the electronic bandgaps of A_2TiSiO_6 (A = Ca, Sr, Ba), and the results were summarized

in Table 2. The dispersion of the conduction and valence bands, especially around the high-symmetry points of the first Brillouin zone, is highly desired to determine the nature of the bandgap and the electronic transitions possible. According to Figure 3, the three A_2TiSiO_6 compounds all have a direct bandgap, and both the valence band maximum (VBM) and conduction band minimum (CBM) are at the Γ-point. This direct bandgap property gives it an advantage in obtaining an efficient optical absorption and electron to hole pair generation, which can be used in optoelectronic and photovoltaic devices. Moreover, the bandgaps calculated with the HSE06 put these materials in the wide-bandgap semiconductor regime, and this aspect suggests their applications in the stable optoelectronic devices of ultraviolet and visible light.

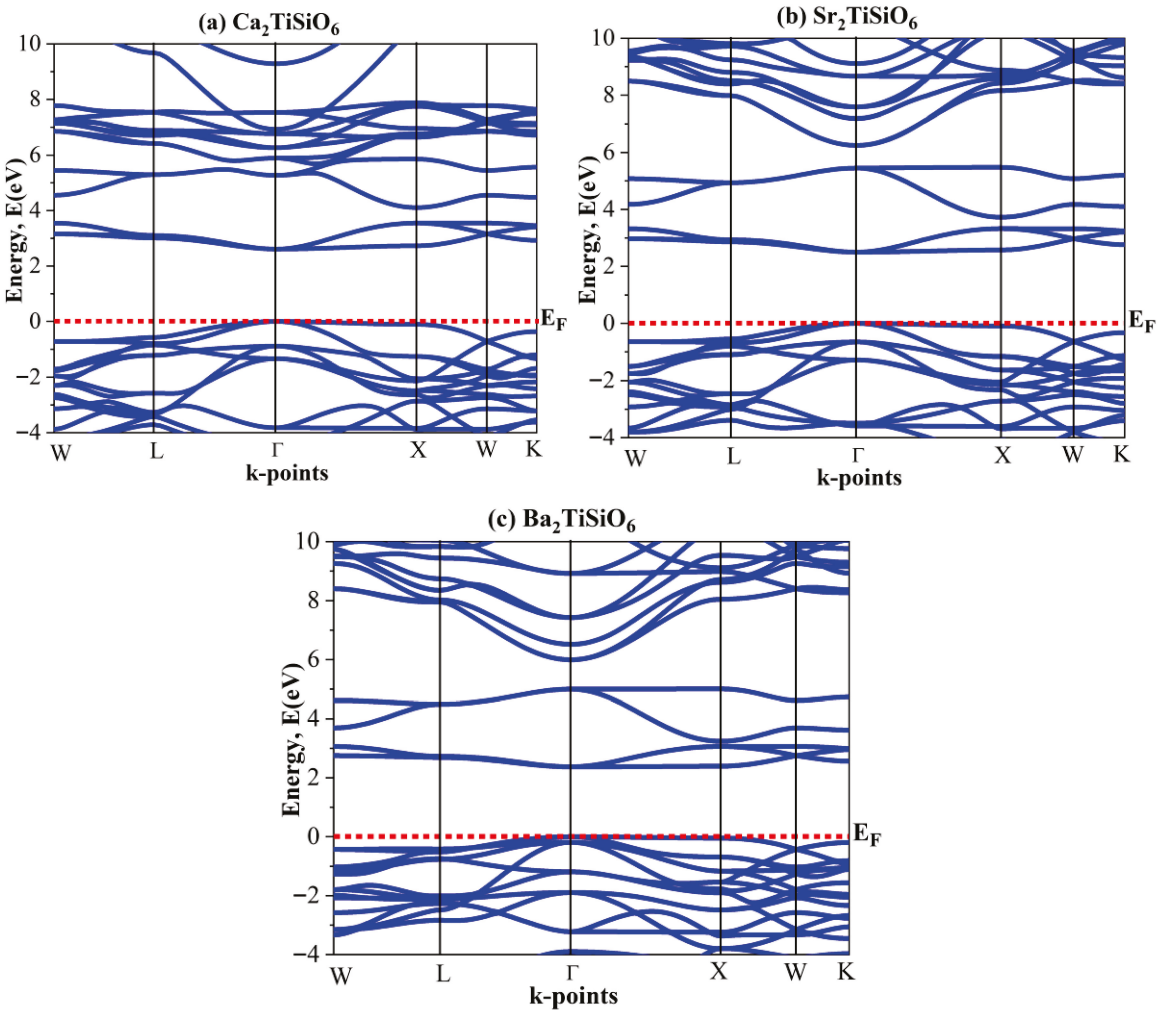

Figure 3. Computed electronic band structures of (**a**) Ca_2TiSiO_6, (**b**) Sr_2TiSiO_6, and (**c**) Ba_2TiSiO_6 compounds.

2.4.2. Density of State (DOS)

Figure 4a–c shows the total and partial density of states (TDOS and PDOS) of A_2TiSiO_6 (A = Ca, Sr, and Ba) calculated with HSE06 hybrid. All those figures indicate clearly that the valence and conduction bands do not intersect the Fermi energy level at all, which proves that all three compounds of the double perovskite are semiconducting.

The total and partial density of state (DOS) shows that there are common electronic characteristics within the series. The O-2*p* states, which are mainly O-2*p* states with some hybridization of Ti-3*d* orbitals are the dominant structure in the region of 0–6 eV, which means that the bond between Ti and O is strong. The alkaline-earth metal atoms (Ca, Sr, and

Ba) play an insignificant role at the Fermi level, which implies that they play an insignificant role in charge transport. Conduction band is above Fermi level, and it is dominated by Ti-3*d* orbital, with minor contributions of Si-*p* and O-*p* orbital. The DOS intensity, especially in the conduction band, shows a gradual increase between Ca_2TiSiO_6 and Ba_2TiSiO_6 that could be explained by increased orbital contributions of the heavier A-site cation. The zero-point energy of the DOS at the Fermi level also proves the semiconducting nature of the systems studied.

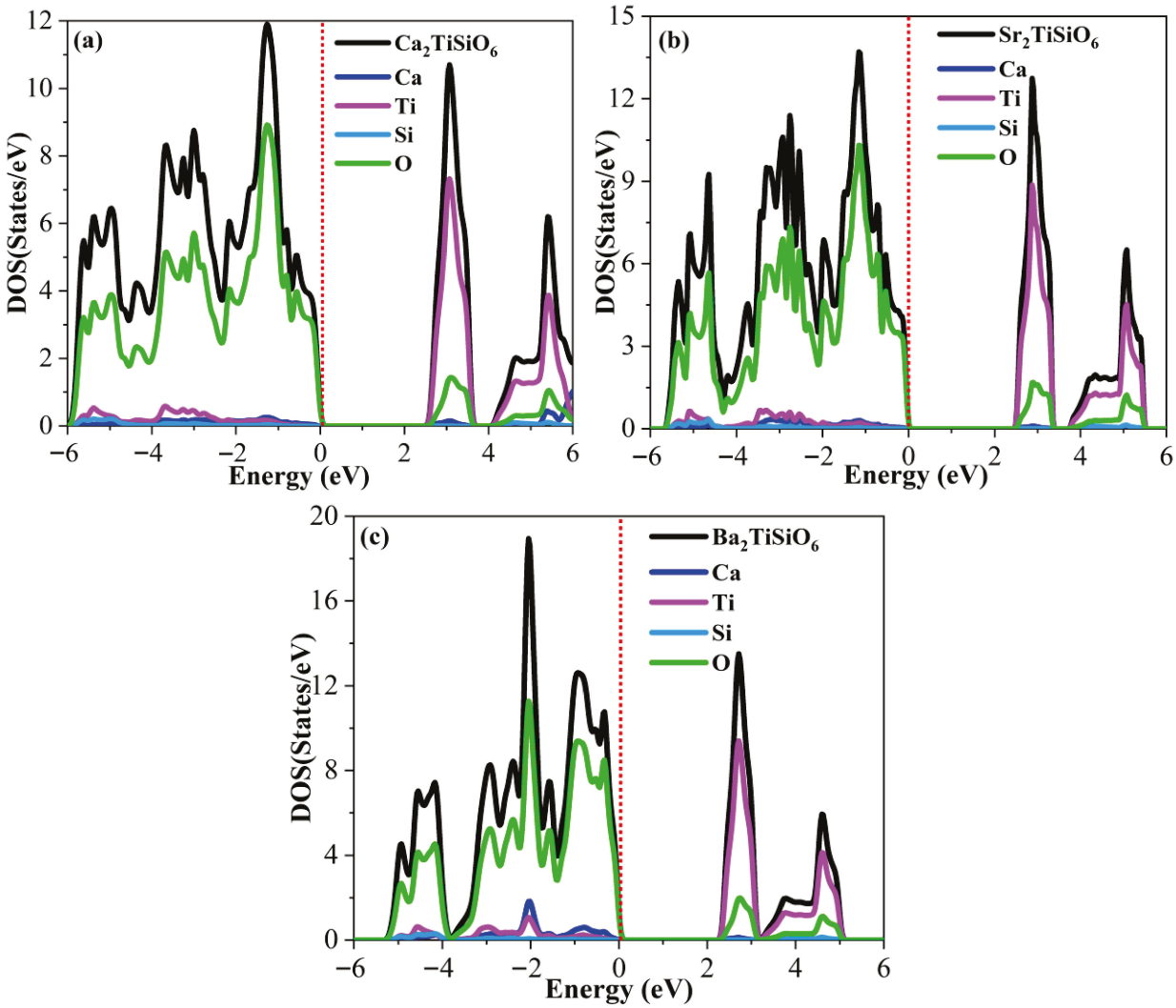

Figure 4. The total and partial density of states of (**a**) Ca_2TiSiO_6, (**b**) Sr_2TiSiO_6, and (**c**) Ba_2TiSiO_6 compounds.

2.4.3. Charge Density

The analysis of charge density is important in the study of the nature of chemical bonding and the mechanism of charge transfer in crystalline materials. Figure 5a–c shows maps of charge density difference $\Delta n\ (r)$ of A_2TiSiO_6 (A = Ca, Sr, Ba), which are a direct measure of the way electronic charge has been redistributed during the formation of the bonds. A large amount of charge accumulation has been observed around the O atoms in all three compounds and the equivalent amount of charge depletion around the A-site cations (Ca/Sr/Ba) and in part around Ti atoms. This indicates that the electron is being transferred off the electropositive atoms in the A-site, along with the Ti atoms to the less electronegative oxygen atoms, which points to the fact that the A–O bonds are predominantly ionic. In the meantime, the accumulated charge along the Ti-O bonds is observable indicating a high

degree of orbital hybridization, indicating the presence of mixed ionic-covalent character of bonds. Gradual charge transfer occurs between Ca_2TiSiO_6 and Ba_2TiSiO_6 which may be explained by the growing ionic radius and electro positivity of the A-site cation.

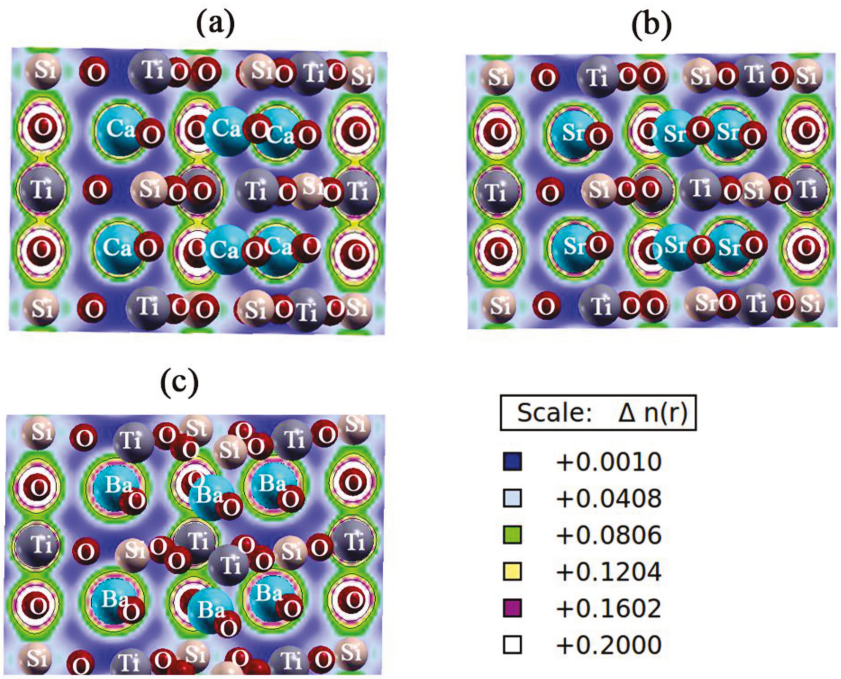

Figure 5. Change density of (**a**) Ca_2TiSiO_6, (**b**) Sr_2TiSiO_6, and (**c**) Ba_2TiSiO_6 compounds.

2.5. Optical Properties

The photovoltaic performance of solar cell devices is strongly governed by the optical properties of the constituent materials, which play a decisive role in the selection of high-efficiency photovoltaic absorbers and are intrinsically linked to their electronic structures [59]. When incident electromagnetic radiations interact with a material, they cause optical responses that determine the efficiency of photon absorption and energy conversion [60,61]. Here, a high optical absorption and a high dielectric constant is very desirable. In this work, all optical properties have been calculated using the HSE06 hybrid functional to ensure improved accuracy in describing the electronic structure and related optical response. In the linear response theory, optical properties of a material are characterized by the complex, frequency dependent dielectric function $\varepsilon(\omega)$, which is given by [61,62]:

$$\varepsilon(\omega) = \varepsilon_1(\omega) + i\varepsilon_2(\omega) \tag{17}$$

where $\varepsilon_1(\omega)$ and $\varepsilon_2(\omega)$ are the real and imaginary components of the dielectric tensor, respectively. The real component $\varepsilon_1(\omega)$ represents the polarization response of the material to the incident electromagnetic field, and the imaginary component $\varepsilon_2(\omega)$ is the absorption of electromagnetic radiation [63,64]. Fundamental material properties such as electronic band structure, lattice vibrations, impurity states and excitonic effects can also be determined through optical properties [60,61]. The Kramers–Kronig relations relate the real and imaginary part of the dielectric function [65]:

$$\varepsilon_1(\omega) = \frac{2}{\pi}\rho\int_0^\infty \frac{\omega'^2\varepsilon_2\omega}{\omega'^2 - \omega^2} \tag{18}$$

$$\varepsilon_2(\omega) = \frac{-2}{\pi}\rho\int_0^\infty \frac{\omega'^2\varepsilon_2\omega}{\omega'^2 - \omega^2} \tag{19}$$

where ρ represents the principal of the integral.

Based on the dielectric function calculated, a number of optical parameters were obtained of A_2TiSiO_6 (A = Ca, Sr, Ba) such as reflectivity $R(\omega)$, the refractive index $n(\omega)$, the extinction coefficient $k(\omega)$, the optical conductivity $\sigma(\omega)$, the electron energy loss function $L(\omega)$, and absorption coefficient $\alpha(\omega)$ over the photon energy range 0–25 eV. The HSE06 hybrid functional was used to calculate all the results. The dielectric function is connected with the optical constants in the following way:

$$\sigma(\omega) = \frac{\omega}{4\pi}\varepsilon_2(\omega) \tag{20}$$

$$n(\omega) = \sqrt{\frac{|\varepsilon(\omega)| + \varepsilon_1(\omega)}{2}} \tag{21}$$

$$K(\omega) = \sqrt{\frac{|\varepsilon(\omega)| - \varepsilon_1(\omega)}{2}} \tag{22}$$

$$L(\omega) = \frac{\varepsilon_2}{\varepsilon_1^2 + \varepsilon_2^2} \tag{23}$$

$$R(\omega) = \frac{(n-1)^2 + k^2}{(n+1)^2 + k^2} \tag{24}$$

$$\alpha(\omega) = \sqrt{2}\omega\left(\frac{\varepsilon_1(\omega)^2 + \varepsilon_2(\omega)^2 - \varepsilon_1(\omega)}{2}\right)^{\frac{1}{2}} \tag{25}$$

Importantly, the spectral features of $\varepsilon_2(\omega)$ are directly associated with interband transitions between O-2p dominated valence band states and Ti-3*d* dominated conduction band states, as confirmed from the electronic density of states analysis. Thus, the major peaks in the dielectric spectra can be explicitly correlated with these orbital-resolved transitions.

The interband electronic transitions in the investigated alkaline-earth titanate silicates A_2TiSiO_6 (A = Ca, Sr, Ba) contribute directly to their calculated dielectric functions and are intrinsically linked to their electronic band structures. Figure 6a presents the real part of the dielectric function, $\varepsilon_1(\omega)$, as a function of photon energy. The low-energy (static) limit of this function yields the static dielectric constant, $\varepsilon_1(0)$, which is directly proportional to the electronic polarizability of the materials. The $\varepsilon_1(0)$ values at rest are 4.68, 4.89, and 5.47 of $Ca_2Ti\ SiO_6$, Sr_2TiSiO_6, and $Ba_2Ti\ SiO_6$ respectively. The growing trend shows that the polarizability improves as the ionic radius of the alkaline-earth metal increases. The gradual increase in $\varepsilon_1(0)$ from Ca to Ba reflects enhanced electronic polarizability due to the larger ionic radius and more delocalized electronic cloud, which is beneficial for dielectric and optoelectronic device applications. This large dispersion at low photon energies can be primarily connected with the transitions which depend on the bandgap and the appearance of negative $\varepsilon_1(\omega)$ at higher energies indicates plasma-like behavior and high reflectivity. The energy range where $\varepsilon_1(\omega)$ becomes negative corresponds to the screened plasma frequency, indicating strong collective oscillations of conduction electrons and marking the transition from dielectric to metallic-like optical response.

The imaginary component of the dielectric function describes the behavior of a substance to incident electromagnetic radiation and is directly related to interband electronic transfers between occupied states of the valence band and unoccupied states of the conduction band [66]. More specifically, the first onset of $\varepsilon_2(\omega)$ corresponds to the fundamental direct bandgap transition (VBM → CBM), while the higher-energy peaks originate from deeper O-2p states to higher Ti-3d/Si-p conduction bands. This element is commonly employed to determine the optical gap because optical gap is equal to onset $\varepsilon_2(\omega)$, which is the minimum photon energy necessary to create an electron–hole pair [67]. All the

excitonic peaks recorded to all the studied compounds are within the bandgap energy region. Whenever the energy range of visible light coincides with the excitonic transition energy, the material will have low reflectivity and high absorption coefficient meaning the material can be useful in optoelectronics application [68]. The imaginary component of the dielectric function, $\varepsilon_2(\omega)$ of A_2TiSiO_6 is shown in Figure 6b. Ca_2TiSiO_6 exhibits the highest absorption peak with a value of 7.29 at 4.09 eV, while Sr_2TiSiO_6 shows a maximum peak of 6.44 at 3.91 eV, and Ba_2TiSiO_6 displays a peak value of 6.56 at 3.64 eV. These peak positions fall within the near-UV region and correspond to strong O-2p $\rightarrow$ Ti-3d charge transfer transitions, which dominate the optical response in oxide perovskites. The red-shift of peak positions from Ca to Ba indicates bandgap narrowing and enhanced optical activity in the visible–UV boundary region. The gradual loss of the peak positions of Ca_2TiSiO_6 to Ba_2TiSiO_6 is evidence of the alkaline-earth cation changing the electronic structure.

The refractive index of the material at zero photon energy is equal to the static refractive index [69]. Figure 6c indicates that the calculated static refractive indices are 2.17 of Ca_2TiSiO_6, 2.20 of Sr_2TiSiO_6 and 2.34 of Ba_2TiSiO_6. The three compounds have a sharp peak in the index of refraction at 3–3.1 eV, rising to a value of about 2.9–3.0, in the visible–near-ultraviolet part of the spectrum. This aspect means that they could be applicable in solar cells and optoelectronics. Beyond this range, the refractive index gradually decreases with increasing photon energy, reaching a minimum of 0.5–0.8 near 22–25 eV, suggesting that these materials become increasingly transparent in the extreme ultraviolet region.

Optical conductivity $\sigma(\omega)$ captures formation of the free charge carriers through absorption of incident photons [70,71] and directly proportional to the imaginary part of the dielectric function [69]. As it can be seen in Figure 6d, the three perovskites all have a zero optical conductivity at low photon energies. As the energy increases, σ increases and possesses clear peaks that are related to solid electronic transitions. Particularly, Ca_2TiSiO_6 has a maximum of 7.04 at 17.59 eV, Sr_2TiSiO_6 peaks at 11.42 at 23.14 eV and Ba_2TiSiO_6 peaks at 9.38 at 18.54 eV. These peaks represent the presence of high levels of photon absorption and imply the possible optoelectronic behavior in the ultraviolet energy spectrum.

Figure 6e shows the optical absorption coefficient, $\alpha(\omega)$, versus the photon energy of A_2TiSiO_6. In the low-energy region, all three compounds exhibit nearly zero absorption, indicating optical transparency at low photon energies. The absorption coefficient grows exponentially with the photon energy, and this is indicative of the interband electronic transitions. Ca_2TiSiO_6, Sr_2TiSiO_6, and Ba_2TiSiO_6 show the first prominent absorption peaks at 4.26 eV (0.66×10^6 cm^{-1}), 3.99 eV (0.58×10^6 cm^{-1}), and 3.76 eV (0.54×10^6 cm^{-1}), respectively. The average maximum absorption coefficients are 2.2×10^6 cm^{-1} at 17.76 eV with Ca_2TiSiO_6, 4.1×10^6 cm^{-1} at 24.37 eV with Sr_2TiSiO_6, and 3.1×10^6 cm^{-1} at 19.56 eV with Ba_2TiSiO_6. The weakest absorption intensity is observed in Ca_2TiSiO_6 and the strongest absorption is observed in Sr_2TiSiO_6 and Ba_2TiSiO_6 with coefficients of the order of 10^6 cm^{-1}. At increased photon energies, $\alpha(\omega)$ exhibits strong oscillatory character and this character is because of complicated high-energy electronic transitions in the conduction bands.

Figure 6f depicts the energy loss function $L(\omega)$. At low energy, the loss of all compounds is negligible, which means that there is a weak loss of energy. Ca_2TiSiO_6, Sr_2TiSiO_6 and Ba_2TiSiO_6 have the values of the static energy losses as 2.56 eV, 2.59 eV and 2.24 eV, respectively. In the intermediate energy range, several loss peaks appear due to interband transitions and plasmon excitations. At higher energies, pronounced loss maxima are observed, with Ca_2TiSiO_6 exhibiting the highest loss intensity of about 1.20 at 22.29 eV, followed by Ba_2TiSiO_6 with a peak of 0.85 at 23.98 eV, and Sr_2TiSiO_6 showing a lower maximum of 0.75 at 18.59 eV. These differences show the effect of the alkaline-earth cations on the plasmonic response of the materials.

The amplitude of incident and reflected electromagnetic waves are used to compute the reflection coefficient $R(\omega)$ [72]. The relatively low reflectivity values (~0.13–0.16 in the visible region) indicate minimal optical losses due to reflection, which is desirable for maximizing absorption in photovoltaic devices [73]. The obtained reflectivity spectra $R(\omega)$ are demonstrated in Figure 6g. The static reflectivity values are approximately 0.13 for Ca_2TiSiO_6, 0.14 for Sr_2TiSiO_6, and 0.16 for Ba_2TiSiO_6. All three compounds in the low-energy region (below about 5 eV) show a slow rise in reflectivity, which is then followed by a sharp rise at about 3–4 eV, attributed to intense optical transitions at the band edge. The reflectivity oscillates in intermediate energy (5–15 eV) region with many peaks and dales, which is the result of numerous interband transitions. Ba_2TiSiO_6 tells a much-improved reflectivity at higher energies (above ~15 eV) with a pronounced peak at 19–20 eV, but Sr_2TiSiO_6 shows a sharp rise ~22 eV and becomes the highest of the three compounds. On the contrary, Ca_2TiSiO_6 retains relatively low reflectivity in this high energy region.

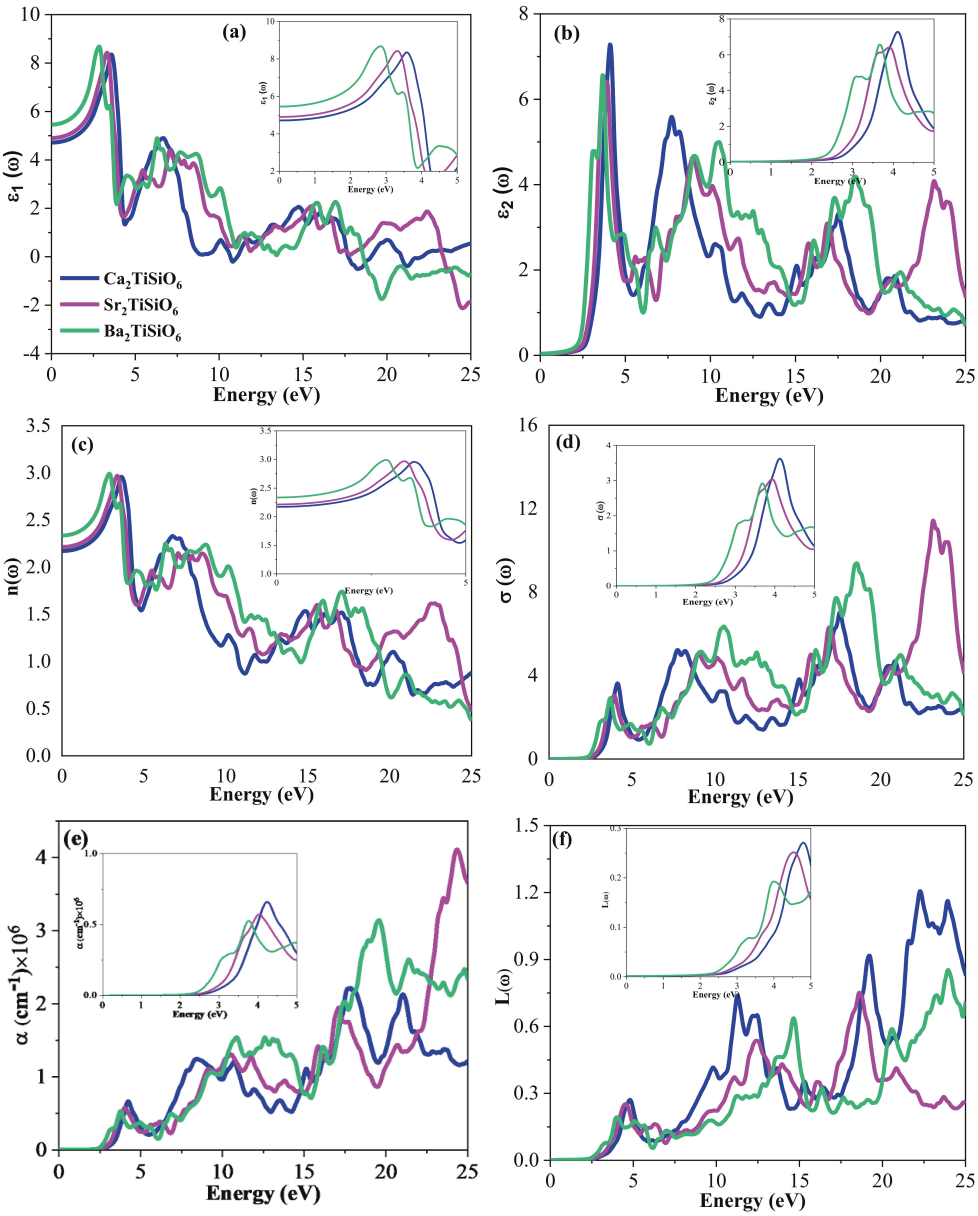

Figure 6. *Cont.*

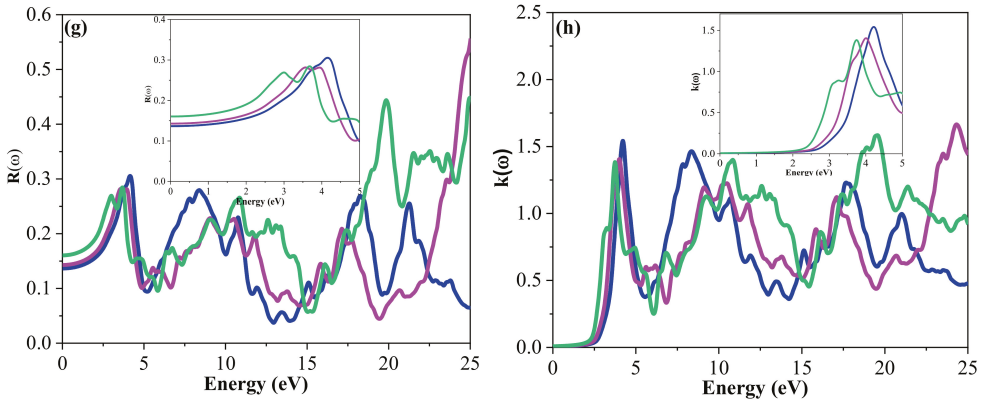

Figure 6. Calculated optical parameters (**a**) Real dielectric part ($\varepsilon_1(\omega)$), (**b**) Imaginary dielectric part ($\varepsilon_2(\omega)$), (**c**) Refractive index ($n(\omega)$), (**d**) Conductivity ($\sigma(\omega)$), (**e**) Absorption coefficient ($\alpha(\omega)$), (**f**) Loss function ($L(\omega)$), (**g**) Reflectivity ($R(\omega)$) and (**h**) Extinction coefficient ($k(\omega)$) of A_2TiSiO_6 (A = Ca, Sr, Ba) compounds.

The extinction coefficient is a property of a material which describes its capability to absorb incident light, a major aspect of optoelectronic materials [62,74]. It also defines how electromagnetic radiations attenuate with the material at a given wavelength [75]. The extinction coefficient $k(\omega)$ of the compounds studied is depicted in Figure 6h. In the low-energy region (below ~3 eV), $k(\omega)$ is nearly zero for all compounds, indicating negligible optical absorption. A steep rise in $k(\omega)$ takes place in the visible to near-UV spectrum, which is associated with the beginning of interband electronic transitions. Ca_2TiSiO_6 absorbs strongly in the long wavelengths with a maximum extinction coefficient of about 1.54 at 4.23 0 eV. At higher energies Sr_2TiSiO_6 has its maximum of about 1.66 at 24.34 eV and the value of Ba_2TiSiO_6 is sharp 1.58 at 19.52 eV. The variation in the positions and strengths of the various compounds at their peaks shows the influence of the alkaline-earth cations on the optical absorption of the compounds.

3. Materials and Methods

The physical properties of the cation-decorated double perovskites A_2TiSiO_6 (A = Ca, Sr, Ba) were studied by the use of first-principles calculations based on the framework of Density Functional Theory (DFT) through the Quantum ESPRESSO version 7.4.1. package [76,77]. Plane-wave pseudo potential method was used and the interaction between the valence electrons and cores of the ion was modeled by the use of ultrasoft pseudopotentials which were chosen to form an optimal balance of efficiency and accuracy in computations. All calculations were performed in a non-spin-polarized framework, and test spin-polarized calculations confirmed a zero net magnetic moment for all compounds, indicating a non-magnetic ground state. The optimization of the structure was carried out by means of the generalized gradient approximation (GGA) in which the Perdew–Burke–Ernzerhof (PBE) exchange correlation functional was used [78]. The lattice parameters and internal atomic coordinates were also completely relaxed until the total energy reached its minimum. The convergence tests were used to select a plane-wave kinetic energy cutoff of 60 Ry and a Monkhorst packing k-point mesh of 10 × 10 × 10, which gave reliable and converged results on all compounds investigated. To achieve more precise electronic band structures and optical properties, the HSE06 hybrid functional [79] was used and the well-known bandgap underestimation of the standard GGA functional sets were overcome. The energy strain method of arriving at elastic constants as in the thermo_pw module [80], allowed the determination of the mechanical stability and elastic behavior. In general, the given multiscale computational methodology offers an in-depth insight into the structural, me-

chanical, electronic, and optical characteristics of A_2TiSiO_6 double perovskites, which may be utilized in optoelectronics.

4. Conclusions

A systematic first-principles investigation of the structural, dynamical, mechanical, electronic, and optical properties of cubic quaternary silicon-based double perovskite oxides A_2TiSiO_6 (A = Ca, Sr, Ba) was performed within density functional theory using the Quantum ESPRESSO package, employing both PBE–GGA and HSE06 exchange correlation functionals. Structural optimization together with ab initio molecular dynamics simulations confirm the structural integrity and dynamical stability of all compounds in the cubic phase.

The calculated elastic constants satisfy the mechanical stability criteria, indicating that A_2TiSiO_6 compounds are mechanically stable, elastically anisotropic, and brittle in nature, with bonding characteristics dominated mainly by covalent interactions. Electronic band structure calculations reveal that all studied materials exhibit direct wide-bandgap semiconducting behavior.

Furthermore, the strong optical absorption in the visible–ultraviolet region, along with positive dielectric constants and appreciable refractive indices, highlights their potential for optoelectronic applications such as ultraviolet photodetectors, light-emitting devices, and photovoltaic absorbers. Overall, the results demonstrate a clear correlation between A-site cation chemistry and the resulting physical properties, suggesting that A_2TiSiO_6 double perovskites are promising candidates for advanced optoelectronic and photovoltaic technologies.

Author Contributions: Conceptualization, Ł.S. and M.G.; methodology, Ł.S. and M.G.; software, Ł.S.; validation, Ł.S. and M.G.; formal analysis, Ł.S. and M.G.; investigation, Ł.S., M.G. and K.M.-G.; resources, Ł.S.; data curation, Ł.S.; writing—original draft preparation, Ł.S. and M.G.; writing—review and editing, Ł.S. and K.M.-G.; visualization, Ł.S.; supervision, Ł.S.; project administration, Ł.S.; funding acquisition, Ł.S. All authors have read and agreed to the published version of the manuscript.

Funding: This research received no external funding.

Institutional Review Board Statement: Not applicable.

Informed Consent Statement: Not applicable.

Data Availability Statement: The original contributions presented in this study are included in the article. Further inquiries can be directed to the corresponding author.

Conflicts of Interest: The authors declare no conflicts of interest.

References

1. Bhattacharjee, S.; Parida, R.K.; Parida, B.N. Investigation of multifunction features of double perovskite oxide A_2FeVO_6 (where A = Ba, Ca). *Phys. B Condens. Matter* **2023**, *659*, 414849. [CrossRef]
2. Dar, S.A.; Murtaza, G.; Zelai, T.; Nazir, G.; Alkhaldi, H.; Albalawi, H.; Kattan, N.A.; Irfan, M.; Mahmood, Q.; Mahmoud, Z. Study of structural, electronic, magnetic, and optical properties of A_2FeMnO_6 (A = Ba, La) double perovskites, experimental and DFT analysis. *Colloids Surf. A Physicochem. Eng. Asp.* **2023**, *664*, 131145. [CrossRef]
3. Huang, Z.; Luo, P.; Jia, S.; Zheng, H.; Lyu, Z. A sulfur-doped carbon-enhanced $Na_3V_2(PO_4)_3$ nanocomposite for sodium-ion storage. *J. Phys. Chem. Solids* **2022**, *167*, 110746. [CrossRef]
4. Yi, K.; Tang, Q.; Wu, Z.; Gu, J.; Zhu, X. Structural, magnetic, and electrical transport properties of half-metallic double perovskite La_2CrNiO_6 oxides. *J. Alloys Compd.* **2023**, *933*, 167742. [CrossRef]
5. Mishra, S.; Choudhary, R.N.P.; Parida, S.K. A multifunctional transition metal based double perovskite $Ba_2(FeW)O_6$: Structural, microstructural, optical, electrical and ferroelectric properties. *Ceram. Int.* **2023**, *49*, 22702–22717. [CrossRef]
6. Katayama, T.; Mo, S.; Chikamatsu, A.; Kurauchi, Y.; Kumigashira, H.; Hasegawa, T. Half-Metallicity and Magnetic Anisotropy in Double-Perovskite $GdBaCo_2O_6$ Films Prepared via Topotactic Oxidation. *Chem. Mater.* **2023**, *35*, 1295–1300. [CrossRef]

7. Huang, Z.; Luo, P.; Wu, Q.; Zheng, H. Constructing one-dimensional mesoporous carbon nanofibers loaded with $NaTi_2(PO_4)_3$ nanodots as novel anodes for sodium energy storage. *J. Phys. Chem. Solids* **2022**, *161*, 110479. [CrossRef]
8. Chen, X.-F. Periodic Density Functional Theory (PDFT) Simulating Crystal Structures with Microporous CHA Framework: An Accuracy and Efficiency Study. *Inorganics* **2023**, *11*, 215. [CrossRef]
9. Zhang, B.; Zhang, S.; Han, H.; Tang, K.; Xia, C. Cobalt-Free Double Perovskite Oxide as a Promising Cathode for Solid Oxide Fuel Cells. *ACS Appl. Mater. Interfaces* **2023**, *15*, 8253–8262. [CrossRef]
10. Singh, P.; Kumar, A. Device engineering of double perovskite based solar cells towards high-performance, eco-friendly solar cells. *Opt. Quantum Electron.* **2023**, *55*, 304. [CrossRef]
11. Hossain, A.; Alharbi, H.F.; Hasan, M.M.; Selvanathan, V.; Islam, M.d.A.; Homyra, S.; Hasan, A.K.M.; Haque, M.; Shahiduzzaman, M.; Uddin, M. First-principles investigation of electronic, optical, and thermal properties of zintl phase MgX_2N_2 (X = Be, Ca, Sr) for optoelectronic applications: A DFT study. *Comput. Condens. Matter* **2025**, *43*, e01042. [CrossRef]
12. Bairwa, J.K.; Rani, M.; Kamlesh, P.K.; Singh, R.; Rani, U.; Al-Qaisi, S.; Kumar, T.; Kumari, S.; Verma, A.S. Modeling and simulation of multifaceted properties of X_2NaIO_6 (X = Ca and Sr) double perovskite oxides for advanced technological applications. *J. Mol. Model.* **2023**, *29*, 379. [CrossRef]
13. Irfan, M.; Murtaza, G.; Muhammad, N.; Tahir, S.; Raza, H.H.; Sabir, B.; Iftikhar, M.; Sharif, S. Experimental and theoretical studies of structural, electronic and magnetic properties of RE_2NiCrO_6 (RE = ce, Pr and Nd) double perovskites. *Phys. E Low-Dimens. Syst. Nanostructures* **2023**, *148*, 115635. [CrossRef]
14. Li, X.; Aftab, S.; Hussain, S.; Kabir, F.; Henaish, A.M.A.; Al-Sehemi, A.G.; Pallavolu, M.R.; Koyyada, G. Dimensional diversity (0D, 1D, 2D, and 3D) in perovskite solar cells: Exploring the potential of mixed-dimensional integrations. *J. Mater. Chem. A* **2024**, *12*, 4421–4440. [CrossRef]
15. Liu, Y.P.; Fuh, H.R.; Wang, Y.K. Study of the half-metallic materials double perovskites Sr_2ZnBO_6 (B = Tc, Re, Ru, Os, Co, Pd, and Au) via first-principle calculations. *J. Magn. Magn. Mater.* **2013**, *341*, 25–29. [CrossRef]
16. Philipp, J.B.; Majewski, P.; Alff, L.; Erb, A.; Gross, R.; Graf, T.; Brandt, M.S.; Simon, J.; Walther, T.; Mader, W.; et al. Structural and doping effects in the half-metallic double perovskite A_2CrWO_6 (A = Sr, Ba, and Ca). *Phys. Rev. B* **2003**, *68*, 144431. [CrossRef]
17. Li, M.; Retuerto, M.; Deng, Z.; Stephens, P.W.; Croft, M.; Huang, Q.; Wu, H.; Deng, X.; Kotliar, G.; Sánchez-Benítez, J.; et al. Giant Magnetoresistance in the Half-Metallic Double-Perovskite Ferrimagnet Mn_2FeReO_6. *Angew. Chem. Int. Ed.* **2015**, *54*, 12069–12073. [CrossRef]
18. Zhang, J.; Ji, W.-J.; Xu, J.; Geng, X.-Y.; Zhou, J.; Gu, Z.-B.; Yao, S.-H.; Zhang, S.-T. Giant positive magnetoresistance in half-metallic double-perovskite Sr_2CrWO_6 thin films. *Sci. Adv.* **2017**, *3*, e1701473. [CrossRef] [PubMed]
19. Liu, R.; Kliem, B.; Titov, V.S.; Chen, J.; Wang, Y.; Wang, H.; Liu, C.; Xu, Y.; Wiegelmann, T. Structure, Stability, and Evolution of Magnetic Flux Ropes from the Perspective of Magnetic Twist. *Astrophys. J.* **2016**, *818*, 148. [CrossRef]
20. Wei, X.-P.; Cao, T.-Y.; Sun, X.-W.; Gao, Q.; Gao, P.; Gao, Z.-L.; Tao, X.-M. Structural, electronic, and magnetic properties of quaternary Heusler CrZrCoZ compounds: A first-principles study. *Chin. Phys. B* **2020**, *29*, 077105. [CrossRef]
21. Teli, N.A.; Mir, S.H.; Sirajuddeen, M.M.S.; Banu, I.S. A computational study of TiHfPtZ (Z = Al, Ga, In) quaternary heusler compounds for spintronics applications. *Phys. Scr.* **2024**, *99*, 025974. [CrossRef]
22. Tang, Q.; Zhu, X. Half-metallic double perovskite oxides: Recent developments and future perspectives. *J. Mater. Chem. C* **2022**, *10*, 15301–15338. [CrossRef]
23. Saha-Dasgupta, T. Double perovskites with 3d and 4d/5d transition metals: Compounds with promises. *Mater. Res. Express* **2020**, *7*, 014003. [CrossRef]
24. Vasala, S.; Karppinen, M. $A_2B'B''O_6$ perovskites: A review. *Prog. Solid State Chem.* **2015**, *43*, 1–36. [CrossRef]
25. Alam, M.; Chatterjee, S. B-site order/disorder in $A_2BB'O_6$ and its correlation with their magnetic property. *J. Phys. Condens. Matter* **2023**, *35*, 223001. [CrossRef]
26. Khandy, S.A.; Gupta, D.C. Study of ferromagnetism, spin-polarization, thermoelectrics and thermodynamics of layered perovskite Ba_2FeMnO_6 under pressure and temperature. *J. Phys. Chem. Solids* **2019**, *135*, 109079. [CrossRef]
27. Ullah, R.; Ali, M.A.; Haq, B.U.; Khan, A.; Mahmood, Q.; Murtaza, G. Exploring electronic, structural, magnetic and thermoelectric properties of novel Ba_2EuMoO_6 double perovskite. *Mater. Sci. Semicond. Process.* **2022**, *137*, 106218. [CrossRef]
28. Haid, S.; Matougui, M.; Benatmane, S.; Bouadjemi, B.; Houari, M.; Zitouni, A.; Lantri, T.; Bentata, S. Predictive Study of the Rare Earth Double Perovskite Oxide Ba_2ErReO_6 and the Influence of the Hubbard Parameter U on its Half-Metallicity. *J. Supercond. Nov. Magn.* **2021**, *34*, 2893–2903. [CrossRef]
29. Mandal, T.K.; Poltavets, V.V.; Croft, M.; Greenblatt, M. Synthesis, structure and magnetic properties of $A_2MnB'O_6$ (A = Ca, Sr; B′ = Sb, Ta) double perovskites. *J. Solid State Chem.* **2008**, *181*, 2325–2331. [CrossRef]
30. Rameshe, B.; Murugan, R.; Palanivel, B. First principle study on electronic structure, structural phase stability, optical and vibrational properties of Ba_2ScMO_6 (M = Nb, Ta). *Int. J. Mod. Phys. B* **2016**, *30*, 1550246. [CrossRef]
31. Cheah, M.C.L.; Kennedy, B.J. Synthesis and structures of chromium double perovskites A_2CrTaO_6 (A = Sr, Ca). *Phys. B Condens. Matter* **2006**, *385–386*, 184–186. [CrossRef]

32. Zhang, S.; Shi, L. Pressure-dependent structural, elastic, electronic and vibrational studies of Ba_2InMO_6 (M = Ta, Nb) from first principles. *Comput. Mater. Sci.* **2018**, *142*, 99–107. [CrossRef]
33. Ghosh, B.; Halder, S.; Shannigrahi, S.; Sinha, T.P. X-ray photoelectron spectroscopic study and electronic structure of double-perovskites A_2SmTaO_6 (A = Ba, Sr, Ca). *Solid State Sci.* **2017**, *67*, 114–118. [CrossRef]
34. Toro, C.E.D.; Rodríguez, M.J.A.; Téllez, D.A.L.; Salazar, N.O.M.; Roa-Rojas, J. First principles study of the structural and electronic properties of double perovskite Ba_2YTaO_6 in cubic and tetragonal phases. *Phys. B Condens. Matter* **2014**, *455*, 18–21. [CrossRef]
35. Saad, H.-E.M.M.; Elhag, A. DFT study on the crystal, electronic and magnetic structures of tantalum based double perovskite oxides Ba_2MTaO_6 (M = Cr, Mn, Fe) via GGA and GGA + U. *Results Phys.* **2018**, *9*, 793–805. [CrossRef]
36. Sheikh, M.S.; Ghosh, D.; Dutta, A.; Bhattacharyya, S.; Sinha, T.P. Lead free double perovskite oxides Ln_2NiMnO_6 (Ln = La, Eu, Dy, Lu), a new promising material for photovoltaic application. *Mater. Sci. Eng. B* **2017**, *226*, 10–17. [CrossRef]
37. Kitamura, M.; Ohkubo, I.; Matsunami, M.; Horiba, K.; Kumigashira, H.; Matsumoto, Y.; Koinuma, H.; Oshima, M. Electronic structure characterization of La_2NiMnO_6 epitaxial thin films using synchrotron-radiation photoelectron spectroscopy and optical spectroscopy. *Appl. Phys. Lett.* **2009**, *94*, 262503. [CrossRef]
38. Chanda, S.; Saha, S.; Dutta, A.; Sinha, T.P. Structural and transport properties of double perovskite Dy_2NiMnO_6. *Mater. Res. Bull.* **2015**, *62*, 153–160. [CrossRef]
39. Lan, C.; Zhao, S.; Xu, T.; Ma, J.; Hayase, S.; Ma, T. Investigation on structures, band gaps, and electronic structures of lead free La_2NiMnO_6 double perovskite materials for potential application of solar cell. *J. Alloys Compd.* **2016**, *655*, 208–214. [CrossRef]
40. Winkler, A.; Narayanan, N.; Mikhailova, D.; Bramnik, K.G.; Ehrenberg, H.; Fuess, H.; Vaitheeswaran, G.; Kanchana, V.; Wilhelm, F.; Rogalev, A.; et al. Magnetism in Re-based ferrimagnetic double perovskites. *New J. Phys.* **2009**, *11*, 073047. [CrossRef]
41. Majewski, P.; Geprägs, S.; Sanganas, O.; Opel, M.; Gross, R.; Wilhelm, F.; Rogalev, A.; Alff, L. X-ray magnetic circular dichroism study of Re 5d magnetism in Sr_2CrReO_6. *Appl. Phys. Lett.* **2005**, *87*, 202503. [CrossRef]
42. Leinenweber, K.; Parise, J.B. Rietveld refinement of Ca_2TiSiO_6 perovskite. *Am. Mineral.* **1997**, *82*, 475–478. [CrossRef]
43. Husain, M.; Rahman, N.; Azzouz-Rached, A.; Tirth, V.; Ullah, H.; Elhadi, M.; Uzair, M.; Alotaibi, A.; Humayun, Q.; Sfina, N.; et al. Exploring Silicon-Based Ca_2TiSiO_6 Ordered Double Perovskite Oxides: A Comprehensive DFT Investigation of Structural, Dynamical, Mechanical Stability, and Optoelectronic Properties. *Silicon* **2024**, *16*, 2781–2790. [CrossRef]
44. Du, X.; He, D.; Mei, H.; Zhong, Y.; Cheng, N. Insights on electronic structures, elastic features and optical properties of mixed-valence double perovskites $Cs_2Au_2X_6$ (X = F, Cl, Br, I). *Phys. Lett. A* **2020**, *384*, 126169. [CrossRef]
45. Sholagberu, A.A.; Yahya, W.A.; Adewale, A.A. Pressure effects on the opto-electronic and mechanical properties of the double perovskite $Cs_2AgInCl_6$. *Phys. Scr.* **2022**, *97*, 085824. [CrossRef]
46. Akter, H.; Hossain, M.M.; Uddin, M.M.; Naqib, S.H.; Ali, M.A. Effects of S substitution on the structural, optoelectronic, and thermomechanical properties of $KTaO_3$ through density functional theory. *J. Phys. Chem. Solids* **2024**, *190*, 112021. [CrossRef]
47. Dar, S.A.; Srivastava, V.; Sakalle, U.K.; Parey, V. Electronic structure, magnetic, mechanical and thermo-physical behavior of double perovskite Ba_2MgOsO_6. *Eur. Phys. J. Plus* **2018**, *133*, 64. [CrossRef]
48. Reuss, A. Berechnung der Fließgrenze von Mischkristallen auf Grund der Plastizitätsbedingung für Einkristalle. *ZAMM—J. Appl. Math. Mech./Z. Angew. Math. Mech.* **1929**, *9*, 49–58. [CrossRef]
49. Hill, R. The Elastic Behaviour of a Crystalline Aggregate. *Proc. Phys. Soc. Sect. A* **1952**, *65*, 349. [CrossRef]
50. Chung, D.H.; Buessem, W.R. The Voigt-Reuss-Hill (VRH) Approximation and the Elastic Moduli of Polycrystalline ZnO, TiO_2 (Rutile), and α-Al_2O_3. *J. Appl. Phys.* **1968**, *39*, 2777–2782. [CrossRef]
51. Audu, A.; Yahya, W.; Abdulkareem, A. Ab initio Studies of the Structural, Electronic and Mechanical Properties of $Zn_{1-x}Cr_xTe$. *J. Theor. Appl. Phys.* **2021**, *3*, 38.
52. Szeleszczuk, Ł.; Mądra-Gackowska, K.; Gackowski, M. Optoelectronic and thermoelectric performance of cubic X_2YInO_6 (X = Ba, Sr; Y = Nb, V) double perovskites: A first-principles approach. *Phys. B Condens. Matter* **2025**, *719*, 417958. [CrossRef]
53. Adewale, A.A.; Chik, A.; Adam, T.; Yusuff, O.K.; Ayinde, S.A.; Sanusi, Y.K. First principles calculations of structural, electronic, mechanical and thermoelectric properties of cubic $ATiO_3$ (A = Be, Mg, Ca, Sr and Ba) perovskite oxide. *Comput. Condens. Matter* **2021**, *28*, e00562. [CrossRef]
54. Qing, W.; Peng, J.; Wang, X. First principles investigation of pressure dependent stability, phonon, Debye temperature, physical, mechanical and thermodynamic properties of Rh3Al intermetallic compound. *Mol. Simul.* **2018**, *44*, 1554–1563. [CrossRef]
55. Anderson, O.L. A simplified method for calculating the debye temperature from elastic constants. *J. Phys. Chem. Solids* **1963**, *24*, 909–917. [CrossRef]
56. Tian, J.; Zhao, Y.; Hou, H.; Wang, B. The Effect of Alloying Elements on the Structural Stability, Mechanical Properties, and Debye Temperature of Al_3Li: A First-Principles Study. *Materials* **2018**, *11*, 1471. [CrossRef]
57. Marathe, M.; Grünebohm, A.; Nishimatsu, T.; Entel, P.; Ederer, C. First-principles-based calculation of the electrocaloric effect in $BaTiO_3$: A comparison of direct and indirect methods. *Phys. Rev. B* **2016**, *93*, 054110. [CrossRef]
58. Tariq, M.; Ali, M.A.; Laref, A.; Murtaza, G. Anion replacement effect on the physical properties of metal halide double perovskites Cs_2AgInX_6 (X = F, Cl, Br, I). *Solid State Commun.* **2020**, *314–315*, 113929. [CrossRef]

59. Yahya, W.; Yahaya, A.A.; Adewale, A.A.; Sholagberu, A.A.; Olasunkanmi, N.K. A DFT study of optoelectronic, elastic and thermo-electric properties of the double perovskites Rb_2SeX_6 (X = Br, Cl). *J. Niger. Soc. Phys. Sci.* **2023**, *5*, 1418. [CrossRef]
60. Huma, M.; Rashid, M.; Mahmood, Q.; Algrafy, E.; Kattan, N.A.; Laref, A.; Bhatti, A. Physical properties of lead-free double perovskites A_2SnI_6 (A = Cs, Rb) using ab-initio calculations for solar cell applications. *Mater. Sci. Semicond. Process.* **2021**, *121*, 105313. [CrossRef]
61. Zhao, S.; Lan, C.; Ma, J.; Pandey, S.S.; Hayase, S.; Ma, T. First principles study on the electronic and optical properties of B-site ordered double perovskite Sr_2MMoO_6 (M = Mg, Ca, and Zn). *Solid State Commun.* **2015**, *213–214*, 19–23. [CrossRef]
62. Hossain, A.; Ali, M.A.; Uddin, M.M.; Naqib, S.H.; Hossain, M.M. Theoretical studies on phase stability, electronic, optical, mechanical and thermal properties of chalcopyrite semiconductors $HgXN_2$ (X = Si, Ge and Sn): A comprehensive DFT analysis. *Mater. Sci. Semicond. Process.* **2024**, *172*, 108092. [CrossRef]
63. Shah, S.; Ali, Z.; Mehmood, S.; Khan, I.; Ahmad, I. Electronic structure, optical and magnetic properties of double Perovskites La_2MTiO_6 (M = Co, Ni, Cu and Zn). *Mater. Chem. Phys.* **2021**, *272*, 125050. [CrossRef]
64. Hossain, M.K.; Toki, G.F.I.; Samajdar, D.P.; Mushtaq, M.; Rubel, M.H.K.; Pandey, R.; Madan, J.; Mohammed, M.K.A.; Islam, R.; Rahman, F.; et al. Deep Insights into the Coupled Optoelectronic and Photovoltaic Analysis of Lead-Free $CsSnI_3$ Perovskite-Based Solar Cell Using DFT Calculations and SCAPS-1D Simulations. *ACS Omega* **2023**, *8*, 22466–22485. [CrossRef]
65. Carcione, J.M.; Cavallini, F.; Ba, J.; Cheng, W.; Qadrouh, A.N. On the Kramers-Kronig relations. *Rheol. Acta* **2019**, *58*, 21–28. [CrossRef]
66. Yang, B.-Y.; Zhang, J.-M.; Ali, A.; Huang, Y.-H.; Wei, X.-M. Computational investigation of structural, magnetic, electronic and optical properties of the cluster Mn-X_6 (X = P, S, Cl, Br or Te) doped monolayer WSe_2. *Thin Solid Film.* **2021**, *732*, 138793. [CrossRef]
67. Zarabinia, N.; Rasuli, R. Electronic and optical properties of halide double-perovskites under strain: A density functional study. *Energy Sources Part A Recovery Util. Environ. Eff.* **2021**, *43*, 2443–2455. [CrossRef]
68. Hossain, A.; Akhtaruzzaman, M.; Uddin, M.M. DFT-based design of X_3BiY_3 (X = Mg, Sr, Ba; Y = F, Cl) perovskites: From wide-gap insulators to promising semiconductors for solar cell applications. *J. Phys. Chem. Solids* **2026**, *208*, 113094. [CrossRef]
69. Abdulkadhim, T.M.J.; Alsaati Sa, A.; Shinen, M.H. Theoretical Investigation of Diameter Effects and Edge Configuration on the Optical Properties of Graphdiyne Nanotubes in the Presence of Electric Field. *J. Niger. Soc. Phys. Sci.* **2023**, *5*, 1083. [CrossRef]
70. Adewale, A.A.; Chik, A.; Yusuff, O.K.; Ayinde, S.A.; Sanusi, Y.K. First principle calculation of structural, electronic and optical properties of CdS and doped $Cd_{x-1}A_xS$ (A = Co, Fe, Ni) compounds. *Mater. Today Commun.* **2021**, *26*, 101882. [CrossRef]
71. Onuegbu, S.C.; Oluyamo, S.S.; Olusola, O.I. Influence of Bath pH values on the Structural and Optical Properties of Electrodeposited MgO Thin Films for Optoelectronic applications. *J. Niger. Soc. Phys. Sci.* **2023**, *5*, 931. [CrossRef]
72. Li, W.; Zhu, S.; Zhao, Y.; Qiu, Y. Structural, electrical, optical properties and stability of Cs_2InBr_5-yXy·H_2O (X = Cl, I, y = 0, 1, 2, 3, 4, 5) perovskites: The first principles investigation. *Thin Solid Film.* **2021**, *733*, 138805. [CrossRef]
73. Ali, M.H.; Islam, M.J.; Kumer, A.; Hossain, M.S.; Chakma, U.; Howlader, D.; Islam, T.; Hossain, T. Investigation of Structural, Electronic and Optical Properties of $Na_2InAgCl_6$, $K_2InAgCl_6$, and $Rb_2InAgCl_6$ Lead-Free Halide Double Perovskites Regarding with Cs2InAgCl6 Perovskites Cell and a Comparative Study by DFT Functionals. *Mater. Res.* **2021**, *24*, e20210086. [CrossRef]
74. Umm-e-Hani Murtaza, G.; Raza, H.H. Optoelectronic and thermal properties of cubic $SiMO_3$ (M = Sn, Pb) oxides for device application: A first principle study. *Opt. Quantum Electron.* **2020**, *52*, 456. [CrossRef]
75. Adewale, A.A.; Chik, A.; Adam, T.; Joshua, T.M.; Durowoju, M.O. Optoelectronic behavior of ZnS compound and its alloy: A first principle approach. *Mater. Today Commun.* **2021**, *27*, 102077. [CrossRef]
76. Giannozzi, P.; Andreussi, O.; Brumme, T.; Bunau, O.; Buongiorno Nardelli, M.; Calandra, M.; Car, R.; Cavazzoni, C.; Ceresoli, D.; Cococcioni, M.; et al. Advanced capabilities for materials modelling with Quantum ESPRESSO. *J. Phys. Condens. Matter* **2017**, *29*, 465901. [CrossRef]
77. Giannozzi, P.; Baroni, S.; Bonini, N.; Calandra, M.; Car, R.; Cavazzoni, C.; Ceresoli, D.; Chiarotti, G.L.; Cococcioni, M.; Dabo, I.; et al. QUANTUM ESPRESSO: A modular and open-source software project for quantum simulations of materials. *J. Phys. Condens. Matter* **2009**, *21*, 395502. [CrossRef]
78. Perdew, J.P.; Burke, K.; Ernzerhof, M. Generalized Gradient Approximation Made Simple. *Phys. Rev. Lett.* **1996**, *77*, 3865–3868. [CrossRef]
79. Heyd, J.; Scuseria, G.E.; Ernzerhof, M. Hybrid functionals based on a screened Coulomb potential. *J. Chem. Phys.* **2003**, *118*, 8207–8215. [CrossRef]
80. Nielsen, O.H.; Martin, R.M. First-Principles Calculation of Stress. *Phys. Rev. Lett.* **1983**, *50*, 697–700. [CrossRef]

Disclaimer/Publisher's Note: The statements, opinions and data contained in all publications are solely those of the individual author(s) and contributor(s) and not of MDPI and/or the editor(s). MDPI and/or the editor(s) disclaim responsibility for any injury to people or property resulting from any ideas, methods, instructions or products referred to in the content.

inorganics

MDPI

Article

Enhanced Secondary Electron Emission from Strontium Titanate Films via High-Temperature Annealing

Weiqiang Li [1,2,3], Dan Wang [1,4,5,*], Wei Zhao [2,3,*], Xiangping Zhu [2,3,6], Yongning He [1,4,5] and Guohe Zhang [1,4,5]

1 School of Microelectronics, Xi'an Jiaotong University, Xi'an 710049, China
2 State Key Laboratory of Ultrafast Optical Science and Technology, Xi'an Institute of Optics and Precision Mechanics, Chinese Academy of Sciences, Xi'an 710119, China
3 University of Chinese Academy of Sciences, Beijing 100049, China
4 Key Laboratory of Electronic Devices and Advanced Chips in Shaanxi Province, Xi'an 710049, China
5 Key Laboratory of Micro-Nano Electronics and System Integration of Xi'an City, Xi'an 710049, China
6 ZhongKe Atomically Precise Manufacturing Technology Co., Ltd., Xi'an 710119, China
* Correspondence: alexaustin@xjtu.edu.cn (D.W.); weiz@opt.ac.cn (W.Z.)

Abstract

The versatile surface reconstruction mechanisms, tunable surface properties, and exceptional electron emission characteristics of $SrTiO_3$ films have garnered significant research interest. In this study, $SrTiO_3$ films were synthesized on n-Si(100) substrates via radio frequency magnetron sputtering. To evaluate the impact of thermal annealing, the as-deposited films underwent post-deposition annealing in an oxygen ambient at 600 °C, 800 °C, and 1000 °C for a duration of 2 h each. The structural, chemical, and secondary electron emission (SEE) characteristics of the $SrTiO_3$ films were characterized as a function of their high thermal process. Post-deposition annealing induced a significant improvement in crystallinity, which directly correlated with a heightened SEE yield (SEY). Furthermore, composition analysis revealed a marked stoichiometric reconfiguration at the surface, with the Sr:Ti:O ratio evolving from 1:0.32:1.14 to 1:0.22:0.94, suggesting a move toward an Sr-O terminated surface. The Sr-O terminated surface inherent to these $SrTiO_3$ films promotes efficient electron escape due to its reduced work function. Following a 1000 °C annealing process, the peak SEY undergoes a significant shift from 2.11 to 2.76, representing a thermal optimization of the SEE performance by approximately 30.8%. High-temperature annealing enhances the SEE performance of $SrTiO_3$ films, validating their significant potential for electron multiplication applications. This study provides a scalable pathway for developing highly efficient SEE materials with optimized crystalline and surface properties.

Keywords: strontium titanate; secondary electron emission; thermal annealing

1. Introduction

Strontium titanate ($SrTiO_3$, denoted as STO), a typical ABO_3-type perovskite oxide, has become a cornerstone material in the emerging field of oxide electronics due to its high dielectric constant, low leakage current, and excellent optical properties [1–3]. Due to their excellent bulk and surface properties, STO single crystals and polycrystalline thin films have been extensively researched for diverse applications, ranging from photocatalytic water splitting to their use as substrates for high-temperature superconductors and components in micro/nanoelectronics devices [4–6]. Furthermore, STO thin films exhibit multifunctional properties that are highly dependent on their unique surface structures,

such as the specific (2 × 1) reconstruction of the STO (001) surface [7]. The physical properties of STO thin films are closely linked to their surface microstructure, morphology, chemical composition, and chemical states—all of which play a critical role in determining their electronic characteristics [8,9]. STO thin films exhibit distinct optoelectronic behaviors compared to their single-crystal counterparts [10]; variations in the oxidation states of metal cations serve as the primary cause of these property changes. The optical bandgap of STO films exhibits significant variability, ranging from 2.70 eV to 4.26 eV [11,12], as influenced by specific fabrication techniques and processing parameters. Ti-O or Sr-O terminated surfaces on STO can be achieved using various processes, including Ar^+ etching, chemical etching, or annealing [13,14]. Vienna Ab initio simulation package (VASP) and experimental studies confirm that the work function of SrO-terminated STO (001) surfaces is generally lower than that of TiO_2-terminated surfaces, regardless of whether the samples are subjected to thermal annealing or surface pretreatment [15,16]. STO thin films can be prepared using various deposition techniques, including atomic layer deposition [17], molecular beam epitaxy [18], metalorganic chemical vapor deposition [19], and RF magnetron sputtering [12]. Among these methods, RF magnetron sputtering stands out as a low-cost and efficient fabrication technique that is also suitable for wafer-scale mass production.

A common strategy for studying the electronic properties of STO involves high-temperature annealing to improve film crystalline quality and surface characteristics. This yields several important periodic reconstructions—e.g., (1 × 1), (2 × 2), and (4 × 4)—some of which have been analyzed in detail. In 2019, Kim et al. grew STO thin films via atomic layer deposition [20], applying rapid thermal annealing before depositing a main STO layer on the seed layer, thereby achieving in situ crystallization. In a low work function surface study in 2022, Kamaratos et al. exposed the STO (100) surface to water vapor and cesium vapor [21], observing the formation of cesium oxide (Cs_2O), which further reduced the surface work function by up to 0.35 eV. In 2023, Hong et al. reported that anomalously strong and coherent secondary photoelectron emission was observed on the reconstructed $SrTiO_3$ (100) surface following simple vacuum annealing [22]. The low work function surface formed after annealing is key to determining these unique secondary electron emission characteristics. In 2024, Pérez reported an optical bandgap of 3.06 eV after annealing STO thin films in a reducing atmosphere [23], and this sample demonstrated superior performance regarding overpotential, Tafel slope, and 24-h stability. In 2025, Chien synthesized $SrTiO_3/TiO_2/TiN$ heterostructure films [24], annealing them under varying partial pressures of nitrogen and oxygen, and the introduction of oxygen vacancies at the interfaces promoted efficient charge separation and suppressed recombination during photoelectrochemical responses.

Although research on STO thin films has been quite extensive, most studies primarily focus on the relationships among preparation methods, surface reconstruction, film quality, and optical/electrochemical properties. There are few reports that research the secondary electron emission (SEE) of STO films. Within the field of SEE research, the use of surface microstructure [25–28] and functional coatings [29–31] to regulate surface SEE yield (SEY) is of paramount importance. For functional coatings engineering, typically, functional films such as titanium nitride are applied within particle accelerators to reduce SEY and further mitigate the risk of cloud effect occurrence [32,33]. Materials such as magnesium oxide possessing high SEY are frequently employed in the dynodes of electron multipliers to achieve efficient amplification of electronic signals within the device [30,34–36]. Moreover, materials possessing high SEY can also be effectively utilized in engineering scenarios where the suppression of electrostatic discharge is required [37,38]. Since STO is a ceramic material possessing a high bandgap (approximately 3.2 eV) [39], STO functional films are supposed to demonstrate efficacy in scenarios involving the modulation of SEY like various

https://doi.org/10.3390/inorganics14030071

other functional coatings, such as in the dynode of photomultiplier tubes requiring high SEE capability [30].

In this study, we employed magnetron sputtering to deposit STO thin films on n-Si substrates, followed by annealing in an oxygen atmosphere, to characterize the film properties. For comparison, additional STO films were deposited under varying argon and oxygen partial pressures. The primary objective is to investigate how these different sputtering and annealing conditions affect the secondary electron emission characteristics of the STO thin films.

2. Results and Discussion

2.1. Film Morphology of the STO Films

The surface morphology of the STO thin films, as characterized by plan-view field emission scanning electron microscopy (FESEM) [23,40], is illustrated in Figure 1. Figure 1a depicts the as-deposited state, while Figure 1b illustrates the morphological changes following a 2 h annealing treatment at 1000 °C under an oxygen atmosphere. The STO film exhibited a thickness reduction from 178.6 nm in the as-deposited state to 163.8 nm following high-temperature annealing. This volumetric contraction of approximately 8.3% is fundamentally attributed to thermal densification and the elimination of residual porosity inherent in room-temperature magnetron-sputtered oxide films. A detailed examination of the STO thin-film morphology reveals that the films remain dense both before and after annealing, with surface grain sizes in the range of several tens of nanometers. The thermal treatment did not significantly alter the overall surface morphology. It is inferred that while annealing promoted Ostwald ripening [41,42]—thereby improving crystalline quality and reducing surface energy—the surface remained continuous and devoid of observable cracks.

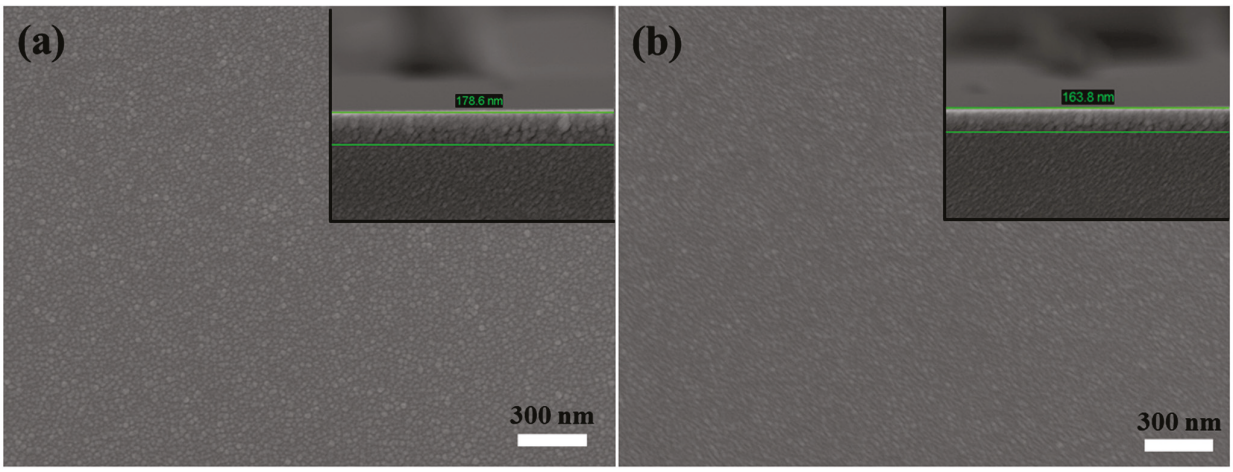

Figure 1. FESEM images of STO thin film on n-Si substrates: (**a**) as-deposited (unannealed) and (**b**) annealed. The inset in the upper right corner of (**a**,**b**), confirm a thickness reduction from 178.6 nm (as-deposited) to 163.8 nm (post-annealing).

2.2. Elemental Composition of the STO Films

In addition to morphological characterization, we employed energy-dispersive X-ray spectroscopy (EDS) to examine the elemental distribution across the surface of the prepared STO films, as illustrated in Figure 2. Figure 2a–c, respectively, show the elemental densities of Sr, Ti, and O within the EDS testing regions. The distribution results of planar elements in Figure 2 show the uniform distribution of the three elements within the test are, and reveal a high density of Sr, while Ti and O exhibit relatively low densities. This indicates that the Sr content is markedly higher than that of Ti and O. Furthermore, based

https://doi.org/10.3390/inorganics14030071

on the operating principle of EDS [43,44], we understand that its detection depth ranges from several hundred nanometers to the micrometer scale. Consequently, the elemental composition results measured in Figure 2 also indirectly indicate that the thickness of the prepared STO film is comparable to the EDS detection depth at accelerating voltage of 5 kV.

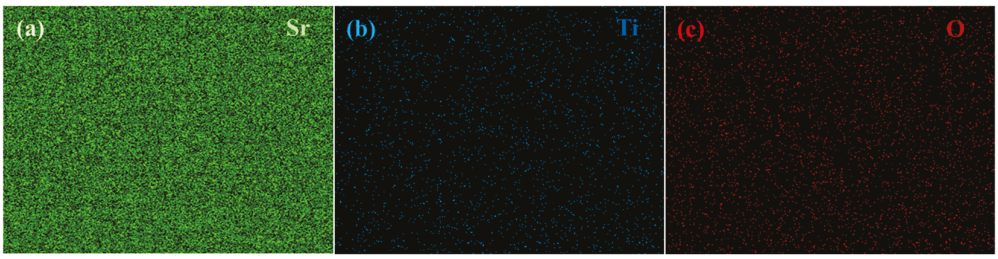

Figure 2. EDS elemental mapping images of (**a**) Sr, (**b**) Ti, and (**c**) O.

In addition to the elemental distribution density, we also employed EDS to determine the relative abundance of each element of the STO perovskite material after annealing, including the EDS spectra and elemental percentages, as shown in Figure 3. In Figure 3, the spectrum exhibits prominent peaks at the characteristic K-shell emission positions for Sr, Ti, and O. The quantitative elemental data are summarized in the inset table. The mass fractions (Wt. %) for Sr, Ti, and O—before and after annealing—were 72.2%/77.5%, 12.8%/9.2%, and 15.0%/13.3%, respectively. These correspond to atomic percentages (At. %) of 40.6%/46.3% (Sr), 13.1%/10.1% (Ti), and 46.3%/43.6% (O). Strontium and Titanium are major metal elements, and their relative atomic ratios should therefore be precise within a ±1.0% range; however, oxygen (a light element) typically has a much higher relative error a ±5.0% due to low X-ray yield and high absorption. The elemental atomic ratio in the unannealed sample (1:0.32:1.12) deviates sharply from ideal $SrTiO_3$, revealing substantial Ti and O vacancies. After annealing, this ratio shifts to 1:0.22:0.93, demonstrating that high-temperature treatment exacerbates the surface Ti and O loss and increases the stoichiometric deviation. The elemental stoichiometry of sputtered STO films inherently deviates from the ideal 1:1:3 single-crystal ratio due to non-congruent sputtering. Multi-component perovskite targets rarely exhibit equal ejection rates; lighter species and those with lower binding energies are preferentially sputtered. While theoretical sputtering yields for Ti often exceed those of strontium Sr due to superior mass-matching with Ar, several synergistic factors contribute to the measured Sr enrichment:

(1) Instrumental Sensitivity: The higher X-ray emission efficiency of heavier cations (Sr) can influence quantitative software results, particularly in standardless models where ZAF correction algorithms may carry inherent analytical uncertainties.
(2) Target Stoichiometry: The initial $SrTiO_3$ target may exhibit a slight Sr-rich bias, which is propagated during the deposition process.
(3) Non-Congruent Transport: Specific sputtering parameters, such as low working pressures or elevated substrate temperatures, may modulate the sticking coefficients and re-sputtering rates, favoring Sr-incorporation over Ti.
(4) Thermal Annealing: During annealing, the relative instability of Ti leads to preferential migration and volatilization, facilitating the formation of a stable SrO_x-rich surface layer.

Given that the EDS interaction range significantly exceeds the thin-film thickness, the reported data represent a volumetric average of the Sr-rich surface and the stoichiometric bulk. Thus, the observed Sr > Ti ratio is a physical manifestation of integrated Ti-depletion rather than a preparation artifact. This fundamental alteration of the surface chemical

state is likely responsible for the modified electronic properties and electron emission characteristics of the films.

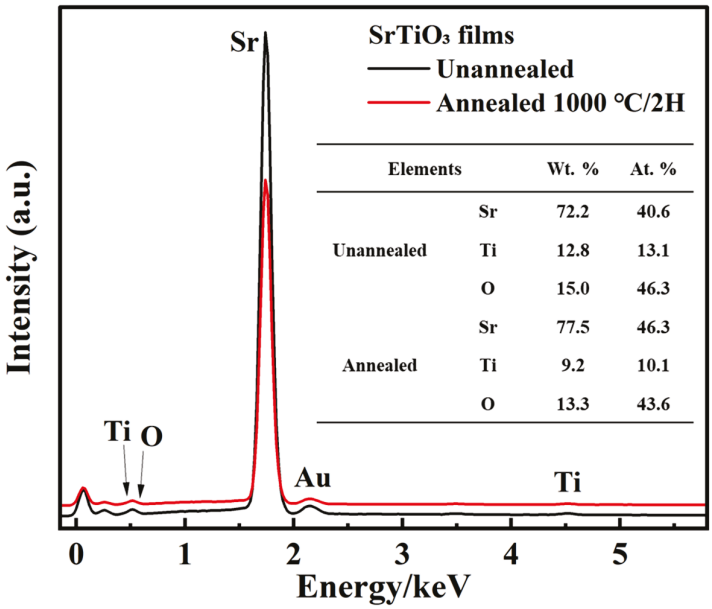

Figure 3. The corresponding EDS spectrum for these samples. The inset in image presents the EDS quantification data, showing the mass percentage (Wt. %) and atomic percentage (At. %) for Sr, Ti, and O, respectively.

In fact, under high-temperature oxidizing conditions, Ti species are prone to volatilization via the formation of TiO_2 or volatile suboxides, especially at high-energy sites like grain boundaries. This process, coupled with thermally induced oxygen vacancies or chemical interactions with the underlying n-Si substrate, fundamentally alters the surface stoichiometry. The formation of a SrO–rich surface termination after thermal treatment is proposed to account for the signal attenuation of Ti, as the enriched overlayer limits the depth-sensitive detection of titanium cations. In 2019, investigations by Chambers and Sushko [16], utilizing UPS experiments and DFT calculations, revealed that the work function of STO (001) surfaces is highly termination-dependent: 3.1~3.6 eV for SrO-terminated surfaces and 4.5~4.8 eV for TiO_2-terminated surfaces. A Sr-rich surface significantly reduces the samples' effective work function, representing one of the most viable strategies for enhancing the SEE of STO films. Additionally, trace peaks associated with adsorbed carbon and the gold coating (sputtered for conductivity) were detected. The EDS elemental mapping of the annealed STO thin film in Figure 2a–c demonstrates a uniform spatial distribution of Sr, Ti, and O across the surface. Qualitatively, the higher image contrast observed in the Sr map suggests a significantly greater signal intensity compared to those of Ti and O, which aligns with the Sr enrichment observed in the quantitative analysis.

2.3. Phase Structure of the STO Films

The crystallinity and phase evolution of the thin films are strictly governed by the deposition parameters and post-deposition annealing temperatures. Therefore, to further characterize the phase structure changes in STO films before and after annealing, we employed X-ray diffraction (XRD) techniques to examine the phase structure of the STO films. Figure 4 illustrates the XRD patterns for the as-deposited and thermally treated STO films. In the as-deposited state, the room-temperature-sputtered samples exhibited a purely amorphous phase, as corroborated by the reference patterns. Subsequent annealing at 600 °C, 800 °C, and 1000 °C in an oxygen (O_2) ambient for two hours induced a progressive enhancement in crystallinity, facilitating a transition into a well-defined polycrystalline

state. Compared to the amorphous as-deposited state, the emergence of sharp diffraction peaks between 30° and 70° signifies the development of a well-ordered crystalline phase. On the one hand, the polycrystalline structure was indexed to tetragonal STO (JCPDS PDF card No.: 97-018-2764), with characteristic reflections from the (112), (200), (202), (004), (220), (204), (312), and (321) planes identified at 2θ positions of 32.4°, 32.4°, 40.0°, 46.4°, 46.5°, 57.8°, 57.8°, and 61.7°, respectively. Notably, the proximity diffraction peaks from the (112) and (200) planes, as well as those from the (204) and (312) planes, results in peak overlap that precludes their individual resolution within the measured XRD patterns. On the other hand, the diffraction features observed at 33.0° and 65.9° in the sample annealed at 1000 °C are indexed to the n-Si substrate (JCPDS PDF card No.: 97-017-0488). Given the high-temperature treatment in an oxygen ambient, we have evaluated and subsequently ruled out the precipitation of titanium oxide (TiO_x) or strontium oxide (SrO_x) phases. Instead, the reflections identified at 47.8°, 54.6°, 55.5°, 56.4°, and 65.9° are attributed to the interfacial formed SiO_2 layer (JCPDS PDF card No.: 97-017-0488) formed via thermal oxidation of the substrate. The broad diffraction envelope observed between 66.1° and 72° in Figure 4 results from the overlapping diffraction peaks from the n-Si substrate, the interfacial SiO_2 layer, and the STO film. This high peak intensity, combined with the high degree of spectral congestion, precludes the precise resolve of individual peak positions within this range. Overall, the XRD results confirm that the crystalline quality of the room-temperature-sputtered STO films is significantly enhanced through high-temperature annealing in an oxygen ambient.

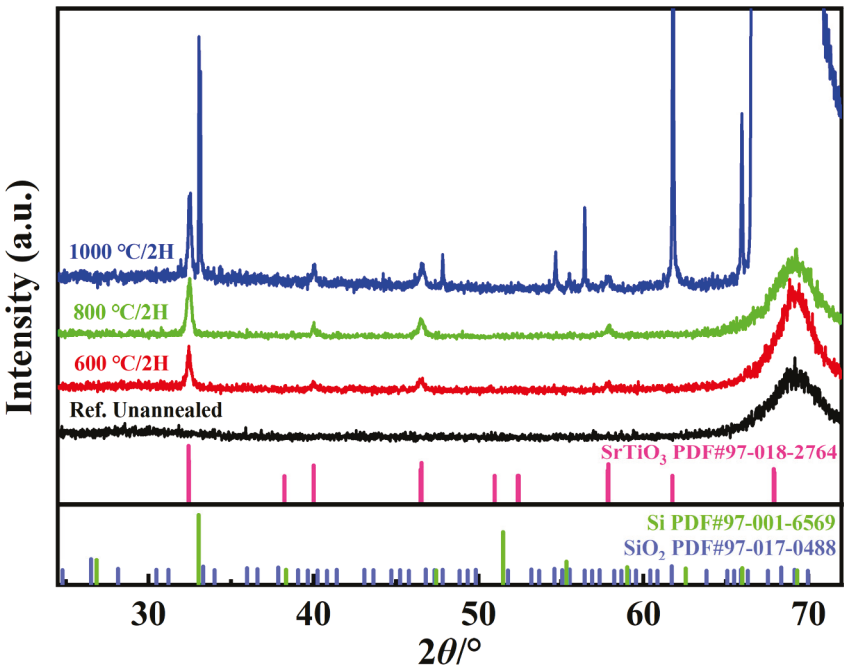

Figure 4. XRD patterns of as-synthesized and annealed STO films (600 °C, 800 °C, and 1000 °C) in O_2 for 2 h.

2.4. SEE Properties of the STO Films

The impact of the post-deposition annealing process under an O_2 atmosphere on the SEE properties of STO films was investigated through SEY measurements. The data confirm that thermal processing markedly improved the secondary electrons emission efficiency of the films. As illustrated in Figure 5, the SEY values exhibit a clear upward shift following the annealing treatment, far exceeding the SEY of the amorphous as-deposited samples. The critical parameters of the SEY profiles, specifically the optimal primary electron energy (E_{pm}) and maximum yield (δ_m), are tabulated in Table 1 for the as-deposited and thermally

https://doi.org/10.3390/inorganics14030071

treated STO thin films. The initial SEY curve's peak of the as-deposited STO film, defined by ($E_{p,m}$, δ_m), was recorded at (260 eV, 2.11). Following thermal treatment in an oxygen ambient at 600 °C for two hours, the SEE characteristics exhibited a marginal enhancement to (306 eV, 2.19), representing a yield increase ($\Delta\delta$%) of approximately 3.8%. Notably, the STO films annealed at 800 °C and 1000 °C demonstrate substantial performance further enhancements; their SEY peaks shifted to (304 eV, 2.43) and (305 eV, 2.76), respectively, corresponding to $\Delta\delta$% improvements of 15.2% and 30.8% relative to the as-deposited state. While δ_m increases, E_{pm} remains relative stable at approximately 305 eV, suggesting that the secondary electron escape depth in the STO thin films undergoes negligible variation. Consequently, the observed enhancement is primarily attributed to improved long-range crystalline order and refined surface conditions, which facilitate more efficient electron transport to the surface and a higher probability of emission following generation. Thermal treatment in an oxygen ambient effectively decontaminates the surface and mitigates structural defects, thereby optimizing the overall SEE efficiency. The results provide a scalable pathway for improving the performance of materials with modest inherent SEY, thereby broadening their suitability for high-performance secondary electron multiplication applications.

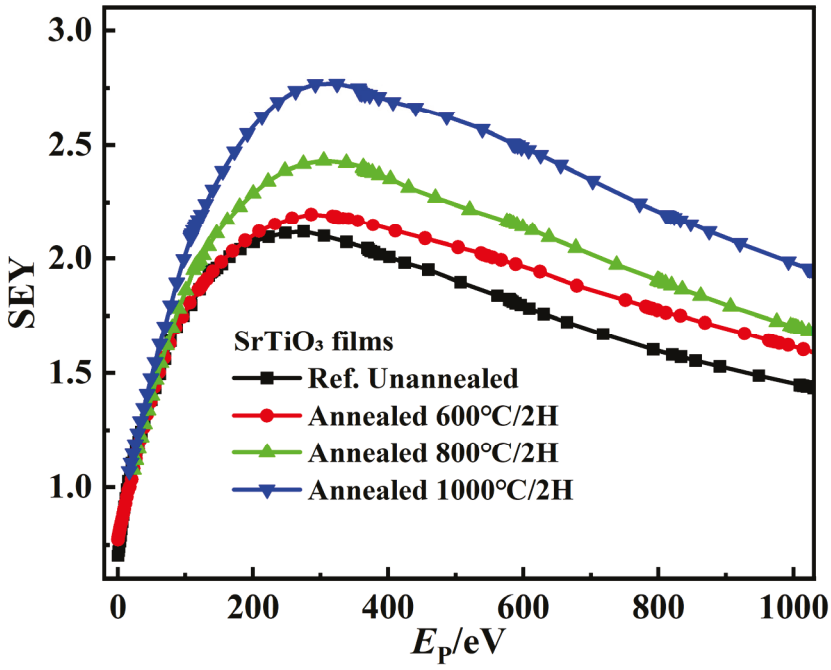

Figure 5. SEY characteristics of STO films on n-Si substrates. SEY curves are presented for samples in the as-deposited (unannealed) state and annealed temperatures at 600 °C, 800 °C, and 1000 °C.

Table 1. SEY characteristics of as-synthesized and annealed STO films.

Samples	E_m/eV	δ_m
Ref. Unannealed	260	2.11
Annealed 600 °C/2H	306	2.19
Annealed 800 °C/2H	304	2.43
Annealed 1000 °C/2H	305	2.76

3. Experimental Methodology

3.1. Film Deposition

STO thin films were deposited onto n-Si(100) substrates at ambient temperature using a GJP-400 dual-target magnetron sputtering system. High-purity argon and oxygen were

utilized as the reaction gases. The deposition utilized a commercially sourced (Hefei Kejing Material Technology Co., Ltd., Hefei, China) high-purity ceramic STO target (3-inch diameter), with the target-to-substrate distance maintained at a fixed 55 mm. Prior to deposition, the n-Si substrates underwent sequential ultrasonic cleaning using deionized water, anhydrous ethanol, and acetone, and the substrates were then immediately dried using high-purity nitrogen flow. The chamber background vacuum was maintained at better than 10^{-4} Pa. The argon and oxygen flow rates were maintained at 20 sccm and 10 sccm, respectively, resulting in a fixed Ar:O_2 flow ratio of 2:1. Deposition occurred at an RF power of 120 W, with a total pressure of approximately 1 Pa. To investigate the effect of annealing on the film structure and SEE properties, samples were annealed in an oxygen atmosphere, maintained at a constant pressure of 0.22 MPa. The annealing temperatures used were 600 °C, 800 °C, and 1000 °C, each maintained for 2 h with a heating rate of 5 °C/min. Annealed samples were stored in a vacuum container. The STO target was pre-sputter cleaned for 10 min before deposition and sealed for storage when not in use.

3.2. Film Characterization

The morphology of the STO thin films was investigated using FESEM with a Zeiss Gemini 500 instrument (Carl Zeiss AG, Oberkochen, Germany). Elemental composition was determined by EDS using an Oxford Instruments UltimMax 100 system attached to the FESEM (the UK). The crystal structure of the samples was characterized by XRD using a Bruker D8 ADVANCE (Bruker Corporation, Karlsruhe, Germany) diffractometer equipped with a Cu Kα radiation source (λ = 1.5405 Å), and the scans were performed in the 2θ range of 10~80°.

3.3. SEY Measurement

The SEE characteristics of the STO thin films were measured using a self-built SEY system based on the collector method. The working principle, instrument configuration, and testing procedure are detailed in our group's previously published literature [45]. Measurements were conducted in a test chamber maintained under high vacuum (better than 10^{-5} Pa). The primary electron beam impinged on the sample surface, generating both a sample absorption current (I_s) and a secondary electron beam/collector current (I_c). The primary electron current (I_P) is defined as the sum of these two components ($I_p = I_s + I_c$). The SEY can then be calculated using the following formula:

$$\delta = \frac{I_C}{I_P} = \frac{I_C}{I_S + I_C}$$

Due to the presence of backscattered electrons, the measured collector current (I_c) actually represents the total emitted electron current from the sample surface, which is the sum of both the true secondary electrons and the backscattered electrons.

4. Conclusions

In this study, we evaluated the evolution of SEE characteristics in STO films across their as-deposited and annealed states. The results demonstrate that high-temperature annealing conditions fundamentally modulate the surface chemical states, stoichiometry, and long-range crystalline order, which in turn govern the resulting electron emission performance. The room-temperature sputtered STO films exhibit robust adhesion to the n-Si substrate and initially possess a purely amorphous structure. EDS analysis reveals a surface stoichiometry of Sr:Ti:O = 1:0.32:1.14, highlighting an Sr-rich phase. Following the annealing process, the surface composition evolves to Sr:Ti:O = 1:0.22:0.94. This surface reconstruction toward an Sr-O termination is critical, as the associated reduction in work function facilitates a

higher SEY at the film–vacuum interface. Thermal treatment in an oxygen ambient at 600 °C initiates the crystallization of the STO films, subsequently modulating their SEE properties. As the annealing temperature is further elevated to 800 °C and 1000 °C, the long-range crystalline order is progressively refined. This structural maturation drives a substantial enhancement in the SEE performance of the resulting polycrystalline STO films. At an annealing temperature of 1000 °C, the peak of the STO emission profile undergoes a significant transition from its initial state of (260 eV, 2.11) to (305 eV, 2.76). This evolution reflects a thermal optimization of the SEE process, signifying an enhancement of approximately 30.8% in the maximum yield. Optimizing STO-deposited conditions and subsequent thermal annealing enables the formation of a low-work-function Sr-O-terminated surface. This processing strategy significantly enhances the SEY, confirming the suitability of annealed STO films as a practical and efficient material for secondary electron multiplication applications.

Author Contributions: Conceptualization, W.L. and D.W.; methodology, W.L. and D.W.; software, W.L.; validation, W.L. and D.W.; formal analysis, D.W. and X.Z.; investigation, W.Z.; resources, Y.H.; data curation, W.L. and D.W.; writing—original draft preparation, W.L. and D.W.; writing—review and editing, D.W., Y.H. and G.Z.; visualization, W.L.; supervision, D.W., W.Z. and G.Z.; project administration, X.Z.; funding acquisition, X.Z. and G.Z. All authors have read and agreed to the published version of the manuscript.

Funding: This study was supported by the Natural Science Foundation of Gansu Province, China (Grant No. 23ZDGE001), the major scientific research instrument development project of the National Natural Science Foundation of China (Grant No. 52127817), the Fundamental Research Funds for the Central Universities (Grant. No. xzy012025052), the National Natural Science Foundation of China (Grant. No. 62101425), and the Shenzhen Science and Technology Program (Grant No. KJZD20231023100501003).

Data Availability Statement: The original contributions presented in the study are included in the article; further inquiries can be directed to the corresponding authors.

Conflicts of Interest: Author Xiangping Zhu was employed by the company ZhongKe Atomically Precise Manufacturing Technology Co., Ltd. The remaining authors declare that the research was conducted in the absence of any commercial or financial relationships that could be construed as a potential conflict of interest.

References

1. Anderson, C.P.; Scuri, G.; Chan, A.; Eun, S.; White, A.D.; Ahn, G.H.; Jilly, C.; Safavi-Naeini, A.; Van Gasse, K.; Li, L.; et al. Quantum critical electro-optic and piezo-electric nonlinearities. *Science* **2025**, *390*, 394–399. [CrossRef]
2. Siebenhofer, M.; Viernstein, A.; Morgenbesser, M.; Fleig, J.; Kubicek, M. Photoinduced electronic and ionic effects in strontium titanate. *Mater. Adv.* **2021**, *2*, 7583–7619. [CrossRef] [PubMed]
3. Kim, J.Y.; Jin, M.J.; Hou, B.; Kim, M.P.; Um, D.-S.; Kim, C.-I. Reducing the oxygen vacancy concentration in $SrTiO_3$-δ thin films via an optimized O_2 plasma treatment for enhancing device properties. *Appl. Surf. Sci.* **2023**, *639*, 158271. [CrossRef]
4. Kaiya, K.; Ueki, Y.; Kawamoto, H.; Watanabe, K.; Yoshino, S.; Yamaguchi, Y.; Kudo, A. Water splitting over transition metal-doped $SrTiO_3$ photocatalysts with response to visible light up to 660 nm. *Chem. Sci.* **2024**, *15*, 16025–16033. [CrossRef] [PubMed]
5. Scheerer, G.; Boselli, M.; Pulmannova, D.; Rischau, C.W.; Waelchli, A.; Gariglio, S.; Giannini, E.; van der Marel, D.; Triscone, J.-M. Ferroelectricity, Superconductivity, and $SrTiO_3$—Passions of K.A. Müller. *Condens. Matter* **2020**, *5*, 60. [CrossRef]
6. Shi, X.L.; Wu, H.; Liu, Q.; Zhou, W.; Lu, S.; Shao, Z.; Dargusch, M.; Chen, Z.-G. $SrTiO_3$-based thermoelectrics: Progress and challenges. *Nano Energy* **2020**, *78*, 105195. [CrossRef]
7. Matsuda, T.; Yoshida, Y.; Mitsuhara, K.; Kido, Y. The structure of $SrTiO_3$(001)-2 × 1 surface analyzed by high-resolution medium energy ion scattering coupled with ab initio calculations. *J. Chem. Phys.* **2013**, *138*, 244705. [CrossRef]
8. Deshmukh, V.V.; Ravikumar, C.R.; Kumar, M.R.A.; Ghotekar, S.; Kumar, A.N.; Jahagirdar, A.; Murthy, H.A. Structure, morphology and electrochemical properties of $SrTiO_3$ perovskite: Photocatalytic and supercapacitor applications. *Environ. Chem. Ecotoxicol.* **2021**, *3*, 241–248. [CrossRef]

9. Phoon, B.L.; Lai, C.W.; Juan, J.C.; Show, P.; Chen, W. A review of synthesis and morphology of $SrTiO_3$ for energy and other applications. *Int. J. Energy Res.* **2019**, *43*, 5151–5174. [CrossRef]
10. Liu, Y.; Wang, Z.; Meng, Q.; Zeng, Y.; Yin, Z.; Liu, Y.; Zhang, J.; Yang, J.; Li, W.; Li, Z.; et al. Tuning of optoelectronic performance of $SrTiO_3$ by surface termination and thickness. *Appl. Surf. Sci.* **2024**, *672*, 160821. [CrossRef]
11. Gao, Y.; Masuda, Y.; Yonezawa, T.; Koumoto, K. Preparation of $SrTiO_3$ thin films by the liquid phase deposition method. *Mater. Sci. Eng. B* **2003**, *99*, 290–293. [CrossRef]
12. Goldenberg, E.; Bayrak, T.; Ozgit-Akgun, C.; Haider, A.; Leghari, S.; Kumar, M.; Biyikli, N. Effect of O_2/Ar flow ratio and post-deposition annealing on the structural, optical and electrical characteristics of $SrTiO_3$ thin films deposited by RF sputtering at room temperature. *Thin Solid Film.* **2015**, *590*, 193–199. [CrossRef]
13. Gellé, F.; Chirita, R.; Mertz, D.; Rastei, M.V.; Dinia, A.; Colis, S. Guideline to atomically flat TiO_2-terminated $SrTiO_3$(001) surfaces. *Surf. Sci.* **2018**, *677*, 39–45. [CrossRef]
14. Yue, C.; Ying, P.; Xu, B.; Tian, Y. Surface Reconstructions of $SrTiO_3$(110) Calibrated with STM and LEED. *Phys. Status Solidi (B)* **2019**, *256*, 1900277. [CrossRef]
15. Ma, T.; Jacobs, R.; Booske, J.; Morgan, D. Understanding the interplay of surface structure and work function in oxides: A case study on $SrTiO_3$. *APL Mater.* **2020**, *8*, 071110. [CrossRef]
16. Chambers, S.A.; Sushko, P.V. Influence of crystalline order and defects on the absolute work functions and electron affinities of TiO2-and SrO-terminated n-$SrTiO_3$(001). *Phys. Rev. Mater.* **2019**, *3*, 125803. [CrossRef]
17. Chung, H.K.; Jeon, J.; Kim, H.; Jang, M.; Kim, S.-C.; Won, S.O.; Baek, I.-H.; Chung, Y.J.; Han, J.H.; Cho, S.H.; et al. Low temperature crystallization of atomic-layer-deposited $SrTiO_3$ films with an extremely low equivalent oxide thickness of sub-0.4 nm. *Appl. Surf. Sci.* **2024**, *664*, 160243. [CrossRef]
18. Yoon, H.; Truttmann, T.K.; Liu, F.; Matthews, B.E.; Choo, S.; Su, Q.; Saraswat, V.; Manzo, S.; Arnold, M.S.; Bowden, M.E.; et al. Freestanding epitaxial $SrTiO_3$ nanomembranes via remote epitaxy using hybrid molecular beam epitaxy. *Sci. Adv.* **2022**, *8*, eadd5328. [CrossRef]
19. Baki, A.; Abdeldayem, M.; Morales, C.; Flege, J.I.; Klimm, D.; Bierwagen, O.; Schwarzkopf, J. Potential of La-Doped $SrTiO_3$ Thin Films Grown by Metal–Organic Vapor Phase Epitaxy for Thermoelectric Applications. *Cryst. Growth Des.* **2023**, *23*, 2522–2530. [CrossRef]
20. Kim, S.H.; Lee, W.; An, C.H.; Kim, D.; Kwon, D.S.; Cho, S.T.; Cha, S.H.; Lim, J.I.; Hwang, C.S. Effect of the Annealing Temperature of the Seed Layer on the Following Main Layer in Atomic-Layer-Deposited $SrTiO_3$ Thin Films. *Phys. Status Solidi (RRL)-Rapid Res. Lett.* **2019**, *13*, 1800557. [CrossRef]
21. Kamaratos, M.; Giotopoulou, E.; Vlachos, D. The interaction mechanism of cesium with water on the $SrTiO_3$(100) surface at room temperature. *React. Kinet. Mech. Catal.* **2022**, *135*, 3257–3274. [CrossRef]
22. Hong, C.; Zou, W.; Ran, P.; Tanaka, K.; Matzelle, M.; Chiu, W.-C.; Markiewicz, R.S.; Barbiellini, B.; Zheng, C.; Li, S.; et al. Anomalous intense coherent secondary photoemission from a perovskite oxide. *Nature* **2023**, *617*, 493–498. [CrossRef] [PubMed]
23. Pérez, J.J.P.; Solís-Cortés, D.; Jiménez, F.M.; Escalante, M.C.L. Reduced band gap $SrTiO_3$ thin film prepared by magnetron sputtering for the oxygen evolution reaction. *Mater. Today Commun.* **2024**, *41*, 110492. [CrossRef]
24. Chien, Y.T.; Yang, X.X.; Lu, F.H. High photoelectrochemical response of $SrTiO_3/TiO_2$/TiN films synthesized via hydrothermal-galvanic couple method with reductive annealing. *Commun. Mater.* **2025**, *6*, 230. [CrossRef]
25. Wang, J.L.; Meng, X.C.; Liu, H.J.; Lian, Z.X.; Yao, K.W.; Li, J.L.; Li, R.B.; Zhang, G.H.; Wang, D. Circular coaxial filters with organic dielectric-loaded for secondary electron multiplication modulation and multipactor verification. *IEEE Trans. Microw. Theory Technol.* **2025**, *73*, 8415–8427. [CrossRef]
26. Zeng, W.; Li, Z.; Wang, Y.; Cao, L.; Fu, L.; Wang, C. Nonlinear Electrical Conductance Triggered by Partial Discharge of Fluorinated Carbon Nanotube Clusters and its Applications in Field Grading. *Inorganics* **2025**, *14*, 18. [CrossRef]
27. Wang, C.; Yang, Y.L.; Shi, X.R.; Li, W.D.; Sun, G.Y.; Chen, S.L.; Ran, S.L.; Zhang, G.J.; Chen, Z.Q. Secondary electron emission characteristics of 3D-printed ceramic insulators with functionally graded lattice structures. *Appl. Phys. Lett.* **2025**, *126*, 121601. [CrossRef]
28. Wang, C.; Chen, Z.Q.; Yang, Y.L.; Chen, S.L.; Shi, X.R.; Jin, X.; Yang, X.; Ran, S.L.; Sun, G.Y.; Zhang, G.J. Design and 3D printing of ceramic insulation for surface flashover mitigation in vacuum. *High Volt* **2024**, *10*, 1593–1601. [CrossRef]
29. Michizono, S.; Kinbara, A.; Saito, Y.; Yamaguchi, S.; Anami, S.; Matuda, N. TiN film coatings on alumina radio frequency windows. *J. Vac. Sci. Technol. A* **1992**, *10*, 1180–1184. [CrossRef]
30. Lian, Z.X.; Wang, D.; Zhu, X.P.; He, Y.N. High-performance microchannel plates based on atomic layer deposition for the preparation of functional layers. *J. Phys. D Appl. Phys.* **2025**, *58*, 115106. [CrossRef]
31. Gu, Y.Q.; Li, J.N.; Wang, D.; Zhang, N. Effect of Nitrogen Ratio in Sputtering on the Quality of Film Formation and Electron Emission Properties of Nitride Films. *Coatings* **2025**, *15*, 55. [CrossRef]
32. Suetsugu, Y.; Fukuma, H.; Ohmi, K.; Tobiyama, M.; Flanagan, J.; Ikeda, H.; Mulyani, E.; Shibata, K.; Ishibashi, T.; Shirai, M. Mitigating the electron cloud effect in the SuperKEKB positron ring. *Phys. Rev. Accel. Beams* **2025**, *28*, 120101. [CrossRef]

33. Kirby, R.E.; King, F.K. Secondary electron emission yields from PEP-II accelerator materials. *Nucl. Instrum. Methods Phys. Res. A* **2001**, *469*, 1–12. [CrossRef]
34. Popecki, M.A.; Adams, B.; Craven, C.A.; Cremer, T.; Foley, M.R.; Lyashenko, A.; O'MAhony, A.; Minot, M.J.; Aviles, M.; Bond, J.L.; et al. Microchannel plate fabrication using glass capillary arrays with atomic layer deposition films for resistance and gain. *J. Geophys. Res. Space Phys.* **2016**, *121*, 7449–7460. [CrossRef]
35. Gorelikov, D.; Sullivan, N.; Rouffignac, P.; Li, H.; Narayanamoorthy, J.; Tremsin, A.S. Development of atomic layer deposition-activated microchannel plates for single particle detection at cryogenic temperatures. *J. Vac. Sci. Technol. A* **2014**, *32*, 020605. [CrossRef]
36. Li, W.Q.; Zhou, N.; Lian, Z.X.; Wang, S.Z.; Wang, D.; Zhang, G.H. Evolution impact of key parameters on device gain for the microchannel plates with secondary electron emission functional layer. *Vacuum* **2025**, *241*, 114703. [CrossRef]
37. Tavant, A.; Croes, V.; Lucken, R.; Lafleur, T.; Bourdon, A.; Chabert, P. The effects of secondary electron emission on plasma sheath characteristics and electron transport in an ExB discharge via kinetic simulations. *Plasma Sources Sci. Technol.* **2018**, *27*, 124001. [CrossRef]
38. Lian, Z.X.; Yao, K.W.; Wang, D.; Zhang, K.Y.; Wang, R.; He, Y.N. Surface potential evolution and DC discharge measurement of the microstrip antenna dielectric under electron beam irradiation. *Vacuum* **2025**, *138*, 114270. [CrossRef]
39. Fareed, I.; Farooq, M.U.; Khan, M.D.; Ali, Z.; Butt, F.K. Band gap engineering of Strontium Titanate ($SrTiO_3$) for improved photocatalytic activity and excellent bio-sensing aptitude. *Mater. Sci. Semicond. Process.* **2024**, *177*, 108327. [CrossRef]
40. Jaya, R.P. 14-Porous concrete pavement containing nanosilica from black rice husk ash. In *New Materials in Civil Engineering*; Butterworth-Heinemann: Oxford, UK, 2020; pp. 493–527. [CrossRef]
41. Yang, M.; Zhang, T.; Schulz, P.; Li, Z.; Li, G.; Kim, D.H.; Guo, N.; Berry, J.J.; Zhu, K.; Zhao, Y. Facile fabrication of large-grain $CH_3NH_3PbI_3-xBr_x$ films for high-efficiency solar cells via CH_3NH_3Br-selective Ostwald ripening. *Nat. Commun.* **2016**, *7*, 12305. [CrossRef]
42. Mahmud, M.A.; Elumalai, N.K.; Upama, M.B.; Wang, D.; Puthen-Veettil, B.; Haque, F.; Wright, M.; Xu, C.; Pivrikas, A.; Uddin, A. Controlled Ostwald ripening mediated grain growth for smooth perovskite morphology and enhanced device performance. *Sol. Energy Mater. Sol. Cells* **2017**, *167*, 87–101. [CrossRef]
43. Frankel, R.S.; Aitken, D.W. Energy-Dispersive X-Ray Emission Spectroscopy. *Appl. Spectrosc.* **1970**, *24*, 557–566. [CrossRef]
44. Hanson, V.F. Quantitative Elemental Analysis of Art Objects by Energy-Dispersive X-Ray-Fluorescence Spectroscopy. *Appl. Spectrosc.* **1973**, *27*, 309–334. [CrossRef]
45. Lian, Z.X.; Xu, Y.N.; Meng, X.C.; Wang, D.; Chen, J.X.; Qi, K.C.; He, Y.N. Secondary electron emission reduction from boron nitride composite ceramic surfaces by the artificial microstructures and functional coating. *J. Phys. D Appl. Phys.* **2024**, *57*, 315304. [CrossRef]

Disclaimer/Publisher's Note: The statements, opinions and data contained in all publications are solely those of the individual author(s) and contributor(s) and not of MDPI and/or the editor(s). MDPI and/or the editor(s) disclaim responsibility for any injury to people or property resulting from any ideas, methods, instructions or products referred to in the content.

inorganics

MDPI

Article

Comparation of Graph Neural Networks and Traditional Machine Learning for Property Prediction in All-Inorganic Perovskite Materials

Jingyu Liu [1], Xueqiong Su [1,*], Lishan Yang [1], Jiansen Ding [1], Jin Wang [1], Xing Ling [1], Yong Pan [2], Zhijun Wang [3], Wei Zhao [4] and Yang Bu [3]

1 School of Physics and Optoelectronic Engineering, Beijing University of Technology, Beijing 100124, China
2 College of Science, Xi'an University of Architecture and Technology, Xi'an 710055, China
3 The First School of Clinical Medicine, General Hospital of Ningxia Medical University, Yinchuan 750004, China
4 Department of Biochemistry and Molecular Biology, School of Basic Medicine, Ningxia Medical University, Yinchuan 750004, China
* Correspondence: nysxq@bjut.edu.cn

Abstract

Machine learning (ML) methods have been widely explored for predicting material properties. However, due to the rapid development of ML techniques and the diversity of available models, performance comparisons between traditional and graph-based machine learning models remain limited. Therefore, we evaluate 11 conventional ML models alongside the graph neural network-based Crystal Graph Convolutional Neural Network (CGCNN) for predicting three key properties—formation energy (E_f), band gap (E_g), and energy above hull (E_h)—across a dataset comprising single perovskites, double perovskites, and their combined structures. The results demonstrate that for single perovskites, CGCNN exhibits gains of over 20% in the root mean square error (RMSE) relative to the second-best model (Gradient Boosting Regression), achieving values of 0.205 eV/atom (E_f), 0.718 eV (E_g), and 0.167 eV/atom (E_h). Prediction accuracy for double perovskites is significantly enhanced by training CGCNN on a combined dataset, particularly for E_h, where the coefficient of determination (R^2) improves approximately 68.1-fold compared to models trained exclusively on double-perovskite data. Feature importance analysis via one-shot, permutation-based, and recursive feature elimination (RFE) methods reveals that optimal model performance requires retention of at least the top 20 critical features. Furthermore, feature utilization patterns of CGCNN across different prediction tasks are visualized. This work provides actionable guidelines for model selection and feature engineering in perovskite property prediction, establishing a benchmark for future ML-driven materials discovery.

Keywords: machine learning; graph neural network; single perovskite; double perovskite; formation energy; band gap; energy above hull

1. Introduction

In recent years, perovskite-structured materials have drawn significant attention by virtue of their excellent optoelectronic and optical properties. These materials have been extensively studied in various application domains, including catalysts [1,2], solar cells [3], light-emitting diodes [4], X-ray scintillators [5], and others [6–8]. Perovskites are typically defined as compounds with the general chemical formula ABX_3, characterized by a crystal

structure in which B atoms occupy the center of octahedra formed by X atoms at the corners, and encapsulating A atoms, where A-site is a monovalent organic or inorganic cation, B-site is a divalent cation, and X-site commonly is a halide anion. Based on the state of corner-sharing network BX_6 octahedra, perovskites can be classified into 3D (where octahedra share corners in three dimensions), 2D, 1D, and 0D (where octahedra are isolated and separated by A-site cations) [9]. The occupancy of B-site in perovskite is not necessarily limited to a single type of atom. From this perspective, perovskite also can be categorized into single perovskite with the formula ABX_3 and double perovskite [10] with $A_2BB'X_6$, for example, the widely studied cesium lead halide perovskites [11] and lead-free cesium silver-bismuth halide perovskites [12].

Perovskite materials exhibit significant property differences due to their diverse compositional variations. Traditional trial-and-error experimental approaches severely hinder the discovery step of perovskite materials. Meanwhile, first-principles computational methods are challenged in rapid material discovery due to their slow computation speed and dependence on computational materials science experts. ML is a computational approach that establishes mapping relationships between inputs and outputs [13]. It offers faster and more cost-effective advantages compared to experimental approaches. As early as around 2000, pioneering studies had already explored using ML methods for predicting material properties [14,15]. In recent years, with the development of open material databases based on first-principles calculations such as Joint Automated Repository for Various Integrated Simulations(JARVIS) [16], Materials Project (MP) [17], Open Quantum Materials Database (OQMD) [18], and others [19–21], extensive studies have been conducted on ML-based material property prediction [22–29]. Sadat and Wang compared logistic regression, artificial neural networks, and random forest for rapid screening of photonic crystals regarding band gap existence and central frequency [30]. Without rapid screening, random selection yielded only a 17% probability of identifying materials with an existing band gap, while random forest-based screening increased this probability to 89%. Sharma et al. employed random forest regression to identify the most influential factors for defect formation energy in oxide perovskites, finding dopant ion size, formation enthalpy, effective tolerance factor, and oxidation state as key determinants [31]. Rath et al. achieved 81% precision in predicting direct band gap characteristics for ABX_3 perovskites by using eXtreme Gradient BOOST [32].

Deep learning (DL), a subset of machine learning, has gained significant attention due to its powerful representation learning capabilities. In recent years, DL has been widely explored in fields such as autonomous driving [33,34], image recognition [35,36], and recommendation systems [37]. Specifically, graph neural networks (GNNs) [38], a type of DL network that takes non-Euclidean graph structures [13,39,40] describing nodes and their relationships as input, show great potential for modeling complex phenomena [41,42], such as N-body simulations [43], protein property prediction [44,45], and material property prediction [46–48]. Crystal Graph Convolutional Neural Network (CGCNN) [49] was the first to represent crystal structures as graphs and use GNN to predict properties such as band gap, formation energy, and energy above hull, achieving better performance than traditional machine learning models. Based on CGCNN's features and basic structure, Orbital Graph Convolutional Neural Network (OGCNN) [50] incorporates an encoder–decoder architecture to learn important features from atomic element characteristics, orbital–orbital interactions, and geometric features. MatErials Graph Network (MEGNet) [51] builds upon CGCNN and Message Passing Neural Network (MPNN) [52], introducing temperature, entropy, and pressure as global state variables. When predicting properties related to these global states, such as internal energy, enthalpy, and Gibbs free energy at room temperature and 0 K, its integrated model outperforms individual models for each

https://doi.org/10.3390/inorganics14020058

property. Inspired by SchNet [53], Atomistic Line Graph Neural Network (ALIGNN) [54] uses both traditional graphs (with atoms as nodes and existing edges between atoms within a certain distance) and line graphs (where edges become nodes and relationships between edges become edges). This approach incorporates more atomic interaction information. There are other developments including Materials Graph neural Network architecture that incorporates three-body interactions (M3GNet) [55], which adds atomic coordinates and lattice matrices to predict interatomic potentials while maintaining strong scalability and flexibility, and Crystals with Transformers on Graphs (CrysToGraph) [56], which incorporates Transformer layers for improving long-range interactions modeling.

The improvement for traditional machine learning algorithms performance relies on feature engineering [57], which involves manually input features design. This process heavily depends on experts with theoretical calculation experience and understanding of model characteristics. While traditional machine learning models have relatively weak fitting capabilities and struggle with highly complex problems, they offer the advantage of being easy to train. Deep learning models can learn data representations directly from raw data [58,59], eliminating the need for manual feature design required in traditional machine learning. However, they face limitations such as large data requirements and strict data distribution demands. Currently, there is limited systematic comparative research between traditional machine learning models and graph neural network-based models, and their differences in feature utilization under conditions of imbalanced data distributions and relatively large datasets. This study can provide guidance for subsequent model selection and feature selection when predicting properties of perovskite materials.

In this work, we compare the performance of machine learning and deep learning models for band gap-related properties of perovskites, and feature importance is revealed. The complete workflow is shown in Figure 1. Specifically, we evaluate 11 commonly used traditional machine learning models against the CGCNN, a classical graph neural network in material property prediction tasks, for predicting three key properties—formation energy (E_f), band gap (E_g), and energy above hull (E_h)—of both single and double inorganic perovskite structures. Additionally, we reveal the differences in feature utilization between the best-performing traditional machine learning model and CGCNN across different tasks.

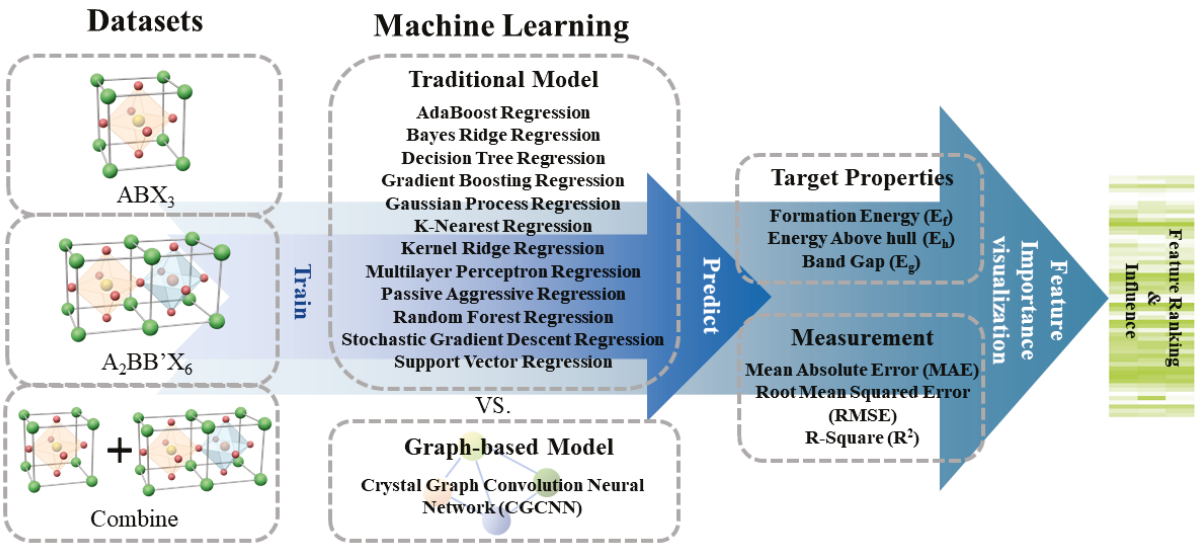

Figure 1. Schematic showing the workflow of this work.

We first construct a dataset for traditional machine learning by selecting compositions of single and double perovskites and using 57 features as input. While maintaining the chemical formula consistency, we extract samples from the MP database that meet

CGCNN's input requirements and contain E_f, E_g, and E_h labels to form the CGCNN dataset. Both traditional machine learning models, optimized using Bayesian optimization, and CGCNN, with its recommended parameters, are evaluated on the three target properties using performance metrics: root mean square error (RMSE), mean absolute error (MAE), and coefficient of determination (R^2). Finally, we discuss potential reasons for performance differences between the best-performing traditional machine learning model and CGCNN, focusing on the cases where $R^2 > 0$.

2. Results and Discussion

In the task for predicting E_f, under the single-perovskite dataset condition (Figure 2A), CGCNN achieves a MAE of 0.126 eV/atom, a RMSE of 0.205 eV/atom, and a R^2 of 0.943 (Figure 3D) on the test set. Relative to GBR, the second-highest performing approach, CGCNN, exhibits respective gains of 35.1%, 34.5%, and 6.0%, with GBR yielding 0.194 eV/atom, 0.313 eV/atom, and 0.889 (Figure 3A).

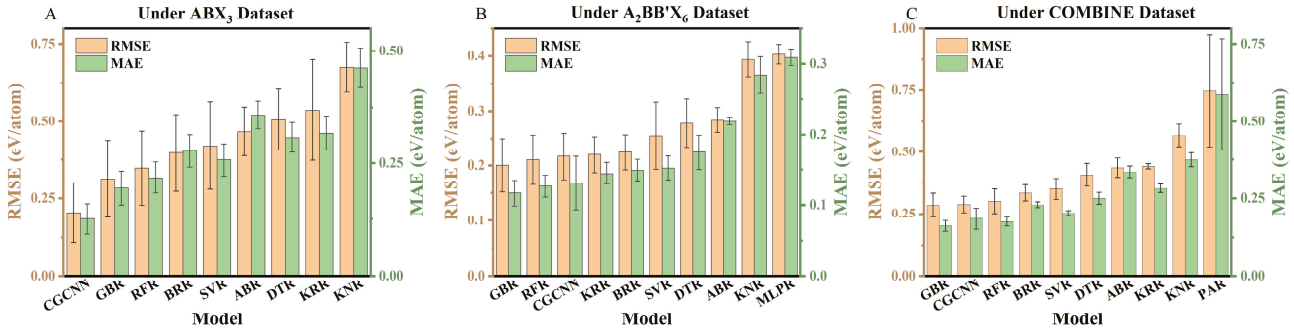

Figure 2. RMSE, MAE achieved by models for predicting formation energy in ABX_3, $A_2BB'X_6$, and combine dataset. The height of the bar chart represents the mean value obtained from 5-fold cross-validation, and the upper and lower bounds of the error bars are determined by adding and subtracting the standard deviation of 5-fold cross-validation to and from the mean value, respectively.

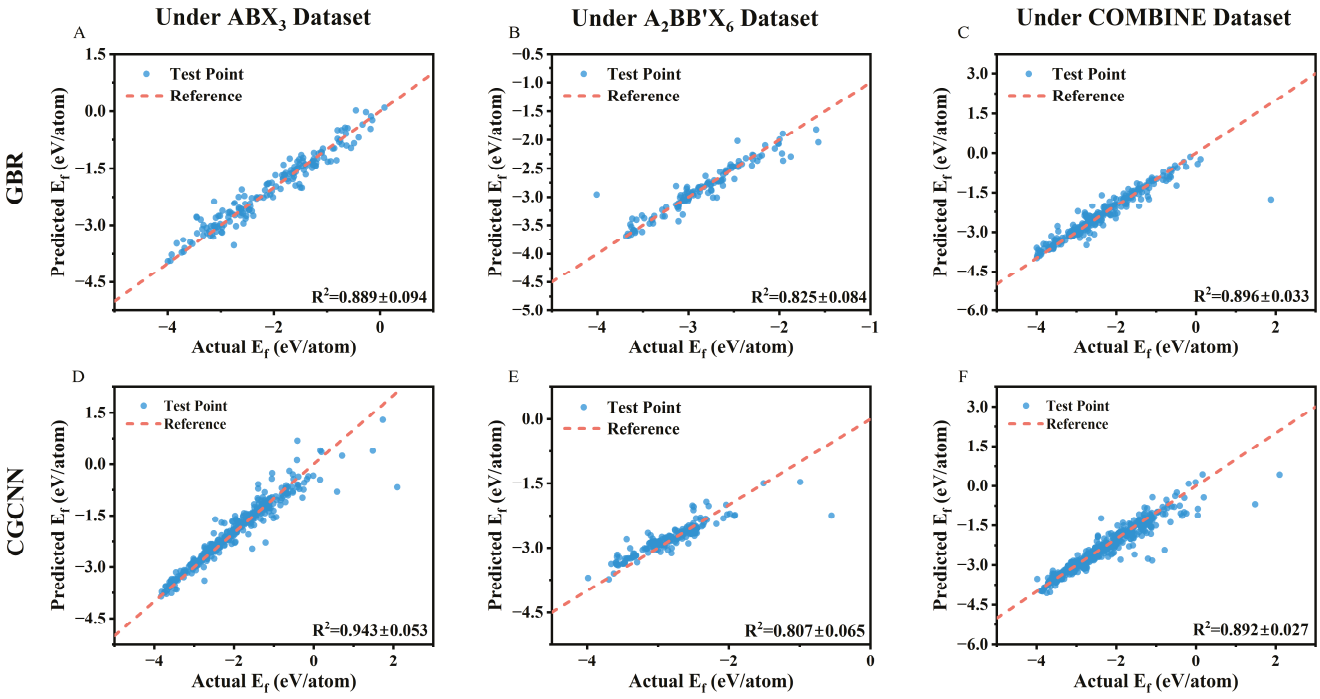

Figure 3. In the task of predicting formation energy, the distribution of the prediction result achieved by the best-performing model among traditional machine learning and graph-based methods.

In Figure 2B, a MAE of 0.116 eV, a RMSE of 0.200 eV, and a R^2 of 0.896 (Figure 3B), achieved by GBR, showing improvements of 5.3%, 7.5%, and 1.3% to 0.126 eV, 0.210 eV, and 0.808 reached by Random Forest Regression (RFR). GCGNN got MAE of 0.131 eV, RMSE of 0.217 eV, and R^2 of 0.807, marginally lower than that of RFR. Under the combine dataset condition, as Figure 2C illustrated, the best performance of RMSE of 0.284 eV/atom, MAE of 0.160 eV/atom, and R^2 of 0.896 (Figure 3C) was still got by GBR. Compared to GBR, CGCNN achieved a comparable result in RMSE but exhibited a 12.6% higher MAE. In terms of R^2, 0.896 got by Gaussian Process Regression (GPR) compared to 0.892 got by CGCNN, as shown in Figure 3C,F, the two models displayed no significant difference; however, the distribution of GBR results was more narrowly concentrated. This empirical evidence suggests CGCNN is more appropriate for ABX_3 structures, whereas GBR represents the preferred choice for double perovskites.

All the valid results for predicting E_g are illustrated in Figure 4. In the ABX_3 dataset (Figure 4A), CGCNN exhibited better performance than the GBR with a RMSE of 0.718 eV, a MAE of 0.517 eV, and a R^2 of 0.814. In contrast, the GBR achieved less favorable results, with a RMSE of 1.03 eV, a MAE of 0.722 eV, and a R^2 of 0.624 (Figure 5A). In the double-perovskite dataset (Figure 4B), GBR with a RMSE of 0.873 eV, a MAE of 0.628 eV, and a R^2 of 0.763 (Figure 5B) delivered comparable results to RFR, while CGCNN showed lower performance relative to the traditional machine learning models, and Figure 5E shows that CGCNN's predictions are predominantly concentrated around 1.5 eV. Under the mixed-dataset condition (Figure 4C), CGCNN's performance lagged behind that of Gradient Boosting Regression (GBR) and Decision Tree Regression (DTR). CGCNN achieved a RMSE of 1.08 eV, a MAE of 0.763 eV, and a R^2 of 0.605 (Figure 5F), which were 13%, 23%, and 25.7% higher than those of the GBR method with 0.956 eV, 0.711 eV, and 0.814 (Figure 5C), respectively, placing it in the third position. That empirical evidence support differentiated model selection based on perovskite structure. For predicting E_g, CGCNN is well-suited for single perovskites and RFR for double perovskites.

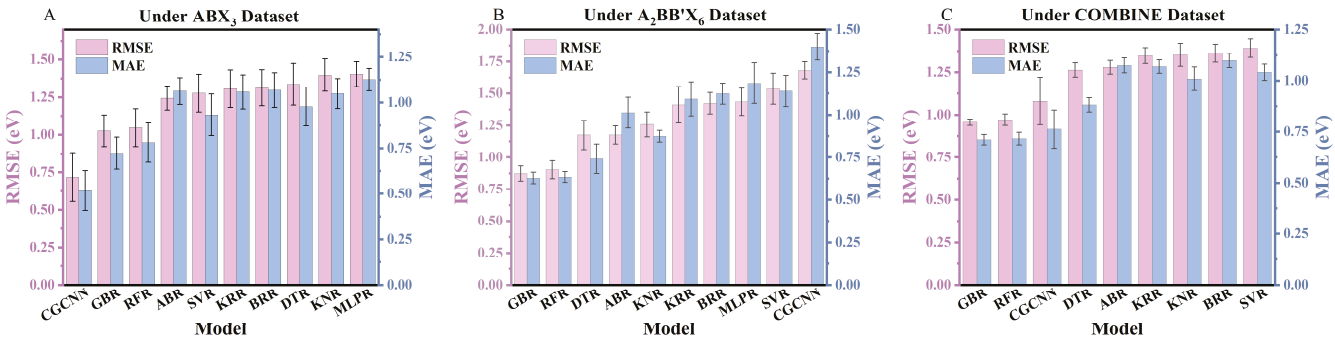

Figure 4. RMSE, MAE achieved by models for predicting band gap in ABX_3, $A_2BB'X_6$, and combine dataset. The height of the bar chart represents the mean value obtained from 5-fold cross-validation, and the upper and lower bounds of the error bars are determined by adding and subtracting the standard deviation of 5-fold cross-validation to and from the mean value, respectively.

Compared with the first two prediction tasks, the prediction of energy above hull exhibited a distinct trend, with detailed results presented in Figure 6. For both the ABX_3 and mixed datasets (Figure 6A,C), CGCNN achieved the best performance, ranking first. In the ABX_3 dataset, CGCNN recorded a RMSE of 0.167 eV/atom, a MAE of 0.073 eV/atom, and a R^2 of 0.787 (Figure 7A), with these values showing improvements of 24.4%, 24.0%, and 300.1% relative to the second-best model, RFR. In the mixed dataset, it reaches scores of 0.184 eV/atom, 0.073 eV/atom, and 0.713 (Figure 7C) for RMSE, MAE, and R^2, respectively, with performance gains of GBR of 18.2%, 20.7%, and 337.4% over GBR. As shown in

Figure 6B, only two methods achieve a R^2 between 0 and 1 for predicting E_h in the double-perovskite dataset, and it can be found that CGCNN and KRR are valid with R^2 close to 0, and most predicted sample points distribute around 0 (from Figure 7B,E).

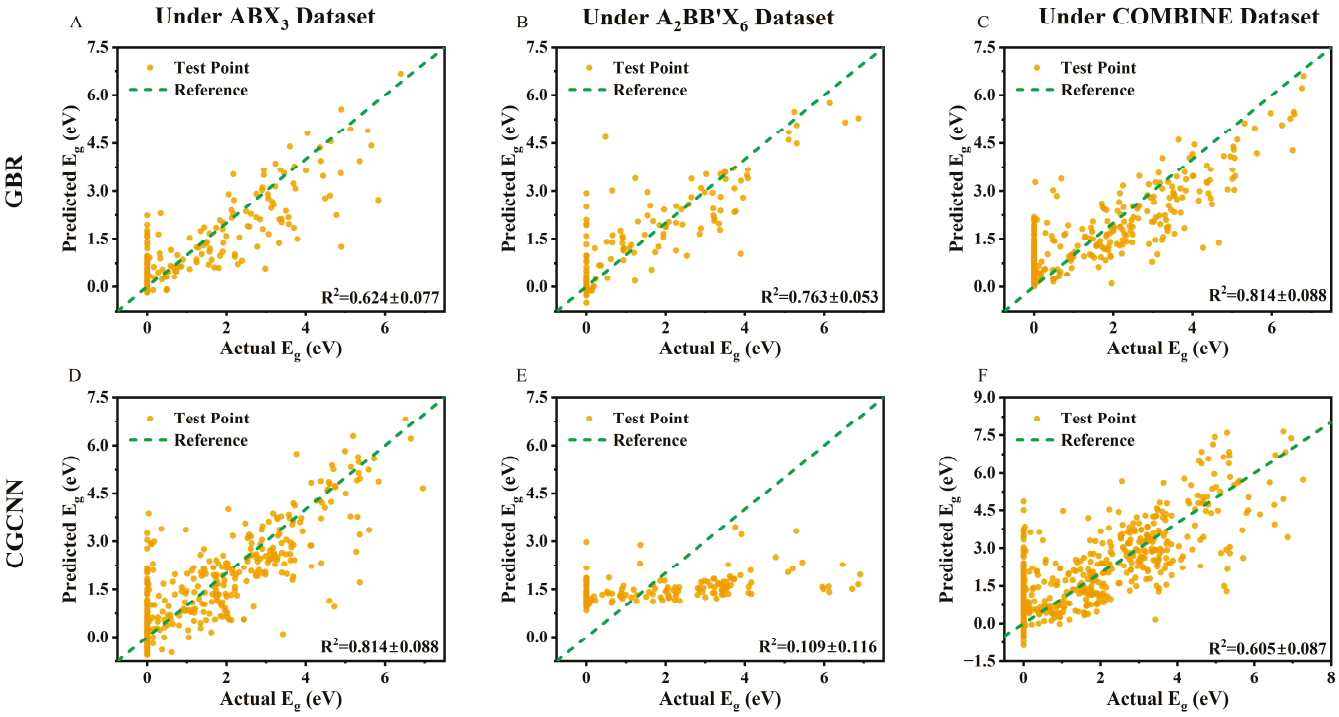

Figure 5. In the task of predicting band gap, the distribution of the prediction result achieved by the best-performing model among traditional machine learning and graph-based methods.

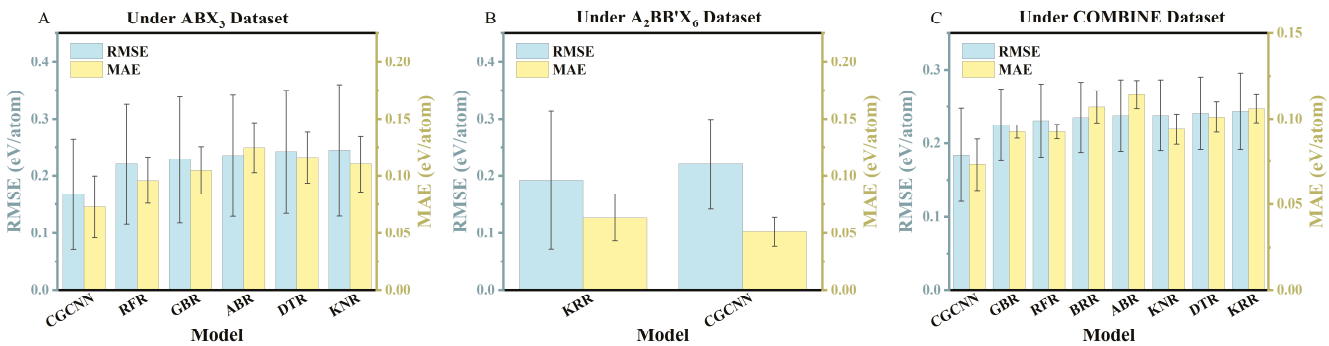

Figure 6. RMSE, MAE achieved by models for predicting energy above hull in ABX_3, $A_2BB'X_6$, and combine dataset. The height of the bar chart represents the mean value obtained from 5-fold cross-validation, and the upper and lower bounds of the error bars are determined by adding and subtracting the standard deviation of 5-fold cross-validation to and from the mean value, respectively.

The rapid performance degradation of CGCNN in predicting two key perovskite properties (E_g and E_h) is inherently due to the dual constraints of the double-perovskite dataset—small sample size and extreme distribution imbalance—and CGCNN's intrinsic reliance on sufficient data for structural representation learning and high sensitivity to data skewness. These constraints have no obvious effect on the E_f task, where relatively balanced data distribution enables CGCNN to achieve satisfactory results. They are most pronounced in the E_h task, leading to stepwise performance decline (single perovskite > combined dataset > double perovskite), with the degradation magnitude positively correlated with the constraint severity (harsher for E_h than E_g).

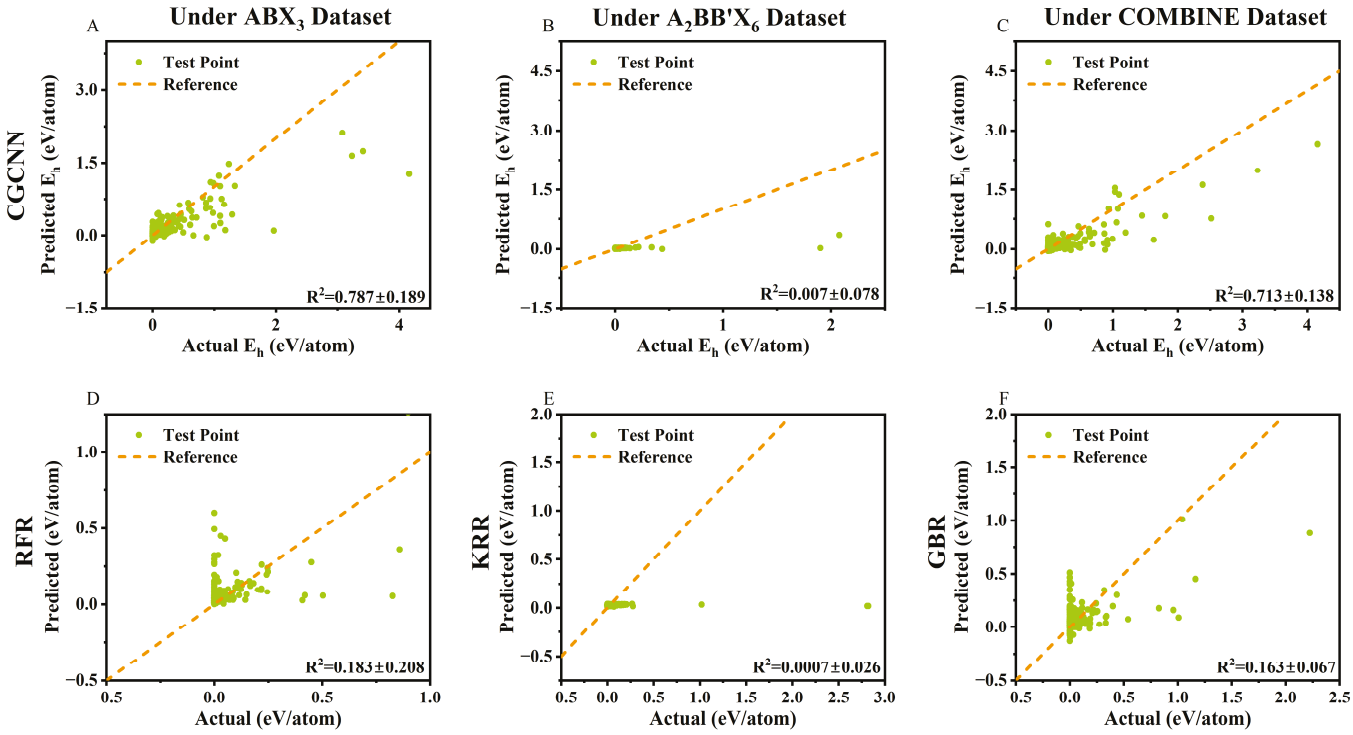

Figure 7. In the task of predicting energy above hull, the distribution of the prediction result achieved by the best-performing model among traditional machine learning and graph-based methods.

For the E_h prediction task, both single- and double-perovskite datasets exhibit extreme distribution imbalance, with over 80% of samples concentrated near 0 eV/atom (Figure 8C,F). The double-perovskite dataset is further constrained by limited sample size. This dual constraint hinders CGCNN from learning the nonlinear mapping between E_h and interatomic geometric and elemental relationships via its graph–structural representation, as CGCNN's core advantage of mining implicit crystal structure patterns relies on sufficient data, resulting in a R^2 of merely 0.007 for double-perovskite E_h prediction. The extreme E_h distribution imbalance probably stems from the perovskite simulation's core objective: prioritizing stable, synthesizable candidates by excluding unstable samples and retaining near-zero E_h samples. This research-driven selection induces data skewness, impairing diversity-dependent models, like CGCNN, in learning generalizable patterns.

For E_g, similar distribution patterns but a milder imbalance explain CGCNN's better performance than E_h both for single- and double-perovskite datasets, while it also exhibits limited E_g prediction performance for double perovskites ($R^2 = 0.109 \pm 0.116$, Figure 5E)—a result attributed to dataset constraints, double-perovskite structural complexity, and CGCNN's architectural limitations. Unlike ABX_3, $A_2BB'X_6$ has dual B/B′ cations plus potential lattice distortions and cation ordering, making E_g sensitive to bond angles (not explicitly encoded in CGCNN input). Additionally, CGCNN prioritizes short-range atomic interactions, failing to effectively incorporate long-range effects. These factors introduce training uncertainty, thus preventing effective fitting and meaningful predicted actual E_g correlations.

To evaluate the generalization ability of CGCNN, we trained the models on mixed-perovskite datasets and only assessed their predictions on double-perovskite data. As Figure 9A illustrates, the model trained only on the ABX_3 dataset (upper branch) shows poor prediction performance, while the model trained on the combined dataset (lower branch) achieves improvement across all three tasks. The prediction performance for double-perovskite properties was compared between the mixed-dataset and double-

perovskite-dataset training conditions, as shown in Figure 9B–D. For predicting E_f, under the combine dataset training condition, RMSE 0.198 eV/atom, MAE 0.12 eV/atom, and R^2 0.84 were achieved, representing improvements of 8.7%, 8.4%, and 4.1%, respectively, compared to the double-perovskite training condition; for E_g, the values were 1.43 eV, 1.04 eV, and 0.355, showing improvements of 14.9%, 25.7%, and 225.7%; most notably, for E_h prediction, 0.106 eV/atom, 0.0397 eV/atom, and 0.519 were achieved, demonstrating significant improvements of 51.8%, 22.3%, and 6720.0%, respectively. It can be revealed that under the combine dataset condition, the performance is not merely an average of good and bad results from sub-datasets. This result indicates that for small-scale datasets with an imbalanced distribution, the model performance can be enhanced by supplementing with data of similar types. Even if the additional data also exhibits an imbalanced distribution, it can still improve the model performance to a certain extent. For the present work, this implies supplementing the double-perovskite dataset with single-perovskite samples.

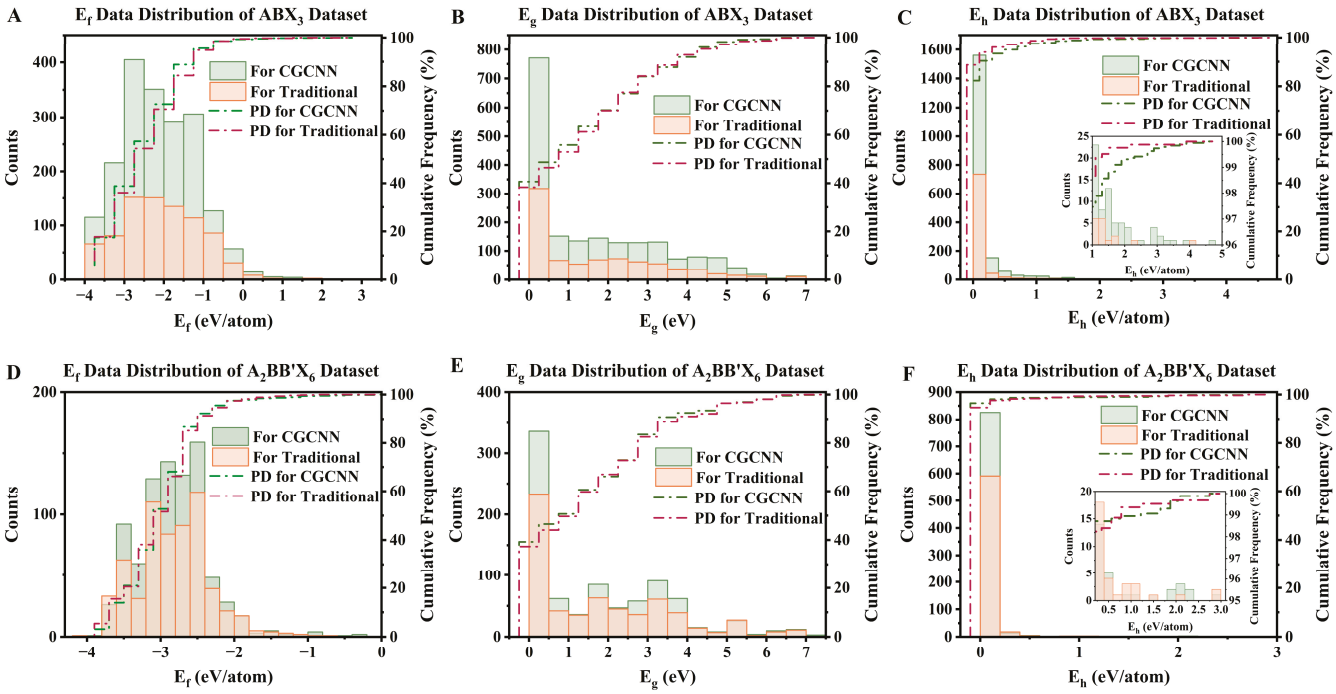

Figure 8. Dataset distributions for traditional machine learning model and CGCNN in predicting E_f, E_g, and E_h.

To reveal the best-performing traditional machine learning model's utilization of input features across different tasks and training datasets, this work employed Permutation-based, Recursive-Feature-Elimination (RFE), and One-shot feature selection methods to evaluate feature importance. Since the GBR model demonstrated the best performance among traditional machine learning algorithms for E_f and E_g, GBR was selected as the subject for feature importance analysis. For CGCNN, this work assessed the impact of different input features on prediction performance by masking specific features, thereby revealing their relative importance. The values shown in Figures 10–12 represent the changes in performance metrics relative to the unmasked condition. Group and Period denote the group number and period number of an element in the periodic table, respectively, while Block refers to the orbital of its valence electrons (i.e., s, p, d, f blocks).

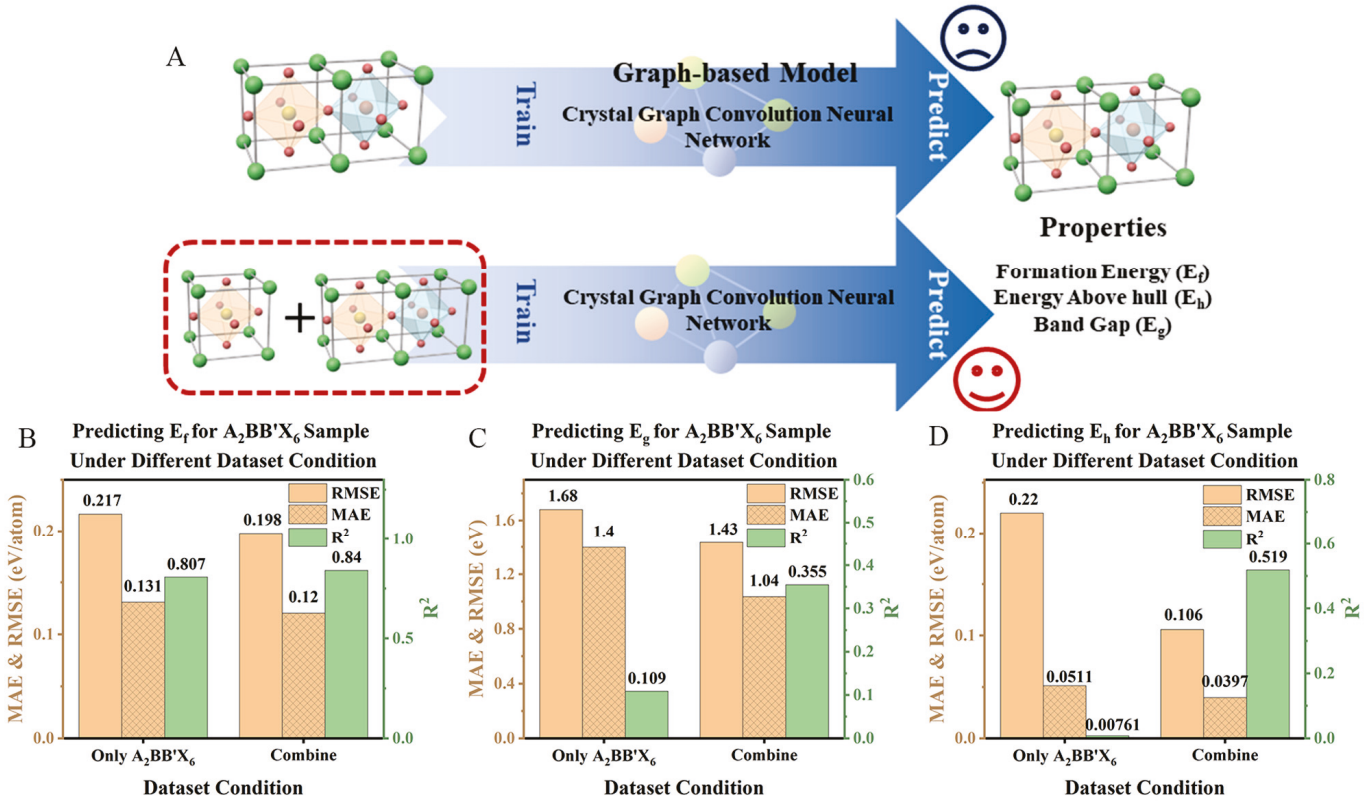

Figure 9. (**A**) Schematic illustration of CGCNN trained under different dataset conditions for predicting $A_2BB'X_6$ structure's property. For predicting (**B**) E_f, (**C**) E_g, and (**D**) E_h properties of $A_2BB'X_6$, the performances of CGCNN under different training dataset conditions.

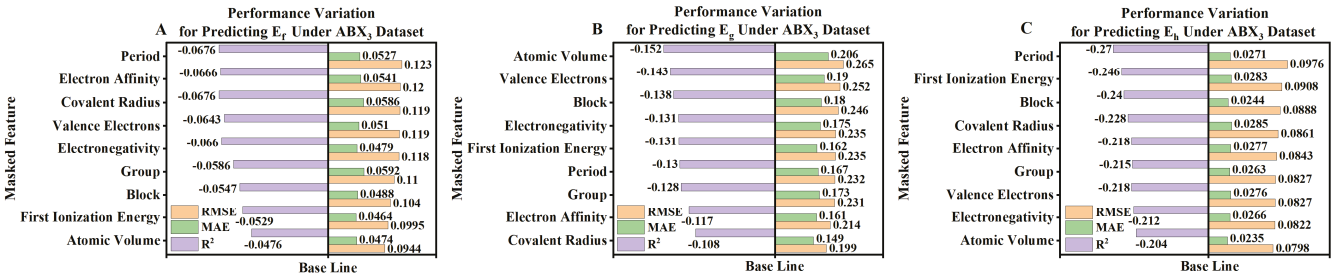

Figure 10. Impacts to performances of CGCNN with masking different feature for predicting E_f, E_g, and E_h under ABX_3 dataset condition. The units of MAE and RMSE for E_f, E_g, and E_h are eV/atom, eV, and eV/atom, respectively.

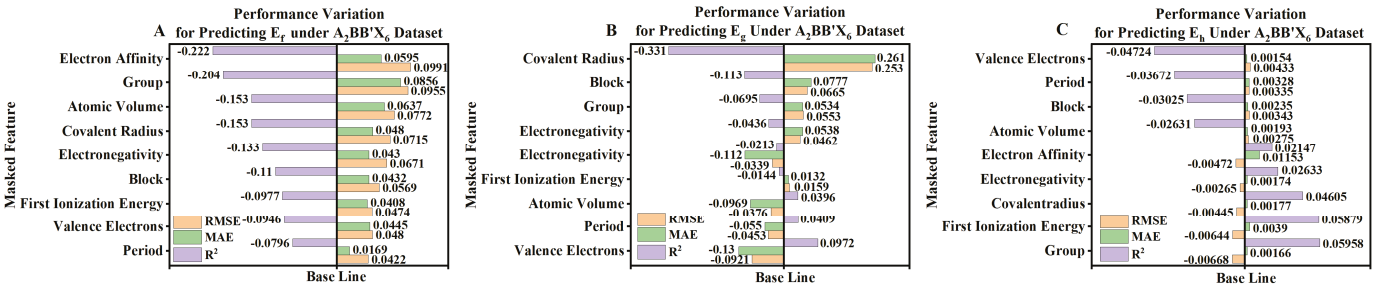

Figure 11. Impacts to performances of CGCNN with masking different feature for predicting E_f, E_g, and E_h under $A_2BB'X_6$ dataset condition. The units of MAE and RMSE for E_f, E_g, and E_h are eV/atom, eV, and eV/atom, respectively.

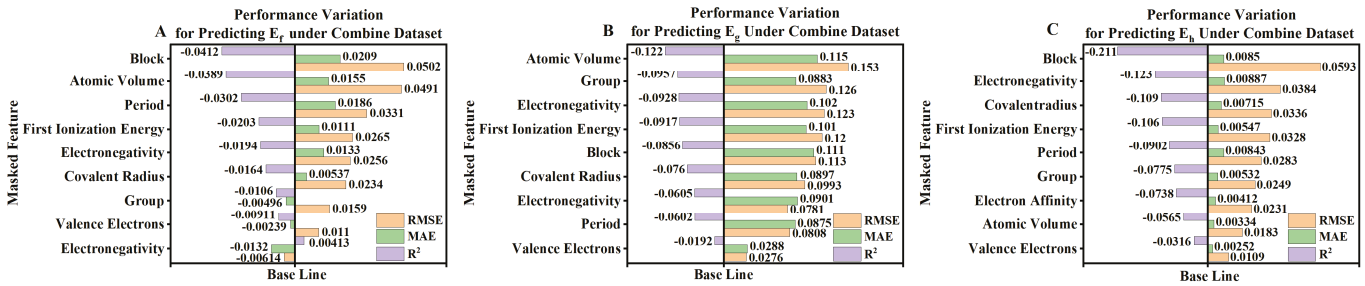

Figure 12. Impacts to performances of CGCNN with masking different feature for predicting E_f, E_g, and E_h under Combine dataset condition. The units of MAE and RMSE for E_f, E_g, and E_h are eV/atom, eV, and eV/atom, respectively.

For the E_f prediction task, Figure 13 presents the feature importance rankings derived from the GBR model under different dataset conditions using three feature selection methods, and abbreviations and full names of input features are given in Table 1. Figure 14 reveals that when fewer than the top 20 features are selected, the R^2, RMSE, and MAE undergo dramatic changes with the increase in the number of selected features (n), generally showing improving trends. When n exceeds 20, the three feature selection methods exert a negligible influence on these metrics, all achieving optimal model performance. For CGCNN, Figures 10A–12A illustrate the effects of masking input features across three datasets. Under the ABX_3 and combine datasets, removing any single feature leads to a change in R^2 by less than 7%. However, under $A_2BB'X_6$, masking any feature except period number results in more than a 9% reduction of R^2. In particular, masking electron affinity and group number causes a performance degradation of over 20%; specifically, the second-ranked feature (group number) shows a respective performance gain of 5.1% relative to the third-ranked one (atomic volume), which is approximately 1.33 times higher, indicating these two features show significant correlation with E_f in $A_2BB'X_6$ structures. As shown in Figure 12A, an anomalous improvement in model performance is observed when masking electronegativity. This phenomenon can be attributed to the insignificant impact of electronegativity on model performance, which is smaller than the performance fluctuations caused by dataset partitioning.

Table 1. Table of full names and abbreviations for input features in traditional machine learning.

Features	Abbreviation	Unit	Title 1	Title 2	Title 3
Atomic Number	Z	-	entry 1	data	data
Group Number	group	-	entry 2	data	data
Row Number	row	-			
Pettifor Mendeleev Number	pet_mn	-			
Villars Modified Mendeleev Number	vil_mn	-			
IUPAC Ordering Number	iupac	-			
Average Ionic Radius	av_ion_rad	angstrom			
Atomic Radius	atom_rad	angstrom			
Calculated Atomic Radius	cal_ atom_rad	angstrom			
Covalent Radius	cov_rad	angstrom			
Van der Waals Radius	vdw_rad	angstrom			
Pauling Electronegativity	x	pauling			
Electron Affinity	ea	eV			
First Ionization Energy	ie	eV			
Static Average Electric Dipole Polarizability	p	10^{-24} cm^3			
Valence Electrons	val	-			

Table 1. *Cont.*

Features	Abbreviation	Unit	Title 1	Title 2	Title 3
Atomic Mass	atom_mass	g/mol			
Elemental Solid Density	rho	g/cc			
Molar Volume	mol_vol	cc			
Boiling Point	bp	k			
Melting Point	mp	k			
Thermal Conductivity	k	W/m·K			
Heat of Fusion	heat_fus	eV			
Heat of Vaporization	heat_vap	eV			
Specific Heat	spec_heat	KJ/kg·K			
Sum of sp-Bonding Radius	sum_rsp	atomic unit			
Average of sp-Bonding Radius	av_rsp	atomic unit			
Goldschmidt Tolerance Factor	gtf	-			
Octahedral Factor	of	-			
Structural Density	st_rho	g/cc			

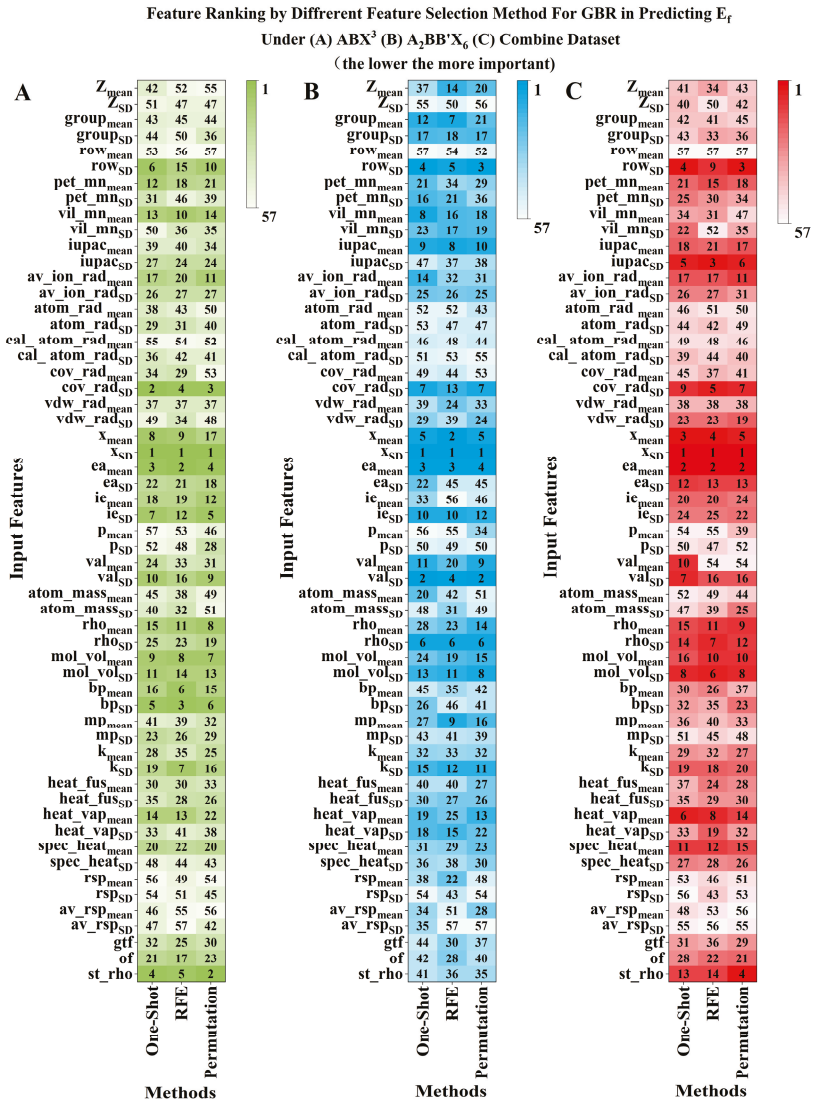

Figure 13. Rank of input features for GBR model by using permutation, RFE, and one-shot method under (**A**) ABX_3, (**B**) $A_2BB'X_6$, and (**C**) combine dataset in the task for predicting E_f. Abbreviations and full names of input features are given in Table 1.

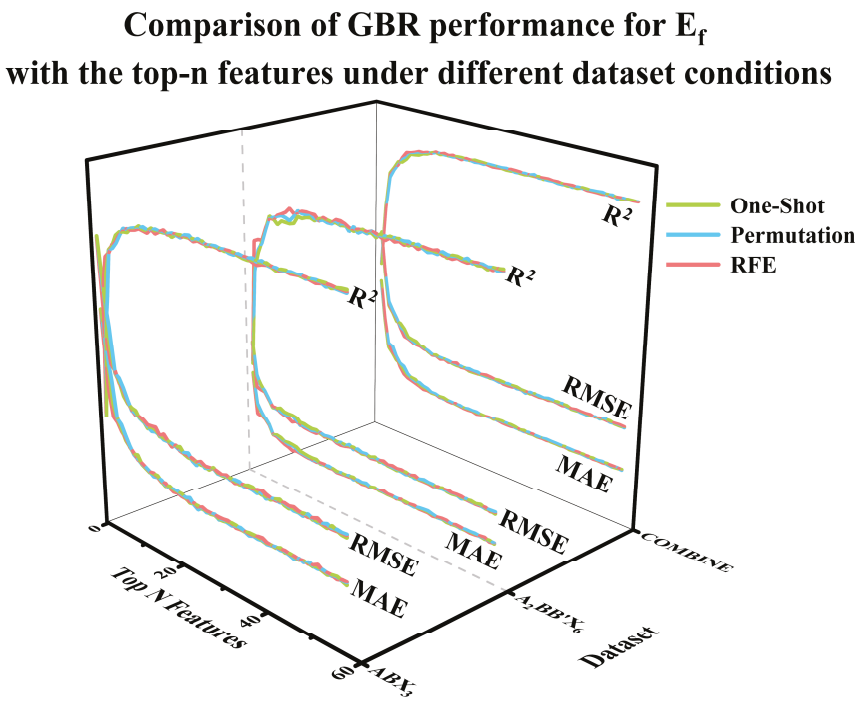

Figure 14. Comparison of GBR performance for E_f with the top-n features under ABX_3, $A_2BB'X_6$, and Combine dataset conditions.

For predicting E_g in the single-perovskite dataset, Figure 15 shows feature importance rankings of GBR, while Figure 16 reveals similar trends to those observed in the E_f prediction task. Metrics change significantly with $n < 20$ and stabilize when $n > 20$. Figures 10B–12B illustrate feature masking effects of CGCNN. Under the single-perovskite dataset, all features reduce R^2 by over 10%, with the maximum degradation occurring when the atomic volume is masked (15.2% and 12.2% in the ABX_3 and combine datasets, respectively). This result indicates strong correlation intensity between atomic volume and E_g. In the $A_2BB'X_6$ structure, numerous cases of performance improvement are observed upon feature removal. Considering the wide distribution ranges of the three metrics with original input features, this anomalous phenomenon can be attributed to performance fluctuations caused by extreme distributions and limited data volume. Similarly, Figure 11C can also be explained by the same reasons.

For E_h, traditional machine learning models exhibited excessively poor performance, rendering their analysis meaningless. The effects of masking CGCNN's input features are shown in Figures 10C–12C. The ABX_3 dataset exhibits a relatively uniform distribution of feature impacts, while in the combine dataset, the Block feature exerts a substantial influence on all three metrics, with its R^2 exceeding that of the second-ranked feature (electronegativity) by 8.8%, which is approximately 1.72 times higher. This indicates that the Block feature demonstrates significantly stronger correlation with E_h prediction capability compared to other features.

The feature importance analysis uncovers both the fundamental physical distinctions and shared underlying principles across the three property prediction tasks. As core metrics of thermodynamic stability, E_f and E_h exhibit a high degree of overlap in their key influencing features, including period, covalent radius, and electron affinity. This overlap stems from their strong physical linkage, as both properties are governed by the same atomic bonding strength and lattice stability that dictate thermodynamic behavior. The elevated importance of first ionization energy in E_h further highlights its unique physical connotation of phase competition, where the electronic stability of competing phases mod-

ulates the convex hull baseline. In contrast, the feature importance profile for band gap E_g—dominated by atomic volume, valence electron count, and electronegativity—aligns directly with its electronic structure origin: valence electrons dictate valence band filling, atomic volume governs orbital overlap and band broadening, and electronegativity drives orbital level splitting. This distinct feature set sharply differentiates E_g from the thermodynamic properties, emphasizing the intrinsic physical divergence between electronic structure and thermodynamic stability. Across all three properties, period, group, and Block emerge as universal features, reflecting the pervasive control of elemental electronic configurations over material properties.

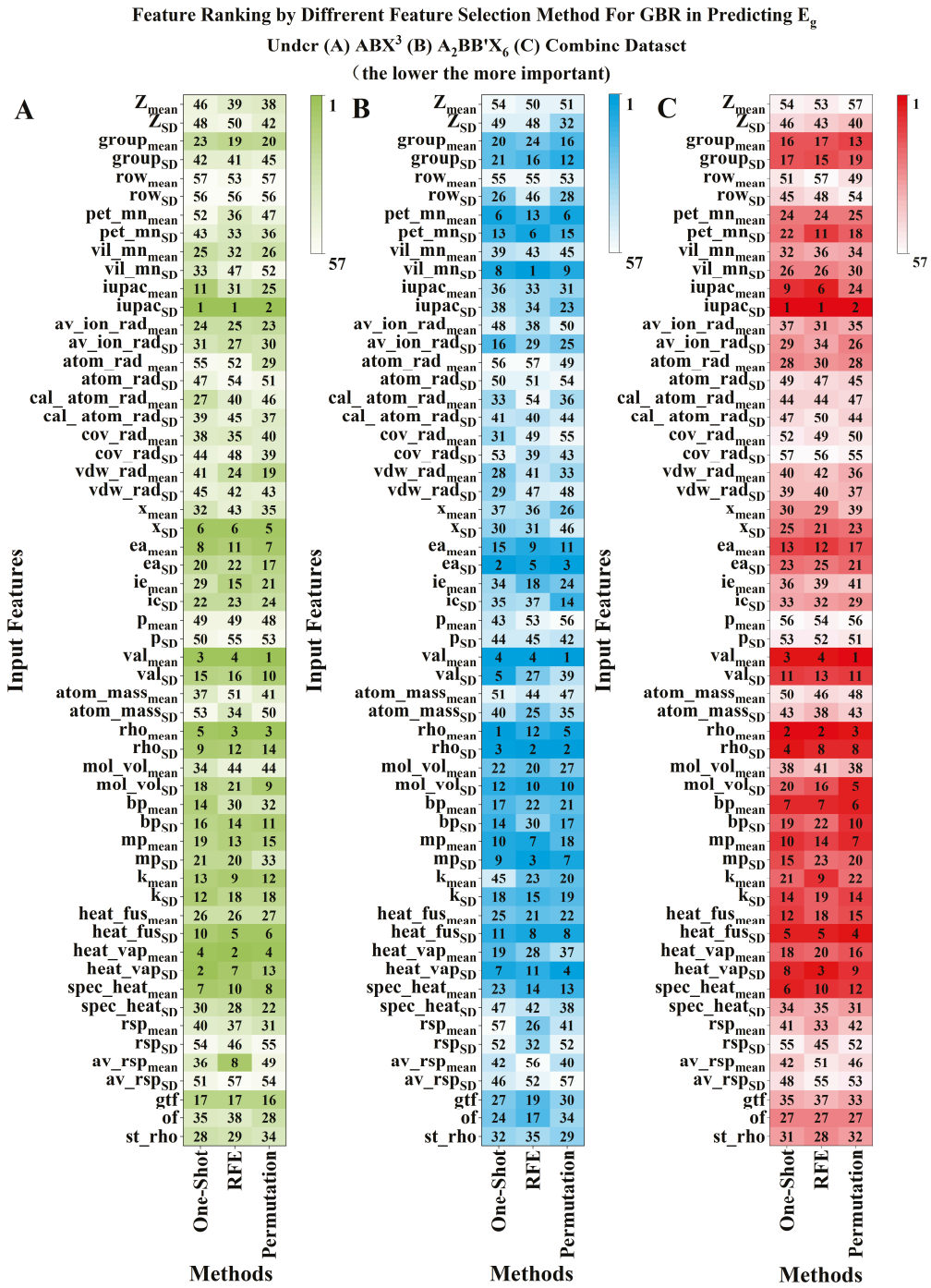

Figure 15. Rank of input features for GBR model by using permutation, RFE, and one-shot method under (**A**) ABX_3, (**B**) $A_2BB'X_6$, and (**C**) combine dataset in the task for predicting E_g. Abbreviations and full names of input features are given in Table 1.

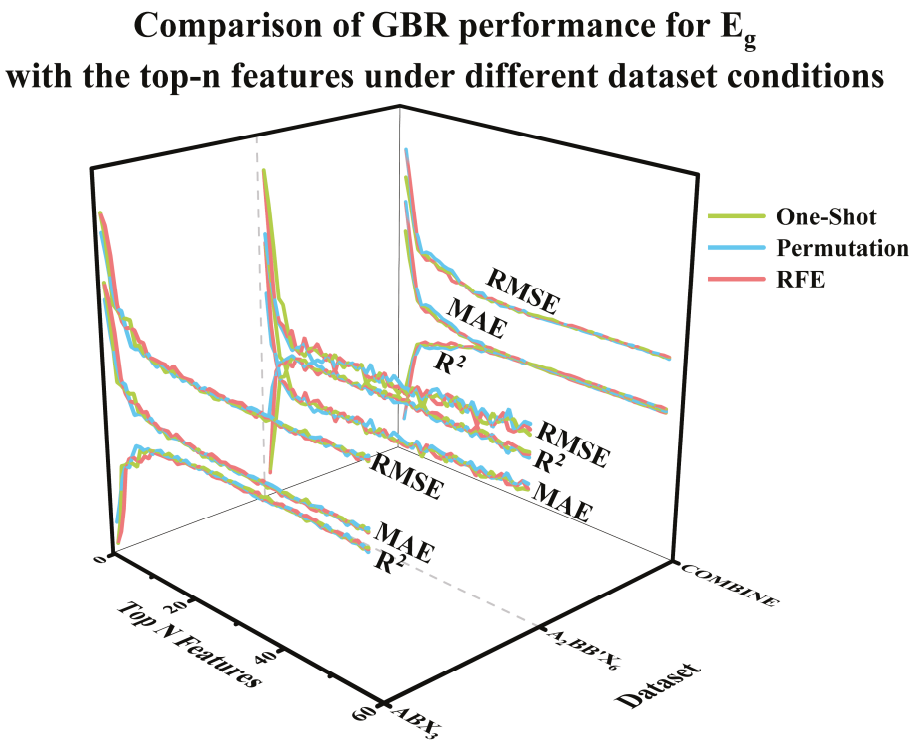

Figure 16. Comparison of GBR performance for E_g with the top-n features under ABX_3, $A_2BB'X_6$, and Combine dataset conditions.

3. Method

The dataset includes perovskite and double perovskite, which are represented as ABX_3 and $A_2BB'X_6$ structure, respectively, and collected from MP and OQMD. There are 829 ABX_3 and 624 $A_2BB'X_6$ samples for traditional machine learning, since graph neural networks inherently account for structural factors, and in order to maintain the component invariant for traditional and graph-based methods, the latter dataset is constructed according to the former chemical formula. There are 1895 and 856 samples for the graph-based method. From the aspect of the proportion of anions composed with a different variety of X elements in the dataset, they include oxide, fluoride, chloride, sulfide, bromide, selenide, iodide and other type.

There are 57 descriptors used to characterize perovskites. The features are divided into 3 categories: features determined by element type describing basic chemical properties, features used for measuring stability, and crystallography features. Those descriptors can be further divided into six categories: position in the periodic table, atomic and ionic size, electrical properties, thermochemical properties and Zunger pseudopotential radii.

Those features are used as the input of several machine learning models to predict target features, including E_f, E_g, and E_h. Each machine learning approach is evaluated on three datasets (exclusively ABX_3, exclusively $A_2BB'X_6$, and the combined dataset) for predicting the three target properties (E_f, E_g, and E_h). The reason a combined dataset is constructed is to enable comparative evaluation of models' adaptability to gradient data quality and generalization via structural commonalities, and to align with real-world materials discovery scenarios where well-studied and understudied materials coexist. All datasets are split into training and testing sets with a ratio of 80% and 20%, respectively. Twelve traditional and 1 graph-based model are evaluated in this work: AdaBoost Regression (ABR), Bayes Ridge Regression (BRR), Decision Tree Regression (DTR), Gradient Boosting Regression (GBR), Gaussian Process Regression (GPR), K-Nearest Regression (KNR), Kernel Ridge Regression (KRR), Multilayer Perceptron Regression (MLPR), Passive Aggressive Regression (PAR),

Random Forest Regression (RFR), Stochastic Gradient Descent Regression (SGDR), Support Vector Regression (SVR), CGCNN.

For each model, the Bayes optimization algorithm is used to determine hyperparameters. Three measurements, which are evaluated by 5-fold cross-validation, are introduced to quantify model performance, including MAE, Root Mean Square Error (RMSE), and R^2. MAE, RMSE, and R^2 are defined by the following formulas:

$$\text{MAE} = \frac{1}{n}\sum_{i}^{n}|y_i - \widehat{y_i}|$$

$$\text{RMSE} = \sqrt{\frac{1}{n}\sum_{i}^{n}(y_i - \widehat{y_i})^2}$$

$$R^2 = 1 - \frac{\sum_i^n (y_i - \widehat{y_i})^2}{\sum_i^n (y_i - \overline{y})^2}$$

where y_i is ground truth, $\widehat{y_i}$ is predicted value, and $\overline{y}$ is the mean value of ground truth. MAE and RMSE are both the lower the better; however, RMSE is more sensitive than MAE for those anomalies points predicted by model. In contrast, R^2 is the closer to 1 the better, and any result out of the range between 0 and 1 means that the model is not able to learn the relationship between the input and output, and that makes the MAE and RMSE achieved by the same model invalid.

Recursive-Feature-Elimination (RFE), Permutation, and one-shot are used for the best performance model to identify the optimum input feature dimension. To be clear, RFE, Permutation, and the one-shot method all are feature selection methods, but they are different in the selection process. RFE is firstly training the model on origin input; then the least important feature is pruned, and the modified input is the new input for the next round, which means the dimension of the new-round training input is reduced. This cycle will not end until the input dimension reaches the goal of the user setting. The Permutation method is a technique that measures the contribution of each feature to a fitted model. This technique involves randomly shuffling the values of a single feature and observing the resulting degradation of the model's score. From this process, a feature's importance to the prediction result can be measured. Then, the feature can be sorted by importance. The one-shot method is simply a sort feature determined by the feature weight of the model.

4. Conclusions

This work systematically compared the performance of 11 conventional machine learning models and the graph neural network-based deep learning model (CGCNN) for predicting E_f, E_g, and E_h properties across single-perovskite, double-perovskite, and combine datasets. For the ABX_3 dataset, CGCNN shows superior performance over all traditional machine learning models in all three metrics (MAE, RMSE, R^2). Compared to the second-best GBR model, CGCNN shows improvements of 59.6%, 5.4%, and 6.0% for E_f; 13%, 23%, and 25.7% for E_g; and 24.4%, 24.0%, and 300.1% for E_h, establishing CGCNN as the preferred choice for a uniformly distributed dataset. In contrast, for the $A_2BB'X_6$ and combine datasets (where balanced distributed ABX_3 data was combined with imbalanced $A_2BB'X_6$ data), the traditional GBR model achieved optimal performance in E_g and E_f tasks, suggesting that GBR had better suitability for imbalanced datasets. Notably, CGCNN showed remarkable improvement in predicting $A_2BB'X_6$ structures' properties when training under the combine dataset, with R^2 for E_h increasing from 0.007 to 0.519, 68.1× improvement, and for E_g showing a 3.3× enhancement, demonstrating that incorporating balanced ABX_3 data can significantly boost CGCNN's predictive capability

for double perovskites. Feature selection analysis revealed that for GBR in E_g and E_f tasks, three methods (One-shot, permutation-based, RFE-based) showed optimal model performance requires retention of at least the top 20 critical features. In the ABX_3 dataset, CGCNN showed uniform feature importance distribution. In the combine dataset, Block, Atomic volume, and Block showed strong correlations with E_f, E_g, and E_h, respectively. In summary, this work provides guidance for subsequent model selection and feature screening methods when using machine learning approaches to predict properties of perovskite structures.

Author Contributions: J.L.: Writing—original draft, Software, Methodology, Visualization, Formal analysis. X.S.: Supervision, Writing—review and editing, Resources, Funding acquisition, Project administration. L.Y.: Data curation, Visualization. J.D.: Validation, Visualization. J.W.: Validation, Software. X.L.: Investigation, Methodology. Y.P.: Funding acquisition, Resources. Z.W.: Funding acquisition, Resources. W.Z.: Funding acquisition, Resources. Y.B.: Funding acquisition, Resources. All authors have read and agreed to the published version of the manuscript.

Funding: This work was supported by the National Natural Science Foundation of China (81860538, 32360175, 62305262), Natural Science Foundation of Shanxi Province (2022JQ-652), Introduction and Cultivation Foundation of Beijing University of Technology (2024GW06), Central Guidance on Local Science and Technology Development Foundation of Ningxia Province (2024FRD05095), and Featured Discipline Construction Project in Oncology of Ningxia Medical University (NXMUZLXK-202505).

Data Availability Statement: The original contributions presented in this study are included in the article. Further inquiries can be directed to the corresponding author.

Conflicts of Interest: The authors declare no conflicts of interest.

References

1. Xu, X.; Wang, W.; Zhou, W.; Shao, Z. Recent Advances in Novel Nanostructuring Methods of Perovskite Electrocatalysts for Energy-Related Applications. *Small Methods* **2018**, *2*, 1800071. [CrossRef]
2. Xu, X.; Zhong, Y.; Shao, Z. Double Perovskites in Catalysis, Electrocatalysis, and Photo(electro)catalysis. *Trends Chem.* **2019**, *1*, 410–424. [CrossRef]
3. Jiang, Q.; Zhu, K. Rapid advances enabling high-performance inverted perovskite solar cells. *Nat. Rev. Mater.* **2024**, *9*, 399–419. [CrossRef]
4. Pacchioni, G. Highly efficient perovskite LEDs. *Nat. Rev. Mater.* **2021**, *6*, 108. [CrossRef]
5. Lu, L.; Sun, M.; Wu, T.; Lu, Q.; Chen, B.; Huang, B. All-inorganic perovskite nanocrystals: Next-generation scintillation materials for high-resolution X-ray imaging. *Nanoscale Adv.* **2022**, *4*, 680–696. [CrossRef]
6. He, J.; Li, C.-Y.; Qi, D.-X.; Cai, Q.; Liu, Y.; Fan, R.-H.; Su, J.; Huo, P.; Xu, T.; Peng, R.; et al. Improving Photoelectric Conversion with Broadband Perovskite Metasurface. *Nano Lett.* **2022**, *22*, 6655–6663. [CrossRef]
7. Long, G.; Adamo, G.; Tian, J.; Klein, M.; Krishnamoorthy, H.N.S.; Feltri, E.; Wang, H.; Soci, C. Perovskite metasurfaces with large superstructural chirality. *Nat. Commun.* **2022**, *13*, 1551. [CrossRef]
8. Cong, G.; Fung, V. Improving materials property predictions for graph neural networks with minimal feature engineering *. *Mach. Learn. Sci. Technol.* **2023**, *4*, 035030. [CrossRef]
9. Sun, S.; Lu, M.; Gao, X.; Shi, Z.; Bai, X.; Yu, W.W.; Zhang, Y. 0D Perovskites: Unique Properties, Synthesis, and Their Applications. *Adv. Sci.* **2021**, *8*, 2102689. [CrossRef]
10. Akkerman, Q.A.; Manna, L. What Defines a Halide Perovskite? *ACS Energy Lett.* **2020**, *5*, 604–610. [CrossRef]
11. Stoumpos, C.C.; Kanatzidis, M.G. The Renaissance of Halide Perovskites and Their Evolution as Emerging Semiconductors. *Acc. Chem. Res.* **2015**, *48*, 2791–2802. [CrossRef]
12. Volonakis, G.; Filip, M.R.; Haghighirad, A.A.; Sakai, N.; Wenger, B.; Snaith, H.J.; Giustino, F. Lead-free halide double perovskites via heterovalent substitution of noble metals. *J. Phys. Chem. Lett.* **2016**, *7*, 1254–1259. [CrossRef]
13. Cai, J.; Chu, X.; Xu, K.; Li, H.; Wei, J. Machine learning-driven new material discovery. *Nanoscale Adv.* **2020**, *2*, 3115–3130. [CrossRef] [PubMed]
14. Sumpter, B.G.; Noid, D.W. On the design, analysis, and characterization of materials using computational neural networks. *Annu. Rev. Mater. Sci.* **1996**, *26*, 223–277. [CrossRef]

15. Manuel Serra, J.; Allen Baumes, L.; Moliner, M.; Serna, P.; Corma, A. Zeolite synthesis modelling with support vector machines: A combinatorial approach. *Comb. Chem. High Throughput Screen* **2007**, *10*, 13–24. [CrossRef]
16. Choudhary, K.; Garrity, K.F.; Reid, A.C.E.; DeCost, B.; Biacchi, A.J.; Hight Walker, A.R.; Trautt, Z.; Hattrick-Simpers, J.; Kusne, A.G.; Centrone, A.; et al. The joint automated repository for various integrated simulations (JARVIS) for data-driven materials design. *npj Comput. Mater.* **2020**, *6*, 173. [CrossRef]
17. Jain, A.; Ong, S.P.; Hautier, G.; Chen, W.; Richards, W.D.; Dacek, S.T.; Cholia, S.; Gunter, D.; Skinner, D.; Ceder, G.; et al. Commentary: The Materials Project: A materials genome approach to accelerating materials innovation. *APL Mater.* **2013**, *1*, 011002. [CrossRef]
18. Kirklin, S.; Saal, J.E.; Meredig, B.; Thompson, A.; Doak, J.W.; Aykol, M.; Rühl, S.; Wolverton, C. The Open Quantum Materials Database (OQMD): Assessing the accuracy of DFT formation energies. *npj Comput. Mater.* **2015**, *1*, 15010. [CrossRef]
19. Curtarolo, S.; Setyawan, W.; Hart, G.L.W.; Jahnatek, M.; Chepulskii, R.V.; Taylor, R.H.; Wang, S.; Xue, J.; Yang, K.; Levy, O.; et al. AFLOW: An automatic framework for high-throughput materials discovery. *Comput. Mater. Sci.* **2012**, *58*, 218–226. [CrossRef]
20. Ramakrishnan, R.; Dral, P.O.; Rupp, M.; von Lilienfeld, O.A. Quantum chemistry structures and properties of 134 kilo molecules. *Sci. Data* **2014**, *1*, 140022. [CrossRef]
21. Hellenbrandt, M. The Inorganic Crystal Structure Database (ICSD)—Present and Future. *Crystallogr. Rev.* **2004**, *10*, 17–22. [CrossRef]
22. Manavalan, B.; Shin, T.H.; Lee, G. PVP-SVM: Sequence-Based Prediction of Phage Virion Proteins Using a Support Vector Machine. *Front. Microbiol.* **2018**, *9*, 476. [CrossRef] [PubMed]
23. Wang, Q.; Garrity, G.M.; Tiedje, J.M.; Cole, J.R. Naive Bayesian classifier for rapid assignment of rRNA sequences into the new bacterial taxonomy. *Appl. Environ. Microbiol.* **2007**, *73*, 5261–5267. [CrossRef] [PubMed]
24. Oliynyk, A.O.; Antono, E.; Sparks, T.D.; Ghadbeigi, L.; Gaultois, M.W.; Meredig, B.; Mar, A. High-Throughput Machine-Learning-Driven Synthesis of Full-Heusler Compounds. *Chem. Mater.* **2016**, *28*, 7324–7331. [CrossRef]
25. Pyzer-Knapp, E.O.; Li, K.; Aspuru-Guzik, A. Learning from the Harvard Clean Energy Project: The Use of Neural Networks to Accelerate Materials Discovery. *Adv. Funct. Mater.* **2015**, *25*, 6495–6502. [CrossRef]
26. Liu, Z.; Zhang, J.; Rao, G.; Peng, Z.; Huang, Y.; Arnold, S.; Liu, B.; Deng, C.; Li, C.; Li, H.; et al. Accelerating Photostability Evaluation of Perovskite Films through Intelligent Spectral Learning-Based Early Diagnosis. *ACS Energy Lett.* **2024**, *9*, 662–670. [CrossRef]
27. Jacobs, R.; Liu, J.; Abernathy, H.; Morgan, D. Machine Learning Design of Perovskite Catalytic Properties. *Adv. Energy Mater.* **2024**, *14*, 2303684. [CrossRef]
28. Zhang, R.; Motes, B.; Tan, S.; Lu, Y.; Shih, M.-C.; Hao, Y.; Yang, K.; Srinivasan, S.; Bawendi, M.G.; Bulović, V. Machine Learning Prediction of Organic–Inorganic Halide Perovskite Solar Cell Performance from Optical Properties. *ACS Energy Lett.* **2025**, *10*, 1714–1724. [CrossRef]
29. Sudha Priyanga, G.; Sampath, S.; Shravan, P.V.; Sujith, R.N.; Mohamed Javeed, A.; Latha, G. Advanced prediction of perovskite stability for solar energy using machine learning. *Sol. Energy* **2024**, *278*, 112782. [CrossRef]
30. Sadat, S.M.; Wang, R.Y. A machine learning based approach for phononic crystal property discovery. *J. Appl. Phys.* **2020**, *128*, 025106. [CrossRef]
31. Sharma, V.; Kumar, P.; Dev, P.; Pilania, G. Machine learning substitutional defect formation energies in ABO3 perovskites. *J. Appl. Phys.* **2020**, *128*, 034902. [CrossRef]
32. Rath, S.; Sudha Priyanga, G.; Nagappan, N.; Thomas, T. Discovery of direct band gap perovskites for light harvesting by using machine learning. *Comput. Mater. Sci.* **2022**, *210*, 111476. [CrossRef]
33. Zhao, J.; Zhao, W.; Deng, B.; Wang, Z.; Zhang, F.; Zheng, W.; Cao, W.; Nan, J.; Lian, Y.; Burke, A.F. Autonomous driving system: A comprehensive survey. *Expert Syst. Appl.* **2024**, *242*, 122836. [CrossRef]
34. Chen, L.; Wu, P.; Chitta, K.; Jaeger, B.; Geiger, A.; Li, H. End-to-end autonomous driving: Challenges and frontiers. *IEEE Trans. Pattern Anal. Mach. Intell.* **2024**, *46*, 10164–10183. [CrossRef]
35. Archana, R.; Jeevaraj, P.S.E. Deep learning models for digital image processing: A review. *Artif. Intell. Rev.* **2024**, *57*, 11. [CrossRef]
36. Manakitsa, N.; Maraslidis, G.S.; Moysis, L.; Fragulis, G.F. A Review of Machine Learning and Deep Learning for Object Detection, Semantic Segmentation, and Human Action Recognition in Machine and Robotic Vision. *Technologies* **2024**, *12*, 15. [CrossRef]
37. Liu, Q.; Hu, J.; Xiao, Y.; Zhao, X.; Gao, J.; Wang, W.; Li, Q.; Tang, J. Multimodal recommender systems: A survey. *ACM Comput. Surv.* **2024**, *57*, 1–17. [CrossRef]
38. Scarselli, F.; Gori, M.; Tsoi, A.C.; Hagenbuchner, M.; Monfardini, G. The graph neural network model. *IEEE Trans. Neural Netw.* **2008**, *20*, 61–80. [CrossRef]
39. Hoang, V.T.; Jeon, H.-J.; You, E.-S.; Yoon, Y.; Jung, S.; Lee, O.-J. Graph Representation Learning and Its Applications: A Survey. *Sensors* **2023**, *23*, 4168. [CrossRef]
40. Han, J.; Cen, J.; Wu, L.; Li, Z.; Kong, X.; Jiao, R.; Yu, Z.; Xu, T.; Wu, F.; Wang, Z.; et al. A Survey of Geometric Graph Neural Networks: Data Structures, Models and Applications. *Front. Comput. Sci.* **2024**, *19*, 1911375. [CrossRef]

41. Guo, Z.; Wang, H. A Deep Graph Neural Network-Based Mechanism for Social Recommendations. *IEEE Trans. Ind. Inform.* **2021**, *17*, 2776–2783. [CrossRef]
42. Wu, L.; Zhang, Q.; Chen, C.H.; Guo, K.; Wang, D. Deep learning techniques for community detection in social networks. *IEEE Access* **2020**, *8*, 96016–96026. [CrossRef]
43. Satorras, V.G.; Hoogeboom, E.; Welling, M. E(n) Equivariant Graph Neural Networks. In Proceedings of the 38th International Conference on Machine Learning, Virtual, 18–24 July 2021; pp. 9323–9332.
44. Meller, A.; Ward, M.D.; Borowsky, J.H.; Lotthammer, J.M.; Kshirsagar, M.; Oviedo, F.; Ferres, J.L.; Bowman, G. Predicting the locations of cryptic pockets from single protein structures using the PocketMiner graph neural network. *Nat. Commun.* **2023**, *14*, 1177. [CrossRef] [PubMed]
45. Yu, Y.; Wang, R.; Teo, R.D. Machine Learning Approaches for Metalloproteins. *Molecules* **2022**, *27*, 1277. [CrossRef]
46. Schütt, K.T.; Sauceda, H.E.; Kindermans, P.-J.; Tkatchenko, A.; Müller, K.-R. SchNet—A deep learning architecture for molecules and materials. *J. Chem. Phys.* **2018**, *148*, 241722. [CrossRef]
47. Huang, G.; Guo, Y.; Chen, Y.; Nie, Z. Application of Machine Learning in Material Synthesis and Property Prediction. *Materials* **2023**, *16*, 5977. [CrossRef]
48. Wieder, O.; Kuenemann, M.; Wieder, M.; Seidel, T.; Meyer, C.; Bryant, S.D.; Langer, T. Improved Lipophilicity and Aqueous Solubility Prediction with Composite Graph Neural Networks. *Molecules* **2021**, *26*, 6185. [CrossRef]
49. Xie, T.; Grossman, J.C. Crystal Graph Convolutional Neural Networks for an Accurate and Interpretable Prediction of Material Properties. *Phys. Rev. Lett.* **2018**, *120*, 145301. [CrossRef]
50. Karamad, M.; Magar, R.; Shi, Y.; Siahrostami, S.; Gates, I.D.; Barati Farimani, A. Orbital graph convolutional neural network for material property prediction. *Phys. Rev. Mater.* **2020**, *4*, 093801. [CrossRef]
51. Chen, C.; Ye, W.; Zuo, Y.; Zheng, C.; Ong, S.P. Graph Networks as a Universal Machine Learning Framework for Molecules and Crystals. *Chem. Mater.* **2019**, *31*, 3564–3572. [CrossRef]
52. Gilmer, J.; Schoenholz, S.; Riley, P.F.; Vinyals, O.; Dahl, G.E. Neural Message Passing for Quantum Chemistry. In Proceedings of the 34th International Conference on Machine Learning, Sydney, Australia, 6–11 August 2017.
53. Schütt, K.T.; Kindermans, P.-J.; Sauceda, H.E.; Chmiela, S.; Tkatchenko, A.; Müller, K.-R. SchNet: A continuous-filter convolutional neural network for modeling quantum interactions. *Adv. Neural Inf. Process. Syst.* **2017**, *30*, 992.
54. Choudhary, K.; DeCost, B. Atomistic Line Graph Neural Network for improved materials property predictions. *npj Comput. Mater.* **2021**, *7*, 185. [CrossRef]
55. Chen, C.; Ong, S.P. A Universal Graph Deep Learning Interatomic Potential for the Periodic Table. *Nat. Comput. Sci.* **2022**, *2*, 718–728. [CrossRef] [PubMed]
56. Wang, H.; Sun, J.; Liang, J.; Zhai, L.; Tang, Z.; Li, Z.; Zhai, W.; Wang, X.; Gao, W.; Gong, S.; et al. Crystals with Transformers on Graphs, for Prediction of Unconventional Crystal Material Properties and the Benchmark. *arXiv* **2024**, arXiv:2407.16131. [CrossRef]
57. Deng, L.; Yu, D. Deep Learning: Methods and Applications. *Found. Trends Signal Process.* **2014**, *7*, 197–387. [CrossRef]
58. LeCun, Y.; Boser, B.; Denker, J.S.; Henderson, D.; Howard, R.E.; Hubbard, W.; Jackel, L.D. Backpropagation Applied to Handwritten Zip Code Recognition. *Neural Comput.* **1989**, *1*, 541–551. [CrossRef]
59. Zeiler, M.D.; Fergus, R. Visualizing and Understanding Convolutional Networks. In *Proceedings of the Computer Vision—ECCV, Zurich, Switzerland, 6–12 September 2014*; Fleet, D., Pajdla, T., Schiele, B., Tuytelaars, T., Eds.; Springer International Publishing: Cham, Switzerland, 2014; pp. 818–833.

Disclaimer/Publisher's Note: The statements, opinions and data contained in all publications are solely those of the individual author(s) and contributor(s) and not of MDPI and/or the editor(s). MDPI and/or the editor(s) disclaim responsibility for any injury to people or property resulting from any ideas, methods, instructions or products referred to in the content.

inorganics

MDPI

Article

Texturing $(Na_{0.5}Bi_{0.5})TiO_3$-$KNbO_3$-$SrTiO_3$ Electrostrictive Ceramics by Templated Grain Growth Using $(Na_{0.5}Bi_{0.5})TiO_3$ Platelets

Arum Ayuningsih [1], Nazım Ecebaş [1], Tran Thi Huyen Tran [1], John G. Fisher [1,*], Jong-Sook Lee [1,*], Woo-Jin Choi [2] and Wook Jo [2]

[1] Department of Materials Science and Engineering, Chonnam National University, 77 Yongbong-ro, Buk-gu, Gwangju 61186, Republic of Korea
[2] School of Materials Science and Engineering, Ulsan National Institute of Science and Technology, Unist-gil 50, Eonyang-eup, Ulju-gun, Ulsan 44919, Republic of Korea
* Correspondence: johnfisher@jnu.ac.kr (J.G.F.); jongsook@jnu.ac.kr (J.-S.L.)

Abstract: Electrostriction is an intriguing behaviour of dielectric materials, characterized by stable electrostrain with minimal hysteresis. $(Na_{0.5}Bi_{0.5})TiO_3$-based ceramics show promising electrostrictive behaviour, particularly the $0.90(Na_{0.5}Bi_{0.5})TiO_3$-$0.08KNbO_3$-$0.02SrTiO_3$ composition located near the morphotropic phase boundary between ferroelectric rhombohedral and relaxor pseudocubic phases. The templated grain growth method has been effectively used to control the grain orientation of NBT-based systems, thereby enhancing their electrical properties. In this study, texturing was introduced to $0.90(Na_{0.5}Bi_{0.5})TiO_3$-$0.08KNbO_3$-$0.02SrTiO_3$ ceramics through homoepitaxial NBT platelets prepared via a three-step molten salt/topochemical microcrystal conversion method. By adding 4 wt% of NBT platelets combined with optimized sintering conditions, textured ceramics were prepared exhibiting a high Lotgering factor of 83% with enhancement of strain (0.02%) and polarization (3 $\mu C/cm^2$) at an electric field of 40 kV/cm, as well as stable dielectric permittivity between 130 and 300 °C. Moreover, the electrostrictive coefficient of textured ceramics increased by ~0.004 C^2m^{-4} compared to that of untextured ceramics, confirming the improvement of the electrostrictive response. These results demonstrate that homoepitaxial templating effectively improves the electrical properties of NBT-KN-ST ceramics while preserving their electrostrictive nature, which offers a viable route for designing lead-free electrostrictive materials.

Keywords: electrostrictive; lead-free perovskite; templated grain growth; $(Na_{0.5}Bi_{0.5})TiO_3$

1. Introduction

The development of advanced motion technology has always been related to high-precision motion systems, especially in modern manufacturing or scientific equipment [1]. In materials engineering, development trends are focused on sensor or actuator materials, which play a significant role in sensing and responding to stimuli in motion technology. Additionally, actuator materials play a crucial role in motion technology, converting electronic signals into physical actions. Piezoelectric and electrostrictive materials are popular for their excellent motion performance, particularly in high-precision actuators [2–7]. Electrostrictive materials, such as $Pb(Mg_{1/3}Nb_{2/3})O_3$ (PMN)-based multilayer actuators, are already in commercial use in optical applications. According to Pan et al., when comparing commercial high-precision actuator materials, the types of piezoelectric and electrostrictive materials were mostly lead-based materials such as PMN, $Pb(Mg_{1/3}Nb_{2/3})O_3$-$PbTiO_3$

(PMN-PT), $Pb(Zn_{1/3}Nb_{2/3})O_3$ (PZN), or $Pb(Zn_{1/3}Nb_{2/3})O_3$-$PbTiO_3$ (PZN-PT) [6]. These lead-based materials have high electrostrain, e.g., Nd-doped PMN-PT has a strain of 0.231% at an electric field of 50 kV/cm [8], and PZT-based materials have strain > 0.35% at electric fields of under 20 kV/cm [9,10]. They concluded that electrostrictive and piezoelectric materials can be applied as high-precision actuators, with the piezoelectric materials giving the best performance among other materials by achieving higher strain in actuator applications. However, piezoelectric materials also show a high strain hysteresis and temperature sensitivity, affecting the precision of movement [11]. On the other hand, electrostrictive actuators exhibit small hysteresis, making them more stable and providing better performance under specific conditions. In electrostrictive materials, the strain occurs as a quadratic response to the electric field. Particularly in centrosymmetric crystal structures, where electrostriction appears more dominantly and no spontaneous polarization is present, ion shifting of cations and anions almost cancel each other out, and the difference in shifts due to the potential anharmonicity in the lattice induces only a small strain [7,12,13]. The trend in manufacturing, which requires actuators capable of fine alignment that can be used for an extended period and are more efficient, indicates that stable actuators with low ageing rates are preferred. As explained above, most of the commercial electrostrictive materials were lead-based. They are mature technologies with excellent properties and performance. However, due to the toxicity of lead-containing substances, which are dangerous to health and the environment, specific regulations controlling the utilization of hazardous substances in electrical and electronic equipment restrict the use of lead-containing materials, e.g., RoHS [7,14,15]. These restrictions are prompting research into developing electrostrictive lead-free materials as alternative materials for actuators.

One of the lead-free materials that has great potential is $(Na_{0.5}Bi_{0.5})TiO_3$ (NBT), which exhibits excellent electromechanical performance. NBT-based materials have a high electric field-induced strain compared to other lead-free materials [16,17]. NBT also shows a large remnant polarization of 38μC/cm^2 and a high coercivity of 73 kV/cm [18–20]. At room temperature, NBT has a rhombohedral structure with a relative permittivity maximum around 320 °C and a depolarization temperature (T_d) at 190 °C [21–23]. As T_d approaches room temperature, a giant electrostrain will be formed due to the low coercive field, as the material will require only a low electric field for switching polarization. However, depolarization may also easily occur, and potentially the strain hysteresis will be higher, which increases the energy loss [14,24]. This can limit the efficiency of the actuator because the power consumption will increase. NBT has a phase transition from a nonergodic relaxor rhombohedral (*R*3*c*) phase to an ergodic relaxor tetragonal (*P*4*bm*) phase at 200–320 °C, and to a paraelectric cubic ($Pm\bar{3}m$) phase at 320–540 °C [23,25]. Shifting T_d to near room temperature will promote the ergodic relaxor phase, associated with unstable ferroelectric domains, and increase the electrostrictive strain [26].

To improve the mobility of the domains and the electrostrain of NBT, several approaches can be employed, such as chemical modification and microstructure control. Chemical modification can be achieved by adding a metal dopant ion [27], an ABO_3 perovskite component [28–33], or co-addition of a metal ion and an ABO_3 perovskite component [34]. Incorporating ABO_3 perovskite components into NBT can induce a morphotropic phase boundary (MPB), which enhances the electroactive response due to the coexistence of two different phases [12]. Phase coexistence facilitates the polarization rotation near this region, and the change in electrical properties emerges. The addition of ABO_3 perovskite components in NBT can produce two typical types of MPB, the first of which is between the rhombohedral and tetragonal phases in binary systems such as $(Na_{0.5}Bi_{0.5})TiO_3$-$BaTiO_3$ and $(Na_{0.5}Bi_{0.5})TiO_3$-$(K_{0.5}Bi_{0.5})TiO_3$ [32,33,35]. The other is be-

tween rhombohedral and pseudo-cubic (tetragonal) phases, such as in NBT-$SrTiO_3$ and NBT- $KNbO_3$ [24,28,29,36–38].

The inclusion of $KNbO_3$ (KN) or $SrTiO_3$ (ST) in the NBT system can expand the unit cell volume and decrease the rhombohedral distortion. This reduction in distortion will reduce the stability of the ferroelectric domains, leading to the shifting of T_d toward room temperature [24,29,36]. Both NBT-KN and NBT-ST binary systems exhibited improvements in the reversible electrostrain, which were around 0.22% at 90 kV/cm and 0.20% at 70 kV/cm, respectively [39,40]. According to the phase diagram of the NBT-KN-ST ternary system, a critical composition of 0.90NBT-0.05KN-0.5ST revealed a large strain of around 0.34% at 70 kV/cm with an MPB phase transition from ferroelectric rhombohedral to relaxor pseudocubic. However, the strain hysteresis was very large. The strain response, which can also be influenced by the tolerance factor, is maximized near the MPB and shifts concomitantly with the increased ST content [41,42]. Concerning the effect of the tolerance factor on the system, the inclusion of a high tolerance factor perovskite will increase the strain [42]. Also, increasing the KN content can shift the T_d to room temperature [28]. Strain hysteresis can be reduced by shifting the composition away from the MPB, at a cost of a reduction in electrostrain. For the $0.90(Na_{0.5}Bi_{0.5})TiO_3$-$0.08KNbO_3$-$0.02SrTiO_3$ (0.90NBT-0.08KN-0.02ST) composition, the applied electric field was reduced to 60 kV/cm with an electrostrain around 0.148% and the shape of the strain hysteresis loop indicated partially electrostrictive behaviour with low strain hysteresis [43]. The electrostrictive coefficient Q_{11} had a value of 0.0236 m^4C^{-2}, which is comparable to that of other NBT-based electrostrictive materials and PMN [44–49]. However, the available electrostrain is low compared to conventional lead-based and lead-free piezoelectric materials [23,50]. To increase the performance of this composition further, it is necessary to increase the electrostrain without increasing strain hysteresis.

The other approach of controlling microstructure has also been applied to achieve high electrostriction behaviour and high strain [41,48,51]. Based on the type of material, textured ceramics were the prospective choice between expensive single crystals and low-performance polycrystals. Because of their improved properties, textured ceramics are better than polycrystals and are even similar to single crystals. On the other hand, the synthesis process is inexpensive compared to single-crystal growth [16,52,53]. In texture engineering, the templates will promote grain alignment in a preferred orientation [41]. Thereby, electrostrictive deformation will be uniform, leading to the increased electrostrictive response. This study aims to enhance the electrostrictive properties of 0.90NBT-0.08KN-0.02ST ceramics by texturing techniques using NBT platelets as the template. By optimizing the texturing degree, high electrostrain and low hysteresis are expected to be obtained, making the material more viable for high-precision actuator applications. The difference in electrical behaviour between random and textured ceramics will be observed through the measurement of dielectric, ferroelectric, and piezoelectric properties.

2. Results and Discussion

2.1. $(Na_{0.5}Bi_{0.5})TiO_3$ Platelet Preparation

In the XRD diffraction patterns in Figure 1, it can be seen that NBT platelets were successfully formed via BiT and NBiT precursors. The BiT precursor exhibits anisotropic growth, as confirmed in Figure 1a. The XRD pattern of BiT obtained is similar to that of the Crystallography Open Database (COD) pattern # 96-152-8446 for $Bi_4Ti_3O_{12}$ (orthorhombic, space group *Aba*2), although some of the peaks have shifted position. There are also peaks (marked *) that belong to a $BiNaO_3$ secondary phase (COD pattern # 96-152-6789). Most of the intense peaks are (00*l*) peaks, i.e., (008) and (0016), which indicate that the BiT precursors are highly oriented [54,55]. It is also evident from the SEM micrograph in

Figure 2a that the morphology of BiT is plate-like. The particle size of BiT appears uniform, with particles of size up to ~30 µm.

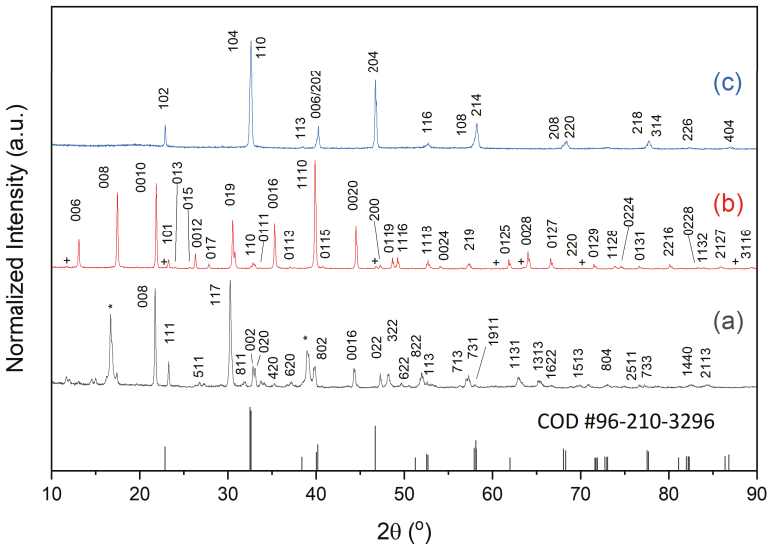

Figure 1. X-ray diffraction patterns of: (**a**) $Bi_4Ti_3O_{12}$ precursors; (**b**) $Na_{0.5}Bi_{4.5}Ti_4O_{15}$ precursors; (**c**) $(Na_{0.5}Bi_{0.5})TiO_3$ platelets. * = $BiNaO_3$ secondary phase; + = unknown secondary phase.

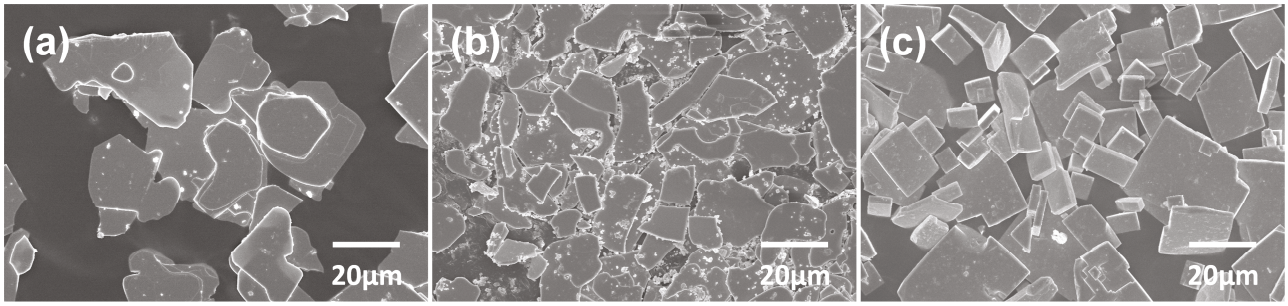

Figure 2. SEM Micrographs of: (**a**) $Bi_4Ti_3O_{12}$ precursors; (**b**) $Na_{0.5}Bi_{4.5}Ti_4O_{15}$ precursors; (**c**) $(Na_{0.5}Bi_{0.5})TiO_3$ platelets.

The XRD pattern in Figure 1b shows the NBiT platelets and was indexed using COD pattern #96-153-8361 for $Na_{0.5}Bi_{4.5}Ti_4O_{15}$ (tetragonal, space group $I4/mmm$). Small peaks (marked +) belonging to an unknown secondary phase are present. The NBiT platelets also exhibit a high degree of orientation by showing high intensity (00*l*) peaks around 2θ = 13°, 17°, 21°, 26°, 35°, and 44°, which have (006), (008), (0010), (0012), (0016), and (0020) Miller indices, respectively. The morphology of the NBiT platelets in Figure 2b retains the plate-like shape of the BiT precursor. However, it showed that the particle size of the NBiT platelets is smaller than that of the BiT precursor.

According to the XRD results, the NBT platelets have a rhombohedral structure (space group $R3c$), which can be indexed using COD pattern #96-210-3296 for $(Na_{0.5}Bi_{0.5})TiO_3$, as shown in Figure 1c and the stick pattern. The plate-like morphology of NBiT is still retained in the NBT platelets, as shown in Figure 2c. The NBT platelets have a clean lateral morphology, regular rectangular shapes, and smooth surfaces. The NBT platelets are of similar size to the NBiT platelets. Based on the microstructure of the obtained NBT platelets, their high aspect ratio and plate-like morphology make them suitable as a template for texturing ceramics.

The Aurivillius structure of BiT is a layered perovskite-type structure with the general formula $Bi_2O_2(A_{m-1}B_mO_{3m+1})$ [56,57]. The Bi_2O_2 layers in the structure can hinder the

epitaxial growth and promote anisotropic growth, which produces plate-like shapes with a high aspect ratio [56]. Moreover, the Bi_2O_2 layers are also flexible in that they can be extracted by the exfoliation process at high temperature during the topochemical conversion process [58]. Through the exfoliation process, the transformation of the perovskite block in the Aurivillius structure occurs while maintaining the morphology and macroscopic form of the crystal [59]. Therefore, in NBT platelet preparation, Aurivillius-structured precursors are suitable for obtaining NBT platelets of high aspect ratio.

In addition, the thickness of the perovskite block in the Aurivillius structure, which is determined by the type of A and B-site cations, significantly influences particle characteristics such as the morphology, aspect ratio, etc. Consequently, selecting the type of Aurivillius precursor for NBT platelet preparation is important. In the present work, two types of Aurivillius structures were used for NBT template preparation, $Bi_4Ti_3O_{12}$ (BiT, m = 3) and $Na_{0.5}Bi_{4.5}Ti_4O_{15}$ (NBiT, m = 4).

BiT and NBiT exhibit highly anisotropic growth and a high aspect ratio, as the Bi_2O_2 layer suppresses c-axis growth, resulting in a significantly higher growth rate along the a (b) axis [54,60]. As a result, these compounds can easily form plate-like particles. Jiang et al. [61] also confirmed that NBT platelets retained their plate-like morphology when prepared directly from BiT or NBiT, making them suitable for texturing. However, preparing NBT templates directly from NBiT has several challenges, primarily attributed to the high volatility of Na at high temperatures, which complicates the determination of the ratio of starting materials [56,62]. To address this challenge, previous research reported that the growth of NBiT could be precisely controlled using BiT as the first precursor, which produced a more uniform shape and smooth surface with a high aspect ratio and well-defined morphology of NBiT particles [56,63]. Therefore, in this study, BiT was employed as the primary precursor to serve as a nucleation framework to overcome the limitations associated with direct NBT platelet synthesis from the NBiT precursor.

In the previous research, due to the high thermodynamic stability of NBiT, Na_2CO_3-rich conditions were used to avoid incomplete conversion reactions from NBiT to NBT [57]. Excess Na_2CO_3 was added to make use of the eutectic formed between the molten NaCl salt and the Na_2CO_3 reactant, which decreased the melting point of the system to approximately 636 °C [62]. The total evaporation rate of the salt also increases with temperature, rising from 9.9% at 800 °C to nearly 60% at 1000 °C [64]. In this case, using the excess carbonate compensates for the loss of evaporated carbonate and maintains the stoichiometric ratio of reactants, leading to complete conversion in the reaction [62,63]. Additionally, Dursun et al. [63] reported that applying excessive carbonate during the transformation of NBiT to NBT can improve the morphology of NBT platelets. Therefore, in this study, NBT platelets were synthesized using a 1.875:1 molar ratio of Na_2CO_3 and NBiT.

2.2. Textured Ceramic Development

The 0.90NBT-0.08KN-0.02ST powder was prepared by conventional solid-state reaction. The phase purity and crystal structure of the matrix powder were confirmed by X-ray diffraction analysis, as shown in Figure 3. The diffraction pattern reveals no impurities and is indexed as a single phase of $(Na_{0.5}Bi_{0.5})TiO_3$ with a tetragonal phase and *P4bm* space group (COD# 96-210-2069). As the peaks are sharp and well-defined, the matrix powder has good crystallinity.

Initially, the textured and untextured NBT-KN-ST ceramics were sintered at 1175 °C for 4 h with varying NBT platelet compositions, i.e., 0, 1, 2, 3, 4, and 5 wt%. Figure 4 shows that all the samples have the NBT perovskite structure. Some of the patterns have a small secondary phase peak at ~29.5° 2θ, but the identity of this peak could not be determined. The pattern of the untextured sample could be indexed with COD # 96-210-2069 as above.

However, for the purpose of calculating the Lotgering factor, the patterns were indexed using a pseudo-cubic unit cell, as shown in Figure 4. The XRD diffraction patterns exhibit intense (00*l*) peaks at 2θ ≈ 22° for (001) and ≈ 46° for (002), while the intensity of the other peaks decreases with an increase in NBT platelet amount. These results indicate that the NBT-KN-ST ceramics were textured in a specific orientation, the (00*l*) planes, as the NBT platelets were added. Notably, the (001) peak at 2θ ≈ 22° begins to broaden into a hump in samples with ≥ 4 wt% NBT platelets, while extra peaks (marked 3rd and 4th in Figure 4) appear on the high-angle side of the peak at 2θ ≈ 46.5° (marked 1st and 2nd in Figure 4) in all samples with NBT platelet addition. These extra peaks become more intense as the amount of NBT templates increases. The position of these extra peaks matches the position of the (204) peaks of the NBT templates (Figure 1), indicating that they may be caused by the NBT templates. The peaks at 2θ ≈ 46.5° are labelled as follows: tetragonal *P*4*bm* phase (1st peak) with its Kα_2 radiation peak (2nd peak), and rhombohedral *R*3*c* phase (3rd peak) with its Kα_2 radiation peak (4th peak). The peak positions of the 1st and 2nd peaks also shift to slightly higher 2θ values as more NBT templates are added. This indicates that the lattice parameters of the NBT-KN-ST ceramics were changed as more templates were added.

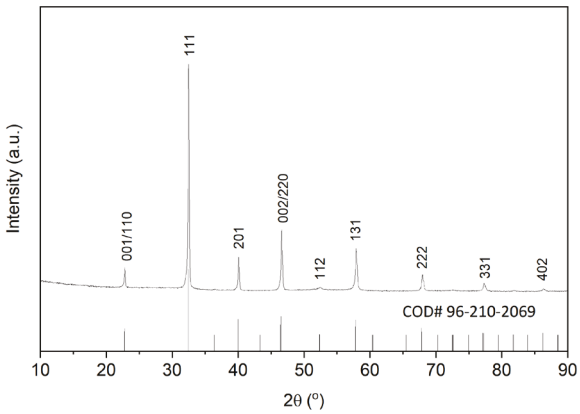

Figure 3. X-ray diffraction pattern of 0.90($Na_{0.5}Bi_{0.5}$)TiO_3-0.08$KNbO_3$-0.02$SrTiO_3$ powder.

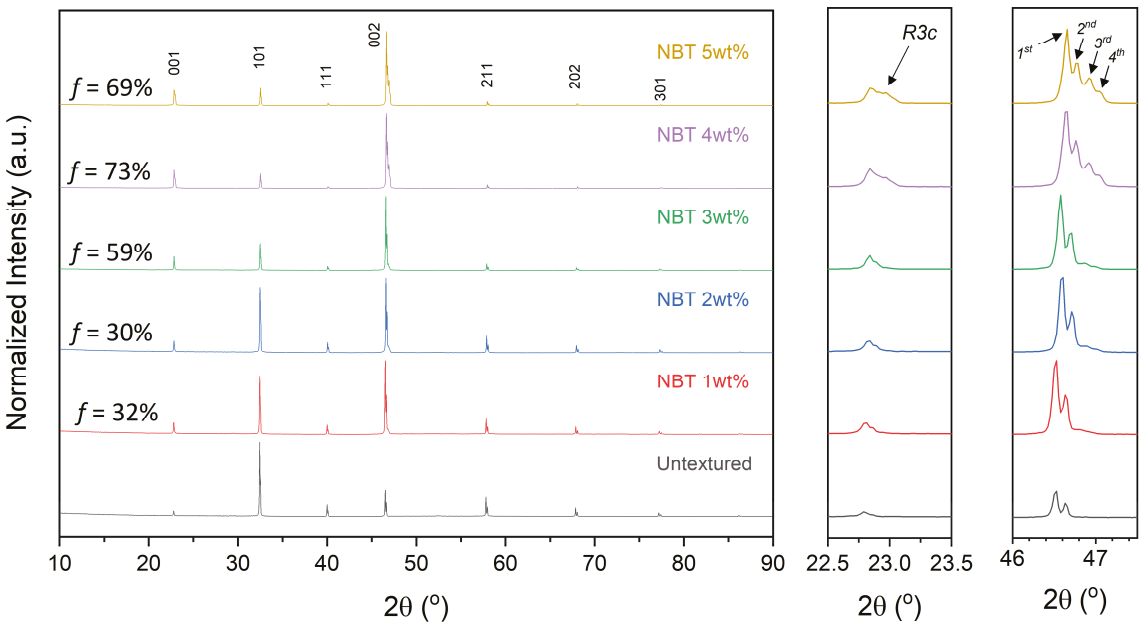

Figure 4. X-ray diffraction patterns of 0.90($Na_{0.5}Bi_{0.5}$)TiO_3-0.08$KNbO_3$-0.02$SrTiO_3$ ceramics sintered at 1175 °C for 4 h with different additions of NBT platelets.

The degree of texture was determined as the result of NBT platelet amount, which formed an optimum trend, with the highest textured degree observed at 4 wt% addition of NBT platelets. The decline in texture degree with the addition of 5 wt% NBT platelets can be attributed to agglomeration and impingement of platelets [65]. It was also demonstrated that the relative density of the textured samples followed a similar trend to the degree of texture (Figure 5). The reduction in relative density of 0.5% at the addition of 5 wt% of NBT platelets is due to platelet impingement, which can hinder oriented growth and lead to the trapping of pores inside the material, decreasing the relative density [66].

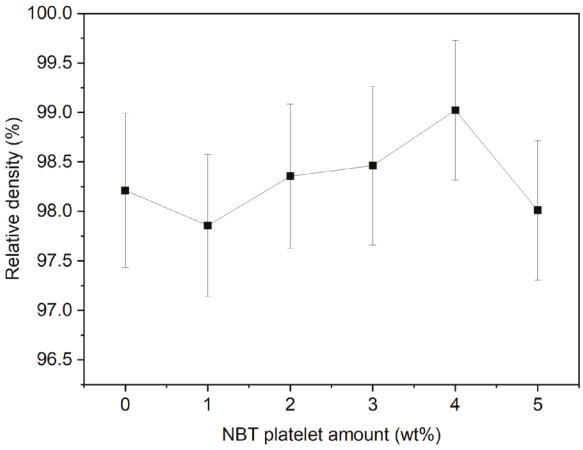

Figure 5. Relative density plots of $0.90(Na_{0.5}Bi_{0.5})TiO_3$-$0.08KNbO_3$-$0.02SrTiO_3$ ceramics sintered at 1175 °C for 4 h with different additions of NBT platelets.

Based on the optimal degree of texturing at 4 wt% NBT platelet addition, further optimization involved increasing the sintering temperature to 1200 °C and extending the sintering time to 20 h. The results in Figure 6 confirm that all the sintered samples remain as a perovskite phase regardless of the sintering conditions. As before, some of the patterns contain a small peak at ~29.5°. Increasing the sintering time at 1175 °C from 4 h to 20 h results in only a slight increase in the Lotgering factor from 73% to 78.2%. However, as the sintering temperature increases to 1200 °C, the texture degree improves to 85% after 20 h of sintering. At both 1175 and 1200 °C, the intensity of the extra 3rd and 4th peaks at ~46.7° 2θ decreases as sintering time increases. This suggests that the NBT platelets are forming a solid solution with the surrounding matrix grains. These changes indicate that the grain growth process is accompanied by solid solution formation, indicating that the NBT templates have been incorporated into the surrounding matrix. The relative density also slightly increases with sintering temperature and follows an optimal trend with time, peaking at 10 h (Figure 7). This trend suggests that both grain growth and pore elimination are most effectively promoted at around 10 h of sintering time. These results align with previous studies [67,68], which reported that increased sintering temperature and time can enhance the texture degree by promoting abnormal grain growth and platelet alignment.

X-ray diffraction patterns of the untextured and textured samples after Rietveld refinement are shown in Figure 8. Refinement results are shown in Table 1. Both samples contain coexisting tetragonal (*P*4*bm*) and rhombohedral (*R*3*c*) phases, with the rhombohedral (*R*3*c*) phase dominant. The fraction of the rhombohedral phase increases by ~28% in the textured sample. The increase in the amount of rhombohedral phase in the textured sample is due to two reasons: (1) rhombohedral NBT platelets were added to the textured sample, thus increasing the amount of rhombohedral phase; (2) the grains that grow on the NBT platelets are more likely to have a rhombohedral structure following the structure of the platelets. The lattice parameters of the two phases in the textured sample showed changes for the tetragonal phase and a decrease for the rhombohedral phase. The XRD pattern for the NBT

templates was fitted using Rietveld refinement with an *R3c* phase and was found to have lattice parameters a = 5.4850Å and c = 13. 5127 Å (R_{wp} = 16.20%, R_p = 12.34%). The lattice parameters of the rhombohedral phase in the textured sample may decrease because this phase is growing on NBT platelets with smaller lattice parameters [69]. Changes in lattice parameter can also happen due to the alignment of grains in the textured sample. In the untextured sample, the grains are randomly oriented, leading to local lattice distortion because of the misorientation of crystallographic planes between differently oriented grains. As texturing develops, more uniform grain orientation is formed, reducing intergranular misorientation and leading to relaxation of the lattice.

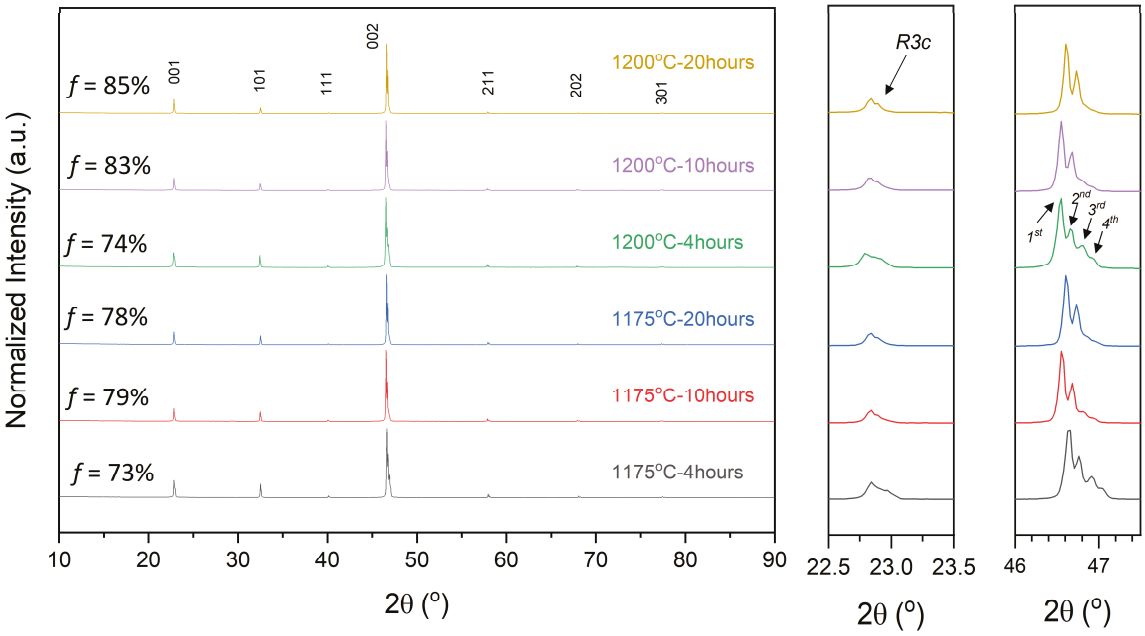

Figure 6. X-ray diffraction patterns of $0.90(Na_{0.5}Bi_{0.5})TiO_3$-$0.08KNbO_3$-$0.02SrTiO_3$ textured ceramics with 4 wt% NBT platelet addition and different sintering conditions.

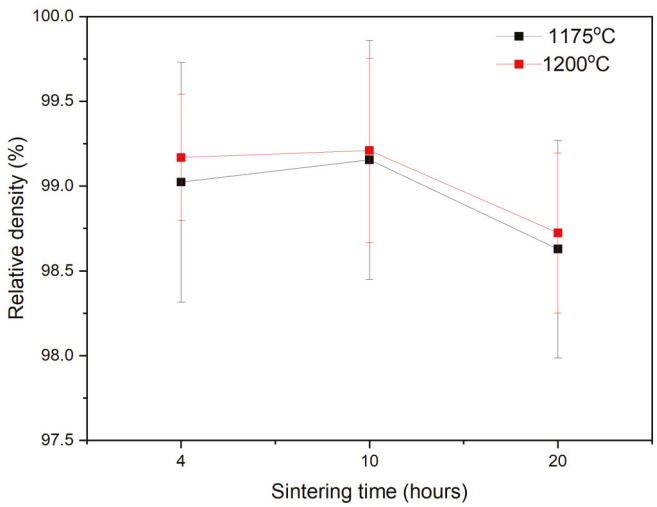

Figure 7. Relative density plots of $0.90(Na_{0.5}Bi_{0.5})TiO_3$-$0.08KNbO_3$-$0.02SrTiO_3$ textured ceramics with 4 wt% NBT platelet addition and different sintering conditions.

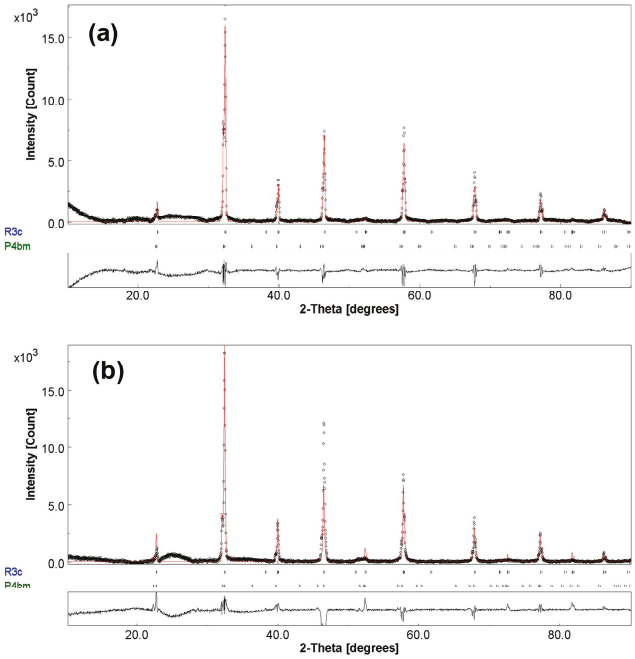

Figure 8. X-ray diffraction patterns of (**a**) untextured and (**b**) textured 0.90($Na_{0.5}Bi_{0.5}$)TiO_3-0.08$KNbO_3$-0.02$SrTiO_3$ ceramics (sintered at 1200 °C for 10 h) after Rietveld refinement. The circles are the raw data points, the red lines are the fitted patterns, the vertical lines are peak positions for the *R*3*c* and *P*4*bm* phases and the subfigures are difference plots between the raw data and fitted pattern.

Table 1. Rietveld refinement results for untextured and textured 0.90($Na_{0.5}Bi_{0.5}$)TiO_3-0.08$KNbO_3$-0.02$SrTiO_3$ ceramics.

	Untextured		**Textured**	
Crystal system	Tetragonal	Rhombohedral	Tetragonal	Rhombohedral
Space group	*P4bm*	*R3c*	*P4bm*	*R3c*
a (Å)	5.5501	5.5205	5.5245	5.5160
b (Å)	5.5501	5.5205	5.5245	5.5160
c (Å)	3.9526	13.5624	3.9751	13.5183
α (°)	90	90	90	90
β (°)	90	90	90	90
γ (°)	90	120	90	120
Weight fraction%	46.1	53.9	17.9	82.1
R (weighted profile)%	9.5496		8.7159	
R profile%	7.7909		5.4665	

2.3. Microstructure

The cross-sectional micrographs of the untextured ceramic in Figure 9a,b show that the grains are randomly oriented, indicating a typical polycrystalline microstructure. The grains are cubic in shape, with rounded edges and corners. Abnormal grain growth appears to be just beginning, as there are many grains ~2–3 times larger than the surrounding matrix grains [70]. There is no evidence of preferential grain alignment, and the structure appears densely packed with minimal visible porosity, indicating that densification through the sintering process was successful. In contrast, large, plate-like grains are elongated in the same direction in the textured sample, as observed in Figure 9c,d. The preferential alignment of large rectangular grains shows that the highly oriented NBT platelets effectively enhance the development of crystallographic texture through templated grain growth. At higher magnification, the plate-like grains display rectangular shapes with well-defined facets, characterized by flat surfaces and rounded edges. The small grains surrounding

the larger aligned ones appear to be randomly oriented. This condition provides evidence that homoepitaxial growth with the Ostwald ripening process occurred, where the large particles (NBT platelets) consumed the finer 0.90NBT-0.08KN-0.02ST grains in order to grow [71,72]. Also, it confirms that the abnormal grain growth mechanism occurred with the NBT platelets acting as sites for rapid grain growth. According to Kimura et al. [67], the abnormal grain growth mechanism forms a bi-modal grain size distribution where the large grains coexist with the fine grains and cause an abrupt increase in the orientation. The sharp difference in grain size between the grains growing on NBT platelets and the surrounding matrix grains was due to interface reaction-controlled growth; rapid growth on the NBT platelets occurred with the activation of abnormal grain growth [73,74]. Large pores are visible in the textured ceramic, often adjacent to the large textured grains. When the large grains impinge upon each other, they tend to form pores that are very difficult to remove. In some of the textured grains, elongated depressions are visible. These correspond to the position of the NBT templates. The disappearance of distinct templates indicate that the grain growth process is accompanied by solid solution formation. It is not clear if the NBT templates diffused into the surrounding grain, leaving an elongated pore behind, or if they were pulled out of the sample during polishing.

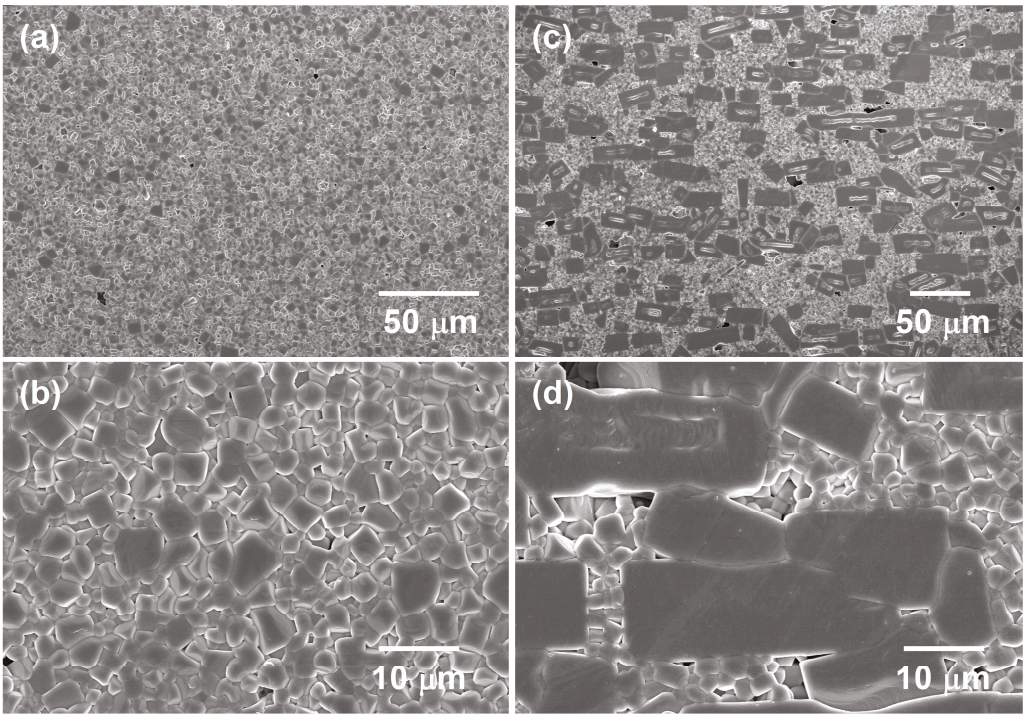

Figure 9. Micrograph of (**a**,**b**) untextured; (**c**,**d**) textured (4 wt% NBT platelets) 0.90($Na_{0.5}Bi_{0.5}$)TiO_3-0.08$KNbO_3$-0.02$SrTiO_3$ ceramics sintered at 1200 °C for 10 h.

To gain more insight, EPMA analysis was conducted to investigate the elemental distribution and quantitative composition of both samples, as presented in Figure 10 and Table 2. The elemental mapping in Figure 10a shows that the elements in the untextured sample are generally uniformly distributed. Some local variations for Na, Bi, K, and Ti indicate a K- and Ti-rich second phase. In the textured sample, although the NBT platelets as templates share a similar composition with the matrix powder (0.90NBT-0.08KN-0.02ST), their presence can be distinguished through the distribution of the minor constituents. As shown in Figure 10b, the textured sample exhibits regions lacking K, Sr, and Nb signals, while having increased Bi (and possibly Ti) signals. Additionally, these regions show a distinct rectangular shape and orientation. These regions are most likely associated with

the NBT platelets. The K- and Ti-rich second phase that appeared in the untextured sample also appears in the textured sample.

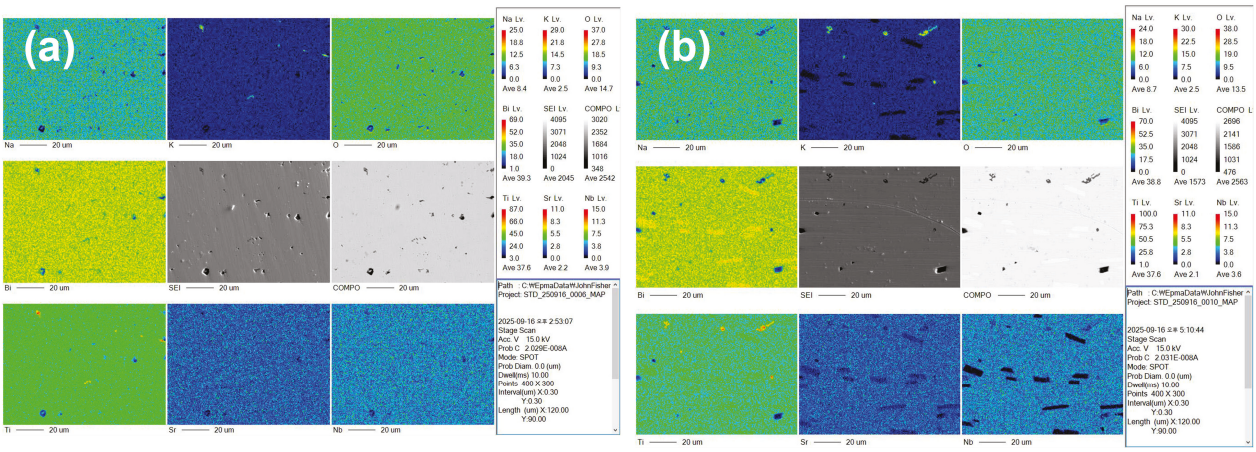

Figure 10. Elemental distribution map by EPMA analysis of (**a**) untextured; (**b**) textured (4 wt% NBT platelets) $0.90(Na_{0.5}Bi_{0.5})TiO_3$-$0.08KNbO_3$-$0.02SrTiO_3$ ceramics sintered at 1200 °C for 10 h. Scale bar = 20 μm.

Table 2. The elemental composition by EPMA analysis of untextured and textured (4 wt% NBT platelets) $0.90(Na_{0.5}Bi_{0.5})TiO_3$-$0.08KNbO_3$-$0.02SrTiO_3$ ceramics sintered at 1200 °C for 10 h.

Oxide (mol%)	Untextured	Textured	Nominal $0.90(Na_{0.5}Bi_{0.5})TiO_3$-$0.08KNbO_3$-$0.02SrTiO_3$	Templates	Nominal $(Na_{0.5}Bi_{0.5})TiO_3$
Na_2O	13.39 ± 0.64	13.89 ± 0.41	15.31	14.05 ± 0.51	16.67
K_2O	2.33 ± 0.12	2.38 ± 0.10	2.72	1.83 ± 0.59	0
TiO_2	64.28 ± 0.33	64.12 ± 0.35	62.59	65.36 ± 1.13	66.67
SrO	1.15 ± 0.05	1.07 ± 0.07	1.36	0.68 ± 0.48	0
Bi_2O_3	16.06 ± 0.25	15.79 ± 0.22	15.31	16.17 ± 0.51	16.67
Nb_2O_5	2.80 ± 0.08	2.75 ± 0.14	2.72	1.91 ± 1.05	0

Quantitative compositional analysis was performed using point analysis, in which 10 representative points were selected from each sample. For the textured sample, 10 points were measured away from the templates, and an additional 5 points were measured on the templates. The results are given as the amount in mol% of each constituent oxide. The results indicate that the untextured sample exhibits relatively homogeneous composition with low deviations across all elements (Table 2). In contrast, the textured sample shows larger deviations, particularly for K, Sr, and Nb. The untextured sample has a composition close to the nominal 0.90NBT-0.08KN-0.02ST composition. It appears Na-deficient and Bi-excess. Na is likely lost by evaporation during sintering. Bi may replace Na in the lattice to maintain charge balance [75]. Similar behaviour occurs in the textured sample. The compositions of the untextured and textured samples are very close to each other. EPMA of the NBT templates indicates that some K, Sr, and Nb have diffused into the templates. The amounts of Na, Bi, and Ti in the templates are also lower than the nominal amounts, indicating that interdiffusion between the templates and surrounding grains has taken place. This explains why the XRD peaks associated with the NBT templates become weaker with increased sintering time.

2.4. Polarization and Strain Behaviour

Each measurement consisted of three cycles. The second cycle of each measurement is shown. The polarization hysteresis loops of the untextured sample in Figure 11a exhibit behaviour typical of a lossy linear dielectric or an ergodic relaxor phase, which is a slim

and linear loop with a minimal remanent polarization ≈1.5 μC/cm^2. Increasing the electric field can gradually elevate the maximum polarization value to ≈17 μC/cm^2, as indicated by the height of the loops. At the same time, the textured sample in Figure 11c exhibited an enhancement in maximum polarization to ≈20 μC/cm^2 and remanent polarization to ≈4.5 μC/cm^2 as the electric field increased. The increases in maximum and remanent polarization may be due to an increased amount of nonergodic rhombohedral phase (Table 1). The increasing polarization in the different electric fields without any saturation exhibited that both materials have relaxor behaviour in the ergodic phase, with dynamic polar nanoregions with no stable ferroelectric domains [43].

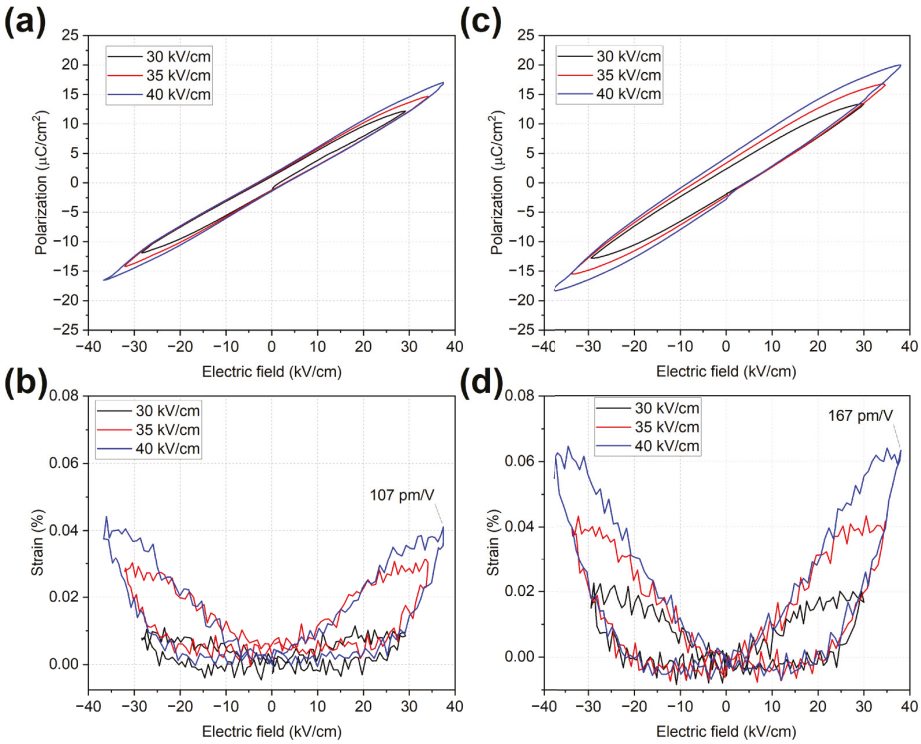

Figure 11. Polarization hysteresis loops and bipolar strain curves of (**a**,**b**) untextured; (**c**,**d**) textured (4 wt% NBT platelets) 0.90($Na_{0.5}Bi_{0.5}$)TiO_3-0.08$KNbO_3$-0.02$SrTiO_3$ ceramics sintered at 1200 °C for 10 h.

The strain response in the bipolar measurements also confirmed the polarization result, where the sprout-shaped loops emerge as seen in Figure 11b,d. This is the typical electric field-induced electrostrictive response in an ergodic relaxor phase, characterized by a quadratic dependence on the electric field (Figure 12c) [12,38,41]. Both untextured and textured samples showed symmetric and reversible strain centred at zero field. This behaviour matches that of ergodic NBT-based relaxor systems [37,43,51]. Hysteresis in the loops is caused by reorientation of polar nanoregions [49]. Similarly to polarization, the increase in the electric field also induces strain enhancement for both samples. However, the textured sample has a higher strain than the untextured sample, showing that texturing in the [001] direction can improve the inverse piezoelectric properties. The addition of NBT templates to the textured ceramic may also improve the inverse piezoelectric properties, with the templates acting as a nonergodic relaxor phase in a nonergodic/ergodic relaxor composite [76,77]. On the other hand, the decrease in the amount of the tetragonal phase (Table 1) may decrease the inverse piezoelectric properties as the electric field-induced phase transition from the tetragonal to rhombohedral phase is known to cause a large strain [78]. The increasing electric field enhanced the magnitude of the polarization and strain without altering the shape of the loops, indicating that the ergodic relaxor and

electrostrictive behaviour remained consistent. The loops are quite broad, indicating that the strain behaviour is not entirely electrostrictive, i.e., ferroelectric domains may form and disappear under the influence of the electric field. The actual electric field is lower than the nominal electric field, particularly at 40 kV/cm. This may be caused by the low resistivity of the samples. A leakage current may allow charge flow across the sample, leading to a lower measured voltage. Hysteresis loop measurements were not carried out at higher electric fields due to concerns about sample electrical breakdown.

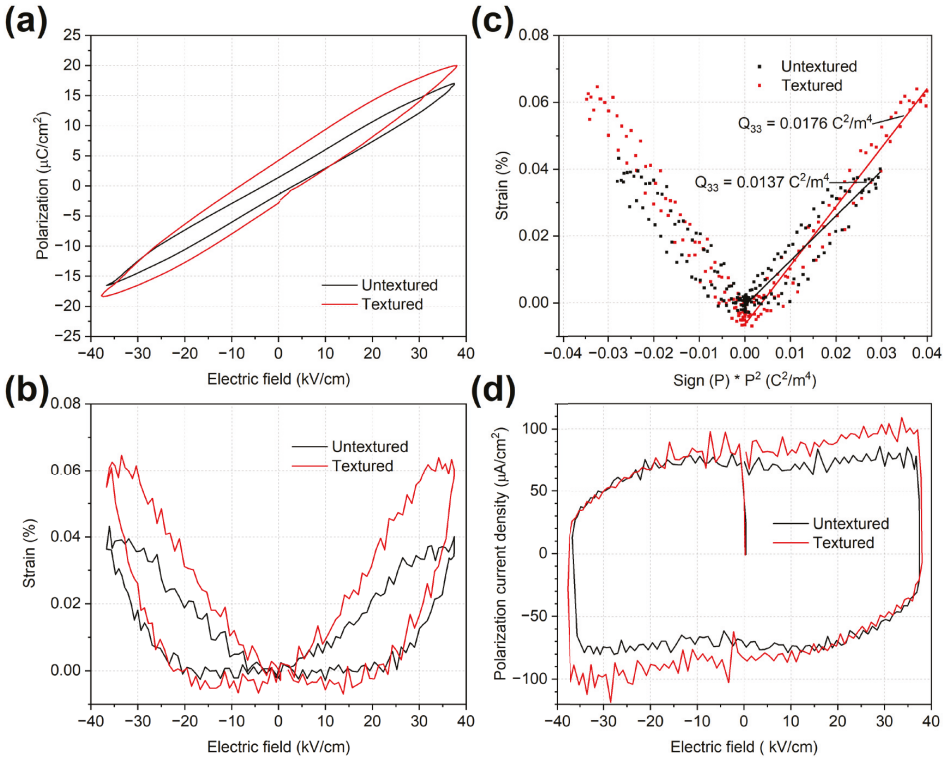

Figure 12. (**a**) Polarization hysteresis loops; (**b**) bipolar strain curves; (**c**) S-P^2 plots; (**d**) polarization current density of untextured and textured (4 wt% NBT platelets) $0.90(Na_{0.5}Bi_{0.5})TiO_3$-$0.08KNbO_3$-$0.02SrTiO_3$ ceramics sintered at 1200 °C for 10 h.

To observe the impact of texturing, the polarization, strain, and polarization current density loops at an electric field of 40 kV/cm are compared. Figure 12a shows that texturing slightly expanded the polarization hysteresis loop, resulting in the enhancement of the remanent polarization and maximum polarization. Although the hysteresis loop becomes slightly wider, both polarization loops maintain a slim, linear shape without saturation at high electric fields. This suggests that both materials still retain their ergodic relaxor phase and do not undergo the complete domain switching characteristic of classical ferroelectrics.

Both samples exhibit symmetric, sprout-like strain hysteresis loops, characterized by rounded and reversible shapes centred at the origin, as illustrated in Figure 12b. It confirmed that electrostrictive behaviour emerged with no remanent strain, and that irreversible domain wall motion did not contribute significantly to the strain response [79]. The S-E loops also showed that texturing enhances the strain from 0.04% in the untextured sample to ~0.06% in the textured sample. Figure 12c exhibits the relation between strain and Sign(P) × P^2 (C^2/m^4) to evaluate the electrostrictive behaviour by observing the linear correlation between both parameters. (Sign (P) is set to positive or negative to correspond to a positive or negative electric field.) As the slope of the regression line represents the longitudinal electrostrictive coefficient (Q_{33}), the textured sample shows a steeper slope than the untextured sample. This indicates a stronger electrostrictive response in

the textured sample with an electrostrictive coefficient = 0.0176 C^2/m^4 compared to the untextured sample with Q_{33} = 0.0137 C^2/m^4. This increase in Q_{33} is due to the increased {001} orientation of the textured ceramics. Crystallographic orientation is known to have an effect on the electrostrictive properties of relaxor ferroelectric single crystals [49]. There is scatter between the data points and the linear fit, indicating that the samples have mixed electrostrictive and relaxor behaviour [49].

To understand the rate of polarization change, the polarization current density–electric field (J-E) curves were examined, as shown in Figure 12d. The untextured and textured samples have broad and smooth loops, indicating that both samples exhibit relaxor/electrostrictive or lossy dielectric behaviour [80,81]. This refers to the presence of dynamic polar nanoregions that continuously reorient in response to a changing electric field and exhibit reversible ergodic behaviour. The absence of sharp peaks in the J-E diagram also shows that there are no remanent ferroelectric domains, with no sharp rise or fall in polarization [82]. Thus, both materials exhibit characteristics of ergodic relaxor ferroelectrics, dominated by field-induced polarization through dynamic PNR activity rather than classical domain switching. The homoepitaxial TGG process uses templates with a similar structure and elemental composition. In this situation, compositional deviation may occur due to the interdiffusion of elements between the templates and the matrix. This can lead to a compositional shift and change the electrical behaviour of the textured sample [71,83,84].

The unipolar hysteresis measurements also exhibit similar behaviour to the bipolar measurements, as shown in Figure 13. The polarization of the textured sample is slightly larger than that of the untextured sample, with larger hysteresis (Figure 13a,c). The slim unipolar hysteresis loop confirms that the untextured sample has mostly electrostrictive behaviour. The addition of NBT platelets as templates resulted in a larger polarization hysteresis of the textured sample, shifting the behaviour from electrostrictive to more ferroelectric behaviour. The unipolar strain also shows a half-sprout shape without any saturated strain. Figure 13b shows that the untextured sample exhibits poor strain under various electric fields, with the maximum strain <0.02% at an electric field of 40 kV/cm. Figure 13d shows that the enhancement of strain occurred with the addition of NBT platelets as a template; the maximum strain at an electric field of 30 kV/cm started around 0.03%, which is higher than that of the untextured sample at an electric field of 40 kV/cm. The maximum strain of the textured sample continued to increase with the electric field, reaching a corresponding strain value of ~0.07% at an electric field of ~40 kV/cm.

Figure 14 shows the first and second cycles of unipolar and bipolar strain hysteresis loops for the untextured and textured samples. The unipolar strain hysteresis loop of the untextured sample shows a remnant strain of ~0.01% after the first cycle (Figure 14a), while the textured sample does not show any remnant strain (Figure 14b). The remnant strain in the untextured sample indicates that ferroelectric domains are forming during application of the electric field and that some of them remain stable after the field is removed. It is noteworthy that if the unipolar hysteresis loops are measured again on the same sample after a pause of a few seconds, the remnant strain disappears, and the behaviour seen in Figure 14a repeats itself. This implies that any remanent ferroelectric domains are unstable and quickly disappear. The poor unipolar strain vs. electric field behaviour of the untextured sample is due to the remnant strain. The bipolar hysteresis loops of the untextured (Figure 14c) and textured (Figure 14d) samples are both noisy in the first cycle, but they both appear to show a remnant strain which then disappears in subsequent cycles (for the textured sample, the 1st and 3rd cycles are shown as the second cycle was distorted). The difference in unipolar strain behaviour between the untextured and textured samples is due to the crystallographic orientation of the textured sample

in the [001] direction. Previous work on NBT-based single crystals has shown that their strain–electric field behaviour can change with sample orientation between electrostrictive and incipient ferroelectric [85].

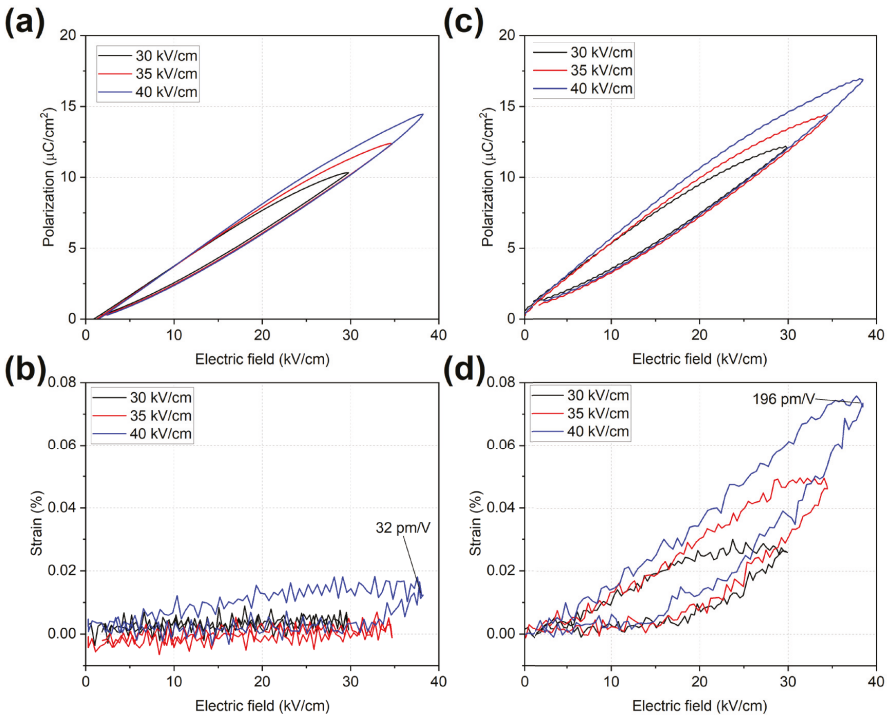

Figure 13. Unipolar polarization hysteresis loops and strain curves of (**a**,**b**) untextured; (**c**,**d**) textured (4 wt% NBT platelets) $0.90(Na_{0.5}Bi_{0.5})TiO_3$-$0.08KNbO_3$-$0.02SrTiO_3$ ceramics sintered at 1200 °C for 10 h.

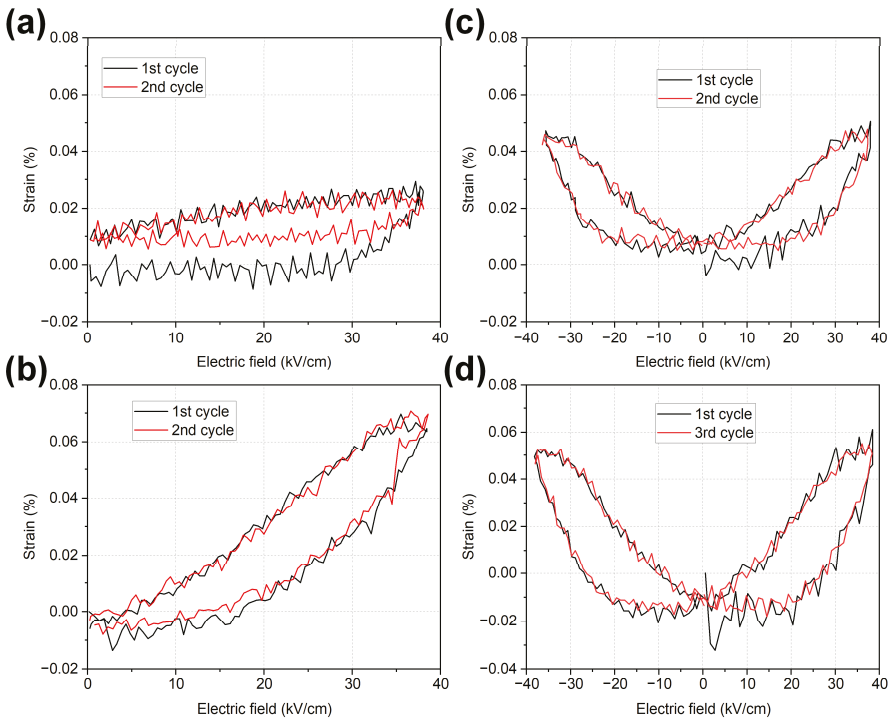

Figure 14. First and second cycles of unipolar strain hysteresis loops of (**a**) untextured; (**b**) textured (4 wt% NBT platelets) $0.90(Na_{0.5}Bi_{0.5})TiO_3$-$0.08KNbO_3$-$0.02SrTiO_3$ ceramics sintered at 1200 °C for 10 h. First and second cycles of bipolar hysteresis loops of (**c**) untextured; (**d**) textured (4 wt% NBT platelets) $0.90(Na_{0.5}Bi_{0.5})TiO_3$-$0.08KNbO_3$-$0.02SrTiO_3$ ceramics sintered at 1200 °C for 10 h (for the textured sample, the 1st and 3rd cycles are shown as the second cycle was distorted).

2.5. Dielectric Property Measurements

The temperature dependence of dielectric properties on cooling is presented in Figures 15 and 16 for untextured and textured samples sintered at 1200 °C for 10 h, as a function of temperature and frequency. The values of characteristic parameters of the untextured and textured ceramics are given in Table 3. Comparing the real part of the permittivity plot between the untextured and textured samples in Figures 15a and 16a, it is seen that the dielectric behaviour of the samples is typical of NBT-based materials [65,86]. The temperature-induced relaxation of the polar nanoregions (PNR) can be observed as a shoulder peak marked as T_s in the real-permittivity plot, which exhibits a slight increase in temperature from untextured to textured samples. T_s varies with measurement frequency, so T_{sm}, the temperature at which frequency dispersion reaches a minimum value, is measured instead. T_{sm} increases in the textured sample, while the temperature of maximum relative permittivity T_m is almost the same in both samples. The depolarization temperature T_d is not observed, as it falls below the measurement range. Both untextured and textured samples exhibit typical relaxor behaviour with broad and stable permittivity over 130~300 °C, driven by polar nanoregion (PNR) dynamics [87,88]. The increase of T_{sm} from untextured to textured samples indicates modified PNR relaxation due to the increase in the fraction of rhombohedral phase caused by the addition of NBT templates (Figures 4 and 8 and Table 1). NBT has a T_{sm} between 230~250 °C [39,86,89].

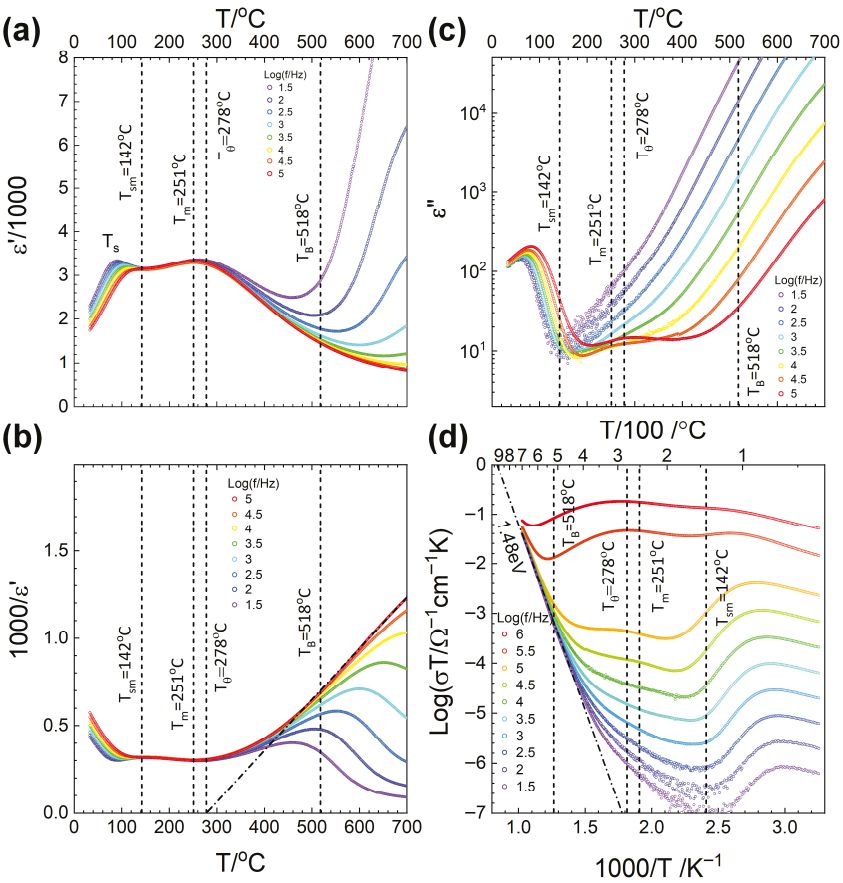

Figure 15. Dielectric properties and AC conductivity of the untextured sample at certain frequencies with a temperature range of 30 °C to 700 °C: (**a**) plot of the real part of the relative permittivity; (**b**) the inverse permittivity; (**c**) the imaginary part of the relative permittivity; (**d**) the Arrhenius plots of the AC conductivity.

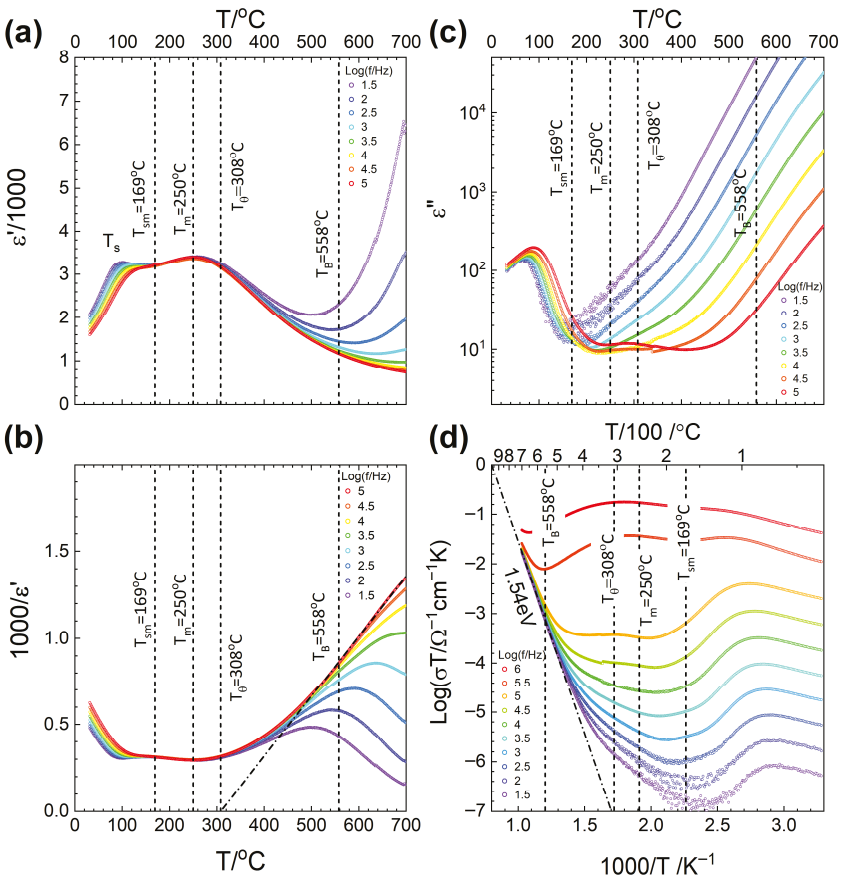

Figure 16. Dielectric properties and AC conductivity of the textured sample with certain frequencies at a temperature range of 30 °C to 700 °C: (**a**) plot of relative permittivity; (**b**) the inverse permittivity; (**c**) the imaginary permittivity; (**d**) the Arrhenius plots of the AC conductivity.

Table 3. Comparison of the dielectric property parameters of untextured and textured $0.90(Na_{0.5}Bi_{0.5})TiO_3$-$0.08KNbO_3$-$0.02SrTiO_3$ samples.

Parameter	Untextured	Textured
T_d (°C)	-	-
T_{sm} (°C)	142	169
T_m (°C)	251	250
T_θ (°C)	278	308
T_B (°C)	518	558
E_a (eV)	1.48	1.54

Beyond T_{sm} and T_m, the dielectric response of relaxor ferroelectrics can be further interpreted in terms of two additional characteristic temperatures: the Curie–Weiss temperature (T_θ) and the Burns temperature (T_B). T_θ is obtained by fitting the Curie–Weiss law to the inverse permittivity plot at temperatures above the Curie temperature, according to the equation below (Figures 15b and 16b) [90]:

$$\varepsilon' = \frac{C}{T - T_\theta}$$

where C is the Curie-Weiss constant. The extrapolation of the Curie–Weiss fit (the dot-dash line) to the temperature axis provides T_θ, which in normal ferroelectrics would be equal to or be less than the actual paraelectric-ferroelectric transition temperature [91,92]. In relaxors, however, long-range ferroelectric order does not develop, and instead T_θ marks the stage when PNRs begin to interact more strongly and influence dielectric behaviour [93,94]. At

the same time, a deviation of the relative permittivity from the linear fit is observed at a much higher temperature, defined as the Burns temperature (T_B), where the formation of PNRs begins from the paraelectric matrix [95]. Above T_B, the material is purely paraelectric, while below T_B, local polar clusters form and gradually grow upon cooling toward T_θ. T_B increases in the textured sample, again due to the presence of the NBT templates and the increase in the fraction of rhombohedral phase [86,93].

To support the presence of dielectric relaxation processes and distinguish the dielectric contribution from thermally activated conduction, the imaginary permittivity (ε'', Figures 15c and 16c) data were plotted. The plots reveal clear frequency-dispersive peaks at T_s, which shift toward higher temperatures with increasing frequency, indicating thermally activated relaxation behaviour. This frequency dispersion is strongly associated with the diffusion of charge carriers that becomes prominent during the rhombohedral–tetragonal phase transition [96]. Consequently, the dielectric response of the system is governed not only by dipole polarization but also by diffusional dynamics triggered by structural transformation [89]. The observed frequency-dependent behaviour originates from a combination of the dynamic response of polar nanoregions and charge migration, while the continuous increase in ε'' at higher temperatures reflects thermally activated conduction.

The AC conductivity was plotted as log (σT) versus 1000/T (Figures 15d and 16d), following the Arrhenius relation [97]:

$$\sigma T = \sigma_0 \exp(-\frac{E_a}{kT})$$

where k is the Boltzmann constant and σ_0 is the pre-exponential factor. In this way, the conduction mechanism can be quantitatively distinguished by determining the activation energy (E_a) from the slope of the Arrhenius plot. Figures 15d and 16d show that at high temperatures between 600 °C and 700 °C, the slopes of the conductivity plots are steep, which also confirms the previous explanation about thermally activated conduction in the imaginary permittivity plots (ε'', Figures 15c and 16c). The increase in conductivity with increasing frequency shows that higher-frequency AC fields promote charge carrier hopping and enhance conduction [98]. The activation energies were also at high values of above 1.2 eV, indicating that conduction may be controlled by oxygen vacancies or hole conduction at high temperature [26,65,98].

EPMA analysis confirms that alkali loss occurs during sintering, generating A-site vacancies (V'_A) and accompanying oxygen vacancies ($V_{\ddot{O}}$) for charge compensation. The volatilization of alkali oxides and their associated charge-compensating process to preserve charge neutrality can be represented in a combined form as:

$$2A_A^x + O_O^x \rightarrow 2V'_A + V_{\ddot{O}} + A_2O(g)$$

where A denotes the alkali cations (Na^+ or K^+) occupying their A-site.

The EPMA data further reveal the presence of a K- and Ti-rich secondary phase, implying that not all of the K entered solid solution, as also found for NBT-KN single crystals [89]. At the B-site, Nb^{5+} substitutes Ti^{4+} according to [99,100]:

$$Nb_2O_5 + 2Ti_{Ti}^x + V_{\ddot{O}} \rightarrow 2Nb_{\dot{Ti}} + TiO_2 + O_O^x$$

Hence, an oxygen vacancy formed by alkali evaporation can be filled. The positively charged donor $Nb_{\dot{Ti}}$ can compensate for the negatively charged alkali vacancies generated during alkali loss [99,101]. The oxygen vacancies serve as charge-compensating defects to stabilize the donor substitution of Nb^{5+} at the B-site, representing an indirect stabilization between A-site and B-site defect chemistry.

EPMA analysis also shows that the samples are slightly Bi-excess. Excess Bi_2O_3 is possibly supplied by the packing powder. Bi can substitute for Na as follows:

$$Bi_2O_3 + 2V_{\ddot{O}} \rightarrow 2Bi_{\ddot{Na}} + 3O_O^x$$

Consequently, the population of oxygen vacancies decreases, reducing the number of mobile ionic carriers and suppressing oxide-ion conduction.

On the other hand, hole-type defects ($h^{\cdot}$) are produced due to oxygen incorporation during sintering in the oxidizing atmosphere (air) according to:

$$\frac{1}{2}O_2(g) + V_{\ddot{O}} \rightarrow O_O^x + 2h^{\cdot}$$

These holes are not free but are localized on Bi–O hybrid orbitals (Bi 6*s*–O 2*p*), forming deep acceptor states that conduct via thermally activated small-polaron hopping:

$$h^{\cdot} + (\text{Bi–O}) \rightarrow (\text{Bi–O})^{\cdot}$$

This localization can also be associated with the second-order Jahn–Teller distortion due to the presence of the Bi^{3+} ($6s^2$) lone-pair electrons. The coupling between the filled Bi-6*s* and empty Bi-6*p* orbitals through O-2*p* states induces off-centring of Bi and creates asymmetric Bi–O bonds [102]. When a hole is introduced, the hybrid orbital (Bi 6*s*–O 2*p*) relaxes further, deepening the local potential well and trapping the hole more strongly.

This trapping of holes by the Bi–O hybrid orbital might be enhanced, since the alkali loss in the A-site increases the polarity of the Bi–O bonds and makes them more effective in trapping holes. Also, the higher tolerance factor introduced by $KNbO_3$ smooths out long-range lattice distortions but strengthens local bonding asymmetry around Bi–O due to the reduced structural relaxation [99]. Therefore, the effect of alkali loss, Nb donor substitution, and oxidizing atmosphere was a reduction in defect-assisted ionic conduction and would push the system toward a deep p-type regime, where a mechanism of holes trapped on Bi–O bonds requires a large lattice relaxation energy and gives rise to a high activation energy, such as that (~1.9 eV) reported by Abbas et al. for NBT-KN [89].

However, in the present work, NBT-KN-ST showed lower activation energies (~1.5 eV), indicating that $SrTiO_3$ decreased the activation energy. The addition of $SrTiO_3$ can shift the tolerance factor toward 1, making the structure more stable due to the large cationic size of Sr [41]. As Sr^{2+} possesses a non-polarizable character and lacks a lone pair of electrons, it suppresses the local polarization fluctuations induced by the stereochemically active Bi^{3+} $6s^2$ lone pair, thereby flattening the local potential landscape [101]. Consequently, these structural relaxations reduce the localization of hole carriers on Bi–O bonds, facilitating their migration and lowering the activation energy required for hole migration in the NBT–KN–ST system.

A slight increase in the activation energy in the textured sample could be attributed to its microstructural characteristics. Conductivity varies with crystallographic orientation for an anisotropic material such as a single crystal, whereas for a polycrystalline ceramic, the random orientation of the grains makes conductivity isotropic [103]. Examples of such behaviour include $LiCoO_2$ and olivine phosphates, which show a two- and one-dimensional Li ion conductivity, respectively [104,105]. The textured NBT–KN–ST sample is more oriented in the [001] direction than the untextured sample and is expected to behave more like a single crystal, hence the difference in activation energy.

3. Materials and Methods

3.1. $(Na_{0.5}Bi_{0.5})TiO_3$ Platelet Preparation

$(Na_{0.5}Bi_{0.5})TiO_3$ platelets were prepared using a three-stage molten salt and topochemical microcrystal conversion method. The process is based on the reactions below [63,106]:

$$2Bi_2O_3 + 3TiO_2 \rightarrow Bi_4Ti_3O_{12} \quad (1)$$

$$4.5Bi_4Ti_3O_{12} + Na_2CO_3 + 2.5TiO_2 \rightarrow 4Na_{0.5}Bi_{4.5}Ti_4O_{15} + CO_2 \quad (2)$$

$$4Na_{0.5}Bi_{4.5}Ti_4O_{15} + 3Na_2CO_3 \rightarrow 16Na_{0.5}Bi_{0.5}TiO_3 + 5Bi_2O_3 + 3CO_2 \quad (3)$$

To remove adsorbed moisture, all materials were dried before use at 250 °C for 5 h. The $Bi_4Ti_3O_{12}$ (BiT) precursor was fabricated by the molten salt method using NaCl (Sigma-Aldrich, Burlington, MA, USA, ≥99.5%) as the salt. Dried Bi_2O_3 (Alfa Aesar, Ward Hill, MA, USA, 99.9%) and TiO_2 (Thermo Fisher Scientific, Waltham, MA, USA, 99.8%) are mixed according to the stoichiometric reaction (1) with a NaCl/oxide weight ratio of 1.25:1 in a planetary mill (Pulverisette 7, Fritsch GmbH, Idar-Oberstein, Germany) in ethanol (Daejung Chemicals, Siheung, Republic of Korea, 99.9%) with zirconia balls as the milling media. The materials were milled at 500 rpm using 36 alternating 5 min milling and 1 min rest cycles, for a total milling time of 3 h. The ethanol in the slurry was removed using a hotplate/magnetic stirrer. Then the slurry was dried in an oven at 70 °C. The dried slurry was ground using an agate mortar and pestle and sieved through a 180 μm sieve. The powder was heat-treated in an alumina crucible with a lid at 1100 °C for 2 h with heating and cooling rates of 5 °C/min. The NaCl was removed from the BiT precursor by stirring it in 500 mL of hot deionized water at 100 rpm and 80 °C for 1.5 h. The presence of Cl^- in the BiT sample was checked using a 0.1 M $AgNO_3$ solution. After the BiT sample was found to be free from Cl^-, it was filtered and dried in an oven at 70 °C.

In the second step, by using the same procedure as for BiT precursor preparation, BiT precursors were transformed into $Na_{0.5}Bi_{4.5}Ti_4O_{15}$ (NBiT) precursors according to reaction (2) with a NaCl/(oxide + carbonate) weight ratio of 1:1. NaCl, Na_2CO_3 (Acros Organics, Geel, Belgium, 99.5%), and TiO_2 were dried and mixed in ethanol in a planetary mill as before. After that, the $Bi_4Ti_3O_{12}$ precursor was added to the mixture and stirred at 100 rpm and room temperature for 5 h using a magnetic stirrer. The slurry mixture was dried at 70 °C as before and heat-treated in an alumina crucible with a lid at 1060 °C for 3.5 h with a heating rate of 5 °C/min, a cooling rate of 3 °C/min down to 700 °C, and a cooling rate of 5 °C/min from 700 °C to room temperature. NaCl was removed as before.

The topochemical microcrystal conversion method was used to obtain the $(Na_{0.5}Bi_{0.5})TiO_3$ (NBT) platelets from the NBiT precursor. A molar ratio of Na_2CO_3 and NBiT of 1.875:1 was used, with a NaCl/(oxide + carbonate) weight ratio of 1.5:1. NaCl and Na_2CO_3 were mixed in ethanol using a planetary mill as before. The NBiT precursor was added to the mixture and stirred at 100 rpm and room temperature for 5 h using a magnetic stirrer. The mixture was dried and heat-treated in an alumina crucible with a lid at 950 °C for 6 h with a heating rate of 5 °C/min and a cooling rate of 3 °C/min down to 700 °C, then 5 °C/min from 700 °C to room temperature. The molten NaCl was removed in hot deionized water as before, and the NBT templates were then soaked in 50 mL of 3 M HCl (Samchun, Seoul, Republic of Korea) for 1 h at room temperature to remove the Bi_2O_3 by-product. After that, the remaining Cl^- is removed from the NBT templates by stirring in hot deionized water at 80 °C and 100 rpm for 1.5 h. The presence of Cl^- in the NBT sample was checked using a 0.1 M $AgNO_3$ solution. Finally, the NBT templates are filtered and dried.

3.2. Preparation of $0.90(Na_{0.5}Bi_{0.5})TiO_3$-$0.08KNbO_3$-$0.02SrTiO_3$ Powder

A conventional solid-state reaction was applied to obtain $0.90(Na_{0.5}Bi_{0.5})TiO_3$-$0.08KNbO_3$-$0.02SrTiO_3$ (0.90NBT-0.08KN-0.02ST) powder. Bi_2O_3, TiO_2, Na_2CO_3, K_2CO_3 (Daejung Chemicals, Siheung, Republic of Korea, 99.5%), Nb_2O_5 (Daejung Chemicals, Siheung, Republic of Korea, >99.9%), and $SrCO_3$ (Sigma-Aldrich, Burlington, MA, USA, 99.9%) were ball-milled in a polypropylene bottle in ethanol using zirconia balls for 24 h. The ethanol was evaporated using a hot plate/magnetic stirrer, and the slurry was dried in an oven at 70 °C. The dried slurry was ground using an agate mortar and pestle and sieved through a 180 μm sieve. The powder was calcined in an alumina crucible with a lid at 850 °C for 4 h at a heating/cooling rate of 5 °C/min. The phase purity of the calcined powder was examined using X-ray diffraction (XRD, Empyrean, Malvern Panalytical, Malvern, UK) with CuKα radiation set at 2θ = 10–90°, a scan rate of 3°/minute, and a 0.026° scan step.

3.3. Textured Ceramic Development

The Templated Grain Growth (TGG) method was employed using the tape-casting technique and NBT platelets as template seeds to obtain the textured 0.90NBT-0.08KN-0.02ST ceramics. The composition of the tape-casting slurry (in wt% of the final slurry, not taking excess solvent into account) is given in Table 4. The tape-casting slurry is prepared in three steps. First, the ethanol (Daejung Chemicals, Siheung, Republic of Korea, 99.9%) and methyl-ethyl-ketone (Daejung Chemicals, Siheung, Republic of Korea, >99.5%) were stirred for 10 min to prepare the solvent (methyl-ethyl-ketone:ethanol weight ratio of 66:34). The solvent and the components for the organic binder (PVB, PEG 400, and BBP) were then mixed to prepare the organic binder solution. Finally, the 0.90NBT-0.08KN-0.02ST powder and organic binder solution were ball-milled using a polypropylene bottle with zirconia balls for 24 h. During this final milling stage, 6.6 wt% excess solvent was added. Various additions of NBT templates (0, 1, 2, 3, 4, and 5 wt%) were added to the mixture, which was then stirred using a magnetic stirrer at 80 rpm for 3 h in a closed beaker at room temperature. The 6.6 wt% excess solvent was then allowed to evaporate, and the slurry was cast on mylar-coated PET film using a doctor blade with a blade gap of ~180 μm at a 13 mm/s casting rate. The green tape was cut, laminated in a 1 cm × 1 cm die, and pressed in a uniaxial press with a pressure of 2 MPa. The organic binder was removed by heating at 300 °C and 600 °C for 1 h each with a heating/cooling rate of 1 °C/min. The ceramic was embedded in 0.90NBT-0.08KN-0.02ST powder inside a double alumina crucible and lid arrangement to reduce volatilization losses for the sintering process. Samples were sintered at 1175 °C and 1200 °C for various sintering times of 4, 10, and 20 h and a heating/cooling rate of 5 °C/min.

Table 4. Batch formulation of tape-casting slurry.

Component	Composition wt%	Function
Matrix powder: 0.90NBT-0.08KN-0.02ST	51.61	
Organic Binder: Polyvinyl-Butyral PVB (Butvar B79, Eastman, Kingsport, TN, USA)	4.65	Binder
Polyethylene-Glycol PEG 400 (Daejung Chemicals, CP grade)	0.33	Plasticizer
n-Butyl Benzyl Phthalate BBP (Alfa Aesar, 98%)	1.59	Plasticizer
Methyl-ethyl ketone (Daejung Chemicals, >99.5%)	27.60	Solvent
Ethanol (Daejung Chemicals, 99.9%)	14.22	Solvent

3.4. Characterization

The phase purity of the BiT, NBiT, and NBT platelets was examined using X-ray diffraction (XRD; SmartLab SE, Rigaku, Tokyo, Japan) with a scan range of 10–90° 2θ, a scan speed of 10°/min, and a beam voltage and current of 40 kV and 50 mA. The BiT, NBiT, and NBT platelets were coated using Pt, and their morphology was observed by scanning electron microscopy (SEM; S-4700, Hitachi, Tokyo, Japan).

The densities of the sintered samples were determined by Archimedes' method using deionized water. Based on the tetragonal unit cell parameters calculated from the XRD pattern of the untextured sample, the theoretical density was calculated to be 5.92 g/cm^3. The crystal phase and the degree of texture of bulk samples were investigated using X-ray diffraction (XRD, Empyrean, Malvern PANalytical, Malvern, UK) with CuKα radiation set at 2θ = 10–90°, a scan rate of 3°/minute, and a 0.026° scan step. The degree of texture was calculated using the Lotgering factor (f) formulae as below [60,61,107,108]:

$$f_{(00l)} = \frac{P - P_0}{1 - P_0} \tag{4}$$

$$P_0 = \frac{\sum I_{0(00l)}}{\sum I_{0(hkl)}} \tag{5}$$

$$P = \frac{\sum I_{(00l)}}{\sum I_{(hkl)}} \tag{6}$$

P and P_0 are the fractions of orientation for a textured sample and a randomly oriented sample, and I is the integrated intensity of the diffraction peak. To determine the structure of the samples in more detail, an untextured and a textured sample (sintered at 1200 °C for 10 h) were crushed into powder, annealed at 550 °C for 1 h, and cooled to room temperature at a rate of 1 °C/min to remove strains induced by crushing. XRD was carried out as before, but with a scan speed of 1°/min. Rietveld refinement was conducted using MAUD (version 2.99993 build 1147). Since NBT-KN-ST can form a morphotropic phase boundary between ferroelectric rhombohedral and relaxor pseudocubic phases, rhombohedral (*R*3*c*) and tetragonal (*P*4*bm*) unit cells were applied as a model for the fitting process [44].

Analysis of the microstructure was carried out on cross-sections of untextured and textured samples that were sintered at 1200 °C for 10 h. The samples were polished to a 1 μm finish using diamond paste and thermally etched. Samples were Pt-coated, and microstructure was observed by scanning electron microscopy (SEM; Hitachi model S-4700, Tokyo, Japan). Electron probe microanalysis (EPMA, JEOL JXA-8530F PLUS, Tokyo, Japan) was carried out on cross-sections of untextured and textured samples that were sintered at 1200 °C for 10 h. The samples were polished to a 1 μm finish using diamond paste but not thermally etched. Wavelength-dispersive spectroscopy (WDS) analysis was carried out using an accelerating voltage of 15 kV. $NaAlSi_2O_6$, $Bi_4Ge_3O_{12}$, $KNbO_3$ and $SrTiO_3$ were used as standards. The samples were carbon-coated.

To examine the electrical behaviour, samples (sintered at 1200 °C for 10 h) were parallel polished on both sides by using grade #2000 and #4000 SiC papers. For dielectric measurement, samples were coated with silver paste electrodes (16032 PELCO, Ted Pella, Redding, CA, USA) on both major surfaces and loaded in a high-temperature heating stage (TS1500, Linkam Scientific Instruments Ltd., Salfords, UK). The impedance was measured using an impedance analyzer (Agilent/HP4284A Precision LCR Meter, Agilent Technologies, Santa Clara, CA, USA) in the frequency range 10^6 Hz to $10^{1.4}$ Hz (25.1 Hz) at 0.1 intervals in logarithmic frequencies from 30 °C to 700 °C in flowing air (100 sccm) and a heating/cooling rate of 1 °C/min. For the measurement of the ferroelectric and inverse piezoelectric properties, the polished samples were coated on both major surfaces with

silver electrodes, which were fired at 600 °C for 1 h and the properties measured using an aixPES hysteresis loop testing machine (aixACCT system GmbH, Aachen, Germany) at 1 Hz under electric fields up to 40 kV/cm for three cycles in each measurement. The thickness of the samples for ferroelectric and inverse piezoelectric property measurement was between 0.97~1 mm.

ChatGPT (version 5.0) was used to identify relevant keywords for searching references, to search for references, to summarize some references about the dielectric and electrical properties of NBT, to explain the equations used to analyze the impedance spectroscopy data, and to improve the writing in the discussion about hole conduction.

4. Conclusions

Texturing of $0.90(Na_{0.5}Bi_{0.5})TiO_3$-$0.08KNbO_3$-$0.02SrTiO_3$ using homoepitaxial NBT platelets induced grain alignment and abnormal grain growth, resulting in a Lotgering factor of 83% and a relative density of 99% at the addition of 4 wt% NBT platelets and optimum sintering conditions. The improvement in the electrical properties, such as electrostrain, polarization, electrostrictive coefficient, and activation energy for conduction, proved that the microstructural changes have influenced the performance of the materials. Notably, the use of homoepitaxial NBT platelets preserved the intrinsic ergodic relaxor behaviour and electrostrictive nature of NBT-KN-ST, evidenced by the stable permittivity (130~300 °C), small polarization hysteresis, and sprout-shaped bipolar strain vs. electric field profiles. This confirms that homoepitaxial templating is a reliable route to tailor both the microstructure and electrostrictive properties of NBT-KN-ST ceramics. Further investigation into sintering parameters, such as sintering atmosphere, may further improve the texturing behaviour and electrical properties.

Author Contributions: Conceptualization, J.G.F.; methodology, J.G.F. and J.-S.L.; formal analysis, A.A.; investigation, A.A., N.E., T.T.H.T. and W.-J.C.; resources, J.G.F., J.-S.L. and W.J.; data curation, A.A. and J.G.F.; writing—original draft preparation, A.A.; writing—review and editing, J.G.F., N.E., T.T.H.T., J.-S.L., W.-J.C. and W.J.; visualization, A.A., J.G.F. and J.-S.L.; supervision, J.G.F., J.-S.L. and W.J.; project administration, J.G.F. and J.-S.L.; funding acquisition, J.G.F. and J.-S.L. All authors have read and agreed to the published version of the manuscript.

Funding: This study was financially supported by Chonnam National University (Grant number: 2024-1096-01). This work was supported by a National Research Foundation of Korea (NRF) grant funded by the Korean Government (MSIT) (No. 2021R1F1A1046778). Jong-Sook Lee was supported by a National Research Foundation of Korea (NRF) grant funded by the Ministry of Science and ICT (MSIT) (Grant No. NRF-2018R1A5A1025224).

Institutional Review Board Statement: Not applicable.

Informed Consent Statement: Not applicable.

Data Availability Statement: The original contributions presented in the study are included in the article; further inquiries can be directed to the corresponding authors.

Acknowledgments: The authors would like to thank Kyeong-Kap Jeong and Jung-Yeol Park (Centre for Research Facilities, Chonnam National University) for operating the Empyrean XRD and EPMA, respectively, and Hye-Jeong Kim (Centre for Development of Fine Chemicals, Chonnam National University) for operating the SmartLab SE XRD and SEM. During the preparation of this manuscript, the authors used ChatGPT (version 5.0) to identify relevant keywords for searching for references, to search for references, to summarize some references about the dielectric and electrical properties of NBT, to explain the equations used to analyze the impedance spectroscopy data and to improve the writing in the discussion about hole conduction. The authors have reviewed and edited the output and take full responsibility for the content of this publication.

Conflicts of Interest: The authors declare no conflicts of interest. The funders had no role in the design of the study; in the collection, analyses, or interpretation of data; in the writing of the manuscript; or in the decision to publish the results.

References

1. Taniguchi, N. Current Status in, and Future Trends of, Ultraprecision Machining and Ultrafine Materials Processing. *CIRP Ann.* **1983**, *32*, 573–582. [CrossRef]
2. Coutte, J.; Debus, J.C.; Dubus, B.; Bossut, R.; Granger, C.; Haw, G. Finite Element Modeling of PMN electrostrictive Materials and Application to the Design of Transducers. In Proceedings of the 1998 IEEE International Frequency Control Symposium (Cat. No.98CH36165), Pasadena, CA, USA, 29 May 1998; pp. 703–708.
3. Uchino, K.; Tsuchiya, Y.; Nomura, S.; Sato, T.; Ishikawa, H.; Ikeda, O. Deformable Mirror Using The PMN Electrostrictor. *Appl. Opt.* **1981**, *20*, 3077–3080. [CrossRef] [PubMed]
4. Nomura, L.S.; Gomi, M.; Uchino, K. Bistable Optical Device with a PMN-Based Ceramic Electrostrictor. *Ferroelectrics* **1985**, *63*, 209–216. [CrossRef]
5. Nomura, S.; Uchino, K. Recent Applications of PMN-based Electrostrictors. *Ferroelectrics* **1983**, *50*, 197–202. [CrossRef]
6. Pan, M.-J.; Rehrig, P.W.; Kucera, J.P.; Park, S.-E.; Hackenberger, W.S. Comparison of Actuator Properties for Piezoelectric and Electrostrictive Materials. In Proceedings of the SPIE 3992, Smart Structures and Materials 2000: Active Materials: Behavior and Mechanics, Newport Beach, CA, USA, 6–9 March 2000; pp. 80–90. [CrossRef]
7. John, S.; Sirohi, J.; Wang, G.; Wereley, N.M. Comparison of Piezoelectric, Magnetostrictive, and Electrostrictive Hybrid Hydraulic Actuators. *J. Intell. Mater. Syst. Struct.* **2007**, *18*, 1035–1048. [CrossRef]
8. Guo, Q.; Meng, X.; Li, D.; Yao, Z.; Sun, H.; Hao, H.; Liu, H.; Zhang, S. Ultrahigh Electrostrictive Strain and Its Response to Mechanical Loading in Nd-doped PMN-PT Ceramics. *Acta Mater.* **2024**, *266*, 119695. [CrossRef]
9. Wang, Q.; Li, F. A Low-Working-Field (2 kV/mm), Large-Strain (>0.5%) Piezoelectric Multilayer Actuator Based On Periodically Orthogonal Poled PZT Ceramics. *Sens. Actuators A Phys.* **2018**, *272*, 212–216. [CrossRef]
10. Fu, J.; Zuo, R. Giant Electrostrains Accompanying The Evolution of A Relaxor Behavior in Bi(Mg,Ti)O_3-$PbZrO_3$-$PbTiO_3$ Ferroelectric Ceramics. *Acta Mater.* **2013**, *61*, 3687–3694. [CrossRef]
11. Uchino, K.; Nomura, S.; Cross, L.E.; Newnham, R.E.; Jang, S.J. Review Electrostrictive Effect in Perovskites and Its Transducer Applications. *J. Mater. Sci.* **1981**, *16*, 569–578. [CrossRef]
12. Li, F.; Jin, L.; Xu, Z.; Zhang, S. Electrostrictive Effect in Ferroelectrics: An Alternative Approach to Improve Piezoelectricity. *Appl. Phys. Rev.* **2014**, *1*, 011103. [CrossRef]
13. Santucci, S.; Esposito, V. Electrostrictive Ceramics and Their Applications. In *Encyclopedia of Materials: Technical Ceramics and Glasses: Volume 1–3*; Elsevier: Amsterdam, The Netherlands, 2021; Volume 3, pp. 369–374.
14. Hao, J.; Li, W.; Zhai, J.; Chen, H. Progress in High-Strain Perovskite Piezoelectric Ceramics. *Mater. Sci. Eng. R Rep.* **2019**, *135*, 1–57.
15. Rödel, J.; Webber, K.G.; Dittmer, R.; Jo, W.; Kimura, M.; Damjanovic, D. Transferring Lead-Free Piezoelectric Ceramics into Application. *J. Eur. Ceram. Soc.* **2015**, *35*, 1659–1681. [CrossRef]
16. Fan, P.; Liu, K.; Ma, W.; Tan, H.; Zhang, Q.; Zhang, L.; Zhou, C.; Salamon, D.; Zhang, S.T.; Zhang, Y.; et al. Progress and Perspective of High Strain NBT-based Lead-free Piezoceramics and Multilayer Actuators. *J. Mater.* **2021**, *7*, 508–544. [CrossRef]
17. Yin, J.; Liu, G.; Zhao, C.; Huang, Y.; Li, Z.; Zhang, X.; Wang, K.; Wu, J. Perovskite $Na_{0.5}Bi_{0.5}TiO_3$: A Potential Family of Peculiar Lead-free Electrostrictors. *J. Mater. Chem. A Mater.* **2019**, *7*, 13658–13670.
18. Dunce, M.; Birks, E.; Antonova, M.; Bikse, L.; Dutkevica, S.; Freimanis, O.; Livins, M.; Eglite, L.; Smits, K.; Sternberg, A. Influence of Sintering Temperature on Microstructure of $Na_{0.5}Bi_{0.5}TiO_3$ Ceramics. *J. Alloys Compd.* **2021**, *884*, 160955.
19. Hiruma, Y.; Nagata, H.; Takenaka, T. Thermal Depoling Process and Piezoelectric Properties of Bismuth Sodium Titanate Ceramics. *J. Appl. Phys.* **2009**, *105*, 084112. [CrossRef]
20. Wang, F.; Zhu, C.; Zhao, S. Good Energy Storage Properties of $Na_{0.5}Bi_{0.5}TiO_3$ Thin Films. *J. Alloys Compd.* **2021**, *869*, 159366.
21. Suchanicz, J.; Nowakowska-Malczyk, M.; Kania, A.; Budziak, A.; Kluczewska-Chmielarz, K.; Czaja, P.; Sitko, D.; Sokolowski, M.; Niewiadomski, A.; Kruzina, T.V. Effects of Electric Field Poling on Structural, Thermal, Vibrational, Dielectric and Ferroelectric Properties of $Na_{0.5}Bi_{0.5}TiO_3$ Single Crystals. *J. Alloys Compd.* **2021**, *854*, 157227.
22. Ramesh Babu, P.; Selvamani, R.; Singh, G.; Kalainathan, S.; Babu, R.; Tiwari, V.S. Growth, Mechanical and Domain Structure Studies of $Na_{0.5}Bi_{0.5}TiO_3$ Single Crystal Grown by Flux Growth Method. *J. Alloys Compd.* **2017**, *721*, 199–204.
23. Rödel, J.; Jo, W.; Seifert, K.T.P.; Anton, E.M.; Granzow, T.; Damjanovic, D. Perspective on the development of lead-free piezoceramics. *J. Am. Ceram. Soc.* **2009**, *92*, 1153–1177.
24. Duong, T.A.; Han, H.-S.; Hong, Y.-H.; Park, Y.-S.; Nguyen, H.T.K.; Dinh, T.H. Dielectric and Piezoelectric Properties of $Bi_{1/2}Na_{1/2}TiO_3$–$SrTiO_3$ Lead–free Ceramics. *J. Electroceram.* **2018**, *41*, 73–79. [CrossRef]
25. Jones, G.O.; Thomas, P.A. Investigation of the structure and phase transitions in the novel A-site substituted distorted perovskite compound $Na_{0.5}Bi_{0.5}TiO_3$. *Acta Crystallogr. B.* **2002**, *58*, 168–178. [CrossRef] [PubMed]

26. Kruzina, T.V.; Sidak, V.M.; Trubitsyn, M.P.; Popov, S.A.; Tuluk, A.Y.; Suchanicz, J. Impedance Spectra of As-Grown and Heat Treated $Na_{0.5}Bi_{0.5}TiO_3$ Crystals. *Acta Phys. Pol. A* **2018**, *133*, 816–818. [CrossRef]
27. Aksel, E.; Forrester, J.S.; Kowalski, B.; Deluca, M.; Damjanovic, D.; Jones, J.L. Structure and Properties of Fe-modified $Na_{0.5}Bi_{0.5}TiO_3$ at Ambient and Elevated Temperature. *Phys. Rev. B Condens. Matter Mater. Phys.* **2012**, *85*, 024121. [CrossRef]
28. Fan, G.; Lu, W.; Wang, X.; Liang, F.; Xiao, J. Phase Transition Behaviour and Electromechanical Properties of $(Na_1/_2Bi_1/_2)TiO_3$-$KNbO_3$ Lead-free Piezoelectric Ceramics. *J. Phys. D Appl. Phys.* **2008**, *41*, 035403. [CrossRef]
29. Wang, G.; Hall, D.A.; Li, Y.; Murray, C.A.; Tang, C.C. Structural Characterization of The Electric Field-induced Ferroelectric Phase in $Na_{0.5}Bi_{0.5}TiO_3$ -$KNbO_3$ Ceramics. *J. Eur. Ceram. Soc.* **2016**, *36*, 4015–4021. [CrossRef]
30. Tong, X.; Li, H.; Zhou, J.; Liu, H.; Fang, J. Giant Electrostrain under Low Driving Field in $Bi_1/_2Na_1/_2TiO_3$-$SrTiO_3$ Ceramics for Actuator Applications. *Ceram. Int.* **2016**, *42*, 16153–16159. [CrossRef]
31. Kashif, M.; Bashir, R.; Ullah, S.; Wang, J.; Hu, W. Enhanced Energy Storage Properties of $0.7Bi_{0.5}Na_{0.5}TiO_3$ -$0.3SrTiO_3$ Ceramic through The Addition of $NaNbO_3$. *Ceram. Int.* **2021**, *47*, 30922–30928.
32. Ünal, M.A.; Karakaya, M.; Irmak, T.; Yıldırım-Özarslan, G.; Murat Avcı, A.; Fulanovic, L.; Suvacı, E.; Adem, U. Electrocaloric Behaviour of Tape Cast Grain Oriented NBT-KBT Ceramics. *J. Eur. Ceram. Soc.* **2024**, *44*, 2128–2134. [CrossRef]
33. Zhao, W.; Ya, J.; Xin, Y.; E, L.; Zhao, D.; Zhou, H. Fabrication of $Na_{0.5}Bi_{0.5}TiO_3$-$BaTiO_3$-Textured Ceramics Templated by Plate-like $Na_{0.5}Bi_{0.5}TiO_3$ Particles. *J. Am. Ceram. Soc.* **2009**, *92*, 1607–1609.
34. Wu, Y.; Wang, X.; Zhong, C.; Li, L. Enhancement of Piezoelectric and Ferroelectric Performances in $(Na_{0.85}K_{0.15})_{0.5}Bi_{0.5}TiO_3$ Films with $BaTiO_3$ interlayers. *J. Eur. Ceram. Soc.* **2018**, *38*, 1434–1441. [CrossRef]
35. Jiang, C.; Zhou, X.; Zhou, K.; Chen, C.; Luo, H.; Yuan, X.; Zhang, D. Grain Oriented $Na_{0.5}Bi_{0.5}TiO_3$-$BaTiO_3$ Ceramics with Giant Strain Response Derived from Single-Crystalline $Na_{0.5}Bi_{0.5}TiO_3$-$BaTiO_3$ Templates. *J. Eur. Ceram. Soc.* **2016**, *36*, 1377–1383. [CrossRef]
36. Wang, G.; Li, Y.; Murray, C.A.; Tang, C.C.; Hall, D.A. Thermally-induced phase transformations in $Na_{0.5}Bi_{0.5}TiO_3$–$KNbO_3$ ceramics. *J. Am. Ceram. Soc.* **2017**, *100*, 3293–3304. [CrossRef]
37. Berksoy-Yavuz, A.; Kaya, M.Y.; Yalcin, E.; Gozuacik, N.K.; Mensur, E. Effect of Texture on Ultra-high Strain Behavior in Eco-friendly NBT-0.25ST Ceramics using NBT Template. *J. Am. Ceram. Soc.* **2024**, *107*, 5502–5511. [CrossRef]
38. Wang, F.; Jin, C.; Yao, Q.; Shi, W. Large Electrostrictive Effect in Ternary $Bi_{0.5}Na_{0.5}TiO_3$-based Solid Solutions. *J. Appl. Phys.* **2013**, *114*, 027004. [CrossRef]
39. He, H.; Lu, X.; Li, M.; Wang, Y.; Li, Z.; Lu, Z.; Lu, L. Thermal and Compositional Driven Relaxor Ferroelectric Behaviours of Lead-free $Bi_{0.5}Na_{0.5}TiO_3$-$SrTiO_3$ Ceramics. *J. Mater. Chem. C Mater.* **2020**, *8*, 2411–2418. [CrossRef]
40. Hiruma, Y.; Nagata, H.; Takenaka, T. Phase Diagrams and Electrical Properties of $(Bi_1/_2Na_1/_2)TiO_3$-based Solid Solutions. *J. Appl. Phys.* **2008**, *104*, 124106. [CrossRef]
41. Bai, W.; Chen, D.; Zheng, P.; Zhang, J.; Wen, F.; Shen, B.; Zhai, J.; Ji, Z. Phase transition, switching characteristics of MPB compositions and large strain in lead-free $(Bi_{0.5}Na_{0.5})TiO_3$-based piezoceramics. *J. Alloys Compd.* **2017**, *709*, 646–657. [CrossRef]
42. Bai, W.; Li, L.; Li, W.; Shen, B.; Zhai, J.; Chen, H. Phase Diagrams and Electromechanical Strains in Lead-Free BNT-Based Ternary Perovskite Compounds. *J. Am. Ceram. Soc.* **2014**, *97*, 3510–3518. [CrossRef]
43. Bai, W.; Li, L.; Wang, W.; Shen, B.; Zhai, J. Phase Diagram and Electrostrictive Effect in BNT-based Ceramics. *Solid. State Commun.* **2015**, *206*, 22–25. [CrossRef]
44. Han, H.S.; Jo, W.; Kang, J.K.; Ahn, C.W.; Kim, I.W.; Ahn, K.K.; Lee, J.S. Incipient piezoelectrics and electrostriction behavior in Sn-doped $Bi_1/_2(Na_{0.82}K_{0.18})_1/_2TiO_3$ lead-free ceramics. *J. Appl. Phys.* **2013**, *113*, 154102. [CrossRef]
45. Bai, W.; Li, L.; Li, W.; Shen, B.; Zhai, J.; Chen, H. Effect of $SrTiO_3$ template on electric properties of textured BNT-BKT ceramics prepared by templated grain growth process. *J. Alloys Compd.* **2014**, *603*, 149–157. [CrossRef]
46. Ahn, C.W.; Choi, G.; Kim, I.W.; Lee, J.S.; Wang, K.; Hwang, Y.; Jo, W. Forced electrostriction by constraining polarization switching enhances the electromechanical strain properties of incipient piezoceramics. *NPG Asia Mater.* **2017**, *9*, e346. [CrossRef]
47. Wang, Y.; Zhao, Y.; Shi, J.; Liu, X. Strain performance and thickness-induced asymmetry in $SrTiO_3$ doped BNT-based lead-free ferroelectrics from nonergodic to ergodic phase. *J. Phys. Chem. Solids* **2024**, *193*, 112188. [CrossRef]
48. Bai, W.; Chen, D.; Zheng, P.; Zhang, J.; Shen, B.; Zhai, J.; Ji, Z. Grain-orientated lead-free BNT-based piezoceramics with giant electrostrictive effect. *Ceram. Int.* **2017**, *43*, 3339–3345. [CrossRef]
49. Li, F.; Jin, L.; Xu, Z.; Wang, D.; Zhang, S. Electrostrictive effect in $Pb(Mg_1/_3Nb_2/_3)O_3$-$xPbTiO_3$ crystals. *Appl. Phys. Lett.* **2013**, *102*, 152910. [CrossRef]
50. Hong, C.H.; Kim, H.P.; Choi, B.Y.; Han, H.S.; Son, J.S.; Ahn, C.W.; Jo, W. Lead-free piezoceramics—Where to move on? *J. Mater.* **2016**, *2*, 1–24. [CrossRef]
51. Bai, W.; Li, H.; Xi, J.; Zhang, J.; Shen, B.; Zhai, J. Effect of different templates and texture on structure evolution and strain behavior of <001>-textured lead-free piezoelectric BNT-based ceramics. *J. Alloys Compd.* **2016**, *656*, 13–23.
52. Wu, J.; Zhang, S.; Li, F. Prospect of Texture Engineered Ferroelectric Ceramics. *Appl. Phys. Lett.* **2022**, *121*, 120501. [CrossRef]
53. Moriana, A.D.; Zhang, S. Lead-free Textured Piezoceramics using Tape Casting: A Review. *J. Mater.* **2018**, *4*, 277–303. [CrossRef]

54. Wu, M.; Li, Y. Topochemical Synthesis of Plate-like $Na_{0.5}Bi_{0.5}TiO_3$ Templates from $Bi_4Ti_3O_{12}$. *Mater. Lett.* **2010**, *64*, 1157–1159. [CrossRef]
55. Li, H.; Huang, R.; Lin, H.T.; Du, Z.; Dai, Y. Effect of the Template Particles Size on Structure and Piezoelectric Properties of <001>-textured BNT-Based Ceramics. *J. Am. Ceram. Soc.* **2024**, *107*, 3219–3229. [CrossRef]
56. Zhao, W.; Zhou, H.; Yan, Y.; Liu, D. Topochemical Synthesis of Plate-like $Na_{0.5}Bi_{0.5}TiO_3$ from Aurivillius Precursor. *J. Am. Ceram. Soc.* **2008**, *91*, 1322–1325. [CrossRef]
57. Saito, Y.; Takao, H. Synthesis of Plate-Like $(Bi_{0.5}Na_{0.5})TiO_3$ Particles by Using a Topochemical Microcrystal Conversion Method and Grain-Oriented Ceramics. *J. Korean Phys. Soc.* **2007**, *51*, 790–797. [CrossRef]
58. Sanjaya Ranmohotti, K.G.; Josepha, E.; Choi, J.; Zhang, J.; Wiley, J.B. Topochemical Manipulation of Perovskites: Low-temperature Reaction Strategies for Directing Structure and Properties. *Adv. Mater.* **2011**, *23*, 442–460. [CrossRef]
59. Poterala, S.F.; Chang, Y.; Clark, T.; Meyer, R.J.; Messinge, G.L. Mechanistic Interpretation of the Aurivillius to Perovskite Topochemical Microcrystal Conversion Process. *Chem. Mater.* **2010**, *22*, 2061–2068. [CrossRef]
60. Zeng, J.T.; Kwok, K.W.; Tam, W.K.; Tian, H.Y.; Jiang, X.P.; Chan, H.L.W. Plate-like $Na_{0.5}Bi_{0.5}TiO_3$ Template Synthesized by a Topochemical Method. *J. Am. Ceram. Soc.* **2006**, *89*, 3850–3853. [CrossRef]
61. Jiang, C.; Zhou, K.; Zhou, X.; Li, Z.; Zhang, D. Synthesis and Characterization of $Na_{0.5}Bi_{0.5}TiO_3$ Platelets with Preferred Orientation using Aurivillius Precursors. *Ceram. Int.* **2015**, *41*, 6858–6862. [CrossRef]
62. Li, J.; Huang, R.; Peng, C.; Dai, Y.; Xiong, S.; Cai, C.; Lin, H.T. Low Temperature Synthesis of Plate-like $Na_{0.5}Bi_{0.5}TiO_3$ via Molten Salt Method. *Ceram. Int.* **2020**, *46*, 19752–19757. [CrossRef]
63. Dursun, S.; Mensur-Alkoy, E.; Sabuncu, A.; Berksoy-Yavuz, A.; Gülgün, M.A.; Alkoy, S. Growth of NBT Template Particles through Topochemical Microcrystal Conversion and Their Structural Characterization. *J. Am. Ceram. Soc.* **2017**, *100*, 937–944. [CrossRef]
64. Ye, L.; Tang, C.; Chen, Y.; Yang, S.; Tang, M. The Thermal Physical Properties and Stability of the Eutectic Composition in a Na_2CO_3-NaCl Binary System. *Thermochim. Acta* **2014**, *596*, 14–20. [CrossRef]
65. Andleeb, K.; Trung, D.T.; Fisher, J.G.; Tran, T.T.H.; Lee, J.S.; Choi, W.J.; Jo, W. Fabrication of Textured $0.685(Na_{0.5}Bi_{0.5})TiO_3$-$0.065BaTiO_3$-$0.25SrTiO_3$ Electrostrictive Ceramics by Templated Grain Growth Using $NaNbO_3$ Templates and Characterization of Their Electrical Properties. *Crystals* **2024**, *14*, 861. [CrossRef]
66. Bai, W.; Hao, J.; Shen, B.; Fu, F.; Zhai, J. Processing optimization and piezoelectric properties of textured $Ba(Zr,Ti)O_3$ ceramics. *J. Alloys Compd.* **2012**, *536*, 189–197. [CrossRef]
67. Kimura, T.; Yi, Y.; Sakurai, F. Mechanisms of texture development in lead-free piezoelectric ceramics with perovskite structure made by the templated grain growth process. *Materials* **2010**, *3*, 4965–4978. [CrossRef] [PubMed]
68. Kimura, T.; Yoshida, Y. Origin of Texture Development in Barium Bismuth Titanate Prepared by the Templated Grain Growth Method. *J. Am. Ceram. Soc.* **2006**, *89*, 869–874. [CrossRef]
69. Liu, K.; Liu, F.; Zhang, W.; Dou, Z.; Ma, W.; Samart, C.; Takesue, N.; Tan, H.; Fan, F.; Ye, Z.G.; et al. Design and development of outstanding strain properties in NBT-based lead-free piezoelectric multilayer actuators by grain-orientation engineering. *Acta Mater.* **2023**, *246*, 118696. [CrossRef]
70. Moon, K.S.; Kang, S.J.L. Coarsening behavior of round-edged cubic grains in the $Na_{1/2}Bi_{1/2}TiO_3$-$BaTiO_3$ system. *J. Am. Ceram. Soc.* **2008**, *91*, 3191–3196. [CrossRef]
71. Messing, G.L.; Trolier-McKinstry, S.; Sabolsky, E.M.; Duran, C.; Kwon, S.; Brahmaroutu, P.; Park, P.; Yilmaz, H.; Rehrig, P.W.; Eitel, K.B.; et al. Templated Grain Growth of Textured Piezoelectric Ceramics. *Crit. Rev. Solid State Mater. Sci.* **2004**, *29*, 45–96. [CrossRef]
72. Ma, Y.; Liu, L.; Xie, H.; Zhang, Z.; Kou, Q.; Lv, R.; Yang, B.; Chang, Y.; Li, F. Enhanced Piezoelectric Properties and Depolarization Temperature in Textured $(Bi_{0.5}Na_{0.5})TiO_3$-based Ceramics via Homoepitaxial Templated Grain Growth. *J. Mater. Sci. Technol.* **2024**, *176*, 91–98. [CrossRef]
73. Fisher, J.G.; Kang, S.J.L. Strategies and Practices for Suppressing Abnormal Grain Growth during Liquid Phase Sintering. *J. Am. Ceram. Soc.* **2018**, *102*, 717–735. [CrossRef]
74. Kang, S.J.L.; Lee, M.G.; An, S.M. Microstructural Evolution during Sintering with Control of the Interface Structure. *J. Am. Ceram. Soc.* **2009**, *92*, 1464–1471. [CrossRef]
75. Zhang, A.; Jing, R.; Zhuang, M.; Hou, H.; Zhang, L.; Zhang, J.; Lu, X.; Yan, Y.; Du, H.; Jin, L. Nonstoichiometric Effect of A-site Complex Ions on Structural, Dielectric, Ferroelectric, and Electrostrain Properties of Bismuth Sodium Titanate Ceramics. *Ceram. Int.* **2021**, *47*, 32747–32755. [CrossRef]
76. Fan, P.; Zhang, Y.; Zhu, Y.; Ma, W.; Liu, K.; He, X.; Marwat, M.A.; Xie, B.; Li, M.; Zhang, H. Large strain under low driving field in lead-free relaxor/ferroelectric composite ceramics. *J. Am. Ceram. Soc.* **2019**, *102*, 4113–4126. [CrossRef]
77. Zhang, H.; Groh, C.; Zhang, Q.; Jo, W.; Webber, K.G.; Rödel, J. Large Strain in Relaxor/Ferroelectric Composite Lead-Free Piezoceramics. *Adv. Electron. Mater.* **2015**, *1*, 1500018. [CrossRef]

78. Hinterstein, M.; Knapp, M.; Hölzel, M.; Jo, W.; Cervellino, A.; Ehrenberg, H.; Fuess, H. Field-induced phase transition in $Bi_{1/2}Na_{1/2}TiO_3$-based lead-free piezoelectric ceramics. *J. Appl. Crystallogr.* **2010**, *43*, 1314–1321. [CrossRef]
79. Song, M.; Sun, X.; Li, Q.; Qian, H.; Liu, Y.; Lyu, Y. Enhanced electrostrictive coefficient and suppressive hysteresis in lead-free $Ba_{(1-x)}Sr_xTiO_3$ piezoelectric ceramics with high strain. *Crystals* **2021**, *11*, 555. [CrossRef]
80. Viola, G.; Saunders, T.; Wei, X.; Chong, K.B.; Luo, H.; Reece, M.J.; Yan, H. Contribution of piezoelectric effect, electrostriction and ferroelectric/ferroelastic switching to strain-electric field response of dielectrics. *J. Adv. Dielectr.* **2013**, *3*, 1350007. [CrossRef]
81. Jin, L.; Li, F.; Zhang, S. Decoding the fingerprint of ferroelectric loops: Comprehension of the material properties and structures. *J. Am. Ceram. Soc.* **2014**, *97*, 1–27. [CrossRef]
82. Shi, J.; Fan, H.; Liu, X.; Li, Q. Ferroelectric Hysteresis Loop Scaling and Electric Field-induced Strain of $Bi_{0.5}Na_{0.5}TiO_3$-$BaTiO_3$ Ceramics. *Phys. Status Solidi (A) Appl. Mater. Sci.* **2014**, *211*, 2388–2393. [CrossRef]
83. Thi, M.P.; March, G.; Colomban, P. Phase Diagram and Raman Imaging of Grain Growth Mechanisms in Highly Textured $Pb(Mg_{1/3}Nb_{2/3})O_3$–$PbTiO_3$ Piezoelectric Ceramics. *J. Eur. Ceram. Soc.* **2005**, *25*, 3335–3346. [CrossRef]
84. Motohashi, T.; Kimura, T. Formation of Homotemplate Grains in $Bi_{0.5}Na_{0.5}TiO_3$ Prepared by The Reactive-Templated Grain Growth Process. *J. Am. Ceram. Soc.* **2008**, *91*, 3889–3895. [CrossRef]
85. Le, P.G.; Tran, T.L.; Kim, H.P.; Jo, W.; Lee, J.S.; Fisher, J.G. Growth of Single Crystals of $0.75(Na_{0.5}Bi_{0.5})TiO_3$-$0.25(Sr_{0.7}Ca_{0.3})TiO_3$ and Characterisation of Their Electrical Properties. *Open Ceram.* **2021**, *6*, 100099. [CrossRef]
86. Liu, G.; Dong, J.; Zhang, L.; Yan, Y.; Jing, R.; Jin, L. Phase Evolution in $(1-x)(Na_{0.5}Bi_{0.5})TiO_3$-$xSrTiO_3$ Solid Solutions: A Study Focusing on Dielectric and Ferroelectric Characteristics. *J. Mater.* **2020**, *6*, 677–691. [CrossRef]
87. Thawong, P.; Prasertpalichat, S.; Suriwong, T.; Pinitsoontorn, S.; Jantaratana, P.; Chootin, S.; Sriondee, M.; Charoonsuk, T.; Vittayakorn, N.; Rittidech, A.; et al. Optimal $Bi_{0.8}Ba_{0.2}FeO_3$ Doping in $Bi_{0.5}(Na_{0.77}K_{0.20}Li_{0.03})_{0.5}TiO_3$ Multiferroic Ceramics Synthesized by The Solid-State Combustion Technique. *Sci. Rep.* **2025**, *15*, 23340. [CrossRef] [PubMed]
88. Zeb, A.; Jan, S.U.; Bamiduro, F.; Hall, D.A.; Milne, S.J. Temperature-stable Dielectric Ceramics Based on $Na_{0.5}Bi_{0.5}TiO_3$. *J. Eur. Ceram. Soc.* **2018**, *38*, 1548–1555. [CrossRef]
89. Abbas, A.; Jung, W.-G.; Moon, W.-J.; Uwiragiye, E.; Pham, T.L.; Lee, J.-S.; Fisher, J.G.; Ge, W.; Naqvi, F.U.H. Growth of $(1-x)(Na_{1/2}Bi_{1/2})TiO_3$–$xKNbO_3$ Single Crystals by The Self-Flux Method and Their Characterisation. *J. Korean Ceram. Soc.* **2024**, *61*, 342–365. [CrossRef]
90. Wu, C.C.; Yang, C.F. Effects of $NaNbO_3$ concentration on the relaxor and dielectric properties of the lead-free $(Na_{0.5}Bi_{0.5})TiO_3$ ceramics. *CrystEngComm* **2013**, *15*, 9097–9103. [CrossRef]
91. M'peko, J.-C.; Peixoto, A.G.; Jiménez, E.; Jiménez, J.; Gaggero-Sager, L.M. Electrical Properties of Nb-Doped PZT 65/35 Ceramics: Influence of Nb and Excess PbO. *J. Electroceram.* **2005**, *15*, 167–176. [CrossRef]
92. Strukov, B.A.; Levanyuk, A.P. *Ferroelectric Phenomena in Crystals*; Physical Foundations Springer: Berlin/Heidelberg, Germany, 1998. [CrossRef]
93. Qiao, X.; Wu, D.; Zhang, F.; Niu, M.; Chen, B.; Zhao, X.; Liang, P.; Wei, L.; Chao, X.; Yang, Z. Enhanced Energy Density and Thermal Stability in Relaxor Ferroelectric $Bi_{0.5}Na_{0.5}TiO_3$-$Sr_{0.7}Bi_{0.2}TiO_3$ Ceramics. *J. Eur. Ceram. Soc.* **2019**, *39*, 4778–4784. [CrossRef]
94. Cheng, Z.-Y.; Katiyar, R.S.; Yao, X.; Bhalla, A.S. Temperature Dependence of The Ferroelectrics. *Phys. Rev. B* **1998**, *57*, 8166–8177. [CrossRef]
95. Sundari, S.S.; Kumar, B.; Dhanasekaran, R. Structural, Dielectric, Piezoelectric and Ferroelectric Characterization of NBT-BT Lead-free Piezoelectric Ceramics. *IOP Conf. Ser. Mater. Sci. Eng.* **2013**, *43*, 012010. [CrossRef]
96. Suchanicz, J.; Roleder, K.; Kwapuliński, J.; Jankowska-Sumara, I. Dielectric and Structural Relaxation Phenomena in $Na_{0.5}Bi_{0.5}TiO_3$ Single Crystal. *Phase Transit.* **1996**, *57*, 173–182. [CrossRef]
97. Selvamani, R.; Singh, G.; Tiwari, V.S.; Gupta, P.K. Oxygen vacancy related relaxation and conduction behavior in $(1-x)$NBT-$xBiCrO_3$ solid solution. *Phys. Status Solidi (A) Appl. Mater. Sci.* **2012**, *209*, 118–125. [CrossRef]
98. Suchanicz, J.; Kluczewska-Chmielarz, K.; Sitko, D.; Jagło, G. Electrical Transport in Lead-free $Na_{0.5}Bi_{0.5}TiO_3$ Ceramics. *J. Adv. Ceram.* **2021**, *10*, 152–165. [CrossRef]
99. Yang, F.; Li, M.; Li, L.; Wu, P.; Pradal-Velázquez, E.; Sinclair, D.C. Defect chemistry and electrical properties of sodium bismuth titanate perovskite. *J. Mater. Chem. A* **2018**, *6*, 5243–5254. [CrossRef]
100. Li, M.; Li, L.; Zang, J.; Sinclair, D.C. Donor-doping and reduced leakage current in Nb-doped $(Na_{0.5}Bi_{0.5})TiO_3$. *Appl. Phys. Lett.* **2015**, *106*, 102904. [CrossRef]
101. Koch, L. *First-Principle Study of The Defect Chemistry and Conductivity in Sodium Bismuth Titanate*; Technische Universität Darmstadt: Darmstadt, Germany, 2021.
102. Bersuker, I.B. Pseudo-Jahn-teller effect—A two-state paradigm in formation, deformation, and transformation of molecular systems and solids. *Chem. Rev.* **2013**, *113*, 1351–1390. [CrossRef] [PubMed]
103. Nye, J.F. *Physical Properties of Crystals: Their Representation by Tensors and Matrices*; Oxford University Press: Oxford, UK, 1985.

104. Fisher, C.A.J.; Islam, M.S.; Moriwake, H. Atomic Level Investigations of Lithium Ion Battery Cathode Materials. *J. Phys. Soc. Jpn.* **2010**, *79*, 59–64. [CrossRef]
105. Nishimura, S.I.; Kobayashi, G.; Ohoyama, K.; Kanno, R.; Yashima, M.; Yamada, A. Experimental visualization of lithium diffusion in Li_xFePO_4. *Nat. Mater.* **2008**, *7*, 707–711. [CrossRef] [PubMed]
106. Zhao, W.; Liu, N.; Gao, K.; Wang, Z.; Zhang, S. Synthesis of Anisotropic $Na_{0.5}Bi_{0.5}TiO_3$ Crystals Using Different Topochemical Microcrystal Conversion Methods. *Int. J. Appl. Ceram. Technol.* **2016**, *13*, 871–875. [CrossRef]
107. Lotgering, F.K. Topotactical Reactions with Ferrimagnetic Oxides Having Hexagonal Crystal Structures-I. *J. Inorg. Nucl. Chem.* **1959**, *9*, 113–123. [CrossRef]
108. Jones, J.L.; Slamovich, E.B.; Bowman, K.J. Critical Evaluation of the Lotgering Degree of Orientation Texture Indicator. *J. Mater. Res.* **2004**, *19*, 3414–3422. [CrossRef]

Disclaimer/Publisher's Note: The statements, opinions and data contained in all publications are solely those of the individual author(s) and contributor(s) and not of MDPI and/or the editor(s). MDPI and/or the editor(s) disclaim responsibility for any injury to people or property resulting from any ideas, methods, instructions or products referred to in the content.

inorganics

MDPI

Article

Hidden Magnetic-Field-Induced Multiferroic States in A-Site-Ordered Quadruple Perovskites $RMn_3Ni_2Mn_2O_{12}$: Dielectric Studies

Alexei A. Belik [1,*], Ran Liu [1,2,3] and Kazunari Yamaura [1,2]

[1] Research Center for Materials Nanoarchitectonics (MANA), National Institute for Materials Science (NIMS), Namiki 1-1, Tsukuba 305-0044, Ibaraki, Japan; liu.ran@sanken.osaka-u.ac.jp (R.L.); yamaura.kazunari@nims.go.jp (K.Y.)
[2] Graduate School of Chemical Sciences and Engineering, Hokkaido University, North 10 West 8, Kita-ku, Sapporo 060-0810, Hokkaido, Japan
[3] Institute of Scientific and Industrial Research, Osaka University, Mihogaoka 8-1, Ibaraki 567-0047, Osaka, Japan
* Correspondence: alexei.belik@nims.go.jp

Abstract: The appearance of spin-induced ferroelectric polarization in the so-called type-II multiferroic materials has received a lot of attention. The nature and mechanisms of such polarization were intensively studied using perovskite rare-earth manganites, $RMnO_3$, as model systems. Later, multiferroic properties were discovered in some $RFeO_3$ perovskites and possibly in some $RCrO_3$ perovskites. However, R_2NiMnO_6 double perovskites have ferromagnetic structures that do not break the inversion symmetry. It was found recently that more complex magnetic structures are realized in A-site-ordered quadruple perovskites, $RMn_3Ni_2Mn_2O_{12}$. Therefore, they have the potential to be multiferroics. In this work, dielectric properties in magnetic fields up to 9 T were investigated for such perovskites as $RMn_3Ni_2Mn_2O_{12}$ with R = Ce to Ho and for $BiMn_3Ni_2Mn_2O_{12}$. The samples with R = Bi, Ce, and Nd showed no dielectric anomalies at all magnetic fields, and the dielectric constant decreases with decreasing temperature. The samples with R = Sm to Ho showed qualitatively different behavior when the dielectric constant started increasing with decreasing temperature below certain temperatures close to the magnetic ordering temperatures, T_N. This difference could suggest different magnetic ground states. The samples with R = Eu, Dy, and Ho still showed no anomalies on the dielectric constant. On the other hand, peaks emerged at T_N on the dielectric constant in the R = Sm sample from about 2 T up to the maximum available field of 9 T. The Gd sample showed peaks on dielectric constant at T_N between about 1 T and 7 T. Transition temperatures increase with increasing magnetic fields for R = Sm and decrease for R = Gd. These findings suggest the presence of magnetic-field-induced multiferroic states in the R = Sm and Gd samples with intermediate ionic radii. Dielectric properties at different magnetic fields are also reported for Lu_2NiMnO_6 for comparison.

Keywords: A-site-ordered quadruple perovskites; B-site double ordering; multiferroics; dielectric constant

1. Introduction

The appearance of spin-induced ferroelectric polarization in the so-called type-II multiferroic materials has received a lot of attention in the literature [1–7]. Because ferroelectric

polarization appears as a result of a magnetic ordering, there is a strong magnetoelectric coupling in such materials, allowing for the control of ferroelectric polarization via a magnetic field and vice versa [8,9]. The nature and mechanisms of such polarization were intensively studied using perovskite-structure rare-earth (R) manganites, $RMnO_3$, as model systems [10–13]. Only some members of the $RMnO_3$ family with specific magnetic structures develop spin-induced ferroelectric polarization, for example, in $RMnO_3$ (R = Tb to Dy) with modulated sinusoidal/spiral antiferromagnetic (AFM) ordering and in $RMnO_3$ (R = Ho to Lu) with the so-called E-type magnetic ordering. Multiferroic properties were discovered in some $RFeO_3$ perovskites [14–20] and possibly in some $RCrO_3$ perovskites [21–23]. While the multiferroic properties of $RFeO_3$ at very low temperatures, where they are caused by additional magnetic orderings of the R^{3+} sublattice, are well established [14–16], the existence of ferroelectric polarization at higher temperatures in $RFeO_3$ and $RCrO_3$ is still under debate [18,19,24].

All R_2NiMnO_6 double perovskites [25–41] have simple ferromagnetic (FM) structures (in the first approximation), which do not break inversion centers and do not produce spin-induced ferroelectric polarization. Nevertheless, there are a few reports with claims of spin-induced ferroelectric properties in R_2NiMnO_6 double perovskites [25,26]. However, such claims were not confirmed [27], and therefore, they are still controversial. The use of cations smaller than Lu^{3+} ($r_{XIII}(Lu^{3+})$ = 0.977 Å [42]) at the R sites (such as Sc^{3+} with $r_{XIII}(Sc^{3+})$ = 0.870 Å and In^{3+} with $r_{XIII}(In^{3+})$ = 0.92 Å [42]) further reduces Ni–O–Mn bond angles in the R_2NiMnO_6 series, weakens the strength of direct FM Ni–Mn exchange interactions, and stabilizes complex AFM structures. For example, Sc_2NiMnO_6 demonstrates two AFM transitions [43]. The dielectric constant of Sc_2NiMnO_6 starts increasing with decreasing temperature when approaching T_{N1} = 35 K and shows a sharp drop below T_{N2} = 17 K. On the other hand, pyroelectric current measurements did not show the development of spin-induced ferroelectric polarization [43]. One AFM transition with an incommensurate structure was found in In_2NiMnO_6 at T_N = 26 K [44,45], and this compound shows spin-induced ferroelectric polarization [45]. Ferroelectric polarization is suppressed by magnetic fields above 6 T. The dielectric constant of In_2NiMnO_6 basically decreases with decreasing temperature between 5 K and 300 K, and a sharp peak is only observed at T_N [45]. It turned out that Lu_2NiMnO_6 is located near a phase boundary between FM and AFM states on the phase diagram of the R_2NiMnO_6 double perovskites, and a moderate pressure can induce a transition from an FM state to an incommensurate AFM state [35].

The R_2NiMnO_6 family of B-site-ordered double perovskites was recently extended further to a subfamily of A-site-ordered quadruple perovskites [46–51] with the composition of $RMn_3Ni_2Mn_2O_{12}$ with R = Bi [52], La [53,54], Ce [52], Nd [55], Sm [55], Gd [55], Dy [55], and Ho [52]. $RMn_3Ni_2Mn_2O_{12}$ behaves differently from R_2NiMnO_6. For example, $LaMn_3Ni_2Mn_2O_{12}$ has two magnetic transitions at T_N = 46 K and T_C = 34 K [53] (similar to Sc_2NiMnO_6 and in comparison with other members of the R_2NiMnO_6 family (R = La to Lu)). Complex magnetic structures are realized in $LaMn_3Ni_2Mn_2O_{12}$ [53]. $NdMn_3Ni_2Mn_2O_{12}$ already shows one magnetic transition at T_N = 26 K [55]. Net FM components are developed at the ground states of $RMn_3Ni_2Mn_2O_{12}$ with R = La and Nd. On the other hand, AFM ground states are basically realized in $RMn_3Ni_2Mn_2O_{12}$ with R = Sm to Ho. Complex AFM ground states are promising for the realization of spin-induced ferroelectric polarization. However, detailed dielectric studies of the $RMn_3Ni_2Mn_2O_{12}$ perovskites have not been performed yet.

Therefore, in this work, we investigated nearly all members of the $RMn_3Ni_2Mn_2O_{12}$ family by performing detailed measurements of dielectric constant in different magnetic fields up to 9 T. While no dielectric constant anomalies were found at a zero magnetic field in all samples, peaks emerge in the dielectric constant in the R = Sm and Gd samples

in intermediate ranges of the magnetic field. These observations suggest the presence of magnetic-field-induced multiferroic states in the R = Sm and Gd samples. Basic physical properties of $EuMn_3Ni_2Mn_2O_{12}$ and dielectric properties at different magnetic fields for Lu_2NiMnO_6 are also reported for comparison.

2. Results and Discussion

2.1. R = Bi, Ce, and Nd

Temperature dependence of dielectric constant and loss tangent of $BiMn_3Ni_2Mn_2O_{12}$ in different magnetic fields is shown in Figure 1. Very weak effects of magnetic fields on dielectric constant values were observed in agreement with the reported weak effects of magnetic fields on specific heat values [52]. No dielectric constant anomalies were observed at T_N = 36 K [52] of $BiMn_3Ni_2Mn_2O_{12}$.

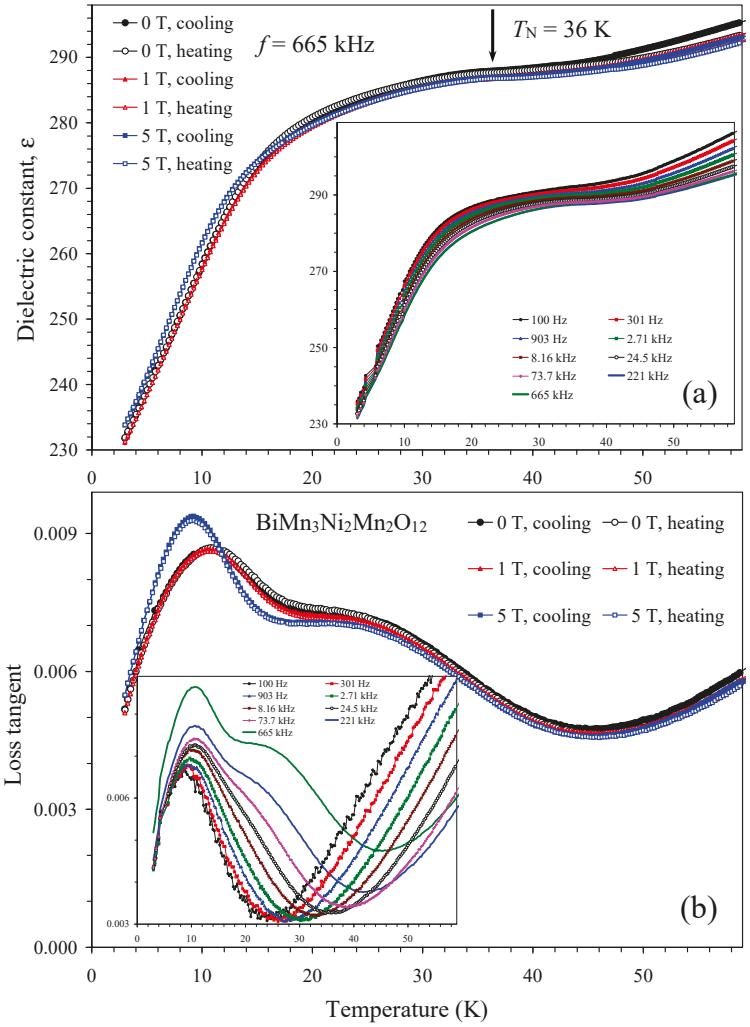

Figure 1. (**a**) Temperature dependence of dielectric constant of $BiMn_3Ni_2Mn_2O_{12}$ at one frequency of 665 kHz and different magnetic fields of 0, 1, and 5 T on cooling and heating. The inset shows the temperature dependence of the dielectric constant at different frequencies at H = 0 T (on cooling). The arrow shows a magnetic transition temperature [52]. (**b**) Temperature dependence of loss tangent of $BiMn_3Ni_2Mn_2O_{12}$ at one frequency of 665 kHz and different magnetic fields of 0, 1, and 5 T on cooling and heating. The inset shows the temperature dependence of the loss tangent at different frequencies at H = 0 T (on cooling).

The temperature dependence of the dielectric constant and loss tangent of $CeMn_3Ni_2Mn_2O_{12}$ (Figure 2) and $NdMn_3Ni_2Mn_2O_{12}$ (Figures 3 and S1) were qualita-

tively similar. The dielectric constant slightly decreased with decreasing temperature, and weak effects of magnetic fields on dielectric constant values were observed below about 60 K. Loss tangent of both samples showed broad anomalies below about 15 K (at the frequency of 665 kHz). No dielectric constant anomalies were observed at their magnetic transition temperatures of 27 K and 33 K (for R = Ce [52]) and 26 K (for R = Nd [55]). In dielectric insulator materials without any ferroelectric or ferroelectric-like transitions, the dielectric constant is usually temperature independent or slightly decreases with decreasing temperature. Therefore, the temperature dependence of the dielectric constant of the R = Ce and Nd samples is typical for ordinary insulators.

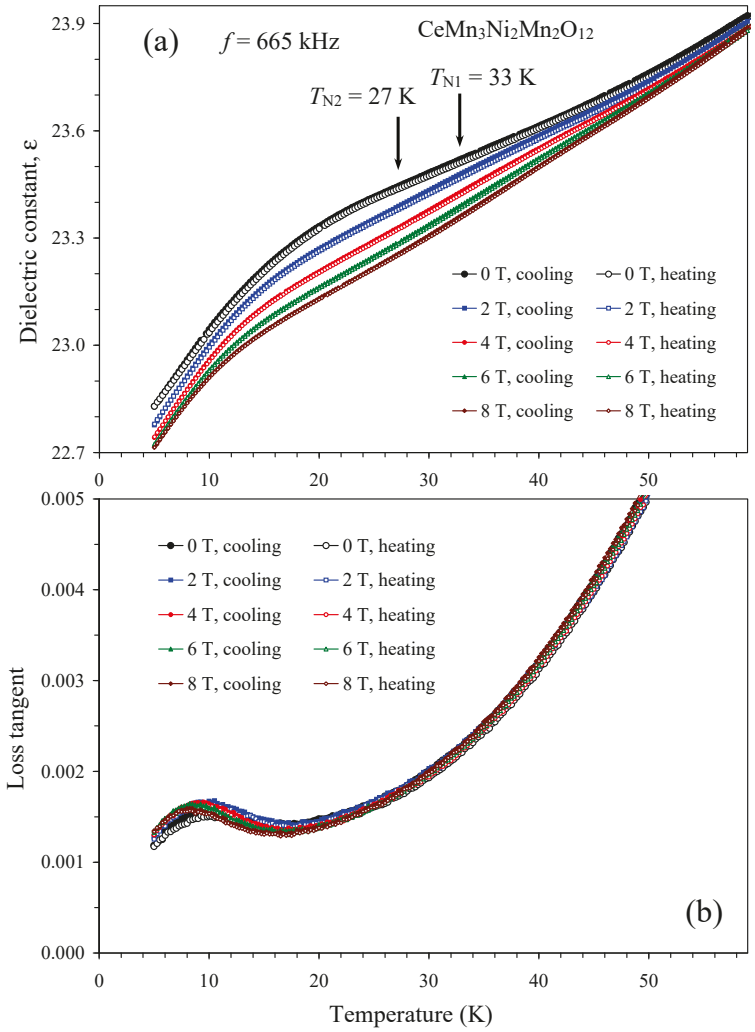

Figure 2. (**a**) Temperature dependence of dielectric constant of $CeMn_3Ni_2Mn_2O_{12}$ at one frequency of 665 kHz and different magnetic fields of 0, 2, 4, 6, and 8 T on cooling and heating. Arrows show magnetic transition temperatures [52]. (**b**) Temperature dependence of loss tangent of $CeMn_3Ni_2Mn_2O_{12}$ at one frequency of 665 kHz and different magnetic fields of 0, 2, 4, 6, and 8 T on cooling and heating.

2.2. R = Sm

The temperature dependence of the dielectric constant of $RMn_3Ni_2Mn_2O_{12}$ with R = Sm to Ho was qualitatively different from that of $RMn_3Ni_2Mn_2O_{12}$ with R = Bi, Ce, and Nd because the dielectric constant started increasing with decreasing temperature below about 30–40 K. The increase of the dielectric constant suggests the development of polar correlations. This change in the behavior of the dielectric constant also correlates with the changes in the magnetic properties because net FM components were observed at the ground states of $RMn_3Ni_2Mn_2O_{12}$ with R = Ce and Nd, while AFM ground states are

basically realized in $RMn_3Ni_2Mn_2O_{12}$ with R = Sm to Ho. This change in the behavior of the dielectric constant could reflect different magnetic structures.

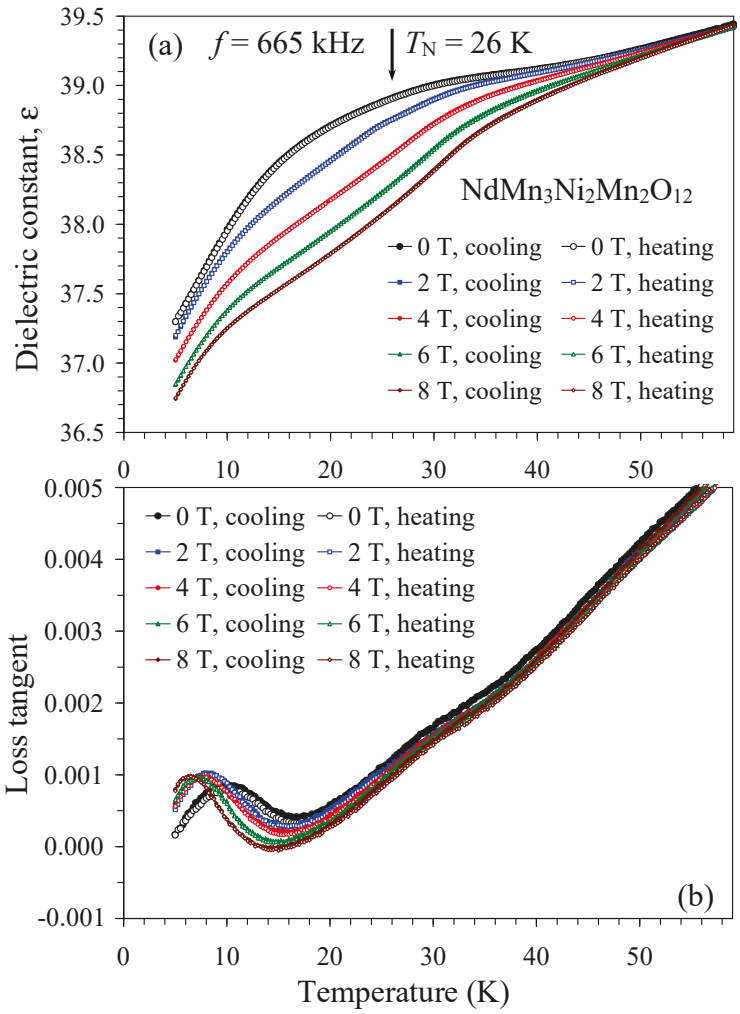

Figure 3. (**a**) Temperature dependence of dielectric constant of $NdMn_3Ni_2Mn_2O_{12}$ at one frequency of 665 kHz and different magnetic fields of 0, 2, 4, 6, and 8 T on cooling and heating. The arrow shows a magnetic transition temperature [55]. (**b**) Temperature dependence of loss tangent of $NdMn_3Ni_2Mn_2O_{12}$ at one frequency of 665 kHz and different magnetic fields of 0, 2, 4, 6, and 8 T on cooling and heating.

The dielectric constant and loss tangent of $SmMn_3Ni_2Mn_2O_{12}$ are shown in Figures 4 and S2–S4. At H = 0 T, the dielectric constant and loss tangent of $SmMn_3Ni_2Mn_2O_{12}$ showed no detectable anomalies. However, at H = 2 T, a small kink appears on the dielectric constant, and a peak is visible on the loss tangent near T_N = 23 K. At higher magnetic fields (4–8 T), a small kink on the dielectric constant transforms to a small peak. Peaks on both dielectric constant and loss tangent are moving to higher temperatures with increasing magnetic field in agreement with the similar shift of specific heat anomalies (Figure 5a), confirming their common magnetic origin. Peaks on loss tangent were observed at 20.5 K (at 2 T), 21.5 K (at 4 T), 23.0 K (at 6 T), 24.5 K (at 8 T), and 25.2 K (at 9 T). Almost no hysteresis in the peak positions was observed during cooling and heating. Therefore, the appearance of peaks on both dielectric constant and loss tangent at magnetic fields of 2–9 T suggests the development of spin-induced ferroelectric polarization in $SmMn_3Ni_2Mn_2O_{12}$ at such magnetic fields.

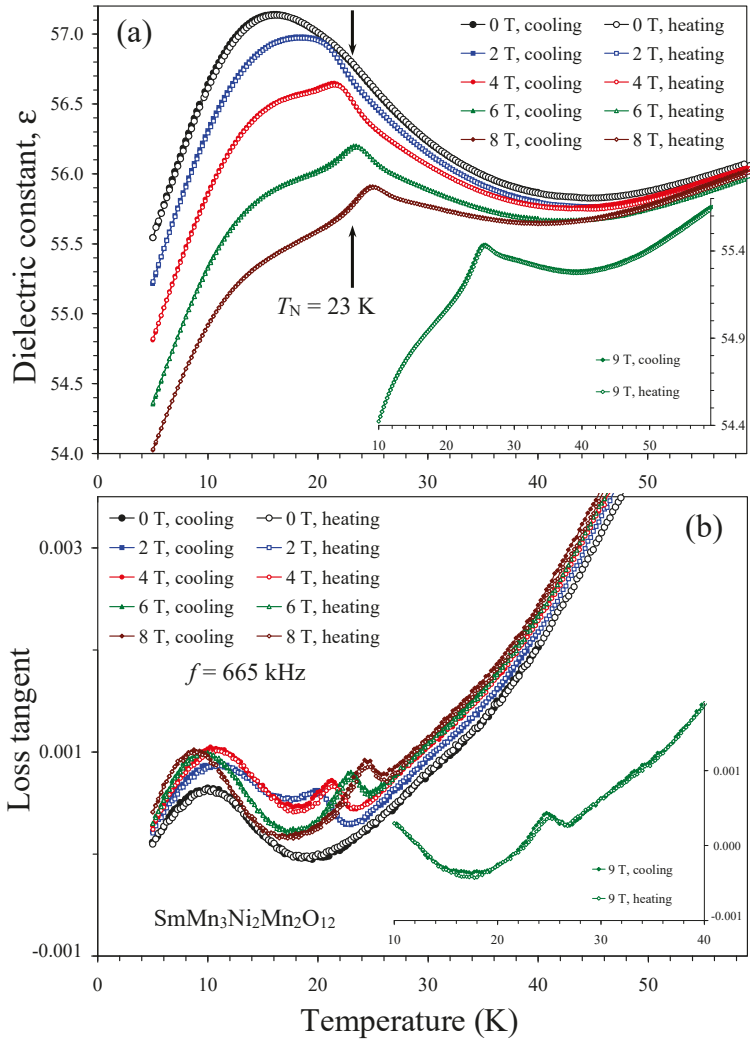

Figure 4. (**a**) Temperature dependence of dielectric constant of $SmMn_3Ni_2Mn_2O_{12}$ at one frequency of 665 kHz and different magnetic fields of 0, 2, 4, 6, and 8 T on cooling and heating. The arrow shows a magnetic transition temperature at H = 0 T [55]. (**b**) Temperature dependence of loss tangent of $SmMn_3Ni_2Mn_2O_{12}$ at one frequency of 665 kHz and different magnetic fields of 0, 2, 4, 6, and 8 T on cooling and heating. The insets show data at a magnetic field of 9 T.

2.3. *R* = *Eu*

As $EuMn_3Ni_2Mn_2O_{12}$ has not been reported yet, we start with the basic characterization of this compound by other methods. $EuMn_3Ni_2Mn_2O_{12}$ crystallized in a cubic structure of the A-site-ordered quadruple perovskite family [46–51] with a = 7.3430(1) Å. The quality of the standard laboratory X-ray diffraction data (with a measurement speed of 3°/min) did not allow detection of superstructure reflections related to (partial) ordering of Ni^{2+} and Mn^{4+} cations and, therefore, to assign the *Im*-3 or *Pn*-3 space groups. Therefore, we measured X-ray diffraction data with a speed of 0.1°/min between 38° and 44° and could detect a very weak (311) superstructure reflection. This fact suggests that there is a partial ordering of Ni^{2+} and Mn^{4+} cations, and the space group is *Pn*-3, similar to some other members of the $RMn_3Ni_2Mn_2O_{12}$ family [55]. Laboratory X-ray diffraction data also showed the presence of some amounts of $(Eu_{1-x}Mn_x)MnO_3$ impurity (space group *Pnma* with a = 5.5357 Å, b = 7.5834 Å, c = 5.3196 Å; about 6.7 wt. %) and NiO impurity (space group *R*-3*m* with a = 2.9597 Å and c = 7.2374 Å; about 2.5 wt. %). The $(Eu_{1-x}Mn_x)MnO_3$ impurity has a ferrimagnetic transition near 140 K.

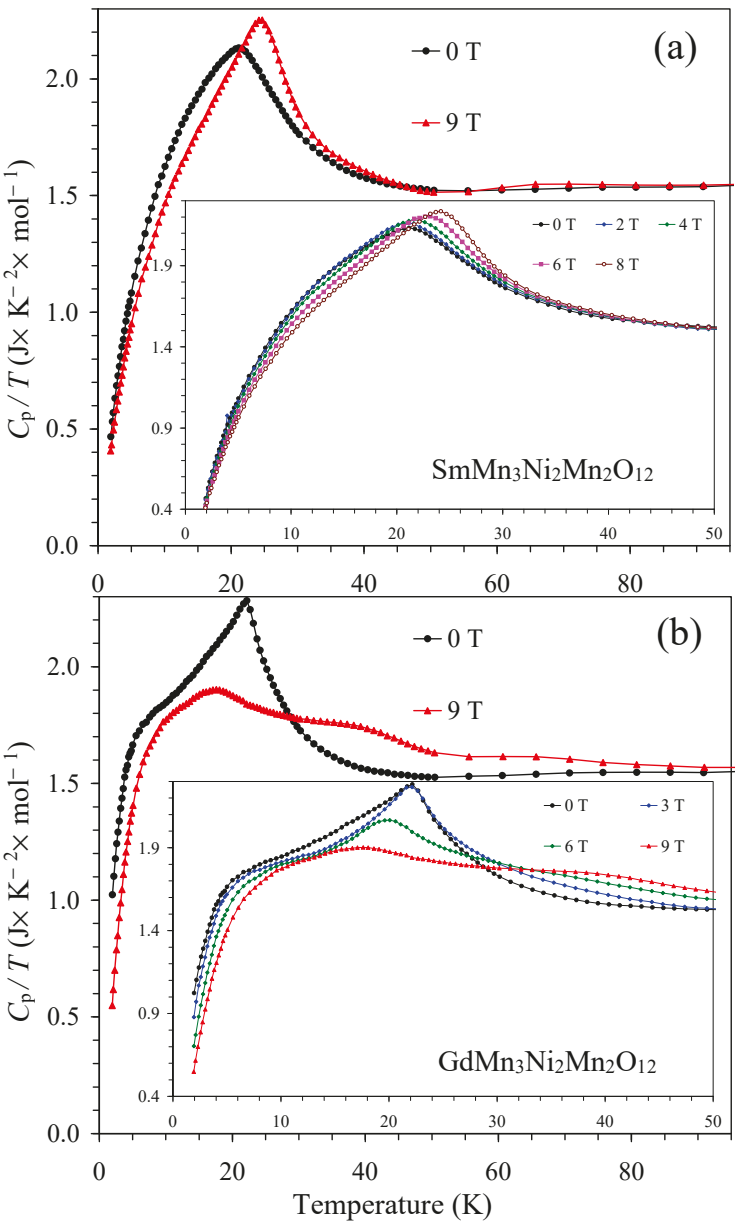

Figure 5. (**a**) C_p/T vs. T curves of $SmMn_3Ni_2Mn_2O_{12}$ measured at H = 0 and 9 T on cooling. The inset shows C_p/T vs. T curves at H = 0, 2, 4, 6, and 8 T. (**b**) C_p/T vs. T curves of $GdMn_3Ni_2Mn_2O_{12}$ measured at H = 0 and 9 T on cooling. The inset shows C_p/T vs. T curves at H = 0, 3, 6, and 9 T.

Temperature dependence of specific heat and magnetic susceptibilities of $EuMn_3Ni_2Mn_2O_{12}$ is shown in Figure 6. Specific heat data clearly showed the presence of one magnetic transition at T_N = 33 K; the specific heat anomaly was slightly dependent on magnetic fields. χ vs. T curves showed a very small kink at T_N = 33 K. On the other hand, differential $d\chi T/dT$ vs. T curves allowed detecting the magnetic anomaly more clearly (the inset of Figure 6b). At high temperatures, inverse magnetic susceptibilities followed the Curie–Weiss law (Figure S5), and the obtained Curie–Weiss parameters (using the 7 T FCC curve in a temperature range of 250–350 K) were μ_{eff} = 11.216μ_B (the experimental effective magnetic moment) and θ = +0.1 K (the Curie–Weiss temperature). The μ_{eff} value was close to the expected calculated value of μ_{calc} = 11.382μ_B (taking 3.4μ_B for Eu^{3+} [56]).

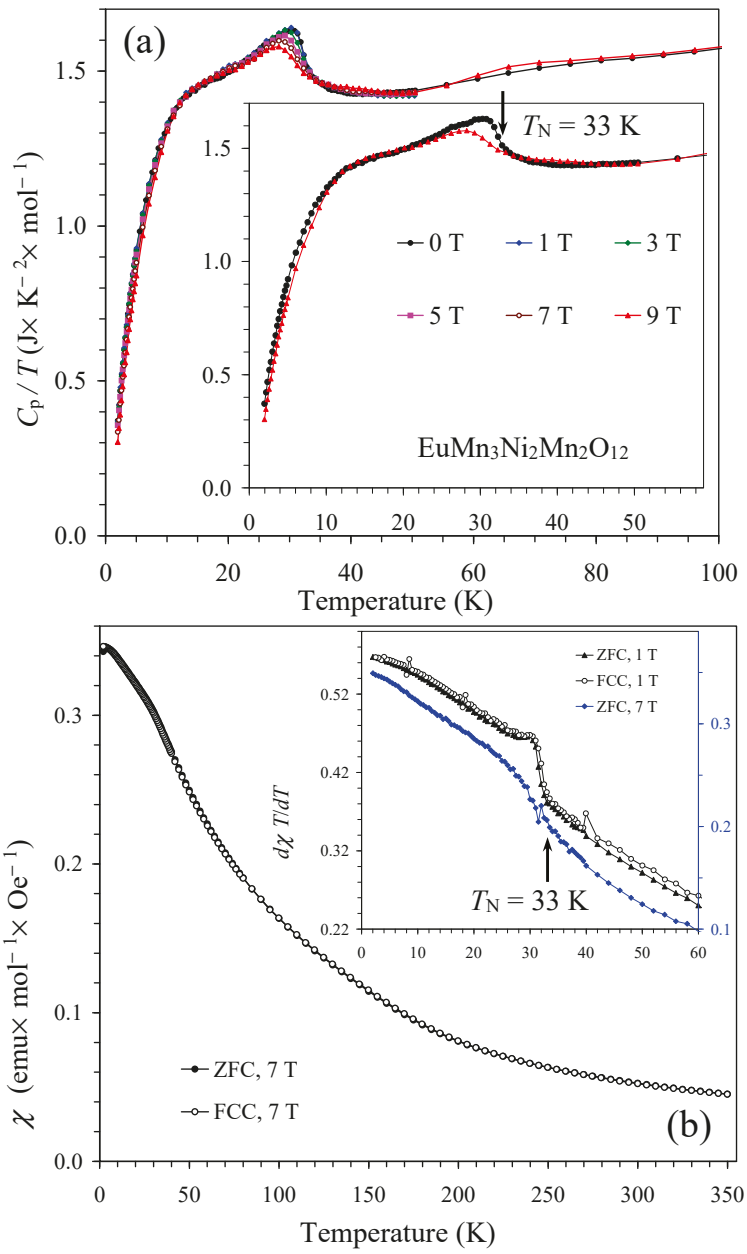

Figure 6. (**a**) C_p/T vs. T curves of $EuMn_3Ni_2Mn_2O_{12}$ measured at H = 0, 1, 3, 5, 7, and 9 T on cooling. The inset shows C_p/T vs. T curves at H = 0 and 9 T. The arrow shows a magnetic transition temperature. (**b**) ZFC (filled symbols) and FCC (empty symbols) dc magnetic susceptibility curves ($\chi = M/H$) of $EuMn_3Ni_2Mn_2O_{12}$ measured at H = 7 T. The inset shows ZFC and FCC $d\chi T/dT$ vs. T curves at H = 1 T and 7 T.

Isothermal magnetization curves (M vs. H) showed nearly linear behavior at T = 5–200 K above about 1 T (Figure S5). The S-type shape was observed near the origin without any significant hysteresis originating from the impurity contribution with soft FM-like properties. Nearly the same S-type contribution was observed at T = 5–100 K, that is, below and above T_N = 33 K of $EuMn_3Ni_2Mn_2O_{12}$. On the other hand, the S-type shape near the origin disappeared at 200 K, that is, above the ferrimagnetic transition of the $(Eu_{1-x}Mn_x)MnO_3$ impurity. Therefore, the χ vs. T and M vs. H curves give evidence that a purely AFM transition takes place in $EuMn_3Ni_2Mn_2O_{12}$ without any net FM-like moments.

Temperature dependence of the dielectric constant and loss tangent of $EuMn_3Ni_2Mn_2O_{12}$ (Figure 7) at different magnetic fields (0–8 T) showed no anomalies at T_N = 33 K, suggesting the absence of any detectable (spin-induced) ferroelectric polarization.

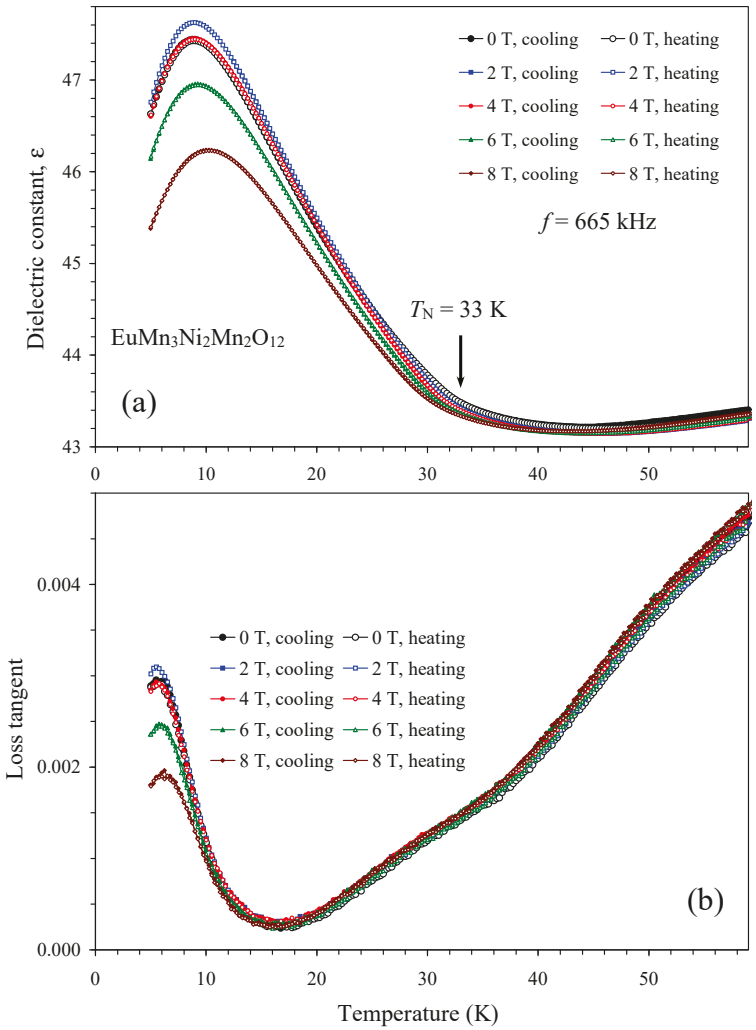

Figure 7. (**a**) Temperature dependence of dielectric constant of $EuMn_3Ni_2Mn_2O_{12}$ at one frequency of 665 kHz and different magnetic fields of 0, 2, 4, 6, and 8 T on cooling and heating. The arrow shows a magnetic transition temperature. (**b**) Temperature dependence of loss tangent of $EuMn_3Ni_2Mn_2O_{12}$ at one frequency of 665 kHz and different magnetic fields of 0, 2, 4, 6, and 8 T on cooling and heating.

2.4. R = Gd

The dielectric constant of $GdMn_3Ni_2Mn_2O_{12}$ showed a small kink near T_N = 22 K at H = 0 T (Figures 8 and S6). The kink transforms to a weak peak already at H = 1 T. The most pronounced peaks on dielectric constant and loss tangent were observed at H = 5 T (Figures 8 and 9). Peaks on the dielectric constant disappear at H = 8 and 9 T. Peaks on the dielectric constant clearly move to lower temperatures with increasing magnetic fields (peaks were observed at 23.2 K at 1 T, 23.0 K at 2 T, 22.5 K at 3 T, 21.5 K at 4 T, 20.5 K at 5 T, and 19.2 K at 6 T) in agreement with specific heat measurements (Figure 5b), confirming their common magnetic origin. Therefore, $GdMn_3Ni_2Mn_2O_{12}$ exhibits spin-induced ferroelectric polarization at about H = 1–7 T.

2.5. R = Dy

The temperature dependence of the dielectric constant and loss tangent of $DyMn_3Ni_2Mn_2O_{12}$ between H = 0 T and H = 8 T (Figure 10) was close to those of $EuMn_3Ni_2Mn_2O_{12}$ (Figure 6). No anomalies were observed at the magnetic transition temperatures of 36 K and 10 K [55].

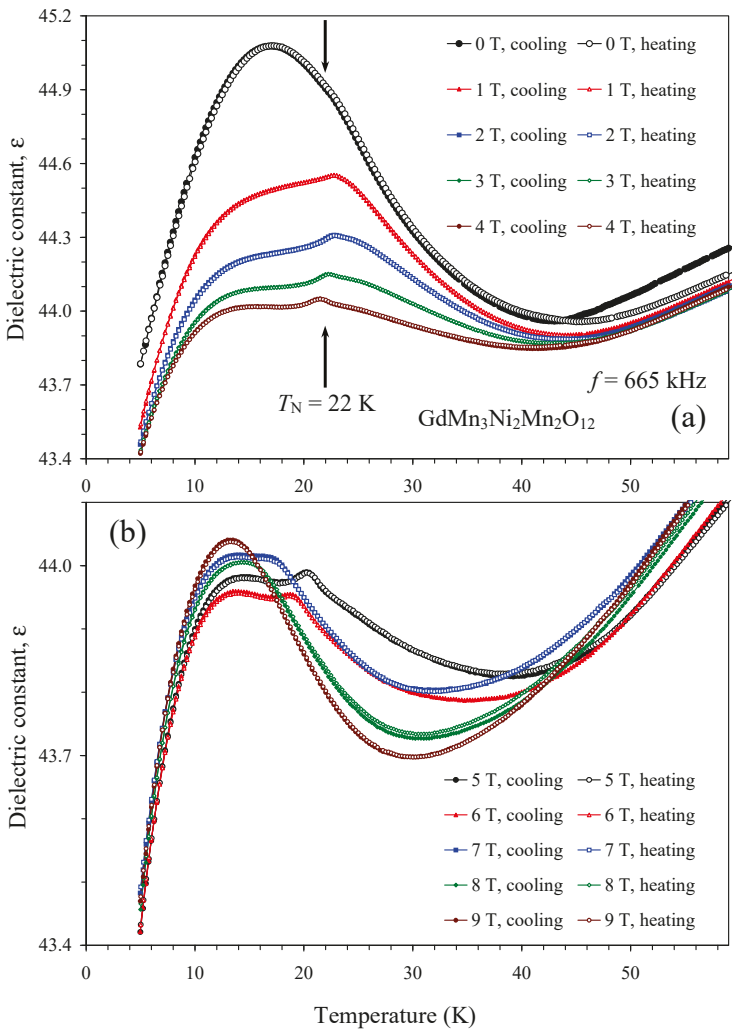

Figure 8. (**a**) Temperature dependence of dielectric constant of $GdMn_3Ni_2Mn_2O_{12}$ at one frequency of 665 kHz and different magnetic fields of 0, 1, 2, 3, and 4 T on cooling and heating. The arrow shows a magnetic transition temperature at H = 0 T [55]. (**b**) Temperature dependence of dielectric constant of $GdMn_3Ni_2Mn_2O_{12}$ at one frequency of 665 kHz and different magnetic fields of 5, 6, 7, 8, and 9 T on cooling and heating.

2.6. R = Ho

Temperature dependence of dielectric constant and loss tangent of $HoMn_3Ni_2Mn_2O_{12}$ between 0 T and 9 T is shown on Figures 11 and 12. Both dielectric constant and loss tangent showed small peaks near 36 K; this temperature matches with the magnetic transition temperature of $HoMn_3Ni_2Mn_2O_{12}$ [52], which was unambiguously determined with specific heat and magnetization measurements [52]. On the other hand, this temperature is also close to the magnetic and ferroelectric transition temperature of the $HoMn_2O_5$ impurity [57–60], which shows very strong and sharp anomalies on both dielectric constant and loss tangent [57–59]. The positions and intensities of the peaks remained nearly the same in all magnetic fields in $HoMn_3Ni_2Mn_2O_{12}$; and there was small hysteresis in the positions of the peaks on cooling and heating. Exactly the same behavior was observed in $HoMn_2O_5$ [57–59]. On the other hand, no hysteresis was observed on the temperature dependence of magnetic susceptibilities of $HoMn_3Ni_2Mn_2O_{12}$ [52] (we note that almost no anomalies were observed on magnetic susceptibilities of $HoMn_2O_5$ [59,60]). Therefore, we believe that there is a high probability that the observed anomalies on dielectric constant and loss tangent are caused by the $HoMn_2O_5$ impurity even though its amount was quite small (about 3 weight % [52]). Therefore, the intrinsic dielectric constant and loss tangent

of $HoMn_3Ni_2Mn_2O_{12}$ are very close to those of $DyMn_3Ni_2Mn_2O_{12}$; that is, there are no detectable anomalies at the magnetic transition temperature between 0 T and 9 T.

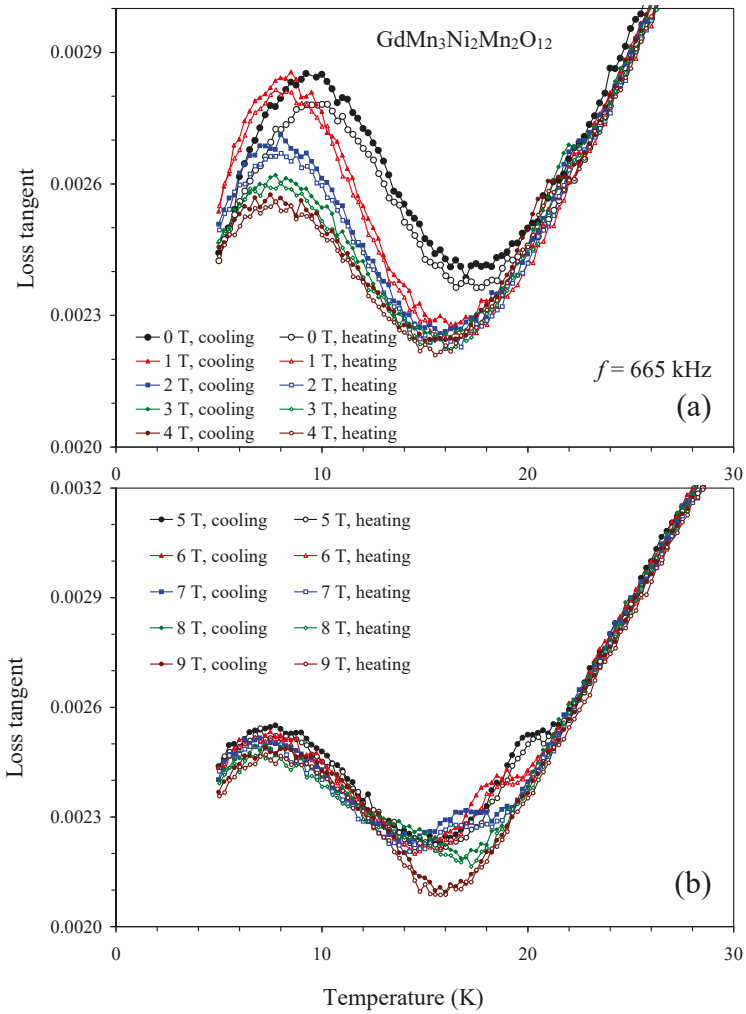

Figure 9. (**a**) Temperature dependence of loss tangent of $GdMn_3Ni_2Mn_2O_{12}$ at one frequency of 665 kHz and different magnetic fields of 0, 1, 2, 3, and 4 T on cooling and heating. (**b**) Temperature dependence of loss tangent of $GdMn_3Ni_2Mn_2O_{12}$ at one frequency of 665 kHz and different magnetic fields of 5, 6, 7, 8, and 9 T on cooling and heating.

2.7. Lu_2NiMnO_6

For comparison, we report here the dielectric properties of one member of the R_2NiMnO_6 family with the smallest R^{3+} cation of R = Lu. Specific heat measurements confirmed the presence of one FM transition at T_C = 41 K (the inset of Figures 13b and S7). Dielectric properties of different members of the R_2NiMnO_6 family were reported in the literature [39,40], and no dielectric anomalies were usually observed. On the other hand, very detailed studies in the vicinity of T_C demonstrated very weak kink-like anomalies at T_C [25,36]; however, effects of magnetic fields have not been studied. Temperature dependence of the dielectric constant and loss tangent of our Lu_2NiMnO_6 sample, prepared by a high-pressure high-temperature method at 6 GPa, is shown in Figure 13. At H = 0 T, we observed a very weak kink-like anomaly at T_C similar to the previous reports [25,36]. The kink-like anomaly could originate from magnetostriction effects because Lu_2NiMnO_6 is a ferromagnet [61,62]. High magnetic fields smeared kink-like anomalies; for example, at H = 7 T and 9 T, no visible dielectric anomalies were detected near T_C. Therefore, Lu_2NiMnO_6 does not develop ferroelectric polarization between 0 T and 9 T. The dielectric

constant decreases with decreasing temperature between 3 K and 300 K, as for ordinary insulators/dielectrics.

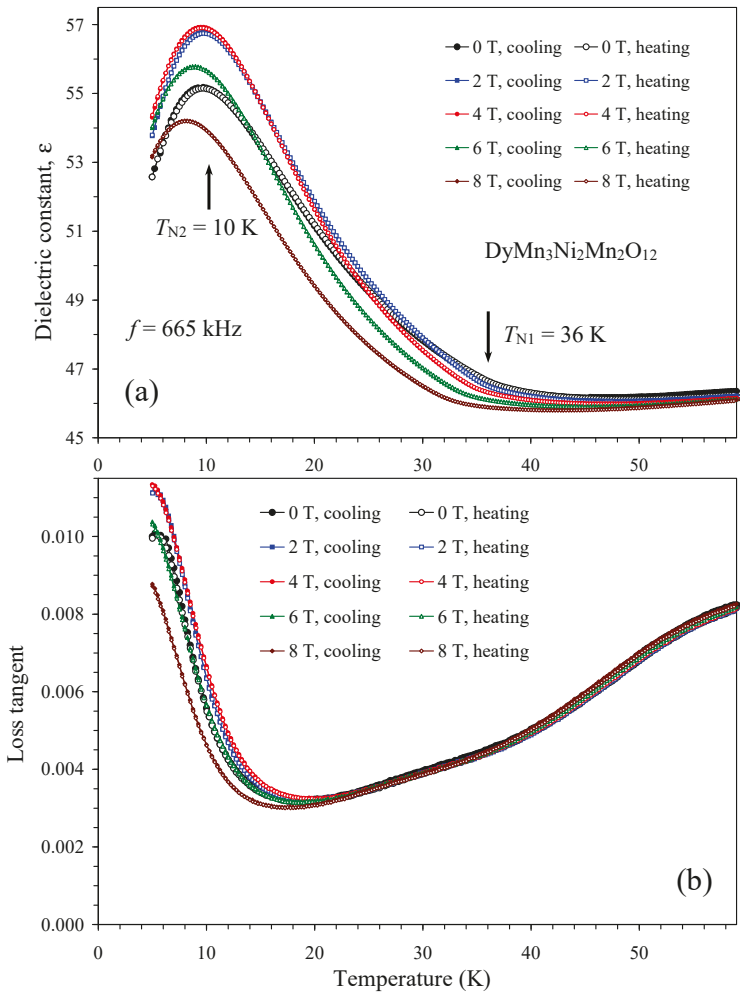

Figure 10. (**a**) Temperature dependence of dielectric constant of $DyMn_3Ni_2Mn_2O_{12}$ at one frequency of 665 kHz and different magnetic fields of 0, 2, 4, 6, and 8 T on cooling and heating. The arrows show the magnetic transition temperatures at H = 0 T [55]. (**b**) Temperature dependence of loss tangent of $DyMn_3Ni_2Mn_2O_{12}$ at one frequency of 665 kHz and different magnetic fields of 0, 2, 4, 6, and 8 T on cooling and heating.

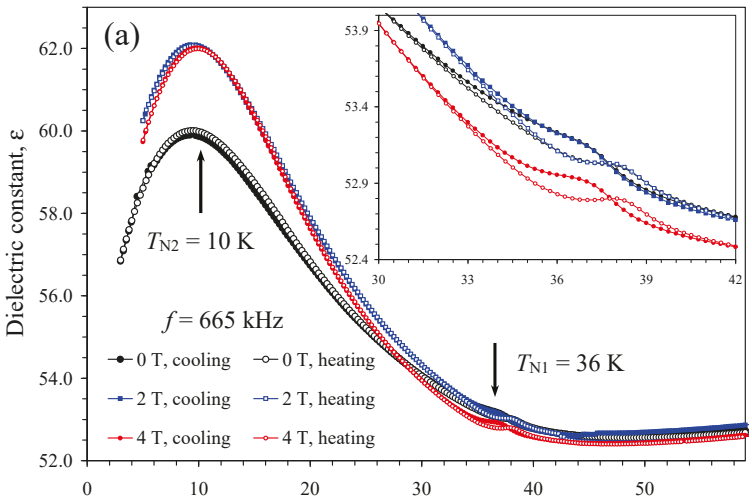

Figure 11. *Cont.*

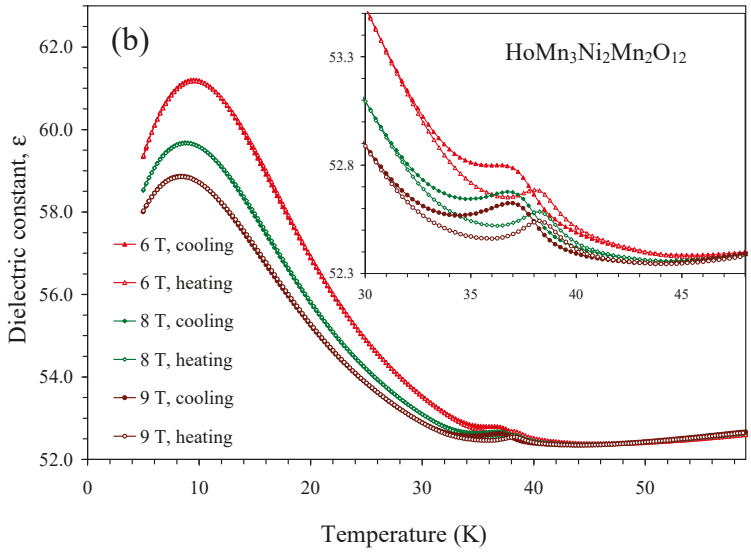

Figure 11. (**a**) Temperature dependence of dielectric constant of $HoMn_3Ni_2Mn_2O_{12}$ at one frequency of 665 kHz and different magnetic fields of 0, 2, and 4 T on cooling and heating. The arrows show the magnetic transition temperatures [52]. (**b**) Temperature dependence of the dielectric constant of $HoMn_3Ni_2Mn_2O_{12}$ at one frequency of 665 kHz and different magnetic fields of 6, 8, and 9 T on cooling and heating. The insets show magnified parts.

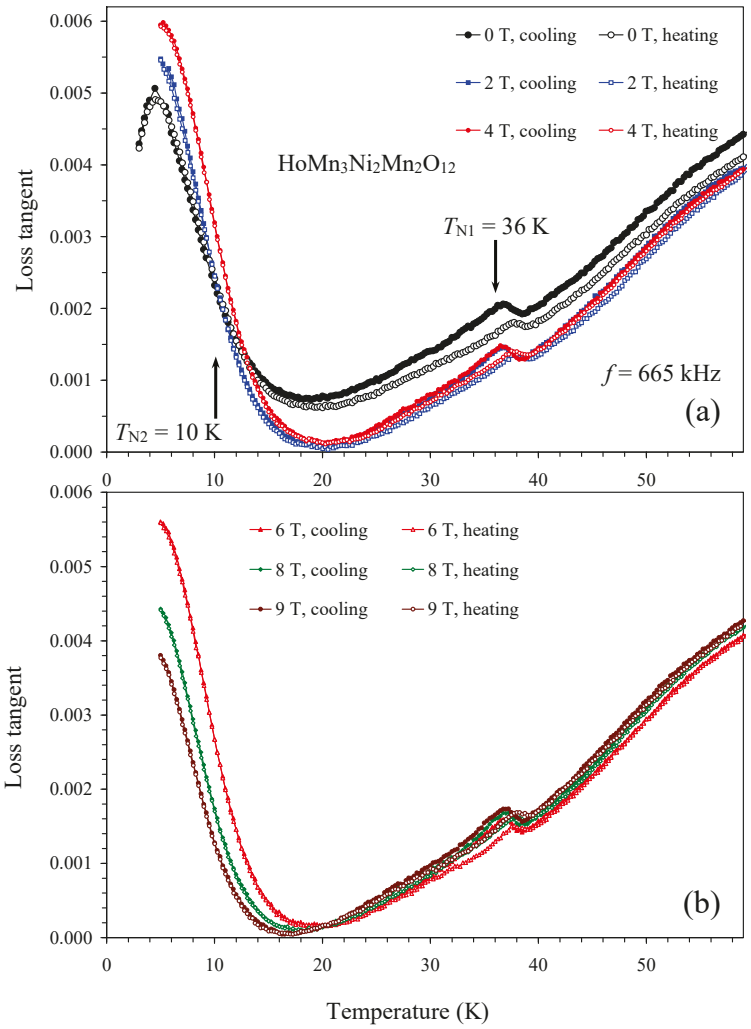

Figure 12. (**a**) Temperature dependence of loss tangent of $HoMn_3Ni_2Mn_2O_{12}$ at one frequency of 665 kHz and different magnetic fields of 0, 2, and 4 T on cooling and heating. The arrows show the

magnetic transition temperatures [52]. (**b**) Temperature dependence of loss tangent of $HoMn_3Ni_2Mn_2O_{12}$ at one frequency of 665 kHz and different magnetic fields of 6, 8, and 9 T on cooling and heating.

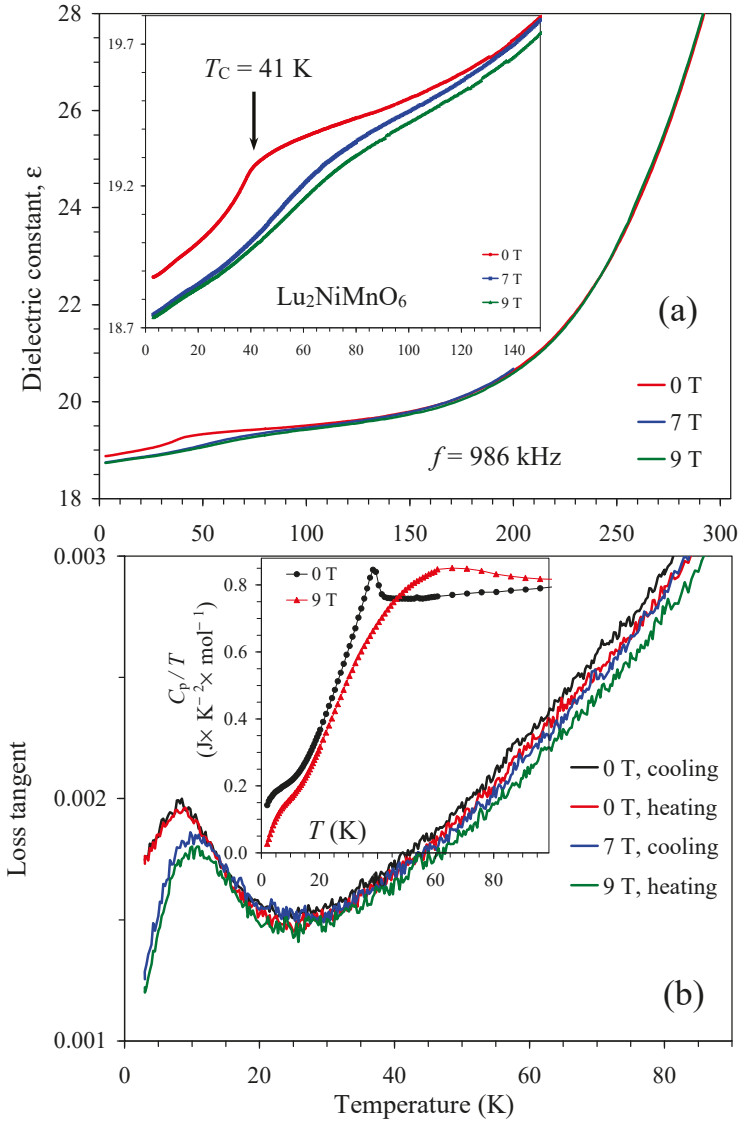

Figure 13. Temperature dependence of (**a**) dielectric constant and (**b**) loss tangent at one frequency of 986 kHz in Lu_2NiMnO_6 at H = 0, 7, and 9 T in different temperature ranges. The inset in the panel (**a**) shows details below 150 K, where the arrow shows a ferromagnetic transition temperature. The inset in the panel (**b**) shows C_p/T vs. T curves of Lu_2NiMnO_6 at H = 0 and 9 T.

3. Materials and Methods

$RMn_3Ni_2Mn_2O_{12}$ samples with R = Bi, Ce, Nd, Sm, Eu, Gd, Dy, and Ho were prepared from stoichiometric mixtures of Bi_2O_3 (Rare Metallic Co., Tokyo, Japan, 99.9999%), CeO_2 (Rare Metallic Co., Tokyo, Japan, 99.99%), R_2O_3 (Rare Metallic Co., Tokyo, Japan, 99.9%), Mn_2O_3 (Rare Metallic Co., Tokyo, Japan, 99.99%), MnO_2 (Alfa Aesar, Ward Hill, MA, USA, 99.99%), and NiO (Rare Metallic Co., Tokyo, Japan, 99.9%). Single-phase Mn_2O_3 was prepared from a commercial MnO_2 chemical (Rare Metallic Co., Tokyo, Japan, 99.99%) by annealing in air at 923 K for 24 h. The synthesis was performed at about 6 GPa and at about 1500 K for 2 h in sealed Au capsules using a belt-type HP instrument. After annealing at 1500 K, the samples were cooled down to room temperature by turning off the heating current, and the pressure was slowly released.

The Lu_2NiMnO_6 sample was prepared from stoichiometric mixtures of Lu_2O_3 (Rare Metallic Co., Tokyo, Japan, 99.9%), MnO_2 (Alfa Aesar, Ward Hill, MA, USA, 99.99%), and NiO (Rare Metallic Co., Tokyo, Japan, 99.9%) by the high-pressure high-temperature method at about 6 GPa and at about 1700 K for 2 h in a sealed Pt capsule. We note that the oxygen content and purity of MnO_2 (Alfa Aesar, Ward Hill, MA, USA, 99.99%) were confirmed before its use by the thermogravimetric analysis and X-ray powder diffraction. The refined lattice parameters of Lu_2NiMnO_6 (space group $P2_1/n$ with a = 5.1490(1) Å, b = 5.5123(1) Å, c = 7.4073(1) Å, and β = 90.441(1)°) were close to the reported values [35].

X-ray powder diffraction data of $EuMn_3Ni_2Mn_2O_{12}$ were collected at room temperature on a MiniFlex600-C diffractometer (Rigaku, Tokyo, Japan) using CuKα radiation (a 2θ range of 10–120°, a step width of 0.02°, and a scan speed of 3°/min; and a 2θ range of 38–44°, a step width of 0.02°, and a scan speed of 0.1 °/min) (Figure S8). The Rietveld analysis of all X-ray powder diffraction data was performed using the *RIETAN-2000* program [63]. The crystallographic characterization of other samples was reported in [52,55].

Magnetic measurements of $EuMn_3Ni_2Mn_2O_{12}$ were performed on SQUID magnetometers (Quantum Design MPMS3, San Diego, CA, USA) between 2 K and 350 K (and between 330 K and 750 K) in applied fields of 0.01 T, 1 T, and 7 T under both zero-field-cooled (ZFC) and field-cooled on cooling (FCC) conditions. Magnetic-field dependence was measured at different temperatures between −7 T and +7 T. Specific heat, C_p, of $RMn_3Ni_2Mn_2O_{12}$ was measured on cooling from 100 K to 2 K at different magnetic fields from 0 T to 9 T by a pulse relaxation method using a commercial calorimeter (Quantum Design PPMS, San Diego, CA, USA).

Dielectric properties were measured using an Alpha-A High Performance Frequency Analyzer (NOVOCONTROL Technologies, Montabaur, Germany) on cooling and heating in a temperature range between 3–5 K and 70–300 K and a frequency range from 100 Hz to 665 kHz (or 986 kHz) at different magnetic fields from 0 T to 9 T. Pieces of pellets were used in all magnetic, specific heat, and dielectric measurements.

4. Conclusions

Dielectric properties of the A-site-ordered quadruple perovskites, $RMn_3Ni_2Mn_2O_{12}$ with R = Bi, Ce, Nd, Sm, Eu, Gd, Dy, and Ho, were investigated at different magnetic fields between 0 T and 9 T. A principal difference in the temperature dependence of the dielectric constant was observed for R = Bi, Ce, and Nd and for R = Sm, Eu, Gd, Dy, and Ho. The dielectric constant of the former group decreases with decreasing temperature down to the lowest temperature. The dielectric constant of the latter group starts increasing with decreasing temperature when approaching magnetic transition temperatures, suggesting different magnetic ground states. Peak-like anomalies were found on dielectric constant and loss tangent in intermediate magnetic-field ranges for the R = Sm and Gd samples, suggesting the existence of "hidden" [64] magnetic-field-induced multiferroic states. Physical properties of a new compound, $EuMn_3Ni_2Mn_2O_{12}$, were also investigated with specific heat and magnetization measurements. Dielectric properties of Lu_2NiMnO_6 at different magnetic fields are reported for comparison.

Supplementary Materials: The following supporting information can be downloaded at: https://www.mdpi.com/article/10.3390/inorganics13100315/s1. Figure S1: Temperature dependence of (a) dielectric constant and (b) loss tangent of $NdMn_3Ni_2Mn_2O_{12}$ at different frequencies from 100 Hz to 665 kHz. Measurements were performed on cooling at H = 0 T; Figure S2: Temperature dependence of dielectric constant of $SmMn_3Ni_2Mn_2O_{12}$ at different frequencies from 100 Hz to 665 kHz. Measurements were performed on cooling at (a) H = 0 T and at (b) H = 8 T; Figure S3: Temperature dependence of loss tangent of $SmMn_3Ni_2Mn_2O_{12}$ at different frequencies from 100 Hz to 665 kHz. Measurements were performed on cooling at (a) H = 0 T and at (b) H = 8 T; Figure S4:

Temperature dependence of dielectric constant of $SmMn_3Ni_2Mn_2O_{12}$ at one frequency of 665 kHz and different magnetic fields of (a) 0, 1, 2, 3, and 4 T and (b) 5, 6, 7, 8, and 9 T on cooling and heating. Different measurements (from Figure 4 in the main text and from Figures S2 and S3) are reported. Temperature dependence of loss tangent of $SmMn_3Ni_2Mn_2O_{12}$ at one frequency of 665 kHz and different magnetic fields of (c) 0, 1, 2, 3, and 4 T and (d) only at 0 and 1 T (to emphasize the absence of anomalies) on cooling and heating. (e) Temperature dependence of loss tangent of $SmMn_3Ni_2Mn_2O_{12}$ at one frequency of 665 kHz and different magnetic fields of 5, 6, 7, 8, and 9 T; Figure S5: (a) M vs. H curves of $EuMn_3Ni_2Mn_2O_{12}$ at T = 5 K, 20 K, 40 K, 60 K, 100 K, and 200 K. The inset shows a magnified part of the M vs. H curves at T = 5 K and 20 K. (b) M vs. H curves of $EuMn_3Ni_2Mn_2O_{12}$ at T = 5 K and 20 K, below its T_N = 33 K. The S-type shape of the M vs. H curves near the origin comes from a contribution from the ferrimagnetic impurity $(Eu_{1-x}Mn_x)MnO_3$ (space group *Pnma*); otherwise, the M vs. H curves were linear without hysteresis. (c) Inverse magnetic susceptibilities of $EuMn_3Ni_2Mn_2O_{12}$ measured at magnetic fields of H = 100 Oe, 10 kOe, and 70 kOe in the low-temperature (LT) region of 2–350 K and in the high-temperature (HT) region of 330–750 K. Red lines show the Curie–Weiss fittings of the LT and HT data at H = 70 kOe; fitting parameters are shown on this figure. The anomaly near 140 K on the LT region originates from the ferrimagnetic impurity $(Eu_{1-x}Mn_x)MnO_3$. A very weak anomaly near 400 K, seen on the HT data at H = 100 Oe, could originate from traces of $NiMnO_3$ impurity observed in some other samples of $RMn_3Ni_2Mn_2O_{12}$ with R = Bi, Ce, and Ho. Magnetic measurements showed that the amount of a possible $NiMnO_3$ impurity was very small, well below the detection limit of laboratory X-ray diffraction; Figure S6: Temperature dependence of dielectric constant of $GdMn_3Ni_2Mn_2O_{12}$ at different frequencies from 100 Hz to 665 kHz. Measurements were performed on heating at (a) H = 0 T and at (b) H = 5 T; Figure S7: C_p/T vs. T curves of Lu_2NiMnO_6 at different magnetic fields of H = 0, 0.2, 1, 2, 3, 5, and 9 T. Measurements were performed on cooling; Figure S8: (a) Experimental (black crosses), calculated (red line), and difference (blue line at the bottom) room-temperature laboratory X-ray powder diffraction patterns of $EuMn_3Ni_2Mn_2O_{12}$ (space group $Pn-3$) in a 2θ range of 16° and 120°. The tick marks show possible Bragg reflection positions for the main phase (brown), $(Eu_{1-x}Mn_x)MnO_3$ impurity (blue), and NiO impurity (green) (from top to bottom). (b) A magnified part of the experimental and calculated patterns in a 2θ range of 38° and 44°, emphasizing the presence of the (311) reflection from the (partial) B-site ordering. The data between 38° and 44° were measured with a speed of 0.1°/min and scaled to match with other data (panel (a)) measured with a speed of 3°/min; because of scaling, the background on panel (b) was not fitted well.

Author Contributions: Conceptualization, A.A.B.; methodology, A.A.B.; validation, A.A.B.; formal analysis, A.A.B.; investigation, A.A.B., R.L., and K.Y.; resources, K.Y.; data curation, A.A.B.; writing—original draft preparation, A.A.B.; writing—review and editing, A.A.B.; supervision, A.A.B. and K.Y.; project administration, A.A.B.; funding acquisition, K.Y. All authors have read and agreed to the published version of the manuscript.

Funding: This work was partially supported by a Grant-in-Aid for Scientific Research (No. JP25K01657) from the Japan Society for the Promotion of Science.

Institutional Review Board Statement: Not applicable.

Informed Consent Statement: Not applicable.

Data Availability Statement: The original data presented in this study are openly available on Zenodo at https://doi.org/10.5281/zenodo.17131358.

Acknowledgments: MANA was supported by the World Premier International Research Center Initiative (WPI), MEXT, Japan.

Conflicts of Interest: The author declares no conflicts of interest.

References

1. Schmid, H. Multi-ferroic magnetoelectrics. *Ferroelectrics* **1994**, *162*, 317–338. [CrossRef]
2. Eerenstein, W.; Mathur, N.; Scott, J.F. Multiferroic and magnetoelectric materials. *Nature* **2006**, *442*, 759–765. [CrossRef]

3. Khomskii, D.I. Multiferroics: Different ways to combine magnetism and ferroelectricity. *J. Magn. Magn. Mater.* **2006**, *306*, 1–8. [CrossRef]
4. Cheong, S.-W.; Mostovoy, M. Multiferroics: A magnetic twist for ferroelectricity. *Nat. Mater.* **2007**, *6*, 13–20. [CrossRef]
5. Khomskii, D. Classifying multiferroics: Mechanisms and effects. *Physics* **2009**, *2*, 20. [CrossRef]
6. Tokura, Y.; Seki, S.; Nagaosa, N. Multiferroics of spin origin. *Rep. Prog. Phys.* **2014**, *77*, 076501. [CrossRef]
7. Fiebig, M.; Lottermoser, T.; Meier, D.; Trassin, M. The evolution of multiferroics. *Nat. Rev. Mater.* **2016**, *1*, 16046. [CrossRef]
8. Heron, J.T.; Trassin, M.; Ashraf, K.; Gajek, M.; He, Q.; Yang, S.Y.; Nikonov, D.E.; Chu, Y.; Salahuddin, H.S.; Ramesh, R. Electric-field-induced magnetization reversal in a ferromagnet-multiferroic heterostructure. *Phys. Rev. Lett.* **2011**, *107*, 217202. [CrossRef]
9. Ueland, B.G.; Lynn, J.W.; Laver, M.; Choi, Y.J.; Cheong, S.-W. Origin of electric-field-induced magnetization in multiferroic $HoMnO_3$. *Phys. Rev. Lett.* **2010**, *104*, 147204. [CrossRef]
10. Kimura, T.; Goto, T.; Shintani, H.; Ishizaka, K.; Arima, T.; Tokura, Y. Magnetic control of ferroelectric polarization. *Nature* **2003**, *426*, 55–58. [CrossRef] [PubMed]
11. Kenzelmann, M.; Harris, A.B.; Jonas, S.; Broholm, C.; Schefer, J.; Kim, S.B.; Zhang, C.L.; Cheong, S.-W.; Vajk, O.P.; Lynn, J.W. Magnetic inversion symmetry breaking and ferroelectricity in $TbMnO_3$. *Phys. Rev. Lett.* **2005**, *95*, 087206. [CrossRef]
12. Pomjakushin, V.Y.; Kenzelmann, M.; Dönni, A.; Harris, A.B.; Nakajima, T.; Mitsuda, S.; Tachibana, M.; Keller, L.; Mesot, J.; Kitazawa, H.; et al. Evidence for large electric polarization from collinear magnetism in $TmMnO_3$. *New J. Phys.* **2009**, *11*, 043019. [CrossRef]
13. Mukherjee, S.; Dönni, A.; Nakajima, T.; Mitsuda, S.; Tachibana, M.; Kitazawa, H.; Pomjakushin, V.; Keller, L.; Niedermayer, C.; Scaramucci, A.; et al. E-type noncollinear magnetic ordering in multiferroic o-$LuMnO_3$. *Phys. Rev. B* **2017**, *95*, 104412. [CrossRef]
14. Tokunaga, Y.; Iguchi, S.; Arima, T.; Tokura, Y. Magnetic-field-induced ferroelectric state in $DyFeO_3$. *Phys. Rev. Lett.* **2008**, *101*, 097205. [CrossRef] [PubMed]
15. Tokunaga, Y.; Taguchi, Y.; Arima, T.H.; Tokura, Y. Electric-field-induced generation and reversal of ferromagnetic moment in ferrites. *Nat. Phys.* **2012**, *8*, 838–844. [CrossRef]
16. Bousquet, E.; Cano, A. Non-collinear magnetism in multiferroic perovskites. *J. Phys. Condens. Matter* **2016**, *28*, 123001. [CrossRef] [PubMed]
17. Lee, J.-H.; Jeong, Y.K.; Park, J.H.; Oak, M.-A.; Jang, H.M.; Son, J.Y.; Scott, J.F. Spin-canting-induced improper ferroelectricity and spontaneous magnetization reversal in $SmFeO_3$. *Phys. Rev. Lett.* **2011**, *107*, 117201. [CrossRef]
18. Johnson, R.D.; Terada, N.; Radaelli, P.G. Comment on "Spin-canting-induced improper ferroelectricity and spontaneous magnetization reversal in $SmFeO_3$". *Phys. Rev. Lett.* **2012**, *108*, 219701. [CrossRef] [PubMed]
19. Kuo, C.-Y.; Drees, Y.; Fernández-Díaz, M.T.; Zhao, L.; Vasylechko, L.; Sheptyakov, D.; Bell, A.M.T.; Pi, T.W.; Lin, H.-J.; Wu, M.-K.; et al. k = 0 magnetic structure and absence of ferroelectricity in $SmFeO_3$. *Phys. Rev. Lett.* **2014**, *113*, 217203. [CrossRef]
20. Rajeswaran, B.; Sanyal, D.; Chakrabarti, M.; Sundarayya, Y.; Sundaresan, A.; Rao, C.N.R. Interplay of 4f-3d magnetism and ferroelectricity in $DyFeO_3$. *EPL* **2013**, *101*, 17001. [CrossRef]
21. Saha, R.; Sundaresan, A.; Rao, C.N.R. Novel features of multiferroic and magnetoelectric ferrites and chromites exhibiting magnetically driven ferroelectricity. *Mater. Horiz.* **2014**, *1*, 20–31. [CrossRef]
22. Oliveira, G.N.P.; Teixeira, R.C.; Moreira, R.P.; Correia, J.G.; Araújo, J.P.; Lopes, A.M.L. Local inhomogeneous state in multiferroic $SmCrO_3$. *Sci. Rep.* **2020**, *10*, 4686. [CrossRef]
23. Zvezdin, A.K.; Gareeva, Z.V.; Chen, X.M. Multiferroic order parameters in rhombic antiferromagnets $RCrO_3$. *J. Phys. Condens. Matter* **2021**, *33*, 385801. [CrossRef]
24. Prado-Gonjal, J.; Schmidt, R.; Romero, J.-J.; Ávila, D.; Amador, U.; Morán, E. Microwave-assisted synthesis, microstructure, and physical properties of rare-earth chromites. *Inorg. Chem.* **2013**, *52*, 313–320. [CrossRef]
25. Zhang, C.; Zhang, T.; Ge, L.; Wang, S.; Yuan, H.; Feng, S. Hydrothermal synthesis and multiferroic properties of Y_2NiMnO_6. *RSC Adv.* **2014**, *4*, 50969–50974. [CrossRef]
26. Su, J.; Yang, Z.; Lu, X.; Zhang, J.; Gu, L.; Lu, C.; Li, Q.; Liu, J.; Zhu, J. Magnetism-driven ferroelectricity in double perovskite Y_2NiMnO_6. *ACS Appl. Mater. Interfaces* **2015**, *7*, 13260–13265. [CrossRef]
27. Nhalil, H.; Nair, H.S.; Kumar, C.M.N.; Strydom, A.M.; Elizabeth, S. Ferromagnetism and the effect of free charge carriers on electric polarization in the double perovskite Y_2NiMnO_6. *Phys. Rev. B* **2015**, *92*, 214426. [CrossRef]
28. Sánchez-Benítez, J.; Martínez-Lope, M.J.; Alonso, J.A.; García-Muñoz, J.L. Magnetic and structural features of the $NdNi_{1-x}Mn_xO_3$ perovskite series investigated by neutron diffraction. *J. Phys. Condens. Matter* **2011**, *23*, 226001. [CrossRef] [PubMed]
29. Retuerto, M.; Muñoz, Á.; Martínez-Lope, M.J.; Alonso, J.A.; Mompeán, F.J.; Fernández-Díaz, M.T.; Sánchez-Benítez, J. Magnetic interactions in the double perovskites R_2NiMnO_6 (R = Tb, Ho, Er, Tm) investigated by neutron diffraction. *Inorg. Chem.* **2015**, *54*, 10890–10900. [CrossRef] [PubMed]

30. Booth, R.J.; Fillman, R.; Whitaker, H.; Nag, A.; Tiwari, R.M.; Ramanujachary, K.V.; Gopalakrishnan, J.; Lofland, S.E. An investigation of structural, magnetic and dielectric properties of R_2NiMnO_6 (R = rare earth, Y). *Mater. Res. Bull.* **2009**, *44*, 1559–1564. [CrossRef]
31. Nasir, M.; Kumar, S.; Patra, N.; Bhattacharya, D.; Jha, S.N.; Basaula, D.R.; Bhatt, S.; Khan, M.; Liu, S.-W.; Biring, S.; et al. Role of antisite disorder, rare-earth size, and superexchange angle on band gap, Curie temperature, and magnetization of R_2NiMnO_6 double perovskites. *ACS Appl. Electron. Mater.* **2019**, *1*, 141–153. [CrossRef]
32. Asai, K.; Fujiyoshi, K.; Nishimori, N.; Satoh, Y.; Kobayashi, Y.; Mizoguchi, M. Magnetic properties of $REMe_{0.5}Mn_{0.5}O_3$ (RE = rare earth element, Me = Ni, Co). *J. Phys. Soc. Jpn.* **1998**, *67*, 4218–4228. [CrossRef]
33. Sobolev, A.V.; Glazkova, I.S.; Akulenko, A.A.; Sergueev, I.; Chumakov, A.I.; Yi, W.; Belik, A.A.; Presniakov, I.A. ^{61}Ni nuclear forward scattering study of magnetic hyperfine interactions in double perovskites A_2NiMnO_6 (A = Sc, In, Tl). *J. Phys. Chem.* **2019**, *123*, 23628–23634. [CrossRef]
34. Ding, L.; Khalyavin, D.D.; Manuel, P.; Blake, J.; Orlandi, F.; Yi, W.; Belik, A.A. Colossal magnetoresistance in the insulating ferromagnetic double perovskites Tl_2NiMnO_6: A neutron diffraction study. *Acta Mater.* **2019**, *173*, 20–26. [CrossRef]
35. Terada, N.; Colin, C.V.; Qureshi, N.; Hansen, T.; Matsubayashi, K.; Uwatoko, Y.; Belik, A.A. Pressure-induced incommensurate antiferromagnetic order in a ferromagnetic B-site ordered double-perovskite Lu_2NiMnO_6. *Phys. Rev. B* **2020**, *102*, 094412. [CrossRef]
36. Zhang, C.; Zhu, W.; Yuan, L.; Yuan, H. B-site ordering, magnetic and dielectric properties of hydrothermally synthesized Lu_2NiMnO_6. *J. Alloys Compd.* **2018**, *744*, 395–403. [CrossRef]
37. Chanda, S.; Saha, S.; Dutta, A.; Murthy, J.K.; Venimadhav, A.; Shannigrahi, S.; Sinha, T.P. Magnetic ordering and conduction mechanism of different electroactive regions in Lu_2NiMnO_6. *J. Appl. Phys.* **2016**, *120*, 134102. [CrossRef]
38. Zhang, L.; Shi, T.L.; Cao, J.J.; Yan, S.M.; Fang, Y.; Han, Z.D.; Qian, B.; Jiang, X.F.; Wang, D.H. Critical behavior and magnetocaloric effect in the multiferroic double perovskite Lu_2NiMnO_6. *J. Alloys Compd.* **2018**, *763*, 613–621. [CrossRef]
39. Katari, V.; Babu, P.D.; Mishra, S.K.; Mittal, R.; Bevara, S.; Achary, S.N.; Deshpande, S.K.; Tyagi, A.K. Effect of preparation conditions on magnetic and dielectric properties of Y_2MMnO_6 (M = Co, Ni). *J. Am. Ceram. Soc.* **2016**, *99*, 499–506. [CrossRef]
40. Kakarla, D.C.; Jyothinagaram, K.M.; Das, A.K.; Adyam, V. Dielectric and magnetodielectric properties of R_2NiMnO_6 (R = Nd, Eu, Gd, Dy, and Y). *J. Am. Ceram. Soc.* **2014**, *97*, 2858–2866. [CrossRef]
41. Zhang, C.Y.; Wang, Z.Z.; Yuan, L.; Ti, R.X.; Wu, H.R.; Yuan, H.M. Double perovskites R_2NiMnO_6 with small R^{3+} cations: Magnetic interactions tuned by R^{3+} ionic radius and the role of orbital ordering. *J. Alloys Compd.* **2025**, *1039*, 182997. [CrossRef]
42. Shannon, R.D. Revised effective ionic radii and systematic studies of interatomic distances in halides and chalcogenides. *Acta Crystall. A* **1976**, *32*, 751–767. [CrossRef]
43. Yi, W.; Princep, A.J.; Guo, Y.F.; Johnson, R.D.; Khalyavin, D.D.; Manuel, P.; Senyshyn, A.; Presniakov, I.A.; Sobolev, A.V.; Matsushita, Y.; et al. Sc_2NiMnO_6: A double-perovskite with a magnetodielectric response driven by multiple magnetic orders. *Inorg. Chem.* **2015**, *54*, 8012–8021. [CrossRef] [PubMed]
44. Yi, W.; Liang, Q.F.; Matsushita, Y.; Tanaka, M.; Belik, A.A. High-pressure synthesis, crystal structure, and properties of In_2NiMnO_6 with antiferromagnetic order and field-induced phase transition. *Inorg. Chem.* **2013**, *52*, 14108–14115. [CrossRef] [PubMed]
45. Terada, N.; Khalyavin, D.D.; Manuel, P.; Yi, W.; Suzuki, H.S.; Tsujii, N.; Imanaka, Y.; Belik, A.A. Ferroelectricity induced by ferriaxial crystal rotation and spin helicity in a B-site-ordered double-perovskite multiferroic In_2NiMnO_6. *Phys. Rev. B* **2015**, *91*, 104413. [CrossRef]
46. Vasil'ev, A.N.; Volkova, O.S. New functional materials $AC_3B_4O_{12}$ (Review). *Low Temp. Phys.* **2007**, *33*, 895–914. [CrossRef]
47. Long, Y. A-site ordered quadruple perovskite oxides $AA'_3B_4O_{12}$. *Chin. Phys. B* **2016**, *25*, 078108. [CrossRef]
48. Yamada, I. Novel catalytic properties of quadruple perovskites. *Sci. Technol. Adv. Mater.* **2017**, *18*, 541–548. [CrossRef]
49. Belik, A.A.; Johnson, R.D.; Khalyavin, D.D. The rich physics of A-site-ordered quadruple perovskite manganites AMn_7O_{12}. *Dalton Trans.* **2021**, *50*, 15458–15472. [CrossRef]
50. Solana-Madruga, E.; Arevalo-Lopez, A.M. High-pressure A-site manganites: Structures and magnetic properties. *J. Solid State Chem.* **2022**, *315*, 123470. [CrossRef]
51. Ding, J.; Zhu, X.H. Research progress on quadruple perovskite oxides. *J. Mater. Chem. C* **2024**, *12*, 9510–9561. [CrossRef]
52. Belik, A.A. A site-ordered quadruple perovskites, $RMn_3Ni_2Mn_2O_{12}$ with R = Bi, Ce, and Ho, with different degrees of B site ordering. *Molecules* **2025**, *30*, 1749. [CrossRef]
53. Yin, Y.Y.; Liu, M.; Dai, J.H.; Wang, X.; Zhou, L.; Cao, H.; Cruz, C.D.; Chen, C.T.; Xu, Y.; Shen, X.; et al. $LaMn_3Ni_2Mn_2O_{12}$: An A-and B-site ordered quadruple perovskite with A-site tuning orthogonal spin ordering. *Chem. Mater.* **2016**, *28*, 8988–8996. [CrossRef]
54. Liu, M.; Hu, C.-E.; Cheng, C.; Chen, X.R. A–B-intersite-dependent magnetic order and electronic structure of $LaMn_3Ni_2Mn_2O_{12}$: A first-principles study. *J. Phys. Chem. C* **2018**, *122*, 1946–1954. [CrossRef]
55. Belik, A.A.; Liu, R.; Tanaka, M.; Yamaura, K. B-site-ordered and disordered structures in A-site-ordered quadruple perovskites $RMn_3Ni_2Mn_2O_{12}$ with R = Nd, Sm, Gd, and Dy. *Molecules* **2024**, *29*, 5488. [CrossRef]

56. Kittel, C.; McEuen, P. *Introduction to Solid State Physics*; John Wiley & Sons, Inc.: New York, NY, USA, 2005.
57. Higashiyama, D.; Miyasaka, S.; Tokura, Y. Magnetic-field-induced polarization and depolarization in $HoMn_2O_5$ and $ErMn_2O_5$. *Phys. Rev. B* **2005**, *72*, 064421. [CrossRef]
58. Mihailova, B.; Gospodinov, M.M.; Güttler, B.; Yen, F.; Litvinchuk, A.P.; Iliev, M.N. Temperature-dependent Raman spectra of $HoMn_2O_5$ and $TbMn_2O_5$. *Phys. Rev. B* **2005**, *71*, 172301. [CrossRef]
59. Radulov, I.; Nizhankovskii, V.I.; Lovchinov, V.; Dimitrov, D.; Apostolov, A. Colossal magnetostriction effect in $HoMn_2O_5$. *Eur. Phys. J. B* **2006**, *52*, 361–364. [CrossRef]
60. Tzankov, D.; Skumryev, V.; Aroyo, M.; Puzniak, R.; Kuz'min, M.D.; Mikhov, M. Magnetic anisotropy of multiferroic $HoMn_2O_5$ single crystal. *Solid State Commun.* **2008**, *147*, 212–216. [CrossRef]
61. Boldrin, M.; Bagri, A.; Barlettani, D.; Teather, E.; Squillante, L.; de Souza, M.; Pontes, R.B.; Silva, A.G.; Mori, T.J.A.; Perry, R.; et al. Magnetostriction as the origin of the magnetodielectric effect in La_2CoMnO_6. *Phys. Rev. Mater.* **2025**, *9*, 094403. [CrossRef]
62. Manikandan, M.; Ghosh, A.; Mahendiran, R. Giant magnetostriction in La_2CoMnO_6 synthesized by microwave irradiation. *Appl. Phys. Lett.* **2023**, *123*, 022403. [CrossRef]
63. Izumi, F.; Ikeda, T. A Rietveld-analysis program RIETAN-98 and its applications to zeolites. *Mater. Sci. Forum* **2000**, *321–324*, 198–205. [CrossRef]
64. Kumar, R.; Sundaresan, A. Unveiling a hidden multiferroic state under magnetic fields in $BaHoFeO_4$. *Phys. Rev. B* **2023**, *107*, 184420. [CrossRef]

Disclaimer/Publisher's Note: The statements, opinions and data contained in all publications are solely those of the individual author(s) and contributor(s) and not of MDPI and/or the editor(s). MDPI and/or the editor(s) disclaim responsibility for any injury to people or property resulting from any ideas, methods, instructions or products referred to in the content.

inorganics

MDPI

Review

A Review of Synthesis, Characterization, Properties, and Applications of Double Perovskite Oxides

Pablo V. Tuza [1,*] and Mariana M. V. M. Souza [2]

[1] Facultad de Ciencia e Ingeniería en Alimentos y Biotecnología, Universidad Técnica de Ambato, Ambato 180216, Ecuador
[2] Escola de Química, Universidade Federal do Rio de Janeiro (UFRJ), Rio de Janeiro 21941-909, RJ, Brazil; mmattos@eq.ufrj.br
* Correspondence: pablo.tuza.alvarado@gmail.com; Tel.: +593-2400987

Abstract: Double perovskites are represented by the formula $A_2BB'O_6$ and $AA'BB'O_6$. These materials have been synthesized using the solid-state reaction, sol–gel, Pechini, and hydrothermal methods. X-ray fluorescence, X-ray diffraction, magnetic measurements, transmission electron microscopy, X-ray photoelectron spectroscopy, temperature-programmed reduction, synchrotron X-ray diffraction, neutron powder diffraction, extended X-ray absorption fine structure, and Raman spectroscopy have been used for the characterization of double perovskites. X-ray diffraction, synchrotron X-ray diffraction, and neutron powder diffraction coupled with the Rietveld method determine the crystal structure of a sample. These materials present various properties and applications. The present review aims (i) to report a process to determine the symmetry, apparent size, and apparent strain using the Rietveld method; (ii) show how experimental characterization techniques complement each other in the investigation of double perovskites; (iii) describe how the synthesis method can help in the uncovering of double perovskites with improved properties; and (iv) exemplify some of the main applications of double perovskites.

Keywords: double perovskites; synthesis; X-ray diffraction; Rietveld method; characterization; applications

1. Introduction

Perovskites are mixed oxides represented by the formula ABO_3, where A is an alkali earth or rare earth metal, and B can be a transition metal [1]. The crystalline structure of this material can be represented using octahedra sharing corners. The oxygen atoms are positioned at the octahedra vertices, the octahedra centers are occupied by B cations, and the A cations are placed in the cavities between the octahedra, as depicted in Figure 1, which was drawn using the Vesta software (version 3.90.0a) [2].

Double perovskites (DPs) can be represented by the formula $A_2BB'O_6$ or $AA'BB'O_6$ [3], where the apostrophe symbol indicates a DP containing distinct metal ions with the same molar composition. There are three types of B-cation arrangement for DPs: random, rock salt, and layered [3], which are indicated in Figure 2. For the case of the random arrangement, the octahedra are randomly distributed in the structure. In the rock salt ordering case, the octahedra are ordered as the sodium and chloride ions in the NaCl structure. As indicated in its name, in the layered DP, BO_6, and $B'O_6$ octahedra layers are intercalated between them. It is worth mentioning that ABO_3 perovskites with B cations with a molar ratio different from 0.5 mol can be represented using the DP random arrangement.

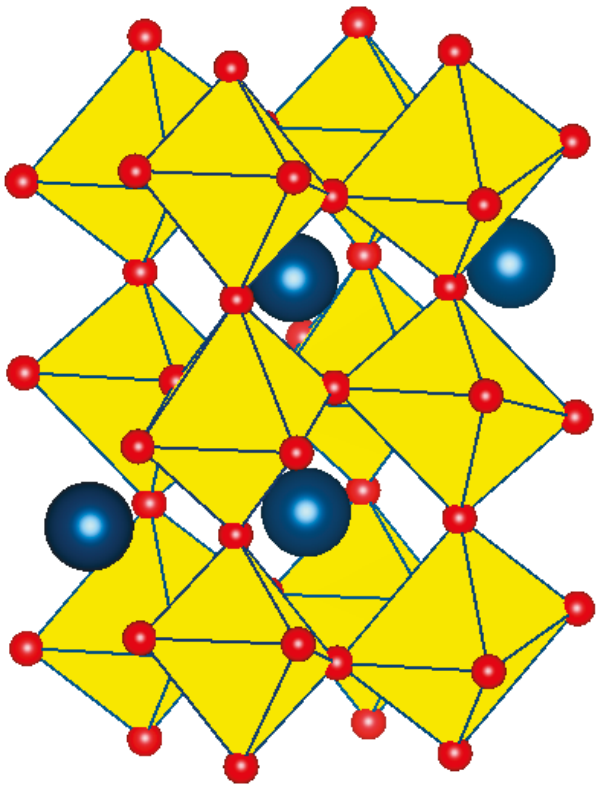

Figure 1. Perovskite crystal structure, where the A cation and oxygen ions are dark-blue and red spheres, and the B cation is in the octahedral center.

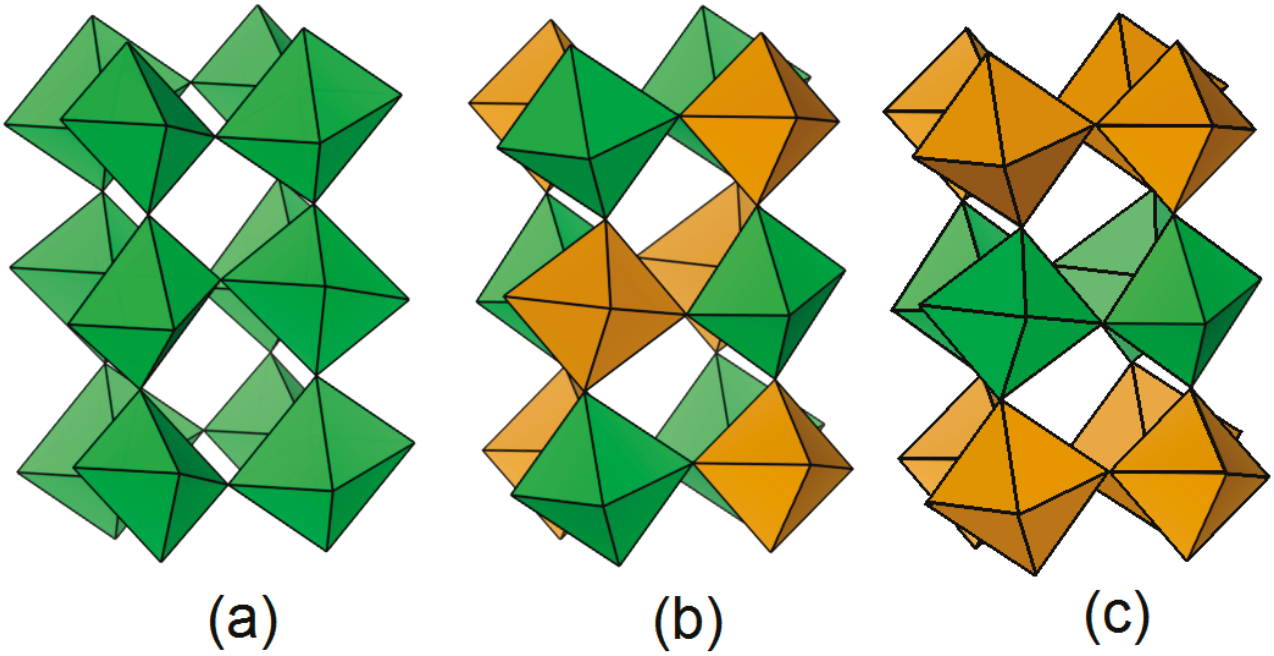

Figure 2. (**a**) Random, (**b**) rock salt, and (**c**) layered arrangements for DPs. For the random arrangement, both BO_6 and $B'O_6$ octahedra are depicted in green. In contrast, for the rock-salt and layered orderings, BO_6 octahedra are shown in green, while $B'O_6$ octahedra are depicted in light brown.

Surface exchange and diffusion of oxygen ions, conductivity enhancement [4], and improvement of catalytic properties are advantages of DPs over ABO_3 materials. For example, La_2NiTiO_6, which contains $LaNiO_3$ and $LaTiO_3$, shows stable catalytic activity for the steam reforming of methane compared to the low-stable Ni or the inactive Ti perovskite,

as the DP presents enhanced metal–support interaction compared to the conventional perovskites [5].

B and B′ cation arrangement in DPs mostly depends on B and B′ valence differences [6], but it also may be influenced by B and B′ ionic radius differences, as occurs for the Bi_2AlGaO_6 and Bi_2AlInO_6 [7]. Furthermore, the calcination time may influence the arrangement, as La-Ni-Ti-containing DPs with random ordering changed to a rock-salt arrangement by modifying the calcination step from 17 h at 800 °C to 135 h at 1000 °C [8].

2. Synthesis

DPs can contain B cations with mixed valences, and this allows for the design of several mixed oxides in accord with the octet rule and the preparation. Four preparation methods are mostly used to prepare these mixed oxides: the solid-state reaction, the sol–gel, the modified Pechini, and the hydrothermal methods.

2.1. Solid-State Reaction Method

The solid-state reaction is the most employed method to synthesize DPs. It consists of mixing adequate amounts of oxide [9] or carbonate [10] precursors of DPs. Then, the mixture is calcined at high temperatures, like 1400 °C [11], for diffusion and chemical reaction of the starting materials. It is worth noting that oxide diffusion is so low at 500 °C [12]. Similarly, higher pressures employed during the synthesis process ensure high diffusion rates [13], and this warrants the formation of the DP phase.

The ball-milling period of the precursors prior to their heating influences the morphology. Zouridi et al. [14] established that the mechanochemical step influences the particle size and produces a spherical nanometric single-phase $La_{0.5}Sr_{0.5}Ti_{0.5}Mn_{0.5}O_{3-\delta}$. Moreover, the perovskite phase can form during the ball-milling process, as observed for the $La_{1-x}Sr_xTi_{1-y}Mn_yO_{3\pm\delta}$ [15]. Furthermore, the microstrain depends on the ball-milling time, as described for the $SrTiO_3$ [16].

An oxygenless atmosphere can influence the formation of DPs. Wlodarczyk et al. [13] established that the Ar atmosphere inhibits cation oxidation during the preparation of the Ba_2CeWO_6. Moreover, the final calcination step for the formation of the single-phase Sr_2FeMoO_6 was 1500 °C for 12 h in 2% H_2/Ar, followed by 1500 °C for 6 h [17], whereas it was 1074 °C for 4 h in 3% H_2/Ar [18]. It is worth noting that the last sample contained about 2 wt% impurities of Fe and $SrMoO_4$.

The sintering temperature affects the coherent length [16], but this condition also affects other properties. Nadig et al. [19] indicated that the $La_{0.67}Ca_{0.33}MnO_3$ calcined from 900 °C to 1200 °C presented the optimal oxygen content for the sample heated to 1100 °C, and this oxygen amount affects its cooling power.

2.2. Sol–Gel Method

The sol–gel method, also known as the citrate sol–gel method [20], is widely used for the preparation of DPs. In this method, nitrates [21], oxides, organometallic compounds [22], and metals [23] of DPs are used as starting materials. As can be found in work by Valdés et al. [24], all precursors are mixed, including the citric acid, in pH-adjusted water using NH_4OH at 80 °C. The resulting mixture was transformed into a gel at 90 °C for 24 h after evaporation at 80 °C. Finally, this last solid was calcined and then reduced.

The sol–gel method can be used to obtain DPs at temperatures lower than those employed in the solid-state reaction method. To illustrate this, Valdés et al. [24] used the sol–gel method for the synthesis of Sr_2FeMoO_6 and employed a reducing atmosphere. The maximum temperature used in this work was 1200 °C, and this is less than that used in the solid-state synthesis for the same material (1500 °C, [17]).

Although the sol–gel method followed by ball milling has not been reported in the literature for DPs, this additional step may improve the mixed oxide properties. For instance, Bartoletti et al. [25] reported that the sol–gel synthesis of $CaCu_3Ti_4O_{12}$, before a ball-milling process, increased its number of defects compared to the same material without the mechanochemical step, and this additional step in the synthesis method improved the $CaCu_3Ti_4O_{12}$ catalytic activity.

Some technological differences in the sol–gel method that influence the DP properties have been reported in the literature. For instance, Xu et al. [26] reported the effect of polyvinyl alcohol (PVA) on the synthesis of La_2CoMnO_6. The final calcination temperature was lower compared to that reported without PVA (700 °C, Xu et al. [26] vs. 900 °C, Yousif et al. [27]). Martinez-Rodriguez et al. [28] prepared the $Pr_{1-x}Ba_xMnO_{3-\delta}$ using EDTA and ethylene glycol (EG) in the preparation method. These authors reported that the sol–gel EDTA synthesis produced a sample with the highest proportion of cubic phase compared to the sol–gel EG preparation for x = 0.5, as the first method produces a better thermally stable sample.

Environmentally friendly fuels, such as lactose, fructose, maltose, sugar, and an organic compound-based powder called liquorice, as well as other types of fuels like oxalic acid, maleic acid, green coffee powder, and pomegranate paste, were employed for the preparation of Tb_2ZnMnO_6 [29] and Tb_2FeMnO_6 [30], respectively. These authors claimed homogeneous and smaller particle sizes for the case of maltose fuel used to synthesize the Zn-containing DP, while the best results in size and morphology corresponded to the maleic acid addition to obtain the Fe-containing DP. Additionally, the grape juice used as fuel can modulate the particle size, as reported for the Y_2CrMnO_6 [31].

2.3. Pechini Method

The Pechini method, also known as Pechini sol–gel [32], is characterized by producing a metal-containing polymer. This method is usually carried out in four stages: (i) metal solution preparation, (ii) chelate production through attachment of solution-containing cations and an organic acid like citric acid, (iii) resin production through chelate polymerization, by employing an alcohol such as the EG, and (iv) synthesis of DPs after multiple thermal treatments.

In the first step, precursor solubilization is required. Some low-cost precursors, such as titanium species produced through titanium isopropoxide evaporation, are not water-soluble. Nitric acid can be employed to help solubilize this titanium precursor, like 3.4 mol/L nitric acid [33].

Moreover, the addition of ammonia hydroxide can be carried out in the first step or to adjust the pH after the third step [34]. The addition of ammonia promotes the production of a foam-like structure. For example, Córdova-Calderón et al. [8] reported the formation of this structure after calcining the resin at 450 °C during La_2NiTiO_6 preparation, and this was not claimed by Pérez-Flores et al. [35] in the same sample produced from the calcination of an NH_4OH-free resin.

Some technical differences in the method include ball-milling of the powder from resin calcination [36] or the use of ethylenediaminetetraacetic acid with citric acid as complexing agents [37]. Related to the $CoFe_2O_4$ preparation, Cheraghi et al. [38] used lemon juice, whereas Al-Wasidi and Abdelrahman [32] employed tartaric acid as a source of complexing agents. This last acid may provide small crystallite sizes, as in the synthesis of $MgAl_2O_4$ [39].

Moreover, the EG may be replaced by another alcohol. For instance, dos Santos et al. [40] employed glycerol instead of EG in the synthesis of SiO_2. These authors claimed a higher surface area for the higher weight alcohol, as a result of the polymeric matrix

influence in the product. Cheraghi et al. [38] reported a mixture of sucrose and EG, while Al-Wasidi and Abdelrahman [32] used 1,2-propanediol.

The resin calcination can be performed using a heating rate of 2 °C/min, which may help maintain low gas production from this polyester decomposition. Bataliotti et al. [41] described that the polymer containing Te ions presented three steps of degradation, and these processes accounted for about 90% weight loss and gas production.

2.4. Hydrothermal Method

The hydrothermal method is carried out by employing nitrates and ammonium salts [42], chlorides [43], and organometallic compounds [44] of double-perovskite-containing metals. To begin with, a solution is obtained from the precursors, and then it is placed in a Teflon-lined stainless-steel autoclave for thermal treatment. Finally, the products are washed and dried.

The hydrothermal method has influenced the structure of DPs. Yi et al. [45] claimed that the dielectric behavior of La_2FeCrO_6 is related to its oxygen vacancies. Irfan et al. [46] reported that the Ce_2NiCrO_6, Pr_2NiCrO_6, and Nd_2NiCrO_6 presented agglomerated particles related to the synthesis method. Valdés et al. [24] reported lower particle sizes of Sr_2FeMoO_6 compared to those from the microwave sol–gel method by providing uniform heating in the particle production. Zhang et al. [47] reported that the hydrothermal method promotes the stabilization of the NiO_6 and MnO_6 structures, which are influenced by the size of R^{3+} ions in the R_2NiMnO_6.

The materials containing DPs prepared using the hydrothermal method have shown better catalytic properties than the conventional catalysts. McGuire et al. [48] used Y_2CoMnO_6 and Y_2NiMnO_6 as supports for the Pt catalyst in performing methanol oxidation. Pt/Y_2CoMnO_6 provided a better performance compared to the commercial Pt/C and the Pt/Y_2NiMnO_6, as it has a stronger metal-to-support interaction. These authors also stated that the Y_2CoMnO_6 was more active and stable than the Y_2NiMnO_6 and the commercial IrO_2 for oxygen evolution reaction (OER). Additionally, Y_2CoMnO_6 is a bifunctional catalyst, as it is also active for the oxygen reduction reaction.

The hydrothermal method has been used to prepare DP-containing composites. Sharma et al. [49] observed that the reduced graphite oxide Sr_2TiMnO_6 (Sr_2TiMnO_6-rGO), prepared by mixing graphite oxide and the DP and then aging the blend using the hydrothermal method, presented activity for the Rhodamine B dye due to its absorbance range and bandgap value. The Sr_2TiMnO_6 was prepared following the solid-state reaction method. Moreover, Khan et al. [50] indicated that the LSTN@NiMn-LDH, where LSTN and LDH are $LaSrTiNiO_6$ and lamellar double hydroxides, were prepared by the hydrothermal method and used as a catalyst for the OER and hydrogen evolution reaction (HER). The authors reported that OER occurs because of the interaction between oxygen species and the catalyst, whereas the HER activity is due to a synergistic effect between LSTN and NiMn-LDH.

3. Characterization

3.1. X-Ray Fluorescence

The chemical composition of DPs can be determined through X-ray fluorescence (XRF) using a spectrometer. The results can be expressed on an oxide or a metal basis. Popov et al. [51] reported that the experimental chemical composition of the Ba_2CoNbO_6 on a metallic basis was 2(0.03):1(0.03):0.998(0.03) for Ba:Nb:Co; hence, the composition was within the interval formed by the mean value of the corresponding experimental chemical composition and the standard deviation. The chemical composition and the presence of impurities were established using the X-ray fluorescence method. A value of 5.4 for oxygen

mols in the $Sr_2CoNbO_{6-\delta}$ and impurities in the sample was determined using XRF and confirmed by magnetization measurements [52]. Jin et al. [53] indicated that the Al:Fe experimental molar ratio for the La_2FeAlO_6 prepared using glucose and citric acid was about 1, and these values were obtained using X-ray fluorescence. Also, the chemical composition quantified using X-ray fluorescence indicates mixed valences of Mn in the $Sr_2MnNbO_{6-\delta}$ [54].

3.2. X-Ray Diffraction (XRD)

XRD can be used to determine the crystal structure, the crystallite size, and the phase composition of DPs. XRD is performed in a diffractometer, and its operating parameters are the 2θ range, step size, and count time. The intensity of the main reflection of the XRD pattern should be at least 10,000 a.u., as reported for the XRD of $NdCaFeSnO_6$ [55].

This characterization technique is largely employed to determine the crystal structure. Fabrelli et al. [56] reported that the $La_{2-x}Ba_xCoMnO_6$ presented an evolution from orthorhombic (*Pnma*) to rhombohedral ($R\bar{3}c$), and then to hexagonal ($P6_3/mmc$) as Ba content increases (Figure 3). Zaraq et al. [57] established that the $Sr_2Co_{0.75}Fe_{0.25}TeO_6$, $Sr_2Co_{0.5}Fe_{0.5}TeO_6$, and $Sr_2Co_{0.25}Fe_{0.75}TeO_6$ present monoclinic symmetry and space group $I2/m$ at room temperature. The symmetry was maintained, but the space group changed to $P2_1/n$ at temperatures below 100 K, whereas the symmetry and the space group changed to tetragonal ($I4/m$) and then to cubic ($Fm\bar{3}m$) at high temperatures up to 1100 K. Córdova-Calderón et al. [8] indicated two different symmetries for the La-Ni-Ti DP as a function of the calcination temperature (Figure 4), fostering the synthesis of DPs with desired crystal structures.

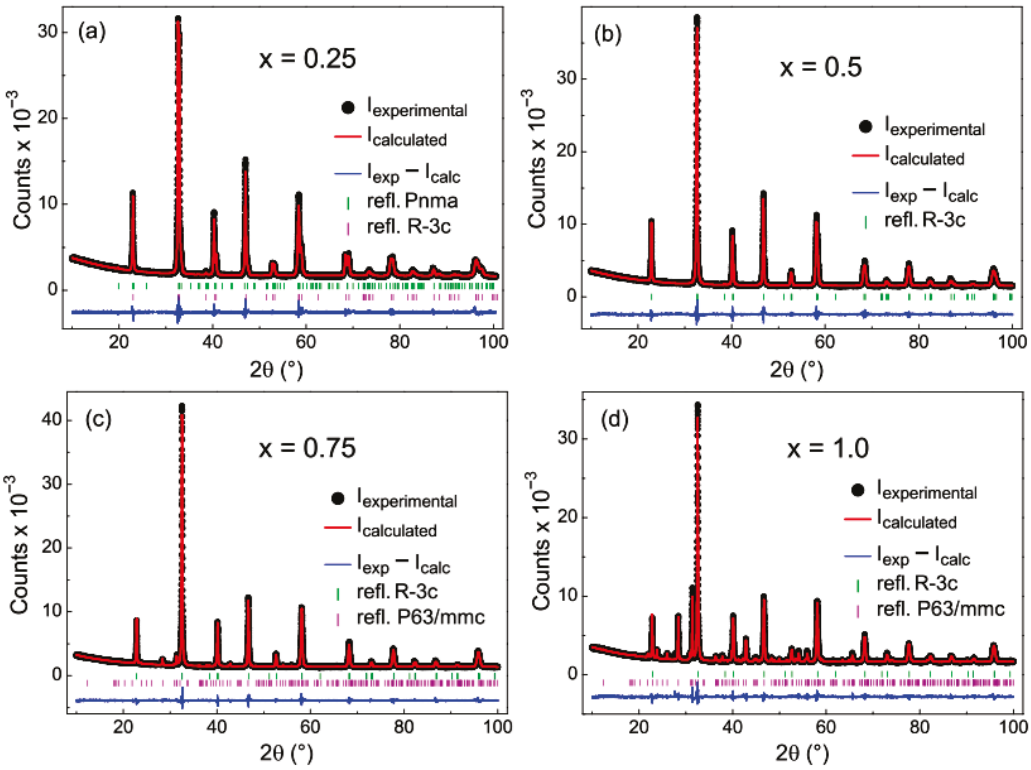

Figure 3. Observed, calculated, and difference XRD patterns of the $La_{2-x}Ba_xCoMnO_6$ for x of (**a**) 0.25, (**b**) 0.5, (**c**) 0.75, and (**d**) 1. Reprinted with permission from Ref. [56].Copyright 2025, Elsevier.

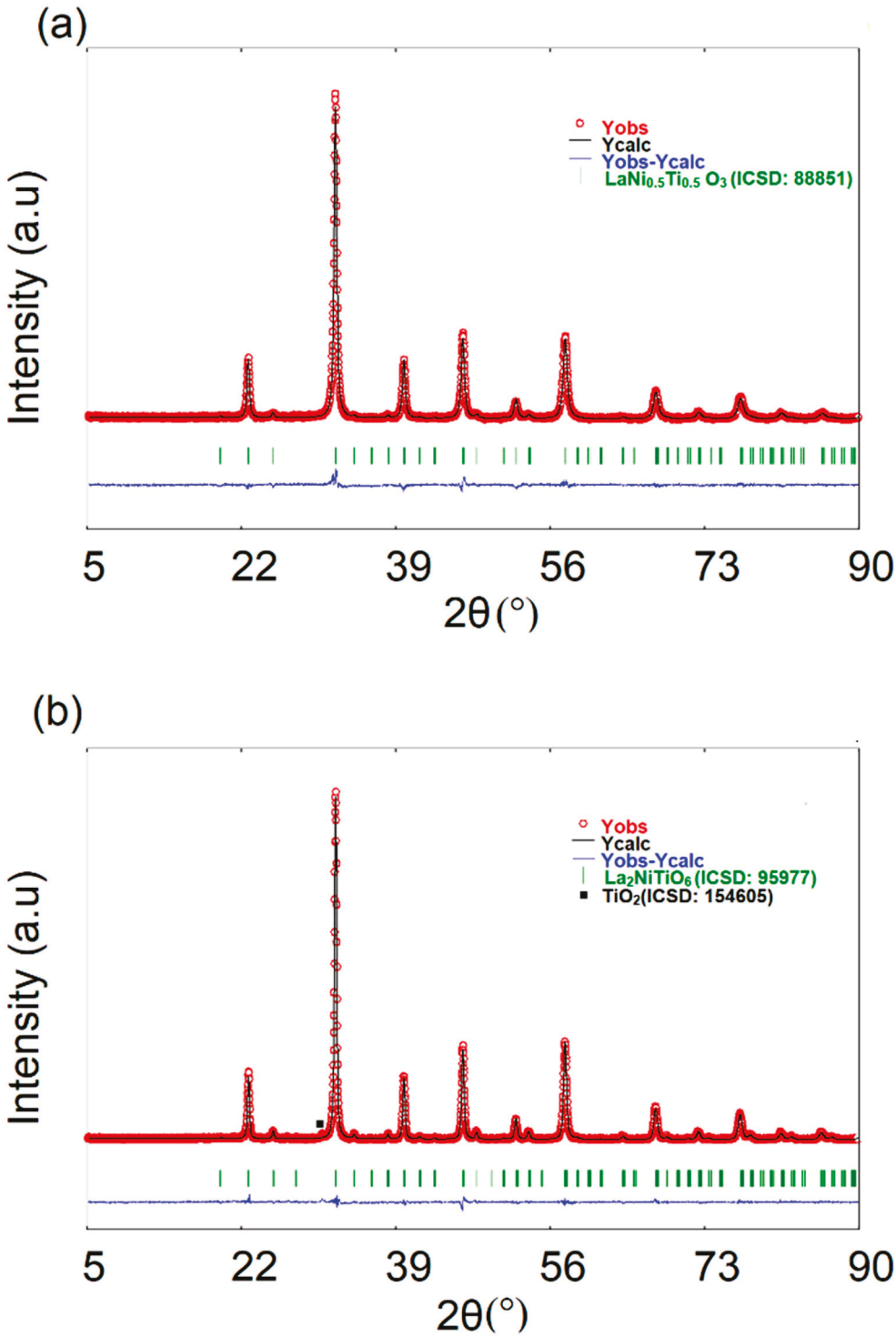

Figure 4. Observed, calculated, and difference XRD patterns of (**a**) $LaNi_{0.5}Ti_{0.5}O_3$ and (**b**) La_2NiTiO_6. Reprinted from Ref. [8].

3.2.1. Crystal Structure Determination

Crystal structures are determined using the Rietveld method, which is implemented in various programs, such as Fullprof [58]. This free and reliable package has been extensively used to refine crystal structures through cyclic steps where the convergence must be achieved.

Free databases like the Crystallographic Open Database share crystallographic information of materials through CIF files. The operator obtains a crystal structure template in a PCR file through the default crystal structure simulation option by opening the CIF

file with the PCR tool of Winplotr [59] and then saving it. The PCR file will be saved in the same CIF file folder. Steps 2 and 3 of Figure 5 depict this procedure, whereas the default and written parameters in a PCR file showing hypothetical values are presented in Table S1. It is important to note that the written parameters in Table S1 should be immediately placed after their prior default row. For instance, row 3 must be added to the PCR file after row 2. In addition, two rows of zeros in rows 8 and 12–17 of Table S1 represent values (top row) and codewords (bottom row) for each parameter, where the codeword enables the parameter refinement. Finally, for the case of the refinement of various parameters in each row, if not specified in the refinement process, the refinement proceeds from left to right.

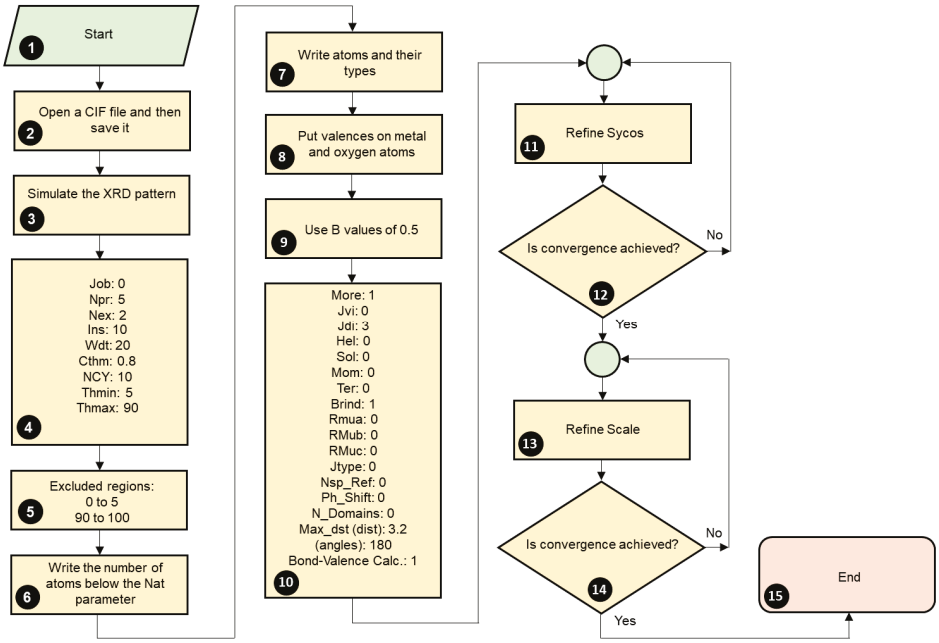

Figure 5. Initial procedure for refining the structure of a DP.

The Rietveld refinement process using the PCR file may be described as five steps: (i) parameter setting, (ii) background, (iii) unit cell parameters, (iv) peak shape parameters, and (v) atomic coordinates refinement.

In the parameter-setting step, an operator changes from simulation to refinement by altering the Job parameter value in row 1 of Table S1 from 2 to 0. Then, the peak shape function is selected and added below the Npr parameter from rows 1 and 9 of Table S1. There are seven different peak functions in Fullprof (version 3.0), and the pseudo-Voigt function is chosen and presented in Table S1. However, other authors prefer the Thompson–Cox–Hastings pseudo-Voigt convoluted with the axial divergence asymmetry function [60]. The suitable function provides better values for the criteria's parameters to judge the quality of refinement.

Next, the researcher specifies the number of excluded 2θ ranges by writing a value for the Nex parameter in row 1 of Table S1 through adding code, depicted in row 6 of Table S1. For instance, if the operator performs the instructions in step 5 of Figure 5, the order-ascending range-containing values, i.e., the lowest and the highest values, replace each row of zeros in row 6 of Table S1.

Moreover, the format of the experimental data, the cut-off of peak profile tails, the monochromator polarization correction, the maximum number of iterations per refinement, the minimum, and the maximum 2θ values are specified through the Ins, Wdt, Cthm, NCY, Thmin, and Thmax parameters in rows 2, 4, and 5 of Table S1.

Furthermore, the operator should add the number of atoms, the atoms, and their valences describing the researched material, as depicted in steps 6 to 8 of Figure 5. The number of atoms (Nat) parameter comprises row 9 of Table S1, whereas the atoms, their types, and valences should be written one above another at row 12 of Table S1. Similarly, the researcher should write literature-based values to isotropic displacement parameters (Biso) for investigations where these values are not refined, as presented by our group [61], and indicated in step 9 of Figure 5. The Biso parameter is contained in row 12 of Table S1.

Additionally, the operator should write 1 for the More parameter located in row 9 of Table S1 and write the code to calculate bond distances and angles, as indicated in row 10 of Table S1. This procedure is shown in step 10 of Figure 5.

Also, the Sycos parameter that accounts for the largest systematic aberration in the Bragg–Brentano geometry [62] and Scale parameters located in rows 7 and 13 of Table S1 are refined, as presented in steps 11 to 14 of Figure 5. In step 11, the operator should select the experimental data saved in the DAT file previously placed in the PCR file folder. Silva et al. [63] refined the Zero parameter in row 7 of Table S1 instead of Sycos. It is worth noting that if the goniometer of the diffractometer is correctly aligned, the Zero parameter should not be refined.

In the background refinement step, four parameters describing the background located in row 8 of Table S1 are refined to ensure convergence is achieved in the program, as depicted in Figure 6.

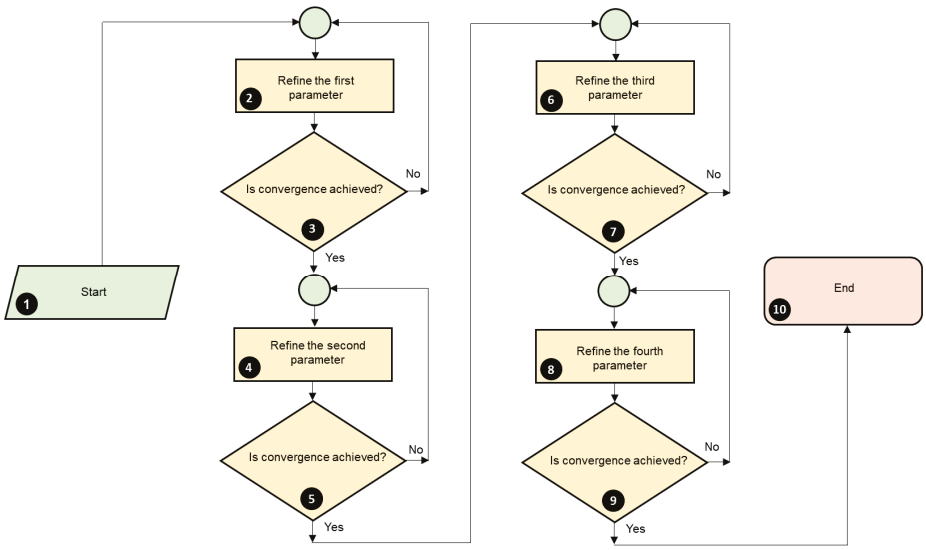

Figure 6. Background refinement through a trial-and-error method.

In the refinement of the unit cell parameters, the operator should refine the unit cell parameters in row 15 of Table S1, as presented in Figure 7, for an orthorhombic symmetry. If the symmetry enables an angle to be refined, like the β angle in the symmetry monoclinic, this angle should be refined after the c parameter (Figure 7), and followed by a convergence verification step, similar to step 7 in Figure 7.

In the refinement step of the peak shape parameters, the operator should refine U, V, W, and X parameters for the peak shape function that are depicted in row 14 of Table S1. It should be observed whether peak shape models enable the refinement of other parameters, like the so-called Shape1; these parameters should be refined right after the X parameter. The procedure of peak shape parameter refinement is presented in Figure 8.

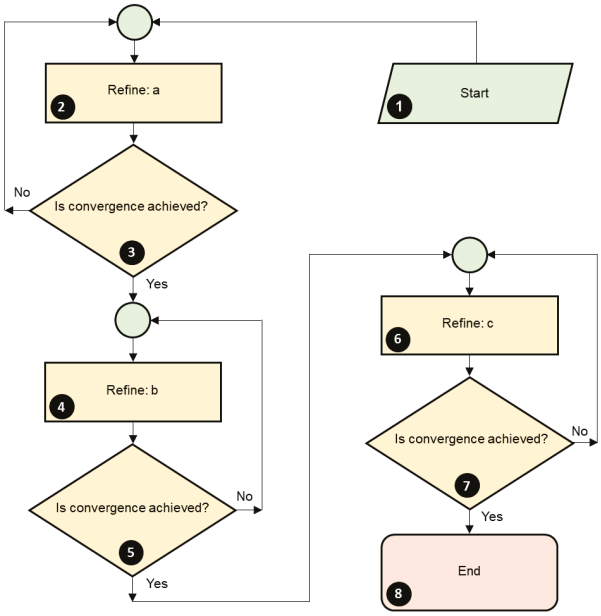

Figure 7. Refinement of unit cell parameters.

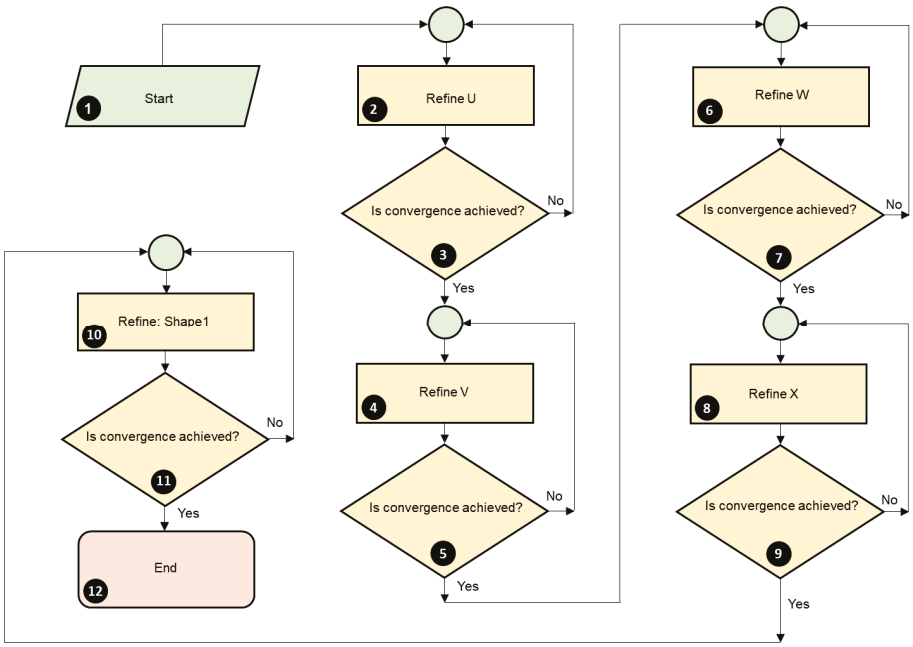

Figure 8. Order of refinement of U, V, W, and X parameters.

The last refinement step involves the atomic coordinates: X, Y, and Z parameters shown in row 14 of Table S1 are refined, as depicted in Figure 9 for a material containing La, Ni, Ti, and O, with orthorhombic symmetry. After the operator has refined all of the atomic coordinates, other parameters, such as Biso and Occ parameters, should be refined.

Furthermore, if the sample powder is packed on a depression of the sample holder prior to the experimental data collection, as recommended by the diffractometer manufacturer, and the diffraction peaks are symmetric, the preferred orientation (Pref1 and Pref2) and asymmetry parameters (Asy1 to Asy4) in row 16 of Table S1 should not be refined. Otherwise, each parameter should be refined after step 16 of Figure 9, following the order of refinement shown in this figure. For this last case, the last 2θ value should be placed under AsyLim located in row 4 of Table S1, to enable the refinement of asymmetry parameters.

It is worth mentioning that preferred orientation is a source of error, as it modifies the diffraction peak intensities [64], and it may occur in compressed samples [65].

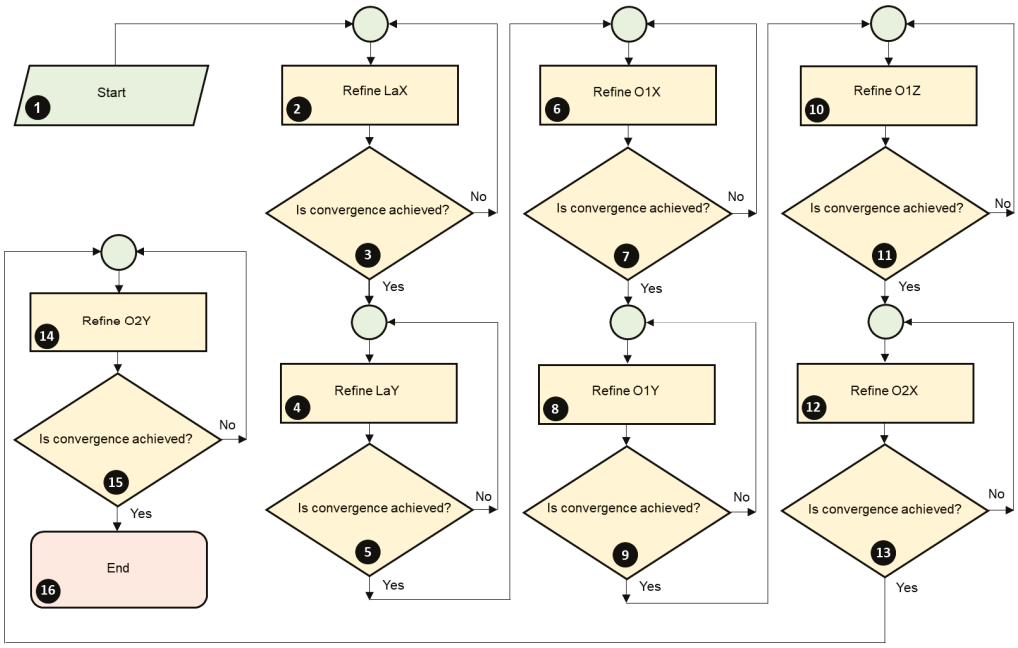

Figure 9. Order of refinement of atomic coordinates for a material containing La, Ni, Ti, and O and an orthorhombic symmetry.

Finally, other authors have refined most of the parameters presented in this work. Silva et al. [63] refined the scale factor, background coefficients, zero-point error, asymmetry, atomic coordinates, Biso, Occ parameters, and unit cell parameters, although they did not describe the order of refinement.

3.2.2. Graph of the Observed and Calculated XRD Pattern

A graph for the observed, calculated, and difference in XRD patterns is presented after finishing the Rietveld refinement method. Bhuyan et al. [66] reported that this graph showed no secondary phase for the Gd_2FeCrO_6 sample. Hosen et al. [20] established the absence of long-range ordering of B cations through the refinement of the crystal structure of Gd_2CoCrO_6 nanoparticles as a result of a peak absence around 20°. However, the graph showed background noise in this sample, which is characteristic of particle sizes at the nanoscale. Guo et al. [67] claimed that the La_2NiRuO_6-calculated pattern corresponds to its experimental profile, as observed in the difference between the data, which is represented below these profiles in the graph. Zaraq et al. [57] reported that the monoclinic $Sr_2Co_{0.5}Fe_{0.5}TeO_6$ presents (111) and $(11\bar{1})$ reflections in the 2θ range 23.5° to 25.5° and (311) $(\bar{3}11)$ (131) $(\bar{1}31)$ reflections in the 2θ range 51° to 53° characterizing the $P2_1/n$ at 100 K; hence, they ensured that the Sr-Co-Fe-Te DP cannot be assigned the space group $I2/m$.

Steps 1 to 5 of Figure 10a present a graph generation procedure for the observed and calculated XRD patterns through the Winplotr tool of the Fullprof package. Step 6 of Figure 10a depicts the edition step, where the operator adds a format to the patterns. Some usual procedures are indicated in Table S2. Step 7 of Figure 10a indicates the export file procedure. This graph is in a BMP file that can be edited in other image-editing programs like Paint.

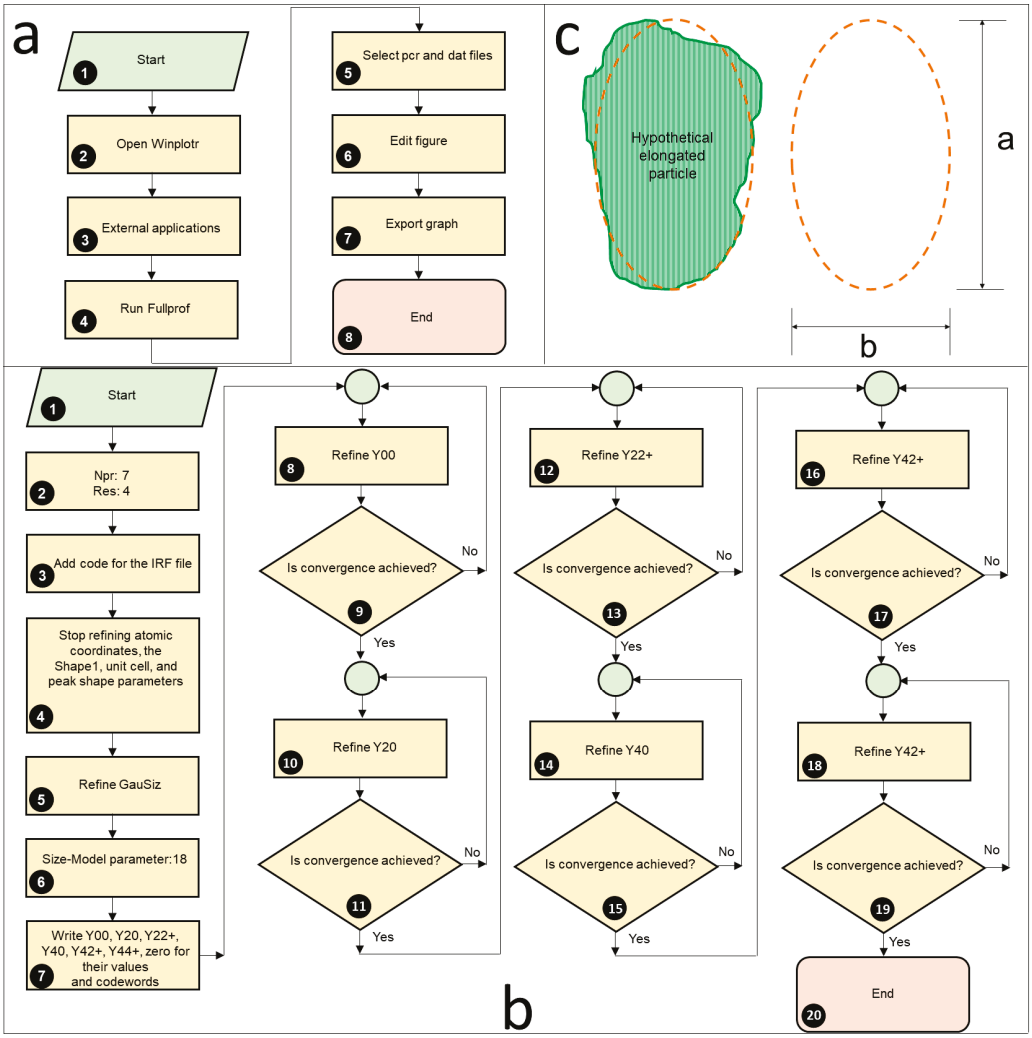

Figure 10. (**a**) Graph generation for the observed and calculated XRD pattern using Fullprof (version 3.0). (**b**) Crystallite size and strain procedure in a PCR file for an orthorhombic symmetry with space group *Pbnm*. (**c**) The a- and b-axes of the orange-dashed ellipse correspond to the axes of the elongated hypothetical particle.

3.2.3. Criteria for Judging the Quality of the Refinement

Several factors, like Rp, Rwp, Rexp, and χ^2, have been used to quantify the quality of a crystal structure refinement. However, there is no consensus on a range of parameter-accepted values. For example, Rp and Rwp values of 21.4 and 26.8 were reported by our group in the refinement of La, Ni, Ti, and Co perovskites [61]. El Hachmi and Sadoune [68] reported values of 4.61 and 5.99 for these same parameters of the crystal structure of the $SrLa_2NiFeNbO_9$.

The R factors should be presented along with bond distances to address the quality of the refinement. For instance, Córdova-Calderón et al. [8] reported Ni-O and Ti-O distances from the structure refinement of $LaNi_{0.5}Ti_{0.5}O_3$ and La_2NiTiO_6 and compared them with previously reported values in the literature to assess the quality of the refinement.

Moreover, the R factors and χ^2 help assign the symmetry and space group for a sample with the same chemical composition but different B cation arrangements. Our group verified that the symmetry and space group for $LaNi_{0.5}Ti_{0.5}O_3$ provided higher R-factor and χ^2 values when used to describe the La_2NiTiO_6 [8].

3.2.4. CIF File Generation

CIF files contain crystallographic sample information that other researchers can use to simulate the XRD pattern using the Fullprof program and then refine the crystal structures of their own samples, as shown in Figures 5–10a. Additionally, they can even draw an image of the crystal structure of the sample using other packages, such as the Vesta software (version 3.90.0a). If the operator has completed the procedures outlined in Figures 5–10a and then enters a codeword of −1 for the Rpa [69] parameter in row 2 of Table S1, the Fullprof program will generate the CIF file for the sample.

3.2.5. Apparent Crystallite Size and Apparent Strain

The apparent crystallite size and apparent strain can be determined through a microstructural analysis in the Fullprof program. Both parameters depend on the full width at half maximum, but the apparent strain is also derived from the Stokes–Wilson apparent strain. Figure 10b presents a summary of the procedure in determining the apparent crystallite size and apparent strain for an orthorhombic structure and space group *Pbnm*. The analysis is performed using the Fullprof program and the default Thompson–Cox–Hastings pseudo-Voigt convoluted with axial divergence asymmetry peak function [70], i.e., Npr of 7, located in rows 1 and 9 of Table S1. The IRF file is derived from a refinement of a standard, such as the CeO_2, and its name and extension are included in the PCR file, as depicted in row 3 of Table S1. A value of 4 for the Res parameter (row 1, Table S1) can describe the information format for this resolution file [62].

Moreover, parameters located from row 12 to 15 of Table S1 should be unchanged by writing zero for their codeword, except for the Scale and the GauSiz. Furthermore, the symmetry and space group should be specified in the Size-Model parameter. For instance, the orthorhombic symmetry with space group *Pbnm* corresponds to a value of 18 [70]. Additionally, the operator should write the crystallite size and strain parameters particular to a crystal structure and space group, as described in steps 7 to 20 of Figure 10b. For example, the parameters shown in row 17 of Table S1 were manually written, and these parameters describe an orthorhombic symmetry, with space group *Pbnm*. As a matter of fact, each symmetry presents its own set of size and strain parameters [70], and these parameters should be refined following the method presented in Figure 10b. On the other hand, it is worth noting that row 17 should replace row 18 in the PCR, and this last row will appear automatically at step 9 of Figure 10b. An MIC file containing the apparent size and apparent strain will be created and saved in the PCR file folder.

3.3. Magnetic Measurements

Magnetic measurements, such as temperature-dependent magnetization in zero-field-cooled (ZFC) and field-cooled (FC) modes at various magnetic fields, can be conducted using a magnetometer. DPs can show various magnetic behaviors. Almadhi et al. [71] demonstrated that $(Ca_{0.5}Mn_{0.5})_2MnTeO_6$ is a spin glass, whereas Shibuya et al. [72] synthesized $Ba_2(Cd_{1-x}Ca_x)ReO_6$ and observed that canted antiferromagnetic (AFM) order and quadrupolar order can be observed for $0 \leq x \leq 0.6$, AFM order and quadrupolar order correspond to $0.6 \leq x \leq 0.9$, and AFM order can be verified for $0.9 \leq x \leq 1$. Agarwal et al. [73] demonstrated different valences and ionic radius mismatches among Co, Cr, and Mn in $La_2Co_{(1-x)}Cr_{(x)}MnO_6$ by increasing the Cr amount through magnetic measurements. This influence reduced the Curie temperature, coercive field, and remanence.

Macchiutti et al. [74] showed the magnetization vs. temperature (M(T)) curves in ZFC and FC modes, the inverse of the magnetic susceptibility vs. temperature ((T)), and the Curie–Weiss law fit for the $La_{1.5}Sr_{0.5}CoMnO_6$ calcined at various temperatures. The authors

observed that a decrease in the M(T) values occurs due to the increase in boundaries, as the number of antiphase domains increases with the grain size [74].

Zhang et al. [75] depicted the ZFC and FC magnetization curves, the first derivative of ZFC curves, the variation in the Curie temperature (T_C), and the glass transition temperature (T_g) as a function of the Ga content for the $La_{1.5}Sr_{0.5}Co_{1-x}Ga_xMnO_6$. It could be observed that the T_g is practically imperceptible for $x \geq 0.3$ due to the dilution effect of the Ga ions in the sample [75].

An important interfacial effect is the Exchange Bias (EB) [76], and it depends essentially on magnetic interactions in the sample. Qiu et al. [77] claimed that an EB field of 1200 Oe at 10 K for the Sr_2FeReO_6-$LaFeO_3$ may be attributed to the B cations arrangement and ferrimagnetic (FiM) nature of the DP interfacing the G-type AFM FeO_6-containing perovskite. Pal et al. [78] contended that the EB results from atoms not occupying their sites and competition of ferromagnetic (FM), AFM, and spin glass interactions in the Sr_2FeRuO_6. Deng et al. [79] described that the EB depends on the spin–orbit coupling on Ir and AFM behavior of the B and B′ cations for the Y_2NiIrO_6. Kush and Srivastava [80] established that the EB depends on surface spins in interfacial frozen glassy states at the FiM particle's interface. Datta et al. [81] indicated that the EB phenomenon results from the competing FiM and AFM interactions for the $NdSrCoIrO_6$. Moreover, while Mahalle et al. [82] reported that the EB is influenced by the applied field for the Gd_2CoRuO_6, Li et al. [83] stated that the EB depends on the FM layer thickness in the $Bi_{0.5}Sr_{0.5}Fe_{0.5}Cr_{0.5}O_3$.

The FM, AFM, FiM, and paramagnetic nature are determined using magnetic scans. While these characteristics are typical of DPs, the AFM behavior is related to B cation ordering. For instance, Córdova-Calderón et al. [8] reported NiO_6 and TiO_6 random ordering in $LaNi_{0.5}Ti_{0.5}O_3$ and a Néel temperature (T_N) of 15 K. Moreover, these authors stated the $LaNi_{0.5}Ti_{0.5}O_3$ Curie–Weiss temperature and the effective magnetic moment by fitting the inverse susceptibility to the Curie–Weiss law. Furthermore, a T_N of 80 K from magnetic measurements is due to the NiO_6 and MoO_6 AFM ordering in the Sr_2NiMoO_6, whereas a T_N of 60 K is related to MoO_6 substitution by the WO_6 [84]. Additionally, a magnetization vs. magnetic field curve justifies FM and AFM domains [20] and indicates multiferroic [85] and ferromagnetic properties [86]. Moreover, the FiM nature in the Ba_2FeMnO_6 depends on the double-exchange interaction of the B and B′ cations through the oxygen [87].

Magnetic susceptibility values derived from magnetization values also present magnetic transitions, as shown by Zaraq et al. [88] for Sr_2FeTeO_6, $Sr_2Fe_{0.75}Ni_{0.25}TeO_6$, $Sr_2Fe_{0.5}Ni_{0.5}TeO_6$, $Sr_2Fe_{0.25}Ni_{0.75}TeO_6$, and Sr_2NiTeO_6. The Curie temperature showed magnetic transitions, and its change with x in $Sr_{2-x}Ce_xFe_{1+x/2}Mo_{1-x/2}O_6$ was identified using magnetic susceptibility measurements [89].

Some structural studies can be performed through magnetic measurements. The progressive Pr substitution in $Sr_{2-x}Pr_xFeTiO_{6-\delta}$ from x = 0.2 to x = 0.8 promoted a transition from AFM to FM [90]. A glassy phase is produced by adding W in $Sr_2NiMo_{1-x}W_xO_6$ ($0 \leq x \leq 1$), as indicated in the ZFC and FC curves at low temperatures [84].

3.4. Transmission Electron Microscopy

Transmission electron microscopy (TEM) provides sample images at the nanometric scale, containing information about the sample morphology and particle size. Guo et al. [67] employed the ImageJ [91] package in the exsolution process of Ni-Ru particles from $La_{1.85}NiRuO_6$ reduced using 3% H_2O-wetted 5% H_2/Ar at 350 °C, finding Ni-Ru particle sizes of about 2.2 nm (Figure 11). Also, these authors measured the interplanar spacing and angles using fringe patterns through the DigitalMicrograph and the ImageJ program. Moreover, these authors manually selected the particles for their size determi-

nation through ImageJ, using a time-consuming procedure. Dara et al. [92] reported that Tb_2CoMnO_6 presented agglomerated particles at the nanoscale, as depicted in Figure 12.

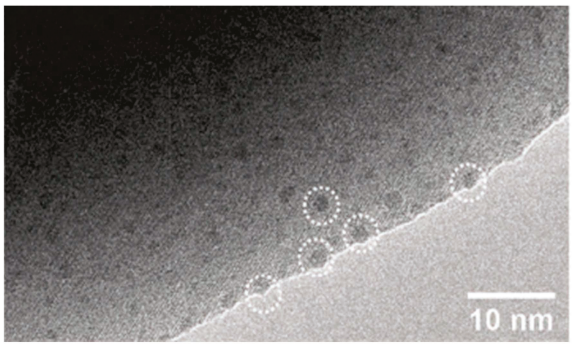

Figure 11. TEM micrograph of reduced $La_{1.85}NiRuO_6$. Reprinted from Ref. [67]. The white-dashed circles indicate Ni-Ru nanoparticles.

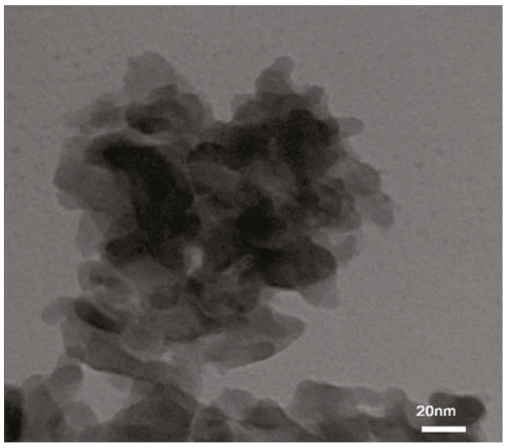

Figure 12. TEM image of Tb_2CoMnO_6. Reprinted from Ref. [92].

The diameter of a spherical particle describes its size. For the case of an elongated particle, its size is the mean of the ellipse axis simulating its shape [93]. Figure 10c presents these axes for a hypothetical particle. Additionally, particle sizes should be equal to or higher than the crystallite size obtained using Size and Strain Analysis from Fullprof, as a particle can be constituted of one or many crystallites. For instance, the Lu_2FeMnO_6's TEM's particle size was 55 nm, whereas its crystallite size was 25.2 nm (Figure 13) [94].

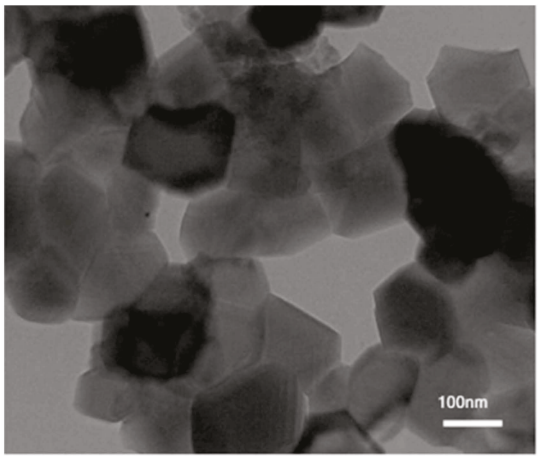

Figure 13. TEM micrograph of the Lu_2FeMnO_6. Reprinted from Ref. [94].

3.5. X-Ray Photoelectron Spectroscopy

X-ray photoelectron spectroscopy (XPS) provides structural information from the surface of the analyzed material, approximately 10 nm deep [95], and indicates the oxidation states of each ion [96]. For example, Ali et al. [97] reported surface $Mn^{3+}O_6$ and $Fe^{3+}O_6$ in La_2MnFeO_6 and surface $Mn^{3+}O_6$ and $Co^{3+}O_6$ in La_2MnCoO_6 using XPS, thereby verifying the structure of a DP in their samples. Sharmili et al. [42] claimed that La_2NiMnO_6 presents a uniform distribution of its constituents. Hosen et al. [20] determined mixed valences for Co and Cr cations in the Gd_2CoCrO_6 through XPS; thus, this DP presents short-range ordering of B cations. Kush and Srivastava [80] established defects in the La_2FeCoO_6 through the analysis of their B cations by using the XPS technique. Bhattacharjee et al. [98] indicated that some Fe^{2+}-O-Fe^{2+} and Fe^{2+}-O-Fe^{3+} interactions for the Ba_2FeVO_6 and Ca_2FeVO_6 were identified through XPS. Zhang et al. [11] reported the La 3d, Mn 2p, and Ni 2p spectra for the La_2MnNiO_6 (Figure 14) that resemble the perovskite characteristic through XPS.

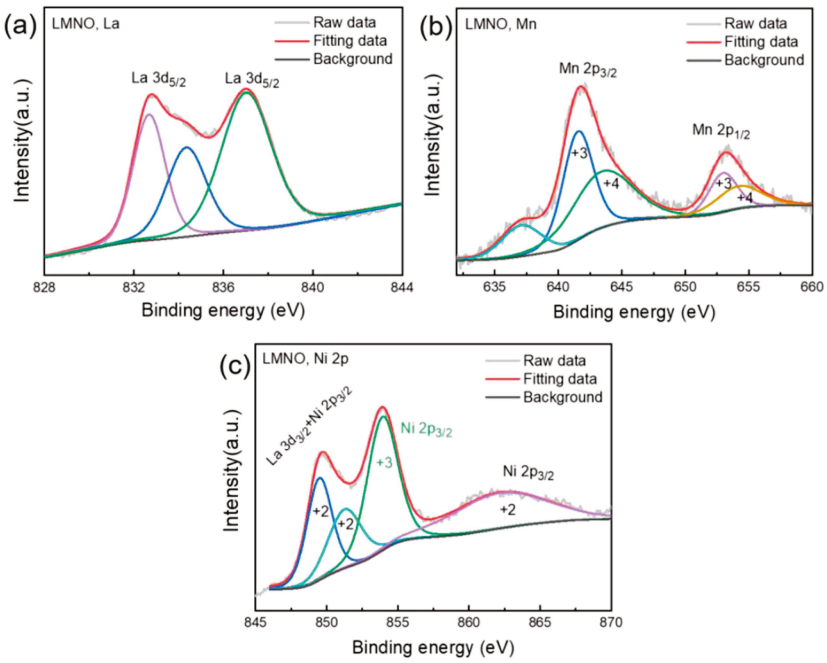

Figure 14. XPS survey scan of the La_2MnNiO_6. XPS spectra of (**a**) La 3d, (**b**) Mn 2p, and (**c**) Ni 2p. Reprinted/adapted with permission from Ref. [11].

Furthermore, XPS provides the surface chemical composition of a sample. For instance, Raji et al. [99] reported that the experimental surface molar ratios for Ba, Co, W, and O in Ba_2CoWO_6 measured through XPS were 1.9, 0.9, 0.85, and 5.8.

Additionally, XPS states the presence of atoms with different valences. For instance, Tang and Zhu [100] reported mixed valences for Fe and Re and two types of oxygen in $La_2FeReO_{6+\delta}$: lattice and adsorbed oxygen. Also, this characterization technique was used to report oxygen vacancies, as in the $NdBaFeTiO_6$ [101]. Additionally, Ghorbani and Ehsani [102] established that the mean oxygen valence of the Ba_2FeMoO_6 was −1.59. Kumar et al. [103] reported an increase in the adsorbed oxygen with a decrease in the Sr content for $Sr_{2-x}FeCoO_{6-\delta}$, as determined by core-level XPS, due to an increase in the number of oxygen vacancies. Furthermore, Ghorbani and Ehsani [104] claimed the generation of mixed valences in $Ba_{2-x}Ag_xFeMoO_6$ for x of 0.025, prepared using the sol–gel method. Yi et al. [105] indicated Cr^{3+}, Cr^{4+}, Ni^{2+}, and Ni^{3+}, lattice and adsorbed oxygen in the La_2CrNiO_6. Moreover, Solanki et al. [106] reported that the ratio of Co^{2+}/Co^{3+} depends on x up to 0.2 for the $La_2CoTi_{1-x}Ni_xO_6$.

3.6. Temperature-Programmed Reduction

The temperature-programmed reduction (TPR) can be carried out in conventional equipment with a TCD or mass detector. Initially, the sample is pretreated to eliminate adsorbed water by heating it under a flow of an inert gas like Ar. Subsequently, the sample is reduced under a flowing reduction mixture like H_2/Ar.

TPR is used to determine surface oxygen species and reduction processes in the sample. La_2AlFeO_6, prepared using glucose and citric acid, demonstrated two peaks: one peak stating the reduction of Fe^{3+} to Fe^{2+} and another peak at high temperatures describing the Fe^{2+} reduction to Fe^0. More Fe^{3+} species are present in the material prepared using glucose, and this was determined through the TPR peak area. Moreover, the mixed oxide prepared using glucose was reduced at lower temperatures than the same material prepared using citric acid [53].

Roozbahania et al. [107] stated that the La_2NiMnO_6 presented two peaks in the TPR profile: the first peak at 378 °C represents the reduction of (i) surface oxygen species, (ii) Mn^{4+} to Mn^{3+}, and (iii) Ni^{3+} to Ni^{2+}. The second peak (at 466 °C) depicts the reduction of (i) lattice oxygen and (ii) Ni^{2+} reduction to Ni^0. These authors also claimed that for La_2CoMnO_6, there was one peak (at 409 °C) showing the reduction of (i) Mn^{4+} to Mn^{3+} and (ii) Co^{3+} to Co^{2+}.

Guamán-Ayala et al. [33] reported that $LaNi_{0.5}Ti_{0.5}O_3$ DP presented two TPR peaks. One peak at low temperatures described the reduction of surface oxygen and Ni^{3+} to Ni^{2+}, whereas the peak at high temperatures indicated the reduction of Ni^{2+} to Ni^0. The peak at high temperatures was confirmed through quantitative phase analysis using the Rietveld method. There is a more delayed H_2 consumption in the La_2NiTiO_6 compared to the $LaNi_{0.5}Ti_{0.5}O_3$ [108].

3.7. Synchrotron X-Ray Diffraction (SXRD)

Synchrotron X-ray powder diffraction measurements can be collected through Debye–Scherrer cameras [109]. Before the data collection, the sample is packed into a capillary, and the measurements can be collected at low temperatures using a cryostat and a blower [110].

These scans can be used to determine the symmetry and space group of a sample. Zhao et al. [111] reported that Pb_2NiMoO_6 presented a monoclinic symmetry with space group *Pc* using synchrotron X-ray powder diffraction dataset. Liang et al. [112] claimed a triclinic crystal structure for Ca_2CuWO_6 with space group $P\bar{1}$ among 100 to 1000 K.

Moreover, these patterns have been used to verify crystal structure stabilities with temperature. da Cruz Pinha Barbosa et al. [113] contended that Ba_2ZnReO_6 presents a transition from cubic to tetragonal at 23 K by using synchrotron radiation. Silva et al. [114] claimed that $SmSrCoFeO_6$ and $EuSrCoFeO_6$ maintain the orthorhombic crystal structure and *Pnma* space group from 9 to 300 K, as stated using a synchrotron X-ray powder diffraction dataset. Morimura and Yamada [109] argued that the CoO_6 and RuO_6 octahedra arrangement in La_2CoRuO_6 changed from rock-salt to random ordering by pressing the sample using 8 GPa and 1373 K, as confirmed by SXRD.

The refinement of the crystal structure can be performed using the Fullprof program, and most of the parameters proposed in this work for the Rietveld method using XRD patterns are fitted in the Rietveld refinement coupled to the SXRD dataset, but following a different refinement strategy. For instance, the unit cell, overall isotropic displacement (Bov, row 13 Table S1), scale, peak shape of the pseudo-Voigt, atomic coordinates, asymmetry, and the background parameters were refined for the $Ce_{1-x}(Nd_{0.74}Tm_{0.26})_xO_{2-x/2}$, where several background points were previously selected, A and B cations were fixed, and the order of refinement is not reported [115].

3.8. Neutron Powder Diffraction (NPD)

The symmetry, space group, and B cation arrangements at low temperatures have been determined using NPD measurements. Ni and Ir moments present ordering below 74 K, as confirmed through 1.5 to 90 K neutron thermodiffractogram [116]. Naveen et al. [117] reported that the $Ca_{2-x}La_xFeRuO_6$ presents orthorhombic symmetry and space group *Pbnm*; hence, these DPs present random ordering of FeO_6 and RuO_6 at temperatures lower than 3 K. The crystal structure and space group at 150 K for $CaMnCoWO_6$ were determined, making use of a neutron-derived fit [118]. Almadhi et al. [71] reported no apparent long arrangement of spins in $(Ca_{0.5}Mn_{0.5})_2MnTeO_6$ at 1.6 K. $Sr_2MnNbO_{6-\delta}$ presents the *Pbnm* space group from 4 to 300 K as established via the NPD method [54].

Magnetic properties can also be studied through neutron diffraction data. Short-range spin orders in $CaMnFeTaO_6$ were verified by the absence of magnetic diffraction peaks in the neutron diffraction patterns [119]. A ferromagnetic order between Mn and Cr in $CaMnCrSbO_6$ was observed through neutron diffraction [120]. Moreover, neutron diffraction patterns of the $CaMnCoWO_6$ revealed magnetic peaks that disappeared through heating from 15 to 20 K [118]. The absence of a magnetic peak at 1.5 K using neutron diffraction was observed for the $CaMnMnWO_6$, and this was related to a spin glass transition at 8 K [121]. A magnetic phase separation for $Sr_2CuTe_{0.3}W_{0.7}O_6$ and $Sr_2CuTe_{0.2}W_{0.8}O_6$ was observed through neutron diffraction measurements [122].

The investigation of the structure has been carried out using neutron diffraction profiles. The amount of Er in $La_{2-x}Er_xNiMnO_6$ preserved the monoclinic symmetry, as verified through Rietveld refinement of neutron diffraction data [123]. Pal et al. [124] stated that the $Pr_{1.5}Sr_{0.5}CoMnO_6$ presented a CoO_6 and MnO_6 random arrangement composed of two symmetries, monoclinic ($P2_1/n$) and orthorhombic (*Pbnm*). Almadhi et al. [71] claimed accurate cation Occ parameters using the contrast in neutron-scattering lengths. Copper sites were partially substituted by iron in $CaCuFeReO_6$, as indicated by the refinement of the mixed oxide crystal structure [125]. Moreover, these authors reported magnetic diffraction peaks in the neutron diffraction patterns collected from 5 to 500 K. To research oxygen positions in $Sr_2Ga_{1-x}Mn_xSbO_6$, the Rietveld refinement of NPD data was employed [126]. Oxygen diffusion paths in the $La_2Ge_{1-x}Cr_xMgO_{6-\delta}$ structure are described through neutron diffraction measurements [127].

The refinement can be performed using the Fullprof program. López et al. [127] reported that in the refinement of the crystal structure of $La_2Ge_{1-x}Cr_xMgO_{6-\delta}$ using NPD, the pseudo-Voigt function was selected, and the scale, background, zero, peak shape, asymmetry, unit cell, and isotropic displacement parameters were refined. The authors also reported the use of scattering lengths in the refinement. The scattering length of oxygen is detectable through NPD [128], compared to XRD, where oxygen cannot be well detected [126]. Similarly, the Ni and Ti in the La_2NiTiO_6 are more detectable in NPD than in XRD, as their scattering lengths are different [108].

3.9. Extended X-Ray Absorption Fine Structure (EXAFS)

EXAFS provides information about the symmetry and the structure. Jeevanandham et al. [129] observed defects in the $La_2Ni_{0.2}Cu_{0.8}MnO_6$. Majumder et al. [130] reported the concentration and distribution of antisite disorders in Sm_2NiMnO_6. Kavaliuk et al. [131] established that the bond length difference between values obtained from EXAFS and XRD are of 0.2 Å in the $BaLn_8Co_2O_{6-\delta}$, $BaLn_{10}Co_2O_{6-\delta}$, $BaLn_{12}Co_2O_{6-\delta}$, and $BaLn_{14}Co_2O_{6-\delta}$, where Ln can be La, Ce, Pr, Nd, Sm, Eu, Gd, Tb, Dy, Ho, Er, Tm, Yb, and Lu, as XRD provides an average value for this parameter.

3.10. Raman Spectroscopy

The crystal structure of DPs has been investigated using Raman spectroscopy. Murthy et al. [132] synthesized the $SrLa_{1-x}Mn_xLiTeO_6$ and claimed the same symmetry for all samples and the Mn inclusion in the perovskite structure. The Cr-O and Fe-O bond lengths in Gd_2FeCrO_6 were calculated using the Raman spectrum and compared to those calculated through XRD, and the difference was 0.04 Å [66]. Chahla et al. [55] indicated that the $NdCaFeSnO_6$ showed bands in the Raman spectrum related to the bending and stretching modes of SnO_6 and FeO_6. Moreover, they reported that the unit cell expansion with the temperature was observed through a peak displacement around 350 cm^{-1} in the Raman spectrum.

Khan et al. [133] established that A-site ordering and anti-site disorder in Gd-doped Y_2CoMnO_6 influence the Raman spectra. Meena et al. [134] stated that $La_{2-x}Ca_xFeMnO_6$ presents improper ordering of FeO_6 and MnO_6 by Raman scattering spectroscopy. Boudad et al. [10] indicated five band shifts in the $LaBaFeTiO_6$ Raman spectrum compared to that of $EuBaFeTiO_6$. Wlodarczyk et al. [13] reported that Ba_2CeWO_6 decomposed in air above 573 K, whereas Silva et al. [135] contended that La_2CoMnO_6 showed phonon energy behaviors associated with short-range Co and Mn ferromagnetic clusters through Raman spectroscopy measurements.

4. Properties and Applications

DPs present several properties like FM [136], magnetoresistance effect [137], ferroelectric [138], AFM [139], FiM [140], multiferroic [141], metal–insulator transition [142], magnetocaloric effect [143], luminescent [144], magnetic [53], optical, electrical, and mechanical [145], semiconducting [146], and half-metallic FM [147].

Some material properties are related to magnetic properties. $BaBiFeTiO_6$ presents ferroelectric properties with remanent polarization, as depicted by the polarization vs. electric field hysteresis loop [138]. The FiM behavior of Sr_2CrHfO_6 was observed at 2 K [140]. Gd_2CrFeO_6 exhibits magnetic entropy changes and refrigerant capacity similar to those of other materials with magnetocaloric effects [143]. The magnetic moments of $La_2BB'O_6$ (BB′ = CrCo, CrNi, ScNi, VNi, VSc) confirm their properties [147].

Other properties are related to their bandgap values. Ba_2GdBiO_6 can be used in ultraviolet and infrared absorption due to its bandgap [145]. The bandgap of the semiconducting Sr_2FeMnO_6 is 1.38 eV [146], whereas the direct bandgap of the semiconducting Gd_2CoCrO_6 justifies its optical property [20]. Other DPs for optoelectronic applications are $LaBaFeTiO_6$ and $EuBaFeTiO_6$, which present high bandgap values [10], whereas the bandgaps of Sr_2InSbO_6 and Ba_2InSbO_6 are 2.55 eV and 1.75 eV [148].

DPs can be used in memory devices [138], sensors [141], cooling [143], LED [144], energy storage and photonics [149], catalytic [53], biomedical [150], photocatalytic [20], electronic, spintronic, optoelectronic, and magnetic [147], solar cell, thermoelectric, and transport [148] applications.

Several characteristics make DPs appealing for their applications. Transport parameters determine the Sr_2PrSnO_6 applications in spintronics [136]. The electronic, magnetic, optical, and mechanical properties foster the photovoltaic applications of the Ca_2TaNiO_6, Sr_2TaNiO_6, and Ba_2TaNiO_6 [139]. The strain-influenced properties promote the $LaSrNiReO_6$ and $LaSr_{0.5}Ca_{0.5}NiReO_6$ for memory devices [142]. Sm-doped Sr_2LaSbO_6 presents excitation at 406 nm, suitable for LED applications [144]. La_2CoMnO_6 exhibits appealing absorption behavior and superior supercapacitor performance, making it suitable for applications in photonics and energy storage [149]. Fe^{2+} from the reduction of surface Fe^{3+} in the La_2FeAlO_6 through artificial light is active for OH production from H_2O_2 in the Fenton reaction [53], a catalytic application of DPs. The Seebeck coefficient and UV

response in the Sr_2NdNbO_6 appeal for its biomedical applications [150]. The magnetoresistance effect, along with the mixed oxide AFM nature, fosters Mn_2CoReO_6 spintronic applications [137]. The FM arrangement, insulating behavior, and ferroelectricity promote the Dy_2MnCoO_6-sensing application [141]. The Ce-doped Ba_2TiMoO_6 degrades methylene blue, which may be related to its capacity to absorb UV radiation that can be used for photocatalytic reactions [151]. The Sr_2FeMoO_6 prepared using the sol–gel method at a pH of 8 and irradiated for 35 min converted methylene blue completely, which can be related to its absorption of UV and VIS radiation and a higher amount of surface oxygen [152]. The Lu_2CrMnO_6 can be used for hydrogen storage, as it presents nanostructures with appealing hydrogen sorption and oxidation-reduction processes [153].

5. Summary

Double perovskites (DP), represented by the formula $A_2BB'O_6$ and $AA'BB'O_6$, present three arrangements (random, rock salt, and layered). They can be synthesized using the solid-state reaction, sol–gel, Pechini, and hydrothermal methods, and characterized using XRF, XRD, magnetic measurements, TEM, XPS, TPR, SXRD, NPD, EXAFS, and Raman spectroscopy.

The Rietveld method was coupled to XRD, SXRD, and NPD and implemented in the Fullprof program. Several options are available in the Winplotr tool of the Fullprof package to draw the Rietveld refinement results. A CIF file can be generated from the sample after refinement of the crystal structure. The results of the Rietveld method can be used to determine the apparent size and apparent strain.

The results from the characterization techniques complement those obtained from the Rietveld method. For the case of La_2NiTiO_6, XRF verifies the occupation number of La, Ni, and Ti in the crystalline structure determined from the Rietveld method coupled to XRD, SXRD, or NPD. Magnetic measurements can verify the Ni and Ti arrangement and symmetry. The apparent crystallite size of the La_2NiTiO_6 can be contrasted with TEM information. The adsorbed oxygen on the surface can be verified by the XPS and the TPR. The Ni-O and Ti-O bond length distances from EXAFS and Raman spectroscopy can complement the results of the Rietveld refinement.

The synthesis method can have an important role in investigating DPs with enhanced properties. Green chemicals in the sol–gel method have been reported to provide DPs with an appealing particle size. The ball-milling step can introduce defects in the sample. NH_4OH can produce a structure-like foam after the resin calcination using the Pechini method. DPs-containing composites have been prepared using the hydrothermal method.

The combination of magnetic, electronic, optical, and catalytic properties makes DPs highly versatile for applications in spintronics, photovoltaics, memory devices, sensors, LEDs, cooling systems, energy storage and photonics, catalysis, photocatalysis, biomedicine, thermoelectric, and hydrogen storage.

6. Outlook and Challenges

Several DPs have been reported in the literature; however, more research on this type of mixed oxides is required. First of all, additional studies should be carried out on cheap ion-containing DPs like Fe, Co, or Cu, as these metals present catalytic properties to produce ammonia, hydrocarbons, or hydrogen. These systems may be designed using active metals with non-active ions to improve the metal–support interaction, as demonstrated for the La_2NiTiO_6. Furthermore, cheap, active, and stable supports like core shell structures should be studied to favor the cost–benefit ratio to implement DPs materials in catalytic applications.

The calcination temperature may influence the oxygen content, as observed in the solid-state reaction method, or the symmetry, as stated for the Pechini method. The partial substitution of B cations may produce vacancies (Pechini method) or mixed valences in the structure (sol–gel). In the sol–gel synthesis, the inclusion of a milling step may modulate the properties of DPs. In the Pechini method, alternative carboxylic acids or alcohols to the citric acid and ethylene glycol may influence the morphology of the samples.

Moreover, more fundamental knowledge about cost-effective systems, such as materials containing DPs and activated carbon, is required to develop technologies for separating, purifying, and storing hydrogen.

Finally, biomedical items may be a new extensive application of DPs, as a result of DP properties, and this new horizon may be fostered by meeting customer needs with starting materials through extensive DP characterization. Therefore, additional research is required on DPs, especially on cost-effective materials and preparation methods, promoting catalytic processes, biomedical applications, and renewable energies.

Supplementary Materials: The following supporting information can be downloaded at https://www.mdpi.com/article/10.3390/inorganics13110372/s1: Table S1: Default (black) and written (blue) parameters in a portion of a PCR file using the Fullprof program with hypothetical values; Table S2: Procedures in the edition step for the observed and calculated XRD pattern.

Author Contributions: Conceptualization, P.V.T. and M.M.V.M.S.; methodology, P.V.T. and M.M.V.M.S.; software, P.V.T. and M.M.V.M.S.; validation, P.V.T. and M.M.V.M.S.; formal analysis, P.V.T. and M.M.V.M.S.; investigation, P.V.T. and M.M.V.M.S.; resources, P.V.T. and M.M.V.M.S.; data curation, P.V.T. and M.M.V.M.S.; writing—original draft preparation, P.V.T. and M.M.V.M.S.; writing—review and editing, P.V.T. and M.M.V.M.S.; visualization, P.V.T. and M.M.V.M.S.; supervision, P.V.T. and M.M.V.M.S.; project administration, P.V.T. and M.M.V.M.S.; funding acquisition, P.V.T. All authors have read and agreed to the published version of the manuscript.

Funding: Mariana M. V. M. Souza thanks Brazilian funding agencies, FAPERJ and CNPq, for the financial support granted to carry out this work.

Data Availability Statement: No new data were created or analyzed in this study. Data sharing is not applicable to this article.

Conflicts of Interest: The authors declare no conflicts of interest.

Abbreviations

The following abbreviations are used in this manuscript:

AFM	Antiferromagnetic
DP	Double perovskite
BMP	File containing a figure of a crystal structure
CIF	Crystallographic information file
DAT	File containing observed X-ray diffraction data
EB	Exchange Bias
EG	Ethylene glycol
EXAFS	Extended X-ray absorption fine structure
FC	Field-cooled mode
FiM	Ferrimagnetic
FM	Ferromagnetic
HER	Hydrogen evolution reaction
IRF	File for an instrumental resolution function containing information of a standard like CeO_2
LED	Light-Emitting Diode
M	Magnetization

MIC	File containing the apparent size and apparent strain
OER	Oxygen evolution reaction
PCR	A tool of the Fullprof program that generates editing files used during the refinement of a crystal structure, called PCR files
PVA	Polyvinyl alcohol
NPD	Neutron Powder Diffraction
SXRD	Synchrotron X-ray diffraction
T	Temperature
T_C	Curie Temperature
TEM	Transmission electron microscopy
T_g	Glass transition temperature
T_N	Néel temperature
TPR	Temperature-programmed reduction
XPS	X-ray photoelectron spectroscopy
XRD	X-ray Diffraction
XRF	X-ray Fluorescence
ZFC	Zero-field cooled mode
χ	Magnetic susceptibility

References

1. Bibi, N.; Usman, M.; Noreen, S. Predictions on new Cu-based ABO_3 (A=Cu and B=Lu, Y) oxide-perovskite for energy storage and optoelectronic applications: A DFT study. *Mater. Sci. Semicond. Process.* **2025**, *185*, 109001. [CrossRef]
2. Momma, K.; Izumi, F. VESTA 3 for three-dimensional visualization of crystal, volumetric and morphology data. *J. Appl. Crystallogr.* **2011**, *44*, 1272–1276. [CrossRef]
3. Malik, S.; Dutta, A. Examining the effects of sintering temperature on double perovskite La_2NiTiO_6: Analysis of structural, optical, electrical properties, and leakage current characteristics. *J. Phys. Chem. Solids* **2024**, *190*, 112027. [CrossRef]
4. Banerjee, A.; Awasthi, M.K.; Maji, P.; Pal, M.; Aziz, S.T.; Lahiri, G.K.; Dutta, A. Double Perovskite Oxides Bringing a Revelation in Oxygen Evolution Reaction Electrocatalyst Design. *ChemElectroChem* **2023**, *10*, e202201098. [CrossRef]
5. Tuza, P.V.; Souza, M.M.V.M. Steam Reforming of Methane over Catalyst Derived from Ordered Double Perovskite: Effect of Crystalline Phase Transformation. *Catal. Lett.* **2016**, *146*, 47–53. [CrossRef]
6. Luo, H.; Li, Y.; Li, T.; Wang, Z.; Wang, L.; Liu, Y.-Q. Double perovskite type catalysts with improved anti-coking and sulfur-resisting performance for diesel reforming. *Int. J. Hydrogen Energy* **2023**, *48*, 9929–9944. [CrossRef]
7. Kaczkowski, J.; Pugaczowa-Michalska, M.; Płowaś-Korus, I. Isovalent cation ordering in Bi-based double perovskites: A density functional analysis. *J. Magn. Magn. Mater.* **2022**, *548*, 168984. [CrossRef]
8. Córdova-Calderón, J.; Tuza, P.V.; Souza, M.M.V.M. Synthesis and Characterization of $LaNi_{0.5}Ti_{0.5}O_3$ and La_2NiTiO_6 Double Perovskite Nanoparticles. *Materials* **2022**, *15*, 2411. [CrossRef]
9. Mohandas, M.; Ugendar, K.; Harsita, M.; Rao, T.D.; Kanakaraju, P.; Mondal, R.; Sattibabu, B. Structural, magnetic and dielectric properties in double perovskite $La_{2-x}Sc_xCoMnO_6$ (x = 0.0, 0.1, and 0.2). *Mater. Today Commun.* **2024**, *41*, 110917. [CrossRef]
10. Boudad, L.; Taibi, M.; Belayachi, A.; Abd-Lefdil, M. Structural, morphological, dielectric and optical properties of double perovskites $RBaFeTiO_6$(R = La, Eu). *RSC Adv.* **2021**, *11*, 40205–40215. [CrossRef]
11. Zhang, C.; Zhang, Y.; Nie, Z.; Wu, C.; Gao, T.; Yang, N.; Yu, Y.; Cui, Y.; Gao, Y.; Liu, W. Double Perovskite La_2MnNiO_6 as a High-Performance Anode for Lithium-Ion Batteries. *Adv. Sci.* **2023**, *10*, 2300506. [CrossRef]
12. Levitas, B.; Piligian, S.; Ireland, T.; Gopalan, S. Elucidating the influence of molten salt chemistries on the synthesis and stability of perovskites oxides. *RSC Adv.* **2021**, *11*, 29156–29163. [CrossRef]
13. Wlodarczyk, D.; Amilusik, M.; Kosyl, K.M.; Chrunik, M.; Lawniczak-Jablonska, K.; Strankowski, M.; Zajac, M.; Tsiumra, V.; Grochot, A.; Reszka, A.; et al. Synthesis Attempt and Structural Studies of Novel A_2CeWO_6 Double Perovskites (A^{2+} = Ba, Ca) in and outside of Ambient Conditions. *ACS Omega* **2022**, *7*, 18382–18408. [CrossRef] [PubMed]
14. Zouridi, L.; Vourros, A.; Garagounis, I.; Marnellos, G.E.; Binas, V. Solvent-free direct salt precursor mechanochemical synthesis of $La_{0.5}Sr_{0.5}Ti_{0.5}Mn_{0.5}O_{3-\delta}$ oxide perovskite and its electrocatalytic behavior as oxygen electrode for solid oxide cells. *J. Solid State Chem.* **2023**, *328*, 124293. [CrossRef]
15. Zouridi, L.; Totnios, D.; Papoutsakis, L.; Daskalos, E.; Karagiannakis, G.; Marnellos, G.E.; Binas, V. Direct Salt Precursor Mechanochemical Synthesis for $La_{1-x}Sr_xTi_{1-y}Mn_yO_{3\pm\delta}$ Perovskite Nanomaterials as Solid Oxide Oxygen Electrodes. *ACS Appl. Nano Mater.* **2025**, *8*, 3389–3401. [CrossRef]

16. Siemek, K.; Olejniczak, A.; Konieczny, P.; Perzanowski, M. Defect engineering in Ba-doped $SrTiO_3$ ball-milled particles. *Appl. Surf. Sci.* **2025**, *710*, 163843. [CrossRef]
17. Phuyal, D.; Mukherjee, S.; Panda, S.K.; Man, G.J.; Simonov, K.; Simonelli, L.; Butorin, S.M.; Rensmo, H.; Karis, O. Nonlocal Interactions in the Double Perovskite Sr_2FeMoO_6 from Core-Level X-ray Spectroscopy. *J. Phys. Chem. C* **2021**, *125*, 11249–11256. [CrossRef]
18. Alvarado-Flores, J.J.; Mondragón-Sánchez, R.; Ávalos-Rodríguez, M.L.; Alcaraz-Vera, J.V.; Rutiaga-Quiñones, J.G.; Guevara-Martínez, S.J. Synthesis, characterization and kinetic study of the $Sr_2FeMoO_{6-\delta}$ double perovskite: New findings on the calcination of one of its precursors. *Int. J. Hydrogen Energy* **2021**, *46*, 26185–26196. [CrossRef]
19. Nadig, P.R.; Murari, M.S.; Daivajna, M.D. Influence of heat sintering on the physical properties of bulk $La_{0.67}Ca_{0.33}$ MnO_3 perovskite manganite: Role of oxygen in tuning the magnetocaloric response. *Phys. Chem. Chem. Phys.* **2024**, *26*, 5237–5252. [CrossRef]
20. Hosen, M.J.; Basith, M.A.; Syed, I.M. Structural, magnetic and optical properties of disordered double perovskite Gd_2CoCrO_6 nanoparticles. *RSC Adv.* **2023**, *13*, 17545–17555. [CrossRef]
21. Islam, M.A.; Sato, T.; Ara, F.; Basith, M.A. Sol-gel based synthesis to explore structure, magnetic and optical properties of double perovskite Y_2FeCrO_6 nanoparticles. *J. Alloys Compd.* **2023**, *94*, 169066. [CrossRef]
22. Boudad, L.; Taibi, M.; Belayachi, A.; Abd-Lefdil, M. Sol-gel synthesis and characterization of novel double perovskites $RBaFeTiO_6$ (R= Pr, Nd). *Ceram. Int.* **2022**, *48*, 6087–6096. [CrossRef]
23. Zhao, X.; Ge, W.; Gu, J.; Tang, Q.; Wu, Z.; Yi, K.; Zhu, X. Effects of synthesis methods on the structural and magnetic properties of double perovskite Sr_2CrReO_6 oxide powders. *J. Alloys Compd.* **2023**, *952*, 170004. [CrossRef]
24. Valdés, J.; Reséndiz, D.; Cuán, Á.; Nava, R.; Aguilar, B.; Cortés-Romero, C.M.; Navarro, O. Sol-Gel Synthesis of the Double Perovskite Sr_2FeMoO_6 by Microwave Technique. *Materials* **2021**, *14*, 3876. [CrossRef]
25. Bartoletti, A.; Gondolini, A.; Sangiorgi, N.; Aramini, M.; Ardit, M.; Rancan, M.; Armelao, L.; Kondrat, S.A.; Sanson, A. Identification of structural changes in $CaCu_3Ti_4O_{12}$ on high energy ball milling and their effect on photocatalytic performance. *Catal. Sci. Technol.* **2023**, *13*, 1041–1058. [CrossRef]
26. Xu, Z.; Feng, Z.; Xu, Y. Preparation and characterization of R_2CoMnO_6 (R=La, Nd) via PVA sol-gel route. *J. Asian Ceram. Soc.* **2021**, *9*, 119–127. [CrossRef]
27. Yousif, N.M.; Makram, N.; Wahab, L.A. Structural, dielectric, and magnetic properties of $LaCo_{0.2}Mn_{0.8}O_3$ and La_2CoMnO_6 perovskite materials. *J. Sol-Gel Sci. Technol.* **2021**, *98*, 238–251. [CrossRef]
28. Martinez-Rodriguez, H.A.; Jurado, J.F.; Herrera-Pérez, G.; Espinoza-Magana, F.; Reyes-Rojas, A. Enhancing $Pr_{1-x}Ba_xMnO_{3-\delta}$ perovskite charge-transport by electronic structure modulation. *J. Mater. Sci.* **2021**, *56*, 16510–16523. [CrossRef]
29. Dara, M.; Hassanpour, M.; Alshamsi, H.A.; Baladi, M.; Salavati-Niasari, M. Green sol-gel auto combustion synthesis and characterization of double perovskite Tb_2ZnMnO_6 nanoparticles and a brief study of photocatalytic activity. *RSC Adv.* **2021**, *11*, 8228–8238. [CrossRef]
30. Dara, M.; Hassanpour, M.; Amiri, O.; Baladi, M.; Salavati-Niasari, M. Sol–gel auto combustion synthesis, characterization, and application of Tb_2FeMnO_6 nanostructures as an effective photocatalyst for the discoloration of organic dye contaminants in wastewater. *RSC Adv.* **2021**, *11*, 26844–26854. [CrossRef]
31. Oroumi, G.; Monsef, R.; Dawi, E.A.; Aljeboree, A.M.; Alubiady, M.H.S.; Al-Ani, A.M.; Salavati-Niasari, M. Achieving new insights on rational design and application of double perovskite Y_2CrMnO_6 nanostructures as potential materials for electrochemical hydrogen storage performance. *J. Energy Storage* **2024**, *85*, 111161. [CrossRef]
32. Al-Wasidi, A.S.; Abdelrahman, E.A. Simple Synthesis and Characterization of Cobalt Ferrite Nanoparticles for the Successful Adsorption of Indigo Carmine Dye from Aqueous Media. *Inorganics* **2023**, *11*, 453. [CrossRef]
33. Guamán-Ayala, M.; Tuza, P.V.; Souza, M.M.V.M. Cation reducibility of $LaNi_{0.5}Ti_{0.5}O_3$, $LaNi_{0.5}Ti_{0.45}Co_{0.05}O_3$, and $LaNi_{0.45}Co_{0.05}Ti_{0.5}O_3$ perovskites from X-ray powder diffraction data using the Rietveld method. *Powder Diffr.* **2022**, *37*, 84–90. [CrossRef]
34. Swadchaipong, N.; Tongnan, V.; Maneesard, P.; Hartley, M.; Li, K.; Ampairojanawong, R.; Makdee, A.; Hartley, U.W.; Seree-watthanawut, I. Study of nitrous oxide utilization for syngas production via partial oxidation of methane using Ni-doped perovskite catalysts. *RSC Adv.* **2025**, *15*, 3080–3088. [CrossRef] [PubMed]
35. Pérez-Flores, J.C.; Castro-García, M.; Crespo-Muñoz, V.; Valera-Jiménez, J.F.; García-Alvarado, F.; Canales-Vázquez, J. Analysis of performance losses and degradation mechanism in porous $La_{2-x}NiTiO_{6-\delta}$:YSZ electrodes. *Materials* **2021**, *14*, 2819. [CrossRef]
36. Zhao, Z.; Zou, M.; Huang, H.; Zhai, X.; Wofford, H.; Tong, J. Insight of $BaCe_{0.5}Fe_{0.5}O_{3-\delta}$ twin perovskite oxide composite for solid oxide electrochemical cells. *J. Am. Ceram. Soc.* **2023**, *106*, 186–200. [CrossRef]
37. Zhai, X.; Ding, F.; Zhao, Z.; Santomauro, A.; Luo, F.; Tong, J. Predicting the formation of fractionally doped perovskite oxides by a function-confined machine learning method. *Commun. Mater.* **2022**, *3*, 42. [CrossRef]

38. Cheraghi, A.; Davar, F.; Homayoonfal, M.; Hojjati-Najafabadi, A. Effect of lemon juice on microstructure, phase changes, and magnetic performance of $CoFe_2O_4$ nanoparticles and their use on release of anti-cancer drugs. *Ceram. Int.* **2021**, *47*, 20210–20219. [CrossRef]
39. Al-Farraj, E.S.; Khairy, M.; Saad, F.A.; Shah, R.K.; Abdelrahman, E.A. Efficient Photocatalytic Decomposition of Acid Blue 25 Dye using Facilely Synthesized Magnesium Aluminate Nanoparticles. *Water Conserv. Sci. Eng.* **2024**, *9*, 3. [CrossRef]
40. dos Santos, T.V.; Pryston, D.B.A.; Assis, G.C.; Meneghetti, M.R.; Meneghetti, S.M.P. Tin, Niobium and Tin-Niobium oxides obtained by the Pechini method using glycerol as a polyol: Synthesis, characterization and use as a catalyst in fructose conversion. *Catal. Today* **2021**, *379*, 62–69. [CrossRef]
41. Bataliotti, M.D.; Costa, F.B.; Minussi, F.B.; Araújo, E.B.; de Lima, N.B.; Moraes, J.C.S. Characterization of tellurium dioxide thin films obtained through the Pechini method. *J. Sol-Gel Sci. Technol.* **2022**, *103*, 378–385. [CrossRef]
42. Sharmili, T.; Preethi, A.J.; Ragam, M. Comprehensive study on double perovskite La_2NiMnO_6 structures synthesized via hydrothermal and sol-gel methods for energy storage applications. *Mater. Today Commun.* **2025**, *48*, 113315. [CrossRef]
43. Wu, Z.; Lv, C.; Fang, J.; Wang, Y.; Jin, X.; Ge, J. Cobalt-doping-controlled synthesis of $CoMnO_3$ as a novel electrode material for supercapacitors. *Inorg. Chem. Commun.* **2025**, *180*, 115005. [CrossRef]
44. Priya, L.S.; Dhanemozhi, A.C.; Mayandi, J.; Pratha Govindaraj, B.S.; Somu, A.R. Structural, optical, morphological and electrochemical properties of dual-shaped $SrTiO_3$ nanostructures with enhanced photocatalytic and supercapacitor performances. *J. Indian Chem. Soc.* **2025**, *102*, 101819. [CrossRef]
45. Yi, K.; Wu, Z.; Tang, Q.; Gu, J.; Ding, J.; Chen, L.; Zhu, X. Microstructural Characterization and Magnetic, Dielectric, and Transport Properties of Hydrothermal La_2FeCrO_6 Double Perovskites. *Nanomaterials* **2023**, *13*, 3132. [CrossRef]
46. Irfan, M.; Murtaza, G.; Muhammad, N.; Tahir, S.; Raza, H.H.; Sabir, B.; Iftikhar, M.; Sharif, S. Experimental and theoretical studies of structural, electronic and magnetic properties of RE_2NiCrO_6 (RE = Ce, Pr and Nd) double perovskites. *Phys. E* **2023**, *148*, 115635. [CrossRef]
47. Zhang, C.; Wang, Z.; Yuan, L.; Ti, R.; Wu, H.; Yuan, H. Double perovskites R_2NiMnO_6 with small R^{3+} cations: Magnetic interactions tuned by R^{3+} ionic radius and the role of orbital ordering. *J. Alloys Compd.* **2025**, *1039*, 182997. [CrossRef]
48. McGuire, S.C.; Wesley, W.; Sasaki, K.; Tong, X.; Wong, S.S. Yttrium-based Double Perovskite Nanorods for Electrocatalysis. *ACS Appl. Mater. Interfaces* **2022**, *14*, 30914–30926. [CrossRef]
49. Sharma, A.; Bhardwaj, U.; Kushwaha, H.S. Efficacious visible-light photocatalytic degradation of toxics by using Sr_2TiMnO_6-rGO composite for the wastewater treatment. *Clean. Eng. Technol.* **2021**, *2*, 100087. [CrossRef]
50. Khan, R.; Mehran, M.T.; Baig, M.M.; Sarfraz, B.; Naqvi, S.R.; K. Niazi, M.B.; Khan, M.Z.; Khoja, A.H. 3D hierarchical heterostructured LSTN@NiMn-layered double hydroxide as a bifunctional water splitting electrocatalyst for hydrogen production. *Fuel* **2021**, *285*, 119174. [CrossRef]
51. Popov, D.V.; Batulin, R.G.; Cherosov, M.A.; Yatsyk, I.V.; Chupakhina, T.I.; Deeva, Y.A.; Makarchenko, A.S.; Fazlizhanova, D.I.; Shustov, V.A.; Eremina, R.M.; et al. Intermediate-spin state of Co ions in magnetic and thermoelectric properties of double perovskite Ba_2CoNbO_6. *J. Alloys Compd.* **2024**, *1009*, 176900. [CrossRef]
52. Popov, D.V.; Batulin, R.G.; Cherosov, M.A.; Yatsyk, I.V.; Chupakhina, T.I.; Deeva, Y.A.; Eremina, R.M.; Maiti, T. Magnetic properties of the double perovskite $Sr_2CoNbO_{6-\delta}$. *Magn. Reson. Solids* **2023**, *25*, 23301. [CrossRef]
53. Jin, Z.; Xu, C.; Zhou, T.; Hu, J.; Hu, R.; Meng, H.; Shen, J.; Yang, M.; Motkuri, R.K. High surface area magnetic double perovskite La_2AlFeO_6 as an efficient and stable photo-Fenton catalyst under a wide pH range. *Appl. Surf. Sci.* **2022**, *574*, 151554. [CrossRef]
54. Popov, D.V.; Batulin, R.G.; Cherosov, M.A.; Chupakhina, T.I.; Deeva, Y.A.; Shustov, V.A.; Agafonov, S.S.; Kolkov, M.I.; Kurbakov, A.I.; Eremina, R.M.; et al. Magnetic phase separation in double perovskite $Sr_2MnNbO_{6-\delta}$. *Mater. Chem. Phys.* **2025**, *345*, 131139. [CrossRef]
55. Chahla, S.; Gagou, Y.; El Marssi, M.; Chaker, H.; Ben Hassen, R. An analysis of the crystal structure, vibrational properties, and optoelectronic behavior of $NdCaFeSnO_6$. *RSC Adv.* **2025**, *15*, 22843–22862. [CrossRef]
56. Fabrelli, H.; Silva, A.G.; Boldrin, M.; Bufaiçal, L.; Bittar, E.M. Structural transitions and spontaneous exchange bias in $La_{2-x}Ba_xCoMnO_6$ series. *J. Solid State Chem.* **2023**, *322*, 123944. [CrossRef]
57. Zaraq, A.; Orayech, B.; Igartua, J.M.; El Bouari, A.; Gregory, D.H.; Gesing, T.M. Crystallography at non-ambient conditions and physical properties of the synthesized double perovskites, $Sr_2(Co_{1-x}Fe_x)TeO_6$. *Dalton Trans.* **2023**, *52*, 4086–4102. [CrossRef] [PubMed]
58. Rodríguez-Carvajal, J. Recent advances in magnetic structure determination by neutron powder diffraction. *Phys. B* **1993**, *192*, 55–69. [CrossRef]
59. Roisnel, T.; Rodríquez-Carvajal, J. WinPLOTR: A Windows Tool for Powder Diffraction Pattern Analysis. In Proceedings of the Seventh European Powder Diffraction Conference (EPDIC 7), Barcelona, Spain, 20–23 May 2020.

60. Graversen, L.G.; Juelsholt, M.; Aalling-Frederiksen, O.; Friis-Jensen, U.; Pittkowski, R.K.; Thomsen, M.S.; Kirsch, A.; Magnard, N.P.L.; Jensen, K.M.Ø. Mechanistic insights into solvent-guided growth and structure of MoO_2 nanoparticles in solvothermal synthesis. *Chem. Sci.* **2025**, *16*, 14350–14365. [CrossRef]
61. Souza, M.M.V.M.; Maza, A.; Tuza, P.V. X-ray powder diffraction data of $LaNi_{0.5}Ti_{0.45}Co_{0.05}O_3$, $LaNi_{0.45}Co_{0.05}Ti_{0.5}O_3$, and $LaNi_{0.5}Ti_{0.5}O_3$ perovskites. *Powder Diffr.* **2021**, *36*, 29–34. [CrossRef]
62. Rodríguez-Carvajal, J. *An Introduction to the Program Fullprof 2000 (Version July 2001)*; Laboratoire Léon Brillouin (CEA-CNRS): Saclay, France, 2001.
63. Silva, R.S.; Gainza, J.; dos Santos, C.; Rodrigues, J.E.F.S.; Dejoie, C.; Huttel, Y.; Biskup, N.; Nemes, N.M.; Martínez, J.L.; Ferreira, N.S.; et al. Magnetoelastic Coupling and Cryogenic Magnetocaloric Effect in Two-Site Disordered $GdSrCoFeO_6$ Double Perovskite. *Chem. Mater.* **2023**, *35*, 2439–2455.
64. Binns, J.; Darmanin, C.; Kewish, C.M.; Pathirannahalge, S.K.; Berntsen, P.; Adams, P.L.R.; Paporakis, S.; Wells, D.; Roque, F.G.; Abbey, B.; et al. Preferred orientation and its effects on intensity-correlation measurements. *IUCrJ* **2022**, *9*, 231–242. [CrossRef]
65. Yotsumoto, Y.; Nakajima, Y.; Takamoto, R.; Takeichi, Y.; Ono, K. Autonomous robotic experimentation system for powder X-ray diffraction. *Digit. Discov.* **2024**, *3*, 2523–2532. [CrossRef]
66. Bhuyan, M.D.I.; Das, S.; Basith, M.A. Sol-gel synthesized double perovskite Gd_2FeCrO_6 nanoparticles: Structural, magnetic and optical properties. *J. Alloys Compd.* **2021**, *878*, 160389. [CrossRef]
67. Guo, J.; Cai, R.; Cali, E.; Wilson, G.E.; Kerherve, G.; Haigh, S.J.; Skinner, S.J. Low-Temperature Exsolution of Ni–Ru Bimetallic Nanoparticles from A-Site Deficient Double Perovskites. *Small* **2022**, *18*, 2107020. [CrossRef]
68. El Hachmi, A.; Sadoune, Z. Synthesis and structural characterization of new perovskite phases, $Ba_2Bi_{0.572}TeO_{6\pm\delta}$ and $SrLa_2NiFeNbO_9$. *Powder Diffr.* **2024**, *39*, 235–244. [CrossRef]
69. Fullprof Suite. Fullprof News—2002. 2002. Available online: https://www.ill.eu/sites/fullprof/Old_FP/php/Fullprof_News_2002.htm (accessed on 8 September 2025).
70. Rodríguez-Carvajal, J. *Rietveld Refinement of Complex Inorganic Materials Using FullProf*; Laboratoire Léon Brillouin (CEA-CNRS): Saclay, France, 2003. Available online: http://ccp14.cryst.bbk.ac.uk/projects/ecm21-durban2003/juan/ecm21_fullprof_juan.pdf (accessed on 9 September 2025).
71. Almadhi, A.; Ji, K.; Injac, S.D.; Ritter, C.; Attfield, J.P. $(Ca_{0.5}Mn_{0.5})_2MnTeO_6$—An Anomalously Stable High-Pressure Double Perovskite. *Chem Asian J.* **2024**, *19*, e202400280. [CrossRef]
72. Shibuya, K.; Hirai, D.; Takenaka, K. Chemical pressure tuning of multipolar and magnetic orders in $Ba_2(Cd_{1-x}Ca_x)ReO_6$ double perovskites. *Phys. Rev. Mater.* **2025**, *9*, 034406. [CrossRef]
73. Agarwal, C.; Verma, J.K.; Bano, T.; Kumawat, S.; Gora, M.K.; Kumar, A.; Chandra, S.; Gautam, Y.K.; Kumar, S. Effect of Cr Substitution for Co on the Structural, Optical, and Magnetic Properties of La_2CoMnO_6 Double Perovskite Nanomaterials: A Facile Auto-Combustion Sol-Gel Approach. *ECS J. Solid State Sci. Technol.* **2025**, *14*, 043012. [CrossRef]
74. Macchiutti, C.; Jesus, J.R.; Carneiro, F.B.; Bufaiçal, L.; Klein, R.A.; Zhang, Q.; Kirkham, M.; Brown, C.M.; dos Reis, R.D.; Perez, G.; et al. Tuning the spontaneous exchange bias effect in $La_{1.5}Sr_{0.5}CoMnO_6$ with sintering temperature. *Phys. Rev. Mater.* **2024**, *8*, 044408. [CrossRef]
75. Zhang, H.; Chen, W.; Xie, L.; Zhao, H.; Li, Q. Tunable exchange bias in $La_{1.5}Sr_{0.5}CoMnO_6$ double perovskite doped with nonmagnetic Ga ions. *Curr. Appl. Phys.* **2022**, *35*, 58–66. [CrossRef]
76. Fourmont, P.; Cho, E.; Cloutier, S.G.; Ross, C.A. Exchange Bias in $La_{0.67}Sr_{0.33}MnO_3/YFeO_3$ Ferromagnet/Antiferromagnet Multilayer Heterostructures. *Small* **2025**, *21*, 2501644. [CrossRef]
77. Qiu, X.; Wang, Z.; Chen, H.; Liang, Y.; Jiang, X.; Zhang, Y.; Ma, J.; Zhu, F.; Nan, T.; Chen, Z.; et al. Enhanced exchange bias in all-oxide heterostructures with cation-ordered ferrimagnetic double-perovskite. *Npj Spintron.* **2024**, *2*, 44. [CrossRef]
78. Pal, K.; Mandal, S.; Dey, S.; Pradhan, K.; Das, I. Unraveling the origins of exchange bias and magnetic anomalies in Sr_2FeRuO_6: Experimental and theoretical insights. *Mater. Today Commun.* **2025**, *46*, 112814. [CrossRef]
79. Deng, Z.; Wang, X.; Wang, M.; Shen, F.; Zhang, J.; Chen, Y.; Feng, H.L.; Xu, J.; Peng, Y.; Li, W.; et al. Giant Exchange-Bias-Like Effect at Low Cooling Fields Induced by Pinned Magnetic Domains in Y_2NiIrO_6 Double Perovskite. *Adv. Mater.* **2023**, *35*, 2370120. [CrossRef]
80. Kush, L.; Srivastava, S. Observation of Giant Zero-Field Cooled Spontaneous Exchange Bias Effect in La_2FeCoO_6 Double Perovskite Ceramic. *J. Supercond. Nov. Magn.* **2025**, *38*, 82. [CrossRef]
81. Datta, R.; Mondal, S.; Mondal, S.; Kalyan Pradhan, S.; Majumdar, S.; Kumar De, S. Evolution of structural, magnetic and transport properties of 3d-5d based double perovskites $Nd_{2-x}Sr_xCoIrO_6$. *J. Phys. Condens. Matter* **2025**, *37*, 065801. [CrossRef]
82. Mahalle, P.; Kumar, A.; Cuello, G.J.; da Silva, I.; Krzystyniak, M.; Yusuf, S.M. Investigating the genesis of negative magnetization, exchange bias, and electrical properties in Gd_2CuRuO_6. *Phys. Rev. Mater.* **2025**, *9*, 104407. [CrossRef]
83. Li, S.Z.; Rahman, A.; Ma, C.L.; Zhao, X.; Sun, Z.Y.; Liu, M.F.; Wang, X.Z.; Xu, X.F.; Liu, J.M. Exchange bias effect in polycrystalline $Bi_{0.5}Sr_{0.5}Fe_{0.5}Cr_{0.5}O_3$ bulk. *Sci. Rep.* **2023**, *13*, 6333. [CrossRef]

84. Patel, R.K.; Chikara, K.S.; Hossain, S.M.; Majumder, M.; Nath, C.; Yusuf, S.M.; Saravanan, M.P.; Bera, A.K.; Pramanik, A.K. Crystal structure, magnetic, and magnetostructural correlations in double perovskite antiferromagnets $Sr_2NiMo_{1-x}W_xO_6$ ($0 \leq x \leq 1$). *Phys. Rev. Mater.* **2025**, *9*, 044406. [CrossRef]
85. Mohanty, S.; Satapathy, S.; Nayak, M.; Rai, S.; Singh, R.; Behera, S. Effect of low Ni- substitution on optical, dielectric and magnetic properties of double perovskite Mg_2FeNbO_6. *Inorg. Chem. Commun.* **2024**, *165*, 112513. [CrossRef]
86. Sahoo, S.; Sahoo, L.; Nayak, N.C.; Parida, B.N.; Parida, R.K. Investigation of the structural, dielectric, magnetic properties and NTC-thermistor response of $CaBiFeMnO_6$ double perovskites. *Mater. Adv.* **2024**, *5*, 5442–5457. [CrossRef]
87. Wu, Z.; Yi, K.; Tang, Q.; Gu, J.; Ding, J.; Chen, L.; Zhu, X. Microstructures and physical properties of sol–gel derived Ba_2FeMnO_6 double perovskite. *J. Am. Ceram. Soc.* **2023**, *106*, 3663–3675. [CrossRef]
88. Zaraq, A.; Gregory, D.H.; Orayech, B.; Igartua, J.M.; El Bouari, A.; Eales, J.D.; Bingham, P.A.; Gesing, T.M. Effects of iron substitution and anti-site disorder on crystal structures, vibrational, optical and magnetic properties of double perovskites $Sr_2(Fe_{1-x}Ni_x)TeO_6$. *Dalton Trans.* **2022**, *51*, 17368–17380. [CrossRef] [PubMed]
89. García-Ruíz, D.L.; Aguilar, B.; Navarro, O.; de la Torre Medina, J.; Soto, T.E.; Cervantes-Solano, M. Effects of the electron-doping on the structural and magnetic properties of the $Sr_{2-x}Ce_xFe_{1+x/2}Mo_{1-x/2}O_6$ double perovskite. *Solid State Commun.* **2025**, *404*, 116046. [CrossRef]
90. Punitha, J.S.; Raji, R.K.; Ramachandran, T.; Kumar, K.S.; Dhilip, M.; Hamed, F.; Nataraj, A. Influence of Pr^{3+} substitution on the structural, optical, magnetic, and dielectric properties of $Sr_2FeTiO6_{-\delta}$ double perovskites. *Solid State Sci.* **2025**, *160*, 107825. [CrossRef]
91. Rasband, W.S. ImageJ: Image Processing and Analysis and Java. Available online: https://imagej.net/ij/ (accessed on 22 August 2025).
92. Dara, M.; Hassanpour, M.; Amiri, O.; Baladi, M.; Salavati-Niasari, M. Tb_2CoMnO_6 double perovskites nanoparticles as photocatalyst for the degradation of organic dyes: Synthesis and characterization. *Arab. J. Chem.* **2021**, *14*, 103349. [CrossRef]
93. Nartova, A.V.; Mashukov, M.Y.; Astakhov, R.R.; Kudinov, V.Y.; Matveev, A.V.; Okunev, A.G. Particle Recognition on Transmission Electron Microscopy Images Using Computer Vision and Deep Learning for Catalytic Applications. *Catalysts* **2022**, *12*, 135. [CrossRef]
94. Rahimkhoei, V.; Salavati-Niasari, M.; Alsultany, F.H.; Aljeboree, A.M.; Hamadanian, M. Exploration of electrochemical energy storage potential of MWCNT scaffolds functionalized with Lu_2FeMnO_6 synthesized via a facile sol–gel Pechini chemical method. *Appl. Water Sci.* **2025**, *15*, 126. [CrossRef]
95. Sha, Z.; Shen, Z.; Calì, E.; Kilner, J.A.; Skinner, S.J. Understanding surface chemical processes in perovskite oxide electrodes. *J. Mater. Chem. A* **2023**, *11*, 5645–5659. [CrossRef]
96. Wlodarczyk, D.; Amilusik, M.; Kosyl, K.M.; Chrunik, M.; Lawniczak-Jablonska, K.; Przybylinska, H.; Kosmela, P.; Strankowski, M.; Bulyk, L.-I.; Tsiumra, V.; et al. Synthesis and Properties of the Ba_2PrWO_6 Double Perovskite. *Inorg. Chem.* **2024**, *63*, 10194–10206. [CrossRef] [PubMed]
97. Ali, A.; Gondal, M.A.; Khan, J.A.; Mustaqeem, M.; Almessiere, M.A.; Baykal, A. Optimizing La_2MnXO_6 Double Perovskite for Superior Electrochemical Efficiency in Supercapacitors. *Energy Storage* **2025**, *7*, e70123. [CrossRef]
98. Bhattacharjee, S.; Parida, R.K.; Parida, B.N. Investigation of multifunction features of double perovskite oxide A_2FeVO_6 (where A = Ba, Ca). *Phys. B* **2023**, *659*, 414849. [CrossRef]
99. Raji, R.K.; Ramachandran, T.; Dhilip, M.; Aravindan, V.; Punitha, J.S.; Hamed, F. Integrating Experimental and Computational Insights: A Dual Approach to Ba_2CoWO_6 Double Perovskites. *Ceramics* **2024**, *7*, 2006–2023. [CrossRef]
100. Tang, Q.; Zhu, X. Structural Characterization and Physical Properties of Double Perovskite $La_2FeReO_{6+\delta}$ Powders. *Nanomaterials* **2022**, *12*, 244. [CrossRef]
101. Islam, Z.U.; Want, B. Structural, optical, and dielectric properties of double perovskite $NdBaFeTiO_6$. *Ceram. Int.* **2025**, *51*, 1585–1594. [CrossRef]
102. Ghorbani, Z.; Ehsani, M.H. Synthesis and magnetic properties of $Ba_{2-x}Sm_xFeMoO_6$ ($0.0 \leq x \leq 0.1$) Double perovskite. *Ceram. Int.* **2023**, *49*, 27362–27372. [CrossRef]
103. Kumar, P.; Tripathi, A.; Verma, H.; Mittal, A.; Bhattacharya, B.; Upadhyay, S. Cation deficiency driven enhancement in electrochemical performance of $Sr_{2-x}FeCoO_{6-\delta}$ double perovskite for supercapacitor electrodes. *Electrochim. Acta* **2025**, *538*, 146992. [CrossRef]
104. Ghorbani, Z.; Ehsani, M.H. Double perovskite oxides $Ba_{2-x}Ag_xFeMoO_6$ (x = 0.0, 0.025, 0.05). *Phys. B* **2024**, *682*, 415867. [CrossRef]
105. Yi, K.; Tang, Q.; Wu, Z.; Gu, J.; Zhu, X. Structural, magnetic, and electrical transport properties of half-metallic double perovskite La_2CrNiO_6 oxides. *J. Alloys Compd.* **2023**, *933*, 167742. [CrossRef]
106. Solanki, N.; Choudhary, R.J.; Kaurav, N. Qualitative study of structural phase transition in nickel doped $La_2CoTi_{(1-x)}Ni_xO_6$ double perovskite. *J. Alloys Compd.* **2023**, *943*, 169126. [CrossRef]

107. Roozbahania, H.; Maghsoodia, S.; Raeia, B.; Kootenaeia, A.S.; Azizi, Z. MgO support mediated enhancement of La_2BMnO_6 (B = Co, Ni) perovskite oxide in catalytic combustion of propane. *Iran. J. Catal.* **2023**, *2*, 211–222.
108. Winterstein, T.F.; Malleier, C.; Mohammadi, A.; Krüger, H.; Kahlenberg, V.; Venter, A.M.; Bekheet, M.F.; Müller, J.T.; Gurlo, A.; Heggen, M.; et al. Lanthanum nickel titanate perovskites as model systems for Ni-perovskite interfacial engineering in methane dry reforming. *Mater. Today Chem.* **2025**, *45*, 102620. [CrossRef]
109. Morimura, A.; Yamada, I. Pressure-Induced Order-Disorder Transition in the Double Perovskite Oxide La_2CoRuO_6. *Mater. Trans.* **2023**, *64*, 2093–2096. [CrossRef]
110. Rodrigues, J.E.F.S.; Gainza, J.; Serrano-Sánchez, F.; Silva, R.S.; Dejoie, C.; Nemes, N.M.; Dura, O.J.; Martínez, J.L.; Alonso, J.A. Thermal Expansion and Rattling Behavior of Gd-Filled Co_4Sb_{12} Skutterudite Determined by High-Resolution Synchrotron X-ray Diffraction. *Materials* **2022**, *16*, 370. [CrossRef] [PubMed]
111. Zhao, J.; Wang, X.; Shen, X.; Sahle, C.J.; Dong, C.; Hojo, H.; Sakai, Y.; Zhang, J.; Li, W.; Duan, L.; et al. Magnetic Ordering and Structural Transition in the Ordered Double-Perovskite Pb_2NiMoO_6. *Chem. Mater.* **2022**, *34*, 97–106. [CrossRef]
112. Liang, X.; Yamaura, K.; Tsirlin, A.A.; Belik, A.A. Ca_2CuWO_6: A triclinically distorted double perovskite with low-dimensional magnetic behavior. *Phys. Rev. B* **2025**, *111*, 094432. [CrossRef]
113. da Cruz Pinha Barbosa, V.; Maharaj, D.D.; Cronkright, Z.W.; Wang, Y.; Cong, R.; Garcia, E.; Reyes, A.P.; Yan, J.; Ritter, C.; Mitrović, V.F.; et al. Exploring the Links between Structural Distortions, Orbital Ordering, and Multipolar Magnetic Ordering in Double Perovskites Containing Re(VI) and Os(VII). *Chem. Mater.* **2024**, *36*, 11478–11489. [CrossRef]
114. Silva, R.S.; Rodrigues, J.E.; Gainza, J.; Serrano-Sánchez, F.; Martínez, L.; Huttel, Y.; Martínez, J.L.; Alonso, J.A. Magnetoelastic Coupling Evidence by Anisotropic Crossed Thermal Expansion in Magnetocaloric $RSrCoFeO_6$ (R = Sm, Eu) Double Perovskites. *Inorg. Chem.* **2024**, *63*, 7007–7018. [CrossRef]
115. Artini, C.; Massardo, S.; Carnasciali, M.M.; Joseph, B.; Pani, M. Evaluation of the Defect Cluster Content in Singly and Doubly Doped Ceria through In Situ High-Pressure X-ray Diffraction. *Inorg. Chem.* **2021**, *60*, 7306–7314. [CrossRef]
116. Sharma, S.; Ritter, C.; Adroja, D.T.; Stenning, G.B.; Sundaresan, A.; Langridge, S. Magnetic structure of the double perovskite La_2NiIrO_6 investigated using neutron diffraction. *Phys. Rev. Mater.* **2022**, *6*, 014407. [CrossRef]
117. Naveen, K.; Rom, T.; Islam, S.S.; Reehuis, M.; Adler, P.; Felser, C.; Hoser, A.; Nath, R.C.; Yadav, A.K.; Jha, S.N.; et al. Evolution of transition metal charge states in correlation with the structural and magnetic properties in disordered double perovskites $Ca_{2-x}La_xFeRuO_6$ ($0.5 \leq x \leq 2$). *Phys. Chem. Chem. Phys.* **2021**, *23*, 21769–21783. [CrossRef]
118. Ji, K.; Chen, R.; Manuel, P.; Attfield, J.P. Coexisting commensurate and incommensurate magnetic orders in the double double perovskite $CaMnCoWO_6$. *Z. Anorg. Allg. Chem.* **2023**, *649*, e202200084. [CrossRef]
119. Kearins, P.; Solana-Madruga, E.; Ji, K.; Ritter, C.; Attfield, J.P. Cluster Spin Glass Formation in the Double Double Perovskite $CaMnFeTaO_6$. *J. Phys. Chem. C* **2021**, *125*, 9550–9555. [CrossRef]
120. Dhawan, R.; Balasubramanian, P.; Nautiyal, T. Origins of multi-sublattice magnetism and superexchange interactions in double–double perovskite $CaMnCrSbO_6$. *J. Phys.:Condens. Matter* **2024**, *36*, 305801. [CrossRef]
121. Ji, K.; Alharbi, K.N.; Solana-Madruga, E.; Moyo, G.T.; Ritter, C.; Attfield, J.P. Double Double to Double Perovskite Transformations in Quaternary Manganese Oxides. *Angew. Chem. Int. Ed.* **2021**, *60*, 22248–22252. [CrossRef]
122. Mustonen, O.H.J.; Fogh, E.; Paddison, J.A.M.; Mangin-Thro, L.; Hansen, T.; Playford, H.Y.; Diaz-Lopez, M.; Babkevich, P.; Vasala, S.; Karppinen, M.; et al. Structure, Spin Correlations, and Magnetism of the S = 1/2 Square-Lattice Antiferromagnet $Sr_2CuTe_{1-x}W_x O_6$ ($0 \leq x \leq 1$). *Chem. Mater.* **2024**, *36*, 501–513. [CrossRef] [PubMed]
123. Harsita, M.; Kodam, U.; Mishra, S.K.; Rao, T.D.; Borole, S.; Rayaprol, S.; Krishna, P.S.R.; Sattibabu, B. Combined structural refinement using x-ray and neutron diffraction and magnetic properties of double perovskites $La_{2-x}Er_xNiMnO_6$. *Mater. Lett.* **2025**, *391*, 138481. [CrossRef]
124. Pal, A.; Anand, K.; Patel, N.; Das, A.; Ghosh, S.; Yen, P.T.-W.; Huang, S.-M.; Singh, R.K.; Yang, H.D.; Ghosh, A.K.; et al. Interplay of spin, phonon, and lattice degrees in a hole-doped double perovskite: Observation of spin–phonon coupling and magnetostriction effect. *J. Appl. Phys.* **2022**, *132*, 223906. [CrossRef]
125. Solana-Madruga, E.; Kearins, P.S.; Ritter, C.; Arévalo-López, Á.M.; Attfield, J.P. 1:1 Ca^{2+}:Cu^{2+} A-site Order in a Ferrimagnetic Double Double Perovskite. *Angew. Chem.* **2022**, *134*, e202209497. [CrossRef]
126. Jin, L.; Ni, D.; Gui, X.; Straus, D.B.; Zhang, Q.; Cava, R.J. Ferromagnetic Double Perovskite Semiconductors with Tunable Properties. *Adv. Sci.* **2022**, *9*, 2104319. [CrossRef]
127. López, C.A.; Singh, P.; Martínez-Coronado, R.; Alonso, J.A. Structural peculiarities of $La_2Ge_{1-x}Cr_xMgO_{6-\delta}$ ($0< x \leq 0.5$): A superior oxide-ion electrolyte for low-temperature solid-oxide fuel cells. *Int. J. Hydrogen Energy* **2023**, *48*, 12485–12492.
128. Yatoo, M.A.; Seymour, I.D.; Skinner, S.J. Neutron diffraction and DFT studies of oxygen defect and transport in higher-order Ruddlesden–Popper phase materials. *RSC Adv.* **2023**, *13*, 13786–13797. [CrossRef] [PubMed]

129. Jeevanandham, K.; Annadata, H.; Vinod, K.; Sathyanarayana, A.T.; Pandian, R.; Chakraborty, S.; Goutam, U.K.; Ghosh, B. Investigations of structural, magnetic, and magnetocaloric properties of $La_2Ni_{1-x}Cu_xMnO_6$ double perovskites. *Phys. Rev. B* **2025**, *111*, 214402. [CrossRef]
130. Majumder, S.; Tripathi, M.; Raghunathan, R.; Rajput, P.; Jha, S.N.; de Souza, D.O.; Olivi, L.; Chowdhury, S.; Choudhary, R.J.; Phase, D.M. Mapping the magnetic state as a function of antisite disorder in Sm_2NiMnO_6 double perovskite thin films. *Phys. Rev. B* **2022**, *105*, 024408. [CrossRef]
131. Kavaliuk, H.; Mielewczyk-Gryń, A.; Gazda, M.; Miruszewski, T.; Gajewska, M.; Wachowski, S.L. High entropy oxides: How many lanthanides can be introduced into Co-based double perovskite oxides? *J. Eur. Ceram. Soc.* **2025**, *45*, 117617. [CrossRef]
132. Murthy, P.S.R.; Salkar, K.; Xec, S.; Zambaulikar, S. Unraveling the role of Mn doping in transforming $SrLaLiTeO_6$ perovskites: Structural, optical, and dielectric insights. *J. Mater. Sci. Mater. Electron.* **2025**, *36*, 369. [CrossRef]
133. Khan, A.; Banerjee, D.; Rawat, D.; Nath, T.K.; Soni, A.; Chatterjee, S.; Taraphder, A. Emergence of spin-phonon coupling in Gd-doped Y_2CoMnO_6 double perovskite oxide: A combined experimental and ab-initio study. *Phys. Chem. Chem. Phys.* **2025**, *27*, 18005–18014. [CrossRef]
134. Meena, B.R.; Chatterjee, S.; Ghosh, A.K. Insight into charge conduction and relaxation in $La_{2-x}Ca_xFeMnO_6$ solid solution double perovskites. *J. Alloys Compd.* **2025**, *1037*, 182341. [CrossRef]
135. Silva, A.V.S.; Silva, R.X.; Paschoal, C.W.A.; Paschoal, A.R.; Nonato, A. Dynamics of magnetic inhomogeneity in La_2CoMnO_6 films probed by Raman spectroscopy. *Spectrochim. Acta Part A* **2025**, *325*, 125112. [CrossRef]
136. Apu, R.S.; Hasan, N.; Haque, R.I.; Kabir, A.; Rashid, M.H. Ferromagnetic double Sr_2PrSnO_6 perovskite: DFT analysis of physical, optoelectronic, and transport properties for advanced opto-spintronics. *AIP Adv.* **2025**, *15*, 035043. [CrossRef]
137. Wang, X.; Zhang, J.; Pan, Z.; Lu, D.; Pi, M.; Ye, X.; Dong, C.; Chen, J.; Chen, K.; Radu, F.; et al. X-ray Absorption Spectroscopic Study of the Transition-Metal-Only Double Perovskite Oxide Mn_2CoReO_6. *J. Phys. Chem. C* **2024**, *128*, 15668–15675. [CrossRef]
138. Sahoo, L.; Parida, B.N.; Parida, R.K.; Padhee, R.; Mahapatra, A.K. Structural, optical dielectric and ferroelectric properties of double perovskite $BaBiFeTiO_6$. *Inorg. Chem. Commun.* **2022**, *146*, 110102. [CrossRef]
139. Ali, H.S.; Murtaza, G.; Ayyaz, A.; Ismail, K.; Touqir, M.; Rehman, H.U.; Alanazi, Y.M. First-principles predictions of structure, half-metallic antiferromagnetism, optoelectronic, and elastic properties of double perovskites A_2TaNiO_6 (A = Ca, Sr, and Ba) for energy harvesting. *Mater. Sci. Semicond. Process.* **2024**, *181*, 108638. [CrossRef]
140. Tang, Q.; Zhu, X. Microstructure and physical properties of Sr_2CrHfO_6 ferrimagnetic double perovskite oxides. *J. Am. Ceram. Soc.* **2024**, *107*, 968–978. [CrossRef]
141. Chatterjee, S.; Das, I. Structural, magnetic, magnetocaloric behavior and magneto-transport, electrical polarization study in 3d based bulk and nano-crystalline multiferroic double perovskite Dy_2MnCoO_6. *J. Phys.: Condens. Matter* **2024**, *36*, 385802. [CrossRef]
142. Faiza-Rubab, S.; Nazir, S. Interplay between spin–orbital coupling and electron-correlation: Induction of phase transitions and giant magnetic anisotropy in strained $LaSr_{1-x}Ca_xNiReO_6$. *Phys. Chem. Chem. Phys.* **2022**, *24*, 17174–17184. [CrossRef]
143. Hao, W.; Ji, R.; Zhu, L.; Huang, S.; Zhang, Y. Structural, magnetic and cryogenic magnetocaloric properties in Gd_2CrFeO_6 ceramic oxide. *Solid State Commun.* **2025**, *399*, 115876. [CrossRef]
144. Verma, S.; Chaurasia, L.; Kumari, S.; Prasad, A.; Rao, A.S. Reddish-Orange emitting thermally stable Sm^{3+} doped Sr_2LaSbO_6 phosphor for applications in w-LEDs. *J. Photochem. Photobiol. A* **2025**, *467*, 116405. [CrossRef]
145. Ali, M.L.; Hasan, Z.; Akter, M.S.; Khan, M. Pressure induced physical properties of lead-free double perovskite Ba_2GdBiO_6 for optoelectronic applications. *Comput. Condens. Matter* **2025**, *44*, e01078. [CrossRef]
146. Rather, M.R.; Bilal, F.; Mushtaq, A.; Parvaiz, A.; Hassan, T.; Ghosh, S.; Sultan, K. Investigating the Multifunctional Role of Sr_2FeMnO_6 Double Perovskite in Spintronic and Thermoelectric Properties. *Phys. Status Solidi B* **2025**, *262*, 2400562. [CrossRef]
147. Arif, S.; Ali, Y. The electronic, magnetic, and optical properties of double perovskite $La_2BB'O_6$ (B = Cr, V and B′ = Co, Ni and Sc). *RSC Adv.* **2022**, *12*, 35279–35289. [CrossRef]
148. Amin, M.A.; Nazir, G.; Mahmood, Q.; Alzahrani, J.; Kattan, N.A.; Mera, A.; Mirza, H.; Mezni, A.; Refat, M.S.; Gobouri, A.A.; et al. Study of double perovskites X_2InSbO_6 (X = Sr, Ba) for renewable energy; alternative of organic-inorganic perovskites. *J. Mater. Res. Technol.* **2022**, *18*, 4403–4412. [CrossRef]
149. Shereef, A.; Aleena, P.A.; Kunjumon, J.; Jose, A.K.; Thomas, S.A.; Tomy, M.; Xavier, T.S.; Hussain, S.; Sajan, D. Third order nonlinear optical properties and electrochemical performance of La_2CoMnO_6 double perovskite. *Mater. Sci. Eng. B* **2023**, *289*, 116262. [CrossRef]
150. Alheibshy, F.; Belhachi, S.; Qureshi, M.T.; Hussein, W.; Alqarni, S.; Younes, K.M.; Abdel-Hameed, R.; Iqbal, M.W.; Sillanpää, M. Biomedical applications of double perovskites Sr_2TmNbO_6 and Sr_2NdNbO_6: A pathway to innovative healthcare solutions. *Talanta* **2026**, *296*, 128440. [CrossRef] [PubMed]
151. Pattanaik, R.; Pradhan, D.; Dash, S.K. A Brief Review on Solar Light Assisted Photocatalytic Degradation of Dyes using Double/Layered Perovskites. *Curr. Nanosci.* **2024**, *21*, 201–217. [CrossRef]

152. Roudgar-Amoli, M.; Abedini, E.; Alizadeh, A.; Shariatinia, Z. Understanding double perovskite oxides capabilities to improve photocatalytic contaminants degradation performances in water treatment processes: A review. *J. Ind. Eng. Chem.* **2024**, *129*, 579–619. [CrossRef]
153. Mahdi, M.A.; Oroumi, G.; Samimi, F.; Dawi, E.A.; Abed, M.J.; Alzaidy, A.H.; Jasim, L.S.; Salavati-Niasari, M. Tailoring the innovative Lu_2CrMnO_6 double perovskite nanostructure as an efficient electrode materials for electrochemical hydrogen storage application. *J. Energy Storage* **2024**, *88*, 111660. [CrossRef]

Disclaimer/Publisher's Note: The statements, opinions and data contained in all publications are solely those of the individual author(s) and contributor(s) and not of MDPI and/or the editor(s). MDPI and/or the editor(s) disclaim responsibility for any injury to people or property resulting from any ideas, methods, instructions or products referred to in the content.

inorganics

MDPI

Review

Recent Progress of Plasmonic Perovskite Photodetectors

Hongki Kim [1], Jeongeun Lee [2], Chae Bin Lee [2] and Yoon Ho Lee [2,*]

[1] Department of Chemistry and Centre for Processable Electronics, Imperial College London, London W120BZ, UK; ghdrl1437@gmail.com
[2] Department of Materials Science and Engineering, Sungshin Women's University, Seoul 01133, Republic of Korea; 20231196@sungshin.ac.kr (J.L.); 20241063@sungshin.ac.kr (C.B.L.)
* Correspondence: yoonhlee@sungshin.ac.kr

Abstract: Perovskite materials have emerged as promising candidates for next-generation photodetectors (PDs) owing to their superior optoelectronic properties and compatibility with low-cost, low-temperature fabrication processes. Broad applicability of PDs spans diverse fields, including X-ray detection, wearable electronics, autonomous vehicles, artificial intelligence, imaging, optical communication, and biomedical sensing, offering advantages over conventional semiconductor PDs based on Si, Ge, InGaAs, and GaN. The integration of plasmonic nanostructures into perovskite-based devices has recently emerged as an effective strategy to enhance performance by amplifying light absorption near the perovskite layer. This review summarizes recent advances and design strategies for plasmonic-integrated perovskite photodetectors (Pe-PDs), with a particular emphasis on plasmonic nanopatterns and nanoparticles as viable approaches for solution-processable Pe-PDs.

Keywords: plasmonic effects; perovskite photodetectors; plasmonic nanopattern; plasmonic nanoparticle

1. Introduction

Metal halide perovskites (MHPs) with the general formular of ABX_3, where A is organic or inorganic cation (e.g., Cs^+, methylammonium (MA^+), or formamidinium (FA^+), B is divalent metal cation (e.g., Pb^{2+}, Sn^{2+}, or Ge^{2+}), and X is halide anion (e.g., Cl^-, Br^-, I^-) have been identified as one of the most promising materials for optoelectronic applications [1–5], due to their high absorption coefficient, long carrier lifetime and diffusion length, and low defect density in conjunction with ease of cost-effective solution processability [6–11]. This surge has made outstanding progress, driven by key applications ranging from photovoltaics to light-emitting diodes and flexible electronics [12–16].

This growing momentum has also driven significant advances in PD technologies [17], particularly in the search for alternatives to conventional semiconductor PDs based on materials such as Si, Ge, InGaAs, and GaN [18,19]. These traditional systems typically require high-temperature fabrication and are limited by their inherent rigidity. As the field moves toward flexible, lightweight, and wearable electronics, there is increasing demand for PDs that are compatible with deformable substrates and possess both mechanical adaptability and high optoelectronic performance [20–23]. In this context, perovskite materials have emerged as strong candidates for next-generation PDs [24–28].

Pe-PDs potentially can offer broad application potential in areas such as X-ray detection [29], wearable electronics [30], autonomous vehicles [31], artificial intelligence [32], polarized imaging [33], optical communication [34], and biomedical sensing [35]

(Figure 1). For instance, the strong X-ray absorption and efficient charge transport properties of perovskites make them well-suited for integration into high-resolution, low-cost medical imaging systems. In addition, Pe-PDs hold significant potential in biomedical applications [36], including non-invasive health monitoring using near-infrared light [37], as well as ultraviolet detection for flame monitoring [38], sterilization [39], and environmental sensing [40,41]. Their compatibility with imaging systems further enables advanced functionalities such as facial recognition and self-powered operation through integration with photovoltaic components. Furthermore, recent advancements in chiral Pe-PDs have facilitated the direct detection of circularly polarized light without the need for bulky external optical components [42,43]. Collectively, these innovations underscore the versatility and transformative potential of Pe-PDs, paving the way for their adoption in next-generation flexible and multifunctional optoelectronic devices.

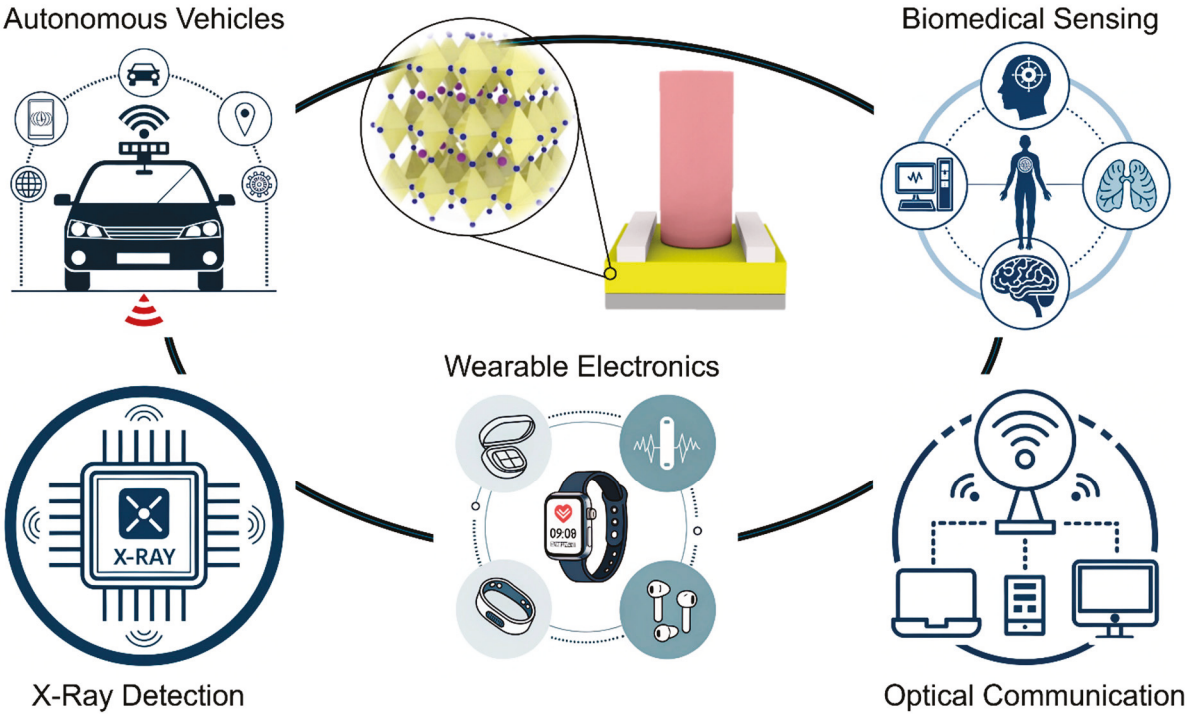

Figure 1. Pe-PDs and their diverse applications in X-ray detection, wearable electronics, autonomous vehicles, artificial intelligence, imaging, optical communication, and biomedical sensing.

Despite the promising properties of perovskite materials, significant challenges remain in advancing their PDs toward practical use. A key obstacle lies in achieving balanced device performance suited for real-world applications, which demand rapid and precise detection of fluctuating signals over a wide range of intensities [44]. To meet these requirements, an ideal PD must concurrently deliver a high signal-to-noise ratio (SNR), a broad linear dynamic range (LDR), and ultrafast response speed [45]. Extensive efforts have been devoted to improving the performance of Pe-PDs by addressing key challenges through strategies such as compositional and additive engineering to suppress bulk and surface defects [46,47], interface engineering using thin buffer layers [48,49], and the introduction of perovskite–organic heterojunction structures [50]. While these material- and interface-driven approaches have yielded notable improvements, they still fall short of fully meeting the stringent performance requirements needed for practical and commercial applications.

Recently, plasmonic-enhanced Pe-PDs have emerged as a promising strategy to surpass the limitations of conventional perovskite-based devices [51,52]. Incorporating plasmonic nanoparticles or nanostructures into the perovskite active layer or the adjacent

charge-collection layer significantly amplifies the local electromagnetic field, enhancing light–matter interactions and boosting photon absorption [53–57]. This approach effectively addresses the challenge of insufficient light absorption in thin perovskite layers, which can otherwise limit device sensitivity and efficiency. Furthermore, plasmonic structures can be precisely engineered to exhibit wavelength-specific resonances, enabling spectral tuning and improved detection selectivity [58]. The resulting strong near-field enhancement also facilitates faster carrier generation and separation [59], contributing to quicker photoresponses and better spectral discrimination. Overall, the integration of plasmonics leads to more efficient light harvesting, enhanced detection sensitivity, faster response times, and greater spectral tunability, collectively overcoming many of the limitations of traditional Pe-PDs.

In this review, we provide a comprehensive discussion focused on three main structures: (1) an overview of viable strategies for integrating plasmonics into Pe-PDs, along with a concise introduction to the two principal plasmonic modes; (2) a division of two types of plasmonic structures: plasmonic nanopatterns and plasmonic nanoparticles (NPs), and their respective impacts on device performance, highlighting their potential in PD applications; and (3) emerging perovskite optoelectronics associated with incorporating chiral plasmonic structures into perovskite optoelectronic devices for advanced light-matter interaction.

2. Introduction of Plasmonics

Plasmonics exploits the collective oscillations of free electrons, excited by electromagnetic radiation, at the interface between metallic and dielectric materials. These oscillations, known as surface plasmons, give rise to surface plasmon resonance (SPR), which enables the confinement and manipulation of light at dimensions well below the diffraction limit [60,61]. This capability has opened new avenues in optical sensing, high-resolution imaging, and the development of advanced photonic and optoelectronic devices [51].

Two principal plasmonic modes are typically distinguished: surface plasmon polaritons (SPPs) and localized surface plasmon resonances (LSPRs). SPPs are electromagnetic waves confined to the metal–dielectric interface, propagating along the surface while tightly binding light and electronic oscillations [62] (Figure 2a). These waves facilitate extreme electromagnetic field enhancement up to 10^5-fold and subwavelength light confinement, making them especially promising for use in thin-film plasmonic optoelectronic devices and PDs. Integrating plasmonic nanostructures directly into the active layer through pattern transfer techniques such as imprinting lithography [63,64] allows the formation of plasmonic features directly on the light-harvesting surface. This approach can significantly amplify optical absorption by enhancing light–matter interaction.

In contrast, LSPRs result from non-propagating electron oscillations confined within metallic nanoparticles (NPs) (Figure 2b). These localized resonances generate intense electromagnetic fields in the immediate vicinity of the nanoparticles, with field enhancement localized within just a few nanometers of the surface. The optical response of LSPRs is highly sensitive to nanoparticle size, shape, and material composition, allowing their resonant frequencies to be precisely tuned across the ultraviolet to infrared spectrum [65]. Strategically positioning these plasmonic nanoparticles, such as embedding them in buffer layers or within the photoactive layer, can enable efficient coupling of the enhanced near fields into adjacent photoactive regions, thereby boosting light absorption and improving device performance. Altogether, plasmonic strategies based on SPP, LSPR, or their combination have emerged as powerful tools for improving the performance of optoelectronic devices and advancing next-generation sensing technologies. Key mechanisms contributing to plasmonic enhancement in perovskite optoelectronics mainly include far-field light scattering,

near-field coupling, and plasmon-driven resonant energy transfer or hot electron transfer (HET) from metals to semiconductors (Figure 2c) [66–70]. In far-field light scattering events, which are representative of plasmonic effects in Pe-PDs, radiative decay involves intense light scattering away from the plasmonic nanostructures. Far-field scattered light effectively extends the optical path length within the photoactive layer, thereby enhancing light absorption [63,68,69,71]. The HET mechanism involves generating energetic hot electrons inside metal nanoparticles such as gold and silver. These hot electrons are produced either by excitations within the metal's conduction band or through transitions from the d-band to the conduction band [72]. Before these hot electrons lose energy, they can be effectively transferred into a semiconductor material by crossing a Schottky barrier formed at the metal-semiconductor interface, thus facilitating charge transfer and improving device performance [66,67,70]. Plasmon resonant energy transfer is a mechanism in which energy absorbed by a plasmonic metal from sunlight is non-radiatively transferred to a nearby semiconductor via dipole–dipole coupling, which enables directional energy flow from the metal to the semiconductor [53]. This process results in the generation of electron–hole pairs below or near the semiconductor's band edge.

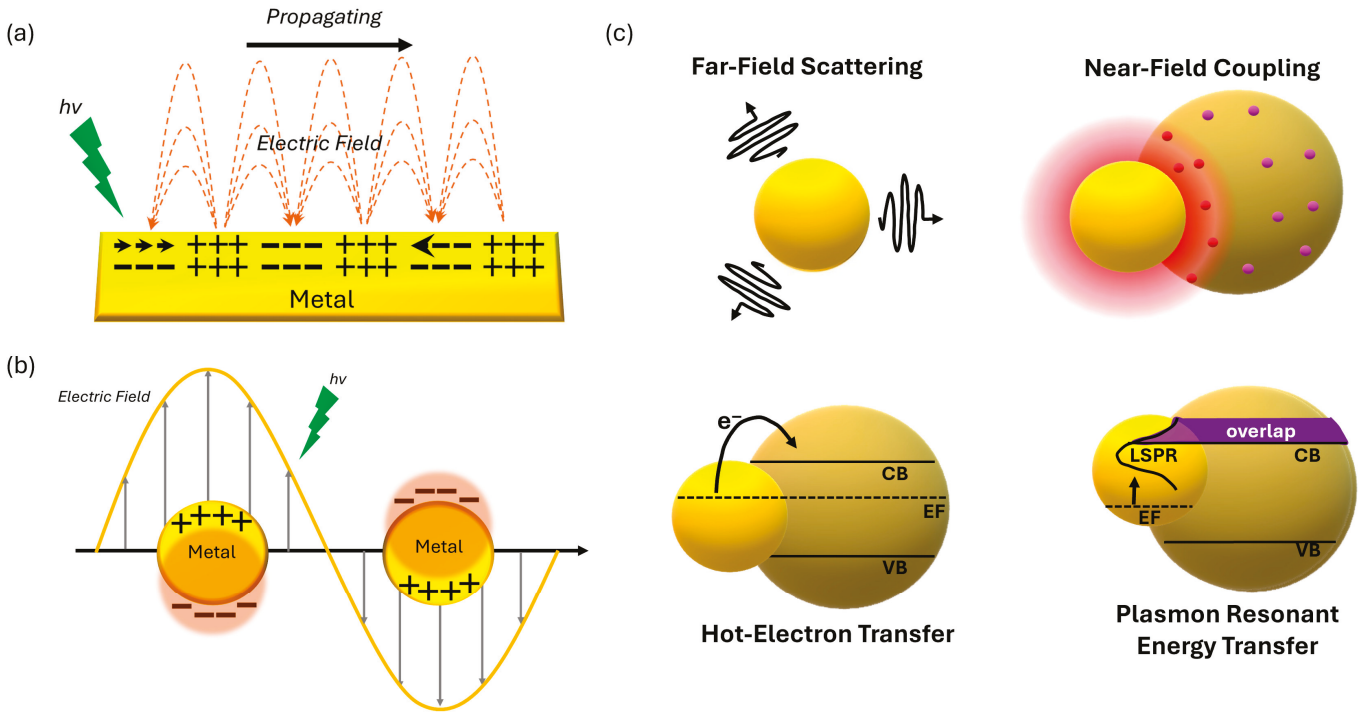

Figure 2. Schematics of the surface plasmons. (**a**) Propagating surface plasmon generated (SPP) at the metal-dielectric interface. (**b**) localized surface plasmon resonance (LSPR) induced in the metal nanoparticles. (**c**) Plasmon-driven far-field and near-field scattering, hot electron transfer (HET), and plasmon resonant energy transfer.

3. Figures of Merits for PDs

To evaluate the performance of a PD, several key figures of merit are typically considered, including responsivity (R), external quantum efficiency (EQE), and detectivity (D^*). These parameters provide critical insights into the optoelectronic properties of the device. R quantifies the electrical response of the PD to incident light and is defined as the ratio of the photocurrent to the incident light power. It is calculated using the following Equation (1):

$$R = \frac{I_{light} - I_{dark}}{P_{in} \cdot S} \tag{1}$$

where I_{light} and I_{dark} are the output currents under illumination and in the dark, respectively, P_{in} is the incident light power density, and S is the effective area of the device. External quantum efficiency (EQE) represents the ratio of the number of charge carriers collected to the number of incident photons, reflecting the PD's photon-to-charge conversion efficiency. It is calculated as Equation (2),

$$\text{EQE} = \frac{hc}{q\lambda} \cdot R \tag{2}$$

where h is Planck's constant, c is the speed of light, q is the elementary charge, and λ is the wavelength of the incident light. D^* is a critical parameter for evaluating the sensitivity of a PD, particularly under low-light conditions. It is defined as Equation (3),

$$D^* = \frac{R\sqrt{S \cdot \Delta f}}{i_n} = \frac{\sqrt{S \cdot \Delta f}}{NEP} \tag{3}$$

where S is the effective area, Δf is the electrical bandwidth, i_{n} is the noise current, and NEP is the noise equivalent power. NEP represents the minimum impinging optical power that a detector can distinguish from the noise. These metrics collectively provide a key assessment of a PD's performance.

In evaluating the performance of PDs, standardized measurement conditions are essential to ensure consistency and comparability across different materials and device architectures. Typically, a bias voltage ranging from 0 to several tens of volts is applied to enhance carrier collection, though self-powered devices operate at zero bias, and higher voltages may be used in specific cases such as transistor-type or avalanche PDs. The active area of a device, which typically varies in area units between mm^2 and cm^2, must be accurately defined, as it directly impacts the calculation of normalized figures of merit such as D^*. Noise characterization, a critical factor in determining NEP and D^*, typically involves measuring the current noise spectral density (in $A/\sqrt{Hz}$) under dark conditions using low-noise current amplifiers and spectrum analyzers or lock-in techniques. Both intrinsic noise sources, such as thermal (Johnson) and shot noise, and extrinsic sources like 1/f noise, are considered [73]. Bandwidths below kHz are commonly used for noise characterization or extending into the MHz range is employed for evaluating response speed and frequency-dependent characteristics. Accurate and transparent reporting of these parameters, bias, active area, bandwidth, and noise estimation methods, is essential for reliable benchmarking and for advancing the development of high-performance PDs.

4. Plasmonic Nanoparticle-Based Pe-PDs

4.1. Perovskite–Plasmonic Nanoparticle

Most studies on plasmonic NP-based Pe-PDs have primarily focused on incorporating plasmonic NPs prior to the deposition of the perovskite layer. Dong et al. demonstrated a Pe-PD with enhanced optoelectronic performance by introducing all-inorganic perovskite ($CsPbBr_3$) nanocrystals (NCs) with a preferred orientation together with gold nanoparticles (Au NPs) exhibiting LSPR effect (Figure 3a) [74]. To fabricate Pe-PDs, Au NPs were spin-coated on a Si substrate, followed by the deposition of a highly dense and uniform $CsPbBr_3$–Au NP film via centrifugal-casting, and the placement of thermally evaporated Au electrodes (Figure 3b). The resulting Pe-PD showed enhanced both light absorption and the near-field electric field due to the LSPR effect of Au NPs through the excellent spectral overlap between the absorption peak of $CsPbBr_3$ (520 nm) and the plasmon resonance peak of Au (530 nm) (Figure 3c). As a result, the photocurrent increased from 245.6 μA to 831.1 μA, representing 238% enhancement, while the on/off ratio rose from 1.6×10^5 to 1.66×10^6, and the detectivity (D^*) improved from 4.56×10^8 Jones to 1.684×10^9 Jones.

Moreover, the fabricated device demonstrated excellent stability, maintaining performance degradation within 3.2% even after more than 10,000 light on/off cycles.

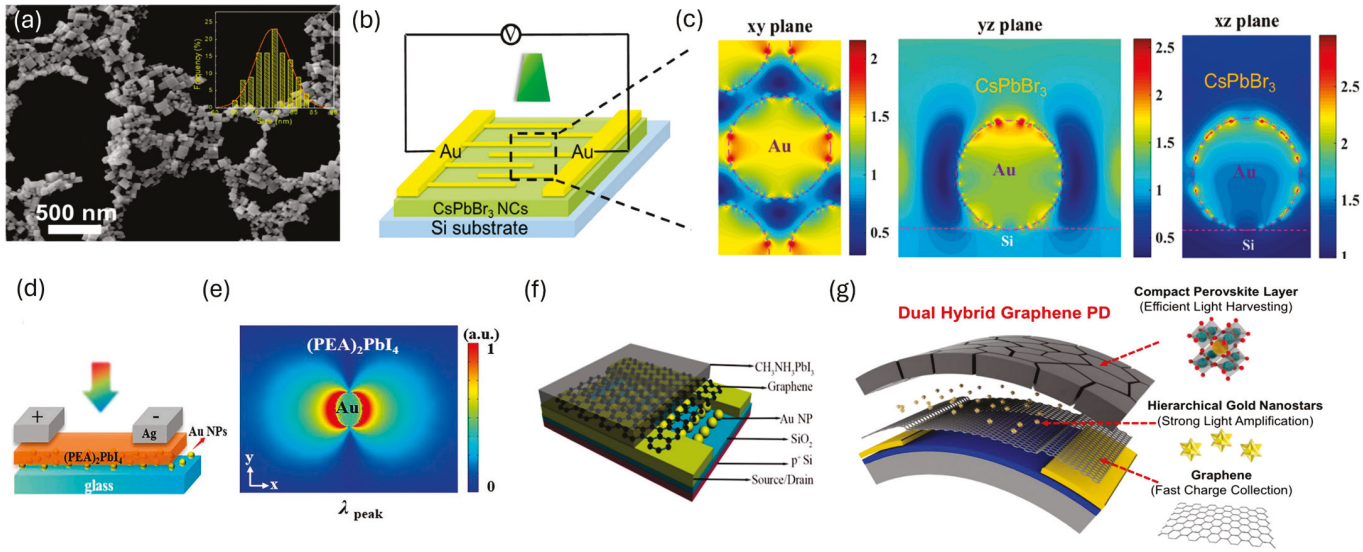

Figure 3. (**a**) SEM images comparing $CsPbBr_3$ nanocrystal (NC) films fabricated by drop-coating. (**b**) Schematic demonstration of device configuration. (**c**) The simplified schematic structures of the simulation model [74]. Copyright © 2016 Wiley-VCH. (**d**) Scheme of the PD based on $(PEA)_2PbI_4$ SC. (**e**) Electric field distributions in the x–y plane at absorption peak wavelength of $(PEA)_2PbI_4$ SC with Au NPs (t_{Au} = 5 nm) [75]. Copyright © 2023 Wiley-VCH GmbH. (**f**) Schematic of the device architecture used in this study [76]. Copyright © 2016 Royal Society of Chemistry. (**g**) Schematic of a graphene dual hybrid PD composed of a perovskite material and GNSs with illustration of the key role of each component in the synergistic effect for optical sensing [77]. Copyright © 2020 Springer Nature.

Conventional 2D single-crystal-based Pe-PDs exhibit a limitation in responsivity (R), being restricted to ultraviolet and visible regions. To overcome this limitation and extend the detection capability to the telecommunication wavelength of 1310 nm, Xi et al. introduced Au NPs [75]. The device was fabricated by thermally evaporating Au NPs onto a glass substrate, transferring a $(PEA)_2PbI_4$ single crystal on top, and subsequently depositing Ag electrodes (Figure 3d). In the long-wavelength region (650–900 nm), an average external quantum efficiency (EQE) was enhanced by up to 1000%, and stable on–off electrical responses were achieved at the 1310 nm telecommunication band. Two mechanisms could explain the enhancement of photodetection performance. First, light absorption was strengthened by the local electric field generated by Au NPs, thereby increasing the photocurrent (Figure 3e). Second, in the long-wavelength region beyond the bandgap of $(PEA)_2PbI_4$, an additional photocurrent was generated through the injection of hot holes from Au NPs. From a performance perspective, the dark current was suppressed to below 100 fA, and the EQE reached 61% at 480 nm, corresponding to an enhancement factor of 68.5% compared with the control device (36.4%). The D^* reached as high as 8.1×10^{14} Jones at 480 nm, representing a 68.5% improvement over the control (4.8×10^{14} Jones). Moreover, the device exhibited excellent stability, maintaining about 70% of its initial photocurrent after 33 days without encapsulation.

4.2. Perovskite–Graphene–Plasmonic Nanoparticle

Plasmonic enhancement has also been explored in hybrid Pe-PDs with 2D materials such as graphene. Sun et al. reported enhanced performance in $CH_3NH_3PbI_3$ perovskite–graphene hybrid Pe-PDs by introducing Au NPs with a diameter of approxi-

mately 40 nm [76]. The device was fabricated by first defining Au electrodes on a Si/SiO_2 substrate, sequentially depositing Au NPs, graphene, and a perovskite thin film, in which Au NPs were positioned beneath the graphene layer and physically separated from the perovskite. This configuration enabled the exploitation of the plasmonic effect of Au NPs without interfering with charge transport pathways in the perovskite, thereby ensuring that the observed enhancement was solely attributed to plasmonic enhancement (Figure 3f). The hybrid device containing perovskite, graphene, and Au NPs (P–G–Au) exhibited nearly twice the *R* and EQE compared with the control device without Au NPs (P–G), achieving a maximum *R* of 2×10^3 A W^{-1}. This enhancement was attributed to the LSPR effect of the Au NPs, which boosted light absorption in the perovskite layer and facilitated the generation of photo-induced carriers near the graphene interface. Faster and more efficient carrier extraction was enabled by shorter transport pathways. As a result, the photoresponse speed of the hybrid device was significantly improved, with the rise time reduced from 1.8 s for the P–G device to 1.5 s for the P–G–Au device, corresponding to an improvement of ~17%. These findings demonstrate that incorporating Au NPs is an effective strategy to simultaneously enhance both the responsivity (*R*) and response speed in perovskite–graphene hybrid PDs.

However, due to the poor affinity of the perovskite precursor solution on the graphene surface, the perovskite layer often forms in an isolated island-like morphology rather than as a dense, continuous film. To overcome this limitation, Lee et al. proposed a hybrid Pe-PD structure by incorporating gold nanostars (GNSs) into graphene–perovskite systems [77]. GNSs possessed a spherical core surrounded by multiple sharp tips, where strong local electromagnetic fields were generated at the tip ends. In this configuration, the perovskite layer acted as an efficient light absorber, graphene provided high-speed charge transport, and GNSs enhanced the local electromagnetic field, thereby enabling complementary functionality among the three components (Figure 3g). The perovskite layer was fabricated by thermal evaporation of PbI_2 followed by spin-coating of MAI, which successfully yielded a dense perovskite film on graphene. The resulting device exhibited outstanding performance under blue light illumination, achieving *R* of 5.90×10^4 A W^{-1} and D^* of 1.31×10^{13} Jones, which represented the highest values reported to date for $MAPbI_3$–graphene Pe-PDs. Compared with pristine Pe–PDs, *R* and D^* were enhanced by 7.7 million-fold and over 100-fold, respectively. Photoluminescence (PL) quenching and enhancement analyses confirmed that the improved performance resulted from both efficient charge transfer at the graphene–perovskite interface and the LSPR effect of GNSs. Furthermore, the device fabricated on a plastic substrate demonstrated remarkable flexibility, maintaining stable operation under bending with a radius of curvature as small as 3 mm and after more than 1000 bending cycles. In addition, a flexible G–GNS–P–PD array (10×10) successfully enabled sensitive photomapping, demonstrating its potential as a high-performance flexible imaging sensor.

Perovskite quantum dots (PQDs) have also been employed in graphene/plasmonic NP hybrid Pe-PDs. Yadav et al. fabricated a device by depositing $MAPbBr_3$ PQDs onto a graphene channel [78] (Figure 4a). In this architecture, PQDs acted as the photo-absorbing layer, generating electron–hole pairs upon illumination; the photogenerated electrons are transferred to graphene, while holes remain in the PQDs, thereby modulating the channel conductivity and inducing a photocurrent. The resulting PQDs/graphene hybrid Pe-PD exhibited a significant enhancement in photoresponse compared with pristine graphene detectors, achieving *R* of ~10^5 A W^{-1} and EQE exceeding 10^7% at 432 nm. Furthermore, the rise and decay times of the photocurrent were reduced from 12 s and 17 s (PQDs/Gr) to 8.9 s and 16 s (PQDs/RD-Au NCs/Gr), respectively, confirming the faster photoresponse. To investigate the plasmonic contribution depending on the shape of plasmonic NPs, three

different morphologies of Au nanocrystals (Au NCs) (e.g., sphere, octahedron (OD), and rhombic dodecahedron (RD)) were incorporated into the PQDs/graphene hybrid structure (Figure 4b). For sphere-shaped Au NCs (∼27 nm), the LSPR peak appeared at 528 nm, resulting in increased absorption and PL intensity, though the enhancement in device performance was relatively modest due to limited local electric field strength. In contrast, OD Au NCs (∼45 nm) exhibited an LSPR peak at 541 nm and provided a larger scattering cross-section and stronger local electric field than spheres, thereby significantly improving both photocurrent and absorption. RD Au NCs (∼50 nm) with an LSPR peak at 544 nm demonstrated the strongest plasmonic effect, featuring the largest scattering cross-section and most intense local electric field among the three shapes. Incorporation of RD Au NCs led to a ~10-fold increase in photocurrent compared with the sphere-based device, yielding a maximum photocurrent of 88.2 μA, R of 2.7 × 10^5 A W^{-1}, D^* of 4.9 × 10^{13} Jones, and EQE of 7.9 × 10^7%.

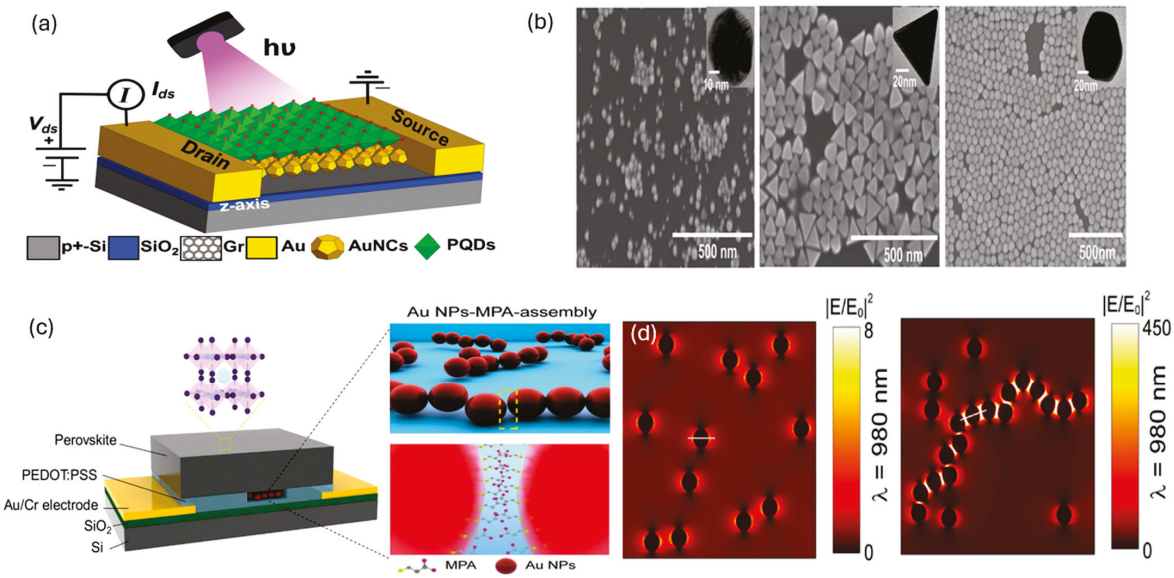

Figure 4. (**a**) The schematic illustration of PQDs/Au NCs/Gr hybrid electrostatic gate-free. (**b**) FE-SEM image of sphere, octahedral (OD), and rhombic dodecahedron (RD) Au NCs, respectively [78]. Copyright © 2023 Wiley-VCH GmbH. (**c**) The scheme of the perovskite/PEDOT–PSS photodetector comprising the Au NPs-MPA assembly embedded in the PEDOT–PSS layer. (**d**) The calculated electric field intensity distribution of plasmonic nanostructures at 980 nm [79]. Copyright © 2021 Elsevier B.V.

4.3. Perovskite–Plasmonic Nanoparticle Assembly

A study by La et al. demonstrated the development of Pe-PDs with both high sensitivity and fast response speed by incorporating plasmonic Au NPs assembled into chain-like structures via 3-mercaptopropionic acid (MPA) [79] (Figure 4c). In this system, MPA serves as a bifunctional linker: its thiol group binds to the Au surface, while its carboxyl group bridges adjacent nanoparticles, thereby inducing ordered chain-like assemblies. Unlike randomly aggregated Au NPs, these MPA-induced assemblies maintain ~0.6 nm interparticle gaps, enabling strong plasmonic coupling, hot spot formation, and enhanced electromagnetic fields compared with isolated Au NPs. The Au NP assemblies were prepared using 3-mercaptopropionic acid (MPA), a short-chain alkanethiol, and embedded within the poly(3,4-ethylenedioxythiophene) polystyrene sulfonate (PEDOT–PSS) hole transport layer. Compared with devices containing only isolated Au NPs, the assembly structure induced plasmon coupling, creating narrow interparticle cavities, which generated strong field enhancement and improved charge extraction and transport simultaneously (Figure 4d). The Au NPs-MPA assembly-based Pe-PDs exhibited R of ~2063 A W^{-1}, which is 4.1 times higher

than that of the pristine device, noise equivalent power (*NEP*) of 1.93×10^{14} W $Hz^{-1/2}$ corresponding to a 15.6-fold reduction, and maximum D^* of 1.16×10^{12} Jones. These enhancements were primarily attributed to three mechanisms: (i) the reduced hole injection barrier induced by Au NPs, leading to improved charge extraction efficiency; (ii) the strong electromagnetic fields generated within the NP chain structure, which facilitated charge separation and transport, thereby accelerating the response speed; and (iii) the excitation of gap plasmons and longitudinal modes, which extended the absorption spectrum from the visible to the near-infrared (NIR) region, contributing additional photocurrent generation. Furthermore, devices fabricated with shortened channel lengths achieved response times as fast as ~300 ns, reduced from ~850 ns in the longer channel devices, corresponding to a 2.8-fold improvement in photoresponse speed. These results demonstrate that embedding Au NPs-MPA assemblies into the PEDOT–PSS layer provides a highly effective strategy for achieving Pe-PDs with both ultrahigh sensitivity and rapid response.

4.4. Perovskite–Interlayer–Plasmonic Nanoparticle

To mitigate the potential increase in dark current caused by the incorporation of plasmonic NPs, strategies involving the interfacial passivation layer into plasmonic nanostructures have also been reported. Lim et al. integrated Au nanorods (NRs) exhibiting LSPR into the ITO electrode to enhance the light absorption of $MAPbI_3$-based Pe-PDs, while simultaneously inserting a thin polyethyleneimine ethoxylated (PEIE) interlayer (~7.9 nm) between the Au NRs and the perovskite active layer [80] (Figure 5a). PEIE, an amine-based cationic polymer, acts as an interfacial passivation layer by blocking electron injection through band alignment and suppressing interfacial trap states, thereby reducing dark current. Among the four fabricated devices ($MAPbI_3$ control, with only Au NRs, with only PEIE, and with Au NRs/PEIE), the hybrid structure incorporating both Au NRs and PEIE exhibited the best photodetection performance. The device achieved *R* of 0.360 A W^{-1} and D^* of 1.81×10^{10} Jones, representing a remarkable enhancement compared with the other devices. In addition, the dark current was significantly suppressed to 2.93×10^{-10} A, corresponding to a ~76% reduction relative to the pristine $MAPbI_3$ control device (1.21×10^{-9} A). These improvements were attributed to the synergistic effects of plasmonic light amplification by Au NRs and interfacial stabilization by the PEIE interlayer (Figure 5b). PL and TRPL analyses revealed that Au NRs facilitated faster charge transfer and reduced recombination, while the PEIE interlayer prevented excessive quenching caused by direct contact between Au NRs and the perovskite, thereby improving charge transport efficiency. Furthermore, finite-difference time-domain (FDTD) simulations confirmed that the electromagnetic field enhancement and scattering effects induced by Au NRs contributed to increased light absorption, consistent with the observed performance improvement.

Another study reported the use of SU-8 encapsulation to reduce recombination losses while simultaneously leveraging the plasmonic enhancement provided by silver nanoparticles (Ag NPs). Ye et al. incorporated Ag NPs exhibiting LSPR together with an SU-8 photoresist encapsulation layer to enhance the performance of $CH_3NH_3PbI_3$-based Pe-PDs [81] (Figure 5c). SU-8 effectively prevented the oxidation of Ag, suppressed Ag^+ ion migration, and passivated surface trap states, thereby optimizing carrier transport. The device was fabricated by spin-coating Ag NPs onto a glass substrate coated with SU-8, forming microelectrodes, and subsequently depositing the perovskite active layer. The resulting Pe-PD showed the photocurrent enhancement from 0.19 μA to 0.86 μA, corresponding to a 352.6% enhancement. The *R* and EQE enhanced from 0.105 A W^{-1} to 0.478 A W^{-1}, while the EQE improved from 0.206% to 0.940%. The D^* was significantly enhanced from 1.11×10^{10} Jones to 5.04×10^{10} Jones (354% increase), and the linear dynamic range (LDR)

expanded from 37.6 dB to 50.7 dB. Additionally, the response speed improved, with the rise and decay times reduced from 277/248 ms to 222/210 ms, respectively. These improvements were attributed to the strong electromagnetic field amplification induced by LSPR around Ag NPs (Figure 5d), which enlarged the light absorption cross-section within the perovskite layer, and to the SU-8 encapsulation layer, which suppressed defect-mediated recombination and enhanced crystallinity for more efficient charge transport. Furthermore, the device maintained stable performance even after 1000 on/off switching cycles, demonstrating device reliability. This work highlights that SU-8 encapsulated Ag NPs can provide a dual benefit of plasmonic enhancement and defect passivation, enabling significant performance improvements in Pe-PDs with simple device architectures.

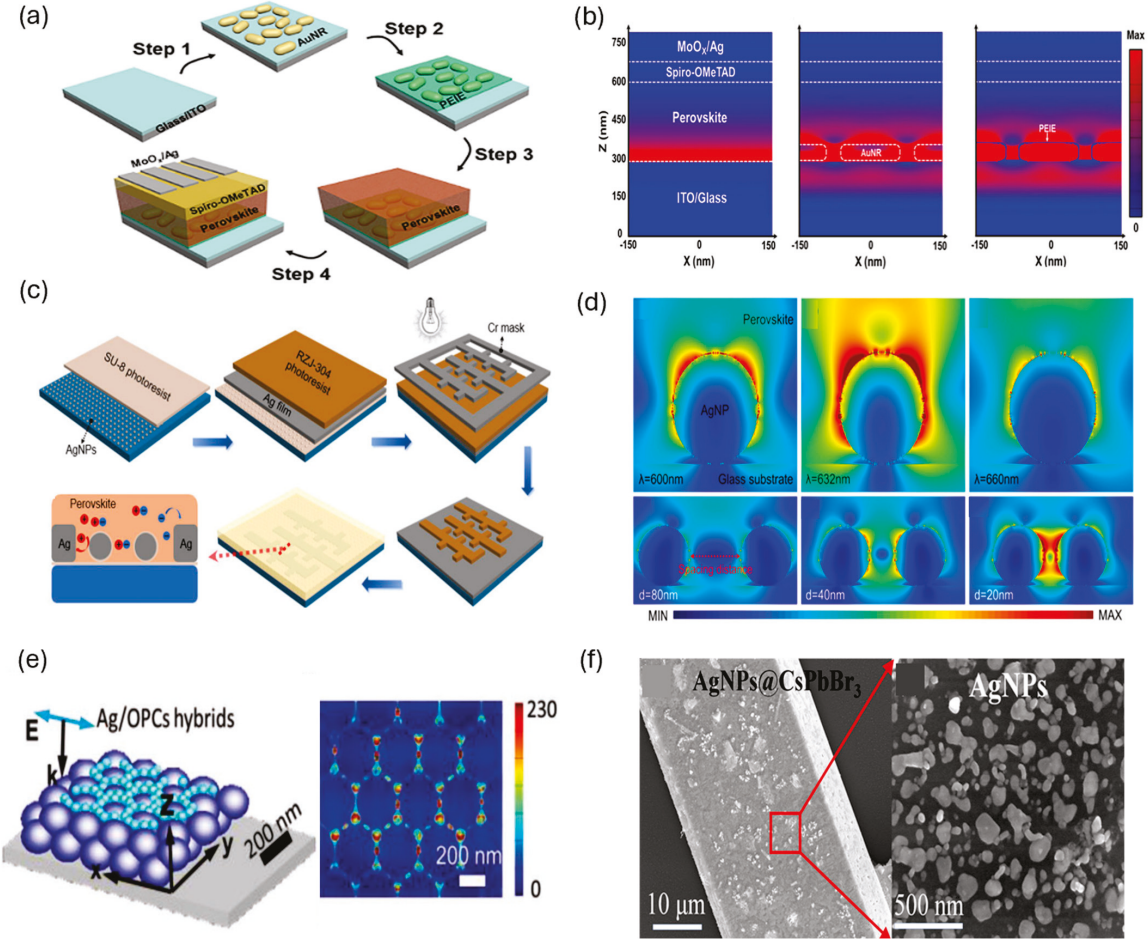

Figure 5. (**a**) Schematic of the fabrication methodology for the perovskite photodetector. (**b**) Absorbance density profiles of the control device, w/Au NR, and w/Au NR/PEIE Pe-PDs at λ = 680 nm, calculated from FDTD simulations [80]. Copyright © 2025 Elsevier Ltd. (**c**) Schematic of fabrication process. (**d**) Analyses of local electric field enhancement of Ag NP with different excitation wavelengths, and the influence of spacing distance under constant excitation wavelength [81]. Copyright © 2024 IEEE. (**e**) Ag/OPCs hybrid model for 3D FDTD simulation and simulated electric field intensity distribution of Ag/OPCs film at 410 nm (top view) [82]. Copyright © 2018 Wiley-VCH GmbH. (**f**) SEM image of a $CsPbBr_3$ NW covered with physically isolated Ag NPs, along with an enlarged view of the Ag NPs [83]. Copyright © 2023 Royal Society of Chemistry.

4.5. Perovskite Photonic Crystal–Plasmonic Nanoparticle

Plasmonic NPs hybridized with photonic crystals have also been incorporated to further enhance the performance of Pe-PDs. Li et al. developed UV-sensitive Pe-PDs by hybridizing plasmonic Ag NPs with opal photonic crystals (OPCs) [82] (Figure 5e). They proposed a new strategy that couples plasmonic metals with photonic crystals,

simultaneously exploiting the LSPR of a Ag NPs-based film and the photonic stop band (PSB) of polymethyl methacrylate (PMMA) OPCs. Ag concentrated incident light into a local electric field to amplify both excitation and emission processes, whereas OPCs control electromagnetic waves via periodic refractive-index modulation to strengthen emission. In particular, the Ag/OPCs hybrid structure exhibited a strong synergistic effect, resulting in an electric field enhancement of up to 230 times near the surface of $CsPbCl_3$ nanocrystals, with the most pronounced enhancement observed when the $CsPbCl_3$ layer thickness was $\leq$ 50 nm. Compared with pristine $CsPbCl_3$, $CsPbCl_3$ deposited on a Ag NPs-based film showed 50 times higher PL intensity; on OPCs it showed 20 times higher; and in the Ag/OPCs hybrid it reached up to 150 times, with an emission efficiency of 51.5%. The PL lifetime is shortened from 3.7 ns to 1.8 ns, evidencing an increased radiative rate, indicating that not only absorption but also emission-field and excitation-field enhancements contributed concurrently. Based on this platform, the resulting UV-sensitive Pe-PDs delivered excellent device performance: a very low dark current on the order of 10^{-11} A, D^* of 9×10^{14} Jones, rise/decay times of 28/31 ms (40~50% reduction versus the control), and R of 8.1 A W^{-1} at 365 nm, exceeding the typical ~1.0 A W^{-1} of commercial UV detectors. The spectral response bandwidth is as narrow as 30 nm. Moreover, devices fabricated on PET substrates maintained high stability and performance under flexible operation.

4.6. Perovskite: Inorganic Heterojunction–Plasmonic Nanoparticle

In addition to Pe-PDs solely using a perovskite layer as an active layer, plasmonic Pe-PDs based on heterojunction systems with inorganic semiconductors have also been investigated. Lin et al. fabricated a heterojunction Pe-PD composed of a $CsPbBr_3$ microwire and a p-GaN substrate, in which Ag NPs were introduced to induce LSPR and simultaneously passivate surface defects, thereby enhancing both device performance and stability [83] (Figure 5f). For the pristine $CsPbBr_3$/GaN heterojunction device without Ag NPs, the R, D^*, and EQE reached 11.6 A W^{-1}, 6.3×10^{11} Jones, and 3781%, respectively, with rise/decay times of 11.98/27.13 ms. Upon integration of Ag NPs, the device performance improved markedly, achieving R of 63.9 A W^{-1} (5.5 times enhancement), D^* of 4.05×10^{12} Jones (6 times enhancement), and EQE of 1.5×10^4%, while the response speed was significantly accelerated to 1.0/21.3 ms. Moreover, stability tests demonstrated that while the pristine $CsPbBr_3$/GaN device exhibited a substantial decrease in photocurrent after 60 days of storage in air, the Ag NPs-integrated device maintained nearly constant photocurrent, confirming a remarkable improvement in long-term stability.

5. Plasmonic Nanopattern-Based Pe-PDs

5.1. Perovskite–Plasmonic Nanopattern

To overcome the limited near-infrared (NIR) response of conventional Pe-PDs, Du et al. introduced Au nanosquare arrays [84]. They fabricated NIR perovskite PDs on a plasmonic functionalized multilayer substrate composed of Au film/SiO_2 spacer/nanosquares arrays (Figure 6a). The plasmonic PD was constructed by sequentially depositing a 100 nm Au film and a 10 nm SiO_2 dielectric layer onto a Si/SiO_2 substrate via electron beam evaporation, followed by the fabrication of 50 nm Au source/drain electrodes and 30 nm Au nanosquare arrays using electron (E)-beam lithography. Subsequently, a 20 nm (2,3,5,6-tetrafluoro-7,7,8,8-tetracyanoquinodimethane (F_4-TCNQ)-doped poly [bis(4-phenyl) (2,4,6-trimethylphenyl) amine] (PTAA) hole transporting layer and an 80 nm $CH_3NH_3PbI_3$ layer were spin-coated on the plasmonic substrate. To investigate the optical properties of the perovskite film, the reflectance spectra and photoluminescence (PL) characteristics were measured. The perovskite film fabricated on the plasmonic substrate exhibited stronger

reflectance than that on the Si/SiO_2 substrate, especially in the near-infrared region from 750 to 850 nm, where a considerable absorption enhancement was observed. Moreover, the film on the plasmonic substrate exhibited approximately twice the PL intensity compared with the Si/SiO_2 substrate, with the PL emission peak located around 765 nm (1.62 eV), indicating improved light absorption and enhanced optoelectronic coupling due to plasmonic effects. Furthermore, time-resolved PL measurements revealed that the perovskite film on the plasmonic substrate exhibited a significantly shortened PL lifetime (2.09 ns vs. 13.87 ns), suggesting faster charge transfer between the perovskite and the hole-transporting layer, thereby facilitating more efficient carrier injection into the electrodes. Device characterization revealed that at 800 nm, the plasmonic Pe-PDs achieved a maximum photocurrent of 4.6 nA, approximately nine times higher than that of the non-plasmonic device, and an EQE of 65%, representing a 2.5-fold enhancement. The enhancement of EQE was maximized at 800 nm, attributed to improved light harvesting via localized surface plasmon resonance (LSPR) absorption, which increased photocurrent generation. Furthermore, as the size of the Au nanosquares increased, the LSPR peak red shifted, demonstrating that tuning the nanosquare dimensions provides an effective strategy for controlling the spectral response of Pe-PDs.

Gu et al. developed plasmonic Pe-PDs with enhanced photodetection properties in the visible range by hybridizing Au triangular arrays with $MAPbI_3$ perovskite [85]. The triangular Au arrays were fabricated by (E)-beam lithography, followed by Au electrode deposition, and then a $MAPbI_3$ solution was spin-coated to construct the plasmonic Pe-PDs (Figure 6b). Plasmonic Pe-PDs showed higher I_{ph} (photocurrent), confirming that the incorporation of Au arrays significantly enhanced the photocurrent generation. This photocurrent enhancement was attributed to the effective electron transfer between the Au arrays and the perovskite film, which suppressed the recombination of electron-hole pairs, and to the enhanced electric field induced by the LSPR effect, which facilitated the generation of more electron-hole pairs in the perovskite-Au system. The resulting Pe-PD exhibited EQE of 12.6%, 15.9%, and 16.9% at excitation wavelengths of 450 nm, 532 nm, and 635 nm, respectively, which were about three times higher than those of the pristine device at the same wavelengths.

5.2. Perovskite–AAO–Plasmonic Nanopattern

In addition to the noble metals Au and Ag, studies have also reported the use of non-noble metals such as Al and Cu to improve the performance of PQD-based PDs. Li et al. reported the fabrication of AAO porous structures via a two-step anodization process, followed by thermal evaporation of metallic sources and annealing to form metallic nanoparticles (Al, Ag, and Cu) on the surface, and subsequent spin coating of $CsPbBr_3$ QD solution to construct plasmonic PDs [86] (Figure 6c). Among the various metals-based plasmonic Pe-PDs fabricated by this method, the Al/AAO hybrid plasmonic Pe-PDs exhibited the highest photodetection performance, with R of 4.8 mA/W at a bias of 1 V, which was 48 times higher than that of bare glass substrate-based pristine Pe-PDs, and the EQE was enhanced by about 40 times from 0.03% to 1.21%. The enhancement has been attributed to multiple interferences within the AAO matrix combined with strong plasmonic coupling among metallic NPs, resulting in spatial light confinement. Notably, the dense distribution of Al nanoparticles provides a stronger electromagnetic field compared with Ag or Cu, leading to superior PL intensity.

5.3. Perovskite–Plasmonic Multiple Pattern

Compared to a single nanograting or nanoparticle (NP), the use of multiple plasmonic patterns significantly enhances light amplification. This approach overcomes the

limitation of single nanogratings, where strong light amplification only occurs when the polarization of the incident light is nearly perpendicular to the grating due to its unidirectional structure. Lee et al. developed high-performance flexible Pe-PDs by applying high-efficiency hierarchical plasmonic nanostructures composed of cross-nanograting patterns (CGs) and nanoposts (NPs) [63]. The hierarchical cross-nanogratings with NPs (CN) patterns were fabricated by combining block copolymer lithography with nanoimprint lithography. A PS-b-PMMA film was spin-coated on a Si/SiO_2 substrate and annealed, followed by nanoimprinting using a poly(dimethylsiloxane) PDMS stamp with CG patterns. Subsequently, UV/acid treatment was carried out to remove PMMA and form nanoholes, which were then used as a mask for dry etching to produce CN-patterned SiO_2 films. Using these SiO_2 films as masters, CN-patterned PDMS stamps were prepared, and Au was deposited on the CN-patterned PS films to complete plasmonic CN-patterned Au films (Figure 6d). The CN patterns induced LSPR, exhibiting superior light trapping performance by concentrating on the electromagnetic field. Under red light illumination (10 $\mu W/cm^2$). The R increased from 140.5 mA/W for flat Pe-PDs to 588.6 mA/W for CN-based Pe-PDs, corresponding to an approximately 4.2-fold enhancement. The EQE improved from 26% to 109%, and the D^* increased from 6.5×10^{11} to 22.5×10^{11} Jones, representing about 4.2-fold and 9.9-fold enhancements, respectively. Particularly, in the 450–670 nm range, the CN-based devices outperformed other single plasmonic structures (GN, CG, and grating). In addition, stable photoresponse characteristics were maintained under a minimum bending radius of 8 mm and after more than 1000 repeated bending cycles, demonstrating both mechanical flexibility and operational stability.

A study has demonstrated that the integration of metasurfaces and nanopatterns can induce stronger plasmonic effects, including SPP resonances and enhanced local thermoelectric fields. These phenomena significantly boost photothermal conversion within the perovskite layer and enhance the photothermoelectric (PTE) effect, thereby overcoming the inherent bandwidth limitations of perovskite-based polarization detectors, which were previously confined to the visible–near-infrared range. Li et al. developed a PD that utilizes the PTE effect [87]. The device was composed of a multilayer structure: $Cs_{0.05}(FA_{0.85}MA_{0.15})_{0.95}Pb(I_{0.85}Br_{0.15})_3$ (CsFAMA) perovskite layer, PEDOT: PSS layer, and metasurface. To optimize the device's structure, the researchers used CST Microwave Studio simulations to compare two types of metasurfaces: T-shaped and I-shaped designs (Figure 6e). The I-shaped metasurface demonstrated superior performance due to stronger boundary effects and enhanced SPP resonance. Under 0.1 THz irradiation, the I-shaped device achieved a high R of 94 V W^{-1}, a low NEP of 5.03 pW $Hz^{-1/2}$, and a fast response time of 138 μs. It also generated a maximum photovoltage of 5.1 mV and a minimum of 3.7 mV, resulting in an anisotropy ratio of 1.38. Even after 240 days of storage in ambient air, the device maintained excellent stability, with the polarization ratio changing by less than 2%. In comparison, the T-shaped metasurface recorded an anisotropy ratio of 1.22, with maximum and minimum photovoltages of 3.4 mV and 2.8 mV, respectively. For a control device without metasurface structures, simulations showed that the maximum electric field intensity reached only 1 kV/m. In contrast, the inclusion of metasurface structures increased this value significantly to 4 kV/m, demonstrating the effectiveness of the metasurface design in enhancing device performance.

5.4. Plasmonic Hot Carrier Inducing Structure

Upon photoexcitation in pristine perovskite materials, both electrons and holes are generated in perovskite materials. Hot carriers are those that possess excess kinetic energy significantly above the thermal equilibrium at ambient temperatures [88]. The generation and distribution of these hot carriers depend on the electronic band structure of the per-

ovskite and the energy of the incident photons. However, due to ultrafast carrier relaxation processes [89,90], only a small fraction of the initially excited hot carriers can be extracted before thermalization occurs [91]. On the other hand, in plasmonic-enhanced perovskite structures, LSPRs in metallic nanostructures play a critical role in facilitating hot carrier generation [92,93]. When these nanostructures absorb light, the decay of excited plasmons can transfer energy to nearby electrons, elevating them to high-energy (hot) states within the conduction band. These hot electrons can be injected into adjacent perovskite layers or other semiconductor components, depending on the device architecture and interface engineering [94]. This process can significantly increase the light-harvesting capability of the system, thereby potentially improving the performance of Pe-PDs [70,85,95]. In addition to the light-harvesting capability, in the field of perovskite solar cells, studies have shown that hot carriers injected from plasmonic nanostructures can effectively fill trap states in the charge transport layers adjacent to the perovskite absorber [96,97]. This effect can reduce the interfacial traps or increase the free carrier density in materials such as TiO_x, thereby enhancing their electrical conductivity and carrier mobility. Furthermore, the efficient transfer of hot excitation supports the idea that hybrid architectures combining metals and perovskite semiconductors are promising platforms for developing highly efficient plasmon-induced and plasmon-enhanced light emission from semiconductors [67].

A study has also reported the enhancement of Pe-PDs performance by utilizing hot electrons generated through plasmonic effects. Park et al. fabricated a plasmonic nanodiode incorporating $MAPbI_3$ perovskite and proposed a structure that improves both the generation and the lifetime of hot electrons [66]. The device consisted of a $MAPbI_3$ layer coated on TiO_2 substrates decorated with plasmonic Au nanoislands, forming a $MAPbI_3$/plasmonic Au/TiO_2 Schottky nanodiode (Figure 6f). The $MAPbI_3$/plasmonic Au/TiO_2 nanodiode exhibited distinct incident photon-to-electron conversion efficiency (IPCE) enhancements at 1.6 eV, 2.2 eV, and 2.5 eV. The enhancement at 1.6 eV originated from the direct p-n junction formed between $MAPbI_3$ and TiO_2, where electrons excited at the conduction band edge of $MAPbI_3$ were extracted. At 2.2 eV, strong LSPR effects generated additional secondary hot electrons, thereby increasing the IPCE. The enhancement above 2.5 eV was attributed to hot electron extraction from the $MAPb_3$ film itself. In terms of photocurrent, the Au/TiO_2 structure generated 25 nA, which increased to 128 nA after introducing plasmonic Au nanoislands. With the subsequent incorporation of the $MAPbI_3$ film, the photocurrent further increased from 139 nA to 552 nA. This improvement arises from the efficient extraction of hot electrons generated within the plasmonic Au via the formation of a three-dimensional Schottky interface, combined with the additional hot electron flux generated in the $MAPbI_3$ film. The $MAPbI_3$ structure, coupled with LSPR, exhibited higher IPCE values across most photon energy regions compared with non-plasmonic structures. At photon energies above 2.7 eV, the $MAPbI_3$/plasmonic Au/TiO_2 nanodiode showed significantly higher IPCE, attributed to the near-field enhancement induced by Au nanostructures. This effect allowed $MAPbI_3$ near the plasmonic Au regions to absorb light more efficiently and generate an increased number of hot electron–hole pairs. Furthermore, since hot electrons are generated close to the hot spots of plasmonic Au, their extraction in the $MAPbI_3$/plasmonic Au structure was much more efficient compared with $MAPbI_3$/thin Au structures. Consequently, $MAPbI_3$ integrated with LSPR active plasmonic Au exhibited superior IPCE and short circuit photocurrent values relative to non-plasmonic $MAPbI_3$ devices.

5.5. Plasmonic-Photonic Hybrid Structure

Kowal et al. proposed a novel plasmonic-photonic hybrid structure based on hybrid plasmonic-photonic modes, providing a pathway to overcome the limitations of

conventional plasmonic Schottky junction PDs [98]. The structure consists of a metasurface incorporating Ag nanopillars integrated with a perovskite film, designed and analyzed using the finite-difference time-domain (FDTD) method. The designed hybrid system exhibited up to a fivefold enhancement of optical field intensity within a 4 × 4 µm pixel unit compared with flat junctions, along with pronounced light-trapping performance in the near-infrared regime, around 300 THz (≈1000 nm). Importantly, the coupling between the guided Bloch mode and the surface lattice resonance (SLR) resulted in strong electromagnetic field confinement at the metal/perovskite interface (Figure 6g), which was identified as a key factor in enhancing photogeneration efficiency. Moreover, the proposed architecture supports both passive and active photodetection, enabling multispectral and multilayer device designs, and offers efficient operation even in relatively thick film configurations. Although the study remains at the simulation stage, this hybrid plasmonic-photonic approach is considered a promising platform for future extension toward infrared, ultraviolet, and X-ray detection.

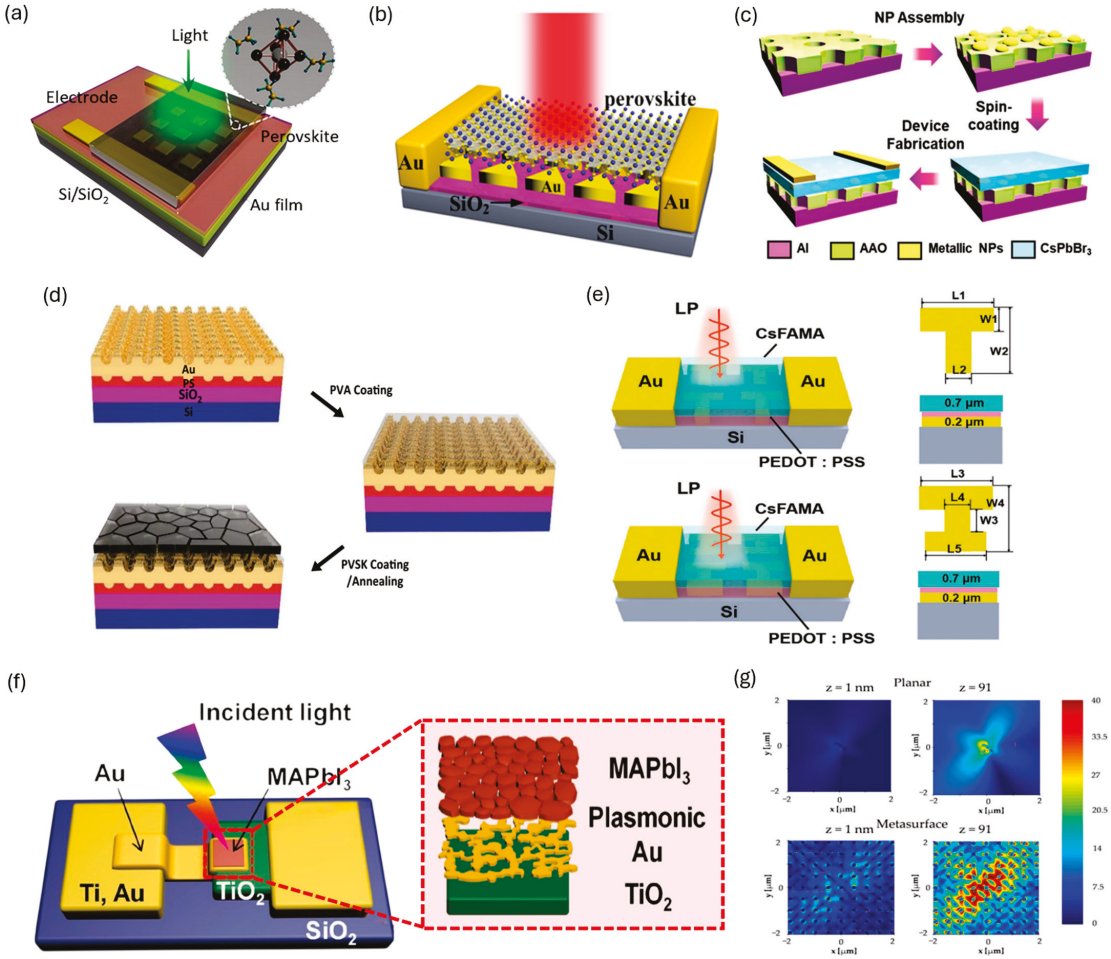

Figure 6. (**a**) Schematic of the device on the plasmonic substrate [84]. Copyright © 2018 Wiley. (**b**) Schematic illustration of the $MAPbI_3$-Au-based PD [85]. Copyright © 2020 Elsevier Ltd. (**c**) Schematic fabrication of hybrid plasmonic nanostructure-based Pe-PDs [86]. © 2020 Wiley. (**d**) Schematic diagram of fabrication process of PVA and $MAPbI_3$ perovskite films on a GN-patterned Au layer [63]. Copyright © 2024 Wiley. (**e**) Schematic diagram of T-shaped and I-shaped PDs structures and dimensions, respectively [87]. Copyright © 2024 Wiley. (**f**) Schematic of the $MAPbI_3$/plasmonic-Au/TiO_2 nanodiode (**left**) and magnified illustration of the active area (**right**) [66]. Copyright © 2019 American Chemical Society. (**g**) Comparison of the electric field magnitude |E| simulated in the planar (**top**) and structured (**bottom**) junction configurations at the vertical coordinate z = 1 nm, which corresponded to the metal patch, and z = 91 nm, which corresponded to the top of the pillars [98].

6. Chiral Plasmonics in Perovskites

6.1. Chiral Plasmonic Nanoparticles

Beyond conventional optoelectronic devices that typically respond to unpolarized light, introducing chirality or chiral plasmonic structures into perovskite materials paves the way for a new generation of technologies [42]. This convergence has led to the observation of a wide range of intriguing phenomena, including circular dichroism (CD), circularly polarized photoluminescence (CPPL), nonlinear optical responses, the chiral-induced spin selectivity (CISS) effect, and spintronic behavior [99,100]. These findings underscore how the synergy between the intrinsic advantages of perovskites and the distinctive nature of chirality is deepening our understanding of this rapidly evolving field in optoelectronics. Chiral optoelectronics provides promising applications such as enantioselective sensing [101], polarization-sensitive imaging [102], and advanced systems for quantum-secure communication and data transmission [103]. As a result, there is increasing focus on the design and development of chiral optical nanostructures by using perovskite materials, leading to enhancement of chiral responses such as CD and CPPL [104–110].

Seo et al. reported a significant enhancement in CPPL at room temperature by leveraging chiral Fano resonances, highlighting the potential of perovskite-based structures for efficient circularly polarized light (CPL) emission [104]. In their approach, triangular silver nanopatterns (with side lengths ranging from 370 to 430 nm) were fabricated on a quartz substrate using E-beam lithography. These nanostructures were then coated with a thin Al_2O_3 insulating layer, followed by the deposition of a ~210 nm-thick $MAPbI_3$ perovskite film via spin-coating (Figure 7a,b). Optical measurements of the resulting structure revealed characteristic Fano resonances, marked by asymmetric spectral features. These arose from the interplay between the broad Fabry–Perot resonance of the perovskite layer and narrow quasi-guided modes induced by the periodic nanopatterns. This interference gave rise to chiral Fano resonances within the perovskite film, resulting in a substantial amplification of CPPL (Figure 7c).

6.2. Chiral Metasurfaces

Aside from conventional plasmonic structures based on metals, significant research efforts have focused on creating chiral metasurfaces by engineering perovskite materials themselves into specific geometries [105,106]. These intrinsically chiral perovskite metasurfaces can offer valuable insight into the design principles for imparting chirality to future plasmonic nanostructures for perovskite optoelectronics. For example, Long et al. successfully created large-area, CPL-active 2D-chiral perovskite metasurfaces by employing a template-assisted self-assembly technique with halide perovskite NCs and pre-patterned elastomeric stamps [105] (Figure 7d). These chiral nanostructures were produced by depositing perovskite NC inks onto glass substrates, then pressing them with one of three distinct PDMS molds featuring 500 nm gammadion-shaped patterns arranged in a square lattice with a 600 nm pitch. The molds created left-handed (L), right-handed (R), and racemic (O) configurations across 9 mm^2 patterned regions. Unlike three-dimensional chiral forms such as helices, these gammadion patterns exhibit two-dimensional chirality; their handedness appears reversed when viewed from opposite sides (Figure 7e,f). This phenomenon is supported by chiral near-field distributions of opposite handedness on each side under illumination. The resulting 2D perovskite metasurfaces demonstrated impressive photoluminescence dissymmetry factors (g_{lum}, $2(I_{LCP} - I_{RCP})/(I_{LCP} + I_{RCP})$; I_{LCP} and I_{RCP} are the intensities of the left- and right-circularly polarized PL) around 0.16, which could be further enhanced to 0.3 by applying a coating with a high refractive index.

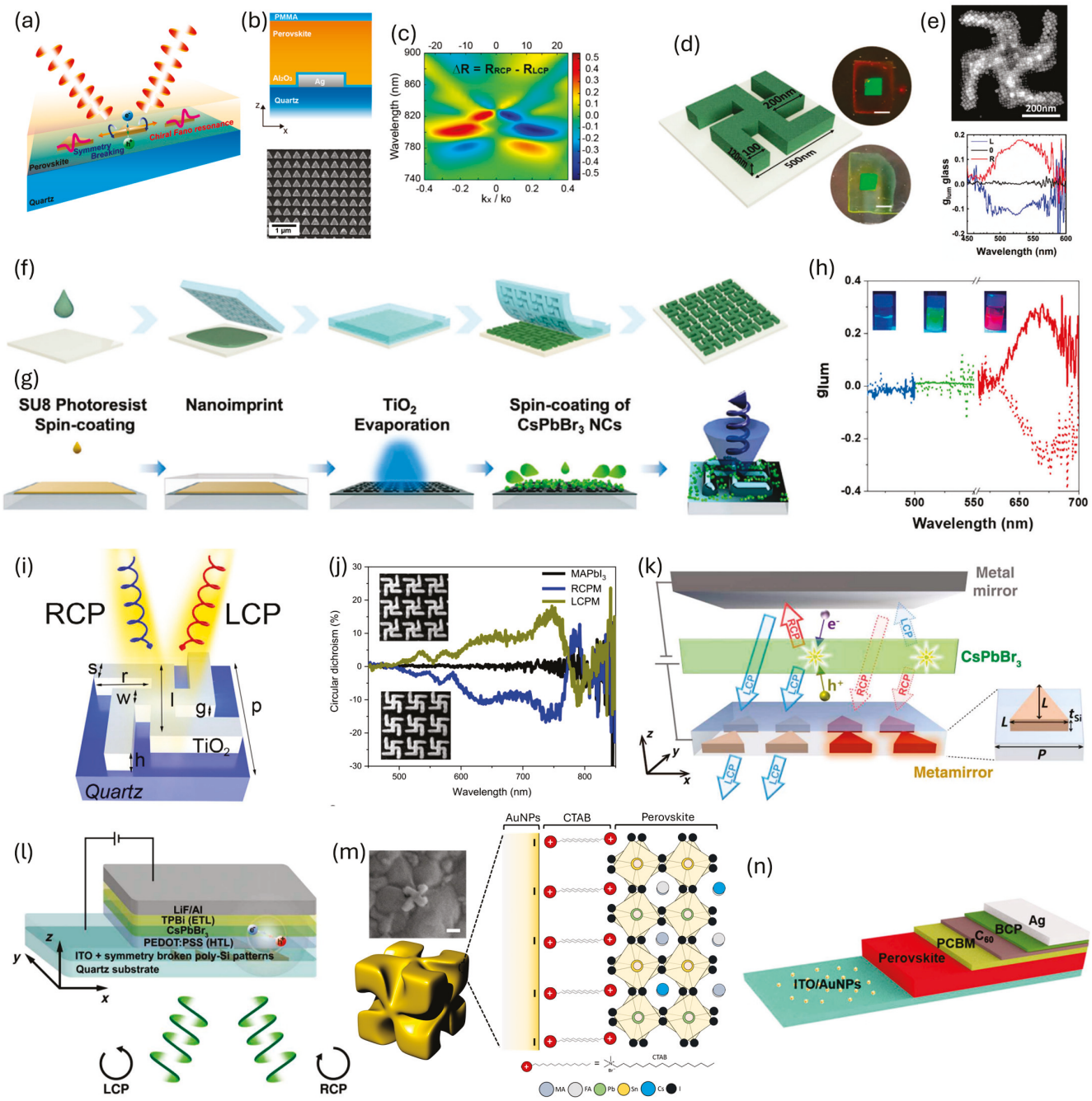

Figure 7. (**a**) Schematic for circularly polarized emission via chiral Fano resonances, (**b**) cross-sectional view of the structure, (**c**) simulated differential reflection spectrum ΔR ($R_{RCP} - R_{LCP}$) [104]. Copyright © 2021 American Chemical Society. (**d**) Schematic of the chiral metasurface unit, (**e**) large-magnification SEM of an L-gammadion unit composed of $CsPbBr_3$ perovskite NCs (**top**) and glum spectra (**bottom**), (**f**) schematic illustration of the fabrication process of chiral metasurfaces [105]. Copyright © 2023 Wiley. (**g**) Scheme of the fabrication process of 2D-chiral metasurfaces, (**h**) g_{lum} spectra [106]. Copyright © 2024 Wiley. (**i**) Schematic of a left-handed perovskite chiral metamolecule on quartz substrate, (**j**) experimental CD spectra of unpatterned $MAPbI_3$ film, right- and left-handed perovskite chiral metasurfaces [107]. Copyright © 2022 Nature Portfolio. (**k**) Schematic of the cavity formed by a metal mirror and a metamirror, (**l**) device geometry [108]. Copyright © 2023 American Association for the Advancement of Science. (**m**) Schematic illustration of possible interactions between Au NPs and $Cs_{0.05}FA_{0.5}MA_{0.45}Pb_{0.5}Sn_{0.5}I_3$, (**n**) device structure of the CPL Pe-PD [109]. Copyright © 2022 Wiley.

Another approach to forming chiral metasurface involves combining perovskite materials with high-refractive-index titanium dioxide (TiO_2), enabling strong light–matter

interactions. Fiuza-Maneiro et al. demonstrated strong chiral light emission from inherently achiral $CsPbBr_3$ nanocrystals by simply depositing them onto pre-formed chiral metasurfaces [106]. The metasurfaces were fabricated using nanoimprint lithography (Figure 7g). A thin 100 nm layer of photoresist was first patterned through hot embossing onto oxygen plasma-treated glass substrates. The embossing mold, made from PDMS, featured a square array of gammadion structures with 600 nm periodicity and 500 nm lateral dimensions, covering a 9 mm^2 area. Three types of metasurfaces were prepared: left-handed (L), right-handed (R), and racemic (O) orientations. To enhance light–matter interactions, a high-refractive-index TiO_2 layer (n = 2.4) was used. Finally, the perovskite nanocrystals were spin-coated directly onto the chiral metasurfaces. This straightforward integration yielded chiral optical systems exhibiting notable g_{lum} values of up to 0.56. The metasurfaces enabled broadband CPPL across the visible spectrum, achieved through resonant coupling between the chiral structures and the emission of both green and red perovskite nanocrystals (Figure 7h).

Although much of the earlier work emphasized the enhancement of chiral photoluminescence using metasurfaces, Long et al. shifted focus toward investigating how such chiral nanostructures influence asymmetric light absorption [107]. In their study, planar gammadion-shaped chiral perovskite metasurfaces, each with opposite handedness, were directly patterned onto $MAPbI_3$ films using focused ion beam (FIB) milling (Figure 7i). The fabricated metasurfaces exhibited pronounced chiroptical responses, achieving CD of 6350 millidegrees and an anisotropy factor for absorption (g_{abs}) of 0.49 (Figure 7j). Simulations further predicted that expanding the metasurface area could push the anisotropy factor to 1.11 and CD values to around 18,900 millidegrees, which approached to the theoretical maximum.

6.3. Chiral Structures in Perovskites Optoelectronics

The integration of chiral plasmonic nanostructures into practical optoelectronic devices (especially for Pe-PDs) has remained limited while a recent study demonstrated enhanced asymmetric light emission in the perovskite-based light-emitting device using chiral metasurfaces. An effort has been made to incorporate chiral metasurface into practical perovskite-based light-emitting devices, providing experimental evidence that these structures can be effectively integrated into practical devices and suggesting their potential applicability in future Pe-PD designs. Kim et al. introduced an interesting concept of chiral light emission using a perovskite-based thin-film metacavity and successfully demonstrated chiral electroluminescence (EL) experimentally [108] (Figure 7k). The device architecture consisted of a $CsPbBr_3$ perovskite emission layer sandwiched between a metallic back reflector and a specially engineered metamirror composed of a square array of triangular polycrystalline silicon (poly-Si) elements (Figure 7l). The metamirror served a dual optical function: it acts as a partially reflective mirror supporting Fabry–Pérot resonances that selectively emit one handedness of circular polarization, while simultaneously suppressing modes of the opposite handedness. This polarization selectivity originated from the intrinsic ability of the metamirror to interact asymmetrically with circularly polarized light. The resulting chiral cavity modes enabled directional, asymmetric EL, producing left- and right-handed circularly polarized emissions that propagate at distinct oblique angles. The device achieved a notable peak circular polarization degree of approximately 0.38.

Following the study on EL based on chiral plasmonic structures, an effort has also been made to integrate chiral plasmonics into CPL Pe-PDs, enhancing their sensitivity and selectivity. Kim et al. developed CPL Pe-PDs incorporating chiral Au NPs into narrow-bandgap tin–lead mixed perovskites [109] (Figure 7m). By embedding chiral Au NPs within a $Cs_{0.05}FA_{0.5}MA_{0.45}Pb_{0.5}Sn_{0.5}I_3$ perovskite matrix, the resulting photodiode-

type device achieved direct CPL detection in the near-infrared (NIR) region (Figure 7n). The optical activity of the chiral Au NPs could be finely controlled by tuning the refractive index of the surrounding environment, due to changes in their dielectric properties. Notably, the spectral overlap between the plasmonic resonance of chiral Au NPs and the absorption profile of the perovskite enabled efficient CPL discrimination in the NIR range. The resulting CPL Pe-PD exhibited a high photocurrent dissymmetry factor (g_{Ph}, $2(I_{LCP} - I_{RCP})/(I_{LCP} + I_{RCP})$; I_{LCP} and I_{RCP} are the photocurrents generated under LCP and RCP illumination) of 0.55 even without external bias.

Recent advances in chiral plasmonics with perovskite materials have shown that incorporating chiral plasmonic structures can substantially enhance the asymmetric optical properties of perovskites. However, despite this promising potential, their integration into practical perovskite-based optoelectronic devices still remains limited. Further research is needed to fully harness the capabilities of chiral plasmonics in real-world applications.

7. Conclusions

In summary, Table 1 presents a comprehensive overview of the performance of plasmonic nanostructure-integrated Pe-PDs. Pe-PDs have rapidly advanced owing to the unique optoelectronic properties of perovskite semiconductors and the versatile opportunities offered by solution-based processing. In particular, the integration of plasmonic nanostructures has recently emerged as a powerful strategy to overcome the intrinsic performance limitations of Pe-PDs, enabling enhanced light absorption, faster carrier dynamics, and improved spectral selectivity. These advances highlight the critical role of plasmonics in bridging the gap between fundamental perovskite research and practical device applications.

Table 1. Performance summary of reported plasmonic Pe-PDs and chiral nanostructure-integrated perovskite emitters and Pe-PD.

Plasmonic Structure	Device Structure	Wavelength (nm)	Performance (with Plasmonics)	Improvement (%)	Ref
Au NPs	Au/$CsPbBr_3$–Au NP film/Au NPs/Si	532	I_{ph} = 831.1 μA, On/Off = 1.66 × 10^6, D^* = 4.56 × 10^8 Jones	I_{ph} = 238, On/Off = 1000	[74]
Au NPs	Ag/$(PEA)_2PbI_4$/Au NPs/Glass	565	D^* = 8.1 × 10^{14} Jones	EQE (650–900 nm) = 1000, EQE (480 nm) = 68.5, D^* = 200	[75]
Au NPs	Perovskite/Graphene/Au NPs/Si/SiO_2	530	R = 2 × 10^3 A W^{-1}	R = 200	[76]
Gold nanostars (GNSs)	Perovskite/Graphene + GNS/Substrate	532	R = 5.90 × 10^4 A W^{-1}, D^* = 1.31 × 10^{13} Jones	R = 7.7 × 10^8, D^* > 10000	[77]
Au NCs (sphere/OD/RD)	PQDs/Graphene + Au NCs/Substrate	432	R = 2.7 × 10^5 A W^{-1}, D^* = 4.9 × 10^{13} Jones, EQE = 7.9 × 10^7%	I_{ph} = 1000	[78]
Au NP chains	Perovskite/PEDOT–PSS + Au NP chains/Substrate	635	R = 2063 A W^{-1}, NEP = 1.93 × 10^{14} W $Hz^{-1/2}$, D^* = 1.16 × 10^{12} Jones	R = 410, NEP = 1560	[79]
Au NRs + PEIE	$MAPbI_3$/Au NRs + PEIE/ITO	700	R = 0.360 A W^{-1}, D^* = 1.81 × 10^{10} Jones, I_{dark} = 2.93 × 10^{-10} A	I_{dark} = 76%	[80]
Ag NPs + SU-8	Perovskite/Ag NPs + SU-8/Glass	632	I_{ph} = 0.86 μA, R = 0.478 A W^{-1}, D^* = 5.04 × 10^{10}	I_{ph} = 352.6, R = 4.6, D^* = 354	[81]

Table 1. *Cont.*

Plasmonic Structure	Device Structure	Wavelength (nm)	Performance (with Plasmonics)	Improvement (%)	Ref
Ag NPs + PMMA OPCs	$CsPbCl_3$/Ag NPs + OPC/Substrate.	410	R = 8.1 A W^{-1}, D^* = 9 × 10^{14} Jones, $\tau_{rise/fall}$ = 28/31 ms	$\tau_{rise/fall}$ = 40–50%	[82]
Ag NPs	$CsPbBr_3$ microwire/Ag NPs/p-GaN	530	R = 63.9 A W^{-1}, D^* = 4.05 × 10^{12} Jones, EQE = 1.5 × 10^4%	R = 550, D^* = 600	[83]
Au nanosquare array	$MAPbI_3$ on patterned Au	800	EQE > 65%, I_{Ph} = 4.6 nA	EQE = 250, I_{Ph} = 900	[84]
Au nanotriangles	$MAPbI_3$ + Au triangles	450	R = 51 mA W^{-1}, EQE = 12.6%	EQE = 300	[85]
Al NP on AAO	$CsPbBr_3$/Al NPs/AAO	490	R = 4.8 mA W^{-1}, EQE: 1.12%	I_{Ph} = 4800, EQE = 4000	[86]
CN-patterned Au	Si/SiO_2/PS/Cr/Au/PVA/ $MAPbI_3$/Au	670	R = 588.6 mA W^{-1}, EQE: 109%, D^* = 22.5 × 10^{11} Jones	R = 420, EQE = 420, D^* =346	[63]
I-shaped perovskite metasurface	CsFAMA/PEDOT: PSS/metasurface	0.1 (THz)	R = 94 A W^{-1}, NEP = 5.03 pW $Hz^{-1/2}$, D^* = 3.28 × 10^{10}, stability retained (<2% change after 240 days)	N/A	[87]
Au nanoislands	$MAPbI_3$/plasmonic Au/TiO_2 nanodiode	563	I_{Ph} = 552 nA	I_{Ph} = 400	[66]
Triangular Ag nanopatterns	Triangular Ag nanopatterns/Al_2O_3/ Perovskite/PMMA	800	g_{lum} (dissymmetry factor for luminescence) = 1.084 ($MAPbI_3$), 0.524 ($MAPbBr_3$)	N/A	[104]
Chiral perovskite metasurfaces	Nanoimprinted gammadion-shaped 2D-chiral perovskite nanocrystal metasurfaces	520	g_{lum} = 0.16 ($CsPbBr_1I_2$)	N/A	[105]
	TiO_2-coated chiral metasurfaces 2D gammadion perovskite nanocrystal arrays	540	g_{lum} = 0.56 ($CsPbBr_3$) at 540 nm	N/A	[106]
	Focused Ion Beam-assisted gammadion perovskite metasurfaces	750	g_{CD} (dissymmetry factor for absorbance) = 0.49 ($MAPbI_3$)	N/A	[107]
Triangular silicon chiral metasurface	Triangular silicon chiral metasurface/ ITO/PEDOT–PSS/$CsPbBr_3$/TPBi/ LiF/Al	520	g_{EL} (dissymmetry factor for electroluminescence) = 0.76	N/A	[108]
Chiral Au NPs	ITO/chiral Au NPs/perovskite/PCBM/ C_{60}/BCP/Ag	808	g_{res} (dissymmetry factor for responsivity) = 0.55 ($Cs_{0.05}FA_{0.5}MA_{0.45}Pb_{0.5}Sn_{0.5}I_3$), R = 0.35 A W^{-1}, D^* = 1.54 × 10^{13} Jones, EQE = 54.2%, Bending radius = 2.5 cm (without degrading g_{res}), 90% retention of initial g_{res} after the 1000 cycle test	N/A	[109]

At the same time, achieving real commercialization of Pe-PDs requires progress on several parallel fronts, including large-area processability, long-term operational stability, and the development of non-toxic lead-free perovskite alternatives. Beyond the development of perovskite material and manufacturing process, the next crucial step lies in

incorporating plasmonic effects into Pe-PDs. Conventional studies on plasmonic Pe-PDs rely on noble metals such as Au and Ag, but their high cost, despite excellent optical properties, limits their viability for industrial adoption. Indeed, the high material cost has driven the semiconductor and display industries to instead rely on cost-effective scattering media, such as TiO_2 particles, to achieve comparable light management.

In the pursuit of environmentally friendly and stable Pe-PDs, lead-free alternatives have garnered increasing attention [111,112]. Among them, Sn-based perovskites are particularly promising due to their suitable bandgaps, high carrier mobilities, and extended spectral response into the near-infrared region, with demonstrated potential in plasmonic PD applications [113]. However, challenges related to Sn^{2+} oxidation and rapid crystallization still hinder their stability and film quality. Bi-based and double perovskites (e.g., Ag_2BiI_5, $Cs_2AgBiBr_6$) also offer excellent long-term stability and decent photodetection capabilities [114,115], particularly in the UV–visible range. With the integration of plasmonic structures, their response can be extended into the NIR region [116]. Nonetheless, their performance still lags behind Pb- and Sn-based counterparts. Additionally, emerging systems based on Sb, Cu, and Ge show unique optoelectronic properties and potential for high-temperature operation [117–120], yet remain underexplored. Overall, while lead-free perovskites offer environmental and stability advantages, further material development, device engineering, and integration of plasmonic structures are essential to match or exceed the performance of traditional lead-based Pe-PDs.

Although the integration of plasmonic nanostructures has shown great promise in enhancing the performance of Pe-PDs, challenges related to scalability and cost-effective manufacturing of plasmonic nanostructures continue to hinder their commercial viability. To overcome these challenges, several scalable fabrication methods have been explored, including wrinkle-assisted colloidal particle assembly [121], bottom-up fabrication using spin-coating techniques [122,123], laser raster patterning [124], roll-to-roll nanoimprint lithography technique [125], AAO-assisted metal patterning [126], dip-coating [127], thermal oxidation of titanium foil followed by silver nanoparticle deposition [128], glancing angle deposition [129], chemical lift-off lithography [130], dynamic shadowing growth [131], and laser inference lithography combined with template-assisted self-assembly [132]. Nonetheless, designing nanostructures with controlled plasmonic effects over large areas is technically still demanding and requires high precision. Moreover, the practical application of scalable fabrication methods of plasmonic nanostructures to PDs with stacked complex structures remains rare. Therefore, developing plasmonic fabrication techniques that are compatible with multilayer device architectures is a critical challenge that must be addressed in the future.

Another key limitation to the large-scale application of plasmonic nanostructures is the high cost and limited availability of noble metals like gold and silver [133]. Although they offer strong plasmonic responses and chemical stability, their narrow operating wavelength range and high price hinder industrial-scale deployment. In contrast, earth-abundant, low-cost metals such as aluminum [134,135], palladium [136], and copper present promising alternatives [137,138], offering broader plasmonic bands suitable for efficient, broadband light harvesting. Thus, to enable sustainable and scalable plasmonic applications, there is a growing need to explore non-noble metal alternatives.

In the future, economically competitive plasmonic Pe-PDs may be realized through the exploration of alternative cost-effective plasmonic materials such as Al, Pd, and organic conductor materials [139–141]. The combined progress in scalable perovskite processing, eco-friendly compositions, and low-cost plasmonic designs will accelerate the transition from laboratory prototypes to practical optoelectronic products, ensuring that plasmonic Pe-PDs become embedded in everyday life.

Author Contributions: Y.H.L. proposed the topic of the review and supervised the writing. H.K., J.L. and C.B.L. equally contributed to writing the main sections. All authors have read and agreed to the published version of the manuscript.

Funding: This work was also supported by the National Research Foundation of Korea (NRF) grant (RS-2025-24533931, RS-2024-00340299) through the NRF by the Ministry of Science and ICT (MSIT), Korea.

Institutional Review Board Statement: Not applicable.

Informed Consent Statement: Not applicable.

Data Availability Statement: No new data were created or analyzed in this study, data sharing is not applicable.

Conflicts of Interest: The authors declare no conflicts of interest.

References

1. Mitzi, D.B. Introduction: Perovskites. *Chem. Rev.* **2019**, *119*, 3033–3035. [CrossRef]
2. Jena, A.K.; Kulkarni, A.; Miyasaka, T. Halide Perovskite Photovoltaics: Background, Status, and Future Prospects. *Chem. Rev.* **2019**, *119*, 3036–3103. [CrossRef]
3. Manser, J.S.; Christians, J.A.; Kamat, P.V. Intriguing Optoelectronic Properties of Metal Halide Perovskites. *Chem. Rev.* **2016**, *116*, 12956–13008. [CrossRef]
4. Zhao, Y.; Zhu, K. Organic–inorganic hybrid lead halide perovskites for optoelectronic and electronic applications. *Chem. Soc. Rev.* **2016**, *45*, 655–689. [CrossRef]
5. Rogalski, A.; Wang, F.; Wang, J.; Martyniuk, P.; Hu, W. The Perovskite Optoelectronic Devices—A Look at the Future. *Small Methods* **2025**, *9*, 2400709. [CrossRef]
6. Stranks, S.D.; Eperon, G.E.; Grancini, G.; Menelaou, C.; Alcocer, M.J.P.; Leijtens, T.; Herz, L.M.; Petrozza, A.; Snaith, H.J. Electron-Hole Diffusion Lengths Exceeding 1 Micrometer in an Organometal Trihalide Perovskite Absorber. *Science* **2013**, *342*, 341–344. [CrossRef]
7. Chen, B.; Baek, S.-W.; Hou, Y.; Aydin, E.; De Bastiani, M.; Scheffel, B.; Proppe, A.; Huang, Z.; Wei, M.; Wang, Y.-K.; et al. Enhanced optical path and electron diffusion length enable high-efficiency perovskite tandems. *Nat. Commun.* **2020**, *11*, 1257. [CrossRef] [PubMed]
8. Wang, P.; Wu, Y.; Cai, B.; Ma, Q.; Zheng, X.; Zhang, W.-H. Solution-Processable Perovskite Solar Cells toward Commercialization: Progress and Challenges. *Adv. Funct. Mater.* **2019**, *29*, 1807661. [CrossRef]
9. Saki, Z.; Byranvand, M.M.; Taghavinia, N.; Kedia, M.; Saliba, M. Solution-processed perovskite thin-films: The journey from lab- to large-scale solar cells. *Energy Environ. Sci.* **2021**, *14*, 5690–5722. [CrossRef]
10. Samiee, M.; Konduri, S.; Ganapathy, B.; Kottokkaran, R.; Abbas, H.A.; Kitahara, A.; Joshi, P.; Zhang, L.; Noack, M.; Dalal, V. Defect density and dielectric constant in perovskite solar cells. *Appl. Phys. Lett.* **2014**, *105*, 153502. [CrossRef]
11. Kim, H.; Figueroa Morales, C.A.; Seong, S.; Hu, Z.; Muyanja, N.; Penukula, S.; Zheng, T.; Pizzo, Z.; Yim, C.S.; Lenert, A.; et al. Molecular design of defect passivators for thermally stable metal-halide perovskite films. *Matter* **2024**, *7*, 539–549. [CrossRef]
12. Docampo, P.; Bein, T. A Long-Term View on Perovskite Optoelectronics. *Acc. Chem. Res.* **2016**, *49*, 339–346. [CrossRef] [PubMed]
13. Zhao, R.; Gu, Z.; Li, P.; Zhang, Y.; Song, Y. Flexible and Wearable Optoelectronic Devices Based on Perovskites. *Adv. Mater. Technol.* **2022**, *7*, 2101124. [CrossRef]
14. Kim, H.; Lee, J.W.; Han, G.R.; Kim, Y.J.; Kim, S.H.; Kim, S.K.; Kwak, S.K.; Oh, J.H. Highly Efficient Hole Transport Layer-Free Low Bandgap Mixed Pb–Sn Perovskite Solar Cells Enabled by a Binary Additive System. *Adv. Funct. Mater.* **2022**, *32*, 2110069. [CrossRef]
15. Lee, Y.H.; Tang, Y.; Dani, R.; Lee, W.-J.; Kim, J.H.; Lee, G.; Sun, J.; Ma, K.; Jeong, S.H.; Xu, W.; et al. Self-Aligned Fluorinated-Organic Ligand for Boosting the Performance of Perovskite Solar Cells. *ACS Appl. Mater. Interfaces* **2025**, *17*, 26751–26758. [CrossRef] [PubMed]
16. Yang, S.J.; Lee, Y.H.; Tateno, K.; Dou, L. Elemental segregation and dimensional separation in halide perovskite light-emitting diodes. *Prog. Quantum Electron.* **2024**, *98*, 100537. [CrossRef]
17. Brenner, T.M.; Egger, D.A.; Kronik, L.; Hodes, G.; Cahen, D. Hybrid organic—Inorganic perovskites: Low-cost semiconductors with intriguing charge-transport properties. *Nat. Rev. Mater.* **2016**, *1*, 15007. [CrossRef]
18. Velilla, E.; Ramirez, D.; Uribe, J.-I.; Montoya, J.F.; Jaramillo, F. Outdoor performance of perovskite solar technology: Silicon comparison and competitive advantages at different irradiances. *Sol. Energy Mater. Sol. Cells* **2019**, *191*, 15–20. [CrossRef]

19. Saif, O.M.; Zekry, A.H.; Abouelatta, M.; Shaker, A. A Comprehensive Review of Tandem Solar Cells Integrated on Silicon Substrate: III/V vs Perovskite. *Silicon* **2023**, *15*, 6329–6347. [CrossRef]
20. Cai, S.; Xu, X.; Yang, W.; Chen, J.; Fang, X. Materials and Designs for Wearable Photodetectors. *Adv. Mater.* **2019**, *31*, 1808138. [CrossRef]
21. Chow, P.C.Y.; Someya, T. Organic Photodetectors for Next-Generation Wearable Electronics. *Adv. Mater.* **2020**, *32*, 1902045. [CrossRef]
22. Hao, D.; Zou, J.; Huang, J. Recent developments in flexible photodetectors based on metal halide perovskite. *InfoMat* **2020**, *2*, 139–169. [CrossRef]
23. Kim, H.; Seong, S.; Gong, X. Heterostructure Engineering of Solution-Processable Semiconductors for Wearable Optoelectronics. *ACS Appl. Electron. Mater.* **2023**, *5*, 5278–5290. [CrossRef]
24. Lee, Y.H.; Song, I.; Kim, S.H.; Park, J.H.; Park, S.O.; Lee, J.H.; Won, Y.; Cho, K.; Kwak, S.K.; Oh, J.H. Perovskite Granular Wire Photodetectors with Ultrahigh Photodetectivity. *Adv. Mater.* **2020**, *32*, 2002357. [CrossRef]
25. Lee, Y.H.; Lee, W.-J.; Lee, G.S.; Park, J.Y.; Yuan, B.; Won, Y.; Mun, J.; Yang, H.; Baek, S.-D.; Lee, H.; et al. Large-Scale 2D Perovskite Nanocrystals Photodetector Array via Ultrasonic Spray Synthesis. *Adv. Mater.* **2025**, *37*, 2417761. [CrossRef]
26. Lee, Y.H.; Park, J.Y.; Niu, P.; Yang, H.; Sun, D.; Huang, L.; Mei, J.; Dou, L. One-Step Solution Patterning for Two-Dimensional Perovskite Nanoplate Arrays. *ACS Nano* **2023**, *17*, 13840–13850. [CrossRef]
27. Demontis, V.; Durante, O.; Marongiu, D.; De Stefano, S.; Matta, S.; Simbula, A.; Ragazzo Capello, C.; Pennelli, G.; Quochi, F.; Saba, M.; et al. Photoconduction in 2D Single-Crystal Hybrid Perovskites. *Adv. Opt. Mater.* **2025**, *13*, 2402469. [CrossRef]
28. Mastria, R.; Riisnaes, K.J.; Bacon, A.; Leontis, I.; Lam, H.T.; Alshehri, M.A.S.; Colridge, D.; Chan, T.H.E.; De Sanctis, A.; De Marco, L.; et al. Real Time and Highly Sensitive Sub-Wavelength 2D Hybrid Perovskite Photodetectors. *Adv. Funct. Mater.* **2024**, *34*, 2401903. [CrossRef]
29. Wei, H.; Fang, Y.; Mulligan, P.; Chuirazzi, W.; Fang, H.-H.; Wang, C.; Ecker, B.R.; Gao, Y.; Loi, M.A.; Cao, L.; et al. Sensitive X-ray detectors made of methylammonium lead tribromide perovskite single crystals. *Nat. Photonics* **2016**, *10*, 333–339. [CrossRef]
30. Min, J.; Demchyshyn, S.; Sempionatto, J.R.; Song, Y.; Hailegnaw, B.; Xu, C.; Yang, Y.; Solomon, S.; Putz, C.; Lehner, L.E.; et al. An autonomous wearable biosensor powered by a perovskite solar cell. *Nat. Electron.* **2023**, *6*, 630–641. [CrossRef]
31. Morteza Najarian, A.; Vafaie, M.; Johnston, A.; Zhu, T.; Wei, M.; Saidaminov, M.I.; Hou, Y.; Hoogland, S.; García de Arquer, F.P.; Sargent, E.H. Sub-millimetre light detection and ranging using perovskites. *Nat. Electron.* **2022**, *5*, 511–518. [CrossRef]
32. Zhang, H.-T.; Park, T.J.; Islam, A.N.M.N.; Tran, D.S.J.; Manna, S.; Wang, Q.; Mondal, S.; Yu, H.; Banik, S.; Cheng, S.; et al. Reconfigurable perovskite nickelate electronics for artificial intelligence. *Science* **2022**, *375*, 533–539. [CrossRef]
33. Hou, H.-Y.; Tian, S.; Ge, H.-R.; Chen, J.-D.; Li, Y.-Q.; Tang, J.-X. Recent Progress of Polarization-Sensitive Perovskite Photodetectors. *Adv. Funct. Mater.* **2022**, *32*, 2209324. [CrossRef]
34. Zheng, D.; Pauporté, T. Advances in Optical Imaging and Optical Communications Based on High-Quality Halide Perovskite Photodetectors. *Adv. Funct. Mater.* **2024**, *34*, 2311205. [CrossRef]
35. Wang, G.; Qi, Y.; Zhou, Z.; Liu, Z.; Wang, R. Research Progress of Halide Perovskite Nanocrystals in Biomedical Applications: A Review. *Inorganics* **2025**, *13*, 55. [CrossRef]
36. Tang, Y.; Jin, P.; Wang, Y.; Li, D.; Chen, Y.; Ran, P.; Fan, W.; Liang, K.; Ren, H.; Xu, X.; et al. Enabling low-drift flexible perovskite photodetectors by electrical modulation for wearable health monitoring and weak light imaging. *Nat. Commun.* **2023**, *14*, 4961. [CrossRef] [PubMed]
37. Zheng, Y.; Zhan, Z.; Chen, Q.; Chen, J.; Luo, J.; Cai, J.; Zhou, Y.; Chen, K.; Xie, W. Highly Sensitive Perovskite Photoplethysmography Sensor for Blood Glucose Sensing Using Machine Learning Techniques. *Adv. Sci.* **2024**, *11*, 2405681. [CrossRef]
38. Zhang, X.; Liu, X.; Sun, B.; Ye, H.; He, C.; Kong, L.; Shi, T.; Liao, G.; Liu, Z. Broadening the Spectral Response of Perovskite Photodetector to the Solar-Blind Ultraviolet Region through Phosphor Encapsulation. *ACS Appl. Mater. Interfaces* **2021**, *13*, 44509–44519. [CrossRef]
39. Zhang, S.; Zhu, W.; Zhang, X.; Mei, L.; Liu, J.; Wang, F. Machine learning-driven fluorescent sensor array using aqueous CsPbBr3 perovskite quantum dots for rapid detection and sterilization of foodborne pathogens. *J. Hazard. Mater.* **2025**, *483*, 136655. [CrossRef] [PubMed]
40. Zhao, D.; Choi, Y.-W.; Yokota, T.; Someya, T.; Park, N.-G. Halide Perovskite Radiation Detectors: Conventional Imaging Applications and New Opportunities. *Adv. Funct. Mater.* **2025**, e13676. [CrossRef]
41. Riisnaes, K.J.; Alshehri, M.; Leontis, I.; Mastria, R.; Lam, H.T.; De Marco, L.; Coriolano, A.; Craciun, M.F.; Russo, S. 2D Hybrid Perovskite Sensors for Environmental and Healthcare Monitoring. *ACS Appl. Mater. Interfaces* **2024**, *16*, 31399–31406. [CrossRef]
42. Long, G.; Sabatini, R.; Saidaminov, M.I.; Lakhwani, G.; Rasmita, A.; Liu, X.; Sargent, E.H.; Gao, W. Chiral-perovskite optoelectronics. *Nat. Rev. Mater.* **2020**, *5*, 423–439. [CrossRef]
43. Kim, H.; Choi, W.; Kim, Y.J.; Kim, J.; Ahn, J.; Song, I.; Kwak, M.; Kim, J.; Park, J.; Yoo, D.; et al. Giant chiral amplification of chiral 2D perovskites via dynamic crystal reconstruction. *Sci. Adv.* **2024**, *10*, eado5942. [CrossRef]

44. Rogalski, A.; Hu, W.; Wang, F.; Wang, Y.; Martyniuk, P. Perovskite versus Standard Photodetectors. *Materials* **2024**, *17*, 4029. [CrossRef]
45. Yang, J.; Wang, W.; Bao, C.; Huang, W.; Wang, J. Toward practical applications of perovskite photodetectors: Advantages and challenges. *Matter* **2025**, *8*, 102207. [CrossRef]
46. Furlan, F.; Nodari, D.; Palladino, E.; Angela, E.; Mohan, L.; Briscoe, J.; Fuchter, M.J.; Macdonald, T.J.; Grancini, G.; McLachlan, M.A.; et al. Tuning Halide Composition Allows Low Dark Current Perovskite Photodetectors with High Specific Detectivity. *Adv. Opt. Mater.* **2022**, *10*, 2201816. [CrossRef]
47. Hong, E.; Nodari, D.; Furlan, F.; Angela, E.; Panidi, J.; McLachlan, M.A.; Gasparini, N. Strain-Induced α-Phase Stabilization for Low Dark Current FAPI-Based Photodetectors. *Adv. Opt. Mater.* **2024**, *12*, 2302712. [CrossRef]
48. Xing, R.; Li, Z.; Zhao, W.; Wang, D.; Xie, R.; Chen, Y.; Wu, L.; Fang, X. Waterproof and Flexible Perovskite Photodetector Enabled By P-type Organic Molecular Rubrene with High Moisture and Mechanical Stability. *Adv. Mater.* **2024**, *36*, 2310248. [CrossRef] [PubMed]
49. Hong, E.; Tremlett, W.D.J.; Hart, L.; Hu, B.; Qiao, Z.; Sukpoonprom, P.; Fearn, S.; Angela, E.; Brunetta, M.; Koutsogeorgis, D.C.; et al. Ferrocene Derivatives Enable Ultrasensitive Perovskite Photodetectors with Enhanced Reverse Bias Stability. *Adv. Funct. Mater.* **2025**, 2424556. [CrossRef]
50. Nodari, D.; Hart, L.J.F.; Sandberg, O.J.; Furlan, F.; Angela, E.; Panidi, J.; Qiao, Z.; McLachlan, M.A.; Barnes, P.R.F.; Durrant, J.R.; et al. Dark Current in Broadband Perovskite–Organic Heterojunction Photodetectors Controlled by Interfacial Energy Band Offset. *Adv. Mater.* **2024**, *36*, 2401206. [CrossRef]
51. Ai, B.; Fan, Z.; Wong, Z.J. Plasmonic–perovskite solar cells, light emitters, and sensors. *Microsyst. Nanoeng.* **2022**, *8*, 5. [CrossRef] [PubMed]
52. Siavash Moakhar, R.; Gholipour, S.; Masudy-Panah, S.; Seza, A.; Mehdikhani, A.; Riahi-Noori, N.; Tafazoli, S.; Timasi, N.; Lim, Y.-F.; Saliba, M. Recent Advances in Plasmonic Perovskite Solar Cells. *Adv. Sci.* **2020**, *7*, 1902448. [CrossRef] [PubMed]
53. Li, J.; Cushing, S.K.; Meng, F.; Senty, T.R.; Bristow, A.D.; Wu, N. Plasmon-induced resonance energy transfer for solar energy conversion. *Nat. Photonics* **2015**, *9*, 601–607. [CrossRef]
54. Cho, S.; Yang, Y.; Soljačić, M.; Yun, S.H. Submicrometer perovskite plasmonic lasers at room temperature. *Sci. Adv.* **2021**, *7*, eabf3362. [CrossRef]
55. Wang, Y.-Y.; Lee, X.-H.; Chen, C.-H.; Yuan, L.; Lai, Y.-T.; Peng, T.-Y.; Chen, J.-W.; Chueh, C.-C.; Lu, Y.-J. Plasmon-enhanced exciton relocalization in quasi-2D perovskites for low-threshold room-temperature plasmonic lasing. *Sci. Adv.* **2025**, *11*, eadu6824. [CrossRef]
56. Carretero-Palacios, S.; Jiménez-Solano, A.; Míguez, H. Plasmonic Nanoparticles as Light-Harvesting Enhancers in Perovskite Solar Cells: A User's Guide. *ACS Energy Lett.* **2016**, *1*, 323–331. [CrossRef] [PubMed]
57. Wang, C.; Wang, X.; Luo, B.; Shi, X.; Shen, X. Plasmonics Meets Perovskite Photovoltaics: Innovations and Challenges in Boosting Efficiency. *Molecules* **2024**, *29*, 5091. [CrossRef]
58. Demydov, P.; Lopatynskyi, A.; Hudzenko, I.; Chegel, V. The approaches for localized surface plasmon resonance wavelength position tuning. Short review. *Semicond. Phys. Quantum Electron. Optoelectron.* **2021**, *24*, 304–311. [CrossRef]
59. Kunwar, S.; Pandit, S.; Jeong, J.-H.; Lee, J. Improved Photoresponse of UV Photodetectors by the Incorporation of Plasmonic Nanoparticles on GaN Through the Resonant Coupling of Localized Surface Plasmon Resonance. *Nano-Micro Lett.* **2020**, *12*, 91. [CrossRef]
60. Wen, X.; Deng, S. Plasmonic Nanostructure Lattices for High-Performance Sensing. *Adv. Opt. Mater.* **2023**, *11*, 2300401. [CrossRef]
61. Li, M.; Cushing, S.K.; Wu, N. Plasmon-enhanced optical sensors: A review. *Analyst* **2015**, *140*, 386–406. [CrossRef]
62. Zhang, J.; Zhang, L.; Xu, W. Surface plasmon polaritons: Physics and applications. *J. Phys. D Appl. Phys.* **2012**, *45*, 113001. [CrossRef]
63. Lee, Y.H.; Lee, S.H.; Won, Y.; Kim, H.; Yang, S.J.; Ahn, J.; Mun, J.; Lee, J.H.; Dou, L.; Rho, J.; et al. Boosting the Performance of Flexible Perovskite Photodetectors Using Hierarchical Plasmonic Nanostructures. *Small Struct.* **2024**, *5*, 2300546. [CrossRef]
64. Lee, Y.H.; Lee, T.K.; Song, I.; Yu, H.; Lee, J.; Ko, H.; Kwak, S.K.; Oh, J.H. Boosting the Performance of Organic Optoelectronic Devices Using Multiple-Patterned Plasmonic Nanostructures. *Adv. Mater.* **2016**, *28*, 4976–4982. [CrossRef]
65. Ha, M.; Kim, J.-H.; You, M.; Li, Q.; Fan, C.; Nam, J.-M. Multicomponent Plasmonic Nanoparticles: From Heterostructured Nanoparticles to Colloidal Composite Nanostructures. *Chem. Rev.* **2019**, *119*, 12208–12278. [CrossRef]
66. Park, Y.; Choi, J.; Lee, C.; Cho, A.-N.; Cho, D.W.; Park, N.-G.; Ihee, H.; Park, J.Y. Elongated Lifetime and Enhanced Flux of Hot Electrons on a Perovskite Plasmonic Nanodiode. *Nano Lett.* **2019**, *19*, 5489–5495. [CrossRef]
67. Huang, X.; Li, H.; Zhang, C.; Tan, S.; Chen, Z.; Chen, L.; Lu, Z.; Wang, X.; Xiao, M. Efficient plasmon-hot electron conversion in Ag–CsPbBr3 hybrid nanocrystals. *Nat. Commun.* **2019**, *10*, 1163. [CrossRef]
68. Bueno, J.; Carretero Palacios, S.; Anaya, M. Synergetic Near- and Far-Field Plasmonic Effects for Optimal All-Perovskite Tandem Solar Cells with Maximized Infrared Absorption. *J. Phys. Chem. Lett.* **2024**, *15*, 2632–2638. [CrossRef] [PubMed]

69. Xu, T.; Li, W.; Wu, X.; Ahmadi, M.; Xu, L.; Chen, P. High-performance blue perovskite light-emitting diodes based on the "far-field plasmonic effect" of gold nanoparticles. *J. Mater. Chem. C* **2020**, *8*, 6615–6622. [CrossRef]
70. Dong, Y.; Xu, L.; Zhao, Y.; Wang, S.; Song, J.; Zou, Y.; Zeng, H. The Synergy of Plasmonic Enhancement and Hot-Electron Effect on CsPbBr3 Nanosheets Photodetector. *Adv. Mater. Interfaces* **2021**, *8*, 2002053. [CrossRef]
71. Ali, A.; Kang, J.H.; Seo, J.H.; Walker, B. Effect of Plasmonic Ag Nanoparticles on the Performance of Inverted Perovskite Solar Cells. *Adv. Eng. Mater.* **2020**, *22*, 1900976. [CrossRef]
72. Erwin, W.R.; Zarick, H.F.; Talbert, E.M.; Bardhan, R. Light trapping in mesoporous solar cells with plasmonic nanostructures. *Energy Environ. Sci.* **2016**, *9*, 1577–1601. [CrossRef]
73. van Vliet, K.M. Noise Limitations in Solid State Photodetectors. *Appl. Opt.* **1967**, *6*, 1145–1169. [CrossRef] [PubMed]
74. Dong, Y.; Gu, Y.; Zou, Y.; Song, J.; Xu, L.; Li, J.; Xue, J.; Li, X.; Zeng, H. Improving All-Inorganic Perovskite Photodetectors by Preferred Orientation and Plasmonic Effect. *Small* **2016**, *12*, 5622–5632. [CrossRef] [PubMed]
75. Xi, Y.; Wang, X.; Ji, T.; Li, G.; Shi, L.; Liu, Y.; Wang, W.; Ma, J.; Liu, S.; Hao, Y.; et al. Plasmonic Resonance Enabling 2D Perovskite Single Crystal to Detect Telecommunication Light. *Adv. Opt. Mater.* **2023**, *11*, 2202423. [CrossRef]
76. Sun, Z.; Aigouy, L.; Chen, Z. Plasmonic-enhanced perovskite–graphene hybrid photodetectors. *Nanoscale* **2016**, *8*, 7377–7383. [CrossRef] [PubMed]
77. Lee, Y.H.; Park, S.; Won, Y.; Mun, J.; Ha, J.H.; Lee, J.H.; Lee, S.H.; Park, J.; Yeom, J.; Rho, J.; et al. Flexible high-performance graphene hybrid photodetectors functionalized with gold nanostars and perovskites. *NPG Asia Mater.* **2020**, *12*, 79. [CrossRef]
78. Yadav, S.N.S.; Hanmandlu, C.; Patel, D.K.; Singh, R.K.; Chen, C.-Y.; Wang, Y.-Y.; Chu, C.-W.; Liang, C.-T.; Lin, C.-T.; Lu, Y.-J.; et al. Enhanced Photoresponsivity of Perovskite QDs/Graphene Hybrid Gate-Free Photodetector by Morphologically Controlled Plasmonic Au Nanocrystals. *Adv. Opt. Mater.* **2023**, *11*, 2300131. [CrossRef]
79. La, J.A.; Kang, J.; Byun, J.Y.; Kim, I.S.; Kang, G.; Ko, H. Highly sensitive and fast perovskite photodetector functionalized by plasmonic Au nanoparticles-alkanethiol assembly. *Appl. Surf. Sci.* **2021**, *538*, 148007. [CrossRef]
80. Kwon, H.; Lim, J.W.; Kim, D.H. Plasmonic perovskite photodetector with high photocurrent and low dark current mediated by Au NR/PEIE hybrid layer. *J. Mater. Sci. Technol.* **2025**, *218*, 45–53. [CrossRef]
81. Ye, X.; Ma, C.; Lou, H.; Dai, J. Effect of SU-8 Encapsulated AgNPs on the Performance Enhancement of $CH_3NH_3PbI_3$ Perovskite Photodetector. *IEEE Photonics Technol. Lett.* **2024**, *36*, 425–428. [CrossRef]
82. Li, D.; Zhou, D.; Xu, W.; Chen, X.; Pan, G.; Zhou, X.; Ding, N.; Song, H. Plasmonic Photonic Crystals Induced Two-Order Fluorescence Enhancement of Blue Perovskite Nanocrystals and Its Application for High-Performance Flexible Ultraviolet Photodetectors. *Adv. Funct. Mater.* **2018**, *28*, 1804429. [CrossRef]
83. Lin, C.; Wan, P.; Yang, B.; Shi, D.; Kan, C.; Jiang, M. Plasmon-enhanced photoresponse and stability of a $CsPbBr_3$ microwire/GaN heterojunction photodetector with surface-modified Ag nanoparticles. *J. Mater. Chem. C* **2023**, *11*, 12968–12980. [CrossRef]
84. Du, B.; Yang, W.; Jiang, Q.; Shan, H.; Luo, D.; Li, B.; Tang, W.; Lin, F.; Shen, B.; Gong, Q.; et al. Plasmonic-Functionalized Broadband Perovskite Photodetector. *Adv. Opt. Mater.* **2018**, *6*, 1701271. [CrossRef]
85. Gu, Q.; Hu, C.; Yang, J.; Lv, J.; Ying, Y.; Jiang, X.; Si, G. Plasmon enhanced perovskite-metallic photodetectors. *Mater. Des.* **2021**, *198*, 109374. [CrossRef]
86. Li, M.-Y.; Shen, K.; Xu, H.; Ren, A.; Lee, J.; Kunwar, S.; Liu, S.; Wu, J. Enhanced Spatial Light Confinement of All Inorganic Perovskite Photodetectors Based on Hybrid Plasmonic Nanostructures. *Small* **2020**, *16*, 2004234. [CrossRef]
87. Li, Y.; Jia, Y.; Yang, H.; Wu, Y.; Cao, Y.; Zhang, X.; Lou, C.; Liu, X.; Huang, L.-B.; Yao, J. A Room-Temperature Terahertz Photodetector Imaging with High Stability and Polarization-Sensitive Based on Perovskite/Metasurface. *Adv. Sci.* **2025**, *12*, 2407634. [CrossRef] [PubMed]
88. Righetto, M.; Lim, S.S.; Giovanni, D.; Lim, J.W.M.; Zhang, Q.; Ramesh, S.; Tay, Y.K.E.; Sum, T.C. Hot carriers perspective on the nature of traps in perovskites. *Nat. Commun.* **2020**, *11*, 2712. [CrossRef]
89. Hopper, T.R.; Gorodetsky, A.; Frost, J.M.; Müller, C.; Lovrincic, R.; Bakulin, A.A. Ultrafast Intraband Spectroscopy of Hot-Carrier Cooling in Lead-Halide Perovskites. *ACS Energy Lett.* **2018**, *3*, 2199–2205. [CrossRef]
90. Fu, J.; Xu, Q.; Han, G.; Wu, B.; Huan, C.H.A.; Leek, M.L.; Sum, T.C. Hot carrier cooling mechanisms in halide perovskites. *Nat. Commun.* **2017**, *8*, 1300. [CrossRef]
91. Kim, H.; Han, G.R.; Kim, S.K.; Lyu, T.; Choi, W.; Lee, J.W.; Oh, J.H. Harnessing Strong Band-Filling in Mixed Pb-Sn Perovskites Boosts the Performance of Concentrator-Type Photovoltaics. *ACS Energy Lett.* **2023**, *8*, 1122–1130. [CrossRef]
92. Jian, C.-c.; Zhang, J.; He, W.; Ma, X. Au-Al intermetallic compounds: A series of more efficient LSPR materials for hot carriers-based applications than noble metal Au. *Nano Energy* **2021**, *82*, 105763. [CrossRef]
93. Wach, A.; Bericat-Vadell, R.; Bacellar, C.; Cirelli, C.; Johnson, P.J.M.; Castillo, R.G.; Silveira, V.R.; Broqvist, P.; Kullgren, J.; Maximenko, A.; et al. The dynamics of plasmon-induced hot carrier creation in colloidal gold. *Nat. Commun.* **2025**, *16*, 2274. [CrossRef] [PubMed]
94. Kuszynski, J.E.; Fabiano, C.J.; Nguyen, E.T.; Mao, K.; Ahuja, A.K.; Schaller, R.D.; Strouse, G.F. Plasmon-Induced Hot-Carrier Excited-State Dynamics in Plasmonic Semiconductor Nanocrystals. *J. Phys. Chem. C* **2023**, *127*, 22654–22661. [CrossRef]

95. Qiu, C.; Zhang, H.; Tian, C.; Jin, X.; Song, Q.; Xu, L.; Ijaz, M.; Blaikie, R.J.; Xu, Q. Breaking bandgap limitation: Improved photosensitization in plasmonic-based CsPbBr3 photodetectors via hot-electron injection. *Appl. Phys. Lett.* **2023**, *122*, 243502. [CrossRef]
96. Dong, H.; Lei, T.; Yuan, F.; Xu, J.; Niu, Y.; Jiao, B.; Zhang, Z.; Ding, D.; Hou, X.; Wu, Z. Plasmonic enhancement for high efficient and stable perovskite solar cells by employing "hot spots" Au nanobipyramids. *Org. Electron.* **2018**, *60*, 1–8. [CrossRef]
97. Yuan, Z.; Wu, Z.; Bai, S.; Xia, Z.; Xu, W.; Song, T.; Wu, H.; Xu, L.; Si, J.; Jin, Y.; et al. Hot-Electron Injection in a Sandwiched TiOx–Au–TiOx Structure for High-Performance Planar Perovskite Solar Cells. *Adv. Energy Mater.* **2015**, *5*, 1500038. [CrossRef]
98. Kowal, D.; Chen, Y.; Birowosuto, M.D. Metal/Perovskite Plasmonic–Photonic Heterostructures for Active and Passive Detection Devices. *Micromachines* **2025**, *16*, 424. [CrossRef]
99. Dong, Y.; Hautzinger, M.P.; Haque, M.A.; Beard, M.C. Chirality-Induced Spin Selectivity in Hybrid Organic-Inorganic Perovskite Semiconductors. *Annu. Rev. Phys. Chem.* **2025**, *76*, 519–537. [CrossRef]
100. Ma, S.; Ahn, J.; Moon, J. Chiral Perovskites for Next-Generation Photonics: From Chirality Transfer to Chiroptical Activity. *Adv. Mater.* **2021**, *33*, 2005760. [CrossRef]
101. Han, Z.; Sun, T.; Cheng, P.; Shi, W. Cation-induced enhanced enantioselective recognition by a chiral covalent-organic framework. *Commun. Chem.* **2025**, *8*, 206. [CrossRef]
102. Khorasaninejad, M.; Chen, W.T.; Zhu, A.Y.; Oh, J.; Devlin, R.C.; Rousso, D.; Capasso, F. Multispectral Chiral Imaging with a Metalens. *Nano Lett.* **2016**, *16*, 4595–4600. [CrossRef]
103. Lodahl, P.; Mahmoodian, S.; Stobbe, S.; Rauschenbeutel, A.; Schneeweiss, P.; Volz, J.; Pichler, H.; Zoller, P. Chiral quantum optics. *Nature* **2017**, *541*, 473–480. [CrossRef] [PubMed]
104. Seo, I.C.; Lim, Y.; An, S.-C.; Woo, B.H.; Kim, S.; Son, J.G.; Yoo, S.; Park, Q.H.; Kim, J.Y.; Jun, Y.C. Circularly Polarized Emission from Organic–Inorganic Hybrid Perovskites via Chiral Fano Resonances. *ACS Nano* **2021**, *15*, 13781–13793. [CrossRef] [PubMed]
105. Mendoza-Carreño, J.; Molet, P.; Otero-Martínez, C.; Alonso, M.I.; Polavarapu, L.; Mihi, A. Nanoimprinted 2D-Chiral Perovskite Nanocrystal Metasurfaces for Circularly Polarized Photoluminescence. *Adv. Mater.* **2023**, *35*, 2210477. [CrossRef] [PubMed]
106. Fiuza-Maneiro, N.; Mendoza-Carreño, J.; Gómez-Graña, S.; Alonso, M.I.; Polavarapu, L.; Mihi, A. Inducing Efficient and Multiwavelength Circularly Polarized Emission From Perovskite Nanocrystals Using Chiral Metasurfaces. *Adv. Mater.* **2024**, *36*, 2413967. [CrossRef]
107. Long, G.; Adamo, G.; Tian, J.; Klein, M.; Krishnamoorthy, H.N.S.; Feltri, E.; Wang, H.; Soci, C. Perovskite metasurfaces with large superstructural chirality. *Nat. Commun.* **2022**, *13*, 1551. [CrossRef]
108. Kim, S.; An, S.-C.; Kim, Y.; Shin, Y.S.; Antonov, A.A.; Seo, I.C.; Woo, B.H.; Lim, Y.; Gorkunov, M.V.; Kivshar, Y.S.; et al. Chiral electroluminescence from thin-film perovskite metacavities. *Sci. Adv.* **2023**, *9*, eadh0414. [CrossRef]
109. Kim, H.; Kim, R.M.; Namgung, S.D.; Cho, N.H.; Son, J.B.; Bang, K.; Choi, M.; Kim, S.K.; Nam, K.T.; Lee, J.W.; et al. Ultrasensitive Near-Infrared Circularly Polarized Light Detection Using 3D Perovskite Embedded with Chiral Plasmonic Nanoparticles. *Adv. Sci.* **2022**, *9*, 2104598. [CrossRef]
110. Kim, H.; Figueroa Morales, C.A.; Seong, S.; Hu, Z.; Gong, X. Perovskite-Supramolecular Co-Assembly for Chiral Optoelectronics. *ACS Appl. Mater. Interfaces* **2024**, *16*, 16515–16521. [CrossRef]
111. López-Fernández, I.; Valli, D.; Wang, C.-Y.; Samanta, S.; Okamoto, T.; Huang, Y.-T.; Sun, K.; Liu, Y.; Chirvony, V.S.; Patra, A.; et al. Lead-Free Halide Perovskite Materials and Optoelectronic Devices: Progress and Prospective. *Adv. Funct. Mater.* **2024**, *34*, 2307896. [CrossRef]
112. Fatima, S.K.; Alzard, R.H.; Amna, R.; Alzard, M.H.; Zheng, K.; Abdellah, M. Lead-free perovskites for next-generation applications: A comprehensive computational and data-driven review. *Mater. Adv.* **2025**. [CrossRef]
113. Ma, X.; Xu, Y.; Li, S.; Lo, T.W.; Zhang, B.; Rogach, A.L.; Lei, D. A Flexible Plasmonic-Membrane-Enhanced Broadband Tin-Based Perovskite Photodetector. *Nano Lett.* **2021**, *21*, 9195–9202. [CrossRef]
114. Wu, S.; Chen, R.; Zhang, S.; Babu, B.H.; Yue, Y.; Zhu, H.; Yang, Z.; Chen, C.; Chen, W.; Huang, Y.; et al. A chemically inert bismuth interlayer enhances long-term stability of inverted perovskite solar cells. *Nat. Commun.* **2019**, *10*, 1161. [CrossRef]
115. Shahiduzzaman, M.; Hossain, M.I.; Gantumur, M.; Yue, F.; Rafij, J.H.; Akhtaruzzaman, M.; Nakano, M.; Karakawa, M.; Tomita, K.; Nunzi, J.-M.; et al. Unlocking high stability in perovskite solar cells through vacuum-deposited Cs3Bi2I9 thin layer. *Nano Energy* **2024**, *127*, 109726. [CrossRef]
116. Liu, Z.; Xi, Y.; Zeng, W.; Ji, T.; Wang, W.; Guo, S.; Shi, L.; Wen, R.; Cui, Y.; Li, G. Lead-free perovskite Cs2AgBiBr6 photodetector detecting NIR light driven by titanium nitride plasmonic hot holes. *Photon. Res.* **2024**, *12*, 522–533. [CrossRef]
117. Ahmed, I.; Prakash, K.; Mobin, S.M. Lead-free perovskites for solar cell applications: Recent progress, ongoing challenges, and strategic approaches. *Chem. Commun.* **2025**, *61*, 6691–6721. [CrossRef]
118. Chiara, R.; Morana, M.; Malavasi, L. Germanium-Based Halide Perovskites: Materials, Properties, and Applications. *ChemPlusChem* **2021**, *86*, 879–888. [CrossRef] [PubMed]
119. Nabi, M.; Gupta, D.C. Potential lead-free small band gap halide double perovskites Cs_2CuMCl_6 (M = Sb, Bi) for green technology. *Sci. Rep.* **2021**, *11*, 12945. [CrossRef]

120. Chen, Q.; Shen, Y.; Cai, R.; Zhao, Z.; Dong, G. The impact of antimony on all-inorganic lead-free perovskites: Progress in optical advancement and applications. *Nanoscale* **2025**, *17*, 4892–4905. [CrossRef]
121. Yu, Y.; Ng, C.; König, T.A.F.; Fery, A. Tackling the Scalability Challenge in Plasmonics by Wrinkle-Assisted Colloidal Self-Assembly. *Langmuir* **2019**, *35*, 8629–8645. [CrossRef] [PubMed]
122. Fang, Y.; Phillips, B.M.; Askar, K.; Choi, B.; Jiang, P.; Jiang, B. Scalable bottom-up fabrication of colloidal photonic crystals and periodic plasmonic nanostructures. *J. Mater. Chem. C* **2013**, *1*, 6031–6047. [CrossRef]
123. Siddique, R.H.; Mertens, J.; Hölscher, H.; Vignolini, S. Scalable and controlled self-assembly of aluminum-based random plasmonic metasurfaces. *Light Sci. Appl.* **2017**, *6*, e17015. [CrossRef]
124. Molinski, J.H.; Zhou, J.; Palinski, T.; Zhang, J.X.J. Rapid, Tunable, and Scalable Patterning of Plasmonic Films for Biosensing Applications. *ACS Appl. Mater. Interfaces* **2025**, *17*, 50227–50236. [CrossRef]
125. Ok, J.G.; Seok Youn, H.; Kyu Kwak, M.; Lee, K.-T.; Jae Shin, Y.; Jay Guo, L.; Greenwald, A.; Liu, Y. Continuous and scalable fabrication of flexible metamaterial films via roll-to-roll nanoimprint process for broadband plasmonic infrared filters. *Appl. Phys. Lett.* **2012**, *101*, 223102. [CrossRef]
126. Xiong, Y.; Zhou, Y.; Tian, J.; Wang, W.; Zhang, W.; Zhang, D. Scalable, Color-Matched, Flexible Plasmonic Film for Visible–Infrared Compatible Camouflage. *Adv. Sci.* **2023**, *10*, 2303452. [CrossRef]
127. Li, Y.; Huang, Z.; Xu, Y.; Zhang, H.; Wang, Q.; Qiao, H.; Shang, W.; Deng, T.; Cui, K. Scalable-Manufactured Plasmonic Metamaterial with Omnidirectional Absorption Bandwidth across Visible to Far-Infrared. *Adv. Funct. Mater.* **2022**, *32*, 2207239. [CrossRef]
128. Khubezhov, S.A.; Ponkratova, E.Y.; Kuzmichev, A.M.; Maleeva, K.A.; Larin, A.O.; Karsakova, M.E.; Yakimchuk, D.V.; Zyuzin, M.V.; Makarov, S.V.; Zuev, D.A. Fast and scalable fabrication of Ag/TiO2 nanostructured substrates for enhanced plasmonic sensing and photocatalytic applications. *Appl. Surf. Sci.* **2024**, *670*, 160669. [CrossRef]
129. Larsen, G.K.; He, Y.; Wang, J.; Zhao, Y. Scalable Fabrication of Composite Ti/Ag Plasmonic Helices: Controlling Morphology and Optical Activity by Tailoring Material Properties. *Adv. Opt. Mater.* **2014**, *2*, 245–249. [CrossRef]
130. Zhao, C.; Xu, X.; Ferhan, A.R.; Chiang, N.; Jackman, J.A.; Yang, Q.; Liu, W.; Andrews, A.M.; Cho, N.-J.; Weiss, P.S. Scalable Fabrication of Quasi-One-Dimensional Gold Nanoribbons for Plasmonic Sensing. *Nano Lett.* **2020**, *20*, 1747–1754. [CrossRef] [PubMed]
131. Larsen, G.K.; He, Y.; Ingram, W.; LaPaquette, E.T.; Wang, J.; Zhao, Y. The fabrication of three-dimensional plasmonic chiral structures by dynamic shadowing growth. *Nanoscale* **2014**, *6*, 9467–9476. [CrossRef]
132. Sarkar, S.; Aftenieva, O.; König, T.A.F. Advances in scalable plasmonic nanostructures: Towards phase-engineered interference lithography for complex 2D lattices. *Colloid Polym. Sci.* **2025**, *303*, 1787–1800. [CrossRef]
133. Naik, G.V.; Shalaev, V.M.; Boltasseva, A. Alternative Plasmonic Materials: Beyond Gold and Silver. *Adv. Mater.* **2013**, *25*, 3264–3294. [CrossRef]
134. Zhang, Y.; Ouyang, Z.; Stokes, N.; Jia, B.; Shi, Z.; Gu, M. Low cost and high performance Al nanoparticles for broadband light trapping in Si wafer solar cells. *Appl. Phys. Lett.* **2012**, *100*, 151101. [CrossRef]
135. Knight, M.W.; King, N.S.; Liu, L.; Everitt, H.O.; Nordlander, P.; Halas, N.J. Aluminum for Plasmonics. *ACS Nano* **2014**, *8*, 834–840. [CrossRef] [PubMed]
136. Sugawa, K.; Tahara, H.; Yamashita, A.; Otsuki, J.; Sagara, T.; Harumoto, T.; Yanagida, S. Refractive Index Susceptibility of the Plasmonic Palladium Nanoparticle: Potential as the Third Plasmonic Sensing Material. *ACS Nano* **2015**, *9*, 1895–1904. [CrossRef]
137. Jiang, Q.; Ji, C.; Riley, D.J.; Xie, F. Boosting the Efficiency of Photoelectrolysis by the Addition of Non-Noble Plasmonic Metals: Al & Cu. *Nanomaterials* **2019**, *9*, 1.
138. Indhu, A.R.; Dharanya, C.; Dharmalingam, G. Plasmonic Copper: Ways and Means of Achieving, Directing, and Utilizing Surface Plasmons. *Plasmonics* **2024**, *19*, 1303–1357. [CrossRef]
139. Sayed, M.; Yu, J.; Liu, G.; Jaroniec, M. Non-Noble Plasmonic Metal-Based Photocatalysts. *Chem. Rev.* **2022**, *122*, 10484–10537. [CrossRef]
140. Lin, D.; Duan, Y.; Bandaru, P.; Li, P.; Ansari, M.S.; Polyakov, A.Y.; Wilhelmsen, J.; Jonsson, M.P. Switchable narrow nonlocal conducting polymer plasmonics. *Nat. Commun.* **2025**, *16*, 4484. [CrossRef] [PubMed]
141. Athanasiou, S.; Martin, O.J.F. Alternative Plasmonic Materials for Fluorescence Enhancement. *J. Phys. Chem. C* **2024**, *128*, 18574–18581. [CrossRef] [PubMed]

Disclaimer/Publisher's Note: The statements, opinions and data contained in all publications are solely those of the individual author(s) and contributor(s) and not of MDPI and/or the editor(s). MDPI and/or the editor(s) disclaim responsibility for any injury to people or property resulting from any ideas, methods, instructions or products referred to in the content.

inorganics

MDPI

Review

Mitigating Lead Toxicity in Halide Perovskite Solar Cells: Strategies for Sustainable Development

Wenguang Li [1,2,†], Tianci Mi [3,†], Tian Tian [2] Meifang Yang [2,*] and Huan Pang [2,*]

[1] School of Chemistry and Environment, Jiaying University, Meizhou 514015, China; wenguang_li@yzu.edu.cn
[2] School of Chemistry and Chemical Engineering, Yangzhou University, Yangzhou 225002, China; tiant91@yzu.edu.cn
[3] Department of Chemical Engineering and Medicine, Guangling College of Yangzhou University, Yangzhou 225002, China; 19083724383@163.com
* Correspondence: yangmf@yzu.edu.cn (M.Y.); panghuan@yzu.edu.cn (H.P.)
† These authors contributed equally to this work.

Abstract: Halide perovskite solar cells (PSCs) exhibit remarkable potential for addressing global energy challenges due to their exceptional photovoltaic properties and cost-effectiveness. However, their widespread adoption is hindered by the presence of toxic lead in the perovskite materials, posing risks to both human health and the environment. This review comprehensively examines the environmental safety concerns associated with PSCs, focusing on the toxicity of lead and its potential for leakage during device operation and end-of-life disposal. Strategies to mitigate lead leakage are explored, including advanced external encapsulation methods, internal lead immobilization techniques, and innovative recycling approaches. These strategies are evaluated based on their effectiveness, feasibility, and potential challenges, highlighting the need for a multi-pronged approach to ensure the responsible and sustainable development of PSC technology. By addressing the toxicity issue and implementing robust prevention and recycling strategies, PSCs can become a driving force for the global transition towards clean and renewable energy while minimizing environmental and health risks.

Keywords: halide perovskite; lead leakage; environmental safety

1. Introduction

In recent years, metal halide perovskites (MHPs) have experienced remarkable advancements as a novel functional material, quickly becoming a focal point in the field of optoelectronics. MHPs exhibit several advantages, including ease of processing, low cost, high light absorption coefficients, high charge carrier mobility, and tunable optoelectronic characteristics [1], which have led to their widespread application in perovskite solar cells (PSCs) [2–5], light-emitting diodes (LEDs) [6–8], photodetectors [9], X-ray detectors [10], gas sensors [11], field-effect transistors [12,13], lasers [14], etc. Despite the rapid development in MHP-based optoelectronic technologies, some stability issues persist, such as ion migration, phase transitions, phase segregation, and component volatilization, which can lead to material degradation and performance deterioration of the devices, particularly under environmental stresses like high temperatures, high humidity, and ultraviolet (UV) exposure [4,15,16]. Furthermore, the deployment of PSC components in commercial applications often occurs in open fields or on rooftops, where they can be subjected to various weather and environmental factors, including debris, hail, snow, strong winds, and fires. In such scenarios, the performance of the devices can decrease dramatically, and since halide

perovskites are ionic compounds, they are prone to decomposition into highly toxic soluble lead salts, halide anions, organic cations, and other components under the influence of moisture, heat, light, or mechanical stress. These constituents can subsequently leach into groundwater or soil along with rainwater, resulting in soil and water contamination [17–19]. Although the lead content in perovskite solar cell modules is only a few hundred milligrams per square meter, the high toxicity of lead to both humans and ecosystems necessitates a careful assessment and management of this issue before the widespread use of lead-based perovskite photovoltaic devices.

Regarding the toxicity issues of perovskites, the industry has raised the question of whether it is possible to achieve excellent optoelectronic performance using lead-free perovskites. Researchers have attempted to replace lead with other metals that have similar orbital configurations, such as group IV elements with identical valence electron configuration [20,21]. Among these, tin (Sn)-based perovskites have been the most extensively studied since Sn^{2+} has an ionic radius (118 pm) similar to that of Pb^{2+} (119 pm) [20,22]. Although Sn-based perovskites also exhibit excellent charge-transport properties, Sn^{2+} is readily oxidized to Sn^{4+} (standard reduction potential E_0 for Sn^{2+}/Sn^{4+} is 0.15 V, while E_0 for Pb^{2+}/Pb^{4+} is 1.67 V) [23], creating defects and degrading optoelectronic performance. Moreover, the acute toxicity of Sn^{2+} ions is considered higher than that of Pb^{2+} [24]. Germanium (Ge), another group IV element, has a smaller ionic radius (73 pm) and is more easily oxidized, leading to inferior stability of Ge-based perovskites [25]. Researchers have also explored other lead-free perovskites based on metals with ns^2 orbital configurations, such as Bi^{3+}, Sb^{3+}, and Ag^{+} [26–29]. However, the metal halides derived from these metals typically form low-dimensional crystal structures, which exhibit wide bandgaps and poor charge transport [30]. Despite some progress in this field, both the power conversion efficiency (PCE) and stability of lead-free PSCs remain substantially inferior to their lead-based halide PSCs [31,32]. By now, lead-based perovskites remain the mainstream choice in terms of the outstanding optoelectronic properties [33]. Therefore, addressing the toxicity issue and mitigating the risk of lead leakage from PSC devices is crucial for the responsible and sustainable development of this promising technology.

To achieve this goal, a comprehensive understanding of the sources and pathways of lead exposure is essential. This involves evaluating the potential for lead release during various stages of the PSC life cycle, including device fabrication, operation, and end-of-life disposal. This review offers an in-depth analysis of the environmental risks linked to PSCs and highlights recent progress in reducing lead leakage. It will explore various strategies, including advanced encapsulation methods, chemical absorption techniques, and innovative recycling approaches, with a focus on their effectiveness, feasibility, and potential challenges. By shedding light on these critical issues, this review seeks to facilitate the development of PSCs into a truly sustainable and responsible technology that can drive the global transition towards clean and renewable energy.

2. Environmental Risks of Halide Perovskite Materials

2.1. Lead Toxicity of Halide Perovskites

As a toxic heavy metal, lead disrupts critical biological functions and adversely impacts multiple organ systems. While its general health and environmental risks are well documented, the unique risks posed by lead leakage from MHP-based optoelectronic devices warrant focused attention. The toxicity of lead arises from its similarity to biologically essential ions (such as Ca^{2+}, Fe^{2+}, and Zn^{2+}), enabling it to mimic these essential cations, compete for binding sites, and disrupt normal physiological functions, such as inhibiting calcium signaling and reacting with proteins [34]. Oxidative stress [35], carcinogenicity [36], and bioaccumulation further exacerbate its hazards [37]. Critically, MHP-derived lead

introduces novel exposure pathways and ecological amplification effects. For example, experimental studies reveal that Pb leaked from perovskite degradation in soil disproportionately enhances plant uptake: mint plants grown in perovskite-contaminated soil (250 mg kg^{-1} Pb) absorbed 366-fold more lead than those in natural lead-polluted soil (36.3 mg kg^{-1} Pb), leading to rapid blackening, rotting, and death (Figure 1) [38]. Although the lead content in perovskite-contaminated soil only increased sevenfold, the absorption of lead by plants increased 366-fold. This highlights the heightened bioavailability of perovskite-associated Pb compared to conventional lead pollutants, threatening the ecological pyramid.

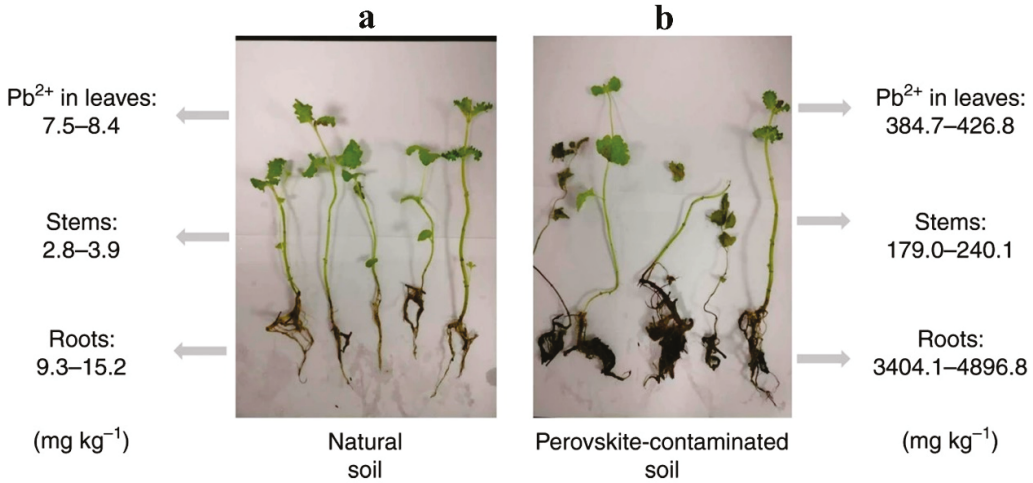

Figure 1. Lead concentration in different parts of mint plants grown in (**a**) control soil and (**b**) perovskite-contaminated soil. Reprinted with permission from Ref. [38]. Copyright 2020 Springer Nature.

More importantly, lead exposure has long-term irreversible toxic effects on humans and animals, which have been confirmed by numerous studies. Babayigit et al. [24] demonstrated PbI_2's developmental toxicity using Danio rerio embryos (85% genetic similarity to humans), linking it to spinal curvature, cardiac edema, and brain vascular defects (Figure 2a). The analysis of heat shock protein 701 further confirmed concentration-dependent developmental impairment (Figure 2b). Such findings underscore the cascading risks of perovskite-derived Pb entering the food chain and affecting vulnerable populations, including infants and children.

When the structure of MHPs is damaged, their perovskite material begins to collapse until complete degradation, and decomposition products such as PbI_2 can easily dissolve in water on rainy days. Then, lead from MHPs may contaminate water and crops, entering the human body. Lead accumulates in bones (half-life: 40–50 years) and organs, causing anemia, neurodevelopmental disorders, and systemic damage [34,39]. Higher exposure levels and younger age (especially fetuses) increase toxicity. Excessive lead affects multiple systems, causing anemia, kidney damage, high blood pressure, and neurological disorders [40–44]. For children, blood lead levels exceeding 100 μg L^{-1} define poisoning, necessitating strict limits on MHP devices used in child-accessible applications. A large-scale deployment of perovskite photovoltaic devices in the future would magnify these risks. While current lead content in perovskite solar cells (0.1 mg cm^{-2}) is lower than in silicon modules [45–47], if all electricity in China and globally were to be supplied by perovskite PV devices, about 493 tons of lead per year in China and 1325 tons globally would be required (assuming 20% efficiency). This scale, driven by rising energy demands from AI and data centers, positions perovskite-derived lead pollution as a critical future challenge. Currently, existing relevant regulations, such as the EU's RoHS2 (2011/65/EU) (no more than 0.1% Pb by weight in

electronic products) [48], may not be sufficient to address the lifecycle risks of MHPs in the future, emphasizing the need for device–human isolation strategies and leakage prevention, especially for indoor applications. In short, the hazards of lead poisoning should be taken seriously and effectively addressed.

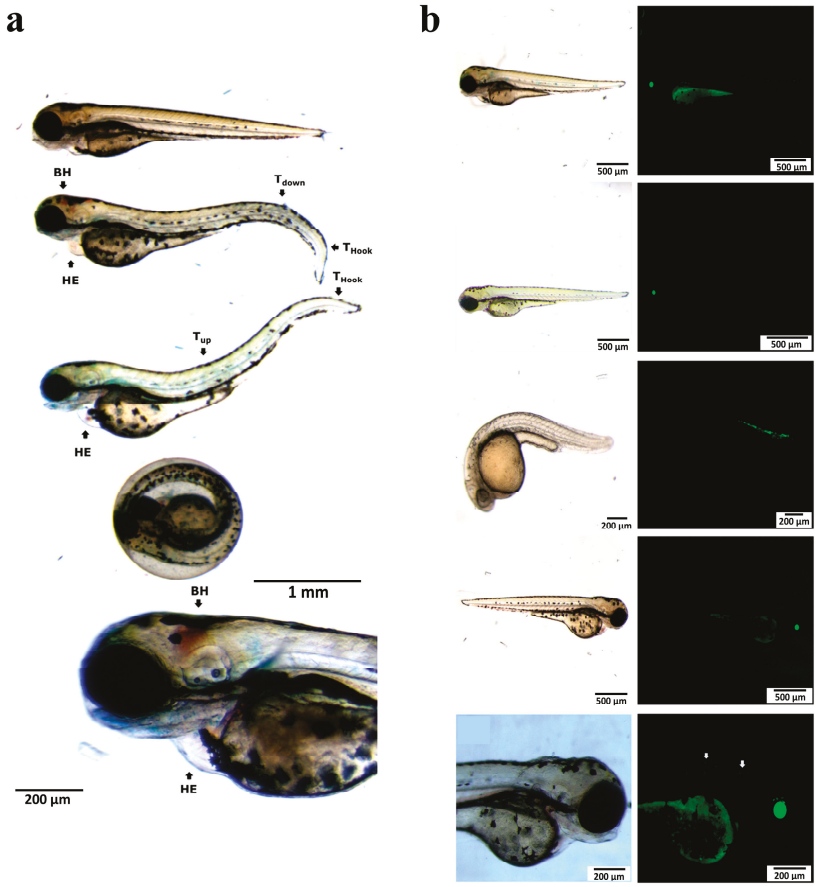

Figure 2. (**a**) PbI_2-induced morphologically defective phenotypes of Danio rerio and the amplification of a cerebrovascular defect in PbI_2-treated group. (**b**) Stereo (**left**) and fluorescence (**right**) images of Tg(hsp70l:GFP) of embryos treated with different PbI_2 concentrations. Reprinted with permission from Ref. [24]. Copyright 2016 Springer Nature.

2.2. Mechanism and Effect of Lead Leakage

Lead mainly exists as divalent ions (Pb^{2+}) in PSCs. The decomposition pathways of MHPs under thermal, aqueous, and environmental stresses have been extensively studied. The degradation mechanism of $MAPbI_3$ exhibits temperature-dependent behavior (Figure 3a): below 200 °C, it primarily decomposes into volatile HI and CH_3NH_2 while retaining solid PbI_2; above this thermal threshold (>200 °C), the decomposition shifts toward producing thermodynamically favored gaseous species including NH_3 and CH_3I, with a persistent formation of crystalline PbI_2 as the inorganic residue [33]. Recent studies have provided deeper insights into the aging atomistic pathway of perovskite $MAPbI_3$ through combined theoretical and experimental approaches [49,50]. At the atomic scale, $MAPbI_3$ degradation follows a two-step pathway: (1) the initial loss of MA^+ cations, forming a metastable intermediate phase $MA_{0.5}PbI_3$ with ordered MA^+ vacancies that preserves the perovskite framework and (2) subsequent collapse into 6H-PbI_2 via Pb^{2+} and I^- diffusion, as revealed by atomic-resolution TEM imaging and DFT calculations [49,50]. This process aligns with the aforementioned thermal decomposition trends.

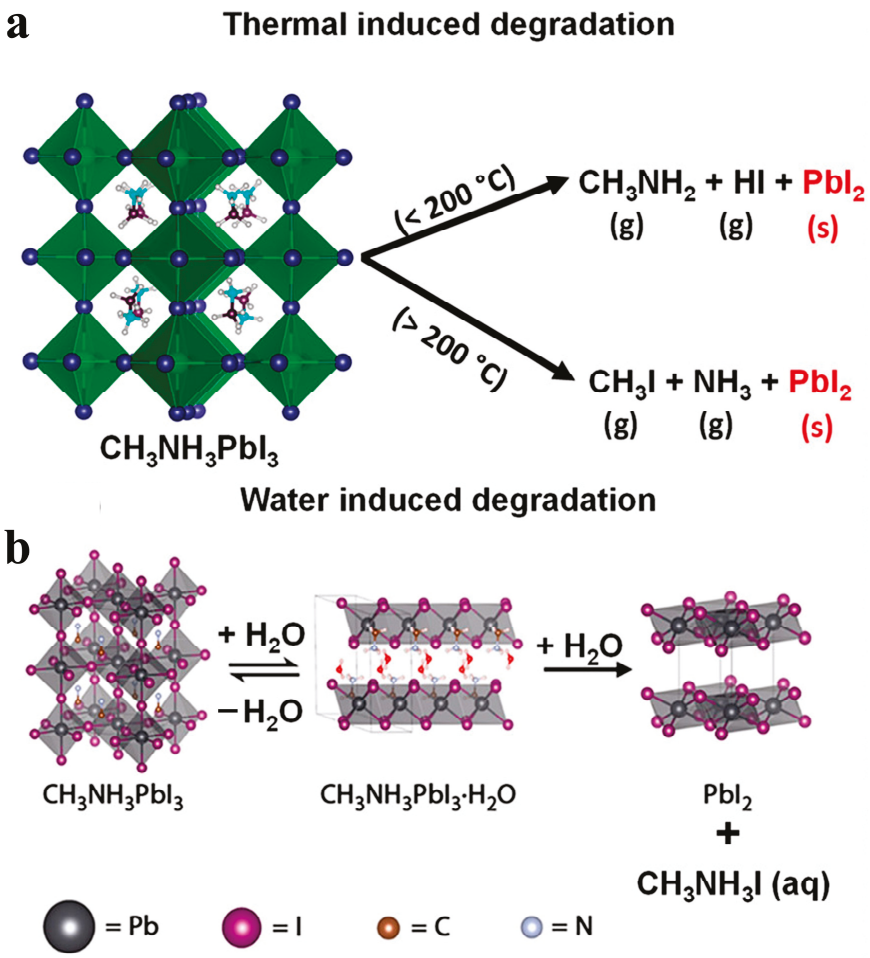

Figure 3. (**a**) Thermally induced degradation reaction of $MAPbI_3$. Reprinted with permission from ref. [33]. Copyright 2020 American Chemical Society. (**b**) Water-induced degradation reaction of $MAPbI_3$. Reprinted with permission from Ref. [51]. Copyright 2020 John Wiley and Sons.

In aqueous environments (Figure 3b), $MAPbI_3$ perovskite undergoes a spontaneous irreversible dissolution process, forming hydrated intermediates ($APbX_3{\cdot}H_2O$) with one-dimensional $[PbI_3]^-$ double chains (Equation (1)) [51]. Subsequently, the perovskite surface dissolves rapidly first, exposing I^- and forming stronger Pb-I bonds on the surface. The low-dimensional hydrated perovskite decomposes into I_2 under ultraviolet or light exposure, further promoting the degradation process (Equations (2) and (3)) [51]. Since there is a strong hydrogen bond between PbX_2 and water molecules, PbX_2 has a high solubility constant in water ($K_{sp} \approx 9.8 \times 10^{-9}$) [52], making it easy to dissolve in water and enter the environment. In acidic environments (such as under acid rain conditions), the irreversible flow of Pb^{2+} from broken devices into water accelerates significantly (Equation (4)), causing more severe Pb leakage and environmental pollution [51]. While mixed cationic systems (such as $FA_{0.85}Cs_{0.15}PbI_3$) have been shown to exhibit relatively good stability, phase segregation is known to occur under humid and light conditions, and PbI_2 degradation products are also inevitably formed [53]. Crucially, PbI_2 serves as the primary lead reservoir across degradation scenarios, with its hydrolysis and dissolution being the dominant pathways for environmental lead release. The understanding of this mechanism is helpful for the subsequent analysis and discussion of lead storage strategy.

$$APbX_3 + H_2O \leftrightarrow APbX_3{\cdot}H_2O \tag{1}$$

(A = MA, FA, Cs, or mixture; X = Br, I, or mixture)

$$(4 - n)APbX_3 + nAPbX_3 \cdot H_2O + (2 - n)H_2O \leftrightarrow A_4PbX_6 \cdot 2H_2O + 3PbX_2 \quad (2)$$

$$A_4PbX_6 \cdot 2H_2O \rightarrow PbX_2 + 4A^+ + 4X^- + 2H_2O \quad (3)$$

$$PbX_2 + 2H_3O^+ \rightarrow Pb^{2+} + 2HX + 2H_2O \quad (4)$$

3. Strategies of Lead Leakage Suppression for Perovskite Solar Cells

3.1. External Encapsulation

Lamination encapsulation constitutes a mature protective method in photovoltaic module manufacturing, effectively isolating the device from ambient environmental degradation factors [54]. Photovoltaic modules are typically encapsulated with ethylene-vinyl acetate (EVA, a copolymer synthesized from ethylene and vinyl acetate), sandwiched between a tempered front glass pane and a reinforced back sheet to provide mechanical protection and environmental isolation for the solar cells [55]. A five-layer stack structure of glass/EVA/PSC/EVA/glass has been adopted for encapsulating PSCs, significantly enhancing the operational stability of the devices [56,57]. EVA has the advantages of good light transmittance, elasticity, adhesion strength to glass, and melt flowability. Therefore, EVA can protect the devices without affecting their efficiency and has been used as an encapsulation material in nearly 80% of photovoltaic modules. The usual UV-curing adhesive was also reported to encapsulate PSCs for better stability [58–60]. In addition, new encapsulation materials and encapsulation methods with better sealing effects and suppression of lead leakage have been developed. For example, Wan et al. combined two encapsulants, polyolefin (PO) and polyisobutylene (PIB), to develop a "sandwich" encapsulation method in which PO was coated on top of the electrode, and the sides of the PSCs were encapsulated with PIB, as shown in Figure 4a [61]. After these devices were damaged under the same conditions, they were immersed in solutions with different pH values (simulating seawater, lake water, and rainwater) to assess the lead leakage (Figure 4b). This "sandwich" encapsulant greatly reduced the damage to the devices caused by hail and acid rain. Under the protection of the "sandwich" encapsulation, the lead leakage in the soil was reduced to 3.4 ppm [61], which is much lower than the 70 ppm predicted by Hailegnaw et al. in 2016 [62].

However, traditional EVA and PO/PIB sandwich encapsulation methods suffer from limitations such as thermomechanical stress-induced delamination and insufficient edge sealing under extreme weather conditions. To address this issue, Wang et al. [63] reported a room-temperature self-cross-linked fluorosilicone polymer (CFDP) that achieved non-destructive encapsulation without requiring high-temperature processing. This material demonstrated exceptional moisture barrier properties, maintaining 98% of normalized PCE after 1000 h in damp heat (85 °C/85% RH) and reducing lead leakage to <0.08 ppm in rainwater immersion tests [63]. The CFDP's strong coordination with Pb^{2+} ions and high thermal conductivity (0.51 W m^{-1} K^{-1}) effectively mitigated heat-induced perovskite decomposition, addressing a critical limitation of traditional encapsulants like EVA and PIB. Recently, Mariani et al. [64] also reported a low-temperature strain-free encapsulation technology using a PIB/hexagonal boron nitride (h-BN) composite. The addition of two-dimensional h-BN flakes enhances the thermal management and barrier properties of the encapsulant. This encapsulation strategy eliminates edge sealants while passing IEC 61215-standard [65] tests (85 °C/85% RH and −40 to 85 °C thermal cycling) with lead leakage below 100 ppb [64]. This strategy minimizes dead zones and is applicable to various cell configurations, including semi-transparent PSCs for building-integrated photovoltaics (BIPVs), with significant potential for large-scale production and commercialization.

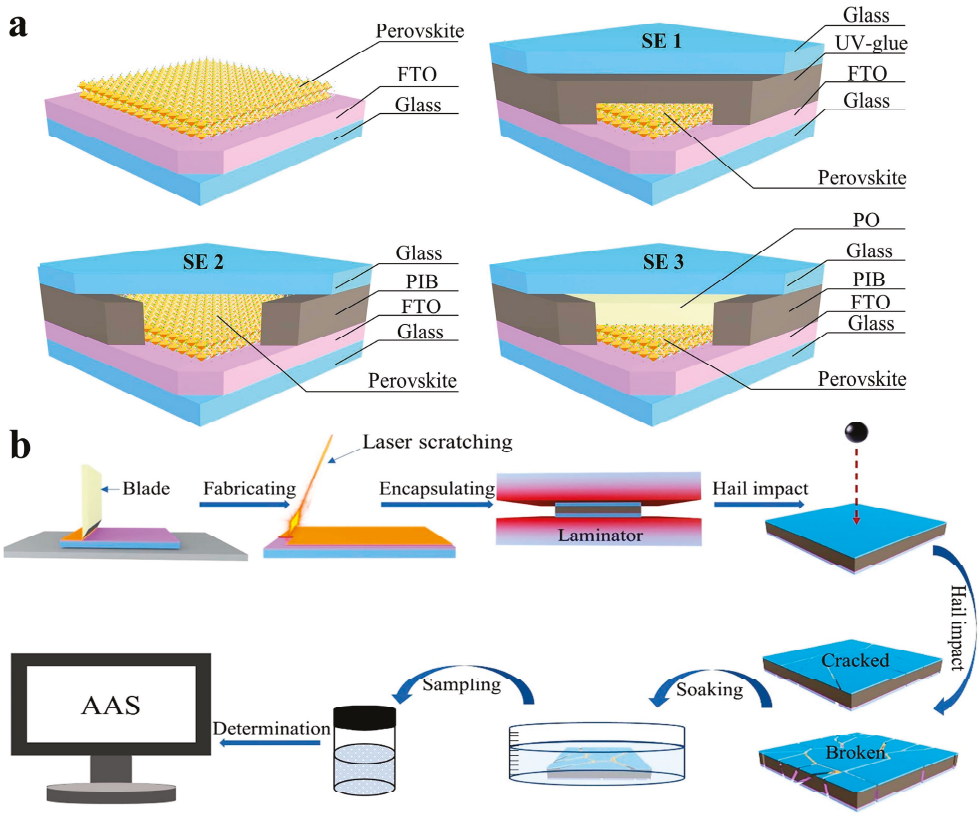

Figure 4. (**a**) Unencapsulated perovskite devices and devices with different "sandwich" encapsulation methods. (**b**) Schematic diagram of the lead leakage testing process of PSCs. Reprinted with permission from Ref. [61]. Copyright 2021 Elsevier.

In the practical application of perovskite photovoltaic devices, lead leakage is not only caused by intrinsic material degradation but more critically from mechanical damage under extreme environmental stressors. For instance, abrupt temperature fluctuations or hail impacts can fracture conventional encapsulation layers, exposing the perovskite active layer and accelerating lead ion diffusion into the environment. To systematically evaluate the efficacy of encapsulation strategies in mitigating lead leakage from damaged PSC modules, Jiang et al. conducted a realistic simulation of mechanical damage (e.g., hail impact) and performed quantitative analysis of lead leakage rates under simulated environmental conditions (Figure 5) [66]. Their comparative study of four encapsulation architectures revealed that lead leakage exhibits a strong dependence on encapsulation design and environmental factors. Notably, combining self-healing polymers with front-side glass encapsulation proves effective in reducing lead leakage. In particular, epoxy resin (ER)-based polymers with a relatively low transition temperature (about 42 °C) are easy to heal at high temperatures, and it is more effective in reducing the lead leakage rate from 30 mg h^{-1} m^{-2} to 0.08 mg h^{-1} m^{-2} in comparison with the method of encapsulating with UV-cured resin-covered glass [66]. These results show that using the appropriate encapsulation materials and methods is the most direct strategy to inhibit lead leakage. The high mechanical strength and self-healing mechanism of ER film can effectively reduce the lead leakage in PSCs, providing new insights into the encapsulation methods of PSCs.

Although appropriate encapsulation architectures can initially inhibit the leakage of lead from PSCs, their long-term operational reliability remains constrained by environmental stressors. Mechanical degradation or chemical corrosion of encapsulation layers, triggered by thermal cycling, exposure to moisture, or physical shock, creates microcracks and interfacial delamination that enable water-soluble Pb^{2+} species to rapidly escape into the surrounding environment via hydrolysis pathway, posing significant ecological

risks [67]. Therefore, simple encapsulation may not be sufficient to completely inhibit lead leakage. In contrast, chemical encapsulation utilizes special lead-capturing materials within the encapsulation matrix to immobilize lead ions through the formation of stable insoluble compounds, as well as their chemical conversion to low-toxicity chelates through coordination bonds. This dual-action approach effectively reduces lead bioavailability and mobility in ecosystems. Coating the front and back of a complete solar cell with an encapsulation layer containing lead capture materials is the most reported effective strategy for PSCs. Compounds containing phosphine [45,68], sulfonic acid [69,70], and carboxyl [71] with strong binding ability to lead ions are usually chosen as lead capture materials. Recently, a series of PSC chemical encapsulation materials and strategies with multiple functions such as enhanced stability, improved resistance to mechanical impact, and reduced lead leakage have been reported.

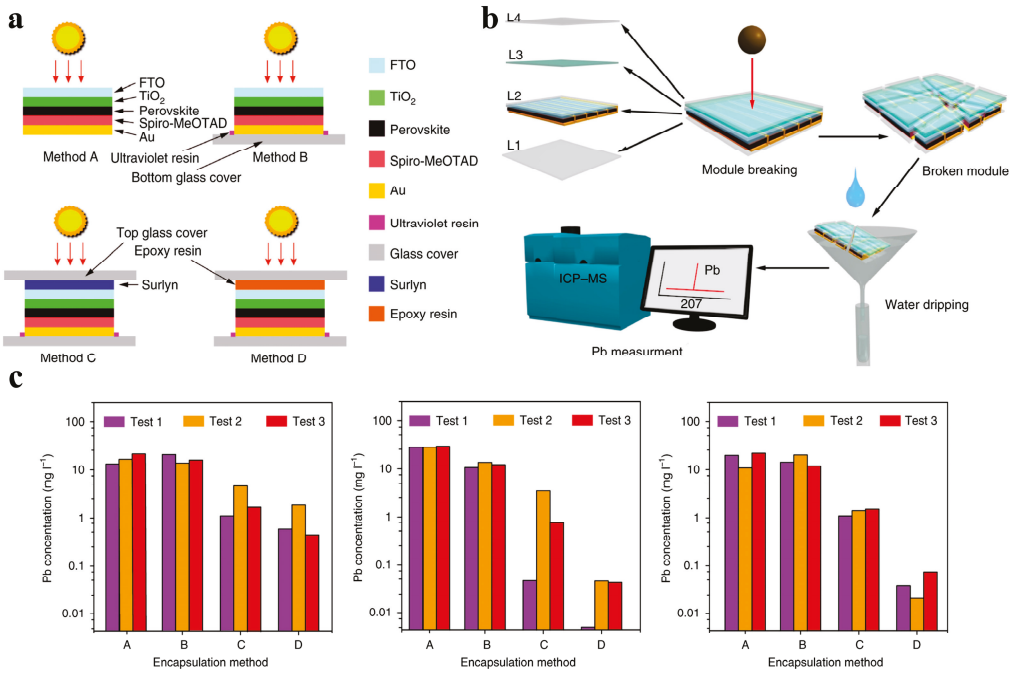

Figure 5. (**a**) Schematic diagram of four encapsulation methods. (**b**) Schematic diagram of Pb leakage test for perovskite solar module damaged by external impact. (**c**) Lead concentration test under different experimental conditions. Reprinted with permission from Ref. [66]. Copyright 2019 Springer Nature.

Li et al. developed a dual-side chemical encapsulation strategy for PSCs, employing distinct functional layers on opposing surfaces [45]. For frontal protection, they implemented a transparent P,P′-di(2-ethylhexyl) methylenediphosphonic acid (DMDP) coating on glass substrates, leveraging its dual phosphonic acid moieties per molecule to strongly chelate Pb^{2+} ions (Figure 6a). The rear encapsulation comprised a composite film blending N,N,N′,N′-ethylendiaminetetramethylphosphonic acid (EDTMP), a potent lead-chelating agent, with polyethylene oxide (PEO), subsequently laminated with EVA. As demonstrated in Figure 6b, both the DMDP and EDTMP-PEO layers exhibited exceptional Pb^{2+} adsorption capacities. Crucially, these films exhibited swelling rather than dissolution upon water exposure, enabling >96% Pb^{2+} retention within damaged devices through physical entrapment and chemical immobilization. Extending this approach, the team engineered an innovative Pb-capturing adhesive by depositing DMDP onto EVA sheets, creating a multifunctional "transparent tape" for device encapsulation (Figure 6c) [72]. This design demonstrated remarkable environmental resilience, maintaining >99.9% Pb absorption efficiency during week-long outdoor exposure while preserving photovoltaic performance.

The delayed Pb release mechanism provides critical time windows for post-damage remediation without compromising initial device functionality.

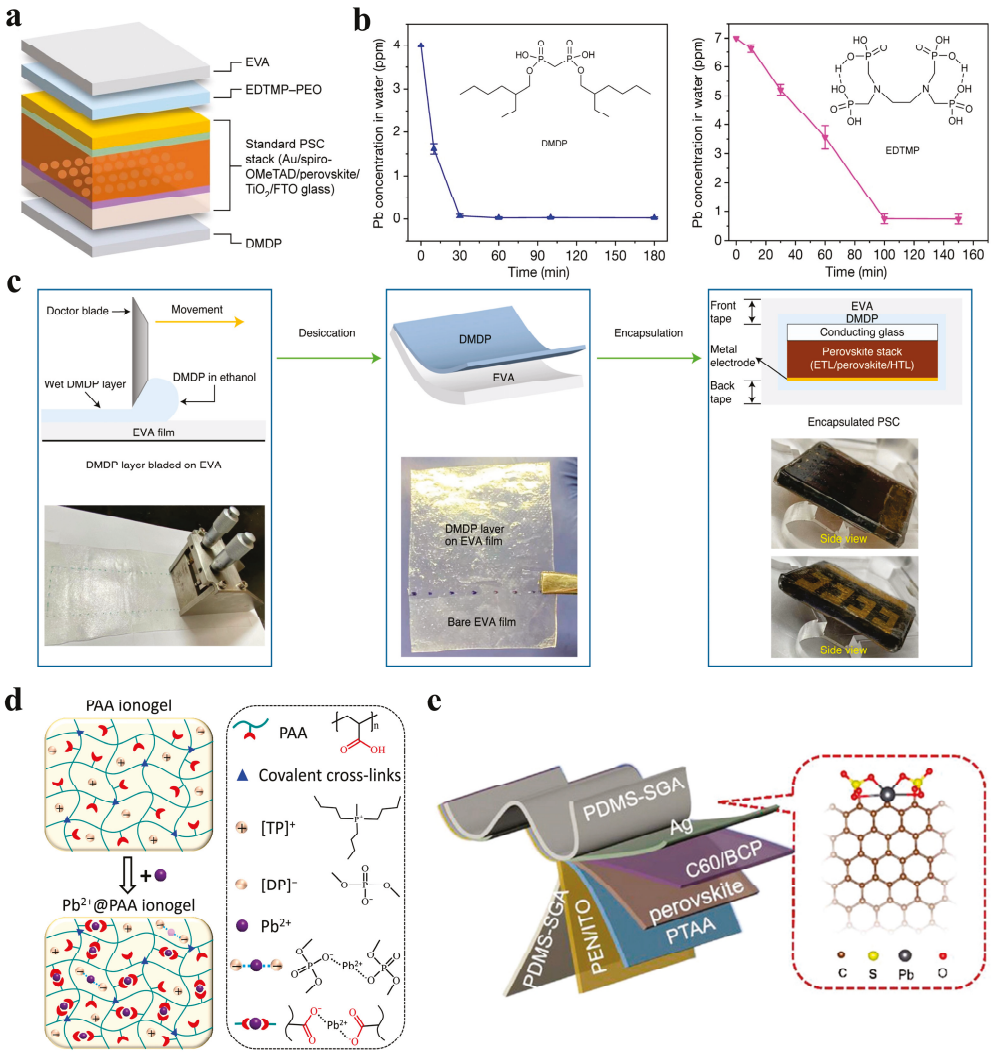

Figure 6. (**a**) The device structure consists of two lead absorbing films (DMDP and EDTMP-PEO). (**b**) Chemical structure and lead trapping capacity of DMDP and EDTMP. Reprinted with permission from Ref. [45]. Copyright 2020 Springer Nature. (**c**) The fabrication and encapsulation process of DMDP and EVA. Reprinted with permission from Ref. [72]. Copyright 2021 Springer Nature. (**d**) Scheme of ionogel microstructure and lead adsorption mechanism. Reprinted with permission from Ref. [73]. Copyright 2021 AAAS. (**e**) Schematic of flexible PSCs encapsulated with S-GA/PDMS mixture on both the front side and back side. Reprinted with permission from Ref. [74]. Copyright 2021 Wiley-VCH.

From a physical mechanics perspective, enhancing the impact resistance of devices can reduce the likelihood of device damage, thereby minimizing lead leakage. Xiao et al. [73] reported a robust and self-healing ionic gel containing lead-adsorbing acrylic acid (AA) and tributyl(methyl)phosphonium dimethylphosphinate (TPDP) ionic liquid, which can be used as a component of encapsulation material for PSCs, simultaneously reducing lead leakage and enhancing device stability (Figure 6d). Wrapping the front and back of PSCs with an ionic gel layer, and subjecting them to a simulated hail test followed by a 24 h water immersion, resulted in lead leakage from the damaged PSC modules of less than 1 ppb, which was undetectable by the instrument. This encapsulation method is more effective in suppressing lead leakage than PO sealant and standard glass cover encapsulation. The high impact resistance of stretchable encapsulation materials and the

strong lead-binding ability of AA monomers are the main reasons for their high lead fixation performance. As shown in Figure 6d, the carboxyl radicals on polyacrylic acid (PAA) are the functional groups for capturing Pb^{2+}. Thanks to the clamp-like cross-linked polymer network of PAA, this encapsulant is very effective in preventing lead leakage. Li et al. [74] developed an encapsulation method for flexible PSCs in which they mixed sulfonated graphene aerogel (S-GA) with PDMS as a lead-absorbing encapsulant and placed it on both sides of the device, as shown in Figure 6e. The large specific surface area and excellent flexibility of S-GA provide sufficient adsorption sites to capture dissociated lead ions, forming strong ionic bonds with Pb^{2+} through SO_3^{2-}, giving it superior lead capture ability in aqueous solutions. Under various simulated conditions, such as scraping, bending, wrinkling, and thermal cycling, the encapsulant can capture more than 99% of the leaked lead from damaged flexible PSCs. This method can reduce the lead leakage after the degradation of flexible PSCs to 10 ppb, far below the hazardous waste limit specified by the US Resource Conservation and Recovery Act [74]. This is a pioneering experimental study on the lead leakage dynamics of flexible PSCs and assesses the efficacy of sulfonated aerogel encapsulation under realistic environmental conditions, offering critical insights for developing safe and reliable flexible PSCs and advancing the commercialization of perovskite-based electronic devices.

Recently, nanostructured adsorption layers have emerged as a promising strategy for mitigating lead leakage in perovskite photovoltaics. Valastro et al. demonstrated this concept through the development of a titanium dioxide (TiO_2) sponge layer synthesized via a scalable, solvent-free sputtering process [75]. The porous structure of TiO_2 layer allows high surface reactivity and accessibility, capturing Pb ions within branched nanopores. Experimental results indicate this approach significantly reduces Pb release into water. For instance, after soaking in water for ten days, the Pb concentration in water with TiO_2-covered PSCs was 0.26 ppm, compared to 2.65 ppm in uncovered PSCs, demonstrating a Pb sequestration efficiency (SQE) of 90.2% [75]. Even under simulated heavy rainfall conditions, the TiO_2 layer achieved an average SQE of 89%. This method offers a sustainable solution for preventing environmental contamination from perovskite devices.

3.2. Lead Immobilization Within PSCs

In addition to physically or chemically encapsulating the entire external structure of the device, incorporating lead-absorbing materials internally can serve as an "additional line of defense" against Pb leakage. Although the addition of lead trapping materials in the PSC encapsulation layers can prevent the ingress of water and oxygen and effectively suppress lead leakage from the device, the lead capture materials on the front of the PSCs are inevitably exposed to ultraviolet radiation from sunlight and may become damaged after prolonged exposure, thereby generating free Pb ions. In PSCs that are not completely damaged, the lead capture materials on the back of the device cannot capture lead that leaks from the front. Moreover, lead capture materials on the surface of the device, when soaked in rainwater for extended periods, may also adsorb other cations such as Cd^{2+}, Ca^{2+}, Mg^{2+}, etc., which can lead to saturation of the metal ion capture function and loss of the ability to continuously adsorb subsequently leaking Pb ions. In contrast, incorporating lead adsorption materials within the PSCs can effectively avoid these issues. This strategy of incorporating lead-absorbing materials internally provides an ideal method that can rapidly capture Pb^{2+} as soon as the perovskite is decomposed by rainwater, and the impact of external factors such as rainwater and ultraviolet light on the lead capture materials is minimal.

An effective approach involves directly incorporating lead-absorbing materials into the perovskite layer to enhance both its stability and lead capture ability. Chen et al. [70]

reported an impressive work, where they developed a novel approach to mitigate lead leakage from damaged perovskite solar modules by incorporating a mesoporous sulfonic acid-based cation exchange resin (CER) directly into the perovskite layer, as shown in Figure 7a. The resin, composed of a cross-linked styrene-divinylbenzene copolymer functionalized with sulfonic acid groups (Figure 7b), operates through a dual mechanism of "ion exchange" and "physical blocking". The sulfonic acid groups act as active adsorption sites, where the Na^+ ions in the resin undergo ion exchange with Pb^{2+} ions from decomposed perovskites under aqueous conditions (e.g., acidic rainwater). This process is driven by the strong affinity of sulfonic acid groups for divalent cations like Pb^{2+}, effectively trapping them within the resin's porous matrix. The mesoporous structure further enhances adsorption capacity by providing a high density of accessible binding sites and prolonging the interaction time between Pb^{2+} and the resin. The authors systematically evaluated Pb leakage in perovskite modules with varying encapsulation strategies through water-dripping tests, simulating highly acidic rainfall conditions (Figure 7c–f). As evidenced by the results of lead leaching concentrations in Figure 7c, the strategy of embedded mesoporous CER within the perovskite layer (Device III) is more effective in preventing lead leakage than just coating lead capture materials on the device's surface (Device II). This built-in lead adsorption framework serves as the first layer of protection against lead leakage, which can be further combined with appropriate external encapsulation to synergistically produce better lead leakage inhibition results, achieving an impressive lowest Pb concentration of 11.9 ± 1.4 ppb.

In addition to lead adsorbing resins, a variety of polymers, organic small molecules, and metal–organic framework (MOF) materials containing amide and carboxyl groups have been developed as lead adsorption materials and added to the perovskite layer. Depending on their structural design, these materials can serve multiple functions: in addition to capturing the leaking lead ions, they can also promote the nucleation and crystallization of perovskite, passivate grain boundary defects, and block the ingress of water vapor. Our group also has proposed a comprehensive strategy of supramolecular complex network to solve the lead leakage issue [46]. As shown in Figure 8a, the cross-linking supramolecular complexes of 2-hydroxypropyl β-cyclodextrin (HPβCD) and 1,2,3,4-butane tetracarboxylic acid (BTCA) were introduced into perovskite films, which were shown to improve the stability of the entire process from perovskite precursor to film and final device, effectively inhibiting lead leakage from severely damaged PSCs and reducing lead toxicity. The built-in HPβCD-BTCA cross-linking complex modification increases the PCE of PSCs to 22.14% and extends the working life to 4000 h. In addition, the external package, combined with the chemical chelation of the built-in supramolecular complex and the flexible HPβCD-BTCA fiber membrane (Figure 8b), retains 97% of the initial efficiency after 522 h of dynamic water scouring, with minimized lead leakage from severely damaged PSCs and resulting in only 14 ppb lead contamination in water [46].

Alternatively, the lead capture materials can be added to the charge transport interface, acting as an interface modifier. In particular, the electron transport layer (ETL) and hole transport layer (HTL), which are adjacent to the perovskite layer, can capture Pb ions immediately upon the occurrence of lead leakage from the perovskite layer. Wu et al. used a two-dimensional conjugated MOF and applied it as an electron extraction layer and lead absorption layer at the perovskite/cathode interface [76]. The Zr (IV)-based MOF ZrL_3 was prepared by solvothermal method, and its densely arranged thiol groups provided spatial shielding and had cross-linked disulfide bonds to capture free lead ions. As shown in Figure 9a, Pb^{2+} from perovskite dissociation did not accumulate on the Ag electrode in the component with the MOF layer, demonstrating that lead ions are trapped by forming Pb-S bonds with the MOF to form insoluble complexes. The concentration of Pb^{2+} in polluted

water for PSCs with ZrL_3:bis-C_{60} as the ETL (7.6 ppm) was much lower than that for control PSCs with bis-C_{60} as the ETL (38.4 ppm, Figure 9b), indicating that more than 80% of Pb^{2+} ions leaked from degraded PSCs could be captured by ZrL_3. This significantly reduced lead leakage due to the formation of water-insoluble Pb^{2+}-ZrL_3 complexes by thiolated ZrL_3 capturing free Pb^{2+} ions. These results show that in PSC devices, the ETL can also serve multiple functions, improving the long-term operational stability of the device while reducing lead leakage into the environment.

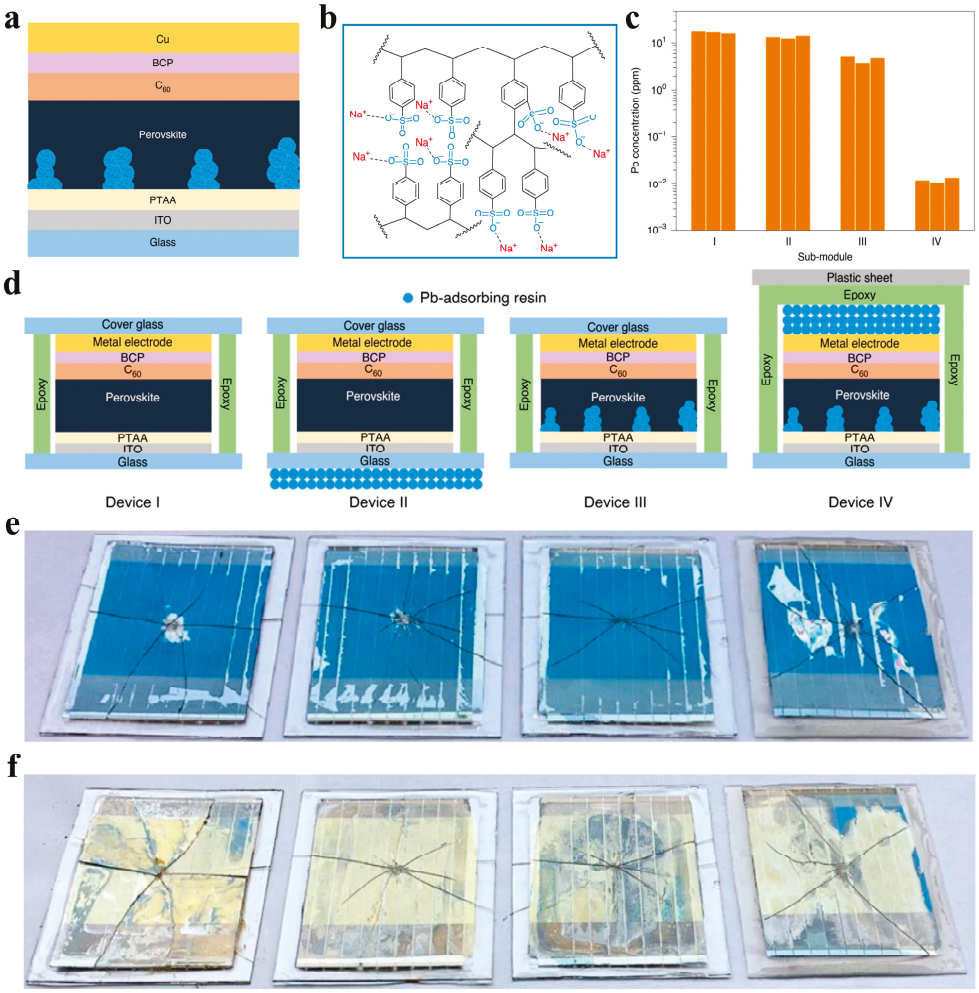

Figure 7. (**a**) The device structure of PSCs containing CERs. (**b**) The chemical structure of CERs. (**c**) Concentrations of lead in polluted water from four types of devices. (**d**) Schematic diagram of four different encapsulation devices. (**e**,**f**) PSCs after (**e**) damage and after (**f**) water-dripping tests. Reprinted with permission from Ref. [70]. Copyright 2021 Springer Nature.

Additionally, the surface of the perovskite layer can be further post-treated, such as with thiol modification, to improve its hydrophobicity and photostability. Other strategies based on surface or interface engineering have also been employed to suppress lead leakage, including superhydrophobic barrier layers, biomimetic shielding interfaces, and polymer resin protective layers [33,66,70,77]. In summary, integrating lead capture materials into the perovskite layer, using post-synthesis treatments, and incorporating these materials at charge transport interfaces are effective strategies for reducing lead leakage of PSCs. In order to alleviate end-user concerns and accelerate the commercialization and practical application of perovskite photovoltaic devices, there is a need to develop more durable, environmentally friendly, and sustainable photovoltaic devices. In this regard, the explo-

ration of optimal strategies for mitigating Pb leakage from MHPs without compromising device performance is a research direction that merits sustained attention.

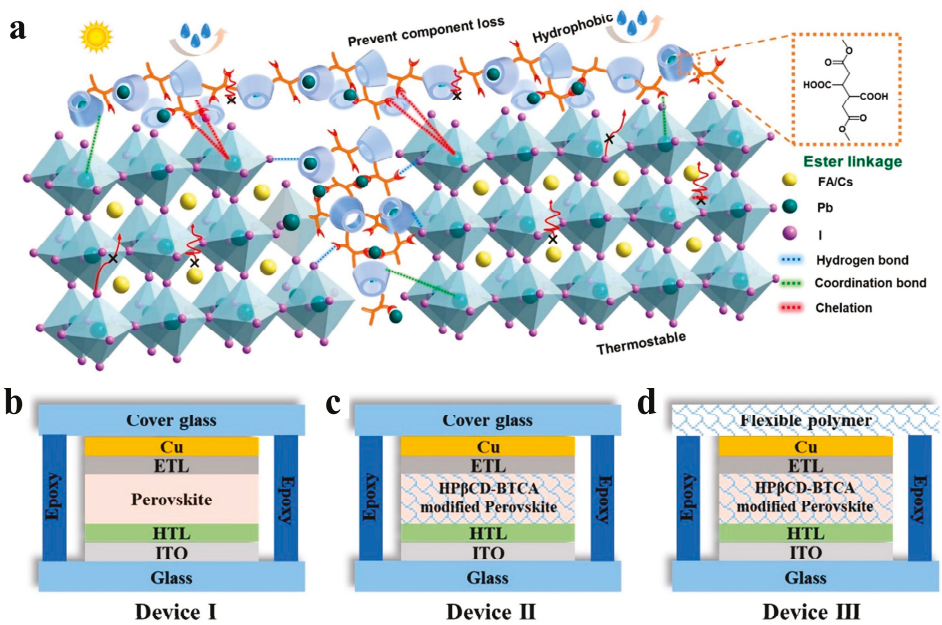

Figure 8. (**a**) Schematic illustration of chemical interactions between cross-linking HPβCD-BTCA supramolecular complex and perovskite structure. (**b**–**d**) Schematic of device configurations with different perovskite films and encapsulation modes. Reprinted with permission from Ref. [46]. Copyright 2023 Springer Nature.

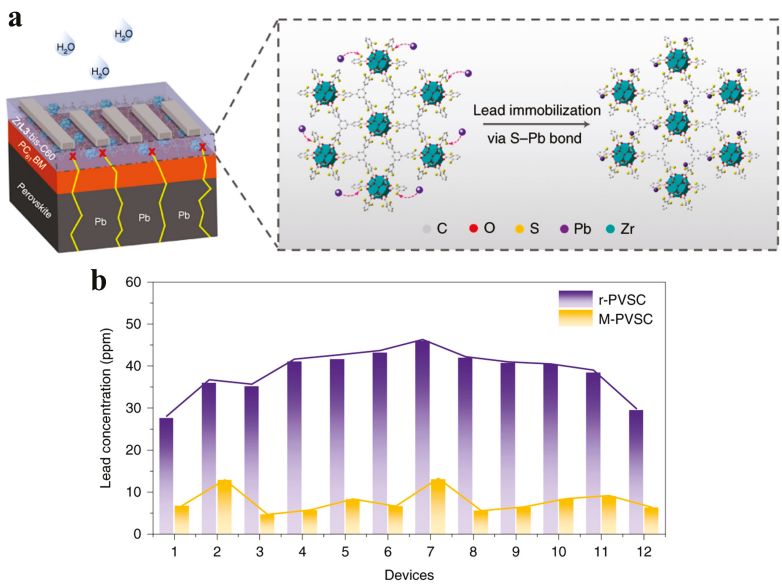

Figure 9. (**a**) Schematic illustration of the lead immobilization by the S-Pb bond between the perovskite and ZrL_3. (**b**) Test of Pb concentration in the contaminated water. Reprinted with permission from Ref. [76]. Copyright 2020 Springer Nature.

4. Sustainable Lead Recovery for Perovskite Solar Cells

Controlling lead leakage in PSCs directly mitigates lead-related health risks and environmental damage. Yet, as the perovskite photovoltaic industry expands, lead will inevitably disperse into the environment over time. Consequently, establishing robust recycling protocols throughout the lifecycle of perovskite devices becomes crucial. Developing an integrated, cost-effective, and secure approach to recover lead and other valuable mate-

rials from PSCs is essential. This recovery process significantly diminishes lead contamination risks, conserves resources, reduces manufacturing time, and decreases energy payback periods. Creating a circular economy model with closed-loop recycling represents the foundation for sustainable large-scale commercialization of perovskite photovoltaic technology.

Recent advancements have yielded multiple methodologies for the extraction and recovery of lead [33,78–81]. Park et al. first used dimethylformamide (DMF) to remove the metal electrode, charge transport layer, and dissolved perovskite (Figure 10) [82]. They employed surface negatively charged iron-modified hydroxyapatite (HAP/Fe) hollow composites, effectively reducing lead concentration to below 15 ppb. Due to the difference in water solubility between HAP/Fe and PbI_2, adding 1 M KI solution can recover PbI_2 with a recovery rate as high as 99.97%. Finally, they fabricated a device using the recovered materials and achieved a PCE of approximately 18%, comparable to that achieved with commercial PbI_2.

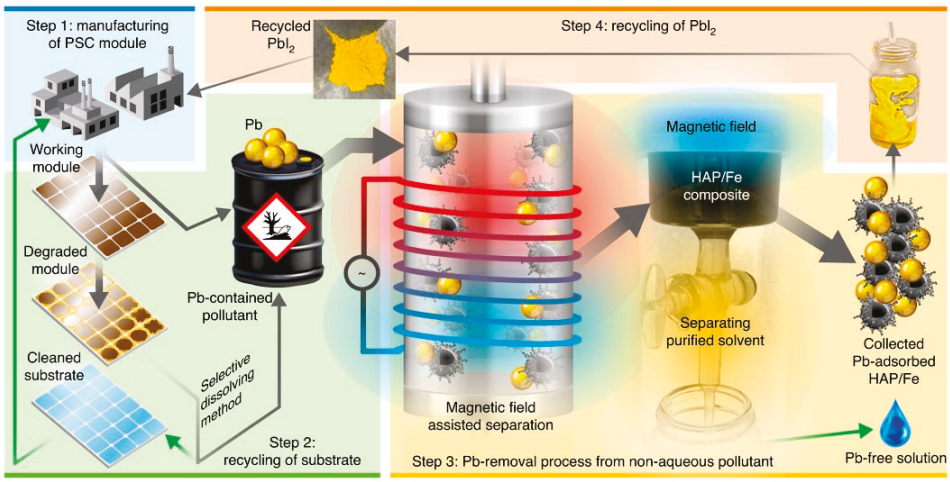

Figure 10. Schematic diagram of PSC preparation and lead-containing pollutant recycling. Reprinted with permission from Ref. [82]. Copyright 2020 Springer Nature.

Chen et al. [83] also used DMF to dissolve the perovskite layers after delaminating the encapsulated devices (Figure 11). They then absorbed lead from the dissolved material using CER and subsequently released it into a clean solvent. The PCE results of PSCs prepared with PbI_2 of different purities showed that the PCE based on recycled PbI_2 was 20.4%, slightly lower than that of commercial PbI_2 with 99.99% purity (21.0%) but higher than that of commercial PbI_2 with 99% purity (19.4%).

A plethora of alternative chemical reagents that are effective in dissolving lead-containing compounds have also been utilized to address the issue of lead recycling in PSCs. As shown in Figure 12a, butylamine (BA) was used to collect valuable materials (lead iodide, PCBM, organic amine salts, NiOx/ITO, and metal electrodes) in perovskite devices, and a series of recovery procedures were designed to recycle these materials [84]. This strategy achieved a high total Pb recovery rate of more than 98.9%, effectively completing the closed-loop of recycling and remanufacturing of the entire perovskite photovoltaic device. Deng et al. [85] screened several polar Pb solubilizers (DMF, DMSO, and BA) and selected DMF as the optimal solvent (strong solubility and weak C=O-Pb coordination) for dissolving Pb in PSCs. Then, KI was used as a multifunctional precipitant to recover high-purity PbI_2 (96.03%). The recovered PbI_2, enriched with K^+ ions, reduced defects and residual strain, enabling re-fabricated PSCs to achieve a record efficiency of 22.78%, surpassing fresh counterparts (20.76%). The process demonstrated exceptional cyclability (maintaining a high efficiency of 20.79% after four cycles), offering a sustainable

pathway to mitigate Pb pollution and reduce production costs, thus advancing scalable PSC commercialization.

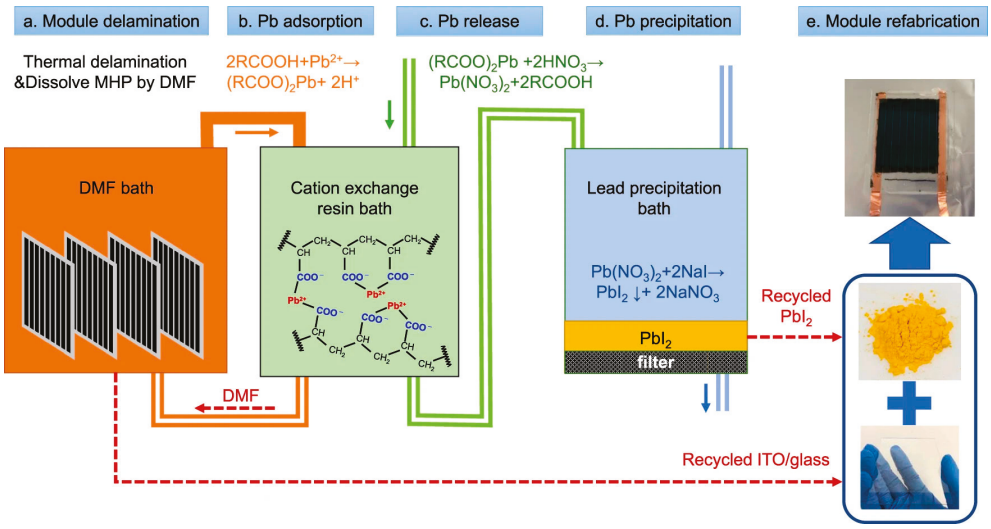

Figure 11. Roadmap for recycling perovskite solar modules. Reprinted with permission from Ref. [83]. Copyright 2021 Springer Nature.

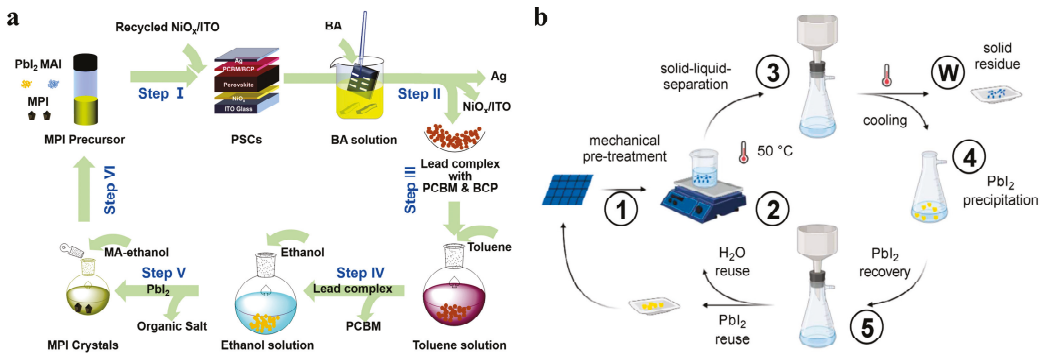

Figure 12. (**a**) Scheme of the closed-loop recycling process. Reprinted with permission from Ref. [84]. Copyright 2021 Elsevier. (**b**) Steps for recycling perovskite solar modules. Reprinted with permission from Ref. [86]. Copyright 2023 Elsevier.

Schmidt et al. demonstrated a simple PbI_2 recovery process that employing hot water as the exclusive solvent to effectively extract lead from precursor mixtures, plastic-based, and glass-based PSCs (with an efficiency of 92.6–100% after two extractions) [86]. They achieved efficient lead recovery from glass-based PSCs through a stepwise cyclic purification process. Upon cooling of the hot extractant, high-purity (>95.9%) PbI_2 crystals precipitated spontaneously from the solution: The first purification cycle recovered 94.4 ± 5.6% of lead, while a subsequent cycle added an additional 10.0 ± 5.2% recovery, making the recovery quantitative (Figure 12b). The remaining solid extraction residue is metal-free and can thus be disposed of as non-hazardous waste. This method exploits the strong temperature dependence of PbI_2 solubility in water to provide a simplified and scalable approach for recovering lead from decommissioned PSCs. By exploiting periodic temperature variations, the process effectively separates Pb species from the residue, mitigating the potential risk of lead leaching at the end of the perovskites' life cycle.

The recovery of perovskite films increases the availability of expensive materials such as transparent conductive substrates and charge transport layers, which can be reused with minimal impact on the device's photovoltaic performance and reduces the impact of lead leakage on the ecosystem. In conclusion, the recycling of Pb has the dual benefits of protecting the environment and reducing costs.

5. Conclusions and Outlook

The burgeoning field of PSCs has heralded a new era in renewable energy, promising high efficiencies and low-cost production. However, the environmental sustainability of these devices, particularly concerning lead leakage, remains a critical challenge that must be addressed to facilitate their widespread commercialization. This review has delved into the intricacies of lead toxicity within PSCs, elucidating the mechanisms of lead leakage and its profound impacts on both the environment and human health. Furthermore, it has explored a plethora of strategies aimed at mitigating lead leakage, ranging from advanced encapsulation techniques to innovative lead immobilization methods and sustainable recycling practices.

In conclusion, the journey towards environmentally safe PSCs is marked by significant advancements and ongoing research efforts. The development of robust encapsulation materials, such as self-healing polymers and ionic gels, alongside the design of sophisticated multi-layer structures, has shown promise in curbing lead leakage. Internal lead immobilization strategies, including the integration of lead-capturing materials like MOFs and the modification of perovskite layers, offer additional layers of protection. Moreover, the advent of in situ and ex situ adsorption techniques provides innovative avenues for lead management. Recycling and reutilization practices, though in their nascent stages, hold potential for creating a circular economy within the PSC industry.

Fortunately, the large-scale commercialization of cadmium telluride (CdTe) photovoltaics provides valuable experience in mitigating the environmental risks associated with heavy metals. After years of industrial optimization, CdTe photovoltaics technology has successfully developed industrial solutions to address cadmium contamination and achieved compliance with the EU RoHS Directive through exemptions. For example, the use of robust glass-to-glass encapsulation [87] has proven effective in preventing cadmium leakage. In addition, the use of closed-loop hydrometallurgical recovery ensures a high rate of cadmium recovery [88], minimizing cadmium emissions to the environment during the end-of-life phase. This recovery process not only reduces the need for new cadmium and tellurium resources but also reduces the overall environmental impact of CdTe photovoltaics devices. These effective strategies could potentially be applied to perovskite PV devices, but the differences between CdTe and perovskite devices need to be taken into account. The lead content in perovskite solar cells is typically low (0.5~1 g/m^2) compared to the high cadmium content in CdTe modules (~7 g/m^2) [88]. However, lead ions in perovskites are highly water soluble and carry a public health stigma, posing unique environmental challenges. This requires innovative encapsulation strategies and lead recovery methods. Although perovskite recycling remains at lab-scale, its solution-processable nature enables direct reuse of PbI_2 with retained device performance. Additionally, perovskite PVs benefit from inherently lower material usage and a shorter energy payback time, potentially offering a more sustainable solution if advanced encapsulation and scalable recycling methods can be successfully implemented. By combining the successful experience of CdTe PV in recycling with the unique advantages of perovskite (such as solution processability and low-energy manufacturing), it is possible to systematically minimize the environmental risks of lead halide perovskite and pave the way for its sustainable large-scale commercialization.

Looking ahead, several key areas demand focused attention. First, future research should focus on advancing encapsulation materials and techniques. Innovations in flexible and stretchable encapsulation materials are crucial, considering the potential application of perovskite devices in flexible electronics. These materials should not only provide excellent barrier properties against water and oxygen but also be mechanically robust to withstand bending, folding, and stretching without losing their integrity. Second, the development of lead-free or low-lead perovskite alternatives is imperative. Recent strides in exploring

tin-based and bismuth-based perovskites offer a glimmer of hope, though their efficiency and stability must be further optimized to match their lead-based counterparts. Third, the scalability of lead mitigation technologies is crucial. The scalability and cost-effectiveness of current recycling technologies need to be improved. Automated recycling processes that can handle large-scale production of perovskite devices should be developed.

In terms of research, interdisciplinary approaches are essential. Collaborations between materials scientists, environmental engineers, and toxicologists can lead to a more comprehensive understanding of lead leakage and its mitigation. Advanced characterization techniques and computational modeling can aid in predicting the long-term behavior of PSCs under various environmental conditions, guiding the development of more resilient materials.

Moreover, the role of policy and regulation cannot be understated. Policymakers need to play an active role in regulating the production, use, and disposal of halide perovskite-based devices. Clear guidelines and standards for lead content limits, device encapsulation requirements, and end-of-life management should be established. Incentives such as subsidies for the development and use of lead-free perovskite technologies can also promote environmentally friendly growth in the industry.

In essence, the path to environmentally safe PSCs is complex but navigable. With continued innovation, collaborative efforts, and a steadfast commitment to sustainability, the promise of perovskite solar cells as a clean, efficient, and safe renewable energy source can be realized, paving the way for a brighter, greener future.

Author Contributions: Conceptualization, W.L. and T.M.; writing—original draft preparation, W.L., T.M. and M.Y.; writing—review and editing, T.T. and H.P.; supervision, H.P. and M.Y.; funding acquisition, W.L. and T.T. All authors have read and agreed to the published version of the manuscript.

Funding: This research was funded by National Natural Science Foundation of China (52402203 and 22305215).

Institutional Review Board Statement: Not applicable.

Informed Consent Statement: Not applicable.

Data Availability Statement: No new data were created or analyzed in this study. Data sharing is not applicable to this article.

Conflicts of Interest: The authors declare no conflicts of interest.

References

1. Huang, J.; Yuan, Y.; Shao, Y.; Yan, Y. Understanding the physical properties of hybrid perovskites for photovoltaic applications. *Nat. Rev. Mater.* **2017**, *2*, 17042. [CrossRef]
2. Chen, H.; Liu, C.; Xu, J.; Maxwell, A.; Zhou, W.; Yang, Y.; Zhou, Q.; Bati, A.S.R.; Wan, H.; Wang, Z.; et al. Improved charge extraction in inverted perovskite solar cells with dual-site-binding ligands. *Science* **2024**, *384*, 189–193. [CrossRef]
3. Correa-Baena, J.-P.; Saliba, M.; Buonassisi, T.; Grätzel, M.; Abate, A.; Tress, W.; Hagfeldt, A. Promises and challenges of perovskite solar cells. *Science* **2017**, *358*, 739–744. [CrossRef]
4. Jiang, Q.; Tong, J.; Scheidt, R.A.; Wang, X.; Louks, A.E.; Xian, Y.; Tirawat, R.; Palmstrom, A.F.; Hautzinger, M.P.; Harvey, S.P.; et al. Compositional texture engineering for highly stable wide-bandgap perovskite solar cells. *Science* **2022**, *378*, 1295–1300. [CrossRef]
5. Kojima, A.; Teshima, K.; Shirai, Y.; Miyasaka, T. Organometal halide perovskites as visible-light sensitizers for photovoltaic cells. *J. Am. Chem. Soc.* **2009**, *131*, 6050–6051. [CrossRef]
6. Cao, Y.B.; Zhang, D.; Zhang, Q.; Qiu, X.; Zhou, Y.; Poddar, S.; Fu, Y.; Zhu, Y.; Liao, J.-F.; Shu, L.; et al. High-efficiency, flexible and large-area red/green/blue all-inorganic metal halide perovskite quantum wires-based light-emitting diodes. *Nat. Commun.* **2023**, *14*, 4611. [CrossRef] [PubMed]
7. Lin, K.; Xing, J.; Quan, L.N.; de Arquer, F.P.G.; Gong, X.; Lu, J.; Xie, L.; Zhao, W.; Zhang, D.; Yan, C.; et al. Perovskite light-emitting diodes with external quantum efficiency exceeding 20 per cent. *Nature* **2018**, *562*, 245–248. [CrossRef] [PubMed]

8. Liu, X.-K.; Xu, W.; Bai, S.; Jin, Y.; Wang, J.; Friend, R.H.; Gao, F. Metal halide perovskites for light-emitting diodes. *Nat. Mater.* **2021**, *20*, 10–21. [CrossRef]
9. Tang, Y.; Jin, P.; Wang, Y.; Li, D.; Chen, Y.; Ran, P.; Fan, W.; Liang, K.; Ren, H.; Xu, X.; et al. Enabling low-drift flexible perovskite photodetectors by electrical modulation for wearable health monitoring and weak light imaging. *Nat. Commun.* **2023**, *14*, 4961. [CrossRef]
10. Li, W.G.; Wang, X.D.; Huang, Y.H.; Kuang, D.B. Ultrasound-assisted crystallization enables large-area perovskite quasi-monocrystalline film for high-sensitive X-ray etection and imaging. *Adv. Mater.* **2023**, *35*, 2210878. [CrossRef]
11. Zhuang, Y.; Yuan, W.; Qian, L.; Chen, S.; Shi, G. High-performance gas sensors based on a thiocyanate ion-doped organometal halide perovskite. *Phys. Chem. Chem. Phys.* **2017**, *19*, 12876–12881. [CrossRef] [PubMed]
12. Senanayak, S.P.; Yang, B.; Thomas, T.H.; Giesbrecht, N.; Huang, W.; Gann, E.; Nair, B.; Goedel, K.; Guha, S.; Moya, X.; et al. Understanding charge transport in lead iodide perovskite thin-film field-effect transistors. *Sci. Adv.* **2017**, *3*, e1601935. [CrossRef]
13. Liu, A.; Zhu, H.; Bai, S.; Reo, Y.; Caironi, M.; Petrozza, A.; Dou, L.; Noh, Y.-Y. High-performance metal halide perovskite transistors. *Nat. Electron.* **2023**, *6*, 559–571. [CrossRef]
14. Deschler, F.; Price, M.; Pathak, S.; Klintberg, L.E.; Jarausch, D.-D.; Higler, R.; Hüttner, S.; Leijtens, T.; Stranks, S.D.; Snaith, H.J.; et al. High photoluminescence efficiency and optically umped Lalsing in solution-rocessed mixed halide perovskite semiconductors. *J. Phys. Chem. Lett.* **2014**, *5*, 1421–1426. [CrossRef]
15. Wu, W.Q.; Rudd, P.N.; Wang, Q.; Yang, Z.; Huang, J. Blading phase-ure formamidinium-alloyed perovskites for high-efficiency solar cells with low photovoltage deficit and improved stability. *Adv. Mater.* **2020**, *32*, 2000995. [CrossRef]
16. Wang, Z.; Zeng, L.; Zhu, T.; Chen, H.; Chen, B.; Kubicki, D.J.; Balvanz, A.; Li, C.; Maxwell, A.; Ugur, E.; et al. Suppressed phase segregation for triple-junction perovskite solar cells. *Nature* **2023**, *618*, 74–79. [CrossRef]
17. Cheng, R.; Liang, Z.B.; Zhu, L.; Li, H.; Zhang, Y.; Wang, C.F.; Chen, S. Fibrous nanoreactors frommicrofluidic blow spinning for mass production of highly stable ligand-free perovskite quantum dots. *Angew. Chem. Int. Ed.* **2022**, *61*, e202204371. [CrossRef]
18. Jeong, M.; Choi, I.W.; Go, E.M.; Cho, Y.; Kim, M.; Lee, B.; Jeong, S.; Jo, Y.; Choi, H.W.; Lee, J.; et al. Stable perovskite solar cells with efficiency exceeding 24.8% and 0.3 V voltage loss. *Science* **2020**, *369*, 1615–1620. [CrossRef] [PubMed]
19. Yang, W.S.; Park, B.-W.; Jung, E.H.; Jeon, N.J.; Kim, Y.C.; Lee, D.U.; Shin, S.S.; Seo, J.; Kim, E.K.; Noh, J.H.; et al. Iodide management in formamidinium-lead-halide–based perovskite layers for efficient solar cells. *Science* **2017**, *356*, 1376–1379. [CrossRef]
20. Wu, T.; Liu, X.; Luo, X.; Lin, X.; Cui, D.; Wang, Y.; Segawa, H.; Zhang, Y.; Han, L. Lead-free tin perovskite solar cells. *Joule* **2021**, *5*, 863–886. [CrossRef]
21. Wang, M.; Wang, W.; Ma, B.; Shen, W.; Liu, L.; Cao, K.; Chen, S.; Huang, W. Lead-free perovskite materials for solar cells. *Nano-Micro Lett.* **2021**, *13*, 62. [CrossRef] [PubMed]
22. Kim, J.Y.; Lee, J.-W.; Jung, H.S.; Shin, H.; Park, N.-G. High-efficiency perovskite solar cells. *Chem. Rev.* **2020**, *120*, 7867–7918. [CrossRef]
23. Awais, M.; Kirsch, R.L.; Yeddu, V.; Saidaminov, M.I. Tin halide perovskites going forward: Frost diagrams offer hints. *ACS Mater. Lett.* **2021**, *3*, 299–307. [CrossRef]
24. Babayigit, A.; Duy Thanh, D.; Ethirajan, A.; Manca, J.; Muller, M.; Boyen, H.-G.; Conings, B. Assessing the toxicity of Pb- and Sn-based perovskite solar cells in model organism Danio rerio. *Sci. Rep.* **2016**, *6*, 18721. [CrossRef] [PubMed]
25. Krishnamoorthy, T.; Ding, H.; Yan, C.; Leong, W.L.; Baikie, T.; Zhang, Z.; Sherburne, M.; Li, S.; Asta, M.; Mathews, N.; et al. Lead-free germanium iodide perovskite materials for photovoltaic applications. *J. Mater. Chem. A* **2015**, *3*, 23829–23832. [CrossRef]
26. Li, W.G.; Wang, X.D.; Liao, J.F.; Jiang, Y.; Kuang, D.B. Enhanced on-off ratio photodetectors based on lead-free $Cs_3Bi_2I_9$ single crystal thin films. *Adv. Funct. Mater.* **2020**, *30*, 1909701. [CrossRef]
27. Wu, X.; Zhang, D.; Wang, X.; Jiang, X.; Liu, B.; Li, B.; Li, Z.; Gao, D.; Zhang, C.; Wang, Y.; et al. Eco-friendly perovskite solar cells: From materials design to device processing and recycling. *EcoMat* **2023**, *5*, e12352. [CrossRef]
28. Zhang, Z.; Sun, Q.; Lu, Y.; Lu, F.; Mu, X.; Wei, S.-H.; Sui, M. Hydrogenated $Cs_2AgBiBr_6$ for significantly improved efficiency of lead-free inorganic double perovskite solar cell. *Nat. Commun.* **2022**, *13*, 3397. [CrossRef]
29. Jin, Z.; Zhang, Z.; Xiu, J.; Song, H.; Gatti, T.; He, Z. A critical review on bismuth and antimony halide based perovskites and their derivatives for photovoltaic applications: Recent advances and challenges. *J. Mater. Chem. A* **2020**, *8*, 16166–16188. [CrossRef]
30. Ning, W.; Gao, F. Structural and functional diversity in llead-free halide perovskite materials. *Adv. Mater.* **2019**, *31*, 1900326. [CrossRef]
31. Ke, W.; Kanatzidis, M.G. Prospects for low-toxicity lead-free perovskite solar cells. *Nat. Commun.* **2019**, *10*, 965. [CrossRef] [PubMed]
32. Giustino, F.; Snaith, H.J. Toward lead-ree perovskite solar cells. *ACS Energy Lett.* **2016**, *1*, 1233–1240. [CrossRef]
33. Ravi, V.K.; Mondal, B.; Nawale, V.V.; Nag, A. *Don't let the lead out*: New aterial Chemicstry approaches for sustainable lead halide perovskite solar cells. *ACS Omega* **2020**, *5*, 29631–29641. [CrossRef]
34. Babayigit, A.; Ethirajan, A.; Muller, M.; Conings, B. Toxicity of organometal halide perovskite solar cells. *Nat. Mater.* **2016**, *15*, 247–251. [CrossRef] [PubMed]

35. Chen, Z.; Huo, X.; Chen, G.; Luo, X.; Xu, X. Lead (Pb) exposure and heart failure risk. *Environ. Sci. Pollut. Res.* **2021**, *28*, 28833–28847. [CrossRef]
36. Landrigan, P.J.; Boffetta, P.; Apostoli, P. The reproductive toxicity and carcinogenicity of lead: A critical review. *Am. J. Ind. Med.* **2000**, *38*, 231–243. [CrossRef]
37. Wang, Z.-K.; Zhou, X.-L.; Song, X.-B.; Zhuang, D.-M.; Wang, Z.-Y.; Yang, D.-B.; Wang, L. Alleviation of lead-induced apoptosis by puerarin via inhibiting mitochondrial permeability ransitionpore opening in primary cultures of rat proximal tubular cells. *Biol. Trace Elem. Res.* **2016**, *174*, 166–176. [CrossRef] [PubMed]
38. Li, J.; Cao, H.-L.; Jiao, W.-B.; Wang, Q.; Wei, M.; Cantone, I.; Lü, J.; Abate, A. Biological impact of lead from halide perovskites reveals the risk of introducing a safe threshold. *Nat. Commun.* **2020**, *11*, 310. [CrossRef]
39. Luo, T.; Shen, M.; Zhou, J.; Wang, X.; Xia, J.; Fu, Z.; Jin, Y. Chronic exposure to low doses of Pb induces hepatotoxicity at the physiological, biochemical, and transcriptomic levels of mice. *Environ. Toxicol.* **2019**, *34*, 521–529. [CrossRef]
40. Czubowicz, K.; Jęśko, H.; Wencel, P.; Lukiw, W.J.; Strosznajder, R.P. The role of ceramide and sphingosine-1-phosphate in alzheimer's disease and other neurodegenerative disorders. *Mol. Neurobiol.* **2019**, *56*, 5436–5455. [CrossRef]
41. Mabrouk, A. Thymoquinone attenuates lead-induced nephropathy in rats. *J. Biochem. Mol. Toxicol.* **2019**, *33*, e22238. [CrossRef] [PubMed]
42. Zeng, X.; Zeng, Z.; Wang, Q.; Liang, W.; Guo, Y.; Huo, X. Alterations of the gut microbiota and metabolomics in children with e-waste lead exposure. *J. Hazard. Mater.* **2022**, *434*, 128842. [CrossRef]
43. Togao, M.; Nakayama, S.M.M.; Ikenaka, Y.; Mizukawa, H.; Makino, Y.; Kubota, A.; Matsukawa, T.; Yokoyama, K.; Hirata, T.; Ishizuka, M. Bioimaging of Pb and STIM1 in mice liver, kidney and brain using Laser Ablation Inductively Coupled Plasma Mass Spectrometry (LA-ICP-MS) and immunohistochemistry. *Chemosphere* **2020**, *238*, 124581. [CrossRef] [PubMed]
44. Lukačínová, A.; Rácz, O.; Lovásová, E.; Ništiar, F. Effect of lifetime low dose exposure to heavy metals on selected serum proteins of Wistar rats during three subsequent generations. *Ecotoxicol. Environ. Saf.* **2011**, *74*, 1747–1755. [CrossRef] [PubMed]
45. Li, X.; Zhang, F.; He, H.; Berry, J.J.; Zhu, K.; Xu, T. On-device lead sequestration for perovskite solar cells. *Nature* **2020**, *578*, 555–558. [CrossRef]
46. Yang, M.; Tian, T.; Fang, Y.; Li, W.-G.; Liu, G.; Feng, W.; Xu, M.; Wu, W.-Q. Reducing lead toxicity of perovskite solar cells with a built-in supramolecular complex. *Nat. Sustain.* **2023**, *6*, 1455–1464. [CrossRef]
47. Wu, P.; Wang, S.; Li, X.; Zhang, F. Beyond efficiency fever: Preventing lead leakage for perovskite solar cells. *Matter* **2022**, *5*, 1137–1161. [CrossRef]
48. Abate, A. Perovskite solar cells go lead free. *Joule* **2017**, *1*, 659–664. [CrossRef]
49. Chen, S.; Wu, C.; Han, B.; Liu, Z.; Mi, Z.; Hao, W.; Zhao, J.; Wang, X.; Zhang, Q.; Liu, K.; et al. Atomic-scale imaging of $CH_3NH_3PbI_3$ structure and its decomposition pathway. *Nat. Commun.* **2021**, *12*, 5516. [CrossRef]
50. Chen, S.; Zhang, X.; Zhao, J.; Zhang, Y.; Kong, G.; Li, Q.; Li, N.; Yu, Y.; Xu, N.; Zhang, J.; et al. Atomic scale insights into structure instability and decomposition pathway of methylammonium lead iodide perovskite. *Nat. Commun.* **2018**, *9*, 4807. [CrossRef]
51. Kundu, S.; Kelly, T.L. In situ studies of the degradation mechanisms of perovskite solar cells. *EcoMat* **2020**, *2*, e12025. [CrossRef]
52. Kadro, J.M.; Hagfeldt, A. The end-of-life of perovskite PV. *Joule* **2017**, *1*, 29–46. [CrossRef]
53. Ho, K.; Wei, M.; Sargent, E.H.; Walker, G.C. Grain transformation and degradation mechanism of formamidinium and cesium lead iodide perovskite under humidity and light. *ACS Energy Lett.* **2021**, *6*, 934–940. [CrossRef]
54. Cheacharoen, R.; Boyd, C.C.; Burkhard, G.F.; Leijtens, T.; Raiford, J.A.; Bush, K.A.; Bent, S.F.; McGehee, M.D. Encapsulating perovskite solar cells to withstand damp heat and thermal cycling. *Sustain. Energy Fuels* **2018**, *2*, 2398–2406. [CrossRef]
55. Huang, Z.; Hu, X.; Liu, C.; Meng, X.; Huang, Z.; Yang, J.; Duan, X.; Long, J.; Zhao, Z.; Tan, L.; et al. Water-resistant and flexible perovskite solar cells via a glued interfacial layer. *Adv. Funct. Mater.* **2019**, *29*, 1902629. [CrossRef]
56. Fu, Z.; Xu, M.; Sheng, Y.; Yan, Z.; Meng, J.; Tong, C.; Li, D.; Wan, Z.; Ming, Y.; Mei, A.; et al. Encapsulation of printable mesoscopic perovskite solar cells enables high emperature and long-term outdoor stability. *Adv. Funct. Mater.* **2019**, *29*, 1809129. [CrossRef]
57. Li, J.; Xia, R.; Qi, W.; Zhou, X.; Cheng, J.; Chen, Y.; Hou, G.; Ding, Y.; Li, Y.; Zhao, Y.; et al. Encapsulation of perovskite solar cells for enhanced stability: Structures, materials and characterization. *J. Power Sources* **2021**, *485*, 229313. [CrossRef]
58. Kim, H.-C.; Jang, T.-W.; Chae, H.-J.; Choi, W.-J.; Ha, M.-N.; Ye, B.-J.; Kim, B.-G.; Jeon, M.-J.; Kim, S.-Y.; Hong, Y.-S. Evaluation and management of lead exposure. *Ann. Occup. Environ. Med.* **2015**, *27*, 30. [CrossRef] [PubMed]
59. Luo, H.; Li, P.; Ma, J.; Han, L.; Zhang, Y.; Song, Y. Sustainable Pb management in perovskite solar cells toward eco-friendly development. *Adv. Energy Mater.* **2022**, *12*, 2201242. [CrossRef]
60. Yin, J.; Cui, J.; Zhou, H.; Cui, S.; Wang, C.; Guo, J.; Wei, J.; Zhang, X. Encapsulation of UV glue, hydrophobicity of binder and carbon electrode enhance the stability of organic-inorganic hybrid perovskite solar cells up to 5 years. *Energy Technol.* **2020**, *8*, 2000513. [CrossRef]
61. Wan, J.; Yu, X.; Zou, J.; Li, K.; Chen, L.; Peng, Y.; Cheng, Y.-b. Lead contamination analysis of perovskite modules under simulated working conditions. *Sol. Energy* **2021**, *226*, 85–91. [CrossRef]

62. Hailegnaw, B.; Kirmayer, S.; Edri, E.; Hodes, G.; Cahen, D. Rain on methylammonium lead iodide based perovskites: Possible environmental effects of perovskite solar cells. *J. Phys. Chem. Lett.* **2015**, *6*, 1543–1547. [CrossRef] [PubMed]
63. Wang, T.; Yang, J.; Cao, Q.; Pu, X.; Li, Y.; Chen, H.; Zhao, J.; Zhang, Y.; Chen, X.; Li, X. Room temperature nondestructive encapsulation via self-crosslinked fluorosilicone polymer enables damp heat-stable sustainable perovskite solar cells. *Nat. Commun.* **2023**, *14*, 1342. [CrossRef] [PubMed]
64. Mariani, P.; Molina-García, M.Á.; Barichello, J.; Zappia, M.I.; Magliano, E.; Castriotta, L.A.; Gabatel, L.; Thorat, S.B.; Del Rio Castillo, A.E.; Drago, F.; et al. Low-temperature strain-free encapsulation for perovskite solar cells and modules passing multifaceted accelerated ageing tests. *Nat. Commun.* **2024**, *15*, 4552. [CrossRef]
65. *IEC 61215-1*; Terrestrial Photovoltaic (PV) Modules—Design Qualification and Type Approval—Part 1: Test Requirements. IEC: Geneva, Switzerland, 2021.
66. Jiang, Y.; Qiu, L.; Juarez-Perez, E.J.; Ono, L.K.; Hu, Z.; Liu, Z.; Wu, Z.; Meng, L.; Wang, Q.; Qi, Y. Reduction of lead leakage from damaged lead halide perovskite solar modules using self-healing polymer-based encapsulation. *Nat. Energy* **2019**, *4*, 585–593. [CrossRef]
67. Ottersböck, B.; Oreski, G.; Pinter, G. Comparison of different microclimate effects on the aging behavior of encapsulation materials used in photovoltaic modules. *Polym. Degrad. Stab.* **2017**, *138*, 182–191. [CrossRef]
68. Meng, X.; Hu, X.; Zhang, Y.; Huang, Z.; Xing, Z.; Gong, C.; Rao, L.; Wang, H.; Wang, F.; Hu, T.; et al. A biomimetic self-shield interface for flexible perovskite solar cells with egligible Lead Lleakage. *Adv. Funct. Mater.* **2021**, *31*, 2106460. [CrossRef]
69. Chen, S.; Deng, Y.; Gu, H.; Xu, S.; Wang, S.; Yu, Z.; Blum, V.; Huang, J. Trapping lead in perovskite solar modules with abundant and low-cost cation-exchange resins. *Nat. Energy* **2020**, *5*, 1003–1011. [CrossRef]
70. Chen, S.; Deng, Y.; Xiao, X.; Xu, S.; Rudd, P.N.; Huang, J. Preventing lead leakage with built-in resin layers for sustainable perovskite solar cells. *Nat. Sustain.* **2021**, *4*, 636–643. [CrossRef]
71. Cho, S.-P.; Lee, H.-J.; Seo, Y.-H.; Na, S.-I. Multifunctional passivation agents for improving efficiency and stability of perovskite solar cells: Synergy of methyl and carbonyl groups. *Appl. Surf. Sci.* **2022**, *575*, 151740. [CrossRef]
72. Li, X.; Zhang, F.; Wang, J.; Tong, J.; Xu, T.; Zhu, K. On-device lead-absorbing tapes for sustainable perovskite solar cells. *Nat. Sustain.* **2021**, *4*, 1038–1041. [CrossRef]
73. Xiao, X.; Wang, M.; Chen, S.; Zhang, Y.; Gu, H.; Deng, Y.; Yang, G.; Fei, C.; Chen, B.; Lin, Y.; et al. Lead-adsorbing ionogel-based encapsulation for impact-resistant, stable, and lead-safe perovskite modules. *Sci. Adv.* **2021**, *7*, eabi8249. [CrossRef] [PubMed]
74. Li, Z.; Wu, X.; Li, B.; Zhang, S.; Gao, D.; Liu, Y.; Li, X.; Zhang, N.; Hu, X.; Zhi, C.; et al. Sulfonated graphene aerogels enable safe-to-use flexible perovskite olar Mmodules. *Adv. Energy Mater.* **2021**, *12*, 2103236. [CrossRef]
75. Valastro, S.; Smecca, E.; Mannino, G.; Bongiorno, C.; Fisicaro, G.; Goedecker, S.; Arena, V.; Spampinato, C.; Deretzis, I.; Dattilo, S.; et al. Preventing lead leakage in perovskite solar cells with a sustainable titanium dioxide sponge. *Nat. Sustain.* **2023**, *6*, 974–983. [CrossRef]
76. Wu, S.; Li, Z.; Li, M.-Q.; Diao, Y.; Lin, F.; Liu, T.; Zhang, J.; Tieu, P.; Gao, W.; Qi, F.; et al. 2D metal-organic framework for stable perovskite solar cells with minimized lead leakage. *Nat. Nanotechnol.* **2020**, *15*, 934–940. [CrossRef]
77. Zhang, H.; Li, K.; Sun, M.; Wang, F.; Wang, H.; Jen, A.K.Y. Design of superhydrophobic surfaces for table perovskite solar cells with reducing lead leakage. *Adv. Energy Mater.* **2021**, *11*, 2102281. [CrossRef]
78. Binek, A.; Petrus, M.L.; Huber, N.; Bristow, H.; Hu, Y.; Bein, T.; Docampo, P. Recycling perovskite solar cells to void lead waste. *ACS Appl. Mater. Interfaces* **2016**, *8*, 12881–12886. [CrossRef] [PubMed]
79. Poll, C.G.; Nelson, G.W.; Pickup, D.M.; Chadwick, A.V.; Riley, D.J.; Payne, D.J. Electrochemical recycling of lead from hybrid organic–inorganic perovskites using deep eutectic solvents. *Green Chem.* **2016**, *18*, 2946–2955. [CrossRef]
80. Xu, J.; Hu, Z.; Huang, L.; Huang, X.; Jia, X.; Zhang, J.; Zhang, J.; Zhu, Y. In situ recycle of PbI_2 as a step towards sustainable perovskite solar cells. *Prog. Photovolt. Res. Appl.* **2017**, *25*, 1022–1033. [CrossRef]
81. Zhang, S.; Shen, L.; Huang, M.; Yu, Y.; Lei, L.; Shao, J.; Zhao, Q.; Wu, Z.; Wang, J.; Yang, S. Cyclic tilization of lead in carbon-based perovskite solar cells. *ACS Sustain. Chem. Eng.* **2018**, *6*, 7558–7564. [CrossRef]
82. Park, S.Y.; Park, J.-S.; Kim, B.J.; Lee, H.; Walsh, A.; Zhu, K.; Kim, D.H.; Jung, H.S. Sustainable lead management in halide perovskite solar cells. *Nat. Sustain.* **2020**, *3*, 1044–1051. [CrossRef]
83. Chen, B.; Fei, C.; Chen, S.; Gu, H.; Xiao, X.; Huang, J. Recycling lead and transparent conductors from perovskite solar modules. *Nat. Commun.* **2021**, *12*, 5859. [CrossRef] [PubMed]
84. Feng, X.; Guo, Q.; Xiu, J.; Ying, Z.; Ng, K.W.; Huang, L.; Wang, S.; Pan, H.; Tang, Z.; He, Z. Close-loop recycling of perovskite solar cells through dissolution-recrystallization of perovskite by butylamine. *Cell Rep. Phys. Sci.* **2021**, *2*, 100341. [CrossRef]
85. Deng, F.; Song, X.; Li, Y.; Zhang, W.; Tao, X. Facile eco-friendly process for upcycled sustainable perovskite solar cells. *Chem. Eng. J.* **2024**, *489*, 151228. [CrossRef]
86. Schmidt, F.; Amrein, M.; Hedwig, S.; Kober-Czerny, M.; Paracchino, A.; Holappa, V.; Suhonen, R.; Schäffer, A.; Constable, E.C.; Snaith, H.J.; et al. Organic solvent free PbI_2 recycling from perovskite solar cells using hot water. *J. Hazard. Mater.* **2023**, *447*, 130829. [CrossRef]

87. Fthenakis, V.M. Life cycle impact analysis of cadmium in CdTe PV production. *Renew. Sustain. Energy Rev.* **2004**, *8*, 303–334. [CrossRef]
88. Vellini, M.; Gambini, M.; Prattella, V. Environmental impacts of PV technology throughout the life cycle: Importance of the end-of-life management for Si-panels and CdTe-panels. *Energy* **2017**, *138*, 1099–1111. [CrossRef]

Disclaimer/Publisher's Note: The statements, opinions and data contained in all publications are solely those of the individual author(s) and contributor(s) and not of MDPI and/or the editor(s). MDPI and/or the editor(s) disclaim responsibility for any injury to people or property resulting from any ideas, methods, instructions or products referred to in the content.

MDPI AG
Grosspeteranlage 5
4052 Basel
Switzerland
Tel.: +41 61 683 77 34

Inorganics Editorial Office
E-mail: inorganics@mdpi.com
www.mdpi.com/journal/inorganics

Disclaimer/Publisher's Note: The title and front matter of this reprint are at the discretion of the Guest Editor. The publisher is not responsible for their content or any associated concerns. The statements, opinions and data contained in all individual articles are solely those of the individual Editor and contributors and not of MDPI. MDPI disclaims responsibility for any injury to people or property resulting from any ideas, methods, instructions or products referred to in the content.

Academic Open
Access Publishing

mdpi.com

ISBN 978-3-7258-8634-0